Advances in Materials Science and Engineering

Fabrication and Machinability of Alloys and Composites

Lead Guest Editor: R. Thanigaivelan
Guest Editors: S. Ramesh and Tadeusz Mikolajczyk

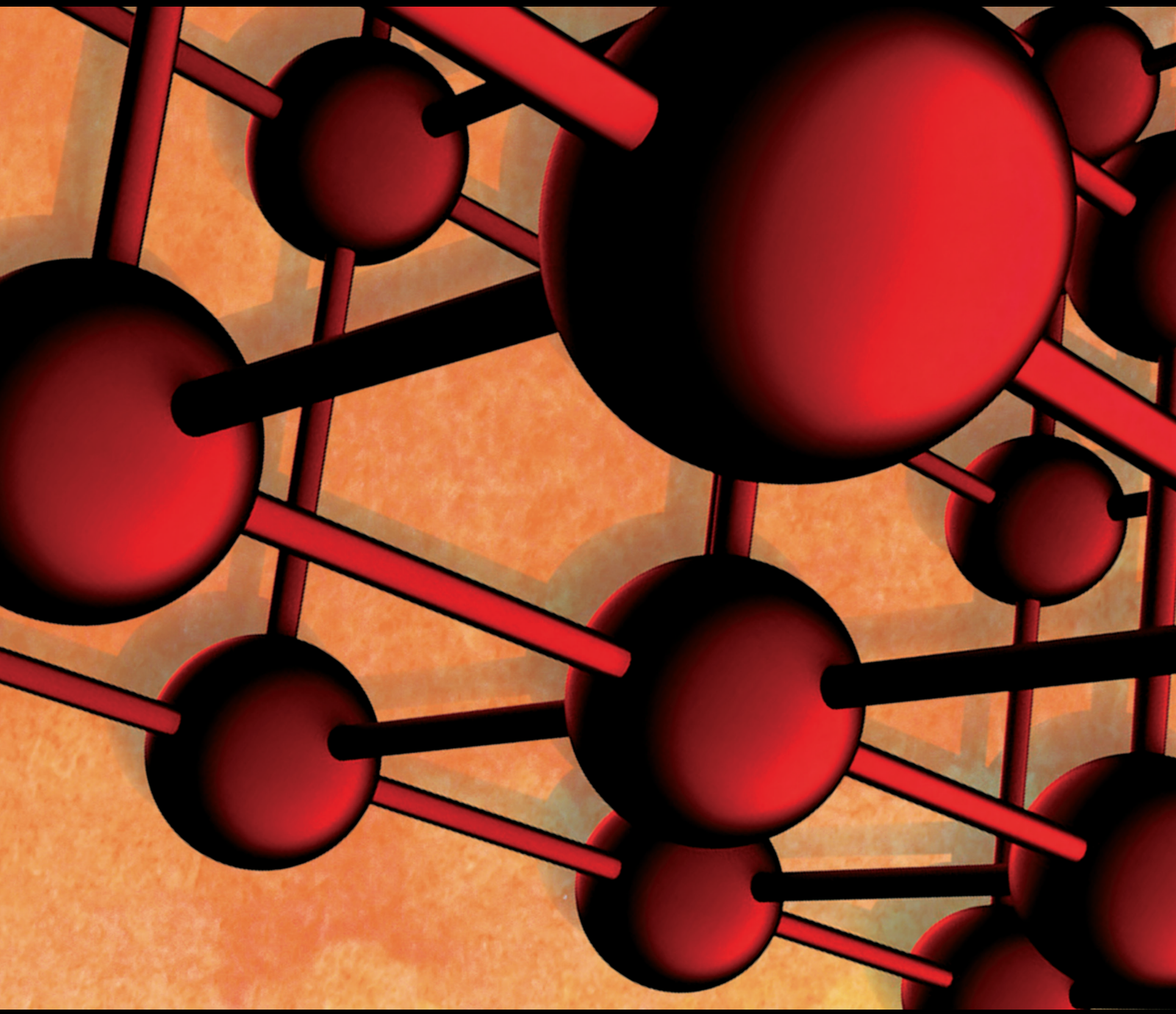

Fabrication and Machinability of Alloys and Composites

Advances in Materials Science and Engineering

Fabrication and Machinability of Alloys and Composites

Lead Guest Editor: R. Thanigaivelan
Guest Editors: S. Ramesh and Tadeusz Mikolajczyk

Contents

Contents

Hindawi
Advances in Materials Science and Engineering
Volume 2023, Article ID 8933844, 8 pages
https://doi.org/10.1155/2023/8933844

Research Article

Estimation of Impact Strength of Kevlar/Basalt and Kevlar/Glass Interwoven Composite Laminate after High-Velocity Bullet Impact

J. Jensin Joshua,[1] **Dalbir Singh**,[1] **Y. Murali Krishna**,[1] **P. Sivaprakasam**,[2] **D. Raja Joseph**,[1] **and P. S. Venkatanarayanan**[1]

[1]*School of Aeronautical Sciences, Hindustan Institute of Technology & Science, Chennai, India*
[2]*Department of Mechanical Engineering, College of Electrical and Mechanical Engineering, Center of Excellence-Nanotechnology, Addis Ababa Science and Technology University, Addis Ababa, Ethiopia*

Correspondence should be addressed to P. Sivaprakasam; shiva@aastu.edu.et

Received 25 June 2022; Revised 1 November 2022; Accepted 25 November 2022; Published 20 November 2023

Academic Editor: R. Thanigaivelan

The application of composite materials has increased so drastically in the aerospace industry. The Impact strength signifies the importance of composite materials when exposed to suddenly applied loads. This paper is focused on describing the behavior of interwoven kevlar/glass-epoxy and kevlar/basalt-epoxy composite laminate under high-velocity bullet impact. The composite lamina of kevlar/glass and that of kevlar/basalt are prepared using three different weaving techniques. The composite laminates are prepared using the compression moulding technique. The laminates have been subjected to high-velocity bullet impact. The velocity range is from 220 m/s to 260 m/s. The impact damage area in the laminate has been assessed through ultrasonic pulse echo submerged nondestructive technique. The impact strength has been calculated using the damaged area derived using the impact energy absorbed by the laminate. The results have shown that the maximum impact which found out to be kevlar/basalt (KB 1×1) is 28.24 J/cm^2.

1. Introduction

The high-velocity impact study has been a major contribution to the aerospace industry ever since Apollo 11 touched down on the moon in the 1960s [1], and the progress has not stopped there. In the aviation sector, the components such as empennage leading edges, windshields, and the intake of engines Nacelles are subjected to high-speed impact loadings; also it was considered that almost 77% of the accidents are caused due to the impact in windshields [2, 3]. In the space sector, the average velocity of debris is 7.5 km/s, and it varies from 0.5 to 16 km/s, which the satellites are supposed to withstand its impact [4, 5]. The military vehicles use organic composites such as kevlar and spectra which absorb energy by deformation of the fiber itself, the same technology is used in formula (1) cars [6]. Kevlar has got its high strength from its interchain bonds and even it is resilient at such low temperatures as −196°C; thus, it has got a wide range of applications in the industry [7].

The kevlar is used in the ballistic application due to its special characteristics such as heat resistance and impact strength. Basalt consists of materials such as olivine, pyroxene, and minerals plagioclase. It has better properties than other fiber materials and the specific strength is three times stronger than that of steel. Shaari and Jumahat, in their work, explained that the addition of kevlar fiber to the glass fiber increases the load-carrying capacity and its resistance to deformation [8]. Velumayil and Palanivel [9] have shown through their experiment that sandwiching kevlar fiber with basalt could yield a maximum impact energy absorption of 8.3 J. Tirillo et al. [10] in their paper carried out ballistic impact on basalt-cabon/epoxy hybrid composite laminate. It is observed from the study that hybridization of basalt has improved the ballistic

limit. Aghamohammadi et al. [11] in their paper fabricated a metal hybrid composite laminate with basalt fiber and aluminium 2024 T3. MWCNT was also added in different percentages to study the flexural and high-velocity impact properties. From the study, it was found out that there was an increase in the flexural property alone. The impact property did not have an immense effect. It has been mentioned that the hybridization of high-strength and high-stiffness fibers would yield better characteristics [12–14]. Hybridization of composites can enhance the mechanical and wear properties of the composites [15]. In thermoset and thermoplastics polymers, glass fiber is used as a reinforcing agent because of its high dimensional stability, high tensile strength, chemical resistance, and low cost with good insulating properties, whereas basalt fiber have good chemical resistance, thermal stability (can also be used in wide range temperature of −200°C to 600°C), mechanical stress, string, and durable. It is obtained naturally as mineral fiber and has impressive performance for advantageous price [16]. When comparing the fibers basalt to glass the chemical stability of basalt fiber in acidic environment is better than glass fiber [17], in the mechanical point of view the elastic modulus of basalt fiber strongly depends on chemical composition but the tensile strength and elongation at break are slightly higher when compared to glass fiber [18].

Also, from the experimental work it is evident that increasing the kevlar content could increase the energy absorption of the material [19]. In glass fiber, the weaving angle between 20° and 30° are observed to be absorbing more energy than that of weaving angle of 60°, 70°, 80°, and 90° [20]. Under the nominal temperature, the tensile strength of basalt fiber is greater than that of glass with 2850 MPa and 2450 MPa, respectively, considering it has a better alternative for glass [21]. At high temperatures of 700°C, the strength of basalt has reduced to 50%, whereas the glass has completely lost its strength characteristics. Due to its increase in load with thermal resistance, basalt fiber has been used in carrying the Space Shuttle [22]. Li et al. [23] have expressed in their experiment that the basalt retains its strength even at the lowest temperature of −96°C. Fu et al., [24] has concluded in his investigation that for the sharp projectile, the woven basalt fiber composites (WBFCs) possess very good low velocity impact resistance than that of unidirectional basalt fiber composites (UBFC) also WBFC has better stiffness than UBFC. It is evident that the damage tolerance and the resistance of a material can be increased by 3D stitching the material. It has also been shown that 3D stitching could increase the impact resistance of the material by up to 20% [25].

To improve the strength of the composite laminate either the composite laminate can be prepared by hybridization or by the addition of the nanoparticles [26]. Enough research in weaving of kevlar with basalt and glass for high-velocity impact studies is not available. So, in the current study, a composite laminate is prepared by weaving (hybridization) the fibers of kevlar-basalt [KB] and kevlar-glass [KG] with epoxy being resin in both cases. Hand loom technique is followed to weave the fibers of basalt and glass with kevlar. The novelty in the current study involves weaving of fibers in three different types and carrying out high-velocity bullet impact on it.

2. Methodology

2.1. Weaving & Preparing Composite Laminate. Weaving in the composite is a process of interlacing warp (fibers in longitudinal direction) and weft (fibers in lateral direction) in a sequence to form a fiber mat. In this research work, weaving is performed in three different types.

2.1.1. Type 01. In type 01, two different kinds of laminas are prepared. One with kevlar/basalt and one with kevlar/glass fibers. Here, every single fiber of basalt [warp] is woven with single fiber of kevlar [weft] and "kb 1 × 1" lamina is prepared [plain weave]. Similarly, every single fiber of glass fiber is interlaced with single fiber of Kevlar and "kg 1 × 1" lamina is prepared.

2.1.2. Type 02. In type 02, two different kinds of laminas are prepared. One with kevlar/basalt and one with kevlar/glass fibers. Here, three fibers of basalt is woven after every three fibers of kevlar and "kb 3 × 3" lamina is prepared. Similarly, every three fibers of glass is interlaced after every three fibers of kevlar and "kg 3 × 3" lamina is prepared.

2.1.3. Type 03. In type 03, two different kinds of laminas are prepared. One with kevlar basalt and one with kevlar glass fibers. Here, five fibers of basalt are woven after every five fibers of kevlar and "kb 5 × 5" lamina are prepared. Similarly five fibers of glass are interlaced after every five fibers of kevlar and "kg 5 × 5" lamina are prepared.

As a result, six different lamina are prepared [kb 1 × 1, kb 3 × 3, kb 5 × 5, kg 1x, kg 3x, and kg 5 × 5]. Then five layers of "kb 1 × 1" lamina with 300 × 300 mm dimension are staked one over the other and "KB 1 × 1" laminate is prepared, epoxy being the resin. Similarly five composite laminates [KB 3 × 3, KB 5 × 5, KG 1 × 1, KG 3 × 3, and KG 5 × 5] are prepared using the compression moulding method with (300 × 300) mm dimension. Then the laminate is cut into 150 mm × 150 mm dimensions using a vertical band saw cutter to fit in the high-velocity impact fixture.

2.2. High-Speed Ballistic Impact Test. The high-velocity impact test has been carried out using a steel projectile on the interwoven composite laminates. The specification of the projectile is given in Table 1.

Table 2 describes the varying velocity of the projectile during initial and impact conditions. It has been observed that the projectile lost its most of the energy in KB 5 × 5 and KG 5 × 5.

The impacted area of the material is extracted using the C scanning method and Phanthom Cine analysis is used to calculate the residual and impact velocity of the projectile. Further, the impact strength has been estimated by finding the absorbed energy of the material.

2.3. Ultrasonic C Scan. The ultrasonic method of inspection is considered to be the most effective way of checking the quality of the materials [27]. Here, a submerged ultrasonic C

Table 1: Specification of the projectile.

Particulars	Specification
Material	Mild steel
Mass	7.34 (g) or 0.00734 (kg)
Length	15.5 (mm)
Diameter	9.66 (mm)

Table 2: Inlet and residual velocity of the projectile.

Material	Average inlet velocity in m/s	Average residual velocity in m/s
KB 1 × 1	225.67	173.67
KB 3 × 3	225	196
KB 5 × 5	250.5	176.67
KG 1 × 1	256	200.33
KG 3 × 3	253	196
KG 5 × 5	249	176.67

scan method is used to obtain the images of the impacted materials and then the area is calculated using Image J software. Then those areas are used to calculate the impact strength of the materials. The system consists of an Ultrasonic Transducer and a receiver to fetch the results from the transducer.

3. Estimation of Absorbed Energy

The study of impact testing is carried out by calculating the absorbed energy from [28, 29]

$$E_{abs} = \frac{1}{2} m_p \left(V_i 2 - V_r 2\right), \tag{1}$$

where, E_{abs} is the energy absorbed by the material, m_p is the mass of the projectile, V_i is the impact velocity of the projectile, and V_r is the residual velocity of the projectile.

As the projectile strikes the material, the kinetic energy of the projectile is converted into absorbed energy. Thus, the energy which is lost is called absorbed energy [29].

From Table 3, we have acquired the impact and the residual velocities of the projectile for different composite materials. The absorbed energy is calculated from this loss of kinetic energy.

The impact strength could be depicted from the absorbed energy of various composite materials which is given in above Table 3.

Figures 1 and 2 display the front face of the material after the bullet impact and their corresponding C scan images. The specimens KG 1 × 1, KG 3 × 3, and KG 5 × 5 has undergone a lot of damage with the impact area of 37.39 cm^2, 33.36 cm^2, 21.16 cm^2, respectively.

Moyo et al. [30] have stated in their work that absorbed energy is linear to that of damaged area. Thus, impact strength for the composites is.

$$\text{impact strength} = \frac{(\text{energy absorbed})}{(\text{damaged area})}. \tag{2}$$

The impact strength of the composite materials is depicted in Table 4. The area is calculated using the Image J software. The impact strength of KB 1 × 1, KB 3 × 3, and KB 5 × 5 are 28.24 J/cm^2, 7.633 J/cm^2, and 19.323 J/cm^2, respectively, while the impact strength of KG 1 × 1, KG 3 × 3, and KG 5 × 5 are 2.494 J/cm^2, 2.816 J/cm^2, and 5.340 J/cm^2, respectively.

4. Results and Discussion

The absorbed energy which was calculated from the energy lost equation is found to be greater for KB 5 × 5 and KG 5 × 5. The absorbed energy for the different kevlar basalt and kevlar glass interwoven laminate is shown in Figure 3.

In order to investigate the influence of the different woven composite materials on the impact properties, the damaged area and impact strength are calculated and the results obtained are presented in Figures 4 and 5.

It is evident from Figure 5, the result that the KB 1 × 1 has is more resistant compared to any other fabricated material with an impact strength of 28.24 J/cm^2 with area of 2.698 cm^2, followed by KB 5 × 5 which has an impact strength of 19.323 J/cm^2 with area of 5.99 cm^2 and the hybrid of glass and kevlar are observed to be having lowest impact strength of 2.494 J/cm^2 with the area of 37.39 cm^2. Basalt has got excellent comprehensive performances because of the presence of silica content. In alkali condition, the basalt fiber is more stable than the glass fibers mainly because of the chemical composition. Added basalt also has got greater failure strain properties [24]. Generally, glass fibers have low knit line strength and low elastic modulus which might have led to low impact strength than kevlar basalt weaving. Lower elastic modulus will tend to make the fiber stiffer resulting in the low breakage of the fibers. The carbon reinforced epoxy composite has impact strength of 27 J/cm^2 [31] which is lesser compared to that of KB 1 × 1. This is because carbon fibers generally have poor impact properties and they are very brittle. The carbon fiber undergoes delamination even under mild impact loads [32].

Table 3: Absorbed energy of composite materials.

Material	Impact velocity (m/s)	Impact energy (J)	Residual velocity (m/s)	Residual energy (J)	Absorbed energy (J)
KB 1 × 1	225.67	186.902	173.67	110.692	76.21
KB 3 × 3	225	185.794	196	140.987	44.807
KB 5 × 5	250.5	230.293	176.67	114.549	115.744
KG 1 × 1	256	240.517	200.33	147.285	93.232
KG 3 × 3	253	234.913	196	140.987	93.926
KG 5 × 5	249	227.544	176.67	114.549	112.995

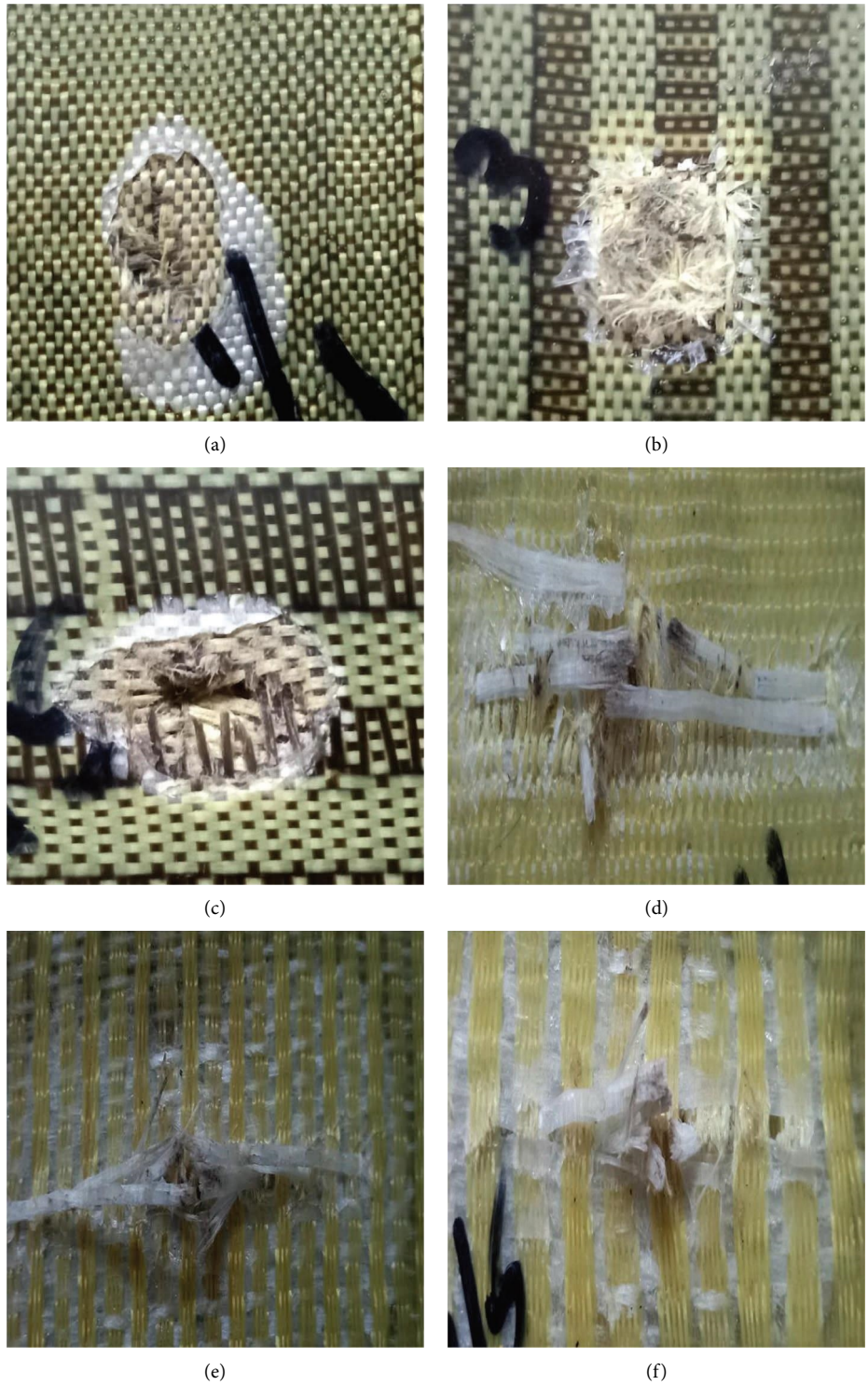

Figure 1: Front face of the impacted specimen (a) KB 1 × 1, (b) KB 3 × 3, (c) KB 5 × 5, (d) KG 1 × 1, (e) KG 3 × 3 and (f) KG 5 × 5.

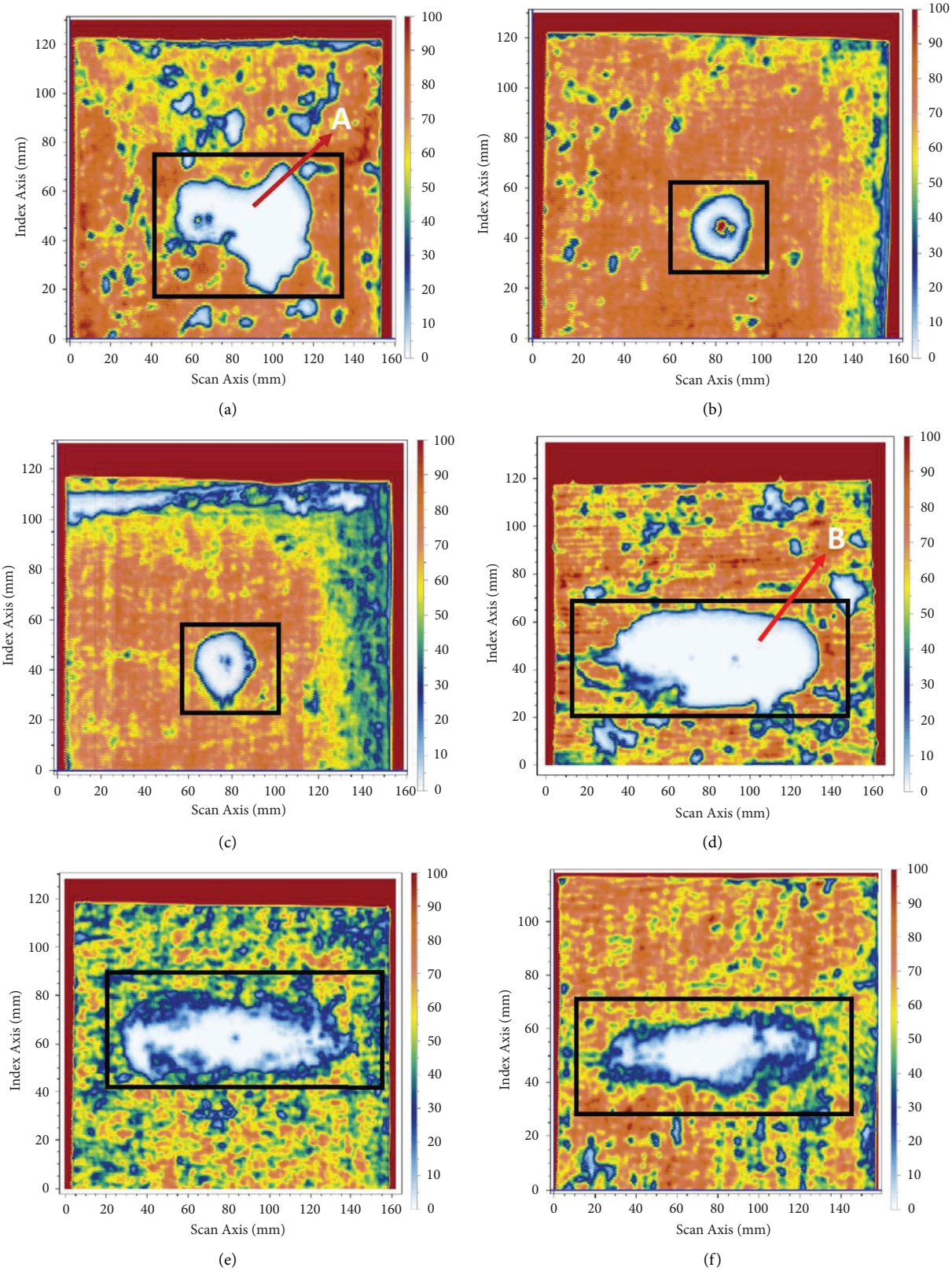

Figure 2: Ultrasonic C scan images (a) KB 1 × 1, (b) KB 3 × 3, (c) KB 5 × 5, (d) KG 1 × 1, (e) KG 3 × 3 and (f) KG 5 × 5.

Table 4: Impact strength of composite materials.

Material	Area in cm^2	Absorbed energy (J)	Impact strength (J/cm^2)
KB 1 × 1	2.698	76.21	28.24
KB 3 × 3	5.87	44.807	7.633
KB 5 × 5	5.99	115.744	19.323
KG 1 × 1	37.39	93.232	2.494
KG 3 × 3	33.36	93.926	2.816
KG 5 × 5	21.16	112.995	5.340

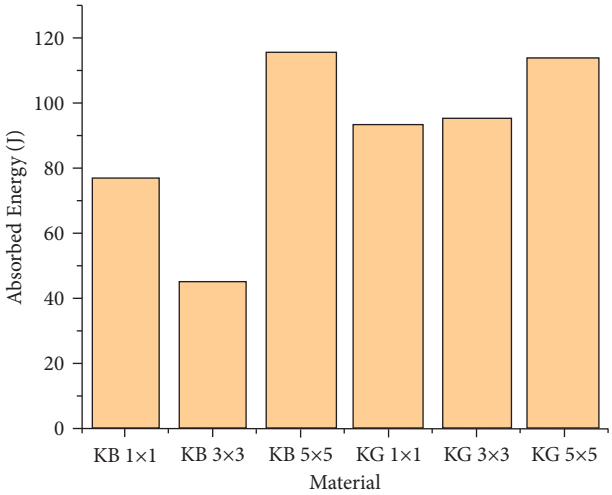

Figure 3: Energy absorbed vs. composite material.

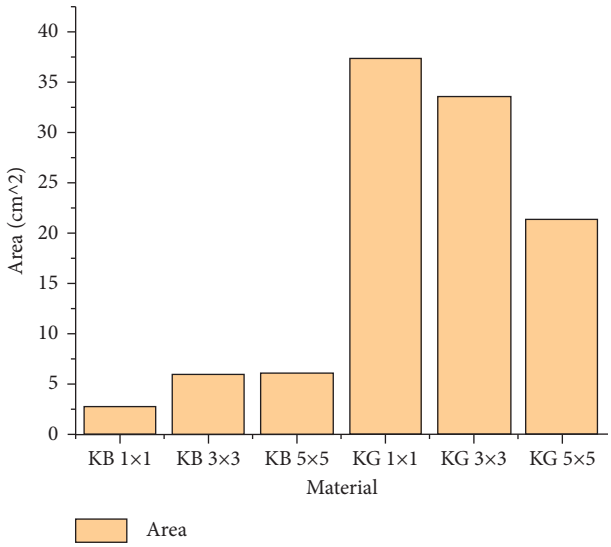

Figure 4: Area vs. composite material.

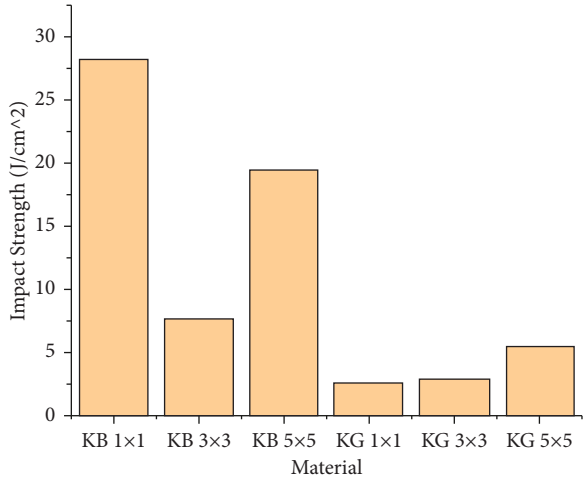

Figure 5: Impact strength vs. composite material.

5. Conclusion

The ballistic impact testing on the interwoven kevlar-basalt/epoxy and kevlar-glass/epoxy composite laminates were carried out and the impact strength for all the laminates was determined.

Following were the observations made from the study:

(1) The impact strength of the impacted specimens is as follows: KB 1 × 1 > KB 5 × 5 > KB 3 × 3 > KG 5 × 5 > KG 3 × 3 > KG 1 × 1. The weaving pattern has direct influence on the impact strength of the material as KB 1 × 1 possesses more impact strength than that of KB 5 × 5.

(2) The damaged area for all the kevlar/glass weaving patterns was higher than the kevlar/basalt weaving pattern. This behavior could be due to the predominant fiber breakage and fibers pull out in the kevlar/glass laminates.

(3) Also, the first few layers of the kevlar/glass have undergone a large amount of damage in the lengthwise direction.

(4) The interwoven laminate of kevlar and basalt which showed improved results can be used in making bullet proof armours. Though the weaving of the laminates can be time consuming the usage of basalt along with kevlar will bring down the cost.

(5) This research can be further extended by adding different nanoparticles in different percentages and testing for the impact strengths.

Data Availability

The data used to support the findings of this study are included in the article.

Conflicts of Interest

The authors declare that they have no conflicts of interest.

Authors' Contributions

J. Jensin Joshua performed planning, design, experimentation, data collection, and initial draft preparations. Dalbir Singh performed figure preparation and reviewing and editing. Y. Murali Krishna performed experimentation and data collection. P. Sivaprakasam performed data analysis, manuscript editing, and reviewing. D. Raja Joseph performed data collection and analysis. P. S. Venkatanarayanan performed reviewing and editing.

References

[1] Y. Sun, C. Shi, Z. Liu, and D. Wen, "Theoretical research progress in high-velocity/hypervelocity impact on semi-infinite targets," *Shock and Vibration*, vol. 2015, Article ID 265321, 15 pages, 2015.

[2] S. N. A. Safri, M. T. H. Sultan, N. Yidris, and F. Mustapha, "Low velocity and high velocity impact test on composite materials—a review," *International Journal of Engineering Science*, vol. 3, pp. 50–60, 2014.

[3] I. Mohagheghian, Y. Wang, J. Zhou et al., "Deformation and damage mechanisms of laminated glass windows subjected to high velocity soft impact," *International Journal of Solids and Structures*, vol. 109, pp. 46–62, 2017.

[4] H. Sylvestre and V. R. R. Parama, "Space debris: reasons, types, impacts and management," *Indian Journal of Radio and Space Physics*, vol. 46, pp. 20–26, 2017.

[5] W. P. Schonberg, "Studies of hypervelocity impact phenomena as applied to the protection of spacecraft operating in the MMOD environment," *Procedia Engineering*, vol. 204, pp. 4–42, 2017.

[6] P. J. Hogg, "Composites in armor," *Science*, vol. 314, pp. 1100-1101, 2006.

[7] M. Hisham, M. Fahaduddin, M. A. Khan, B. C. Ashok, and P. K. Shrivastava, "A research on kevlar and hybrid kevlar composites; A report," *International Journal of Recent Technology and Engineering*, vol. 8, no. 2S3, pp. 830–833, 2019.

[8] N. Shaari and A. Jumahat, "Unhole and open hole compressive behaviours of hybrid Kevlar/glass fibre reinforced silica nanocomposites," *Materials Research Express*, vol. 5, no. 6, Article ID 065009, 2018.

[9] R. Velumayil and A. Palanivel, "Hybridization effect on mechanical properties of basalt/kevlar/epoxy composite laminates," *Polymers*, vol. 14, no. 7, 2022.

[10] J. Tirillò, L. Ferrante, F. Sarasini et al., "High velocity impact behaviour of hybrid basalt-carbon/epoxy composites," *Composite Structures*, vol. 168, 2017.

[11] H. Aghamohammadi, R. F Eslami, and A. Tcharkhtchi, "The effect of multi-walled carbon nanotubes on the mechanical behavior of basalt fibers metal laminates: an experimental study," *International Journal of Adhesion and Adhesives*, vol. 98, Article ID 102538, 2020.

[12] M. Damghani, N. Ersoy, M. Piorkowski, and A. Murphy, "Experimental evaluation of residual tensile strength of hybrid composite aerospace materials after low velocity impact," *Composites Part B: Engineering*, vol. 179, Article ID 107537, 2019.

[13] A. Wondimu, M. Kebede, and S. Palani, "Trash pineapple leaf fiber reinforced polymer composite materials for light applications," in *Bio-Fiber Reinforced Composite Materials*, pp. 13–30, Springer, Singapore, 2022.

[14] A. Divya Sadhana, J. Udaya Prakash, P. Sivaprakasam, and S. Ananth, "Wear behaviour of aluminium matrix composites (LM25/Fly ash)–A Taguchi approach," *Materials Today Proceedings*, vol. 33, pp. 3093–3096, 2020.

[15] J. U. Prakash, P. Sivaprakasam, I. Garip et al., "Wire electrical discharge machining (WEDM) of hybrid composites (Al-Si12/B4C/fly Ash)," *Journal of Nanomaterials*, vol. 2021, Article ID 2503673, 10 pages, 2021.

[16] T. Yashas Gowda, G. Vinod, and P. Madhu, ""A new study on flax-basalt-carbon fiber reinforced epoxy/bioepoxy hybrid composites"," *Polymer Composites*, vol. 42, no. 4, pp. 1891–1900, 2021.

[17] F. Sarasini, J. Tirillò, L. Ferrante et al., "Drop-weight impact behaviour of woven hybrid basalt–carbon/epoxy composites," *Composites Part B: Engineering*, vol. 59, pp. 204–220, 2014.

[18] J. Gustin, A. Joneson, M. Mahinfalah, and J. Stone, "Low velocity impact of combination Kevlar/carbon fiber sandwich composites," *Composite Structures*, vol. 69, no. 4, pp. 396–406, 2005.

[19] R. Yahaya, S. M. Sapuan, M. Jawaid, Z. Leman, and E. S. Zainudin, "Measurement of ballistic impact properties of woven kenaf–aramid hybrid composites," *Measurement*, vol. 77, pp. 335–343, 2016.

[20] T. Sathishkumar, S. Satheeshkumar, and J. Naveen, "Glass fiber-reinforced polymer composites – a review," *Journal of Reinforced Plastics and Composites*, vol. 33, no. 13, pp. 1258–1275, 2014.

[21] E. Kessler, R. Gadow, and J. Straub, "Basalt, glass and carbon fibers and their fiber reinforced polymer composites under thermal and mechanical load," *AIMS Materials Science*, vol. 3, no. 4, pp. 1561–1576, 2016.

[22] V. J. John and B. Dharmar, "Influence of basalt fibers on the mechanical behavior of concrete—a review," *Structural Concrete*, vol. 22, no. 1, pp. 491–502, 2020.

[23] Z. Li, J. Ma, H. Ma, and X. Xu, "Properties and applications of basalt fiber and its composites," *IOP Conference Series: Earth and Environmental Science*, vol. 186, Article ID 012052, 2018.

[24] H. Fu, X. Feng, J. Liu, Z. Yang, C. He, and S. Li, "An investigation on anti-impact and penetration performance of basalt fiber composites with different weave and lay-up modes," *Defence Technology*, vol. 16, no. 4, pp. 787–801, 2020.

[25] D. P. C. Aiman, M. F. Yahya, and J. Salleh, "Impact properties of 2D and 3D woven composites: a review," *AIP Conference Proceedings. Author(s)*, vol. 1774, 2016.

[26] R. F Eslami, H. Aghamohammadi, S. Mohammad Reza Khalili, and J. Hamid, "Recent trend in developing advanced fiber metal laminates reinforced with nanoparticles: a review study," *Journal of Industrial Textiles*, vol. 51, no. 5_supp, pp. 7374S–7408S, 2022.

[27] T. Hasiotis, E. Badogiannis, and N. G. Tsouvalis, "Application of ultrasonic C-scan techniques for tracing defects in laminated composite materials," *Strojniškivestnik – Journal of Mechanical Engineering*, vol. 3, pp. 192–203, 2011.

[28] E. Kazemi-Khasragh, F. Bahari-Sambran, M. HosseinSiadati, and R. EslamiFarsani, "High velocity impact response of basalt fibers/epoxy composites containing GrapheneNanoplatelets," *Fibers and Polymers*, vol. 19, no. 11, pp. 2388–2393, 2018.

[29] V. Mahesh, S. Joladarashi, and S. M. Kulkarni, "Damage mechanics and energy absorption capabilities of natural fiber reinforced elastomeric based bio composite for sacrificial structural applications," *Defence Technology*, vol. 17, no. 1, pp. 161–176, 2021.

[30] M. Moyo, K. Kanny, and R. Velmurugan, "Performance of kenaf non-woven mat/PLA biocomposites under medium velocity impact," *Fibers and Polymers*, vol. 21, pp. 2642–2651, 2020.

[31] T. A. Lenda and S. Mridha, "Impact strength of carbon reinforced epoxy composite at different temperatures," *Advanced Materials Research*, vol. 264, pp. 451–456, 2011.

[32] S. Chocron, A. J. Carpenter, N. L. Scott, R. P. Bigger, and K. Warren, "Impact on carbon fiber composite: ballistic tests, material tests, and computer simulations," *International Journal of Impact Engineering*, vol. 131, no. 143, pp. 39–56, 2019.

Hindawi
Advances in Materials Science and Engineering
Volume 2023, Article ID 7926006, 8 pages
https://doi.org/10.1155/2023/7926006

Research Article

Tribological Behavior of Ni-P Electroless Coating of Inconel 625 with Multiwall Nano Carbon Tubes

D. Jayabalakrishnan,[1] **S. Senthil Kumar**,[2] **R. Suthan**,[3] **P. Babu Aurtherson**,[4] **J. Elanchezhian**,[5] **V. Ramanareddy**,[6] **S. Louies Praveen**,[7] **and Umamahesawari Kandasamy**[8]

[1]*Center for Materials, Chennai Institute of Technology, Chennai 600069, India*
[2]*Department of Mechanical Engineering, R.M.K College of Engineering and Technology, R.S.M Nagar, Puduvoyal, Thiruvallur 601206, India*
[3]*Department of Mechanical Engineering Panimalar Engineering College, Chennai 600123, India*
[4]*Department of Mechanical Engineering, DMI Engineering College, Aralvaimozhi, Kanyakumari, Tamil Nadu, India*
[5]*Department of Mechanical Engineering, Anand Institute of Higher Technology, Chennai 603103, India*
[6]*Department of Mechanical Engineering, Vardhaman College of Engineering, Hyderabad 501218, Telangana, India*
[7]*Department of Mechanical Engineering, Panimalar Institute of Technology, Chennai 600123, India*
[8]*Kebridehar University, Kebridehar, Ethiopia*

Correspondence should be addressed to Umamahesawari Kandasamy; umasashwini@gmail.com

Received 24 June 2022; Revised 26 September 2022; Accepted 14 October 2022; Published 24 July 2023

Academic Editor: R. Thanigaivelan

An attempt was taken to study the wear rate of coated Inconel 625 using 0.3 gm of multiwall carbon tubes (MWCNT).The coating was carried out by the Ni-P electroless coating method. The Ni-P-MWCNT coating was prepared by using nickel phosphorous solution. The sliding wear test was conducted using pin on discs tribometer. The wear rate behavior was investigated at various levels of pin on discs tribometer factors, and a predictive model was developed using regression equations. The wear test experiment was carried out based on the L_{27} orthogonal array. The wear process parameters load, sliding velocity, and sliding distance were chosen. It was observed that the rate of wear increased as the load increases, whereas increase in sliding velocity and sliding distance reduces the rate of wear. The developed regression model was validated with the measured wear rate. The percentage error was observed within 0.99%.

1. Introduction

Inconel alloy is used in automotive, aerospace, and defense industries due to its high-strength and corrosion resistance [1, 2]. Inconel 625 alloy is widely utilized in different area owing to its features such as high work hardening rate and low thermal conductivity. This alloy is particularly used to make turbine blades, aero engine parts, and heat exchangers parts. Inconel 625 is subjected to high temperature environment, and its alloy wear and corrosion resistivity need to be improved in order to withstand the impact of high temperature environment. Naji et al. [3] have studied the corrosion resistivity, biocompatibity of HA/TiO_2, and ZrO_2/HA coating material. Titanium alloy (Ti-6Al-7Nb) was used as substrate material. The anodic microarc oxidizing (MAO) coating technique was used. They have reported that the rutile and anatase phases were present by MAO coating. Furthermore, they have said that the metaphosphates were seen by mixing ZrO_2 to the electrolyte. Guo et al. [4] have studied the effect of nano tubes-coated Ti6Al4V alloy on wear and corrosion resistivity and microstructure. They have carried out coating process on this alloy using various concentric level of sodium chloride solution, and the coating was done by microarc oxidation. They have suggested that

0.15 Gram/liter CNT has shown low porosity and roughness. The corrosion resistivity was enhanced on increasing the CNT concentration up to 0.15 Gram/liter.

Li et al. [5] have done using microarc oxidation coating on Zr alloy substrate using composite coat $Al_2O_3/MoS_2/CeO_2$/graphene oxide. They have investigated the surface status, cross section status, composition, and structure of phase of various composite microarc oxidation coating. They have suggested that the composite coating consisting ZrO_2 s hashown better corrosion resistance and the MAO coating—Al_2O_3 has shown the good resistivity of corrosion.

Askarnia et al. [6] have coated the surface of AZ91 magnesium alloys using various amounts of graphene oxide and they have used microarc oxidation process in the presence of alkaline electrolyte. The test of scratch, behavior of corrosion, antibacterial and bioactivity properties of coated AZ91 magnesium alloys were carried out. They have observed that the MgO and Mg_2SiO_4 ceramics were existed as a result of oxidation and electrolyte reaction. The surface of AZ91 magnesium alloy coated with 20 mg/L of GO leads to minimum pores on the surface. The crashed width of the scratch reduced from about 137 μm to 87 μm for sample coated with 20 mg/GO owing to strengthening of the coating by graphene oxide reinforcement. Küçükosman et al. [7] have deposited composite coat on AZ91 alloy using MAO (microarc oxidation) and the MAO-hydrothermal treatment. Si/ph-based electrolyte/graphite particles size of 5–10 and 75 μm were used. The surface morphology with good appearance was observed in the MAO coating, and also the resistance of wear of the graphite-doped MAO-HT composite coatings was improved identically.

Thanu et al. [8] have used electro deposition of Ni-Ta coating on Nickel-based alloy. Their study revealed that the scanning electron microscopic shows evidently that constant electro deposition generates smooth and uniform coatings. Higher hardness was achieved in the coating done using Ni/Ta: 4 : 1 and it increases to 270 VHN. Reis et al. [9] stated that copper-beryllium is the materials which are widely utilized to make mold in the injection moulding process. Though it has great abrasion resistance, still its resistivity needs to be improved. Therefore, this material is coated using Ni-P coating. They have investigated the hardness, wear test, XRD, and SEM analysis, and the improvement of the coated alloy behavior is reported.

Corona-Gomez et al. [10] stated that radio-frequency magnetron sputtering is used to coat TaZrN on CoCrMo biomedical substrate. The wear and corrosion behaviour in addition to mechanical test of the coated substrate is evaluated. They have reported that the coated specimen has proved lower wear rate and higher corrosion resistivity. Finally, they have said that the coated specimen would improve the hip joint implant's lifetime. Wei et al. [11] reported the wear and corrosion resistivity of coated AZ31 magnesium alloy. The alloy was coated with Al using the magnetron sputtered method after that the coated specimen is treated using plasma electrolytic oxidation (PEO). The aluminate and silicate electrolytes are used for PEO. They have resulted that the aluminate produces better wear resistivity than silicate coat of the specimen. Furthermore, the PEO/Al has improved the corrosion resistivity of AZ31 alloy.

Ma et al. [12] have studied the corrosion and wear resistance including morphology of Mg-Li-coated alloy by adding Al-Y. The microarc oxidation coatings are used. The best corrosion resistance, wear resistance enhanced hardness, and minimum porosity were obtained for Mg-14Li-3Al-1Y alloy. Jiang et al. [13] have investigated the behaviour of microstructure, microhardness, and wear resistance of WC-Co coating on Ti-6Al-4V substrate. The laser cladded coating method is used to coat Ti-6Al-4V substrate. They have seen an improvement in microhardness and wear resistivity of WC-Co coating on Ti-6Al-4V substrate. Qin et al. [14] have deposited SiO_2-Ni on $AZ_{91}D$ substrate using electroplating technique, characterized by AFM, SEM, and mechanical and tribological test. It has found that the corrosion resistivity was more improved owing to composite coating than pure Ni coating. Furthermore, it was noticed that the SiO_2-Ni composite coat has shown great wear resistance. Divya Sadhana et al. investigated the wear characteristic-Specific Wear Rate-is optimized using the Taguchi approach (SWR) [15]. Physical Vapor Deposition (PVD)-based AlTiN can be applied to coat titanium alloy and SS 316LVM materials for biomedical applications since it has greater wear resistance qualities [16, 17]. An innovative multistage micromechanical approach is proposed to explore the function of carbon nanotube (CNT) coating on carbon fibre (CF) surfaces in the effective thermal conductivities of the unidirectional polymer hybrid nanocomposites [18].

The polarisation efficiency of poly (vinylidene fluoride)/barium titanate ($PVDF/BaTiO_3$) composites was increased by coating carbon nanotubes [19]. Titanium alloy was coated with carbon nanotubes (CNTs)-reinforced composites using a laser cladding. Due to the self-lubricating effect, the coating's COF was drastically lowered [20]. Analysis of wear characteristics of titanium nitride had been deposited by DC magnetron sputtering over 6061 aluminium alloy. The Vickers hardness tester was used to assess the hardness of untreated and coated aluminium specimens, and the findings showed that coated specimens had a 26% improvement in comparison to uncoated samples [21].

From the literature review, it is evidently seen that there was no adequate investigation on coated Inconel alloy. Therefore, an attempt is taken to study the MWCNT-coated Inconel 625 using electroless coating technique. The wear rate was observed and the effect of pin on disc wear test on wear rate is analyzed.

2. Materials and Methods

Inconel 625 is selected as the substrate owing to its usage in aerospace industries and heat exchangers manufacturers. Electroless coating technique is chosen to coat on the substrate to improve the wear resistivity. The following steps are about the preparation of the electroless solution:

(i) Take the required vessels, rinse it with soap water, and clean it with deionized water.

(ii) Take 200 ml of nickel phosphorous solution in 250 ml beaker and place it in a magnetic stirrer until it obtains temperature of 88°C which is measured by thermometer.

(iii) Take a sample of Inconel 625, rinse it with soap water, and clean it with deionized water. Now, clean the sample using ultrasonic cleaner at 55°C.

(iv) Take the cleaned sample and dip it in a solution containing 50% of HCl. Now, prepare the MWCNT solution by adding sodium lauryl sulphate`in deionized water.

(v) Place the sample in the holder which is dipped inside the Nickel phosphorous solution; after half an hour, add 0.30 g of MWCNT and leave the sample for 1 hour.

(vi) Now, take the sample, again clean it with deionized water, and dry it.

(vii) Place the sample in the holder which is dipped inside the Nickel phosphorous solution, and leave the sample for 1 ½ hours in the magnetic stirrer.

The specimens are machined equal to 20 mm and cleaned using acetone and diluted HCL, and the specimens are dried. Figure 1 shows the wear test assembly and specimen. The sample size ranges with 20 mm diameters and 15 mm length. The specifications of Pin on disc are as follows: Load (N):5–200 N; disc speed: 100–2000 rpm; motor and drive: AC motor with drive; sliding velocity: 0.5 to 10 m/s; specimen holders: universal holders; wear measurement (μ): ±5000 microns or ±5 mm.

3. Taguchi Analysis

Taguchi analysis is used to design the experiment and it gives reduced variance for the experiment with optimum settings of process factors. The orthogonal array would provide a complete set of very well balanced design of experiments. Taguchi analysis consist experiments' plan, model determination, and adequacy check of the predictive model. Furthermore, it comprises of planning of experiments, determination of model, and checking adequacy of the developed model. The parameters selected to study the wear behavior of the coated work material are sliding distance, velocity, and load. Experiment's plan is carried out by Taguchi analysis. The L_{27} experimental trails are done for the chosen number of factors. Table 1 shows the factors and their levels. Figure 2 shows the SEM images of the coated specimen, in which the CNTs (Carbon Nano Tubes) are agglomerated on the substrate.

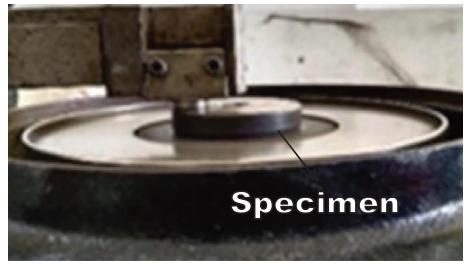

Figure 1: Wear test tribometer.

4. Wear Test

The sliding wear behaviour is studied on the coated Inconel 625 specimen to observe the impact of MWCNT on the improvement of wear resistance. Load applied on the specimen and the specimen adheres to the counterface. The specimen is kept close to this counter face. The disc is cleaned and polished using SiC emery sheets to have clean surface contact of coated specimen surface. The parameters are set in the pin on disc setup, and tests are carried out based on L_{27} orthogonal array. The rate of wear is evaluated by weight loss way as shown in equation (1). The weight of the specimen is calculated before and after the wear test.

$$W = \frac{M}{\rho} * D, \tag{1}$$

where W = wear rate (WR) (mm^3/m), M = weight loss (WL) (g), ρ = density (g/mm^3), D = sliding distance (SL) (m).

5. Results and Discussions

The impact of wear factors on the MWCNT-coated Inconel 625 substrate is analyzed with the help of ANOVA analysis.

The wear test based on 27 experimental trails was carried out and Table 2 shows wear test results. The experimental results are analyzed through the Design Expert, and a predictive model is developed to predict the rate of wear. Table 3 shows the estimation of the coefficients for the development of a model and significance test of the model. The wear rate is expressed in equation (2) using the regression coefficient as given in Table 3, and the average percentage error is found to be within 0.99%. Table 4 shows the difference among the experimental results and forecasted results. The other new levels of factors are substituted in the developed model and verified the model results with experimental results. The comparison of actual with predicted results is shown in Figure 3.

$$\begin{aligned}\text{Wear rate} = {} & 0.000749 + 0.000014 * \text{load} + 0.000033 * \text{Velocity} + 3.72778\text{E} - 08 * \text{Slidi ng di stance} - 6.52778\text{E} \\ & - 07 * \text{load} * \text{velocity} - 2.88333\text{E} - 09 * \text{load} * \text{slidi ng di stance} - 3.67778\text{E} - 08 * \text{Velocity} * \text{slidi ng di stance}.\end{aligned} \tag{2}$$

Table 1: Factors/levels.

S. no	Factors	Levels		
1	Load (L) (N)	10	30	50
2	Velocity (V) (m/s)	1.5	3	4.5
3	Sliding distance (SL) (m)	500	1000	1500

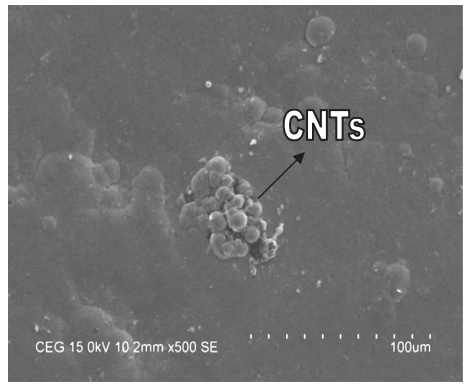

Figure 2: SEM images of MWCNT coated specimen.

Table 2: Experimental results of wear rate: coated inconel 625.

Exp	Load (N)	Velocity (m/s)	Sliding distance (m)	Wear rate (mm^3/m)
1	10	1.5	500	0.000930
2	10	1.5	1000	0.000905
3	10	1.5	1500	0.000877
4	10	3	500	0.000921
5	10	3	1000	0.000856
6	10	3	1500	0.000707
7	10	4.5	500	0.000912
8	10	4.5	1000	0.000838
9	10	4.5	1500	0.00095
10	30	1.5	500	0.001144
11	30	1.5	1000	0.001107
12	30	1.5	1500	0.001068
13	30	3	500	0.001156
14	30	3	1000	0.001064
15	30	3	1500	0.000911
16	30	4.5	500	0.001114
17	30	4.5	1000	0.001041
18	30	4.5	1500	0.000803
19	50	1.5	500	0.001338
20	50	1.5	1000	0.001312
21	50	1.5	1500	0.001271
22	50	3	500	0.001362
23	50	3	1000	0.001231
24	50	3	1500	0.001108
25	50	4.5	500	0.001351
26	50	4.5	1000	0.001226
27	50	4.5	1500	0.001097

5.1. Analysis of Variance. The factor's significance on the wear rate is estimated with the help of ANOVA (Analysis of Variance) analysis. Table 5 shows ANOVA analysis. R^2 and adjusted R^2 such as 91% and 89%, respectively, for significance test are evident that the model developed correlate very well the factors with the wear rate. The ANOVA is used to estimate the impact of every factor. The P-value indicates the statistical importance of every factor. The particular factor can be said to be statically important, if the P-value is identified to be lesser than 0.05. The ANOVA is set with the significance level of 5%. The F-value for every factor on wear rate is evaluated as Load (175.62), velocity (5.84) and sliding

Table 3: Significant test results: wear rate.

Term	Coeff	SE coeff	T	P
Constant	0.0011	$6.136E-06$	0.0010	0.0011
Load	0.0002	$7.516E-06$	0.0002	0.0002
Velocity	−0.0000	$7.516E-06$	−0.0001	−0.0001
Sliding distance	−0.0001	$7.516E-06$	−0.0001	−0.0001
Load*velocity	$1.750E-06$	$9.205E-06$	−0.0000	0.0001
Load*sliding distance	$-7.250E-06$	$9.205E-06$	−0.0000	0.0001
Velocity*sliding distance	−0.0000	$9.205E-06$	−0.0001	−0.0001

Table 4: Predicted vs. experimental trail values.

S. no	Actual	Predicted	Percentage error (%)
1	0.0009	0.0009	0.00
2	0.0009	0.0009	0.00
3	0.0009	0.0009	0.00
4	0.0009	0.0009	0.00
5	0.0009	0.0008	12.50
6	0.0007	0.0008	12.50
7	0.0009	0.0009	0.00
8	0.0008	0.0008	0.00
9	0.0007	0.0007	0.00
10	0.0011	0.0011	0.00
11	0.0011	0.0011	0.00
12	0.0011	0.0011	0.00
13	0.0012	0.0011	9.09
14	0.0011	0.0011	0.00
15	0.0009	0.0010	10.00
16	0.0011	0.0011	0.00
17	0.0010	0.0010	0.00
18	0.0008	0.0009	11.11
19	0.0013	0.0014	7.14
20	0.0013	0.0013	0.00
21	0.0013	0.0012	8.33
22	0.0014	0.0014	0.00
23	0.0012	0.0013	7.69
24	0.0011	0.0012	8.33
25	0.0014	0.0014	0.00
26	0.0012	0.0012	0.00
27	0.0011	0.0011	0.00

distance (31.33). The F-value of every factor on wear rate, the load, and sliding distance is identified to be a more significant impact on wear rate followed by velocity as shown in Table 5.

5.2. Influence of Factors on Wear Rate. The 3D plot developed to study the wear rate as the level of the wear test factors such as load, and sliding distance is shown in Figures 4(a)–4(c). The changes in wear rate at the various level of load and velocity is shown in Figure 4(a). From this Figure 4(a), it is seen that the wear has increased with increase in the level of load and it would be owing to generation of higher pressure and higher stresses during the measurement. However, MWCNT coating on the substrate minimizes the deformation owing to good

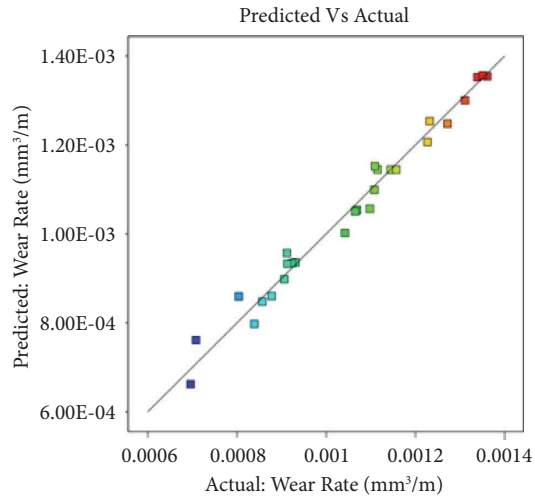

Figure 3: Predicted vs. experimental results.

Table 5: ANOVA results for wear rate.

Source	SoS	DF	MS	F	P
Model	$8.018E-07$	6	$1.336E-07$	36.54	<0.0001
Load	$6.422E-07$	1	$6.422E-07$	175.62	<0.0001
Velocity	$2.136E-08$	1	$2.136E-08$	5.84	0.0253
Sliding distance	$1.146E-07$	1	$1.146E-07$	31.33	<0.0001
Load*velocity	$4.602E-09$	1	$4.602E-09$	1.26	0.2752
load*sliding distance	$9.976E-09$	1	$9.976E-09$	2.73	0.1142
velocity*sliding distance	$9.130E-09$	1	$9.130E-09$	2.50	0.1298
Residual	$7.314E-08$	20	$3.657E-09$		
Total	8.750–07	26			

R^2: 91% and adjusted: R^2 89%.

adherability, stability, and adequate wear resistivity. Lower wear is seen at 10 N load due to lower pressure via lever arm (tribometer/pin on disc). The wear rate increases as the velocity level is reduced, and it would be owing to high contact/interaction time among the disc and the specimen. The change in the wear rate due to change in the level of sliding distance is shown in Figures 4(a) and 4(b). The wear rate is found to be high at lower level of sliding distance and the wear rate is reduced as the level of sliding distance is increased. At low sliding distance, the wear rate is increased. It would owe some irregularities presented in the coating process, and these irregularities would induce improper contact of disc with specimen surface. The worn out surfaces of the coated Inconel 625 are examined with help of SEM as shown in Figure 5. The coated Inconel surfaces worn out at various levels of pin on disc factors are examined. The worn pot coated surface at various levels of the tribometer's factors is shown in Figures 5(a) and 5(b). The minimum of scratches with merciful wear is seen at lower level of load, middle and higher level of velocity, and higher level of sliding distance as shown in Figures 5(a) and 5(b), and it would be owing to minimum pressure induced on the pin on disc.

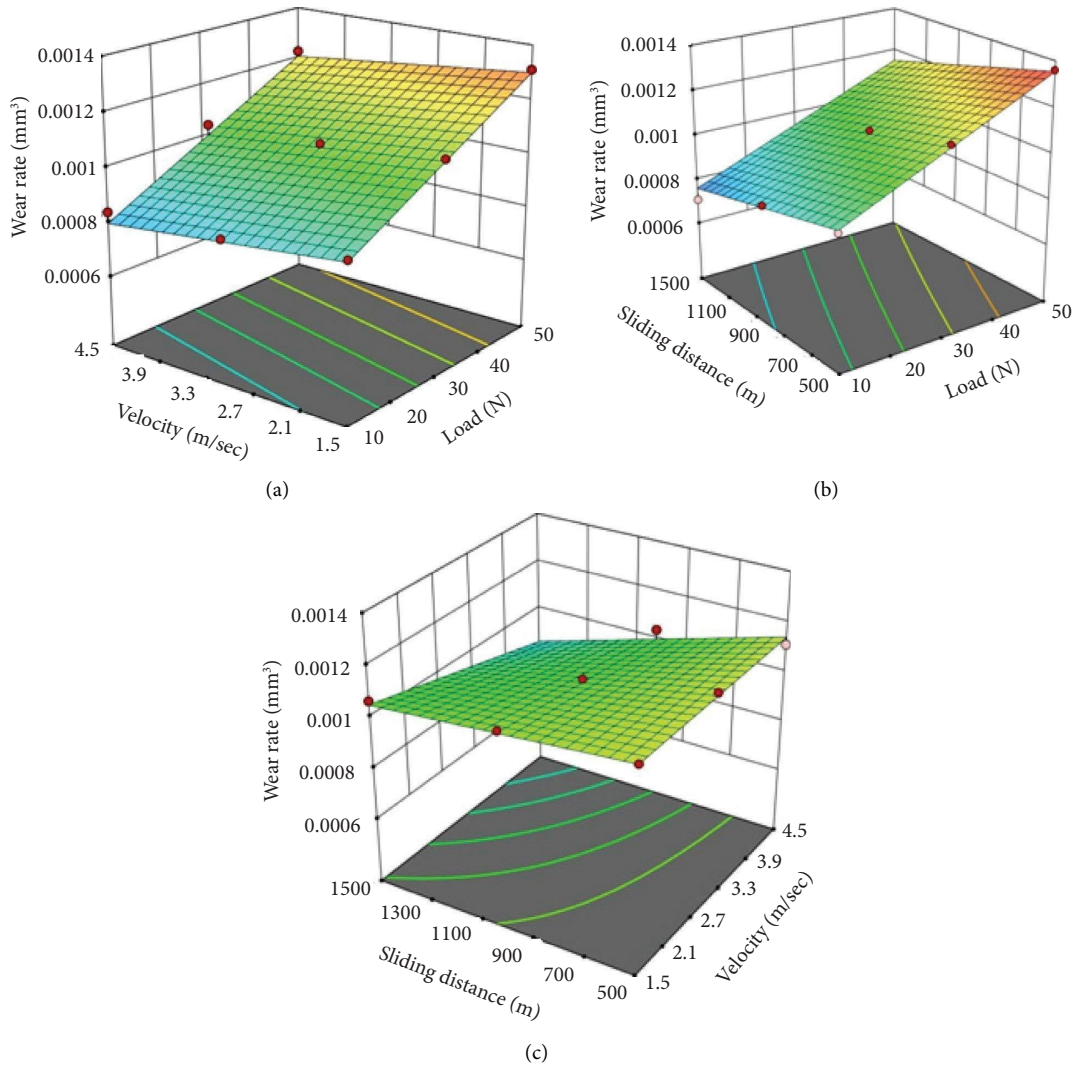

Figure 4: Wear rate at various levels of factors. (a) Wear rate: V vs. L; (b) Wear rate: SD vs. L; (c) Wear rate: SD vs. V.

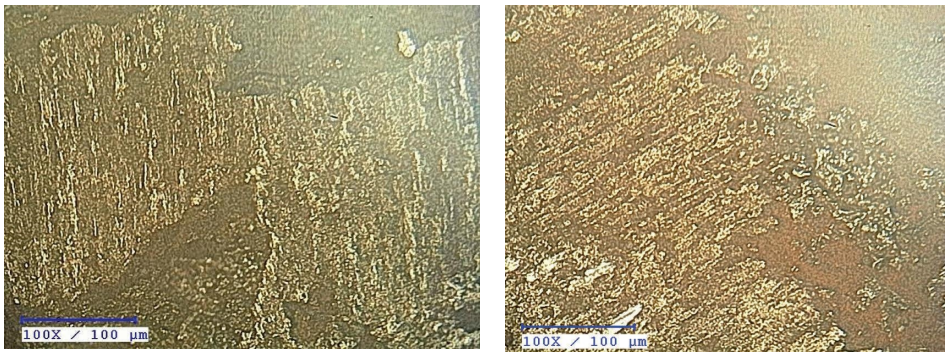

Figure 5: (a-b) Worn out images of the coated surface. (a) Worn out images at 10 N, 4.5 m/sec and 1000 m. (b) Worn out image at 10 N, 3 m/sec and 1500 m.

6. Conclusion

MWCNT is deposited on the Inconel 625 through the Ni-P electroless coating method. The following conclusions were observed:

(i) A predictive model is developed to predict the wear rate and it facilitates a best relation among pin on disc wear process factors with wear rate of MCWNT coated specimen.

(ii) ANOVA test provides and confirms the adequacy of the model with very minimum lack of fit.

(iii) Load is influenced significantly on wear rate followed by sliding distance and velocity.

(iv) The plot of wear rate at various levels of wear process factors shows that increase in load develops the wear rate. The increase in velocity and sliding distance diminishes the rate of wear.

(v) The maximum wear rate observed at load = 50 (N), V = 3 (m/sec), SD = 500 (m) is found to be 1.92 times higher than the wear rate observed at load = 10 (N), $V = 3$ (m/sec), SD = 1500 (m).

(vi) The presence of coating has been ensured via scanning electron microscopy analysis.

Data Availability

The data used to support the findings of this study are included within the article.

Conflicts of Interest

The authors declare that they have no conflicts of interest.

References

[1] P. Sivaprakasam, P. Hariharan, and G. Elias, "Experimental investigations on magnetic field-assisted micro-electric discharge machining of inconel alloy," *International Journal of Ambient Energy*, vol. 43, no. 1, pp. 2619–2626, 2022.

[2] P. Sivaprakasam and P. Hariharan, "Optimization of process parameters of micro-WEDM process on inconel super alloy through response surface methodology," *International Journal of Mechanical and Production Engineering Research and Development*, vol. 8, no. 6, pp. 1001–1012, 2018.

[3] Q. Naji, J. M. Salman, and N. M. Dawood, "Investigations of structure and properties of layered bioceramic HA/TiO2 and ZrO2/Tio2 coatings on Ti-6Al-7Nb alloy by micro-arc oxidation," *Materials Today Proceedings*, vol. 61, 2021.

[4] Y. Guo, L. Xu, J. Luan, Y. Wan, and R. Li, "Effect of carbon nanotubes additive on tribocorrosion performance of micro-arc oxidized coatings on Ti6Al4V alloy," *Surfaces and Interfaces*, vol. 28, pp. 101626–101713, 2022.

[5] Z. Li, Z. Cai, X. J. Cui, R. Liu, Z. Yang, and M. Zhu, "Influence of nanoparticle additions on structure and fretting corrosion behavior of micro-arc oxidation coatings on zirconium alloy," *Surface and Coatings Technology*, vol. 410, no. 25, Article ID 126949, 2021.

[6] R. Askarnia, S. R. Fardi, M. Sobhani, H. Staji, and H. Aghamohammadi, "Effect of graphene oxide on properties of AZ91 magnesium alloys coating developed by micro-arc oxidation process," *Journal of Alloys and Compounds*, vol. 892, no. 5, Article ID 162106, 2022.

[7] R. Küçükosman, E. Emine Şüküroğlu, Y. Totik, and S. Şüküroğlu, "Investigation of wear behavior of graphite additive composite coatings deposited by micro arc oxidation-hydrothermal treatment on AZ91 Mg alloy," *Surfaces and Interfaces*, vol. 22, Article ID 100894, 2021.

[8] V. C. Thanu, C. Andrew, and M. Jayakumar, "Electrodeposition of nickel super alloy from deep eutectic solvent," *Surfaces and Interfaces*, vol. 19, Article ID 100539, 2020.

[9] T. M. Reis, C. D. Boeira, F. L. Serafini, M. C. M. Farias, C. A. Figueroa, and A. F. Michels, "Micro-abrasive wear resistance of heat-treated electroless nickel phosphorus coatings deposited on copper beryllium alloy C17200," *Surface and Coatings Technology*, vol. 438, Article ID 128374, 2022.

[10] J. Corona-Gomez, K. K. Sandhi, and Q. Yang, "Wear and corrosion behaviour of nano crystalline TaN, ZrN, and TaZrN coatings deposited on biomedical grade CoCrMo alloy," *Journal of the Mechanical Behavior of Biomedical Materials*, vol. 130, 2022.

[11] B. Wei, Y. Cheng, Y. Liu, Z. Zhu, and Y. Cheng, "Corrosion and wear resistance of AZ31 Mg alloy treated by duplex process of magnetron sputtering and plasma electrolytic oxidation," *Transactions of Nonferrous Metals Society of China*, vol. 31, no. 8, pp. 2287–2306, 2021.

[12] X. Ma, S. Jin, R. Wu et al., "Influence alloying elements of Al and Y in MgLi alloy on the corrosion behavior and wear resistance of microarc oxidation coatings," *Surface and Coatings Technology*, vol. 432, Article ID 128042, 2022.

[13] C. Jiang, J. Zhang, Y. Chen et al., "On enhancing wear resistance of titanium alloys by laser cladded WC-Co composite coatings," *International Journal of Refractory Metals and Hard Materials*, vol. 107, Article ID 105902, 2022.

[14] B. Qin, S. Zhou, H. Chen, and M. Wang, "Superior corrosion and wear resistance of AZ91D Mg alloy via electrodeposited SiO2–Ni-based composite coating," *Materials Chemistry and Physics*, vol. 283, Article ID 126001, 2022.

[15] A. Divya Sadhana, J. Udaya Prakash, P. Sivaprakasam, and S. Ananth, "Wear behaviour of aluminium matrix composites (LM25/Fly ash)–A Taguchi approach," *Materials Today: Proceedings*, vol. 33, pp. 3093–3096, 2020.

[16] P. Sivaprakasam, A. Kirubel, G. Elias, P. Maheandera Prabu, and P. Balasubramani, "Mathematical modeling and analysis of wear behavior of AlTiN coating on titanium alloy (Ti-6Al-4V)," *Advances in Materials Science and Engineering*, vol. 2021, Article ID 1098605, 9 pages, 2021.

[17] P. Sivaprakasam, G. Elias, P. Maheandera Prabu, and P. Balasubramani, "Experimental investigations on wear properties of AlTiN coated 316LVM stainless steel," *Materials Today: Proceedings*, vol. 33, pp. 3470–3474, 2020.

[18] M. K. Hassanzadeh-Aghdam, M. J. Mahmoodi, and J. Jamali, "Effect of CNT coating on the overall thermal conductivity of unidirectional polymer hybrid nanocomposites," *International Journal of Heat and Mass Transfer*, vol. 124, pp. 190–200, 2018.

[19] C. Yang, S. Song, F. Chen, and N. Chen, "Fabrication of PVDF/BaTiO3/CNT piezoelectric energy harvesters with

bionic balsa wood structures through 3D printing and supercritical carbon dioxide foaming," *ACS Applied Materials & Interfaces*, vol. 13, no. 35, pp. 41723–41734, 2021.

[20] Z. Ye, J. Li, L. Liu, F. Ma, B. Zhao, and X. Wang, "Microstructure and wear performance enhancement of carbon nanotubes reinforced composite coatings fabricated by laser cladding on titanium alloy," *Optics & Laser Technology*, vol. 139, Article ID 106957, 2021.

[21] N. Radhika and R. Raghu, "Influence of parameters on sliding wear of titanium nitride coated 6061 aluminium alloy," *Tribology in Industry*, vol. 40, no. 2, pp. 203–212, 2018.

Hindawi
Advances in Materials Science and Engineering
Volume 2023, Article ID 8033881, 9 pages
https://doi.org/10.1155/2023/8033881

Research Article

Microfriction Stir Welding of Aluminium Using ABB IRB 1410 Robot

R. Manoj Samson,[1] **R. Aravind**,[1] **Solomon Jenoris Muthiya**,[2] **Joshuva Arockia Dhanraj**,[3] **Karthikeyan Velmurugan**,[4,5] **and Saw Lin Oo**[6]

[1]*Department of Mechanical Engineering, SRM Institute of Science and Technology, Kattankulathur, Chennai 603203, India*
[2]*Department of Automobile Engineering, Dayananda Sagar College of Engineering, Bengaluru, Karnataka 560078, India*
[3]*Centre for Automation and Robotics (ANRO), Department of Mechatronics Engineering, Hindustan Institute of Technology and Science, Padur, Chennai 603103, India*
[4]*Center for Alternative Energy Research and Development, Khon Kaen University, Khon Kaen, Thailand*
[5]*Mechanical Engineering Division, Faculty of Engineering, Khon Kaen University, Khon Kaen, Thailand*
[6]*Department of Physics & Universities' Research Centre, University of Yangon, Yangon, Myanmar*

Correspondence should be addressed to Solomon Jenoris Muthiya; jenoris.555@gmail.com and Saw Lin Oo; kosawlinoo@gmail.com

Received 7 August 2022; Revised 22 November 2022; Accepted 13 April 2023; Published 9 May 2023

Academic Editor: R. Thanigaivelan

Industry 4.0 industries are relying on automation processes using robots. Robots are multifunctional reprogrammable machines tuned to be used in any process with high accuracy and repeatability. The advent of intelligent technology allows better precision in the welding process. One such robotic welding process is the robot microfriction welding process which is slowly replacing conventional ones. Robot microfriction stir welding (RMFSW) process mainly relays on friction between the tool and material making it more suitable for joining metals in the industries such as automotive and aerospace applications. The robot-assisted MFSW process can provide better joints without human intervention. In this work, a shrinking flange has been designed and fabricated to grip the end effector with the robot. A microfriction stir welding tool was manufactured using EN24 and used to weld 1 mm thin aluminium 1100 sheets. Both the flange and MFSW tools were designed in SOLIDWORKS software. Taguchi *L9* was designed with three factors such as motor speed, traverse speed, and plunging depth. The robot microfriction stirs welded samples had controlled bead width and depth of penetration. Mechanical results show an improvement in hardness after the welding process. TOPSIS optimization technique was carried out. The motor speed of 20,000 rpm, traverse speed of 2 mm/sec, and plunge depth of 0.7 mm were found to be the best-optimized parameters.

1. Introduction

One of the unique challenges in producing compact products is the making of small and microcomponents. Especially, joining materials of 1000 μm or below it is a difficult process. This microjoining process can be achieved through highly accurate and precise automated robots. Micromanufacturing using industrial robots is possible by designing a special-purpose gripper tool for a particular process. One such microjoining process is microfriction stir welding (MFSW), which was developed in the welding institute by Wayne Thomas. It is an eco-friendly and solid-state welding process [1]. Solid-state welding is a process of joining two metals or alloys by producing friction between the tool and the base materials. The same method is followed in microfriction stir welding where the dimensions are reduced to a micron level. A tool made of a solid rod tougher than the base material is used in microfriction stir welding. The hard MFSW tool is made of a pin and shoulder that is to be rotated at greater velocity and simultaneously moved

through metals to join it by creating moderate heat and friction [2, 3]. Since MFSW is a solid-state process based on friction it produces low-level heat compared to other welding processes. It produces good-appearance welds with low distortion, at a relatively low cost. The only disadvantage of this technique has been its exit keyhole. MFSW is very useful in applications such as welding of complicated products like thin-walled structures, battery covers, and electrical and electronic components [4–6]. The μFSW process has four phases which is conducted in the order mentioned in Figure 1. Some of the principal process parameters of microfriction stir welding are the rotational speed of the tool, forward velocity of the tool and plunge depth. The torque or rotational force of the tool decides the frictional force between the tool and the material which transports the metal around the tool in the plastic zone. This parameter is important to produce the friction at the shoulder of the tool which gives the welding finish [7–9]. Traverse movement of the tool is essential to make the material move around the tool and move it forward. Plunge depth is decided by the thickness of the material. For example, for a sheet with a 1 mm thickness, the maximum plunge depth can be up to 0.9 mm [10]. It is very difficult to carry out fusion welding in a 1 mm sheet due to metallurgical problems and distortion. MFSW is utilized to carry out welding without distortion [11–13]. The disadvantage of the MFSW process is that it has a keyhole at the last stage, this technique is very scale-sensitive so high precision and accuracy are needed. The major advantage in the MFSW process compared to microresistance welding is that the joints are made at lower temperatures without any need of fluxes, gas, or consumable electrodes automatically reducing the risk of contamination or cleaning delicate components. This avoids the need of postwelding treatments which consequently reduces the welding cost. Mahidhar et al. has done TOPSIS optimization for laser-welded haste alloys [14].

The objective of this work is to carry out RMFSW process in aluminum 1100 using ABB IRB 1410 robot. In order to achieve the process a motor with high torque capacity is used as an end effector for the robot. A microfriction stir welding tool has been designed and manufactured in EN24 material. In this project, we are designing and manufacturing a special-purpose shrinking flange to grip the Makita RT0700C alternating current motor to the ABB IRB 1410 Project plan is shown in Figure 1. The aluminum 1100 is welded using RMFSW. The optimization of process parameters of the RMFSW was done using TOPSIS optimization.

2. Experimental Details

Aluminum 1100 alloy of 1 mm thin sheets with a dimension of $70 * 35$ mm was used throughout this study. The composition of Aluminium 1100 alloy is shown in Table 1.

2.1. Design of the Robotic Gripper. A special type of shrinking flange has been designed in SOLIDWORKS software and manufactured in H30 material to withhold the Makita RT0700C motor. Microfriction stir welding tool has been designed in SOLIDWORKS software and manufactured using EN24 material.

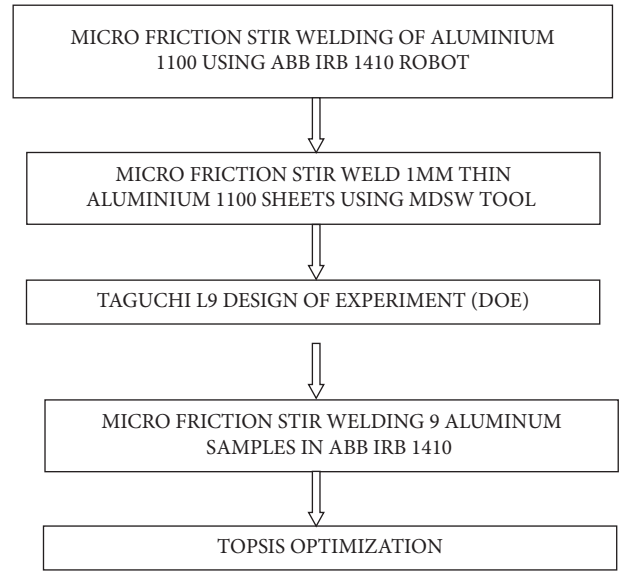

Figure 1: Robot microfriction stir welding.

2.2. Design of Backing Plate. The backing plate was designed in SOLIDWORKS to use in any type of welding process. It is manufactured in mild steel material and the whole setup is coated with blackening powder to prevent rust. The model is designed to act as a backing block and also as a shielding gas provider below the sheets. Turning it upside down it also can be used for RFSW process. The SOLIDWORKS design of the Backing plate is presented and the manufacturing block is presented in Figure 2.

2.3. Design of Microfriction Stir Welding Tool. The tool was designed in SOLIDWORKS software and the tool material was decided by considering workpiece material. In this work, aluminium 1100 alloy was chosen as a work piece material which has a hardness value of 144 HB. MFSW tool was selected based on a higher hardness value than the base material since our aluminum is a soft material. EN24 was chosen as MFSW tool with a hardness value of 248 HB. The tool was designed by considering the bending moment in the account so to reduce it a step-by-step cut design is used (Figure 3).

ABB IRB 1410 robot was used in this project to do the microfriction stir welding process with aid of Makita RT0700C AC motor and specially designed microfriction stir welding tool. The welding setup is shown in Figure 4.

The robot MFSW was done based on the *L9* Taguchi array by considering three levels of factors named as M = Motor speed (RPM), T = Traverse speed (mm/Sec) and P = Plunging depth (mm). Table 2 shows three levels of parameters with three factors.

The *L9* Taguchi design of the experiments table with both input and output parameters is mentioned in Table 3, where DOP, is the depth of penetration, and BW is bead width.

Table 1: Chemical composition of Al 1100 alloy.

Elements	Aluminium (Al)	Copper (Cu)	Iron (Fe)	Manganese (Mn)	Zinc (Zn)	Residuals
Components	99.0–99.95%	0.05–0.20%	0.95% max	0.05% max	0.1% max	0.15% max

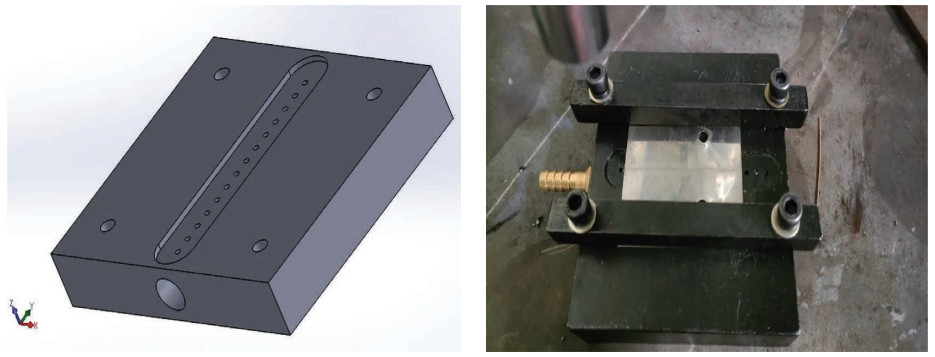

(a) (b)

Figure 2: Backing plate design solid works (a) and manufactured block (b).

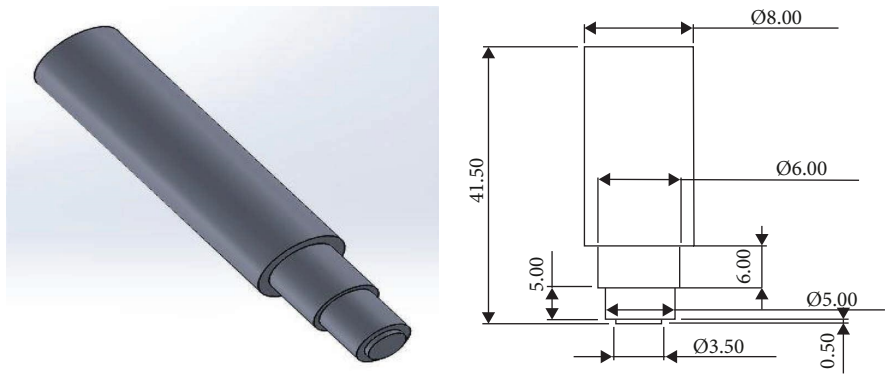

(a) (b)

Figure 3: Microfriction stir welding tool design (a) and tool dimensions (b).

The robot microfriction stir welded (RMFSW) 1 mm thin sheets of aluminium 1100 alloy sheets are shown in Figure 5.

After the RMFSW process, the welded specimen were cut down into 10 × 10 mm samples using the wire-EDM method and then cold-mounted. The cold-mounted samples were polished using emery sheets and the disc was polished using diamond paste. Further, the samples were etched using Keller's reagent [150 ml H_2O, 3 ml HNO_3, and 6 ml HF] for 20 seconds. Macrostructure was taken using a machine vision system and microhardness testing was carried out in a micro-Vickers hardness tester with the model number of HMV-G made by Shimadzu.

3. Results and Discussion

3.1. Macrostructure. The macrostructure of the welded samples is taken from the machine vision system. BW and DOP of the samples are measured using VMS 3.1 software. Measured values are tabulated below. All the samples have achieved a bead width of 3.5 mm approximately and the samples have achieved the applied depth of penetration with a variation of ±0.02 mm. Sample images are revealed in Figure 6 and (see Tables 4 and 5).

3.2. Microhardness. Microhardness test was carried out in Vickers hardness tester. The values are taken in the interval of 10 mm on either side of the weld zone and on the weld zone. The average microhardness values of the welded samples are tabulated below. Samples 7, 8, and 9 had the highest hardness of 43 HV.

3.3. Optimization (TOPSIS). TOPSIS stands to be a technique for order preference by similarity to the ideal solution which is a common technique that has been used in automobile industries for decision making. This technique has six stages as follows:

Stage I: Determination of a Performance Matrix

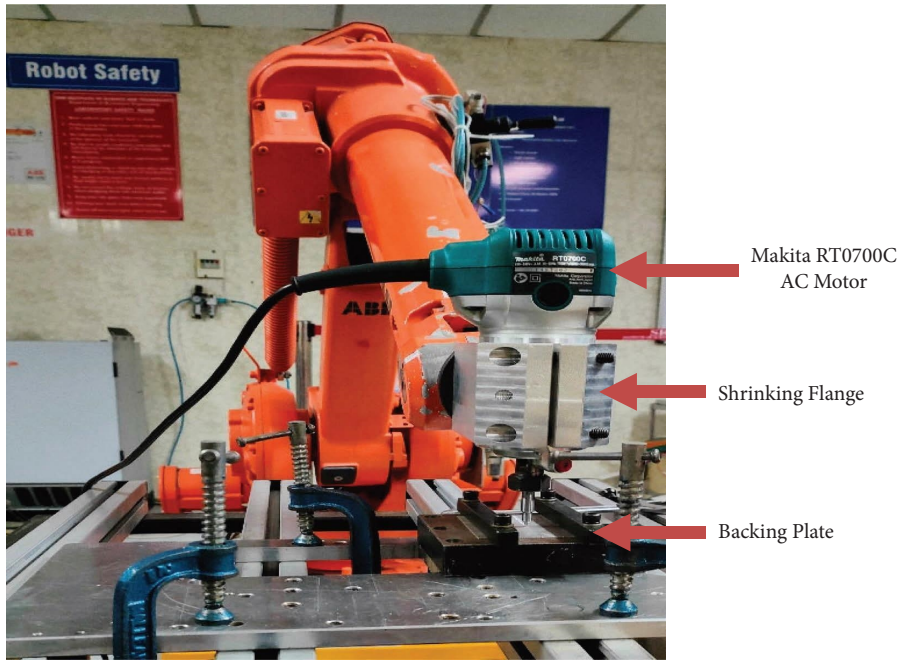

Figure 4: Robot microfriction stir welding setup.

Table 2: Level of parameters.

Factors	*L*1	*L*2	*L*3
M (RPM)	10,000	16,000	20,000
T (mm/Sec)	1	2	3
P (mm)	0.5	0.6	0.7

Table 3: *L9* input and output parameters.

	Input parameters			Output parameters		
Sample no	Motor speed (RPM)	Traverse speed (mm/Sec)	Plunging depth (mm)	DOP (mm)	BW (mm)	Hardness (Hv)
1	10000	1	0.5	0.4989	3.48	42.3
2	10000	2	0.6	0.602	4.42	42
3	10000	3	0.7	0.7233	4.45	42
4	16000	1	0.6	0.5936	4.43	41.3
5	16000	2	0.7	0.7103	4.48	42.6
6	16000	3	0.5	0.4852	3.47	42.3
7	20000	1	0.7	0.7713	4.45	43
8	20000	2	0.5	0.4731	3.43	43.3
9	20000	3	0.6	0.584	4.49	43.3

Stage II: Calculation of Normalized Decision Matrix

Stage III: Calculate Weighted Normalized Decision Matrix

Stage IV: Determination of the Ideal (D_i^+) and (D_i^-)

Stage V: Calculate the Euclidian Distance between Ideal (D_i^+) and Ideal (D_i^-)

Stage VI: Determine the Relative Performance Closeness to the Ideal Soln.

In this project, depth of penetration and hardness is considered to be larger the better criteria whereas bead width is considered to be smaller the better criteria.

Stage I: Determination of a Performance Matrix

Calculate the sum of squares for DOP, BW, and microhardness to calculate the performance matrix. The performance matrix of the above-mentioned parameters is shown in Table 6.

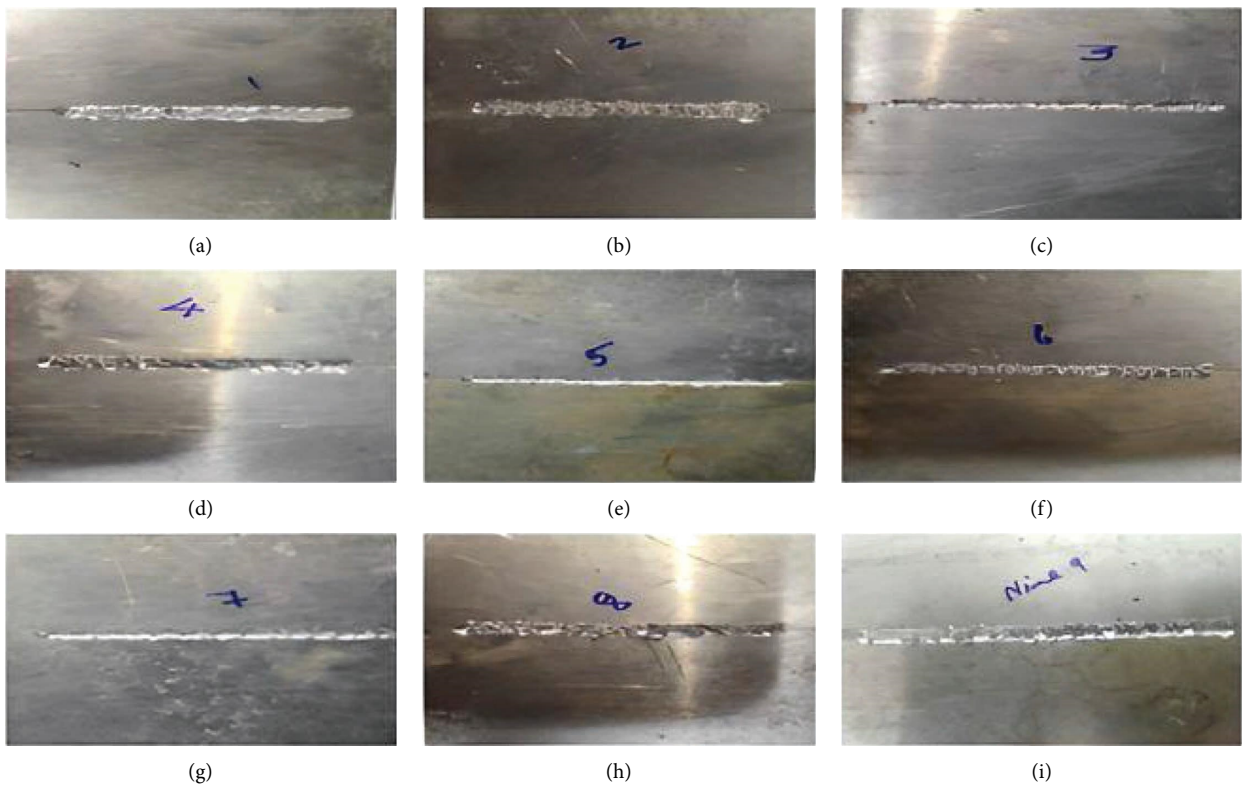

(a) (b) (c)

(d) (e) (f)

(g) (h) (i)

Figure 5: Robot microfriction stir welded *L*9 samples.

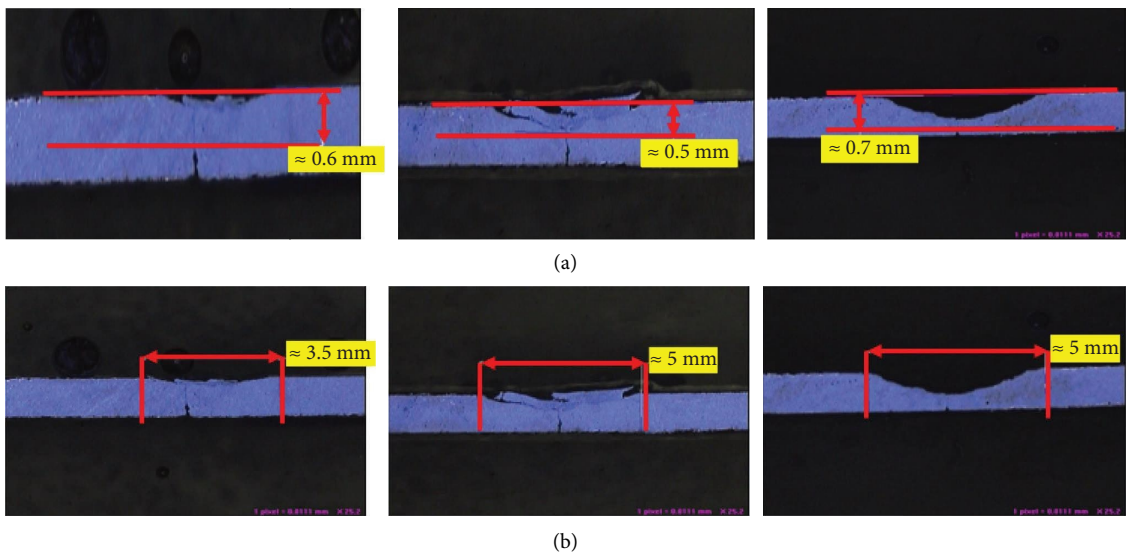

Figure 6: MFSW samples macrostructure: (a) depth of penetration and (b) bead width.

Table 4: DOP and BW of MFSW samples.

Sample no	DOP (mm)	BW (mm)
1	0.4989	3.48
2	0.602	4.42
3	0.7233	4.45
4	0.5936	4.43
5	0.7103	4.48
6	0.4852	3.47
7	0.7713	4.45
8	0.4731	3.43
9	0.584	4.49

Table 5: Microhardness of welded samples.

Sample no	Hardness (Hv)
1	42.3
2	42
3	42
4	41.3
5	42.6
6	42.3
7	43
8	43.3
9	43.3

Table 6: Performance matrix.

Sample no	DOP (mm)	BW (mm)	Hardness (Hv)
1	0.4989	3.48	42.3
2	0.602	4.42	42
3	0.7233	4.45	42
4	0.5936	4.43	41.3
5	0.7103	4.48	42.6
6	0.4852	3.47	42.3
7	0.7713	4.45	43
8	0.4731	3.43	43.3
9	0.584	4.49	43.3
SOS	**3.386557**	**154.913**	**16225.81**

Bold value is the maximum threshold of the values.

Stage II: Calculation of Normalized Decision Matrix

Equation (1) is used to calculate Normalized Decision Matrix. Table 7 shows the corresponding values.

$$U_{ij} = \frac{x_{ij}}{\sqrt{\left(\sum x_{[i]j}^2\right)}}. \quad (1)$$

Stage III: Calculate Weighted Normalized Decision Matrix

Weights are allocated to output parameters based on optimization techniques. Weights are distributed equally in percentage to the input parameters. So, 0.35, 0.3, and 0.35 has been selected as equal percentage weight for the input parameters. Corresponding values are mentioned in Table 8 and the matrix is shown in Table 9.

We can calculate the weighted normalized matrix,

$$B_{ij} = M_{ij} \times N_{ij}. \quad (2)$$

Stage IV: Determination of the Ideal (D_i^+) and (D_i^-)

Table 10 reveals ideal worst and best numbers.

Ideal Positive Soln. = P_j^+ (min or max).

Ideal Negative Soln. = P_j^- (min or max).

Stage V: Calculate the Euclidian Distance between Ideal (D_i^+) and Ideal (D_i^-)

Euclidian Distance values calculated using equations (3) and (4) are shown in Table 11.

Table 7: Normalized decision matrix.

Sample no	DOP (mm)	BW (mm)	Hardness (Hv)
1	0.271103	0.279599	0.332076
2	0.327128	0.355123	0.329721
3	0.393042	0.357533	0.329721
4	0.322563	0.355926	0.324225
5	0.385978	0.359943	0.334431
6	0.263658	0.278795	0.332076
7	0.419126	0.357533	0.337571
8	0.257083	0.275582	0.339926
9	0.317346	0.360747	0.339926

Table 8: Weighted matrix.

Depth of penetration (mm)	Bead width (mm)	Hardness (Hv)
0.35	0.3	0.35

Table 9: Weighted normalized decision matrix.

Sample no	DOP (mm)	BW (mm)	Hardness (Hv)
1	0.094886	0.08388	0.116227
2	0.114495	0.106537	0.115402
3	0.137565	0.10726	0.115402
4	0.112897	0.106778	0.113479
5	0.135092	0.107983	0.117051
6	0.09228	0.083639	0.116227
7	0.146694	0.10726	0.11815
8	0.089979	0.082674	0.118974
9	0.111071	0.108224	0.118974

Table 10: Determination of ideal (D_i^+) and ideal (D_i^-).

	DOP (mm)	BW (mm)	Hardness (Hv)
$B+$	0.146694	0.082674	0.118974
$B-$	0.089979	0.108224	0.113479

Table 11: Euclidian distance between ideal (D_i^+) and ideal (D_i^-).

Sample no	E_i^+	E_i^-
1	0.051895	0.024985522
2	0.040236	0.024648703
3	0.026468	0.047634276
4	0.041874	0.02296354
5	0.027907	0.045255018
6	0.054491	0.024845285
7	0.024599	0.056915002
8	0.056715	0.02613385
9	0.043838	0.021796252

Table 12: Relative performance closeness to ideal solution.

Sample no	Pi	Rank
L1	0.324993	7
L2	0.379883	4
L3	0.642820	2
L4	0.354173	5
L5	0.618556	3
L6	0.313163	9
L7	0.698222	1
L8	0.315441	8
L9	0.332087	6

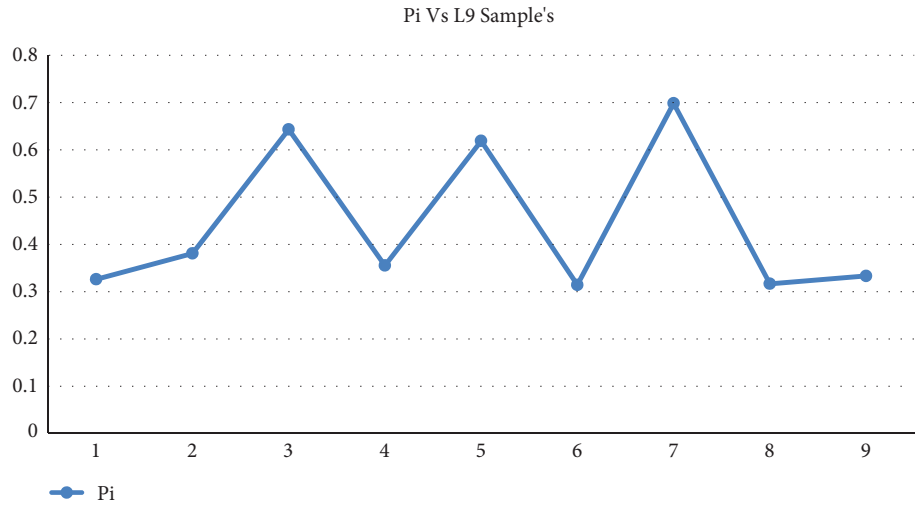

Figure 7: Pi vs. *L9* samples.

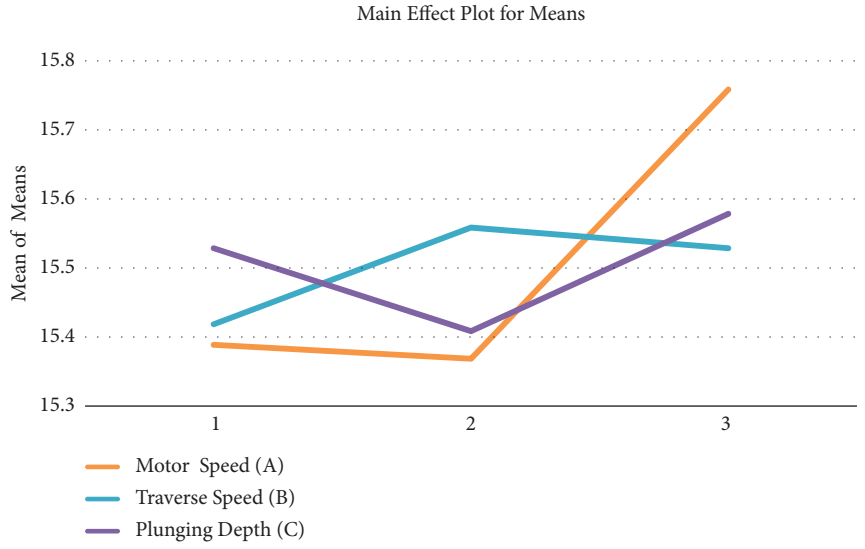

Figure 8: Main effect plot of input parameters.

Table 13: Response table.

Level	Motor speed (A)	Traverse speed (B)	Plunging depth (C)
1	15.39	15.42	15.53
2	15.37	**15.56**	15.41
3	**15.76**	15.53	**15.58**
Delta	0.38	0.13	0.16
Rank	1	3	2

Bold value is the maximum speed attained.

Table 14: Optimized parameter combination.

Factors	Initial values	Optimized parameters	
Setting level	$A_1\ B_1\ C_1$	Prediction $A_3\ B_2\ C_3$	Experiment $A_3\ B_2\ C_3$
DOP (mm)	0.4989	—	0.70012
BW (mm)	3.48	—	3.5
Hardness (HV)	42.3	—	43.3
Pi	0.324993	0.402025	0.410251

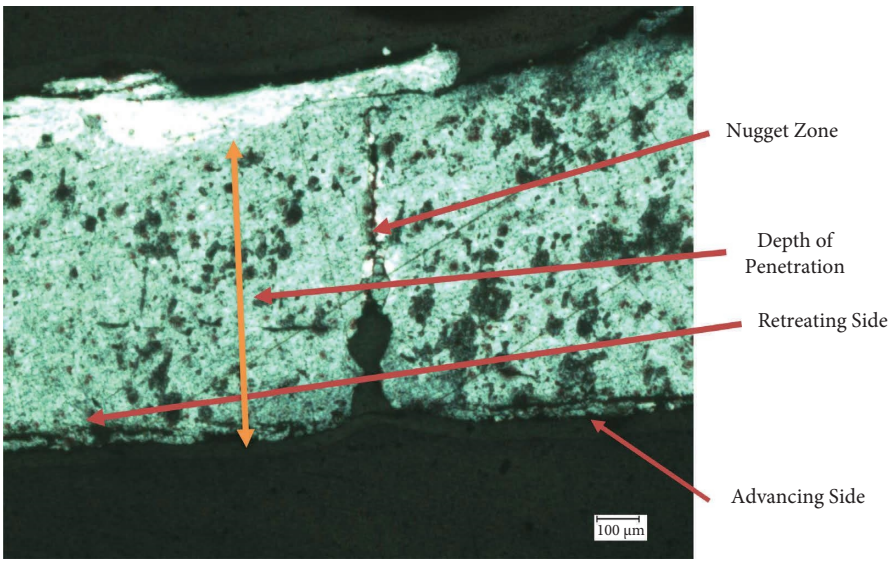

Figure 9: Microstructure of optimized sample.

$$E_i^+ = \left[\sum \left(D_i^+ - B_{ij}\right)^2\right]^{0.5}, \tag{3}$$

$$E_i^- = \left[\sum \left(D_i^- - B_{jj}\right)^2\right]^{0.5}. \tag{4}$$

Stage VI: Determine the Relative Performance Closeness to the Ideal Soln.

$$P_i = \frac{E_i^-}{E_i^+ + E_i^-}. \tag{5}$$

Table 12 reveals relative performance closeness and its rank.

Figure 7 shows graphical representation of Pi (closeness value) vs. $L9$ samples.

3.3.1. Response Value Table Using Closeness Value. $A_3\ B_2\ C_3$ was found to be the best optimal parameter in the Taguchi $L9$. Motor speed had the highest influence on input parameters followed by plunge depth and traverse speed, respectively. Figure 8 shows the best optimal level of the parameter (see Table 13).

The mean line was found around 15.5 above this point all the input good results but our optimal level was found to be out of $L9$ so a confirmatory test was done.

3.3.2. Confirmation Test. In order to find the optimized parameter set Pi value was predicted using the following equation:

$$[ee] = h_{m+} \sum (h - h_m), \tag{6}$$

where h_m average of Pi values, h is the mean of Pi values at the optimum level. The optimized parameters are presented in Table 14.

The experiment was done again using predicted values and the optimal parameter combination is found with DOP = 0.7 mm; BW = 3.5 mm; and hardness = 43.3 HV. Figure 9 shows the microstructure of the optimized parameter.

4. Conclusion

(1) Robot microfriction stir welding (RMFSW) of 1 mm thin aluminum 1100 sheets was successfully done using ABB IRB 1410 robot.

(2) *L*9 Taguchi was designed with three factors and three levels.

(3) In microstructure analysis, the weld zone had a fine grain structure, which increases the hardness value of the material.

(4) Microhardness seemed to be higher after the welding process which has increased up to 43.3 HV.

(5) In TOPSIS sample number 7 had the highest rank compared to all other samples. Sample 7 has input parameters such as motor speed = 20000 rpm; traverse speed = 1 mm/sec; and depth of penetration = 0.7 mm. It had a dop of 0.7 mm; a bead width of 3.45; and a hardness of 43 HV.

(6) A confirmation test was carried out and $A_3B_2C_3$ was found to be the best optimal input parameter.

(7) Motor speed is found to be the most influencing parameter among all three, succeeded by plunge depth and traverse speed, respectively.

Data Availability

The data used to support the findings of this study are made available from the corresponding author upon request.

Conflicts of Interest

The authors declare that they have no conflicts of interest.

References

[1] M. Simoncini, D. Ciccarelli, A. Forcellese, and M. Pieralisi, "Micro-and macro-mechanical properties of pinless friction stir welded joints in AA5754 aluminium thin sheets," *Procedia Cirp*, vol. 18, pp. 9–14, 2014.

[2] B. T. Gibson, D. H. Lammlein, T. J. Prater et al., "Friction stir welding: process, automation, and control," *Journal of Manufacturing Processes*, vol. 16, no. 1, pp. 56–73, 2014.

[3] K. Wang, F. Léonard, and G. Abba, "Dynamic model identification of axial force in robotic friction stir WeldingÕ," *IFAC-PapersOnLine*, vol. 48, no. 3, pp. 1936–1941, 2015.

[4] M. Guillo and L. Dubourg, "Impact & improvement of tool deviation in friction stir welding: weld quality & real-time compensation on an industrial robot," *Robotics and Computer-Integrated Manufacturing*, vol. 39, pp. 22–31, 2016.

[5] J. Qin, F. Léonard, and G. Abba, "Real-time trajectory compensation in robotic friction stir welding using state estimators," *IEEE Transactions on Control Systems Technology*, vol. 24, no. 6, pp. 2207–2214, 2016.

[6] K. Sithole and V. V. Rao, "Recent developments in micro friction stir welding: a review," *IOP Conference Series: Materials Science and Engineering*, vol. 114, no. 1, Article ID 012036, 2016, February.

[7] Y. Huang, X. Meng, Y. Zhang, J. Cao, and J. Feng, "Micro friction stir welding of ultra-thin Al-6061 sheets," *Journal of Materials Processing Technology*, vol. 250, pp. 313–319, 2017.

[8] J. A. Joy, M. Sajjad, and D. W. Jung, "Design and fabrication of friction stir welding machine," in *MATEC Web of Conferences*, vol. 207, EDP Sciences, Article ID 03022, 2018.

[9] Y. Sagheer-Abbasi, S. Ikramullah-Butt, G. Hussain, S. H. Imran, A. Mohammad-Khan, and R. A. Baseer, "Optimization of parameters for micro friction stir welding of aluminum 5052 using Taguchi technique," *The International Journal of Advanced Manufacturing Technology*, vol. 102, no. 1-4, pp. 369–378, 2019.

[10] H. Luo, J. Fu, L. Jiao, G. Liu, C. Yu, and T. Wu, "KiNematics and dynamics analysis of a new-type friction stir welding robot and its simulation," *Advances in Mechanical Engineering*, vol. 11, no. 7, Article ID 168781401986651, 2019.

[11] K. N. Salloomi, F. I. Hussein, and S. N. Al-Sumaidae, "Temperature and stress evaluation during three different phases of friction stir welding of AA 7075-T651 alloy," *Modelling and Simulation in Engineering*, vol. 2020, Article ID 3197813, 11 pages, 2020.

[12] M. Sen, S. Shankar, and S. Chattopadhyaya, "Micro-friction stir welding (μFSW)–A review," *Materials Today: Proceedings*, vol. 27, pp. 2469–2473, 2020.

[13] P. Zolghadr, M. Akbari, and P. Asadi, "Formation of thermomechanically affected zone in friction stir welding," *Materials Research Express*, vol. 6, no. 8, Article ID 086558, 2019.

[14] V. Mahidhar, K. R. Sampreet, R. Kannan, and T. D. B. Kannan, "Parameter optimization in laser welding of Hastelloy C-276 using TOPSIS," *Materials Today: Proceedings*, vol. 21, pp. 595–600, 2020.

Hindawi
Advances in Materials Science and Engineering
Volume 2023, Article ID 2219460, 7 pages
https://doi.org/10.1155/2023/2219460

Research Article

Evaluation of Mechanical Behaviour of Multiwalled Nanotubes Reinforcement Particles in Jute-Glass Fibres Hybrid Composites

S. Kaliappan,[1] T. Mothilal,[2] P. Pravin,[3] B. Raja Bharathi,[4] and E. S. Esakkiraj[5]

[1]*Department of Mechanical Engineering, Velammal Institute of Technology, Chennai-601204, Tamil Nadu, India*
[2]*Department of Automobile Engineering, KCG College of Technology, KCG Nagar, Karapakkam, Chennai-600097, Tamil Nadu, India*
[3]*Department of Mechanical Engineering, Graphic Era Deemed to be University, Bell Road, Clement Town 248002, Dehradun, Uttarakhand, India*
[4]*Department of Mechanical Engineering, Saveetha School of Engineering, SIMATS, Chennai-602105, Tamil Nadu, India*
[5]*Department of Mechanical Engineering, Dambi Dollo University, Dambi Dollo, Ethiopia*

Correspondence should be addressed to E. S. Esakkiraj; essakkiraj@dadu.edu.et

Received 26 August 2022; Revised 11 December 2022; Accepted 12 April 2023; Published 26 April 2023

Academic Editor: R. Thanigaivelan

Fibre-reinforced polymers (FRPs) are composite materials of plastics reinforced with fibres. Cars, sea, aeronautics, and foundation projects progressively utilize fibre-reinforced polymers. This study aims to study the effect of adding multiwalled nanotubes fillers into the hybridized jute-glass FRP composites and their relative properties. This study uses multiwalled nanotubes (MWCNTs), and particles-hybrid jute-glass composites containing jute fibre chopped layer mats, woven glass mats, epoxy resin, and multiwalled nanotubes fillers were created using the hand layup method. After adding multiwalled nanotubes fillers in various weight proportions, the mechanical behaviours of fibre-reinforced polymers were analysed. The mechanical behaviours of laminated composites were tested using the ASTM standard; the following properties are tensile, flexural, and impact strength. The multiwalled nanotubes with 6% wt. attained the maximum mechanical properties compared to the 2 and 4 wt. % of MWCNTs. The E-based specimen contributes the most to the different types of specimens, with a contribution of 24.21% for tensile, 25.03% for flexural, and 24.56% for impact. The microstructures of hybrid composites were studied using a scanning electron microscope.

1. Introduction

The usage of composite materials has developed at an inconceivable rate, and these materials currently have an astounding and different scope of utilization. Composites enjoy different upper hands over metallic materials, including lightweight, high fatigue tolerance, high resistance to corrosion, and low coefficient of thermal expansion and insulation. Polymer matrix composites (PMCs) cover excellent physical and thermal qualities, such as high specific toughness, toughness, and rust resistance. Aeroplanes, battleships, housing, cars, microelectronics components, and maritime construction are among the applications where they have emerged as viable alternatives to traditional metals [1, 2]. The materials utilized in the airframe of a Boeing 777 are 50% aluminium and 12% wt. of plastics. However, recently, 787 aircraft of Boeing are redesigned, 20 and 50% wt. Proportions among aluminium and plastics have been utilized, respectively. High firmness, crack strength execution, harm resilience levels, nonmagnetic properties, high thermal soundness, oxidation opposition, and short assembling energy utilization are only some of the advantages of fibre-reinforced polymer compounds [3, 4]. The most common artificial fibres are fibre glass-reinforced glass, polypropylene, and graphene. More robust and challenging fibres can be added to boost the strength and rigidity of polymer matrix composites. Fibre-reinforced composites have been majorly employed with their excellent qualities, namely high specific fracture toughness, tunable electrical conductivity, temperature resistance, high

fatigue barrier capabilities, and suitability for the manufacture of a variety of contour substances. Composite materials have replaced traditional architectural materials such as metals, hardwoods, and iron in various applications [5, 6]. Composites manufacture automobiles, aeroplanes, wind energy facilities, yachts, and warships, to name a few. Filler-reinforced underlying polymeric or thermoplastic composites have impacted the status quo made. They can now be found in bullet barriers, armament, percussion instruments, fashion items, and much more, in addition to air and ground vehicles, sports gear, and electronics. The requirement for materials of good physical qualities, in combination with lighter weight and low price, grows as demand grows [7].

Polymer-based nanocomposites have sparked a lot of attention in academia and business during the last two decades. This involves a never-ending search for novel ingredients, additives, and manufacturing techniques. The conventional technique is to find a connection that connects the reinforcement to the matrix and improves load transmission while causing little matrix fouling at the boundary, allowing fracture propagation during dynamic loads [8]. Nanostructured membranes comprised of polymer matrices and nanomaterials/nanofillers have caught the interest of researchers and industry in their application due to their increased qualities, resulting in high barrier packing for food and automotive and aviation gadgets. Compared to their standard microscopic and macroscopic or clean equivalents, they offer exceptional feature upgrades, such as enhanced thermal and mechanical properties, permeability resilience, and flame retardancy at various filler levels [9, 10]. Several polymer matrixes and nanoparticles have been examined in various combinations. The expansion of an unobtrusive measure of nanofiller has been displayed to employ on the polymer matrices with physical properties. The highlights of a polymeric-filled composite are affected by the following conditions: structure, content, size, and level of total filler, as well as how much matrix filler bonds. Nanomaterials as fillers generate a more extensive dynamic and interactive zone, which could result in substantially stronger matrices couplings and a superior end product.

Nanoparticles can also give nanocomposites unique properties such as electrical, photonic, magnetic, or transportation capacities, opening up many new opportunities for rapid technological advancement. In polymer-based composites, synergistic effects from combining distinct components contribute to better characteristics [11, 12]. These gains may be approximated in regular composites using mixing processes, but in nanocomposites, interface interactions between constituents become critical for determining bulk features. Microparticles or nanofillers of various types and sizes are strewn haphazardly in matrix materials to create particle polymer composites. Introducing multiwalled nanotubes and aluminium oxide nanoparticles in epoxy achieves maximum hardness, tear dulling, fracture deflecting, and fracture anchoring hardening processes. Due to matrix deformations, region buffering, void creation, particle-matrix delamination, and localised shearing band hardening mechanisms, the integration of nano-SiO_2 boosted mechanical properties and fracture durability with volume concentration. Nanostructured materials' biomechanical, physical, and chemical properties, particularly yield strength, are influenced by their formulation, constituent characteristics, architecture, and interface contact. When evaluating material properties, nanoparticle orientation should be considered if they have an anisometric topology. The maximum stress a material can withstand during uniaxial tensile stress is known as its strength. The effectiveness of stress transmission between the filler and the matrix impacts the intensity of a particle-filled composite. Nanoparticles made out of multiwalled nanotubes are presently one of the most intriguing compounds [13, 14]. After undergoing ultrasonic processing, the mechanical and absorption properties of polymeric composites with multiwalled nanotube nanoparticles and epoxy were compared to composite samples containing multiwalled nanotube microparticles and epoxy, as well as plain resin. The nanocomposites with reasonable nanoparticle scatterings at a stacking of 10 wt % showed a great mix of properties, including further developed sway opposition and flexibility, as well as upgrades in cyclic loading and swelling tolerance, all while keeping up with hardness. The nanofilled composites exhibited without improvements in abrasion resistance and a reduction in strain to disappointment when contrasted with the perfect pitch [15, 16].

This research aims to determine how the multiwalled nanotubes fillers affect the hybrid jute-glass composite's behaviours in terms of mechanical load-bearing effect. Since the natural fibres are coupled with glass, their properties must be studied. If the properties are above average to the expected level, the composites could be used as a functional material for many engineering applications. The following mechanical characteristics test tensile, bending, and impact were conducted and examined using the ASTM standard. The microstructural analysis was carried out using a scanning electron microscope. The composites were made using hand layup procedures.

2. Experimental Techniques

2.1. Materials and Methods. Multiwalled nanotubes particles with 50 nm of molecule size were utilized as filler material to change epoxy matrices. The 350 gsm monetarily accessible jute fibre cleave strand mat was utilized as a supporting material [17]. A 250 gsm woven glass mat with a typical thickness having 0.65 mm is utilized as a strengthened material. GVR fibre industry gave the jute and glass fibres as shown in Figure 1 mats in Madurai, Tamilnadu, and India [18]. The value of warp and Tex are maintained as 0.25 mm for each fabric, followed by the weaving as 1 m/2 h.

The multiwalled nanotubes filler was provided by Naga Chemical Ltd in Chennai, Tamilnadu, India. The reinforcement materials and multiwalled nanotubes fillers are revealed.

2.2. Alkaline Treating. The most remarkable change was produced through alkaline treatment, breaking the hydrogen bonds in the organization formation, which increments

Figure 1: Jute and glass fibres [18].

in surface roughness. When natural fibres are approached with reinforcement by thermoplastics and thermosets, alkaline treatment is also known as mercerization, commonly used as a chemical treatment process. During alkaline treatment, fibres are submerged in a NaOH medium for a particular measure. In this examination, the glass mat was dealt with artificially utilizing sodium hydroxide. Conventional glass was submerged in a treated steel container containing a 5% sodium hydroxide answer for four hours [17]. The fibre mats were then air-dried at room temperature.

2.3. Production of Hybrid Composites. The weight parts of the MWN particle fillers are mixed with fibre to build plastic material by increasing by 2 to 6%, contingent upon the mass of the little multiwalled nanotubes particles to a general load of the jute, glass, epoxy sap, and multiwalled nanotubes particles. Mechanical stirring was employed to mix the multiwalled nanotubes particle fillers into the epoxy resin, followed by the appropriate hardener to make the multiwalled nanotube mixed epoxy resin. The hybrid composites were made by hand layup and comprised three layers of glass, jute, and glass. The top and bottom layers were made of glass, while the middle layer was made of jute. A delivering specialist was initially applied to a level moulding to make the created half and hybrid fibre-supported plastics simpler to eliminate. Over the release chemical layer, a thick coating of nanoscale multiwalled nanotubes blended epoxy resin was applied. The mould's surfaces were then covered in a bottom layer of glass. The nanoscale multiwalled nanotubes blended epoxy resin was then sprayed and evenly spread with a brush onto the surface of the glass that had previously been placed in the mould. A roller was dragged across the bottom layer with little force or any trapped air. Once more, multiwalled nanotubes epoxy resin was applied. The experiment was repeated with the addition of a second interfacial layer of jute. Table 1 shows the list of parameters and their constraints of nanocomposites [18].

2.4. Mechanical Testing. For tensile testing, fabricated specimens are prepared per the ASTM D-638-03 with $150 \times 15 \times 3$ mm sizes. Similarly, the flexural and the impact were conducted and prepared as per the ASTM D-790 and ASTM D-256 standard having the dimensions 10 mm of width, 3 mm of thickness, and 125 mm of length and 12.7 mm of width, 3 mm of thickness, and 64 mm of length, respectively.

2.5. Scanning Electron Microscope (SEM). SEM was utilized to examine the cracked surfaces of fabricated composites before the specimen must be polished and dehydrated and surface coating prepared. During the coating, 10 nm gold particles were coated on the specimens to enhance the electrical conductivity of the fabricated composites.

3. Result and Discussion

The following session briefly discusses the mechanical goods such as flexural, tensile, and impact characteristics of polyester composites based on their input parameters.

3.1. Mechanical Performances of Hybrid Nanocomposites. The mechanical properties of glass-jute based multiwalled nanotubes filler composites, such as their tensile, flexural, and impact properties, are shown in Figure 2. According to this study, the weight% of nanoparticles is very close to the test results. The mechanical characterization of hybrid composites improved as the weight percentage of multiwalled nanotubes particles in the matrix mixture went up. The strength of the composite was affected by the interfacial layer's stiffness, the adhesion components' quality, and their static adherence strength. This will help move the stress and elastic deformation from the matrix to the fibres or fillers and from the fibres to the matrix [18, 19].

There are more interactions between nanomaterials than between microscopic composites. If the connection between the filler matrix and the particles is not strong enough, the particles will not be able to carry any of the material added from the outside. In this case, the strength of the composite cannot be greater than that of the simple matrix material. The filler and its matrix both have good strength, and the nanoparticle composites could have a higher elastic modulus than the matrix material. With the addition of nanocomposite filler particles, the mechanical properties of the processed hybrid composite get better. This is because there are more high-strength multiwalled nanotube filler particles and less epoxy in the matrix [20, 21]. The fact that the hybrid composite has more mechanical properties, such as flexural and impact, suggests that stresses are being transferred across the contact. The synergistic effect of multiwalled nanotubes filler particles, glass, jute, and epoxy improves the

Table 1: List of parameter and their levels of nanocomposites [18].

Specimen type	Woven glass fibre (vol. %)	Woven jute fibre (vol. %)	Epoxy matrix (vol. %)	Multiwalled nanotubes (vol. %)
A	0	0	100	0
B	30	7	63	0
C	30	7	61	2
D	30	7	59	4
E	30	7	57	6

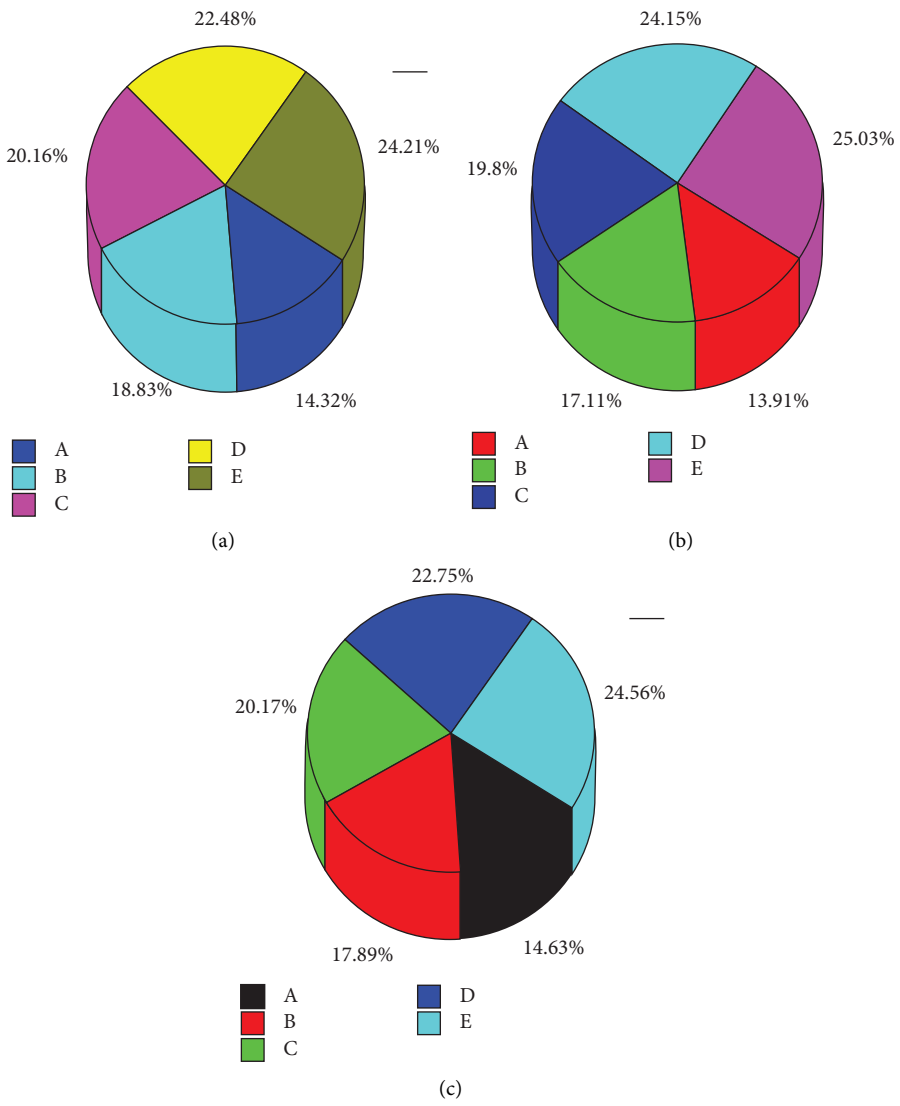

Figure 2: Different specimen contribution in % (a) tensile, (b) flexural, and (c) impact strength of hybrid nanocomposites.

overall mechanical properties of hybrid jute-glass hybrid composites.

When multiwalled nanotubes filler particles are used, the hybrid composite's mechanical properties improve significantly. With their hybrid composites, the tensile strength is 0% wt. Multiwalled nanotubes ranged from 58 MPa for the hybrid composites with no multiwalled nanotubes to 74 MPa for the hybrid composites with 6% multiwalled nanotubes. Flexural strength went from 98 MPa when no multiwalled nanotubes were present to 143 MPa when 6% multiwalled nanotubes were present. With 0% multiwalled nanotubes, the impact strength went up to 49 kg/m^2. With 6% multiwalled nanotubes, the impact strength went up to 67 kg/m^2. When nano multiwalled nanotubes filler particles are added to hybrid composites, they get stronger in all directions. Figures 2(a)–2(c) show how the different samples affect the mechanical properties.

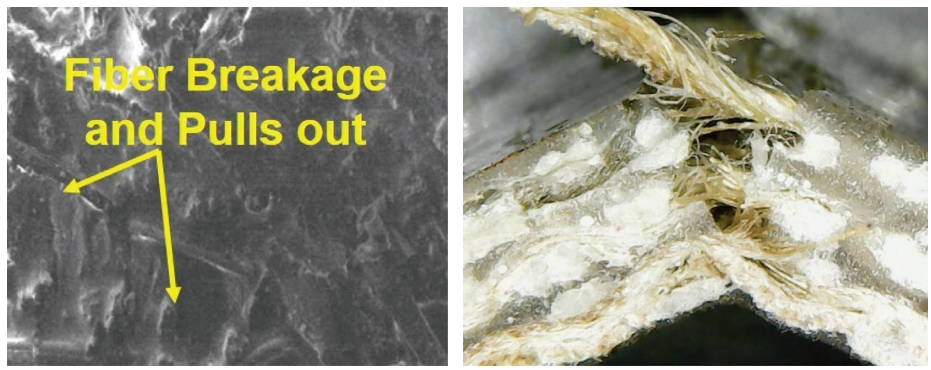

Figure 3: Optical macrostructure and SEM image of multiwalled nanotubes filled glass and jute based hybrid composites.

3.2. Morphological Analysis. The features of tensile surface flaws and the fibre-matrix contact were studied using scanning electron microscopy (SEM). Others have utilized this method to assess nanocomposites' stiffness modulus and durability. SEM micrographs of natural fibre-based nanocomposites after tensile fracture are shown in Figure 3. The dispersion of multiwalled nanotubes in the epoxy matrix is very consistent. The fillers are to form agglomerates on the processed specimens with maximum loadings. It is widely acknowledged that proper filler dispersion in the matrix is critical for optimal mechanical properties [17, 22, 23]. It is well known that as filler loading increases, so does the ability to agglomerate. Using a higher magnification, a single multiwalled nanotubes particle with longitudinal geometries may be observed. The aggregation of multiwalled nanotubes particles can be seen with the biggest ones being seen using the SEM.

In the literature, failure modes for conventional fibre-based polymerics have been identified as polymer pain, fibre breakage, and polymer and reinforcement adhesive catastrophe. Fibre pull-out rather than fracture could result from a weedy border or insufficient contact between fibre and matrix, decreasing mechanical characteristics. Depending on the nanocomposite's composition, numerous combinations of these failures were observed in this investigation. This sample of a nanocomposite with 6 wt. % multiwalled nanotubes was examined using a scanning electron microscope (SEM), and a typical micrograph was obtained. In the SEM photos [24], fibre pull-out and breaking may be seen. The interaction holes surrounding pull-out fibres increased as the organic resin concentration increased, indicating worse adhesion between the fibre and the biobased matrix. It is exhibited that the interface features of pull-out failures have been investigated. Nanocomposites containing 6 wt % multiwalled nanotubes had the same interfacial separation as nanocomposite. This demonstrates that reinforcing using multiwalled nanotubes does not influence the fibre-matrix interfacial bonding. Tensile tests back up the idea that a weaker interface leads to a more spectacular pull-out, as mechanical characteristics deteriorated as the amount of organic-based resin material increased (Figure 3). The fibre pulls allow more oomph to diffuse at the boundaries,

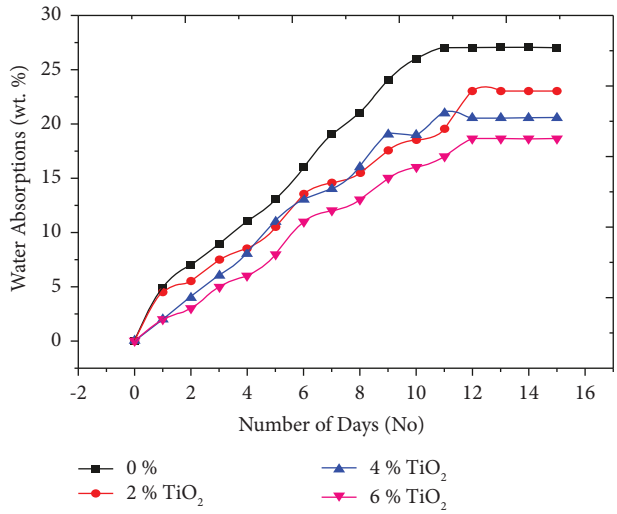

Figure 4: Water absorption behaviour of multiwalled nanotubes filled hybrid nanocomposites [18].

which correlates with improved impact characteristics and endurance during chemical-type epoxy treatment [16].

4. Water Absorption Behaviour

The moisture content of numerous composite materials is depicted in Figure 4 [18]. Water updating was significant initially for all composite materials, but it has subsequently become nearly constant and has declined in the final phase. According to the data, all composite materials show a substantial moisture absorption rate over extended periods. After the first day, moisture content ranged from 12 to 22%, rising to 12–38% for various composites formed. The hybrid nanocomposites constructed using multiwalled nanotubes had the highest proportion of water attraction of all the composite materials. This could be attributed to the hybrid nanocomposite's increased hydrophilic nature resulting in fibre mixing and MWN integration. The glass/jute with 6 wt. % multiwalled nanotubes (Model E) combination had the maximum water uptake values compared to the other composites.

This is owing to the high concentration of OH groups on glass fibre surfaces. The number of hydroxyl clusters and microvoids in glass/epoxy composites increased, which resulted in a significant increase in moisture fascination. The hybrid wood-glass combination absorbed the least water quantity [25–27]. On the other hand, the hydrophilic multiwalled nanotubes in the hybrid nanocomposite absorbed more moisture than the hybrid composite. The moisture absorption of the 6 wt. % multiwalled nanotubes filled hybrid composites is lower than that of the 0, 2, 4 wt. % multiwalled nanotubes filled hybrid composites. This is owing to adequate nanoparticle dispersion in the epoxy matrix mixture. It aids in the reduction of void formation and pushes the fibre out. This may aid in improving moisture absorption properties [28, 29, 30].

5. Conclusion

Jute fibre, glass mat, and epoxy resin with multiwalled nanotubes were employed to make multiwalled nanotubes particles composites. Multiwalled nanotubes composites were created, indicating nanocomposites might be used in various applications. The multiwalled nanotubes filler particles superior the tensile, flexural, and impact strength of the hybrid fibres strengthened polymers, according to mechanical outcomes. When compared to the 2, 4 % wt, MWN, multiwalled nanotubes with 6% wt. showed maximum mechanical strength. With contributions of 24.21 percent for tensile, 25.03 percent for flexural, and 24.56 percent for impact, the E-type specimen contributes the most to the various specimens. With 6 wt. % multiwalled nanotubes, the E-type specimen exhibits more excellent mechanical qualities when compared to other specimens A, B, C, and D kinds.

Data Availability

The data used to support the findings of this study are included within the article and are available from the corresponding author upon request.

Conflicts of Interest

The authors declare that there are no conflicts of interest.

References

[1] H. Alshahrani and V. Arun Prakash, "Mechanical, fatigue and DMA behaviour of high content cellulosic corn husk fibre and orange peel biochar epoxy biocomposite: a greener material for cleaner production," *Journal of Cleaner Production*, vol. 374, no. 2022, Article ID 133931, 2022.

[2] M. S. Chowdary, G. Raghavendra, M. S. R. N. Kumar, S. Ojha, and V. Boggarapu, "Influence of nano-silica on enhancing the mechanical properties of sisal/kevlar fiber reinforced polyester hybrid composites," *Silicon*, vol. 14, no. 2, pp. 539–546, 2022.

[3] S. Kaliappan, S. M. D. P. Nagarajan, and M. R. Kamal, "Analysis of an innovative connecting rod by using finite element method," *Taga Journal Of Graphic Technology*, vol. 14, pp. 1147–1152, 2018.

[4] M. Senthil Kumar, L. Natrayan, R. D. Hemanth, K. Annamalai, and E. Karthick, "Experimental investigations on mechanical and microstructural properties of Al2O3/SiC reinforced hybrid metal matrix composite IOP Conference Series: materials Science and Engineering," *IOP Conference Series: Materials Science and Engineering*, vol. 402, no. 1, Article ID 012123, 2018.

[5] V. A. Vincent, "Strength characterization of caryota urens fibre and aluminium 2024-t3 foil multi-stacking sequenced sic-toughened epoxy structural composite," *Biomass Conversion and Biorefinery*, vol. 12, pp. 1–11, 2020.

[6] M. M. Matheswaran, T. V. Arjunan, S. Muthusamy et al., "A case study on thermo-hydraulic performance of jet plate solar air heater using response surface methodology," *Case Studies in Thermal Engineering*, vol. 34, Article ID 101983, 2022.

[7] S. Sanjeevi, V. Shanmugam, S. Kumar et al., "Effects of water absorption on the mechanical properties of hybrid natural fibre/phenol formaldehyde composites," *Scientific Reports*, vol. 11, pp. 13385–13396, 2021.

[8] K. C. Manikandan Nair, S. Thomas, and G. Groeninckx, "Thermal and dynamic mechanical analysis of polystyrene composites reinforced with short sisal fibres," *Composites Science and Technology*, vol. 61, no. 16, pp. 2519–2529, 2001.

[9] N. Merah and O. Mohamed, "Nanoclay and water uptake effects on mechanical properties of unsaturated polyester," *Journal of Nanomaterials*, vol. 2019, Article ID 8130419, 11 pages, 2019.

[10] V. Fiore, T. Scalici, and A. Valenza, "Effect of sodium bicarbonate treatment on mechanical properties of flax-reinforced epoxy composite materials," *Journal of Composite Materials*, vol. 52, no. 8, pp. 1061–1072, 2018.

[11] R. P. Singh and P. Aggarwal, "Effect of nanosilica on the properties of cement mortar," *Cem. Int.*vol. 13, pp. 65–70, 2015.

[12] E. I. Akpan, X. Shen, B. Wetzel, and K. Friedrich, *Design and Synthesis of Polymer Nanocomposites*, Woodhead Publishing, Sawston, UK, 2018.

[13] G. Raghavendra, S. Ojha, S. K. Acharya, and S. K. Pal, "Influence of micro/nanofiller alumina on the mechanical behavior of novel hybrid epoxy nanocomposites," *High Performance Polymers*, vol. 27, no. 3, pp. 342–351, 2015.

[14] F. Perreault, A. Fonseca De Faria, and M. Elimelech, "Environmental applications of graphene-based nanomaterials," *Chemical Society Reviews*, vol. 44, no. 16, pp. 5861–5896, 2015.

[15] J. Datta, P. Kosiorek, and M. Włoch, "Effect of high loading of titanium dioxide particles on the morphology, mechanical and thermo-mechanical properties of the natural rubber-based composites," *Iranian Polymer Journal (English Edition)*, vol. 25, no. 12, pp. 1021–1035, Iran, 2016.

[16] G. Seshanandan, D. Ravindran, and T. Sornakumar, "Mechanical properties of nano titanium oxide particles - hybrid jute-glass FRP composites," *Materials Today: Proceedings*, vol. 3, no. 6, pp. 1383–1388, 2016.

[17] V. Arun prakash and A. Rajadurai, "Inter laminar shear strength behavior of acid, base and silane treated E-glass fibre epoxy resin composites on drilling process," *Defence Technology*, vol. 13, pp. 40–46, 2017.

[18] C. R. Mahesha, R. Suprabha, M. S. Harne et al., "Mebratu markos, "nanotitanium oxide particles and jute-hemp fiber hybrid composites: evaluate the mechanical, water absorptions, and morphological behaviors"," *Journal of Nanomaterials*, vol. 2022, Article ID 3057293, 7 pages, 2022.

[19] L. Natrayan, S. Kaliappan, S. Baskara Sethupathy et al., "Investigation on interlaminar shear strength and moisture

absorption properties of soybean oil reinforced with aluminium trihydrate-filled polyester-based nanocomposites," *Journal of Nanomaterials*, vol. 2022, Article ID 7588699, 8 pages, 2022.

[20] H. Alshahrani and V. Arun Prakash, "Thermal, mechanical and barrier properties of rice husk ash biosilica toughened epoxy biocomposite coating for structural application," *Progress in Organic Coatings*, vol. 172, no. 2022, Article ID 107080, 2022.

[21] T. Sathish, K. Palani, L. Natrayan, A. Merneedi, M. V. De Poures, and D. K. Singaravelu, "Synthesis and characterization of polypropylene/ramie fiber with hemp fiber and coir fiber natural biopolymer composite for biomedical application," *International Journal of Polymer Science*, vol. 2021, Article ID 2462873, 2028 pages, 2021.

[22] G. Manikandan, "Mechanical and delamination studies on siliconized chitosan and morinda-citrifolia natural fiber-reinforced epoxy composite in drilling," *Polymer Composites*, vol. 42, pp. 181–190, 2021.

[23] D. Jayabalakrishnan, P. Prabhu, and S. Mohamed, "Mechanical, dielectric, and hydrophobicity behavior of coconut shell biochar toughened Caryota urens natural fiber reinforced epoxy composite," *Polymer Composites*, vol. 43, no. 1, pp. 493–502, 2021.

[24] H. Alshahrani, G. Pathinettampadian, A. K. Gujba, and A. Prakash Vincent Rethnam, "Effect of palmyra sprout fiber and biosilica on mechanical, wear, thermal and hydrophobic behavior of epoxy resin composite," *Journal of Industrial Textiles*, vol. 52, no. 2022, Article ID 152808372211373, 2022.

[25] S. Yogeshwaran, "Mechanical properties of leaf ashes reinforced aluminum alloy metal matrix composites," *International Journal of Applied Engineering Research*, vol. 10, no. 13, pp. 11048–11052, 2015.

[26] R. Ramaswamy, "Characterization of prickly pear short fiber and red onion peel biocarbon nanosheets toughened epoxy composites," *Polymer Composites*, vol. 43, 2022.

[27] S. Senthil Kumar, T. C. Anil Kumar, M. Chokkalingam et al., "Mechanical, fracture toughness, and fatigue behavior of spinifex littoreus fiber on echinoidea spike toughened epoxy composite," *Polymer Composites*, vol. 43, pp. 2329–2340, 2022.

[28] T. Sathish, L. Natrayan, S. Prasad Jones Christydass et al., "Experimental investigation on tribological behaviour of AA6066: HSS-Cu hybrid composite in dry sliding condition," *Advances in Materials Science and Engineering*, vol. 2022, Article ID 9349847, 9 pages, 2022.

[29] R., S. K. Subbiah and P. P. Patil, "Effect of nanosilica on mechanical, thermal, fatigue, and antimicrobial properties of cardanol oil/sisal fiber reinforced epoxy composite," *Polymer Composites*, vol. 43, 2022.

[30] L. Natrayan, P. V. Arul Kumar, J. A. Dhanraj et al., "Synthesis and analysis of impregnation on activated carbon in multi-walled carbon nanotube for Cu adsorption from wastewater," *Bioinorganic Chemistry and Applications*, vol. 2022, Article ID 7470263, 8 pages, 2022.

Hindawi
Advances in Materials Science and Engineering
Volume 2023, Article ID 1466963, 7 pages
https://doi.org/10.1155/2023/1466963

Research Article

Mechanical Characterization of Friction-Stir-Welded Aluminum AA7010 Alloy with TiC Nanofiber

S. Kaliappan,[1] T. Mothilal,[2] L. Natrayan ,[3] P. Pravin,[4] and Tewedaj Tariku Olkeba [5]

[1]*Department of Mechanical Engineering, Velammal Institute of Technology, Chennai 601204, Tamil Nadu, India*
[2]*Department of Automobile Engineering, KCG College of Technology, KCG Nagar Karapakkam, Chennai 600097, Tamil Nadu, India*
[3]*Department of Mechanical Engineering, Saveetha School of Engineering, SIMATS, Chennai 602105, Tamil Nadu, India*
[4]*Department of Mechanical Engineering, Graphic Era Deemed to be University, Bell Road Clement Town, Dehradun 248002, Uttarakhand, India*
[5]*Department of Mechanical Engineering, Ambo University, Ambo, Ethiopia*

Correspondence should be addressed to Tewedaj Tariku Olkeba; tewedaj.tariku@ambou.edu.et

Received 26 August 2022; Revised 11 December 2022; Accepted 31 March 2023; Published 24 April 2023

Academic Editor: R. Thanigaivelan

The effects of introducing TiC nanofibers (TiCnf) to the weld pool of Grade AA7010 were investigated in this study. The joints were made on a vertical machining centre with a lap joint arrangement. ASTM standards were followed while testing the strength of tensile and yield and percent of elongation, and hardness strength. According to the data, welds formed with TiCnf at around 1.0 wt % had a maximum tensile strength of 452 MPa. It was discovered that utilizing many nanofibers also enhance microhardness. Because of the nanofiber, the HAZ and TMT grains were polished and distortion-free, resulting in improved mechanical properties.

1. Introduction

Friction stir welding (FSW) is an essential joining process that uses frictional heat and high pressure to solidify materials. Due to their lightweight and high strength, aluminium-based alloys are often welded with brass, copper [1], and other aluminium alloys to make high-performance materials with combined properties for specific uses [2]. So far, much more research has been done to improve the quality of welds and the life of tools, both of which directly affect the overall process economy [3]. It is still hard to make significant welds at least 85% as strong as the metal they are attached to. So, experts are still working on improving weld settings to improve the quality of the welds. Many studies have been done to improve process parameters, such as the speed of the tool's rotation, traverse speed, the time it stays in one place, and plunge depth. Several new ways to finish joining processes have also been thought of [4]. Others work on changing the shape and weaving rate of the tool underwater, while others work on changing the shape and weaving rate of the tool. But there are still problems with the welds' quality and material getting into the weld zone. The strength of the weld bead is less than the minimum requirement of at least 85% of the strength of the source metal [5]. So, scientists started to look into what would happen if nanophases were added to the weld pool during the welding process. When these nanophases come together, they make nanocomposites that strengthen the weld nugget and stop cracks from spreading [6]. Because of this, people often get good results when they weld. Unique fillers like graphene nanoplatelets, graphene oxides, carbon nanotubes (CNTs), and other MoS4 are often used to improve the quality of welds. However, adding these fillers raises the cost and lowers the overall economy of the process [7]. But the cost of these fillers made the process less economical again, which led to the search for new fillers that were less expensive. Titanium carbide is a low-cost filler that works well and is often used to reinforce metal and polymer matrix

composites [8]. Also, TiC works well with aluminium-based alloys, which could be used to process aluminium-based metals [9, 10].

Anil Kumar et al. [11] looked at the mechanical properties and shapes of friction-stir-welded joints made of GRADE AA7010 that had TiC nanoparticles added. Using the state of the butt process before FSW, the edges of each plate were given a rectangular groove along the edge. Four fractional volumes of 0, 5, 8, and 13% TiCNP were put into grooves that were 0 to 0.5 mm wide, and FSW was used to shape metal with metal matrix nanocomposite (MMNC) in the stirred zone or weld nugget zone (WNZ). Compared to FSW samples made without TiCNP, the WNZ achieved grain refinement with TiC by adding different volumes (5, 8, or 13%) of TiCNP after the second pass of FSW. This improved the mechanical properties. In the WNZ, samples with 13 vol % part TiCNP had a higher hardness of 150 HV [12].

Sun and his colleagues [13] looked at what happened when pure copper metal was mixed with TiC particles. During the friction stir welding process, 5 m-sized TiC particles were injected into joints made of pure Cu. The author says that the Vickers hardness of Cu joints with TiC particles dispersed in them is 110 HV, much higher than the hardness of the stir zone without TiC particles, which is only 70 HV. Al-Mg and A316L alloys were welded better by Fallahi et al. [14] using TiC nanopowder. With the intermetallic joints, this work looked at getting two ideal cross speeds of 16 and 20 mm/min while keeping the rotational speed at 250 rpm. With six passes at a cross-sectional speed of 16 mm/min, the FSW achieved a high level of joint strength. The ultimate tensile strength (UTS) of the AA5083 base metal (BM) was increased to 94% and elongation decreased by 3%. There was a 250% increase in Vickers hardness in the stir zone. Mehdi et al. [15] looked into the mechanical performance and characterization of multipass FSWed AA6082-T6 with TiC-strengthened nanoparticles. With multipass FSPed-TiC and AA6082-T6, the mechanical properties were made by keeping the spinning speed at 1350 rpm, the welding speed at 65 mm/min, and the tilt angle at 2°. All TiC nanoparticles were broken up and spread out evenly in the fifth pass. This made AA6082, with a tensile strength of 215.54 MPa in the base metal and 24.91% strain. Along the stirred zone, the Vickers hardness values go from 89 to 133 HV from the first to the fifth pass. Tabasi et al. [16] looked at the role of TiC nanoparticles in FSWed Al-Mg alloys that differed from each other. The strengthened nanoparticle of titanium carbide was put into the stir zone to make a metal matrix composite. Researchers say that using titanium carbide nanoparticles to help support FSW takes into account the fact that a stirred microstructure is possible with the spinning mechanism.

Studies have shown that adding TiC to the weld bead will likely make a weld with a refined microstructure better at carrying loads. Also, research on TiC-based reinforcement in the weld pool has not been as extensive as on fillers such as nanosilica, TiO_2, and B_4C. But there are not many studies that use GRADE AA7010 weld joints. Also, TiC nanoparticles have been used in research instead of whiskers, nanorods, nanoribbons, and nanofibers. Because these one-of-a-kind structures can make microstructures stronger and more precise, this study looks into the mechanical behaviour of AA7010. Joining these different alloys could help make structural, automotive, and aerospace parts because they are lightweight, strong, and easy to make.

2. Materials and Method

The core metals used in this experiment were an AA7010 alloy with dimensions of 100 mm × 50 mm × 3 mm, respectively. Ms Bandari's metal treading company supplied the base metals. Sigma Aldrich in the United States also carried TiC nanofiber with a diameter of 2.5 μm and a length-to-diameter ratio of more than 20. The nanofiber utilized in this investigation has 3.22 grams per cubic centimetre density. Both metals are used in their native state before welding, with no pretreatment. Figure 1 shows the welded AA7010 alloy base metal. The mechanical properties and the chemical compositions of the base materials are displayed in Tables 1 and 2. The process variables are listed in Table 3.

2.1. Welding Process. Following the process parameters specified in Table 3, friction stir welding of parent metal was carried out on a high-precision vertical machining centre (HMT India) with a bed size of 810 × 400 mm, 45 to 1500 rpm of spinning speed, and 0.25 to 500 mm/min of weld speed. The spinning tool was targeted from one end, and the welding metal was organized in a butt joint pattern. The base metals were bonded using a tool with a taper and a 34° angle. The shoulder is 16 mm in diameter, with a 2.5 mm gap between it and the tooltip. The TiC nanofiber was inserted in the grooves at the edges before welding. 0.5, 1, and 1.5 wt. percent TiC nanofibre was used to determine the significance of particle addition [16, 17]. Figure 2 depicts the welding setup, tool image and the welded AA7010.

2.2. Test Specimen Making. Welded components were sliced by wire cut electrical discharge machining to create ASTM test specimens. Distilled water served as the dielectric medium, and the wire diameter was 0.25 mm. The pulse width was 113 volts on time and 25 volts off time, the current density was 230 volts, the gap voltage was 24 volts, and the pulse width was 113 volts on time and 25 volts off time.

3. Characterization of Welds

Tensile properties of friction-stir-welded plates were examined using universal testing equipment with a 20 ton loading capacity and 1.5 mm/min cross-head speed using ASTM E8M-04. Similarly, the impact hardness of weld beads was measured using an ASTM E23-compliant Charpy impact tester with a 70 J capacity. Vickers hardness setups calculated the hardness of weld nuggets, HAZ, and TMAZ following the ASTM 384 standard. The test variables were 5 Hz working frequency, 0.1 stress ratio, and 23°C working temperature. Finally, an OM and SEM examined the

Figure 1: AA7010 alloy base metal to be welded.

Table 1: Mechanical properties of base metal.

S.no	Material	Tensile strength (MPa)	Elongation (%)	Charpy impact (Joules)	Micro hardness (HV)
1	AA7010	452	1367.5	153	

Table 2: Chemical compositions of AA7010.

S.nos	Elements	%
1	Al	95.45
2	Zn	2.4
3	Mg	1.7
4	Cu	0.11
5	Zr	0.15
6	Fe	0.1
7	Si	0.08

Table 3: Description of FSW parameters.

Process variables	Description
Axial load	5 kN
Traverse speed	30 mm/min
Rotating speed	900 rpm
Length of weld	150 mm
Dwell time (s)	5
Plunge depth (mm)	0.2
TiC nanofiber (wt.%)	0.5, 1 and 2

microstructure of GRADE AA7010 weld joints. TESCAN VEGA 3, UNITED KINGDOM.

4. Results and Discussion

4.1. Mechanical Properties. The mechanical responses of the different welds tested in this study are shown in Table 4. The manufacturer says that the GRADE AA7010 weld has a tensile strength of 262 MPa, yield strength of 202 MPa, a condition of 21.6% elongation at break, and a Charpy impact toughness of 68.2 J. Aluminium becomes less flexible when the amount of aluminum alloy increases and TiC is added. Because of this, the alloy gets more brittle and may be harder to stretch because it loses some of its tensile strength. But when many nanofibers were added to the weld pool, it strengthened the weld. Figure 3(a) shows welds that were

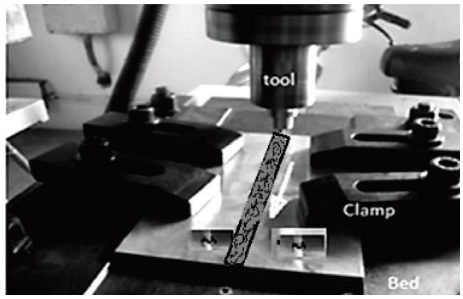

Figure 2: FSW of welding setup plate in bed.

made with 0.5 wt., 1.0 wt., and 2.0 wt. The tensile strengths of TiCnf were 284, 326, and 308 MPa, in that order. This is better than a simple weld by 8.39%, 24.4%, and 17.5%. Yield

Table 4: Mechanical responses on the weldment region.

Weld composition	Tensile strength (MPa)	Yield strength (MPa)	Elongation (%)	Charpy impact (Joules)
AA7010	262 ± 2.6	202 ± 1.7	21.6 ± 1.9	68.2 ± 2.1
AA7010 + 0.5TiCnf	284 ± 1.9	218 ± 2.1	18.2 ± 1.8	70.4 ± 1.9
AA7010 + 1.0TiCnf	326 ± 2.2	238 ± 1.9	16.4 ± 1.8	71.8 ± 2.2
AA7010 + 1.5TiCnf	308 ± 2.1	221 ± 2.3	17.6 ± 2.1	70.2 ± 2.0

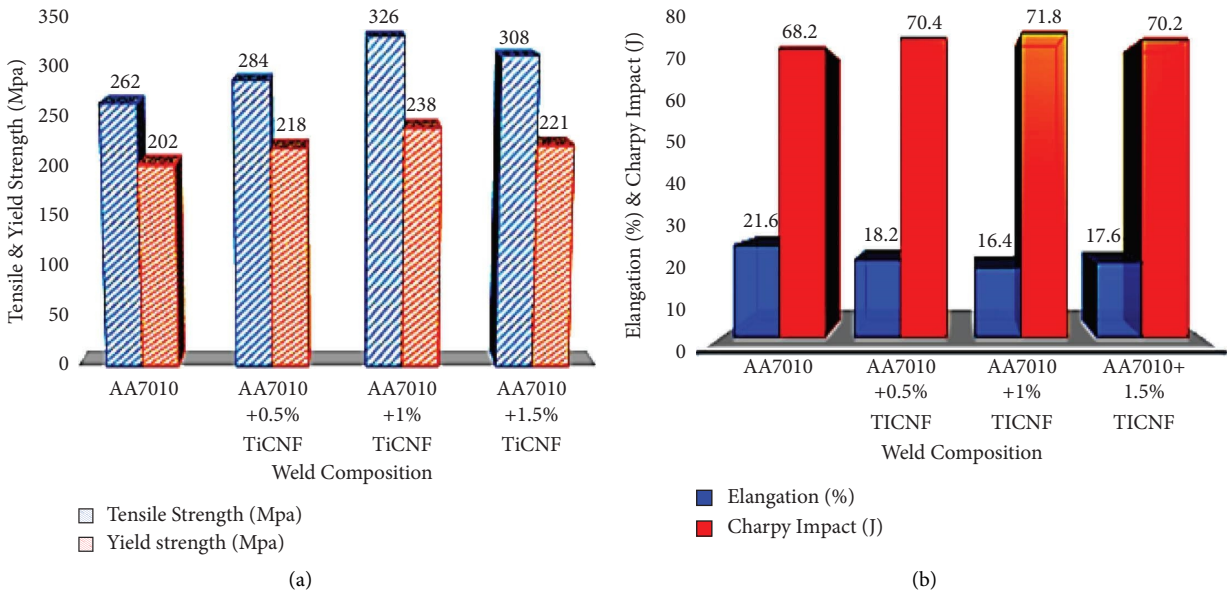

Figure 3: Weld composition of (a) tensile and yield strength (MPa) and (b) elongation (%) and charpy impact (J).

and length qualities both got better. These important changes are due to the effective stir zone and better reinforcing effect of TiC nanofiber [18]. The higher tool speed of the circular taper tool head made it possible for the primary metals and TiCnf reinforcement to mix more evenly [19]. Also, when the weld bead is put under tensile stress, the TiC long fibre structure increases the load-bearing capacity by making it easier for the Al-Mg molecules at the weld bead to lock together [20]. Also, the production of hard intermetallic compounds during the joining process tends to reduce elasticity. However, the presence of TiC nanofibers reduced the excessive formation of these intermetallic compounds and formed a nanocomposite layer on the top of the weld bead [21]. As a result, there was more behaviour that could carry weight. Still, a large amount of nano reinforcement added to the weld pool has almost no effect on the ability to stretch and absorb energy. Figure 3(b) shows a small drop for a GRADE AA7010 weld with 2.0 wt% TiCnf. This drop makes it easier for IMCs to form on the surface of nuggets [22]. When a thick IMC layer forms, it has a terrible effect on the mechanical properties of the weld [9]. When the tool's spinning speed is set, and the welding speed is slowed down, the IMC layer gets thicker, which means the strength of the joint is going down [23]. As a result, there is a big drop in the strength of the weld.

Figure 4 shows the optical microscope images of aluminium and its composites. The grains are coarser with the residues of nanofibers. The grain boundaries are strengthened, and the grains are stiffer. Thus, the crack wouldn't propagate faster through the boundaries; higher strength is noted. Table 3 shows that the Charpy impact toughness levels are significant [24]. The ordinary dissimilar weld has an impact energy of 68.2 J. When the TiC nanofiber was added to the weld pool at the time of joining, the energy absorption increased. This improvement is responsible for lowering ultra-hard brittle intermetallic phases at the weld contact [25]. As a result, weld nugget brittleness increased, resulting in little energy absorption.

In contrast, inserting nano-TiC fibres into the weld pool reduces IMC thickness while retaining flexibility in the nugget zone [26]. As a result, there may be an increase in energy absorption. For 1.0 wt. % TiCnf addition, the highest energy absorption of 21.8 J was found, which is a 19.7% increase over the plain weld [27].

4.2. Hardness Characteristics. Figure 5 shows how the hardness of many different welds varies. The Vickers hardness of a plain weld is 89 HV at the weld nugget, 84 HV at the TMAZ, and 82 HV at the HAZ. When joined, this

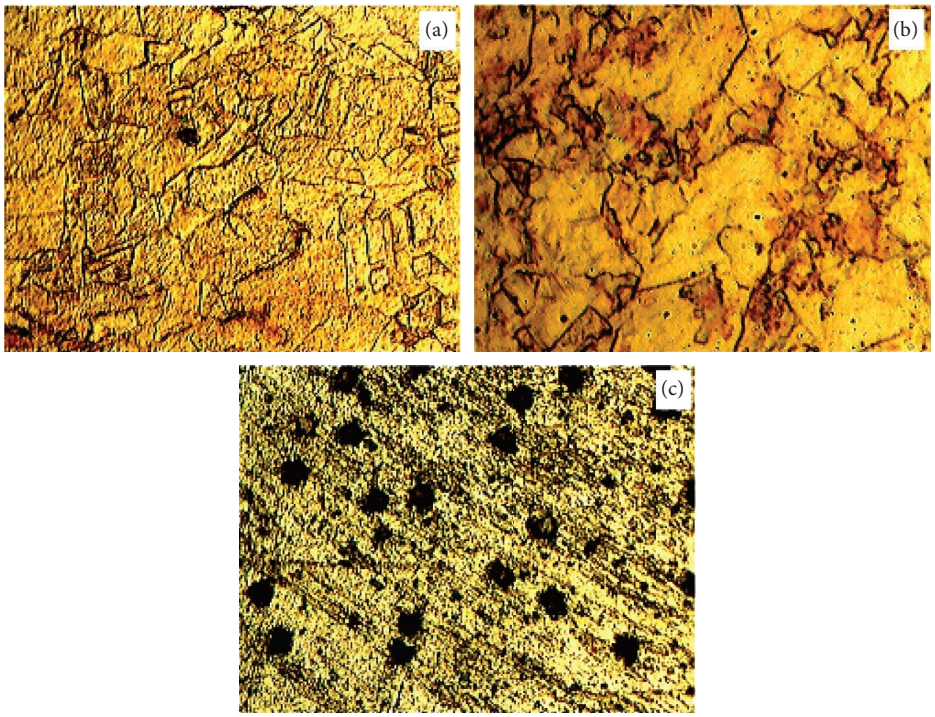

Figure 4: Optical microscope image of composites.

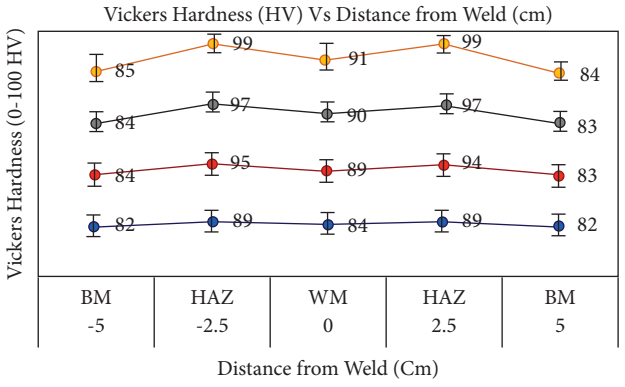

Figure 5: Vicker's hardness of dissimilar welds with TiC.

slightly higher hardness makes for better compounds between metals [28]. This is because the top layer of the joint is covered with too many intermetallic compounds, which makes it more challenging. But adding a lot of TiCnf made it a little bit stronger. The higher speed of the tool's rotation ensures that the TiC nanofibers are spread out evenly in the weld pool area, which has a pleasing reinforcing effect [29]. With 1.5 wt% TiCnf, the friction stir weld has a hardness of 99 HV. It is important to note that the microhardness of the nugget zone is the highest of any weld [30]. Both sides reported slightly less hardness in weld stages like TMAZ and HAZ, which are close to each other. This difference in hardness leads to the intermetallic density at the weld [31]. The higher precipitates IMCs at the weld nugget explain why they are higher than on the other sides. Because of this, the nugget is more complex than the phases around it [32].

5. Conclusions

This work used titanium carbide nanofibers to investigate the mechanical performances of friction stir welded AA7010 alloy. The precise outcomes made as a result of this investigation are as follows:

(i) TiC nanofiber was used to construct sound weld joints in GRADE AA7010 alloys. To achieve very homogeneous welds, predetermined process variables were applied.

(ii) The addition of TiCnf to the weld pool of the GRADE AA7010 alloy improved its tensile characteristics. The maximum tensile strength of 326 MPa was observed for 1 wt % TiCnf reinforced weld beads.

(iii) The addition of TiCnf significantly enhanced the hardness of the nuggets. The hardness has significantly increased. There was no unusual increase in hardness. This demonstrated that incorporating TiCnf into the weld bead reduced the highly saturated IMCs.

(iv) As a result, adding TiCnf to the GRADE AA7010 weld beads significantly improved the joint strength

properties. As a result, the inclusion of TiCnf is notable for producing sound weld connections with about 70% joint efficiency.

Data Availability

The data used to support the findings of this study are included within the article and are available from the corresponding author upon request.

Conflicts of Interest

The authors declare that there are no conflicts of interest.

References

[1] R. Vibin, S. Julyes Jaisingh, G. Ramesh, D. Jayabalakrishnan, and V. R. Arunprakash, "Effect of nanosilica and weave geometry on weld properties of friction stir welded nylon 6–6 thick plates," *Silicon*, vol. 14, pp. 1–9, 2020.

[2] S. Vijayakumar, S. Anitha, R. Arivazhagan, A. D. Hailu, T. V. J. Rao, and H. P. Pydi, "Wear investigation of aluminum alloy surface layers fabricated through friction stir welding method," *Advances in Materials Science and Engineering*, vol. 20228 pages, 2022.

[3] S. Vijayakumar, S. Manickam, S. Seetharaman, T. V. J. Rao, D. Pounraj, and H. P. Pydi, "Examination of friction stir-welded AA 6262/5456 joints through the optimization technique," *Advances in Materials Science and Engineering*, vol. 2022, Article ID 4527595, 11 pages, 2022.

[4] F. O. Edoziuno, C. Nwaeju, A. Adediran, B. Odoni, and V. Arun Prakash, "Mechanical and microstructural characteristics of aluminium 6063 alloy/palm kernel shell composites for lightweight applications," *Scientific African*, vol. 12, Article ID e00781, 2021.

[5] D. Pal, S. Vijayakumar, T. J. Rao, and R. S. R. Babu, "An examination of the tensile strength, hardness and SEM analysis of Al 5456 alloy by addition of different percentage of SiC/flyash," *Materials Today: Proceedings*, vol. 62, pp. 1995–1999, 2022.

[6] R. Ramamoorthi, K. P. Yuvaraj, C. Gokul, S. J. Eashwar, N. Arunkumar, and S. Abith Tamil Dheen, "An investigation of the impact of axial force on friction stir-welded AA5086/AA6063 on microstructure and mechanical properties butt joints," *Materials Today: Proceedings*, vol. 37, no. 2021, pp. 3159–3163, 2021.

[7] H. P. Pydi, A. P. Pasupulla, S. Vijayakumar, and H. A. Agisho, "Study on microstructure, behavior and Al-O3 content flux A-TIG weldment of SS-316L steel," *Materials Today: Proceedings*, vol. 51, pp. 728–734, 2022.

[8] A. Y. Adesina, F. A. Al-Badour, and Z. M. Gasem, "Wear resistance performance of AlCrN and TiAlN coated H13 tools during friction stir welding of A2124/SiC composite," *Journal of Manufacturing Processes*, vol. 33, pp. 111–125, 2018.

[9] B. Rahmatian, K. Dehghani, and S. E. Mirsalehi, "Effect of adding SiC nanoparticles to nugget zone of thick AA5083 aluminium alloy joined by using double-sided friction stir welding," *Journal of Manufacturing Processes*, vol. 52, pp. 152–164, 2020.

[10] M. A. Murugan, D. J. Jayaseelan, T. Maridurai, S. S. Kumar, G. Ramesh, and V. R. A. Prakash, "Low velocity impact and mechanical behaviour of shot blasted TiC wire-mesh and silane-treated aloevera/hemp/flax-reinforced TiC whisker modified epoxy resin composites," *Silicon*, vol. 12, pp. 1–10, 2019.

[11] K. S. Anil Kumar, S. M. Murigendrappa, and H. Kumar, "Experimental investigation on effects of varying volume fractions of SiC nanoparticle reinforcement on microstructure and mechanical properties in friction-stir-welded dissimilar joints of AA2024-T351 and AA7075-T651," *Journal of Materials Research*, vol. 34, no. 7, pp. 1229–1247, 2019.

[12] M. M. Matheswaran, T. V. Arjunan, S. Muthusamy et al., "A case study on thermo-hydraulic performance of jet plate solar air heater using response surface methodology," *Case Studies in Thermal Engineering*, vol. 34, Article ID 101983, 2022.

[13] Y. F. Sun and H. Fujii, "The effect of TiC particles on the microstructure and mechanical properties of friction stir welded pure copper joints," *Materials Science and Engineering A*, vol. 528, pp. 16-17, 2011.

[14] A. A. Fallahi, A. Shokuhfar, A. Ostovari Moghaddam, and A. Abdolahzadeh, "Analysis of SiC nano-powder effects on friction stir welding of dissimilar Al-Mg alloy to A316L stainless steel," *Journal of Manufacturing Processes*, vol. 30, pp. 418–430, 2017.

[15] H. Mehdi and R. S. Mishra, "Effect of multi-pass friction stir processing and SiC nanoparticles on microstructure and mechanical properties of AA6082-T6," *Advances in Industrial and Manufacturing Engineering*, vol. 3, Article ID 100062, 2021.

[16] M. Tabasi, M. Farahani, M. K. B. Givi, M. Farzami, and A. Moharami, "Dissimilar friction stir welding of 7075 aluminum alloy to AZ31 magnesium alloy using SiC nanoparticles," *The International Journal of Advanced Manufacturing Technology*, vol. 86, no. 1-4, pp. 705–715, 2016.

[17] A. Abdollahzadeh, A. Shokuhfar, H. Omidvar et al., "Structural evaluation and mechanical properties of AZ31/SiC nano-composite produced by friction stir welding process at various welding speeds," *Proceedings of the Institution of Mechanical Engineers, Part L: Journal of Materials: Design and Applications*, vol. 233, no. 5, pp. 831–841, 2019.

[18] K. Suresh, K. Karuppasamy, and S. Palani, "Effect of silane treated wheat husk biosilica (WHB) deionized water dielectric on EDM drilling of Ti-6Al-4 V alloy," *Silicon*, vol. 14, 2022.

[19] H. Wang, X. Gao, J. Liu, M. Ren, and A. Lu, "Multi-functional properties of carbon nanofiber reinforced reactive powder concrete," *Construction and Building Materials*, vol. 187, pp. 699–707, 2018.

[20] A. S. Kaliappan, S. Mohanamurugan, and P. K. Nagarajan, "Numerical investigation of sinusoidal and trapezoidal piston profiles for an IC engine," *Journal of Applied Fluid Mechanics*, vol. 13, no. 1, pp. 287–298, 2020.

[21] K. Nagarajan, A. Rajagopalan, S. Angalaeswari, and L. Natrayan, "Wubishet degife mammo, "combined economic emission dispatch of microgrid with the incorporation of renewable energy sources using improved mayfly optimization algorithm"," *Computational Intelligence and Neuroscience*, vol. 2022, Article ID 6461690, 22 pages, 2022.

[22] S. Li, Y. Su, X. Zhu, H. Jin, Q. Ouyang, and D. Zhang, "Enhanced mechanical behavior and fabrication of silicon carbide particles covered by in-situ carbon nanotube reinforced 6061 aluminum matrix composites," *Materials & Design*, vol. 107, pp. 130–138, 2016.

[23] F. Khodabakhshi, A. Simchi, A. H. Kokabi, A. P. Gerlich, M. Nosko, and P. Švec, "Influence of hard inclusions on microstructural characteristics and textural components during dissimilar friction-stir welding of an PM Al–Al2O3–TiC hybrid nanocomposite with AA1050 alloy,"

Science and Technology of Welding & Joining, vol. 22, no. 5, pp. 412–427, 2017.

[24] P. Karthikeyan and K. Mahadevan, "Investigation on the effects of TiC particle addition in the weld zone during friction stir welding of Al 6351 alloy," *International Journal of Advanced Manufacturing Technology*, vol. 80, no. 9, pp. 1919–1926, 2015.

[25] M. Srivastava and S. Rathee, "A study on the effect of incorporation of TiC particles during friction stir welding of Al 5059 alloy," *Silicon*, pp. 1–11, 2020.

[26] V. Subramani, B. Jayavel, and S. Ramesh, "Assessment of microstructure and mechanical properties of stir zone seam of friction stir welded magnesium AZ31B through nano-TiC," *Materials*, vol. 12, no. 7, p. 1044, 2019.

[27] A. Dolatkhah, P. Golbabaei, M. K. B. Givi, and F. Molaiekiya, "Investigating effects of process parameters on microstructural and mechanical properties of Al5052/TiC metal matrix composite fabricated via friction stir processing," *Materials & Design*, vol. 37, pp. 458–464, 2012.

[28] M. Bahrami, N. Helmi, and K. Dehghani, "Exploring the effects of TiC reinforcement incorporation on mechanical properties of friction stir welded 7075 aluminum alloy: fatigue life, impact energy, tensile strength," *Materials Science and Engineering A*, vol. 595, pp. 173–178, 2014.

[29] S. Kaliappan, S. M. D. P. Nagarajan, and M. R. Kamal, "Analysis of an innovative connecting rod by using finite element method," *Taga Journal Of Graphic Technology*, vol. 14, pp. 1147–1152, 2018.

[30] V. Paranthaman, K. Shanmuga Sundaram, and L. Natrayan, "Influence of SiC particles on mechanical and microstructural properties of modified interlock friction stir weld lap joint for automotive grade aluminium alloy," *Silicon*, vol. 14, pp. 1617–1627, 2022.

[31] D. A. Dragatogiannis, E. P. Koumoulos, I. A. Kartsonakis, D. I. Pantelis, P. N. Karakizis, and C. A. Charitidis, "Dissimilar friction stir welding between 5083 and 6082 Al alloys reinforced with TiC nanoparticles," *Materials and Manufacturing Processes*, vol. 31, pp. 2101–2114, 2016.

[32] S. Kaliappan, J. Lokesh, P. Mahaneesh, and M. Siva, "Mechanical design and analysis of AGV for cost reduction of material handling in automobile industries," *Int. Res. J. Automot. Technol*, vol. 1, no. 1, pp. 1–7, 2018.

Hindawi
Advances in Materials Science and Engineering
Volume 2023, Article ID 1366857, 9 pages
https://doi.org/10.1155/2023/1366857

Research Article

Optimization of Process Parameters in Electrochemical Micromachining of AMCs by Using Different Techniques of Weight Evaluation

S. Maniraj,[1] **R. Thanigaivelan**,[2] **K. Gunasekaran**,[3] **and K. G. Saravanan**[4]

[1]*Department of Mechanical Engineering, Paavai Engineering College (Autonomous), Namakkal, Tamilnadu, India*
[2]*Department of Mechanical Engineering, AKT Memorial College of Engineering and Technology, Kallakurichi, Tamilnadu, India*
[3]*Department of Mechanical Engineering, Muthayammal Engineering College (Autonmous), Rasipuram, Tamilnadu, India*
[4]*Department of Mechanical Engineering, Sona College of Technology, Salem, Tamilnadu, India*

Correspondence should be addressed to R. Thanigaivelan; tvelan10@gmail.com

Received 28 April 2022; Revised 3 September 2022; Accepted 30 September 2022; Published 22 February 2023

Academic Editor: Abílio De Jesus

The application of electrode heating is proposed in electrochemical micromachining (EMM). In the EMM process, the temperature of the electrode, voltage, duty cycle, and electrolyte concentration are considered process parameters. Taguchi L_{18} mixed-level orthogonal array (OA) design was adopted for designing the experiments and this study highlights the effect of temperature on responses such as radial overcut (ROC), material removal rate (MRR), and conicity factor (CF). In addition, multicriterion design making (MCDM) with VIKOR (VlseKriterijumska Optimizacija I Kompromisno Resenje, i.e., multi-criteria optimization and compromise solution) technique is used for finding the best alternatives based on the distinct weight assessing methods such as equal weights method (EWM), analytic hierarchy process (AHP), and entropy-based weights method (EBWM). Furthermore, a confirmation test is also conducted to find the best optimal parameters and their levels among the EWM-VIKOR, AHP-VIKOR, and EBWM-VIKOR. The results revealed that AHP-VIKOR provides a maximum improvement of 0.945 among the three methods.

1. Introduction

Composite materials nowadays play a vital role in engineering applications such as automotive, aerospace, and other industrial areas. In particular, MMCs with high specific stiffness and high strength may be used in long-term applications where weight reduction is a key factor, such as robots, turbine blades, high-speed machinery, rotating shafts, and automotive engine and brake components. However, the machining of composite materials is still difficult in the conventional machining process due to the reinforcement present in matrix material [1, 2]. Nonconventional machining processes are commonly utilized regardless of material hardness. In particular, microfabrications of composites are machined through processes such as electrochemical micromachining (EMM), electrical discharge machining (EDM), laser beam machining (LBM), and chemical machining (CM). Among these machining processes, EMM plays a major role due to better surface finish, higher machining rate, and high precision to be achieved. EMM process works on the reverse electroplating process under Faraday's law [3–5]. In this proposed work, the temperature of the electrode is considered one of the parameters for all the experiments run. In electrochemistry, temperature is the most influencing factor in improving the movement of ions between the electrodes. Researchers have performed experiments in EMM with different methods of heating such as ultraviolet light, infrared light source, ultrasonic vibration heating, and coil heating for improving the machining efficiency [6, 7]. Gründler et al. utilized an AC power supply for heating the electrode rather than supplying DC in the perspective of

reducing the faradic impacts that contribute to more electrons being transferred between the electrodes [8]. Qiu et al. implemented a new technique of radiofrequency (Rf) radiation heating the electrode. The heated electrode changes the viscosity property of the electrolyte solution resulting in enhanced flow patterns that contribute to enhanced mass transportation [9]. Wildgoose et al. examined the changed heating strategies in electrochemistry and discussed high-temperature mass transport. During the production of greater current, the phenomenon of mass transport increases through convection [10]. Frank Marken used microwave irradiation to identify a novel approach for heating nonisothermal electrodes. They noted a greater energy supply at high temperatures through this heating principle [11]. Long et al. suggested laser support for the electrochemical processing of stainless steel material. The electrolyte temperature variation creates greater conductivity resulting in a greater material dissolution rate [12].

Any manufacturing process is required to meet the quality and cost. The optimization of process parameters improves productivity and cost. Researchers have used MCDM to optimize the responses. Maniraj et al. adopted the Taguchi technique for optimizing the MRR and ROC by considering different % compositions of GGBS. In addition, the MCDM method of TOPSIS is also utilized for finding the best solution [13]. Singaravel et al. combined the AHP and TOPSIS for maximizing the MRR and minimizing the surface roughness (SR) and microhardness in the turning operation. The AHP method is used for finding the weight factor based on the decision makers and it provides a better solution when compared to other alternatives [14]. Kumar et al. also considered multicriterion optimization by assessing the weight by different methods such as equal weight method (EWM), AHP, and entropy-based weight method (EBWM) for consumption of energy responses along with MRR and SR during the turning operation [15]. Dinesh Singh et al. evaluated the performance of ECM process parameters by using the black hole algorithm (BHA) and the result obtained by using BHA provides better results when compared to other algorithms [16]. Sohrabpoor et al. designed a combined MCDM method of principal component analysis (PCA) with neuro-fuzzy associated with the teaching cuckoo algorithm for finding the optimal parametric condition satisfying maximum MRR, minimum ROC, and SR [17]. Bhuyan et al. optimized the process parameters of the EDM process by using an entropy-based assigning weight with the VIKOR method. Additionally, a confirmation test to validate optimized outcomes is also performed [18]. Maniraj et al. utilized a novel approach for heating the electrode through an AC power supply and corresponding effects were studied based on the temperature of aluminium metal matrix composite (AMC) with 12% reinforced GGBS material [19].

Based on the above literature, the researchers use electrode heating in the field of electrochemistry, but still, researchers are not focused on electrode heating in the EMM process. The heating of the electrode tool is suggested in this research study and an appropriate heating system for heating the cathode device to the given temperature and maintaining the electrode temperature with the aid of a thermostat sensor. In addition, the MCDM optimization technique (VIKOR method) was used to maximize the MRR, minimizing the ROC and CF. In this work, three distinct techniques (EWM, AHP, and EBWM) are used for assessing the weights because these methods have different principles for finding the weights. Furthermore, a confirmation test is also conducted for obtaining optimum parametric conditions by using the VIKOR index and then reported in this study.

2. Experimental Setup and Experimentation

Figure 1 shows the modified experimental setup for conducting the designed work. It consists of a feeding system, a machining unit, a system for supplying the electrolyte, a power supply unit, and a newly designed heating electrode unit. This heating unit is made up of a heating coil, thermostat, regulator unit, power supply unit, and ceramic material. As shown in Figure 2, the heating unit is placed on the electrode tool. In experimentation, the temperature of the electrode tool is set using the regulator for controlling the temperature and then it is heated by using the supply of AC power. Here, the ceramic material is used to prevent the conduction of the AC power supply between the heating coil to the tool electrode. The thermostat is provided in the system for continuous monitoring of temperature and maintains the set electrode tool temperature. If the temperature of the electrode instrument reaches the set temperature, the thermostat breaks the AC power supply automatically to the coil responsible for heating the electrodes. The temperature range varies between 20°C to 60°C.

Al 6061 T6 material is used as a matrix and 12% composition of GGBS by weight is used as reinforcement for fabricating the AMCs in the stir casting technique [20]. Selected matrix material and reinforcement chemical composition are presented in Tables 1 and 2.

The temperature of the electrode, electrolyte concentration, duty cycle, and machining voltage is selected as machining parameters and it is presented in Table 3 with their levels. The different levels of these parameters are selected based on the set of preliminary experiments. In this process, the current and frequencies are kept constant.

The output parameters such as MRR, ROC, and CF evaluate the performance of the EMM process. MRR is determined by the difference in the period of time between the work piece's final and initial weights. The duration of the machining process is calculated for all the experiments for computing the MRR. ROC is computed from the difference between the diameters of the tool electrode to the diameter of the machined hole. CF is deliberated by the expression which is $\mathrm{CF} = (T_d - B_d)/2 * w$, where T_d is the top hole diameter, B_d is the bottom hole diameter, and "w" is the workpiece thickness [21]. Machined hole diameters are identified through the scanning electron microscope (SEM) and it is used to figure out the ROC and CF. L_{18} mixed-level OA is used to design the experiments and it is presented in

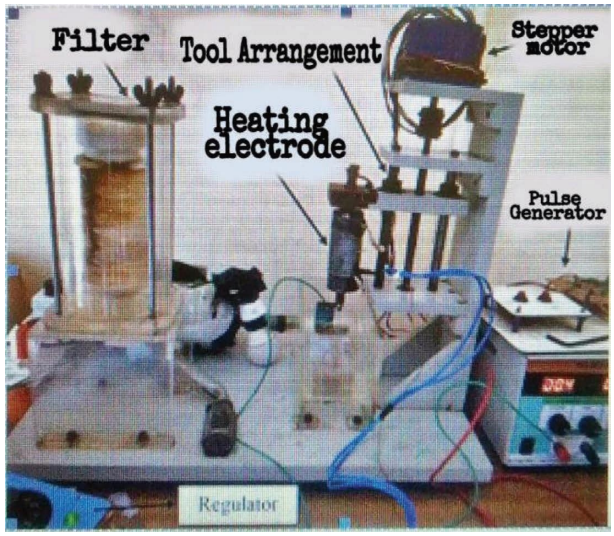

Figure 1: Modified EMM setup used for experimentation.

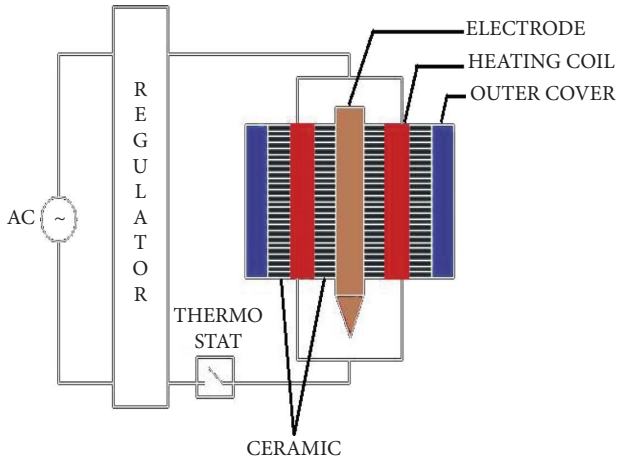

Figure 2: Designed heating unit for EMM process.

Table 4. Higher MRRs reduced ROCs and reduced CFs are preferred in the EMM process.

3. Results and Discussion

Figure 3 illustrates the 3-Dimensional response surface plot of MRR varying with the temperature of the electrode, voltage, duty cycle, and electrolyte concentrations. Figure 3(a) depicts the increase in temperature of the electrode leads to an increase of MRR due to the microstirring effect which is produced because of its temperature changes, irrespective of its voltage [22]. The current density needed for machining the AMCs rises with an increase in the duty cycle, simultaneously contributing to the linear increase of MRR for the heated electrode. The temperature of the electrode and higher current density dissolve the matrix material and at the same time break the reinforcement bond leading to greater MRR and it is evident from Figures 3(b). From Figure 3(c) it's evident that MRR increases with sodium nitrate electrolyte concentration. The precipitation and sludge formations are reduced due to the combined effect of the microstirring effect and proper flushing of electrolytes which leads to an increase in the MRR [23]. Figure 4 illustrates the 3-dimensional response surface plot of ROC varied with voltage, duty cycle, and electrolyte concentration comparatively with the temperature of the electrode. In electrochemistry, the movement of ions in an electrolyte solution is directly proportional to the temperature which contributes to increased conductivity. In AMCs, the distribution of reinforcement also plays a vital role because ceramic reinforcement has lesser conductivity when compared to matrix material [24].

Due to the distinct thermal expansion coefficients, the separation of reinforcement material (GGBS) from the

Table 1: Aluminium 6061 T6 quantified chemical composition in %.

Materials	Si	Cu	Fe	Mg	Cr	Mn	Zn	Ti	Al
Percent	0.80	0.40	0.70	1.2	0.35	0.15	0.25	0.15	Balance

Table 2: GGBS constituents' chemical composition quantified in %.

Materials	SiO_2	CaO	Al_2O_3	MgO	SO_3	K_2O	Na_2O	Fe_2O_3
Percent	34.4	33.2	21.5	9.5	0.47	0.39	0.34	0.2

Table 3: Parameters of machining and their levels.

Symbol	Parameters	Levels		
		1	2	3
A	Temperature of the electrode (°C)	30	40	—
B	Machining voltage(V)	8	10	12
C	Duty cycle (%)	70	80	90
D	Electrolyte concentration (g/lit)	15	20	25

Table 4: L_{18} mixed-level OA-based experimental design.

Experimental no.	A	B	C	D	MRR (gm/min)	ROC(μm)	CF
1	30	8	70	15	0.071	46	0.023
2	30	8	80	20	0.073	57	0.021
3	30	8	90	25	0.074	78	0.018
4	30	10	70	15	0.075	53	0.017
5	30	10	80	20	0.078	68	0.015
6	30	10	90	25	0.080	92	0.013
7	30	12	70	20	0.086	78	0.010
8	30	12	80	25	0.088	94	0.010
9	30	12	90	15	0.081	74	0.009
10	40	8	70	25	0.094	103	0.026
11	40	8	80	15	0.091	82	0.023
12	40	8	90	20	0.093	88	0.024
13	40	10	70	20	0.096	98	0.021
14	40	10	80	25	0.098	112	0.015
15	40	10	90	15	0.093	81	0.016
16	40	12	70	25	0.114	110	0.019
17	40	12	80	15	0.091	96	0.017
18	40	12	90	20	0.094	102	0.016

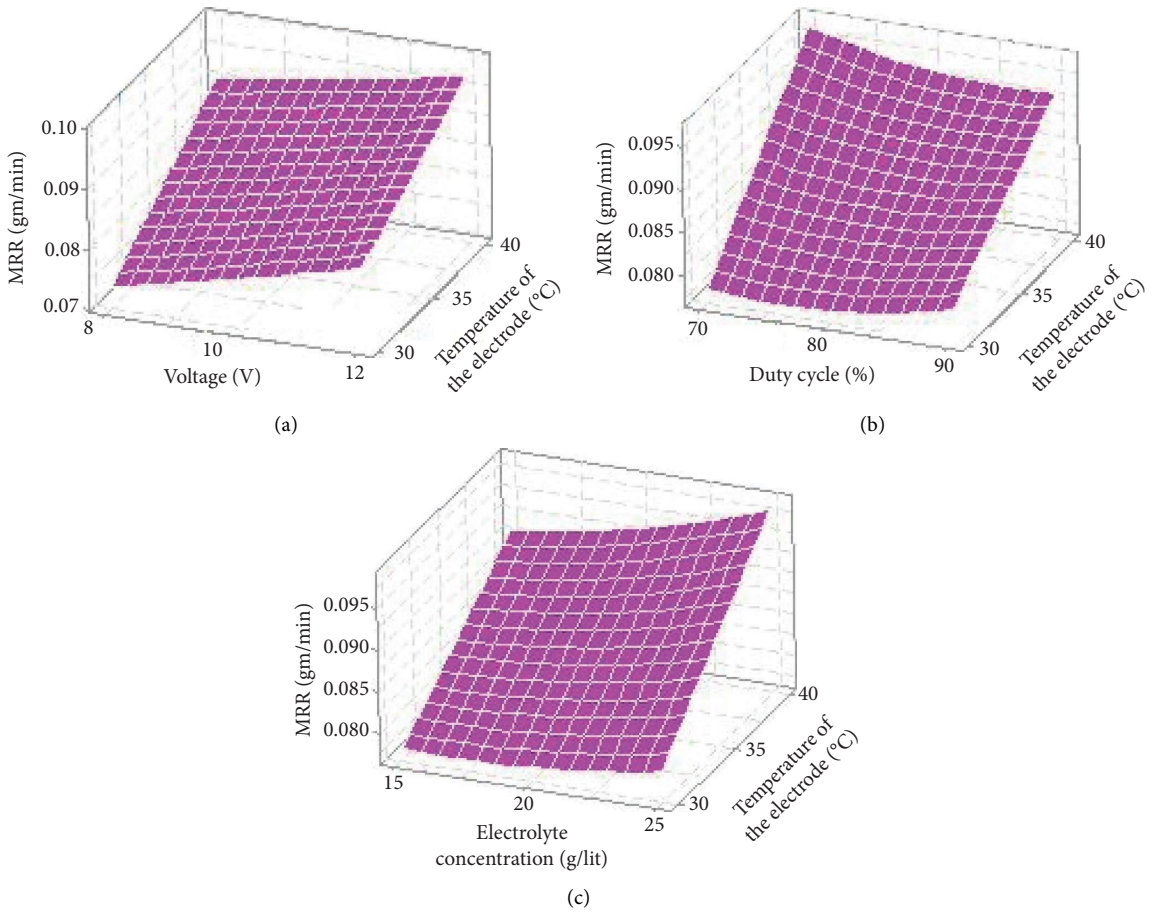

Figure 3: Process parameters effect on MRR.

AMCs also increases with increased the temperature of the electrode. This attribute leads to higher ROC from AMCs and it is evident in Figures 4(a) and 4(b). From Figure 4(c), with the increased concentration of electrolytes, the associated machining ions are also increased. This increase in ion and electrode heating removes more materials in the machining area, including the required material, resulting in higher ROC [25].

Figure 5 illustrates the 3-dimensional response surface plot of CF varied with voltage, duty cycle, and electrolyte concentration comparatively with the temperature of the electrode. The impact of electrode temperature on CF is shown in Figure 5(a). Electrode heating establishes the hot spot/zone in front of the electrode. Gas bubbles form at the electrode attributing to increasing the electrolyte conductivity thereby it reduces the CF when increase in voltage.

Because of the distribution of the reinforcement in the MMC, the removal of bulk material from the microstirring impact leads to an increase in CF during longer pulse duration and it is evident from Figure 5(b). It is clear from Figure 5(c), the temperature of the electrode initiates quicker ion movement and the microstirring impact also dissolves the dissolved products. This impact, resulting in less conicity when compared with increases in the concentration of the electrolyte, replenishes the electrolyte in the machining area [6].

3.1. Integrated MCDM Method with EWM, AHP, and EBWM-VIKOR Approach. In this research work, an integrated MCDM method was adopted. It consists of various weights assessing methods such as EWM, AHP, and EBWM with the VIKOR method [15]. The steps to be followed for implementing the MCDM technique are as follows:

Step 1. Decision Matrix Development

In optimization techniques, the development of a decision matrix is important with considering the alternatives as input/process parameters and the criteria as output parameters. The formulation of the decision matrix by using the expression provided in the following equation:

$$\mathrm{DM}_{ij} = \begin{bmatrix} & C_1 & C_2 & \ldots & C_n \\ A_1 & a_{11} & a_{12} & \ldots & a_{1n} \\ A_2 & a_{21} & a_{22} & .... & a_{2n} \\ \ldots & \ldots & .... & .... & .... \\ A_m & a_{m1} & a_{m2} & .... & a_{mn} \end{bmatrix}, \quad (1)$$

where $i = 1, 2, 3, \ldots, m$ represents the number of possible alternatives present, and $j = 1, 2, 3, \ldots, n$ represents the number of individual criteria.

Step 2. Determination of Normalized Decision Matrix

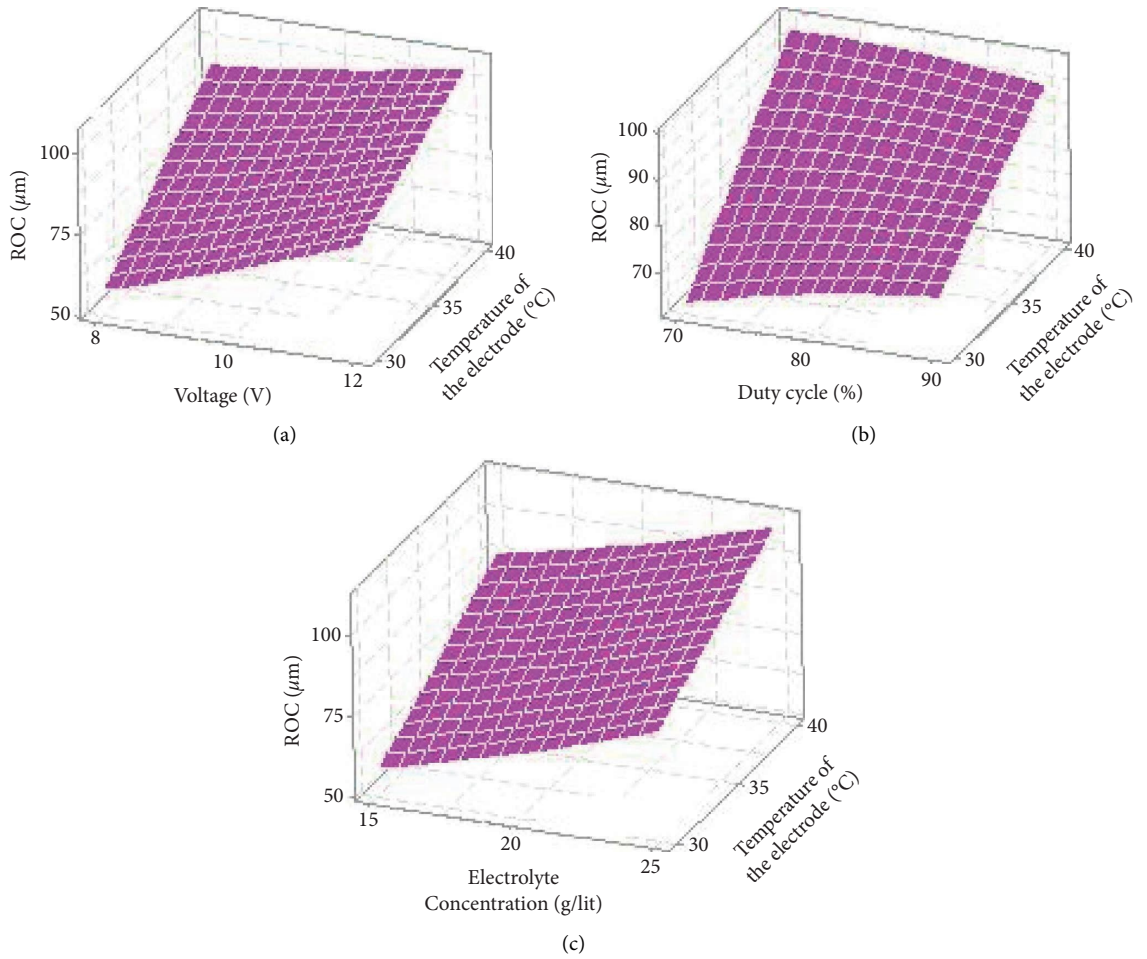

Figure 4: Process parameters effect on ROC.

In this step, all the criteria/output parameters are normalized irrespective of their unit and convert the values of the criteria lie between 0 and 1 by using the following equation:

$$NDM_{ij} = \frac{a_{ij}}{\sum_{i=1}^{m}\left(a_{ij}\right)^2}; \quad i = 1, 2, 3, m; \; j = 1, 2, 3, n; . \tag{2}$$

Step 3. Determination of Weights of Different Criteria/Output Parameters

In this particular step, identifying and assigning the different weights W_j (for $j = 1, 2, 3, \ldots, n$) by using the different weight assessing methods such EWM, AHP, and EBWM.

3.1.1. Equal Weight Method. In this EWM, the weights of individual criteria are considered by dividing 1 by the number of individual criteria (n) as expressed in the following equation:

$$Wj = (\text{for}\, j = 1, 2, n) = \frac{1}{n}. \tag{3}$$

In this research work, there are three (3) criteria are considered, so the weight of individual criteria is calculated by the following expression as shown in the following equation:

$$Wj\,(\text{for}\, j = 1, 2n) = \frac{1}{3}. \tag{4}$$

Based on EWM, the respective weights of MRR, ROC, and CF are 0.33, 0.33, and 0.33, respectively.

3.1.2. Analytic Hierarchy Process. The AHP method requires decision makers to make decisions as to the comparative significance of each criterion and then indicate a preference for each alternative decision on each criterion [25].

Based on AHP, the respective weights of MRR, ROC, and CF are 0.63, 0.26, and 0.11, respectively.

3.1.3. Entropy-Based Weights Method. In this EBWM, the weights of the individual criterion are measured without the influence of the decision maker. Based on the decision matrix as expressed in (1), normalization of the matrix with minimization and maximization criterion is formulated. Criterion weights are critical in measuring the performance

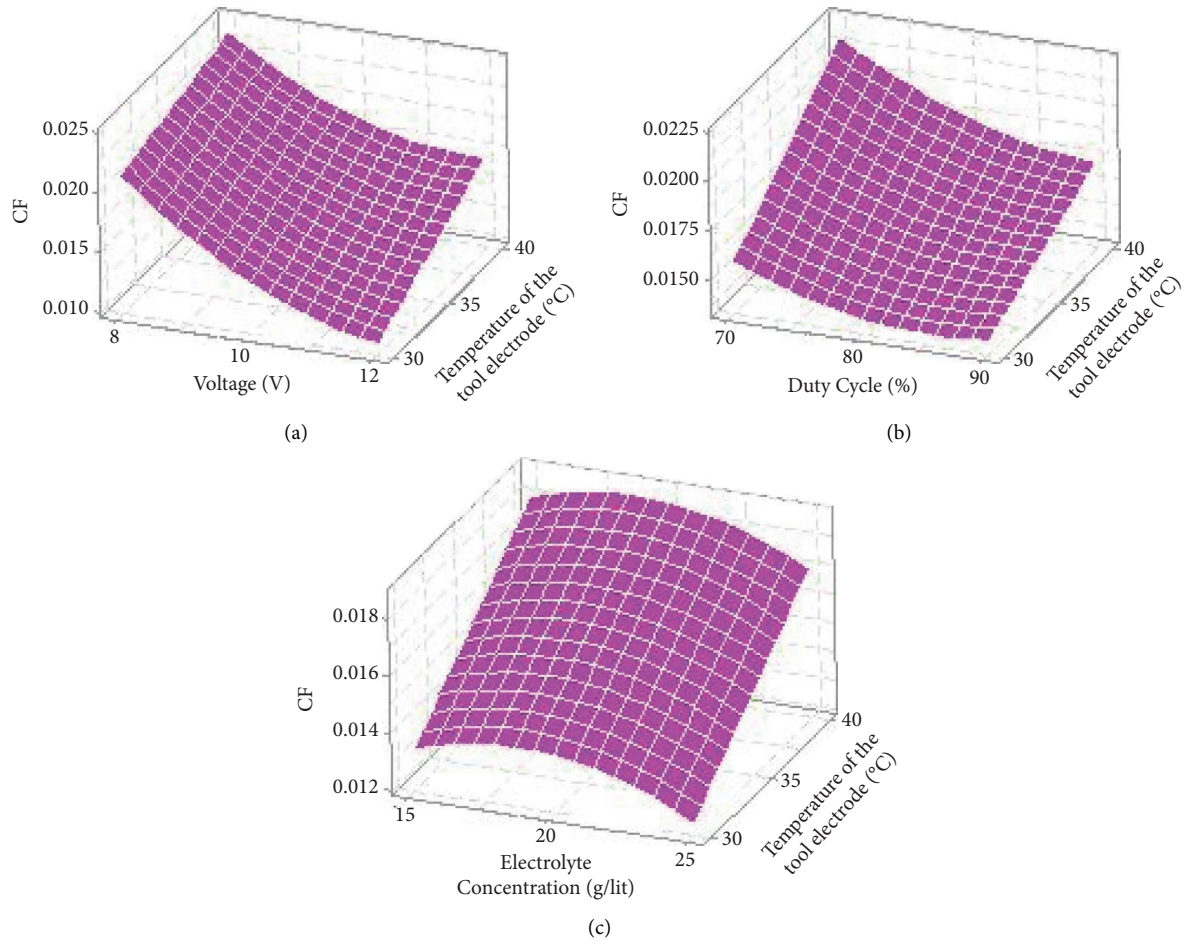

Figure 5: Process parameters effect on CF.

Table 5: VIKOR index and ranking for EWM, AHP, and EBWM.

S.No	Equal weight method (EWM)				Analytic hierarchy process (AHP)				Entropy-based weights method (EBWM)			
	U_i	R_i	Q_i	Rank	U_i	R_i	Q_i	Rank	U_i	R_i	Q_i	Rank
1	0.608	0.333	0.778	17	0.721	0.630	0.945	18	0.552	0.451	0.621	14
2	0.609	0.318	0.729	13	0.722	0.601	0.908	16	0.541	0.386	0.532	12
3	0.648	0.310	0.757	16	0.770	0.586	0.942	17	0.554	0.290	0.421	9
4	0.495	0.302	0.529	8	0.651	0.571	0.791	15	0.387	0.258	0.255	5
5	0.508	0.279	0.473	5	0.653	0.527	0.735	13	0.395	0.193	0.181	3
6	0.574	0.264	0.511	7	0.705	0.498	0.754	14	0.454	0.245	0.289	7
7	0.398	0.217	0.130	2	0.543	0.410	0.458	11	0.268	0.170	0.058	2
8	0.464	0.242	0.297	4	0.576	0.381	0.457	10	0.349	0.256	0.225	4
9	0.397	0.256	0.252	3	0.594	0.483	0.611	12	**0.227**	**0.149**	**0.000**	**1**
10	0.776	0.333	1.000	18	0.628	0.293	0.397	8	0.898	0.548	1.000	18
11	0.635	0.275	0.625	11	0.569	0.337	0.391	7	0.697	0.451	0.729	16
12	0.669	0.294	0.733	14	0.570	0.308	0.353	6	0.756	0.483	0.813	17
13	0.637	0.263	0.591	10	0.546	0.264	0.268	4	0.706	0.386	0.655	15
14	0.575	0.333	0.735	15	0.533	0.260	0.249	2	0.582	0.351	0.519	11
15	**0.477**	**0.177**	**0.105**	**1**	0.491	0.308	0.265	3	0.461	0.225	0.270	6
16	0.519	0.323	0.629	12	**0.317**	**0.252**	**0.000**	**1**	0.663	0.341	0.565	13
17	0.588	0.253	0.493	6	0.586	0.337	0.409	9	0.578	0.266	0.409	8
18	0.575	0.283	0.573	9	0.559	0.293	0.321	5	0.571	0.298	0.443	10

of the diversity index. This diversity index gives the quantitative measure of an individual criterion distributed among the alternatives. The concept of weight measurement is that a greater index value than a lower index value is preferable [26].

Based on EBWM, the respective weights of MRR, ROC, and CF are 0.101, 0.351, and 0.548, respectively.

Step 4. Determine the utility measure (U_i) and regret measure (R_i).

From the NDM, find the maximum value ($NDM_{\max}$) and the minimum value ($NDM_{\min}$) for both beneficial and nonbeneficial criteria. In this machining process, MRR is the beneficial criterion, whereas ROC and CF are the nonbeneficial criteria.

For beneficial criterion, the U_i and R_i terms are expressed in the following equations and represented in Table 5.

$$U_i = \sum_{i=1}^{n} W_i \frac{\left(NDM_{ij} - NDM_{\min}\right)}{\left(NDM_{\max} - NDM_{\min}\right)}, \tag{5}$$

$$R_i = \text{Max.of}\left[W_i \frac{\left(NDM_{\max} - NDM_{ij}\right)}{\left(NDM_{\max} - NDM_{\min}\right)}\right]. \tag{6}$$

For the nonbeneficial criterion, the *Ui* and *Ri* terms are expressed in the following equations:

$$U_i = \sum_{i=1}^{n} W_i \frac{\left(NDM_{\max} - NDM_{ij}\right)}{\left(NDM_{\max} - NDM_{\min}\right)}, \tag{7}$$

$$R_i = \text{Min.of}\left[W_i \left[\frac{\left(NDM_{ij} - NDM_{\min}\right)}{\left(NDM_{\max} - NDM_{\min}\right)}\right]\right]. \tag{8}$$

Step 5. Determine the value of Q_i

The value of Q_i can be computed by the following equation, where U_i is the utility measure, (U_i) max = maximum of U_i, (U_i)min = minimum of U_i.

$$Q_i = \left[\epsilon \left[\frac{\left(U_i - (U_i)_{\min}\right)}{\left((U_i)_{\max} - (U_{i\min})\right)}\right]\right] + \left[[1-\epsilon]\left[\frac{\left(R_i - (R_i)_{\min}\right)}{\left((R_i)_{\max} - (R_{i\min})\right)}\right]\right], \tag{9}$$

whereas R_i is the regret measure, (R_i) max = maximum of R_i, (R_i)min = Minimum of R_i and is introduced for weight for the strategy of maximum criteria. The value normally lies between 0 and 1 and it is now considered as 0.5.

Step 6. Ranking of alternatives

The alternatives ranking is based on the value of Q_i. The minimum value of Q_i gives the best alternative among all alternatives.

3.2. Confirmation Test. After assessing the optimal parameters from the VIKOR method based on different weights by EWM, AHP, and EBWM. A confirmation test was carried out to validate the VIKOR method outcomes. To estimate the optimum MRR, ROC, and CF (10) were used, respectively.

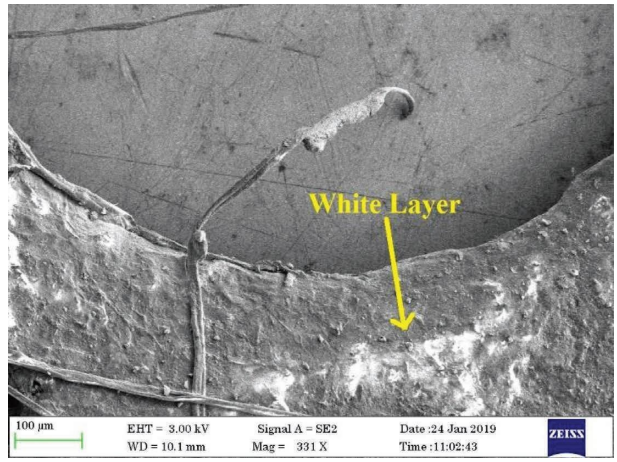

Figure 6: Process parameters effect on CF.

$$\mathfrak{R} = Q_m + \sum_{i=1}^{q} \left(Q_i - Q_m\right), \tag{10}$$

where Q_m is the overall VIKOR index mean, q represents the number of different control parameters and Q_i is the VIKOR index mean at optimal conditions.

Here, (A2, B2, C3, D1), (A2, B3, C1, D3), and (A1, B3, C3, D1) represent the optimum levels of MRR, ROC, and CF based on EW-VIKOR, AHP-VIKOR, and EBWM-VIKOR methods. The improvement in the VIKOR index is found to be 0.673, 0.945, and 0.621 from the different weight methods. Among the three different methods, AHP-VIKOR gives the maximum improvement of 0.945. Thus, the result of the confirmation obtained from the (10) reflects optimization success.

3.3. Micromachined Hole Scanning Electron Microscope (SEM) Image. Figure 6 shows the SEM image of a machined hole at TE = 40°C, MV = 10 V, DC = 90%, EC = 15 g/l trail. This image clearly depicts the formation of a white layer due to the increase in the temperature of the electrode. The heated electrode raises the local temperature of the electrolyte and lowers its viscosity, resulting in electrolyte regeneration in the machining zone.

4. Conclusion

In the present study, electrode heating is proposed for improving the performance of the EMM process. L_{18} mixed-level OA Taguchi design was adopted for conducting the experiments. In addition, the MCDM VIKOR method is used to find out the optimal process parameters of AMCs. The conclusions and results drawn from this research are given as follows:

(i) The EMM setup is altered with an electrode consisting of a heating coil, power supply, and thermostat.

(ii) The effect on MRR, ROC, and CF of process parameters such as the temperature of the electrode, MV, DC, and EC was investigated through L_{18} mixed-level OA, and the effect of heating the electrode on MRR, ROC, and CF was significant.

(iii) The optimal process parameters and their levels for maximizing MRR and minimizing ROC and CF using the VIKOR method were determined based on three distinct weight-assessing methods.

(iv) Optimal levels of EW-VIKOR are observed at A2 B2 C3 D1 (i.e., the temperature of TE = 40°C, MV = 10 V, DC = 90%, EC = 15 g/l). For AHP-VIKOR are observed at A2 B3 C1 D3 (i.e., the temperature of TE = 40°C, MV = 12 V, DC = 70%, EC = 25 g/l) and for EBWM are observed at A1 B3 C3 D1 (i.e., the temperature of TE = 30°C, MV = 12 V, DC = 90%, EC = 15 g/l).

(v) Based on the tests of confirmation results, the AHP-VIKOR provides a better improvement of 0.945 by the VIKOR index.

Nomenclature

AHP: Analytic hierarchy process
AMCs: Aluminium metal matrix composite
CF: Conicity factor
CM: Chemical machining
EBWM: Entropy-based weight method
EDM: Electrical discharge machining
EMM: Electrochemical micromachining
EWM: Equal weight method
GGBS: Ground granulated blast furnace slag
LBM: Laser beam machining
MRR: Material removal rate
MCDM: Multicriterion design making
NDM: Normalized decision matrix
OA: Orthogonal array
R_f: Radiofrequency
ROC: Radial overcut
SEM: Scanning electron microscope
TOPSIS: The technique for order of preference by similarity to an ideal solution
VIKOR: VlseKriterijumska Optimizacija I Kompromisno Resenje, i.e., multicriteria optimization and compromise solution.

Data Availability

The data used to support the results of this study are included within the article and are available from the corresponding author upon request.

Conflicts of Interest

The authors declare that there are no conflicts of interest.

References

[1] D. B. Miracle, "Metal matrix composites – from science to technological significance," *Composites Science and Technology*, vol. 65, no. 15-16, pp. 2526–2540, 2005.

[2] M. B. D. Ellis, "Joining of aluminium based metal matrix composites," *International Materials Reviews*, vol. 41, no. 2, pp. 41–58, 1996.

[3] A. K. Srivastava, A. R. Dixit, and S. Tiwari, "A review on the intensification of metal matrix composites and its nonconventional machining," *Science and Engineering of Composite Materials*, vol. 25, no. 2, pp. 213–228, 2018.

[4] V. K Jain, *Introduction to Micromachining*, Narosa Publishing House, New Delhi, 2010.

[5] V. Venkatesh, N. Swain, G. Srinivas, P. Kumar, and H. C. Barshilia, "Review on the machining characteristics and research prospects of conventional microscale machining operations," *Materials and Manufacturing Processes*, vol. 32, no. 3, pp. 235–262, 2016.

[6] R. Thanigaivelan, R. M. Arunachalam, M Kumar, and B. P. Dheeraj, "Performance of electrochemical micromachining of copper through infrared heated electrolyte," *Materials and Manufacturing Processes*, vol. 33, no. 4, pp. 383–389, 2017.

[7] M. Soundarrajan and R. Thanigaivelan, "Investigation on electrochemical micromachining (ECMM) of copper inorganic material using UV heated electrolyte," *Russian Journal of Applied Chemistry*, vol. 91, no. 11, pp. 1805–1813, 2018.

[8] P. Gründler and A. Kirbs, "The technology of hot-wire electrochemistry," *Electroanalysis*, vol. 11, no. 4, pp. 223–228, 1999.

[9] F. L Qiu, R. G Compton, B. A Coles, and F Marken, "Thermal activation of electrochemical processes in a Rf-heated channel flow cell: experiment and finite element simulation," *Journal of Electroanalytical Chemistry*, vol. 492, no. 2, pp. 150–155, 2000.

[10] G. G Wildgoose, D Giovanelli, N. S. Lawrence, and R. Compton, "High- temperature electrochemistry: a review," *Electroanalysis*, vol. 16, no. 6, pp. 421–433, 2004.

[11] F. Marken, "Chemical and electro-chemical applications of in situ microwave heating," *Annual Reports Section "C" (Physical Chemistry)*, vol. 104, pp. 124–141, 2008.

[12] Y. Long, Q. Liu, Z. Zhong, L. Xiong, and T. Shi, "Experimental study on the processes of laser-enhanced electrochemical micromachining stainless steel," *Optik - International Journal for Light and Electron Optics*, vol. 126, no. 19, pp. 1826–1829, 2015.

[13] S Maniraj and R Thanigaivelan, "Optimization of electrochemical micromachining process parameters for machining of AMCs with different % compositions of GGBS using Taguchi and TOPSIS methods," *Transactions of the Indian Institute of Metals*, vol. 72, no. 12, pp. 3057–3066, 2019.

[14] B Singaravel and T. Selvaraj, "Optimization of machining parameters in turning operation using combined TOPSIS and AHP method," *Tehnički Vjesnik - Technical Gazette*, vol. 22, pp. 1475–1481, 2015.

[15] R. Kumar, P. S Bilga, and S. Singh, "Multi objective optimization using different methods of assigning weights to energy consumption responses, surface roughness and material removal rate during rough turning operation," *Journal of Cleaner Production*, vol. 164, pp. 45–57, 2017.

[16] D. Singh and R. Shukla, "Parameter optimization of electrochemical machining process using black hole algorithm,"

IOP Conference Series: Materials Science and Engineering, vol. 282, Article ID 012006, 2017.

[17] H. Sohrabpoor, S. P. Khanghah, S. Shahraki, and R. Teimouri, "Multi-objective optimization of electrochemical machining process," *International Journal of Advanced Manufacturing Technology*, vol. 82, no. 9-12, pp. 1683–1692, 2015.

[18] R. K. Bhuyan and B. C. Routara, "Optimization the machining parameters by using VIKOR and Entropy Weight method during EDM process of Al–18% SiCp Metal matrix composite," *Decision Science Letters*, vol. 5, pp. 269–282, 2016.

[19] S. Maniraj and R Thanigaivelan, "Effect of electrode heating on performance of electrochemical micromachining," *Materials and Manufacturing Processes*, vol. 34, no. 13, pp. 1494–1501, 2019.

[20] M. K Sahu and R. K. Sahu, *Fabrication of Aluminum Matrix Composites by Stir Casting Technique and Stirring Process Parameters Optimization*Intech, 2018.

[21] Z. W. Fan and L. W. Hourng, "Electrochemical micro-drilling of deep holes by rotational cathode tools," *International Journal of Advanced Manufacturing Technology*, vol. 52, no. 5-8, pp. 555–563, 2011.

[22] P. Gründler, T. Zerihun, A Möller, and A. Kirbs, "A simple method for heating micro electrodes in-situ," *Journal of Electroanalytical Chemistry*, vol. 360, no. 1-2, pp. 309–314, 1993.

[23] G. U. Flechsig and A. Walter, "Electrically heated electrodes: practical aspects and new developments," *Electroanalysis*, vol. 24, no. 1, pp. 23–31, 2011.

[24] C. J. T. Mariapushpam, D. Ravindran, and M. D. Anand, "Machining parameters influencing in electro chemical machining on AA6061 MMC," *Materiali in tehnologije*, vol. 50, no. 6, pp. 951–960, 2016.

[25] C. S. Kalra, V. Kumar, and A. Manna, "Analysis of electrochemical behavior on micro-drilling of cast hybrid Al/(Al2O3p + SiCp + Cp)-MMC using micro-ECM process," *Proceedings of the Institution of Mechanical Engineers - Part L: Journal of Materials: Design and Applications*, vol. 232, no. 1, pp. 67–79, 2015.

[26] T. L. Saaty, "Decision making with the analytic Hierarchy process," *International Journal of Services Sciences*, vol. 1, pp. 83–98, 2008.

Hindawi
Advances in Materials Science and Engineering
Volume 2023, Article ID 8598585, 8 pages
https://doi.org/10.1155/2023/8598585

Research Article

Evaluation of Mechanical Properties for Epoxy Resin in Nano Composite Diffusion

K. Bharadwaja,[1] Sreeram Srinivasa Rao,[1] T. Babu Rao,[2] and Hari Prasadarao Pydi[3]

[1]*Department of Mechanical Engineering, K L University, Vadddeswaram Green Fields, Vijayawada, Andhra Pradesh, India*
[2]*Department of Mechanical Engineering, NIT, Tadepalligudem, Andhra Pradesh, India*
[3]*Department of Mechanical Engineering, Bule Hora University, Bule Hora, Ethiopia*

Correspondence should be addressed to Hari Prasadarao Pydi; haripydi609@gmail.com

Received 25 August 2022; Revised 21 October 2022; Accepted 27 January 2023; Published 6 February 2023

Academic Editor: R. Thanigaivelan

This research work developed a method for the analysis of epoxy matrix nanocomposites used in epoxy resin with the incorporation of Al_2O_3 and SiO_2 nanoparticles. The different tests were performed in order to derive the mechanical characteristics and wear properties of Al_2O_3 and SiO_2 nanoparticles. The mixing is performed using an ultrasound process where the nanoparticles are mixed with the resin for a homogeneous diffusion. The strengths observed for the nanocomposite were higher for bending and impact strength because of the Al_2O_3 and SiO_2 nanoparticle incorporation. The wear rate and friction coefficient is observed to be reduced due to the incorporation of Al_2O_3 and SiO_2 nanoparticles into the epoxy resin. This characteristic has a significant benefit of using Al_2O_3 and SiO_2 nanoparticles for loading conditions. The effects of Al_2O_3 and SiO_2 nanoparticles were more effective in epoxy resin, which were more effectively been derived by reinforcing methods.

1. Introduction

Epoxy resins are mostly useful in various structural fields due to their higher strength and higher modulus, which is useful for optimal thermosetting polymers. The resins have a high chemical resistance and are simple in processing. This resin has been in commercial use for a long time which has good characteristics of electrical insulation and chemical resistance [1]. The epoxy resin shows lower cure shrinkage and is more effective in terms of strength, bonding, and reliability factors. On curing, the epoxy resin forms a network with different curing elements like anhydrides, amines, thiols, etc. [2–8]. The characteristic makes epoxy resin more effective in different usages like coating for protection, electronic usage, flooring purposes, painting etc. In recent years, nanocomposites have primarily been used as a composite material to improve the composite's ability to interact with other materials [9–14]. Nano materials are used to combine polymers and solid phases with nanometer dimensions [15]. Various studies revealed that nanocomposites illustrate a high mechanical and thermal characteristic [16, 17]. The densities of the micrometer fillers are higher in value compared to a low density polymer, which hence needs a higher filler count to enhance the mechanical property. This filling also increases the composite weight in the material [18]. The advantage of the nanocomposite polymer is an advantage in physical properties when compared to existing composites, which makes the nanocomposite polymer more optimal for fillers. The nanocomposite has the characteristic of improving mechanical strength with a low filler, which makes the material light in weight [19]. The nanocomposite inclusion can enhance the material stiffness with no effect on its toughness and can improve the holding properties without reducing the transparency or mechanical characteristic with flame retardant properties without changing the color [20, 21]. In recent times, different nanomaterials are used, such as TiO_2 and SiO_2 [22, 23], with epoxy resin to improve the properties of the epoxy matrix composition [24]. The epoxy matrix/nano-TiO_2 exhibits higher performance of mechanical behavior [25]. The inclusion of nano-sized materials is a more optimal means of improving the mechanical and thermal

characteristics of thermoset polymers in comparison to the existing micrometer-sized fillers. Epoxy/clay type nanocomposites were used as the most commonly used thermosets. Polymer composites are widely employed as structural materials in the aerospace sector due to possession of light weight. The ability of polymers and polymer composites to self-lubricate is advantageous for tribological components including gears, cams, bearings, and seals. Incorporating good distributed nanosize inorganic powder into a polymer matrix which improves the tribological features of polymer composites [14, 26, 27]. Numerous studies have demonstrated experimentally that metallic or inorganic nanoparticles may efficiently strengthen thermoplastic and thermosetting polymer matrices [16–18, 21, 24]. Researchers have outcomes with methods to vary the resin type, agent for curing, and processing methods to develop new materials in fabrication and processing methods. Nanocomposites are now used in various real time usages [25, 28–30]. In deriving the optimal performance, a good dispersion is needed. Various methods for the dispersion of nanoparticles into a polymer were used in the recent past, which is used for the dispersion of nanomaterials from an agglomerated to homogeneous state. The most commonly used method is the ultrasonic method, which is used for mixing to obtain a homogenous dispersion [20, 31–33]. Supersonic plasma spraying was used to deposit an aluminum oxide-phenolic resin composite layer on top of an epoxy resin matrix composite. The coating and matrix's bonding strength was 25.64 MPa. The mass ablative rate of the samples fell from 0.058 to 0.035 g/s in the oxyacetylene ablation experiment, showing that the Al_2O_3-PF composite coating could significantly increase the ablation resistance of an epoxy resin matrix composite [34]. By using a vacuum bagging approach, Vinay and Venkatesh report the manufacturing and mechanical, wear behavior of glass fiber-reinforced epoxy composites that have nano alumina added in various percentages (1%, 2%, 3%, and 4% by weight fraction). The mechanical and wear behavior of composites have been significantly enhanced by the inclusion of nanofillers. With an increase in the percentage of nanofillers, it was found that the tensile strength, bending strength, hardness, and wear rate were all gradually increasing. According to the findings, 4% of the nano-Al_2O_3 particles in the composite were effective for engineering applications [35]. Exfoliated graphite (EG) and any one of Al_2O_3, $BaTiO_3$/ZnO are combined in epoxy to generate bi-filler composites that increase microwave absorption capabilities. By employing SEM, Raman spectroscopy, and X-ray photoelectron spectroscopy, these composites are evaluated for their compositional and morphological characteristics [36]. In order to enhance the mechanical properties of their glass fiber/epoxy composite, Nayak et al. treated the epoxy matrix with Al_2O_3, SiO_2, and TiO_2 microparticles. The hand layup process is used to create the composites. In comparison to other micro modifiers, it has been found that SiO_2-treated epoxy composites have higher flexural strength, flexural modulus, and ILSS. This might be as a result of silica's smaller particle size compared to other materials. In comparison to other modifiers, the alumina-modified epoxy composite has higher hardness and impact energy. SEM shows clustering of Al_2O_3 microparticles in the matrix [37]. This presented work develops a method for study of mechanical property in the epoxy resin using nanocomposite materials. The presented work analyses the impact of mechanical characteristics on the used distribution type and the loading conditions. The mixing process is developed using the ultrasonic process, where the wear property of epoxy Al_2O_3 and SiO_2 is evaluated as a function of Al_2O_3 and SiO_2 nanoparticles.

2. Materials and Methods

This work used the material as epoxy resin (bisphenolA/epichlorohydrin) with an equivalent weight of 185–192 g, at a viscosity of 100–150 poise for a temperature of 25°C. Modified curing agent–cycloaliphaticamine. Al_2O_3 represents the ceramic nanocrystalline phase and consists of primary particles with a size of 100 nm. They are having a specific surface area of 100 m^2/g. The known value of epoxy resin was taken in a beaker. Al_2O_3 nanoparticles were mixed to the resin and stirred using a homogenizer for about 1 to 2 hours. The separation of particle agglomerates is the result of the high shear mixing. After adding the hardener (10 weight percent resin), the mixture was agitated for 14 minutes. After that, the mixture was put into the mold. The composite was cured for 24 hours at 25°C, and then, it underwent a post-cure for 1 hour at 70°C. The mixing of epoxy and nanoparticles of both reinforcements are done by ultrasonic dispersion as shown in Figure 1. Al_2O_3 nanoparticles are very small size and easily bind with the matrix. 100 nm is selected based on the previous studies.

3. Mechanical Properties' Test

3.1. Flexural Test. Bending tests are completed using ENISO 178 with a Zwick universal testing machine at room temperature and deformation rate of 0.05 mm/s with ASTM D790 standards. Five samples of each kind were tested to determine flexural characteristics.

3.2. Izod Impact Test. This test is performed using an impact tester machine in accordance with ASTMD256 standard [26]. The Notched Izod impact test was performed on samples with size of $64 \times 12.7 \times 4$ mm.

3.3. Hardness Test. The hardness test is performed using a durometer called "durometer hardness". The durometer intender foot is penetrated into the test sample for the measurement of hardness of the sample. As per standard ASTMD2240 [27], the hardness is measured using a durometer of type D.

3.4. Pin on Ring Wear Test. Tribological properties of the nanocomposite was performed on the POD apparatus with dry condition. A counter body is made up of carbon sterling which is hardened and smoothly polished sample for POD testing by maintaining pressure of 3 MPa and velocity of

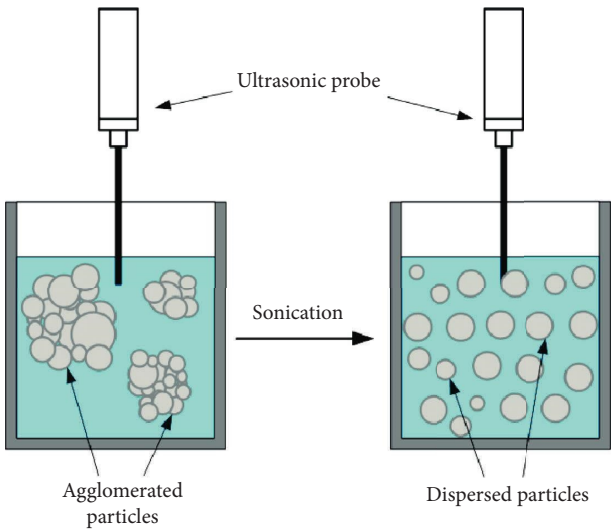

Figure 1: Ultrasonication dispersion.

0.1 m/s. To reduce the running period, all test samples were pre-worn to their average surface area before wear testing. This process minimizes the running time. Under ambient condition, the test was performed for a period of 3 hours. In the test period, the wear process removes certain portion of the material which is computed by the difference in weight [38]. The wear out of a tribological system is described by the wear performance which is defined as follows:

$$W_{\text{ts}} = \frac{\Delta\text{wm}}{\rho F_{nr} D} \frac{\text{mm}^3}{\text{Nm}}, \tag{1}$$

where

$$\begin{aligned} &\Delta\text{wm}-\text{worn mass of test sample},\\ &\rho - \text{Specific gravity}\left(\frac{\text{g}}{\text{cm}}\right),\\ &F_{nr} - \text{Force (N)},\\ &D - \text{Sliding Distance (m)}. \end{aligned} \tag{2}$$

3.5. Scanning Electron Microscopy. To observe the effect of nanoparticles, the morphology of the structure surface is examined which is generated by the Izod impact test. A scanning electron microscope was used for studying the impact due to reinforcement and wearing process.

4. Result and Discussion

4.1. Flexural Test. To test the flexural properties of the epoxy material, a three-point bending test was performed. The test was performed on the composited having Al_2O_3 and SiO_2 nanoparticles. In various past research works, it is outlined that the usage of particles of micrometer size has a rigid behavior in the stress-strain of the polymer composite. The flexural strength is observed to reinforce with a decrease in particle size as the filling content is observed to increase. As the size of the particle is decreased, the nano-sized particles has an increase in the surface area, which results in higher bonding of nanoparticles with the polymer [14]. This results in large interaction of nanoparticles with the polymer matrix and gets higher flexural strength. With varying content of Al_2O_3 and SiO_2 in the filling of nanocomposites, Figure 2 shows flexure strength with varying contents of the nanoparticles before and after test. From the observation of Figure 3, 1% addition of Al_2O_3 and SiO_2 nanoparticles results into 15% increase in flexural strength of the epoxy resin when compared to neat epoxy. 3% alumina is added for improving the flexural strength. The increase in flexural strength can be observed as a quality measure for loading and distribution of Nano particles.

The raise in flexural strength is due to bonding of nanoparticles and matrix Al_2O_3 and SiO_2 in nanocomposites. The interfacing quality of nanocomposites has a greater role in the performance of mechanical property. The distribution of the nanoparticle has a greater impact on the performance of mechanical property, defined by the distribution quality of nanoparticles [24]. A proper choice of mixing, results in a proper dispersion which increases the interaction of nanoparticles and matrix. For an effective load transferring, an optimal dispersion attains a higher surface area which results into higher flexural strength in epoxy resin. The loading condition can highly affect the mechanical performance of a nanocomposite. Higher loading results in rise of van Der Waals force among the particles resulting into lower dispersion in the particles. Hence, a high loading condition will decrease the flexural strength between the matrix and nanoparticles. This results in a non-effective load transferring condition. Polymers filled by inorganic particles are observed to improve the stiffness but with a reduction in toughness of the polymer [16, 17]. Due to the combination of inorganic and organic elements in the polymer, the morphology gets changed which results in increase of mechanical performance at nanosize. The increase in interfacial interaction of epoxy resin and Al_2O_3 and SiO_2 nanoparticles results in an increase in the stiffness.

4.2. Impact Test. Impact tests are carried out in industries to observe the characteristic of a material for loading, bending, torsion, and tension. The Izod test is the most commonly used test for the impact test due to an ease in sample preparation and getting the observation data faster [18]. There are two forms of sample preparation for the Izod impact test which is developed as notched or unnotched samples. The effect on a notched sample is observed to be lower compared to an unnotched sample as the sample strength is effective for both crack initiation and propagation. The impact is observed by the propagation of crack only. So, notches in a sample behave like a stress concentrator. If the mixing is not effected, the effect of a stress concentrator can be observed by the particle agglomerates, which operates as a stress concentrator in the polymer matrix. In the present work, it is observed that computation of energy is needed in transferring the material in the crack. The impact strength of nanocomposites with the variation of

Figure 2: Flexural test specimens before and after test.

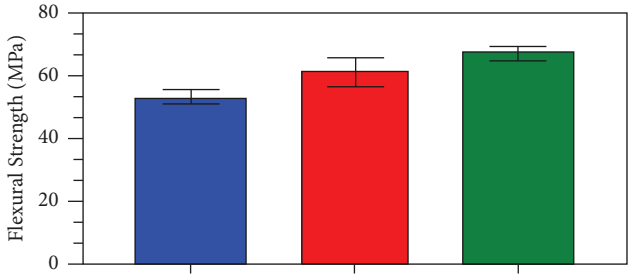

Figure 3: Flexural strength result.

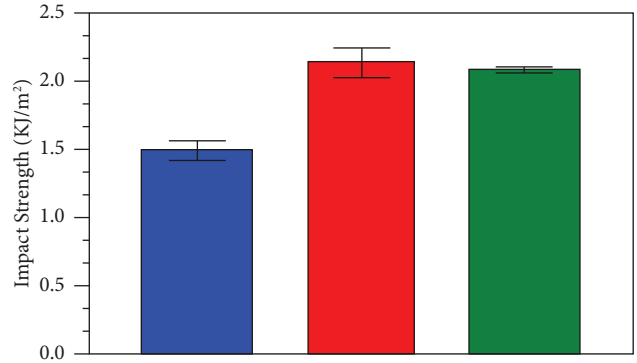

Figure 4: Impact test result.

Al_2O_3 and SiO_2 nanoparticles are shown in Figures 4, and Figure 5 shows impact test specimens.

The addition of Al_2O_3 and SiO_2 nanoparticles shows an improvement in the impact characteristic of the composite. The improvement is more effective at low level of Al_2O_3 and SiO_2 due to a finer distribution of Al_2O_3 while compared to the epoxy reinforcement at low volume of reinforcements. This effect is defined by various factors. The effect of stress concentration is observed to be low as the concentration of nanoparticles are of lower value and the impact strength is not affected by the diffusion of nanoparticles at a lower volume of Al_2O_3 and SiO_2. There is a need of appropriate mixing for a homogenous dispersion. The other factor affecting the impact strength is the loading factor which increases the agglomeration by an increase in stress concentration within the nanocomposite. So, no variations were observed in Figure 5. In comparison to a brittle polymer, the fracture surface of a thermosetting polymer is observed to be featureless in nature. The fracture effect on the surface of thermosetting is based on the testing conditions and the testing polymer structure defining shape and temperature. Three different approaches of propagation modes are seen in the process of curing and testing [21, 24]. For a continuous fracture, the sample is observed to be brittle with smooth surface. The other propagation effect is the unstable brittle which is developed due to stick/slip processing. The microstructure of epoxy with reinforcements (1% and 3%) is displayed in Figure 6.

A crack line is observed in this method. A stable ductile based propagation is observed at a high temperature [28]. The system observes a high plain stress in the epoxy-alumina composite which is used as a stress in yield shearing process. The higher impact strength of the epoxy alumina composite makes them more suitable in usage and set as an optimal replacement to the fibers in a fiber based reinforcement.

4.3. Hardness Test. The variation of the hardness for the epoxy composite with the variation of Al_2O_3 nanofiller content is shown in Figure 7. Due to proper dispersion of Al_2O_3 and SiO_2 nanofiller, the hardness factor is observed to be increased by the addition of Al_2O_3 and SiO_2 nanofillers. A low concentration of Al_2O_3 and SiO_2 nanofillers of 1% shows a larger hardness compared to a 3% Al_2O_3 and SiO_2 nanoparticles. With the increase in filer content, the hardness is observed to increase; however, for a higher filler content ratio, the hardness is observed to be reducing. The process is observed due to reducing adhesion of epoxy matrix and Al_2O_3 and SiO_2 nanofillers [25]. It is found that with increase in filler content, the cluster of Al_2O_3 increases. A minimization of hardness is observed with the epoxy composite. Figure 8 shows hardness test specimens.

4.4. Pin on Disc Wear Test. The mechanical characteristic of the epoxy matrix filled with Al_2O_3 and SiO_2 was observed in previous sections. As there is no association observed for mechanical and tribological performance, the wear characteristic of the epoxy due to change in nanoparticles is addressed in this section. In recent methods, it is observed that the nanocomposite filled with nanoparticles are more uniform in coating surfaces compared to existing coating additives [29, 30] for abrasion resistance. Whereas, it is observed that large particles are more

Figure 5: Impact test specimens before and after test.

Figure 6: Microstructure of neat epoxy, epoxy + 1% Al_2O_3 and SiO_2, and epoxy + 3% Al_2O_3 and SiO_2.

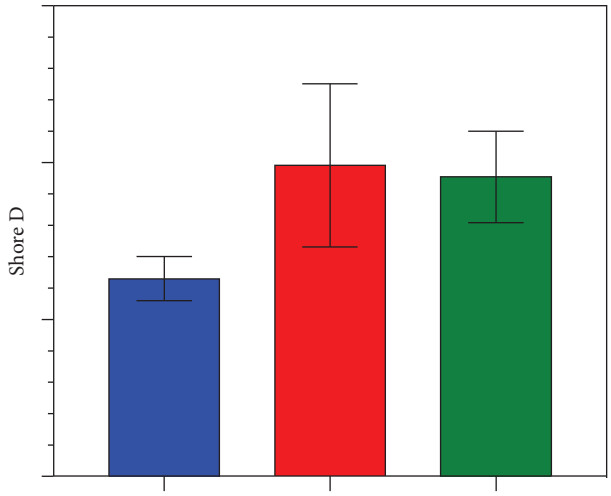

Figure 7: Hardness test outcome.

Figure 8: Hardness specimens.

suitable in protecting the polymer matrix if not been removed [20].

Figure 9 shows the wear rate with varying Al_2O_3 and SiO_2 and Figure 10 shows pin on ring wear test specimens. For reaching a steady state behavior, the wear test would take a considerable time of hours. On the steady state condition, the frictional coefficient and frictional force are observed to be at a constant value and the heat exchanges are at the equilibrium level [39, 40]. All the samples in test are tested under a constant environment. The observation made illustrates a decrease in wear rate with increase in nanoparticles which improves the wear resistance. The wear rate is observed to decrease as observed in Figure 8 with the increase in Al_2O_3 and SiO_2 nanoparticles. The minimization is more effective at a lower filling of Al_2O_3 and SiO_2 nanoparticles for about 1% as compared to 3% volume of Al_2O_3 and SiO_2 nanoparticles. Similar observations were seen with the friction coefficient as seen in Figure 11 for the epoxy matrix filled with Al_2O_3 and SiO_2 nanoparticles. Figure 12 shows set up of pin on ring wear test.

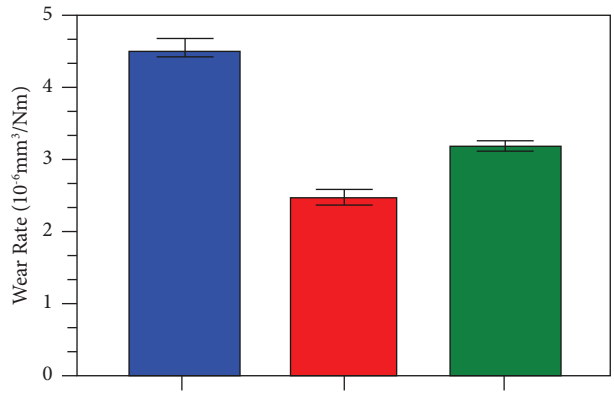

Figure 9: Wear rate result.

Figure 10: Samples for wear test.

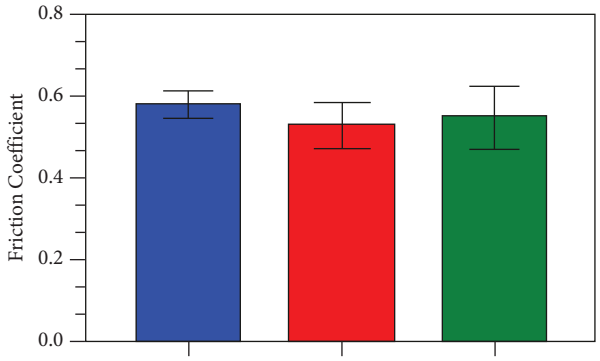

Figure 11: Friction coefficient observation.

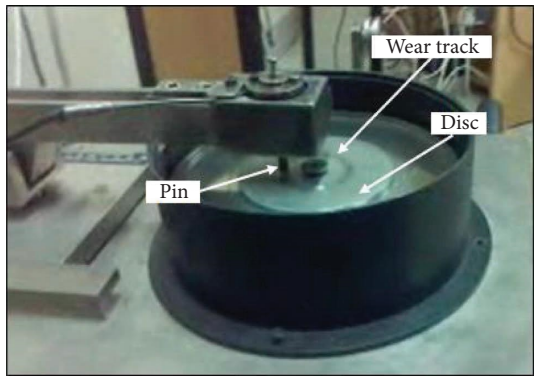

Figure 12: Pin on disc apparatus.

The bonding strength between the filler and matrix has a significant effect on the friction coefficient which improves the wear resistance. Due to shearing stress, the nanoparticle is observed to wear, and particles are observed to separate. The separation process has a great impact on the removal material because of wearing.

5. Conclusion

This paper analyzed the mechanical and tribological characteristic of the epoxy-alumina and silicon nanocomposite. The effect of the epoxy matrix is observed to be effected with the usage of nanoparticles. The presented work applied an

ultrasonic mixing for a higher dispersion quality for the epoxy-alumina and silicon nanocomposite. With the introduction of 1% volume of alumina-silicon nanoparticles, the flexural and impact strength is observed to increase. The stiffness of the material is also observed to improve. Whereas, the wear rate and the friction coefficient are observed to minimized with a 1% inclusion to alumina-silicon nanoparticles. With an increase of volume to 3%, the observation is not optimal due to increase in the agglomeration of particles. With the increase in the mechanical property and wear property, the epoxy-alumina-silicon nanocomposite is observed to replace the existing fiber-reinforced composites.

(i) When compared to other fillers, Al_2O_3, SiO_2-modified epoxy composite has higher mechanical parameters, such as flexural strength and flexural modulus.

(ii) As the size of the ceramic particle decreases, the mechanical characteristics improve.

(iii) When compared to other modifiers, the alumina-modified epoxy composite increases hardness and impact energy due to agglomeration of Al_2O_3, SiO_2 microparticles in the matrix.

(iv) For all types of composites, SEM examination clearly shows that the mode of fracture is a combination of matrix crack, matrix/fibered bonding, and fiber pull out.

Data Availability

The data used to support the findings of this study are included in the article. Should further data or information be required, these are available from the corresponding author upon request.

Disclosure

It was performed as a part of the Employment Bule Hora University, Ethiopia.

Conflicts of Interest

The authors declare that there are no conflicts of interest regarding the publication of this paper.

Acknowledgments

The authors appreciate the technical assistance from Department of Mechanical Engineering, Bule Hora University, Ethiopia, to complete this experimental work. The author convey their thanks to the Department of Mechanical Engineering, K L University, Andhra Pradesh, for their support in draft writing.

References

[1] Q. Wang, Q. Xue, W. Liu, and W. Shen, "Tribological properties of micron silicon carbide filledpoly(ether-etherketone)," *Journal of Applied Polymer Science*, vol. 74, no. 11, pp. 2611–2615, 1999.

[2] M. Vardavoulias and M. Jeandin, "Role of reinforcing ceramic particles in the wear behaviour of polymer-based model composites," *Wear*, vol. 181–183, pp. 833–839, 1995.

[3] M. Q. Zhang, M. Z. Rong, S. L. Yu, B. Wetzel, and K. Friedrich, "Effect of particle surface treatment on the tribological performance of epoxy based nanocomposites," *Wear*, vol. 253, no. 9–10, pp. 1086–1093, 2002.

[4] K. Bhardwaj, S. S. Rao, and T. B. Rao, "Investigation of hardness & tribology behavior of Epoxy and Sio2 composite: an experimental study," *Materials Today Proceedings*, vol. 45, pp. 3343–3347, 2021.

[5] S. S. R. Kbhardwaja and T. B. Rao, "Investigation of tensile and flexural behavior of epoxy and SiO2 composite," *An experimental studyMaterials Today: Proceedings*, vol. 45, pp. 2649–2726, 2021.

[6] S. Bahadur, D. Gong, and J. Anderegg, "The investigation of the action of fillers by XPS studies of the transfer films of PEEK and its composites containing CuS and CuF2," *Wear*, vol. 160, no. 1, pp. 131–138, 1993.

[7] G. Boopathy, V. Vanitha, K. Karthiga et al., "Optimization of tensile and impact strength for injection moulded nylon 66/SiC/B4c composites," *Journal of Nanomaterials*, vol. 2022, Article ID 4920774, 9 pages, 2022.

[8] K. Bhardwaj, S. S. Rao, and T. B. Rao, "Epoxy reinforced with Nano TIO2 particles: an experimental investigation of mechanical &tribological behavior," *Materials Today Proceedings*, vol. 62, 2022.

[9] M. Zhi Rong, M. Qiu Zhang, H. Liu, H. M. Zeng, B. Wetzel, and K. Friedrich, "Microstructure and tribologicalbehavior-ofpolymeric nanocomposites," *Industrial Lubrication & Tribology*, vol. 53, no. 2, pp. 72–77, 2001.

[10] R. P. Singh, M. Zhang, and D. Chan, *Journal of Materials Science*, vol. 37, no. 4, pp. 781–788, 2002.

[11] C. B. Ng, L. S. Schadler, and R. W. Siegel, "Synthesis and mechanical properties of TiO2-epoxy nanocomposites," *Nanostructured Materials*, vol. 12, no. 1-4, pp. 507–510, 1999.

[12] Q. Wang, Q. Xue, and W. Shen, "The friction and wear properties of nanometre SiO2 filled polyetheretherketone," *Tribology International*, vol. 30, no. 3, pp. 193–197, 1997.

[13] Q. Wang, Q. Xue, W. Shen, and J. Zhang, "The friction and wear properties of NanometerZrO2-filledpoly-ether-etherketone," *Journal of Applied Polymer Science*, vol. 69, no. 1, pp. 135–141, 1998.

[14] V. Harshitha and S. Srinivasa Rao, "Design and analysis of ISO standard bolt and nut in FDM 3D printer using PLA and ABS materials," *Materials Today Proceedings*, vol. 19, pp. 583–588, 2019.

[15] P. Paramasivam and S. Vijayakumar, "Mechanical characterization of aluminium alloy 6063 using destructive and non-destructive testing," *Materials Today Proceedings*, vol. 63, pp. 2502–2505, 2021.

[16] B. T. Chintalapudi, C. B. Gonuguntla, M. Pothuri, J. Kant, A. Pathan, and R. K. Pittala, "Investigation of mechanical properties of duralumin sandwich hybrid composite using E-glass fiber," *International Journal of Mechanical Engineering & Technology*, vol. 8, no. 5, pp. 425–431, 2017.

[17] R. A. Braga and P. A. A. Magalhaes, "Analysis of the mechanical and thermal properties of jute and glass fiber as reinforcement epoxy hybrid composites," *Materials Science and Engineering: C*, vol. 56, pp. 269–273, 2015.

[18] A. K. Pathak, M. Borah, A. Gupta, T. Yokozeki, and S. R. Dhakate, "Improved mechanical properties of carbon fiber/graphene oxide-epoxy hybrid composites," *Composites Science and Technology*, vol. 135, pp. 28–38, 2016.

[19] S. Vijayakumar, S. Anitha, R. Arivazhagan, A. D. Hailu, T. V. J. Rao, and H. P. Pydi, "Wear investigation of aluminum alloy surface layers fabricated through friction stir welding method," *Advances in Materials Science and Engineering*, vol. 2022, Article ID 4120145, 8 pages, 2022.

[20] M. R. Sanjay and B. Yogesha, "Studies on mechanical properties of jute/E-glass fiber reinforced epoxy hybrid composites," *Journal of Minerals and Materials Characterization and Engineering*, vol. 4, no. 1, pp. 15–25, 2016.

[21] G. Açıkbas, S. Özcan, and N. ÇalısAçıkbas, "Production and characterization of a hybrid polymer matrix composite," *Polymer Composites*, vol. 39, no. 11, pp. 4080–4093, 2018.

[22] D. Pal, S. Vijayakumar, T. J. Rao, and R. S. R. Babu, "An examination of the tensile strength, hardness and SEM analysis of Al 5456 alloy by addition of different percentage of SiC/flyash," *Materials Today Proceedings*, vol. 62, pp. 1995–1999, 2022.

[23] S. Vijayakumar, P. S. Satheesh Kumar, P. Sampath kumar, S. Manickam, G. B. Ramaiah, and H. P. Pydi, "The effect of stir-squeeze casting process parameters on mechanical property and density of aluminum matrix composite," *Advances in Materials Science and Engineering*, vol. 2022, Article ID 3741718, 10 pages, 2022.

[24] C.-K. Lam, H.-y. Cheung, K.-t. Lau, L.-m. Zhou, M.-w. Ho, and D. Hi, "Cluster size effect on hardness of Nanoclay/epoxy composites," *Composites Part B: Engineering*, vol. 36, no. 3, Article ID 263269, 2005.

[25] G. A. Kumar, S. Surya, G. S. Naidu, G. Phanindra, and Y. Gangaraju, "Investigation of flexural strength for carbon reinforced aluminiumNano composite," *International Journal of Mechanical Engineering & Technology*, vol. 8, no. 12, pp. 1083–1088, 2017.

[26] E. Petrie, *Epoxy Adhesive Formulations*, McGraw Hill Professional, New York, NY, USA, 2005.

[27] N. Domun, H. Hadavinia, T. Zhang, T. Sainsbury, G. H. Liaghat, and S. Vahid, "Improvingthe fracture improving the fracture toughness and the strength of epoxy," *Nanoscale*, vol. 7, 2015.

[28] B. Gugulothu, S. Seetharaman, S. Vijayakumar, and D. Jenila Rani, "Process parameter optimization for tensile strength and Hardness of Al-MMC using RSM technique," *Materials Today Proceedings*, vol. 62, pp. 2115–2118, 2022.

[29] M. S. Anirudh, S. N. Asif, S. V. Nadella, and K. Nagireddy, "Investigation o Investigation of Mechanicalproperties of al 7075/B4C/GR hybrid metal matrix composite," *International Journal of Mechanical Engineering & Technology*, vol. 8, no. 5, pp. 400–408, 2017.

[30] K. Bharadwaja, S. S. Rao, and T. Baburao, "Epoxy/SIO2 nanocomposite mechanical properties and tribological performance," *Materials Today Proceedings*, vol. 62, 2022.

[31] B. Gugulothu, N. Nagarajan, A. Pradeep, G. Saravanan, S. Vijayakumar, and J. Rao, "Analysis of mechanical properties for Al-MMC fabricated through an optimized stir casting process," *Journal of Nanomaterials*, vol. 2022, Article ID 2081189, 7 pages, 2022.

[32] A. A. Aly, S. B. Zeidan, A. A. A. Alshennawy, A. A. El-Masry, and W. A. Wasel, "Friction and wear of polymer composites filled by nano-particles: a review," *World Journal of Nano Science and Engineering*, vol. 2, no. 1, pp. 32–39, 2012.

[33] A. Patnaik1 and S. Biswas, "Investigations on three-body abrasive wear and mechanical properties of particulate filled glass epoxy composites " Malaysian," *Polymer Journal*, vol. 5, no. 2, pp. 37–48, 2010.

[34] Q. Peng, M. Liu, Y. Huang et al., "Development mechanism and performance of Al2O3-PF composite coating on epoxy resin matrix composite surface by supersonic plasma spraying," *Surface and Coatings Technology*, vol. 446, Article ID 128762, 2022.

[35] S. S. Vinay and C. V. Venkatesh, "Effect of nano-Al2O3 particles on mechanical and wear behaviour of glass fibre epoxy composites," *Materials Today Proceedings*, vol. 46, pp. 9004–9007, 2021.

[36] S. K. Singh, M. J. Akhtar, and K. K. Kar, "Impact of Al2O3, TiO2, ZnO and BaTiO3 on the microwave absorption properties of exfoliated graphite/epoxy composites at X-band frequencies," *Composites Part B: Engineering*, vol. 167, pp. 135–146, 2019.

[37] R. K. Nayak, A. Dash, and B. C. Ray, "Effect of epoxy modifiers (Al 2 O 3/SiO 2/TiO 2) on mechanical performance of epoxy/glass fiber hybrid composites," *Procedia Materials Science*, vol. 6, pp. 1359–1364, 2014.

[38] B. Gugulothu, S. L. Sankar, S. Vijayakumar et al., "Analysis of wear behaviour of AA5052 alloy composites by addition alumina with zirconium dioxide using the Taguchi-grey relational method," *Advances in Materials Science and Engineering*, vol. 2022, Article ID 4545531, 7 pages, 2022.

[39] T. B. Rao, P. K. Vamsi, D. S. Ram, M. Jagadeesh, V. Pilli, and P. V. Ramarao, "Experimental investigation on peak temperature and tensile strength during plasma arc welding of ss-316," *International Journal of Mechanical Engineering & Technology*, vol. 9, no. 4, pp. 284–292, 2018.

[40] S. R. Ranganatha, H. C. Chittappa, and T. Dranganatha, "INVESTIGATION ON THREE BODY ABRASIVE WEAR OFAl2O3 FILLER," *ON CFRP COMPOSITES" International Journal of Advanced Engineering Research and Studies*, vol. 2, pp. 83–85, 2013.

Hindawi
Advances in Materials Science and Engineering
Volume 2023, Article ID 4414502, 9 pages
https://doi.org/10.1155/2023/4414502

Research Article

Forging Temperature Effects on Crack Tip Creep Behaviour of Hot Hammer Forged Ti-6Al-4V Alloy

Xiurong Fang,[1] **Yan Liu**,[1] **Yanru Shao**,[2] **Huihui Xu**,[1] **and Fuqiang Yang**[1]

[1]*School of Mechanical Engineering, Xi'an University of Science and Technology, Xi'an, China*
[2]*Kangni Mechanical & Electrical Co. Ltd., Nanjing, China*

Correspondence should be addressed to Xiurong Fang; fangxr098@163.com

Received 3 August 2022; Revised 4 November 2022; Accepted 24 November 2022; Published 23 January 2023

Academic Editor: Sengottuvelu Ramesh

The creep behaviour of hot hammer forged Ti-6Al-4V alloy under different forging temperatures has an essential influence on their high-temperature service performance. In this article, the high-temperature mechanical property and creep behaviour of Ti-6Al-4V alloy forging at different forging temperatures were first investigated experimentally. Then, in view of the critical effect of microcracks and other defects on the service life of components in forging, the creep characteristics at the tip of a 2 mm crack were characterized by the finite element method. The results show that when the Ti-6Al-4V alloy was forged at 1000°C, the high-temperature mechanical property was improved, and the steady-state creep rate and creep residual deformation were significantly reduced. In addition, the creep strain and creep rate at the crack tip were decreased apparently during creep, and the creep strain gradient in the crack tip region was also significantly reduced. This indicates that the creep deformation of Ti-6Al-4V alloy can be controlled by an appropriate forging temperature during hot hammer forging process and might delay the crack propagation to improve the service life of components.

1. Introduction

Ti-6Al-4V alloy is used as a structural material for turbine blades because of its high strength, corrosion resistance, and excellent high-temperature properties [1, 2]. The creep behaviour of titanium alloys is critical to blade's service life and the turbine's safety and credibility in high-temperature and pressure service environments [3]. In recent years, to achieve the development goals of ultra-supercritical generating units with high capacity, high power, and long life, the steam temperature and pressure of the turbine were continuously increased, which puts forward a severe test to the creep property of turbine blades [4, 5]. Therefore, the creep behaviour of titanium alloys has received much attention from many researchers. Dvorak et al. [6] performed constant load creep tests on titanium alloy with different annealing temperatures. It was found that titanium prepared at elevated room temperatures had an ultrafine grain size microstructure, which exhibited a higher creep strength than titanium prepared at low temperatures. Dogan et al. [7] studied the effects of microstructure on creep crack growth behaviour of Ti-6242 alloys in the forged and heat-treated condition. The results showed that the material with lamellar microstructure is more creep deformation resistant than the material with equiaxed microstructure. Consequently, the creep behaviour of titanium alloy components is strongly influenced by the preparation process.

The pre-existing microcracks and other defects may exist before the titanium alloy component is put into service. With the increasing of the creep exposure time, the microcracks or other defects inside the material will further grow until the failure of the component [8, 9]. The forging plastic forming process, a common production method for Ti-6Al-4V alloy blades, is applicable to enhance the mechanical properties and can substantially eliminate internal flaws [10]. And compared with hydraulic press forging, the comprehensive mechanical properties of Ti-6Al-4V alloy forged by hot hammer forging are more excellent due to the high deformation rate that leads to the formation of finer grains [2, 11, 12]. Lou et al. [13–15] showed that the variation

of forging parameters during hot hammer forging could significantly affect the phase transformation process of Ti-6Al-4V alloy, in which the variation of forging temperature has a more significant effect on the phase transformation, dislocation motion, and grain boundary slip state during the forging deformation of titanium alloy. It can be clarified that, in the hot hammer forging plastic forming process, the forging temperature is a vital parameter affecting the forging properties.

Creep deformation is induced when titanium alloy components are subjected to long-term operation at high temperature and pressure. The creep deformation accumulation reaches the critical value, the creep crack begins to initiate and propagate, and creep fracture will occur in severe cases [16, 17]. It is effective and accurate to test the creep behaviour of cracks in high-temperature materials using standard specimens. However, the method is time-consuming and highly expensive. Thus, the finite element method is widely used to investigate crack propagation in high-temperature materials. Zhang et al. [18–20] determined the creep damage model based on the material properties of high-temperature alloys, the loading state of the component in service, and investigated the creep crack propagation behaviour by the finite element method. The final physical experiment verified that the simulated data agreed well with the experimental results, which indicated that the numerical method can be used to simulate the creep crack propagation behaviour of high-temperature alloys.

In summary, creep behaviour and creep crack extension of titanium alloy have been extensively investigated and discussed in the last decade. However, few studies focused on how to produce titanium alloy forgings with excellent creep property by controlling the forging process parameters. In this article, the effect of different forging temperatures on the creep behaviour of Ti-6Al-4V alloy forgings is investigated by designing the hot hammer forging temperature. The creep characteristic parameters of the crack tip were further analyzed. It aims to understand the relationship between forging temperature and creep behaviour of titanium alloys after hot hammer forging, which also provides a basis for backtracking the forging process parameters by the creep property requirements of the titanium alloy components.

2. Materials and Methods

2.1. Materials. The commercially available Ti-6Al-4V alloy bars with a diameter of 100 mm and a height of 150 mm were produced by ingot metallurgy. They were provided by China Heavy Machinery Research Institute and the nominal chemical compositions are listed in Table 1.

Table 1: Main chemical composition of Ti-6Al-4V alloy.

Element	Al	V	Fe	O	Impurity	Ti
Wt. (%)	6.29	4.03	0.098	0.16	<0.40	Bal.

2.2. Experimental Procedure

2.2.1. Forging Experiments. As we all know, forging is an experience-oriented technology [21]. The Institute has accumulated a great experience in titanium alloy forging experiments over the years. Therefore, the forging experiments were conducted based on the standard of the forging manual and forging experience [22]. The experimental procedure of forging is shown in Figure 1. The free forging electro-hydraulic hammer of CZYQ-120 had been used in the forging experiment. It has a maximum strike stroke of 1200 mm and strike energy of 120 kJ, respectively, and the mass of the hammerhead is 3400 kg. The energy consumption for preheating and the heat loss in the forging process were considered. Before forging, the upper and lower anvils had been preheated at 200 to 300°C according to the requirements of the institute's forging process. The samples were heated in a special heating furnace with a heating rate of 6°C/min. When the temperature reached the preset forging temperature, the samples were held for 120 min to ensure uniform temperature distribution inside and outside the samples. Due to the relatively narrow forging temperature band of titanium alloys, the whole forging process needs to be completed within 20 s as far as possible. The height reduction of the forgings was controlled by setting the height of the limit block. Finally, the forging was cooled to room temperature by air cooling when the reduction in the overall height of the forgings reached 50%.

It is generally known that the temperature is an important factor affecting the performance of the component during processing [23]. Ti-6Al-4V alloy will crystallize to α-phase in low temperature and transform to β-phase in high temperature, thus the forging of Ti-6Al-4V alloy is divided into $\alpha+\beta$ forging ($T = T_\beta - (30\sim60^\circ C)$), near β forging ($T = T_\beta - (10\sim15^\circ C)$), and β forging ($T > T_\beta$). The measured β-transition temperature of the material was about 985°C [24]. The forging experiment scheme was formulated based on the relationship between the forging temperature and β phase transition temperature as shown in Table 2.

2.2.2. High-Temperature Tensile and Creep Tests. Five groups of tensile samples with five samples in each group were cut from each forged sample for high-temperature tensile and creep tests. Then, all these samples were mechanically polished, cleaned, and dried before testing. As shown in Figures 2(a) and 2(b), the geometrical sizes of standard high-temperature tensile and creep test samples were determined based on high-temperature tensile test method for metal materials (GB/T 228.2-2015) and uniaxial tensile creep test method for metallic materials (GB/T 2039-2012).

The high-temperature tensile tests were carried out at 400°C based on the temperature of the service environment of the turbine blades. Before the test, the samples had been loaded into the high-temperature furnace of the INSTRON 5982 tensile testing machine for heating and held for 15 min when the temperature reached 400°C. The tensile speed was 10 mm/min and the tensile strain rate was $6.67 \times 10^{-3}\ s^{-1}$ during the experiment. The creep tests were conducted on the RD-100 electronic axial tensile creep test machine at a temperature of 400°C, stress loading of 484 MPa, and creep

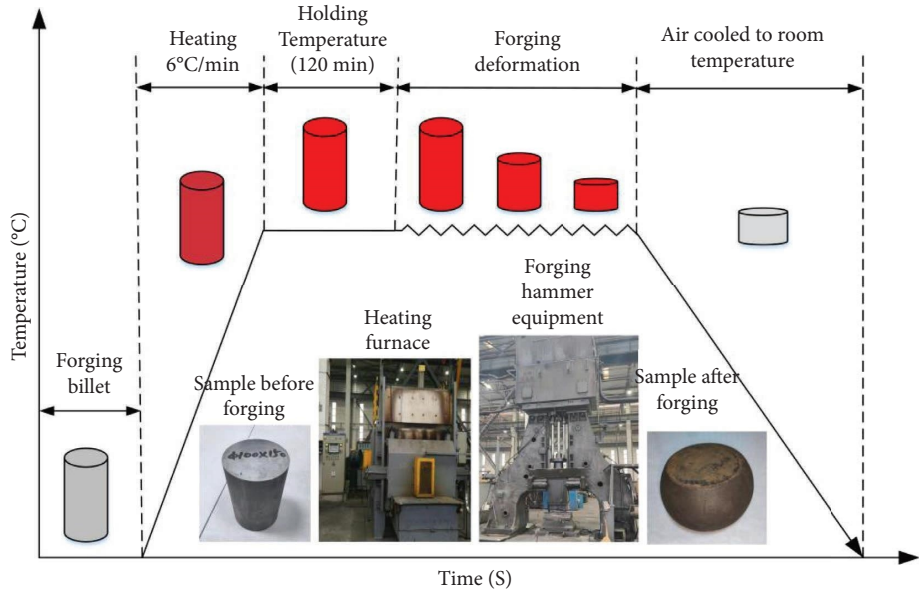

Figure 1: Ti-6Al-4V alloy forging process.

Table 2: Forging experiment scheme of Ti-6Al-4V alloy at different forging temperatures.

Samples	Forging types	Forging temperature (°C)
1#	$\alpha+\beta$	T_β − 60 925
2#	$\alpha+\beta$	T_β − 35 950
3#	Near β	T_β − 10 975
4#	β	T_β + 15 1000
5#	β	T_β + 40 1025

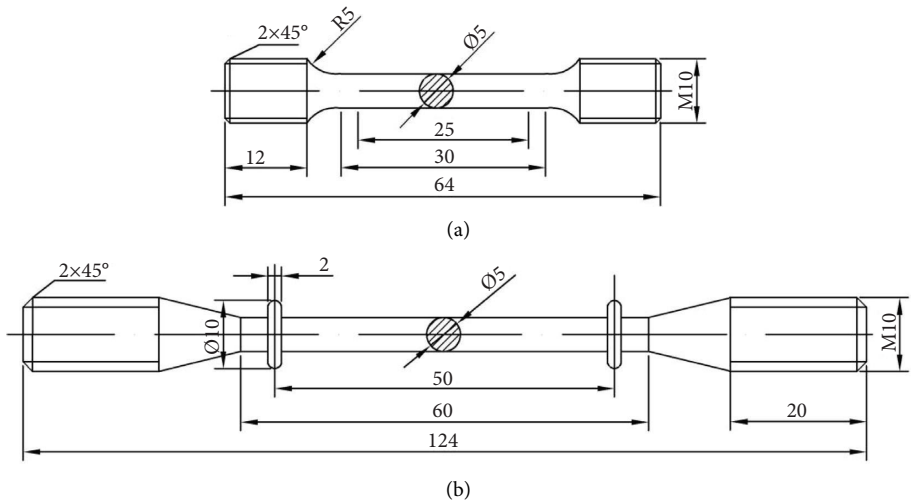

Figure 2: Geometrical sizes of the sample of Ti-6Al-4V alloy (unit: mm): (a) high-temperature tensile sample; (b) creep sample.

time of 80 h. Before testing, the sample had been loaded into the high-temperature furnace for heating and holding for 1 hour when the temperature reached 400°C. The temperature fluctuations were less than ±2°C. Then, the creep stress was loaded with a loading rate of 50 N/s to a preset value and the timing started. The bidirectional extensometer had been

used to measure the creep deformation of the samples and a computerized data acquisition system recorded the creep data in real time.

2.3. Finite Element Method

2.3.1. Constitutive Creep Model. This article studied the creep behaviour of Ti-6Al-4V alloy forging at constant temperature and load, and the time hardening mathematical model is adopted [25, 26]:

$$\dot{\varepsilon} = A\sigma^n t^m, \tag{1}$$

where $\dot{\varepsilon}$ and t are the creep rate and creep time, respectively, A, n, and m are the material constant, stress index, and time index, respectively, A and $n > 0$, and $-1 < m \leq 0$. As shown in equation (2), the expression of creep strain is obtained by integrating equation (1):

$$\varepsilon = \frac{A}{m+1}\sigma^n t^{m+1}, \tag{2}$$

where ε is the creep strain.

2.3.2. Geometry and Mesh Models. The finite element model of the sample with a single-sided crack is shown in Figure 3(a), where W is the width, $2L$ is the length, and the length of the prefabricated crack is a. The constitutive creep model and mechanical property parameters of Ti-6Al-4V alloy at high temperatures were introduced into the CREEP module of ABAQUS. The creep load and creep time were consistent with creep experiments. To balance the calculation efficiency and the accuracy of the results, fine elements were used in the vicinity of the crack tip while coarse elements were used elsewhere. The four-node linear quadrilateral element (CPE4R) was used in the meshing and the global finite element mesh is given in Figure 3(b), and the mesh around the crack tip is shown in Figure 3(c). The geometry of this model was taken as $W = 20$ mm, $L = 25$ mm, and $a = 2$ mm according to the standard SENT sample [27].

3. Results and Discussion

3.1. High-Temperature Mechanical Property. As shown in Figure 4, the averaged mechanical parameters of each sample were calculated after the high-temperature mechanical tensile experiments. When the forging is below the β-phase transition temperature, there is no significant change in the mechanical property of the samples at different forging temperatures. When the forging temperature increases above the β-phase transition temperature to 1000°C, the yield strength and tensile strength are significantly increased with an average increase of 13.8% and 10.6%, respectively. Meanwhile, the reduction of fracture area and elongation also increased by an average of 15.3% and 5.9%. However, when the forging temperature is 1025°C, the comprehensive mechanical property of the sample decreases sharply. This indicates that Ti-6Al-4V alloy forged at a forging temperature of 1000°C has optimum strength and ductility and shows optimal mechanical property.

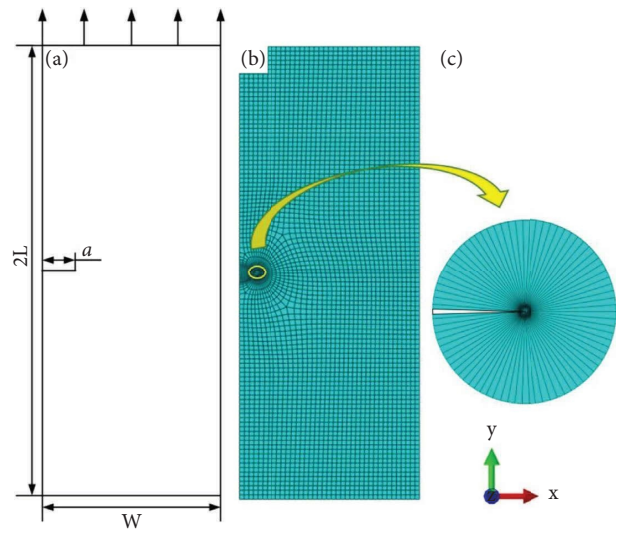

Figure 3: Finite element model: (a) finite element geometry model; (b) global finite element mesh; (c) mesh around the crack tip.

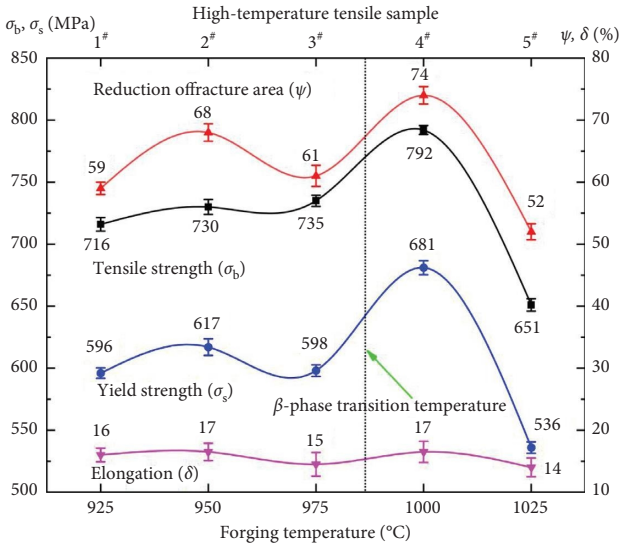

Figure 4: High-temperature mechanical property of Ti-6Al-4V alloy at different forging temperatures (average value of five forged Ti-6Al-4V alloy samples).

3.2. High-Temperature Creep Property. The averaged creep curves of each sample were calculated after the creep experiment, as shown in Figure 5. Creep curves display well-defined two creep stages such as the initial creep stage and steady-state creep stage. When the forging temperature changed, the creep strains of samples 1#, 2#, 3#, and 5# were larger than sample 4# and reached the steady-state creep stage early. This is because, at the forging temperature of 1000°C, the deformation resistance of the forging increases due to the increase in yield strength and ultimate tensile strength; thus, the degree of creep deformation of the forging is reduced.

The majority of creep time is occupied by the steady-state creep stage, and the steady-state creep rate and creep

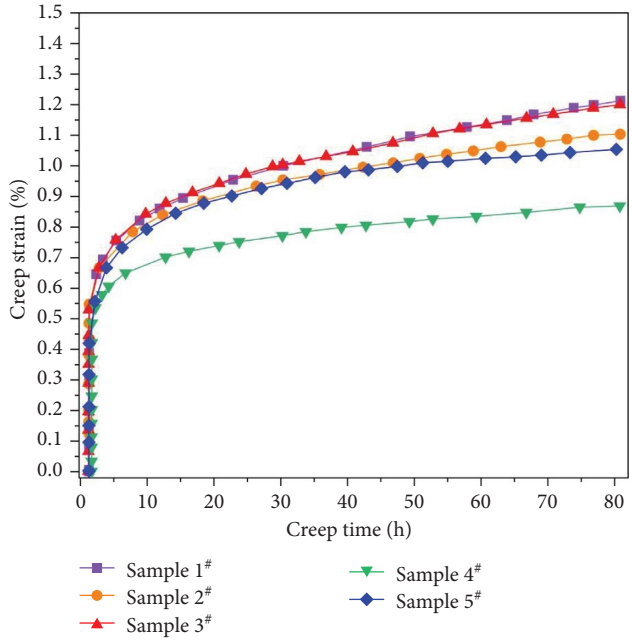

Figure 5: Creep curve of Ti-6Al-4V alloy at different forging temperatures.

residual deformation are usually used to reflect the creep behaviour of the materials [28]. The averaged steady-state creep rate and creep residual deformation of each sample are calculated as shown in Figure 6. With the increase in forging temperature, the steady-state creep rate and creep residual deformation tend to fluctuate downward in general. When the forging temperature is above the β-transition temperature to 1000°C, the steady-state creep rate and creep residual deformation are significantly reduced with an average reduction of 51.3% and 25.6%, respectively. When the forging temperature is 1025°C, the steady creep rate and creep residual deformation increase by another 20% and 30%, respectively. Therefore, during hot hammer forging of Ti-6Al-4V alloy, the creep-induced failure and damage of the forging can be significantly slowed down at a forging temperature of 1000°C. In this way, the service life of the component can be improved.

Studies have shown that the mechanical properties of materials are related to their microstructure. The microstructure of hot hammer forged Ti-6Al-4V at different forging temperatures has been studied by author Fang in the previous work. It was found that the morphology and volume fraction of α and β phases were significantly affected by the forging temperature of hot hammer forging process [2]. As shown in Figures 4–6, when the forging temperature is above the β phase transition temperature to 1000°C, the equiaxed α phase disperses into the $\alpha+\beta$ substrate and the volume fraction of α phase increases. This causes an increase in the forging deformation resistance and a significant improvement in the mechanical property of the forgings. In addition, the lamellar structure is significantly increased, which increases the difficulty of creep slide and hinders the formation of grain boundary voids; the steady-state creep rate and creep residual deformation are reduced after creep. However, with an increasing forging temperature of 1025°C, the α phase nucleates at the grain boundaries and then grows as lamellae into the prior β phase to form the fine needle-like $\alpha+\beta$ lamellar phase, which caused a sharp decrease in the mechanical property of the forgings. Moreover, the numerous $\alpha+\beta$ lamellar phase provides an increasing opportunity for the nucleation of voids, which also aggravates the creep deformation and creep rate of forgings. It can be seen that, with an increasing forging temperature of 1025°C, the creep deformation and creep rate increase the company with a dramatical drop in strength and ductility. Therefore, the finite element analysis of creep was carried out on an alloy forged at 925°C, 950°C, 975°C, and 1000°C, respectively. The critical parameters of the constitutive creep model of equation (2) were fitted according to the experimental creep data, as shown in Table 3.

3.3. The Crack Tip Creep Characteristics

3.3.1. Creep and Creep Rate. The creep curves at the crack tips of the samples is shown in Figure 7(a). During the creep of 80 hours, the creep strain of Ti-6Al-4V alloy at the crack tip under different forging temperatures changed significantly. The creep strain of Ti-6Al-4V alloy forged below β-phase transition temperature is larger than that forged above the β-phase transition temperature. When the creep is carried out for about 70 hours, the creep strain and creep rate of the crack tip gradually stabilizes, and the creep gradually reaches the steady-state creep stage. The minimum creep strain increment at the crack tip of sample 4# is 0.45%, which is reduced by 45.4%, 26.8%, and 42.3% compared to samples 1#, 2#, and 3#, respectively. In addition, as shown in Figure 7(b), sample 4# keeps a low creep rate in the creep process, which not only slows down the creep deformation of the crack tip but also can effectively delay the creep crack propagation. Therefore, at the forging temperature of

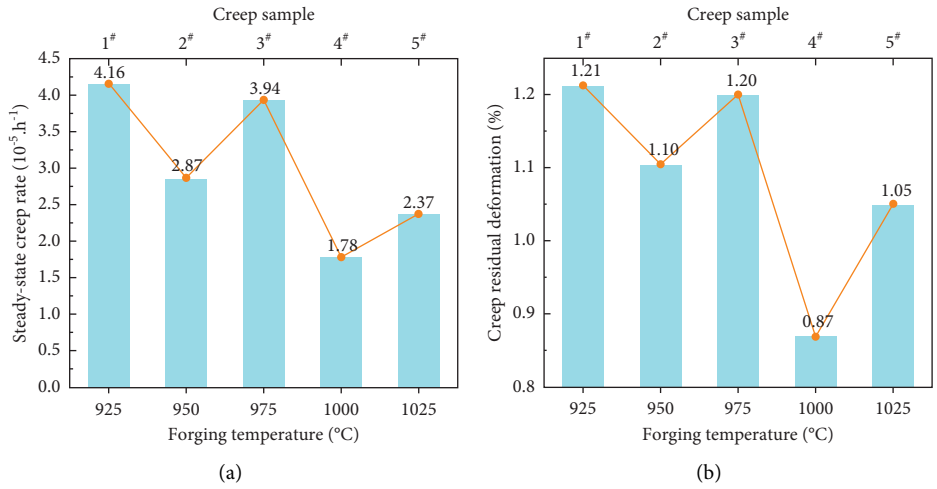

Figure 6: Creep characteristics of Ti-6Al-4V alloy at different forging temperatures: (a) steady-state creep rate; (b) creep residual deformation.

Table 3: Creep equation and parameters of Ti-6Al-4V alloy at different forging temperatures.

Samples	A	n	m
1#	1.7549×10^{-10}	2.5173	−0.8038
2#	3.0787×10^{-9}	2.0278	−0.8509
3#	4.2437×10^{-11}	2.7431	−0.8187
4#	1.1275×10^{-8}	1.7650	−0.8794

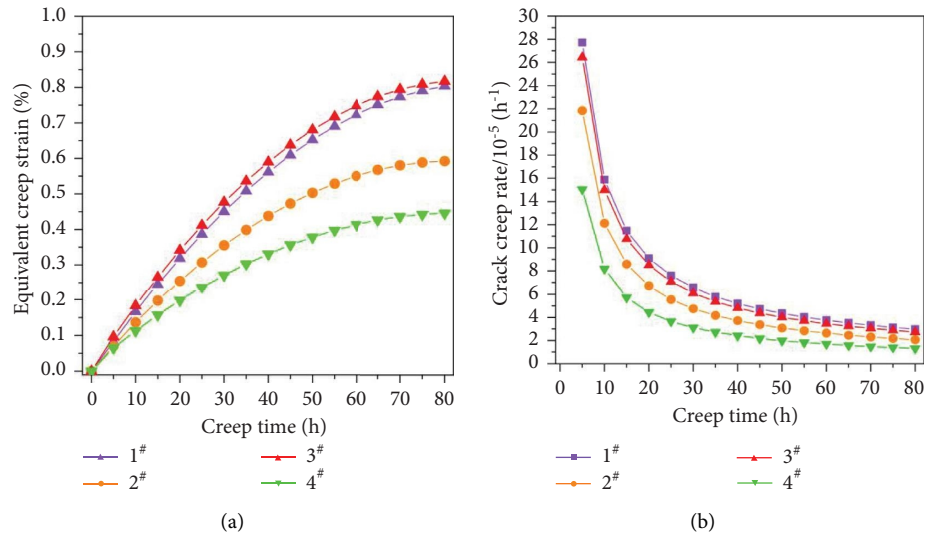

Figure 7: Creep characteristics at the crack tip of Ti-6Al-4V alloy at different forging temperatures: (a) creep curve; (b) creep rate.

1000°C, the creep resistance at the crack tip of the Ti-6Al-4V alloy is significantly improved, which may prolong the service life of titanium alloy components by slowing down the crack expansion process.

3.3.2. Equivalent Creep Strains in the Crack Tip Region. A circular area of $\varphi = 50\,\mu$m at the crack tip was taken to observe the creep strain distribution accurately. As shown in Figure 8, the equivalent creep strains are symmetrically distributed along the direction of crack expansion. The equivalent creep strain gradients at the crack tip of samples 1#, 2#, and 3# are the most obvious, divided into eight regions by seven contours, and the creep strain corresponds to 0.1%, 0.2%, 0.3%, 0.4%, 0.5%, 0.6%, and 0.7%. However, the equivalent creep strain distribution of sample 4# is only divided by contours 0.1%, 0.2%, 0.3%, and 0.4% into five regions. Furthermore, the creep strain gradients in front and

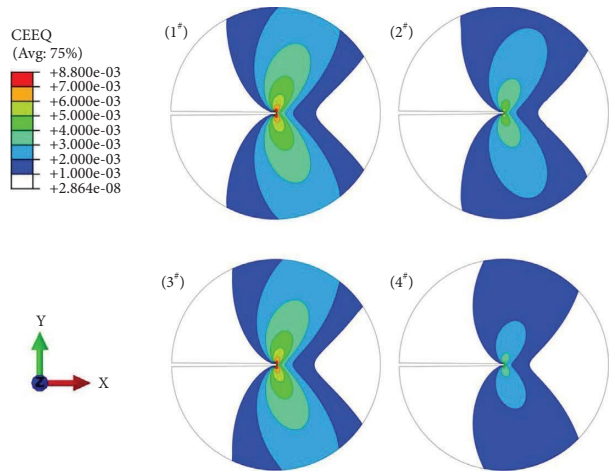

Figure 8: Equivalent creep strain (CEEQ) distribution of Ti-6Al-4V alloy in the crack tip region at different forging temperatures: (1#) 925°C, (2#) 975°C, (3#) 950°C, and (4#) 1000°C.

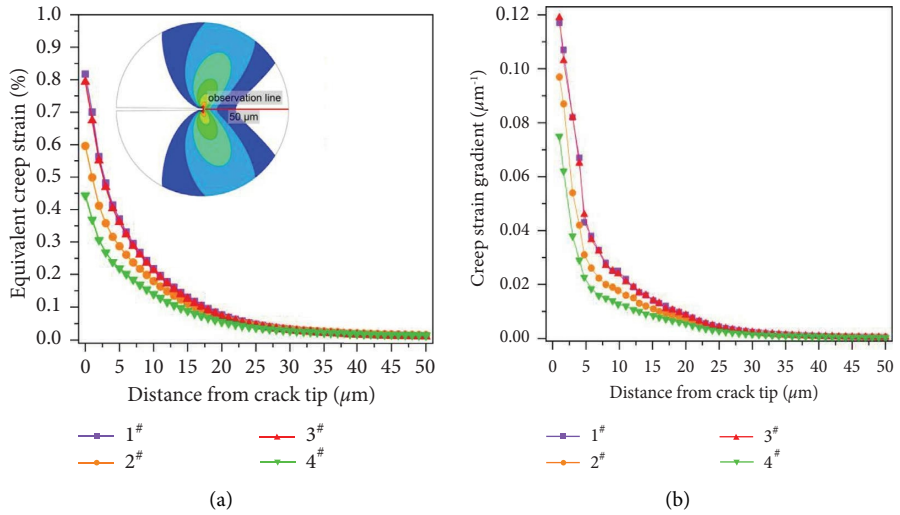

Figure 9: Equivalent creep strain on the observed line in front of the crack tip of Ti-6Al-4V alloy at different forging temperatures. (a) Equivalent creep strain. (b) Creep strain gradient.

on both sides of the crack in samples 1#, 2#, and 3# are larger than those in sample 4#, which indicates that the creep deformation zone is significantly reduced and the equivalent creep strain in the X and Y directions will be a smaller strain gradient in the crack tip region with increasing forging temperature to 1000°C.

The maximum value of mechanical parameters is located in front of the crack propagation. The equivalent creep strain distribution on the 50 μm observation line in front of the crack tip is presented in Figure 9(a). The maximum value of equivalent creep strain at the crack tip decreases sharply and then tends to be flat as the distance from the crack tip increases. The equivalent creep strain values of the 4 samples gradually tend to 0.05% when the distance from the crack tip is beyond 30 μm. It means that the influence of forging temperature on the creep deformation in the crack tip region of the Ti-6Al-4V alloy forging is weakened with the increase of the distance from the crack tip. Moreover, as shown in Table 4, sample 4# exhibits the minimum reduction in equivalent creep strain on the observation line, which decreased by 48.1%, 27.3%, and 46.7%, respectively, compared to samples 1#, 2#, and 3#.

The driving force of creep crack propagation is determined by the creep strain gradient, and it is reasonable to characterize the creep crack propagation behaviour with a creep strain gradient [29]. As shown in Figure 9(b), the creep strain gradient of the crack tip of the sample at different forging temperatures shows the same trend as the creep strain. On the line of observation in front of the crack, the creep strain gradient of sample 4# was significantly reduced compared to samples 1#, 2#, and 3#.

It indicates that when the forging temperature is above the β-phase transition temperature to 1000°C, Ti-6Al-4V alloy forging can keep a low creep strain and creep strain gradient in the crack tip region during the creep process even if there is the appearance of microcracks. The low creep

Table 4: Comparison of equivalent creep strains on observation lines of Ti-6Al-4V alloy at different forging temperatures.

Samples	Maximum equivalent creep strain (%)	Minimum equivalent creep strain (%)	Reduction (%)
$1^{\#}$	0.82	0.05	0.77
$2^{\#}$	0.60	0.04	0.56
$3^{\#}$	0.80	0.05	0.75
$4^{\#}$	0.45	0.05	0.40

strain gradient means that the driving force of crack propagation will be reduced. Therefore, the crack propagation rate will also be effectively slowed down during the service of the components, which is important for improving the service life of Ti-6Al-4V alloy forging.

4. Conclusions

From a sustainability viewpoint, the creep behaviour and creep characteristics at the crack tip of the forged Ti-6Al-4V alloy were investigated by physical experiments. Then, the creep characteristics of the crack tip with the same crack length were analyzed by a finite element method according to the experimental data.

The experimental results show that the forgings forged at 1000°C exhibited optimum high-temperature mechanical and creep property. The yield strength and tensile strength increased by an average of 14.2% and 10.6%, respectively, while the elongation and section shrinkage improved by an average of 15.3% and 5.9%, respectively. In addition, steady-state creep rate and creep residual deformation decreased with an average of 51.3% and 25.6%, respectively.

It was found by the finite element method that Ti-6Al-4V alloy forged at the temperature of 1000°C was creeping for 80 hours, the forging has the minimum creep strain with 0.45%, and it kept the lowest creep rate at the crack tip. Moreover, the creep deformation zone was significantly reduced, and the equivalent creep strain in the X and Y directions will be a smaller strain gradient in the crack tip region. Especially, in the observation line in front of the crack tip, the creep strain was reduced by 0.4% and kept the minimum value, which resulted in a significant reduction of the creep strain gradient and effectively delayed the crack extension.

It also indicated that, in the hot hammer forging process, appropriate forging process parameters such as forging temperature for Ti-6Al-4V alloy can be designed to help reduce the creep deformation, which can effectively improve the service life and reliability of Ti-6Al-4V alloy components as well as lower the billet waste and maintain minimum energy consumption for forging production.

Data Availability

The data used to support the findings of this study are included within the article.

Conflicts of Interest

The authors declare that they have no conflicts of interest.

Acknowledgments

This work was funded by the National Natural Science Foundation of China (Grant nos. 52175145 and 51775427).

References

[1] S. Ramesh, K. Palanikumar, S. B. Boppana, and E. Natarajan, "Analysis of chip formation and temperature measurement in machining of titanium alloy (Ti-6Al-4V)," *Experimental Techniques*, vol. 48, 2022.

[2] X. R. Fang, L. Liu, J. Lu, and Y. Gao, "Optimization of forging process parameters and prediction model of residual stress of Ti-6Al-4V alloy," *Advances in Materials Science and Engineering*, vol. 2021, Article ID 3105470, 2021.

[3] W. Choi, H. Yoon, and B. D. Youn, "Operation-adaptive damage assessment of steam turbines using a nonlinear creep-fatigue interaction model," *IEEE Access*, vol. 8, pp. 126776–126783, 2020.

[4] H. He, Z. B. Zheng, Z. J. Yang, X. Wang, and Y. Wu, "Failure analysis of steam turbine blade roots," *Engineering Failure Analysis*, vol. 115, no. 4, pp. 104629–111281, 2020.

[5] Y. Sun and B. Xu, "On real-time creep damage prediction for steam turbine," *Transactions of the Institute of Measurement and Control*, vol. 44, no. 13, pp. 2603–2610, 2022.

[6] J. Dvorak, P. Kral, A. G. Kadomtsev et al., "Influence of cryo-processing and post-SPD annealing on creep behavior of CP titanium," *Materials*, vol. 15, no. 5, pp. 1646–1653, 2022.

[7] B. Dogan, A. Saxena, and K. H. Schwalbe, "Creep crack growth in creep-brittle Ti-6242 alloys," *Materials at High Temperatures*, vol. 10, no. 2, pp. 138–143, 2016.

[8] Y. C. Wang, X. Y. Xue, H. C. Kou et al., "Quasi-in-situ investigation on microstructure degradation of a fully lamellar TiAl alloy during creep," *Journal of Materials Research and Technology*, vol. 18, pp. 4980–4989, 2022.

[9] I. P. Semenova, K. S. Selivanov, R. R. Valiev et al., "Enhanced creep resistance of an Ultrafine-Grained Ti–6Al–4V alloy with Modified surface by Ion Implantation and (Ti + V)N coating," *Advanced Engineering Materials*, vol. 22, no. 10, pp. 1901219–1901247, 2020.

[10] N. M. Prabu, S. Nallusamy, and G. Sureshkannan, "Investigation of heat transfer enhancement effect on normal and nano coated wick structure heat pipes-A comparative assessment," *International Journal of Engineering Research in Africa*, vol. 51, pp. 191–198, 2020.

[11] J. Cai, M. Guo, P. Peng et al., "Research on hot deformation behavior of as-Forged TC17 titanium alloy," *Journal of Materials Engineering and Performance*, vol. 30, no. 10, pp. 7259–7274, 2021.

[12] G. Sureshkannan, V. Thangarasu, N. Manikanda Prabu, and D. Anburose, "Review on extrusion of magnesium matrix nano composites," *International Journal of Nano-manufacturing*, vol. 14, no. 1, pp. 1–342, 2018.

[13] S. Y. Luo, J. N. Yao, J. Li, H. Du, H. Liu, and F. Yu, "Influence of forging velocity on temperature and phases of

forged Ti-6Al-4V turbine bladefluence of forging velocity on temperature and phases of forged Ti-6Al-4V turbine blade," *Journal of Materials Research and Technology*, vol. 9, no. 6, pp. 12043–12051, 2020.

[14] Q. Ma, K. Wei, Y. Xu, L. Zhao, and X. Zhang, "Exploration of the static softening behavior and dislocation density evolution of TA15 titanium alloy during double-pass hot compression deformation," *Journal of Materials Research and Technology*, vol. 18, pp. 872–881, 2022.

[15] T. R. Prabhu, "Simulations and experiments of the nonisothermal forging process of a Ti-6Al-4V impeller," *Journal of Materials Engineering and Performance*, vol. 25, no. 9, pp. 3627–3637, 2016.

[16] P. Aliprandi, F. Giudice, E. Guglielmino, and A. Sili, "Tensile and creep properties improvement of Ti-6Al-4V alloy specimens produced by electron beam powder bed fusion additive manufacturing," *Metals*, vol. 9, no. 11, pp. 1207–1436, 2019.

[17] W. Zhang, X. W. Wang, H. F. Chen, T. Y. Zhang, and J. M. Gong, "Evaluation of the effect of various prior creep-fatigue interaction damages on subsequent tensile and creep properties of 9%Cr steel," *International Journal of Fatigue*, vol. 125, pp. 440–453, 2019.

[18] Y. C. Zhang, W. C. Jiang, S. T. Tu, X. C. Zhang, Y. J. Ye, and R. Z. Wang, "Experimental investigation and numerical prediction on creep crack growth behavior of the solution treated Inconel 625 superalloy," *Engineering Fracture Mechanics*, vol. 199, pp. 327–342, 2018.

[19] D. Q. Wu, L. Y. Xu, W. Zhai, H. Jing, L. Zhao, and Y. Han, "Analysis of the constraint levels and the creep crack initiation times for pressurized pipes with long surface cracks," *Thin-Walled Structures*, vol. 153, Article ID 106787, 2020.

[20] R. Okamoto, S. Suzuki, M. Sakaguchi, and H. Inoue, "Evolution of short-term creep strain field near fatigue crack in single crystal Ni-based superalloy measured by digital image correlation," *International Journal of Fatigue*, vol. 162, Article ID 106952, 2022.

[21] T. Altan, G. Ngaile, and G. Shen, *Cold and hot Forging: Fundamentals and Applications*, ASM International, Almere, Netherlands, 2005.

[22] Society of Plasticity Engineering, "Chinese mechanical Engineering Society, forging manual - forging workshop equipment," *Machinery Industry, Ver.*,vol. 3, 2013.

[23] R. Viswanathan, S. Ramesh, and N. Elango, "Temperature measurement and optimisation in machining magnesium alloy using RSM and ANOVA," *Pertanika J. Sci. Technol*, vol. 25, no. 1, pp. 255–262, 2017.

[24] J. S. Jha, S. P. Toppo, R. Singh, A. Tewari, and S. K. Mishra, "Understanding flow behavior and microstructure evolution during thermomechanical processing of mill-annealed Ti-6Al-4V titanium alloy," *Matls. Perf. Charact*, vol. 8, no. 5, pp. 20190010–20190021, 2019.

[25] H. Y. Jing, D. B. Su, L. Y. Xu et al., "Finite element simulation of creep-fatigue crack growth behavior for P91 steel at 625°C considering creep-fatigue interaction," *International Journal of Fatigue*, vol. 98, pp. 41–52, 2017.

[26] W. M. Ye, X. T. Hu, and Y. D. Song, "A new creep model and its application in the evaluation of creep properties of a titanium alloy at 500 °C," *Journal of Mechanical Science and Technology*, vol. 34, no. 6, pp. 2317–2326, 2020.

[27] Y. F. Huang and W. X. Zhou, "Stress intensity factor for clamped SENT specimen containing non-straight crack front and side grooves," *Theoretical and Applied Fracture Mechanics*, vol. 93, pp. 116–127, 2018.

[28] Z. Z. Zheng, F. T. Kong, Y. Y. Chen, and X. P. Wang, "Effect of nano-Y2O3 addition on the creep behavior of an as-cast near-α titanium alloy," *Materials Characterization*, vol. 178, pp. 111249–249, 2021.

[29] Y. Liu and S. Cai, "Gradients of strain to increase strength and ductility of magnesium alloys," *Metals*, vol. 9, no. 10, pp. 1028–1036, 2019.

Hindawi
Advances in Materials Science and Engineering
Volume 2023, Article ID 5442809, 17 pages
https://doi.org/10.1155/2023/5442809

Review Article

A Systematic Review on the Mechanical, Tribological, and Corrosion Properties of Al 7075 Metal Matrix Composites Fabricated through Stir Casting Process

M. Sambathkumar,[1] **R. Gukendran**,[1] **T. Mohanraj**,[2] **D. K. Karupannasamy**,[1] **N. Natarajan**,[3] **and David Santosh Christopher**[4]

[1]*Department of Mechanical Engineering, Kongu Engineering College, Erode, Tamilnadu, India*
[2]*Department of Mechanical Engineering, Amrita School of Engineering, Amrita Vishwa Vidyapeetham, Coimbatore, India*
[3]*Department of Mechanical Engineering, Muthayammal Engineering College, Rasipuram, Tamilnadu, India*
[4]*Department of Mechanical Engineering, College of Engineering, Wolaita Sodo University, Sodo, Ethiopia*

Correspondence should be addressed to David Santosh Christopher; david.santosh@wsu.edu.et

Received 24 June 2022; Revised 28 September 2022; Accepted 30 September 2022; Published 21 January 2023

Academic Editor: Tadeusz Mikolajczyk

Aluminium alloy components are used in lightweight engineering applications and lack mechanical properties, wear resistance, and corrosion resistance. When hard reinforcement particulates are dispersed in the aluminium matrix alloy, aluminium matrix composites (AMCs) are formed. This new material exhibits enhanced properties such as better specific stiffness, specific strength, corrosion resistance, elastic modulus, wear resistance, and lightweight. AMCs have many favorable properties compared to their alloy and extensive applications. Especially, in the space industry, where weight reduction and an increase in modulus are prevalent, the strength-to-weight ratio is more important. This study focuses on the tribological, mechanical, and corrosion properties of Al 7075 metal matrix composites (MMCs) reinforced with one or more particulates such as aluminium oxide (Al_2O_3), boron carbide (B_4C), titanium carbide (TiC), silicon carbide (SiC), titanium dioxide (TiO_2), and titanium diboride (TiB_2). In AMCs, the reinforcements are incorporated by either the solid or liquid metallurgy route. The study addresses the findings and shortcomings in the preparation of MMCs with reinforcements and their improvement in corrosion resistance, wear resistance, mechanical properties, and lower coefficient of thermal expansion than the Al 7075 base alloy. A comprehensive survey of reinforcement particulates in MMCs and their influences are outlined from the literature, encompassing recent research trends to enhance the structural properties.

1. Introduction

Airplane and automotive sectors have faced more technological disputes in meeting consumer obligations. Weight reduction is the foremost task among manufacturers. Decreased weight in airplanes can reduce fuel consumption, enhance payload [1], improve performance, and lower emissions [2]. Additionally, the material has ameliorated properties like corrosion, mechanical, wear, and so on, reducing maintenance and repair costs and increasing service life. Reducing weight and cost is essential for aircraft and automobiles. Thus, the need arises to search for suitable advanced material [3, 4]. During the last few decades, researchers have focused on composite materials to develop advanced materials to meet customer requirements. The researchers did a comprehensive review of polymer MMCs [5].

The materials used for constructing airplanes and automobiles ought to have a lightweight, high specific strength, resistance against high temperature, fatigue load, corrosion and crack, and low wear rate [6]. Previously, alloy steels were generally used for airplanes and

automotive components. The benefits of ferrous metals are broad availability and inexpensiveness; and drawbacks include substantial weight, a higher wear rate, and lesser corrosion resistance. Nonferrous metals have low densities compared to ferrous metals, and there has been broad interest in using aluminium, magnesium, titanium, and so on for various applications. Among the various nonferrous materials, Magnesium (Mg) is a lightweight metal but is restricted in airplane production because it quickly seizes fire [7, 8]. Titanium (Ti) expends an equivalent weight to Mg, costing 20 to 30 times more than Aluminium (Al).

The tensile strength of pure Al is about 90 MPa, and its strength can be increased by about two times by rolling or other cold working processes. By alloying with other metals or using heat treatment processes, the tensile strength can be increased to the strength range of structural steel. Aluminium alloy (AA) is often used because it is more robust than most magnesium alloys [9]. Different manufacturing methods fabricate aluminium alloys by adding alloying elements such as copper, manganese, silicon, magnesium, zinc, and lithium to improve their properties.

1.1. Aluminium Matrix Composites. Aluminium matrix composites (AMCs) are a type of MMC that provide a superior combination of physical, mechanical, and thermal properties compared to monolithic materials. Due to their higher performance and environmental benefits, AMCs are used in the aerospace and automobile industries for the benefits of lower fuel consumption and noise. Moreover, the selection of reinforcement and fabrication techniques of AMCs can offer a wide variety of commercial applications [10]. The usage of reinforcement and matrix materials in composites is represented in Figures 1(a) and 1(b).

To the authors' best knowledge, the mechanical, tribological, and corrosion properties of AA 7075-MMCs with different reinforcements were rarely found in the literature. This article investigates the mechanical, tribological, and corrosion properties of Al 7075 MMCs reinforced with different particulates. In this paper, the authors mainly focus on reinforcing Al 7075 alloys with SiC, B_4C, Al_2O_3, etc., by stir casting and analyzing their properties through tensile tests, friction and wear tests, and corrosion tests. The results from the literature are compared to show the variations in properties of MMCs in a comprehensive manner. Due to its potential application and studies, the authors limit the review of Al-based MMCs to Al_2O_3, SiC, Gr, etc. Table 1 shows review articles related to various aluminium alloy composites. From the review, the production of Al-MMCs with different manufacturing techniques and studied their mechanical or wear or corrosion properties. Review papers on Al 7075 are minimal and study their mechanical and wear properties only. This review article discussed the origin of AMCs, the fabrication (stir casting) method compared with other techniques, different reinforcement types, mechanical properties, wear properties, and corrosion properties.

2. Fabrication Methods of AMCs

This section presents an outline of the different fabrication methods of Al-based MMCs and their advantages and disadvantages. The properties of Al, Mg, and Ti are presented in Table 2. The properties of different aluminium alloys and their applications are represented in Table 3.

In Table 3, the heat-treatable aluminium 2xxx and 7xxx series alloys have higher strengths than other aluminium alloy series and are applicable for aerospace and automobile applications. Table 4 provides a comparative study of various manufacturing processes of Al-MMCs. Manufacturing AMC on an industrial scale can be classified as

(i) Liquid state process: spray casting, infiltration, and stir casting

(ii) Solid-state process: powder metallurgy and diffusion bonding processes

Various techniques have been used to develop composite materials. From these available techniques, stir casting (liquid metallurgy) is the best way to produce the composite owing to its low cost, simplicity, and mass production [22]. Aluminium-zinc (Al-Zn) alloys are used widely in automobiles due to their lightweight, castability, mechanical properties, and corrosion resistance. They are widely utilized in various applications [23]. They are ready to cast using all standard casting techniques [24].

Numerous studies on hybrid Al-MMCs reinforced with more than one reinforcement, such as boron carbide (B_4C), alumina (Al_2O_3), titanium carbide (TiC), silicon carbide (SiC), and graphite (Gr), show an enhancement in properties as compared to the base alloy and single reinforcement composites. Adding a little weight/volume fraction of reinforcement to MMCs improves the mechanical and thermal properties. In the liquid metallurgy technique, the homogeneous dispersal of particles into the matrix is the challenging step, affecting the properties and quality of the composites directly. The matrix and reinforcement have an interfacial strength, which determines the properties of MMCs.

In stir casting, the gases are entrapped during melting and mixing/stirring, producing gas bubbles and porosity [25]. The porosity amount depends on the matrix and reinforcement type, weight/volume fraction, and process parameters. The reinforcement particle distribution in the molten metal depends on the geometry, location, stirring parameter of the stirrer, and melting temperature [26]. Al-MMCs were prepared with powder metallurgy (PM) route with different wt.% of SiC reinforcements. An increase in SiC ratio by 5 wt.% enhanced hardness by 14%. The compressive strength is maximum with 25 wt.% of SiC [27]. The Al_2O_3 and collagens were reinforced with Al-MMCs using the stir casting method. They found that there were 38.25% and 45% enhancements in tensile strength (TS) and hardness for the Al + 5% collagen + 5% Al_2O_3 composite, respectively. Though composite material's density, toughness, and ductility were decreased by 0.16%, 25%, and 24.24%, respectively [28]. Mg_2Zn matrix alloy reinforced with Al_2O_3 fabricated through the PM route. Mg alloy composite with

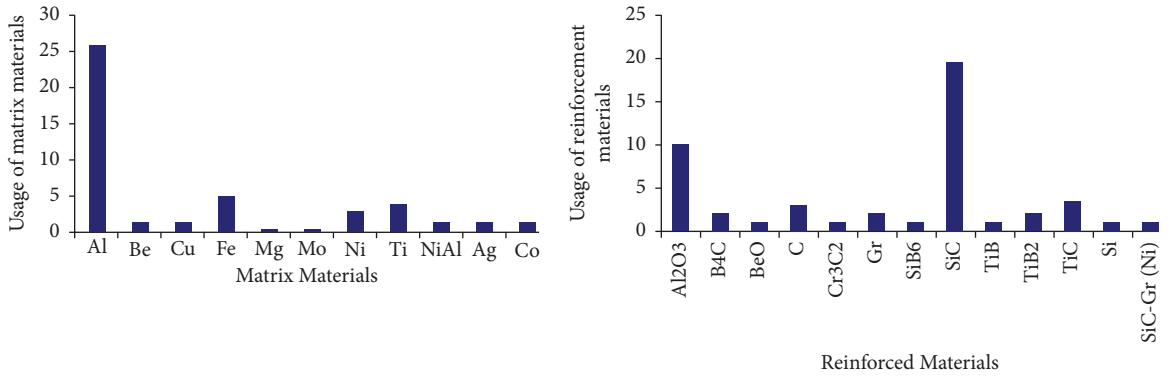

(a) (b)

Figure 1: Usage of (a) matrix and (b) reinforcement materials in MMCs [11].

Table 1: Previous review articles based on aluminium composites.

S. no.	Studies	Materials	Ref.
1	Stress corrosion cracking and its factors	7xxx	[12]
2	Corrosion behavior in a deep-sea environment	Al 5083 H111, Al 6082 T6, Al 7075 T651, and Al 8090 T81	[13]
3	Development of MMCs with optimum furnace processing parameters	Different Al alloys	[14]
4	Different fabrication methods of MMCs and their mechanical properties	Different Al alloys	[15, 16]
5	Mechanical properties of MMCs	Al 7050 and Al 7075	[17]
6	Mechanical properties of hybrid MMCs	Different Al alloy	[18]
7	Tribological properties of MMCs	Different Al alloy	[19]
8	Review based on types of reinforcement	Different Al alloy	[20]

Table 2: Properties of Al, Mg, and Ti [7].

Properties	Al	Mg	Ti
Crystal structure	FCC	hcp	hcp
Density@20°C	2.70 (g/cm^3)	1.74 (g/cm^3)	4.4 (g/cm^3)
Coefficient of thermal expansion 20–100°C	23.6 10^{-6}/C	25.2 10^{-6}/C	8.5 10^{-6}/C
Elastic modulus (MPa)	68.9×10^6	44.1×10^6	110×10^6
Tensile strength (MPa)	320 (for A380)	240 (for AZ91D)	434
Melting point (°C)	660	650	1660

Table 3: Comparison of aluminium alloy properties [9].

S. no.	Alloy		UTS (MPa)	Yield strength (MPa)	Advantages	Applications
1	Nonheat treatable alloys	1xxx	105	25	High electrical conductivity, formability, corrosion resistance, and low strength	Chemical and electrical components
2		3xxx	180	69	High corrosion resistance, formability, indivisibility, and moderate strength	Packaging, heat transfer, and roofing applications
3		5xxx	145	35	Outstanding corrosion resistance, toughness, weldability, and sufficient strength	Construction, automobile, cryogenic, and shipbuilding
4	Heat treatable alloys	2xxx	220	95	High strength at elevated and room temperatures	Transportation and aircraft and applications
5		4xxx	170	165	Good flow attributes and moderate strength	Pistons and intricate shaped forgings
6		6xxx	124	55	Superior corrosion resistance, outstanding extrudability, and sufficient strength	Building, automobile, and shipbuilding
7		7xxx	228	103	Exceptional high toughness and very high strength versions	Automotive and aerospace

Table 4: Comparative study of various manufacturing techniques of MMCs [21].

S. no.	Method	Range of size and shape	Advantages	Disadvantages
1	Stir casting	Larger size and extensive range	Low cost, less reinforcement damage, and very high metal yield (>90%)	Vol. fraction range up to 30%
2	Squeeze casting	Limited by preform shape, up to 2 cm height	Relatively expensive and volume fraction range up to 45%	Serious damage to reinforcement, meager metal yield
3	Powder metallurgy (PM)	Controlled size and a wide range	Very high metal yield and volume fraction range up to 30 to 70%	High-priced and reinforcement fracture
4	Spray casting	Larger size and limited shape	Metal yield is medium	High-priced
5	Infiltration process	Restricted size and limited by preform shape	Vol. fraction is more	High-priced

8 wt.% of Al_2O_3 exhibits the highest TS of 191 MPa. The least weight loss (9%) and corrosion rate (2.5 mm/year) were obtained with a 2 wt.% Al_2O_3 [29].

Al 7005 composite reinforced with fly ash (FA) (5 wt.%, 6 wt.%) and S-glass fiber (5 wt.%) was fabricated through a stir casting route. They found that Al 7005 + 6 wt.% of fly ash exhibited enhanced corrosion resistance compared to other composites. During the corrosion test, the fly ash particles remain inactive and act as a physical fence with corrosive medium [30]. An aluminium hybrid MMCs was produced using the stir casting method and investigated the mechanical and tribological properties [31].

AA7075-Y_2O_3 (0.5 wt.%) composites were successfully produced through the PM (ball milling and hot pressing) route. The fabricated composite exhibits enhanced hardness and TS of 164% and 90%, respectively [32]. The combination of PM and ball milling was utilized to produce the multi-walled carbon nanotubes (MWCNTs)-reinforced AMCs. After 8 hrs of ball milling, hardness was increased by 160%, and after 2 hrs of milling, density increased by 99.96% from the base composite. This result ensures that the employed PM method effectively produces MMCs with enhanced mechanical properties [33].

A summary of various fabrication methods for different AAs explored by various researchers is given in Table 5. Various reinforcement materials are added to enhance the properties of AAs. The addition of one or more particulates into the AA has also been studied and is listed in Table 6.

3. Methods of Structure Analysis

This section describes the microstructure using an optical microscopic image, SEM morphological analysis, and elemental mapping using EDAX.

3.1. Optical Microstructure Analysis. This section discusses the microstructure observations of MMCs and their key characteristics. Equal dispersion of reinforcement particles into the matrix enhances the properties of the MMCs. According to Kalkanlı and Yılmaz [83], the reinforcement material is evenly distributed in the base material, as illustrated in Figure 2. The optical microstructure of the Al 7075 + SiC MMC composite shows that the SiC particles are equally dispersed in the matrix and reveals the composite that increases the content of reinforcement in the base matrix.

3.2. Scanning Electron Microscope (SEM) Analysis. The following section addresses the SEM analysis of various MMCs in the literature. SEM images were used to analyze surface morphology in tensile, tribological, and corrosion studies. The scanning electron microscope (SEM) images of the cast matrix Al 7075/SiC MMCs are presented in Figure 3, and the reinforcement particles are distributed evenly in the Al molten metal. The SEM image depends mainly on the mean atomic number of various phases present in the metals. According to Bhushan et al. [84] SEM images of the Al 7075/SiC with 0%, 10%, and 15% (20–40 μm) composite show an even distribution of the reinforcements, as illustrated in Figures 3(a)–3(c). Figures 3(d)–3(f) present the uniform distribution of Al 7075/15 wt.% of SiC with different particle sizes.

3.3. Energy-Dispersive X-Ray Spectroscopy Analysis. Energy-dispersive X-ray spectroscopy (EDAX) analysis reveals detailed information about the elements present in materials. Figure 4 shows the EDAX of A7075/basalt composite materials. The EDAX of Al 7075/7.5 wt.% of basalt composites is composed mainly of solid diffraction lines of Al phase with Zn, Fe, and so on phases but with weak diffraction lines.

4. Mechanical Properties Research

In this section, the authors report the key findings about the hardness and tensile strength results found in the literature. From this study, other properties such as ductility, elongation, and yield point were also found by using stress-strain.

4.1. Hardness. The composite containing a higher volume percentage of reinforcement exhibits superior hardness. According to Baradeswaran et al. adding Al_2O_3 fragments into the Al 7075 matrix improves the hardness values, as shown in Figure 5. Hard reinforcement particles increase the load-carrying capability of the MMC, constrain the matrix deformation by restricting the movement of disruption, and increase the strength of the composites [76].

4.2. Tensile Strength. Hybrid composites of Al 7075 exhibit improved tensile strength (TS) compared to the base composite. The presence of hard reinforcement particles

Table 5: Fabrication methods for various Al-MMCs.

S. no.	Ref.	Matrix	Fabrication method	Properties studied
1	[34]	1060	Powder metallurgy	Wear
2	[35]	1100	Accumulative roll bonding	Elongation, microhardness, and TS
3	[36]		Stir casting	Yield strength, TS, and % elongation
4	[37]	2009	Powder metallurgy	Corrosion
5	[38]	2011	Stir casting	Wear
6	[39]	2014	Squeeze casting	Wear and friction
7	[40]		Squeeze casting	Hardness and wear
8	[41]		Stir casting	Wear
9	[42]	2024	Pressure infiltration	Bending strength
10	[43]		Powder metallurgy	Wear
11	[44]		Vortex method and applied pressure	Hardness and TS
12	[45]	2124	Powder metallurgy	Fatigue behavior
13	[46]	2219	Liquid metallurgy	Wear
14	[47]	2618	Squeeze casting	Wear
15	[48]	5052	Pressure less infiltration	TS
16	[49]	5059	Stir casting	Hardness and wear
17	[50]	6061	Stir casting	Hardness, ultimate TS, and wear
18	[51]		Vacuum hot pressing	TS
19	[52]	6063	Liquid metallurgy	Wear
20	[53]	6351	Stir casting	Wear
21	[54]	7005	Compo casting	TS, hardness, and fracture
22	[55]	7055	Powder metallurgy	Fatigue behavior
23	[56]	7075	Stir casting	Ultimate TS and hardness
24	[57]		Liquid casting	TS, hardness, and wear
25	[58]	8090	Spray deposition	Wear

Table 6: Various reinforcement materials used in Al-MMCs.

Reinforcements	Ref.
Gr	[59]
SiC	[60]
Al_2O_3	[61]
TiB_2	[62]
B_4C	[63]
SiN_4	[61]
ZrB_2	[53]
TiC	[64]
SiO_2	[65]
FA	[66]
Gr	[67]
TiO_2	[68]
SiC + Gr	[69]
SiC + Al_2O_3	[70]
SiC + MoS_2	[71]
SiC + FA	[72]
SiC + TiO_2	[73]
SiC + B_4C	[74]
SiC + RHA	[75]
Al_2O_3 + Gr	[76]
Al_2O_3 + B_4C	[77]
Al_2O_3 + RHA	[78]
TiC + B_4C	[79]
B_4C + Gr	[80]
TiB_2 + Gr	[81]
SiC + TiC	[82]

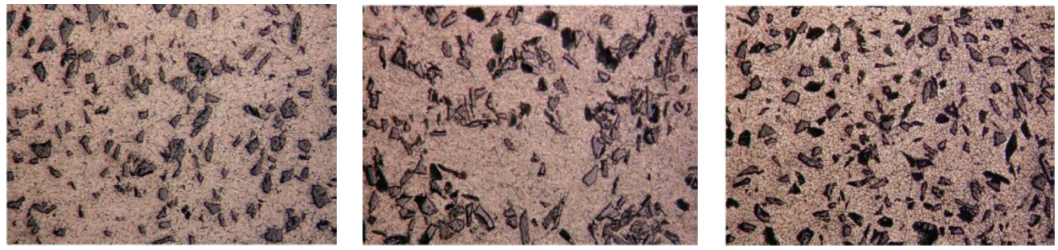

(a) (b) (c)

Figure 2: The optical microstructures of (a) 10 wt.%, (b) 15 wt.%, and (c) 20 wt.% SiC reinforced 7075 Al composites (200x).

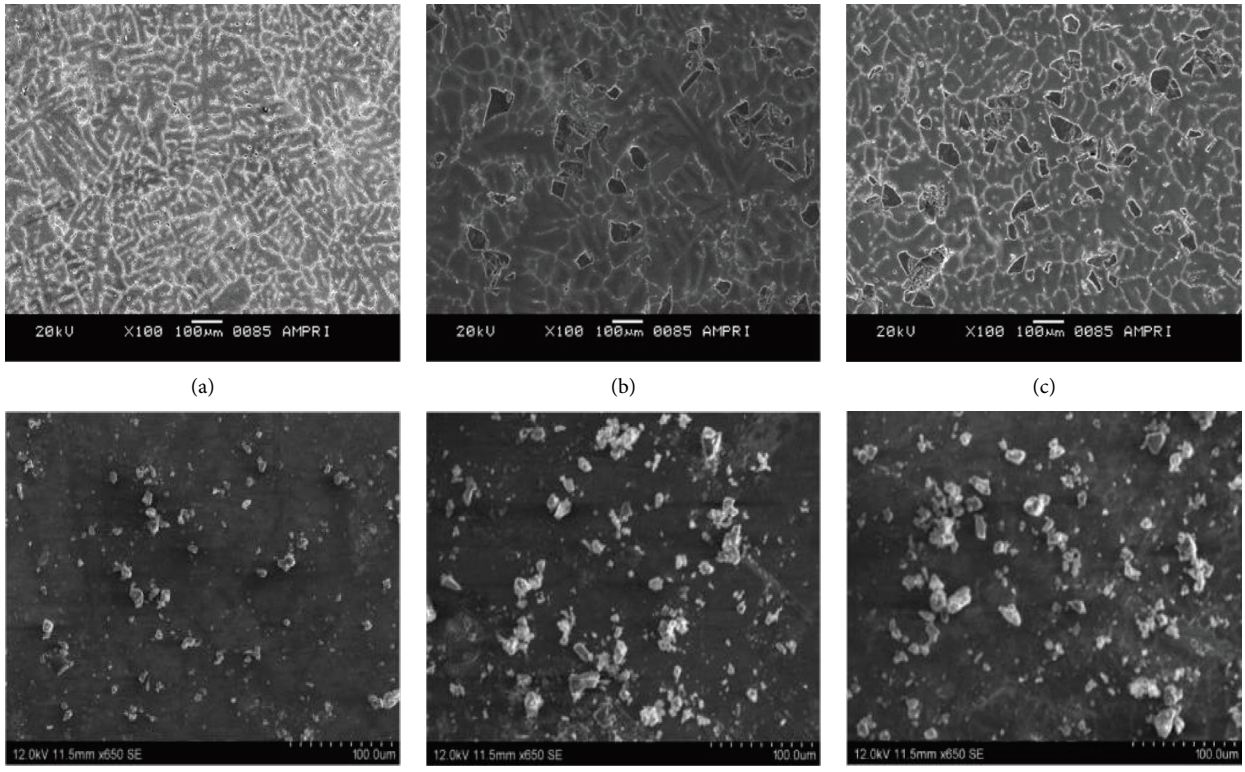

(a) (b) (c)

(d) (e) (f)

Figure 3: SEM image of (a) Al 7075 [84], (b) Al 7075/10 wt.% of SiC (20–40 μm) [84], (c) Al 7075/15 wt.% of SiC (20–40 μm) [84], (d) Al 7075/15 wt.% of SiC (25 μm) [85], (e) Al 7075/15 wt.% of SiC (50 μm) [85], and (f) Al 7075/15 wt.% of SiC (75 μm) [85].

improves the strengthening effect of the composites. In Al 7075 hybrid MMCs, the hard reinforcement particles are scattered consistently, resulting in the act of block-off for dislocation movement. It reduces the rupture of the composite material [87]. Increasing hard reinforcement increases the TS and reduces the fracture of the composite by stress transfer from the Al matrix to the reinforcements. This is due to the orowan mechanism [88], bypassing serious obstacles where dislocation is limited around a reinforcement, which improves TS. Figure 6 presents an SEM image of the Al 7075 fractured surface and its stress-strain curve.

During tensile testing, when applying load on the material, the high local stress concentration will be generated around the particles, enhancing debonding or breaking of SiC particles, as shown in Figure 7 [89]. Al-MMCs reinforced with hard ceramic parts rapidly change conventional materials in different applications [90]. The Al/SiC particles are more rigid than the other ceramic particles and provide a very effective barrier to subsurface shear [91]. Deaquino et al. [92] fabricated Al 7075/graphite composites by hot extrusion and mechanical alloying. Increasing the milling time and Gr wt.% refines the grain size and increases the dislocation density. The addition of graphite particles reacts with Al and forms Al_4C_3 during the extrusion and sintering processes, which enhances the TS of the composite by interrupting the dislocation motion.

Rogal et al. [93] studied the microstructure characterization of the Al 7075 alloy after the thixo forming process. After the formation of semisolid metal, the globular microstructure is obtained, and the size of the average globules is 60–90 μm, whereas the process temperature is 615°C and

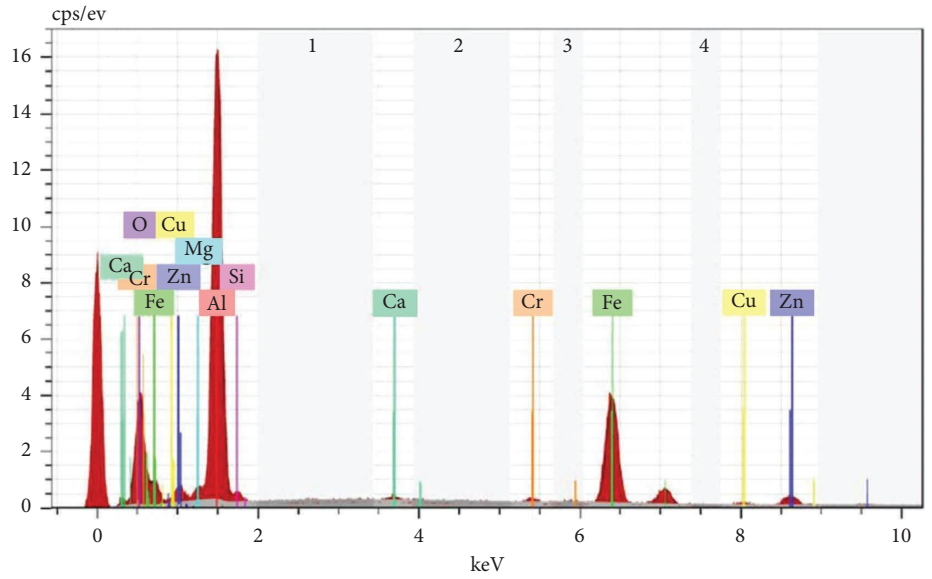

Figure 4: EDAX analyses of Al 7075 and composite with 7.5 wt.% basalt reinforcement [86].

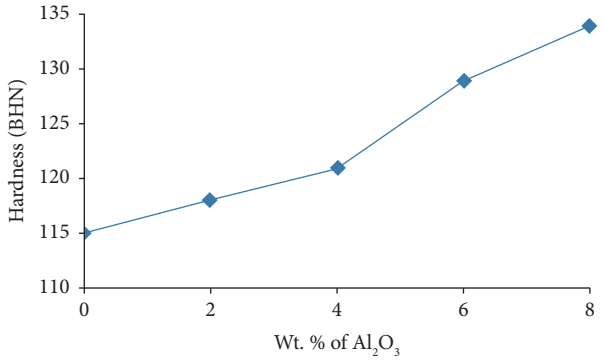

Figure 5: Hardness of Al 7075 MMC with/Al_2O_3 + 5 wt.% of Gr [76].

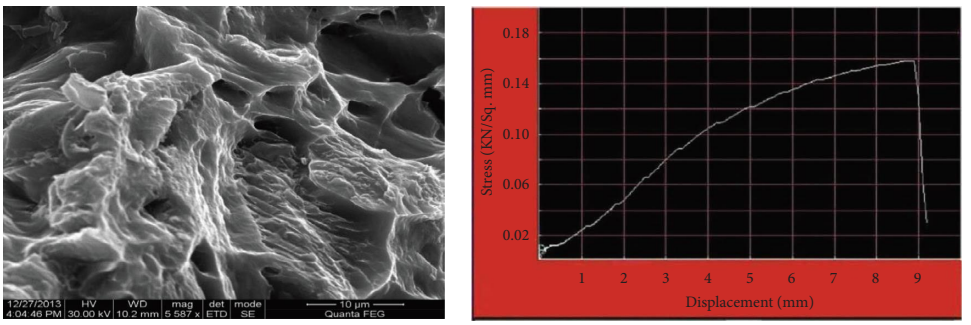

(a) (b)

Figure 6: (a) SEM image of Al 7075 fractured surface. (b) Al 7075 stress-strain curve [80].

the piston velocity is 1.5 m/s. Thixo formed microstructure samples show 19% eutectic, 12% Cu, and 77% Al (all in wt.%). Qu et al. [94] have studied the properties of spray-formed Al 7075 alloys under various heat treatment processes and reported that tiny and disconnected precipitates at grain boundaries improve the alloy's corrosion resistance

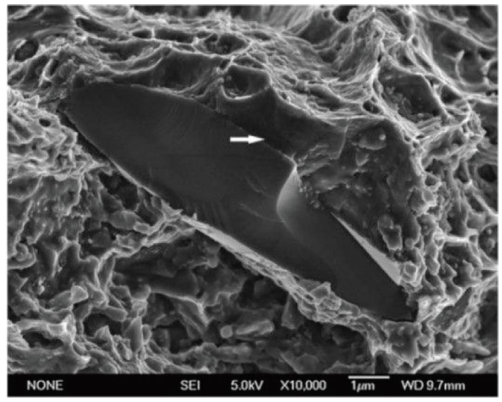

Figure 7: SEM micrographs of the nucleation of cracks result from the breaking of SiC particles [89].

and ultimate tensile strength. The Al-MMCs treated with the U-RRA-H process show higher properties than the T6, T73, and conventional RRA processes.

Similarly, Senthilvelan et al. [95] developed Al 7075/10 wt.% SiC, B_4C, and Al_2O_3 composites using the stir casting method. Al/B_4C composites show a tensile strength improvement of 143% due to the most robust bonding between reinforcement and matrix. However, in the Al/Al_2O_3 and Al/SiC composites, 88% and 46% tensile strength are obtained because of weak interface and porosity. Clark et al. [96] and Reda et al. [97] have deliberated on the retrogagation-treated Al 7075 T6 alloy and reported that preaging material improves the electrical resistivity, tensile properties, and hardness. Kim et al. [98] have reported that aged Al 7075 improves the hardness.

Baradeswaran and Perumal [57] examined the wear and mechanical properties of Al 7075/Gr composites developed by the liquid casting technique. The flexural strength and hardness decrease when raising the Gr content by 5 wt.%. The wear property increases compared to the other samples with increasing sliding distance, sliding speed, and graphite content (up to 5 wt.%). The composite's wear rate rises with increasing load. Lee and Kwon [99] have fabricated Al 7075/SiC composites by a pressureless infiltration process and reported that the composites exhibit higher strength values than the base alloy in all the treated conditions. The addition of Mg improves the wettability and TS.

Chen et al. [100] developed Al 7075 hybrid composite reinforced with 40 vol.% SiC particle and 5 vol.% Ti particle by the squeeze casting process. Casted hybrid Al-MMCs have a TS of 622 MPa and considerable plasticity of 1.2%. The addition of Ti particles improves crack propagation resistance and plastic deformation. The TS of MMC was enhanced due to the good interfacial bonding between Ti reinforcement and the base matrix. Kannan and Ramanujam [101] fabricated Al 7075 hybrid nanocomposites using squeeze and stir casting techniques and analyzed the microstructural and mechanical characterization. The hardness and ultimate TS increase when both single and hybrid composites expand the reinforcements. The hardness of hybrid and single-reinforced nanocomposite by stir casting is improved by 81.1% and 63.7% respectively, while a single-reinforced squeeze cast nanocomposite improves up to 90.5%. The ultimate TS of the nanocomposite is also detected up to 60.1%, 73.8% and 92.3% in the same series of composites compared to base alloy respectively.

In the same way, Lu et al. [102] studied the mechanical and thermophysical properties of Al 7075/SiC/Cr hybrid MMC produced through squeeze casting. Thermophysical and mechanical properties are enhanced by the addition of Cr particles into the 50% SiC composite. 50% SiC + 5% Cr composite show ductile-brittle fracture mode, but 50 SiC composite exhibits brittle fracture mode. Adding Cr particles decreases the dislocation density, forming a good interface between Al matrix and Cr particles and improving fracture toughness and interface conductance. The hybrid composite material has good thermophysical properties and the highest bending strength. Baradeswaran and Perumal [76] studied the wear and mechanical performance of Al 7075/Al_2O_3/5 wt.% of Gr hybrid MMC fabricated through stir casting. In a wear process, the Gr particles act as a solid lubricant and reduce the friction coefficient of the composites. Table 7 shows the mechanical properties of MMCs compared to the base metal.

Al 7075-MMCs reinforced with 1 wt.% of Mg and 1–4 wt.% of Al_2O_3 were fabricated by stir casting and found an augmentation in hardness and TS. 4 wt.% of Al_2O_3 exhibits an increase in 50% and 6.25% of hardness and TS, respectively. On the contrary, % elongation was decreased by 51.16% [109]. Al 7075 with 6 wt.% of Al_2O_3 exhibits an increase of 37.5% and 24.44% hardness and TS, respectively [110]. Al 7075 with 10 wt.% of SiC, Al_2O_3, and B_4C exhibits an increase of 25.52%, 16.98%, and 43.75% hardness and 45.51%, 88.71%, and 143.34% increase in TS, respectively and % elongation also significantly decreased [95]. The heat-treated (500°C) Al-MMCs with 2 wt.% of Al_2O_3 increased the hardness and TS by 61.84% and 60.71%, respectively. Al 7075 + 2% Al_2O_3 + 4% SiC (500°C) exhibits superior properties than Al 7075 and Al 7075 + 2% Al_2O_3. Mechanical properties are slightly dropped with a further increase in the heat treatment temperature. Al-MMCs with 2 wt.% of Al_2O_3 produced through squeeze casting exhibited enhanced properties than all [101].

Al-MMCs with 5 wt.% of SiC and 5 wt.% of CB exhibited a 16.36% and 19.32% rise in hardness and TS. On the other hand, the same MMCs process with FSP yields a 105.98% increase in TS and % elongation to 5.83% [111]. Al 7075 with 5 and 10 wt.% of SiC exhibited a 69.23% and 84.61% increase in hardness and TS, respectively [112]. Al 7075 with 6 wt.% of SiC exhibited a 58.33% and 77.77% increase in hardness and TS, respectively [113]. During the casting of Al-MMCs, different sizes of SiC particles were reinforced. Al-MMCs + 10 wt.% of 75 μm SiC particles exhibited better mechanical properties than other particle sizes. It increased the 22.58% and 8.25% hardness and TS, respectively [114]. Al-MMCs with 15 wt.% of SiC exhibit 10.52%, 17.64% hardness, and TS, respectively. The specimen with heat treatment significantly increases the TS (61.76%) [83].

Al-MMCs with 5 wt.% of TiC increased the hardness by 70% [115]. Al-MMCs with 7.5 wt.% TiC + 7.5 wt.% of SiC increased by 18.11% and 27.77% hardness and TS [116]. Al-

Table 7: Mechanical properties of Al 7075 MMCs.

S. no.	Composition	Density (g/cm^3)	Hardness	UTS (MPa)	Elongation (%)	Ref.
1	Al 7075	—	83 VHN	368.5	—	[103]
	Al 7075 + 1.5% Gr	—	113 VHN	413	—	
	Al 7075 + 15% SiC	—	120 BHN	230	—	
	Al 7075 + 15% Al_2O_3	—	140 BHN	240	—	
	Al 7075 + 15% B_4C	—	160 BHN	260	—	
	Al 7075 + 15% TiB_2	—	150 BHN	250	—	
2	Al 7075	—	127 BHN	114	13.8	[104]
	Al 7075 + 3% CSFA	—	134 BHN	121	13.5	
	Al 7075 + 3%CSFA + 12% B_4C	—	169 BHN	177	9.8	
3	Al 7075 (cast)	—	62 VHN	100	7	[105]
	Al 7075 (hot rolled)	—	70 VHN	250	13	
	Al 7075 + 10% TiB_2 (cast)	—	78 VHN	160	5	
	Al 7075 + 10% TiB_2 (hot rolled)	—	82 VHN	400	11	
4	Al 7075	—	65 VHN	145	8.2	[56]
	Al 7075 + 3% TiB_2	—	80 VHN	195	7.5	
	Al 7075 + 6% TiB_2	—	95 VHN	240	5	
	Al 7075 + 9% TiB_2	—	125 VHN	100280	3.5	
5	Al 7075	2.804	70 BHN	—	—	[106]
	Al 7075 + 2% albite	2.796	80 BHN	—	—	
	Al 7075 + 4% albite	2.793	90 BHN	—	—	
	Al 7075 + 6% albite	2.787	100 BHN	—	—	
	Al 7075 + 8% albite	2.784	115 BHN	—	—	
	Al 7075 + 10% albite	2.78	110 BHN	—	—	
6	Al 7075	2.75	74 BHN	131.8	4.93	[107]
	Al 7075 + 2.5% cenosphere	2.67	81.9 BHN	133.6	5.12	
	Al 7075 + 5% cenosphere	2.52	89 BHN	138.9	5.13	
	Al 7075 + 7.5% cenosphere	2.47	96.3 BHN	146.1	5.22	
	Al 7075 + 10% cenosphere	2.41	100 BHN	143.2	5.17	
7	Al 7075	—	120 HV	166	—	[108]
	Al 7075 + 2% steel powder	—	131 HV	180	—	
	Al 7075 + 4% steel powder	—	139 HV	185	—	
	Al 7075 + 6% steel powder	—	155 HV	170	—	

MMCs with 5 wt.% of TiC with 10 hours of milling exhibit high hardness and TS [117]. Al-MMCs with 6 wt.% of BA and 5 wt.% of Gr had 100 BHN hardness and 300 MPa TS [118].

From Table 7, it was observed that Al 7075 + 15 wt.% B_4C offers 160 BHN hardness and 260 MPa UTS. Along with 12 wt.% of B_4C and 3 wt.% of CSFA, hardness increased to 169 BHN, but UTS decreased to 177 MPa. The particle size of B_4C played a significant role in hardness. The small particle size (20 μm) provides enhanced hardness values [119]. The addition of albite, cenosphere, and steel powder significantly enhances the mechanical properties of Al 7075 AMCs. When the reinforcements are added beyond a significant level, they form a cluster and significantly affect the mechanical properties [106].

Recent studies have shown that by choosing suitable reinforcement and optimizing for optimum reinforcement dispersion, the mechanical characteristics of MMCs can be further enhanced. Impressive improvements in the hardness and mechanical properties were seen. Heat-treated MMCs also improve the mechanical properties of the composites.

4.3. Tribological Properties. In this section, the authors report the key findings about the tribological properties related to different process parameters in the literature. Relative movement between two surfaces can cause the material to fall off one or both surfaces, called wear [83]. The wear process also depends on the nature of the surface, which is determined by the processing route [120]. Two solid surfaces slide over one another with load, which forms adhesive wear [121]. High-hardness materials reduce wear with high strength and toughness [122]. Many researchers have reported that increasing the wt./vol. fraction of reinforcement particles improves the wear resistance of the composites [123]. At a higher vol. fraction, the coefficient of friction is found to be higher without any applied load condition [124]. Adding reinforcement to MMCs improves the wear behavior, increasing the stiffness and specific strength, making it an ideal contender for engineering applications [125, 126].

Material wear resistance is determined by strength, hardness, ductility, toughness, reinforcing material type, wt./vol. fraction, and particle size and shape [65, 127, 128]. MMCs reinforced with higher bond strength particles and matrix support can prevent crack initiation and improve wear resistance [129, 130]. Several researchers examined the wear characteristics of Al-MMCs with various reinforcement materials. The commonly used AMCs are reinforced with hard ceramic particles (like SiC, Al_2O_3 [131]) or soft particles (such as Gr [132]). Venkataraman and

Sundararajan [133] studied the sliding friction and wear characteristics of 7075 AA and SiC particle-reinforced AMCs under dry conditions. Experimental observations show a strong correlation between friction and wear in the mechanical mixed layer (MML). The oxidation mechanism was established from the microphotograph of the worn surface.

Daoud et al. [134] developed Al 7075/Al_2O_3 MMCs through compression casting technology. The presence of the reinforcement creates a fine structure in the MMC. The pressure applied during the extrusion process increases the bond strength at the interface between the matrix and the Al_2O_3, thus reducing superfluous porosity at the interface of the particles. As the vol. fraction of Al_2O_3 rises, the hardness of the composite material increases linearly. Compression casting compounds show better wear resistance than base alloys because Al_2O_3 acts as a load-carrying element during sliding.

In the same way, Michael et al. [135] considered the wear characteristics of the Al 7075/TiB_2 composites developed. TiB_2 particles do not develop intermetallic compounds and are dispersed evenly in the matrix. TiB_2 particles and matrix material bonding and wear resistance are more due to the absence of pores and inclusions. The worn surface at room temperature exhibits parallel grooves, delamination, and grooves through the worn surface. By increasing the reinforcing agent content and the wear transition temperature to 210°C, the wear resistance of the MMC is lowered. TiB_2 particles can resist metal flow and subsurface deformation at 240°C.

Baradeswaran and Perumal [136] explored the mechanical and wear behavior of Al 7075/B_4C composites developed by casting and used K_2TiF_6 as a fluxing agent to increase the wettability during the casting process. Adding reinforcing particles will increase the hardness because it will hinder the movement of dislocations. Compared with the base alloy, adding B_4C particles enhances the mechanical properties. Compared with the base alloy, the compound Al 7075 + 10% vol. of B_4C, their wear rate is reduced by 11%. The MML developed on the worn surface controls the wear characteristics, and composites reached a coefficient of friction (CoF) of 0.32.

Baydoğan et al. [137] analyzed the wear characteristics of retrogression and reaging (RRA) on Al 7075. Under dry sliding conditions, the alloy treated at 220°C shows better resistance against wear than the Al 7075 alloy. However, due to the lubricating effect, RRA with 30 g/l NaCl + 10 g/l HCl solution-treated alloys has lower wear resistance than Al 7075 T6 alloy. Dasgupta and Meenai [138] also developed Al 7075/SiC composites using stir casting and analyzed the sliding wear properties. The composites show appreciably enhanced wear properties compared to the base matrix. The RRA-treated composites exhibit better resistance against wear than T6 heat-treated composites.

Lakshmipathy and Kulendran [139] developed Al 7075/SiC and Al 6061/Al_2O_3 MMCs through stir casting and studied the wear behavior. Increasing reinforcement (SiC, Al_2O_3) improves the hardness of the composites, and 20 wt.% reinforced composites have 50 BHN (SiC) and 37 BHN (Al_2O_3). Composite impact strength decreases when increasing reinforcements. Al with 20 wt.% reinforced composites show enhanced wear properties than base matrix, in which Al 7075/SiC is better than all. The wear rate rises with the load, and the surface temperature increases with increased reinforcement.

Pradeep et al. [82] produced Al 7075/SiC/TiC hybrid MMC through the powder metallurgy route. The composite with 8% TiC and 4% SiC has a higher microhardness value of 52.12 HV than other samples. Adding SiC and TiC particles into the matrix improves the wear resistance. The Al 7075 composite with 4 wt.% SiC and 4 wt.% TiC shows a lower CoF than specimens. Liu et al. [140] examined the dry sliding wear characteristics of Al 7075/SiCp/Ti hybrid MMCs developed by squeeze casting. The addition of Ti particles does not influence the wear mechanism. These particles form microzones that develop synergistic deformation and stress release effects. This type of effect obstructs the formation of cracks beneath and the cracking of SiC particles. At low loads, incorporated Ti particles improve the wear resistance.

Similarly, Kumar and Dhiman [69] developed Al 7075/SiC/Gr hybrid MMCs by stir casting. The specific wear rate reduces with increasing the transition speed (4 m/s) and load. Transition speed increased to 6 m/s, reducing the specific wear rate by forming the tribolayer. The composite-specific wear rate decreases with an expansion in the sliding distance at low load (20–40 N) and low speed (2–4 m/s). With the rise in the sliding distance, the specific wear rate increases with increasing load and speed. The amalgamation of Gr, formation of iron oxide, work-hardening of the specimen surface, and miniature lubricant layer formation between the contact surfaces increase the wear resistance.

The wear rate of 7075 AMCs significantly increased with the load. On the other hand, by increasing the reinforcement of Al_2O_3 from 3% to 5%, the wear rate decreased from 0.3309 to 0.2467 mm^3/min. Further increases in Al_2O_3 wt.% considerably increase the wear rate to 0.0467 mm^3/min at 1.5 N load [141]. Al 7075 + 5 wt.% of Gr + 2 wt.% of Al_2O_3 exhibits the least wear rate of 0.0007 mm^3/min for a 20 N load. Further increasing the wt.% of Al_2O_3 wear rate was considerably increased [76]. Al 7075 MMCs + 10 wt.% of Al_2O_3 + 5 wt.% of FA significantly decrease the wear rate to 0.049 mm^3/min at 10 N load [142]. Al 7075 + 1 wt.% of Mg + 4 wt.% of SiC + 4 wt.% of Al_2O_3 with a 40 N load exhibits the least wear rate of 0.10×10^{-3} mm^3/min. A reverse trend of a decrease in wear rate with an increase in load was observed [143].

A rise in wear rate with an expansion in wt.% of SiC was found [144]. It was noticed that the wear rate boosted with an expansion in sliding distance [145]. Al 7075 AMCs + 9.5 wt.% of SiC exhibit the least wear rate with a sliding distance of 1000 m [146]. An increase in wt.% of TiC (10 wt.%) reduces the wear rate from 2.15 mm^3/km to 1.7 mm^3/km [147]. The impact of TiC wt.% has to be further explored by increasing the wt.% to 15. Al 7075 MMCs, along with 10 wt.% FA and 6 wt.% Gr, significantly decrease the wear rate to 200 mm^3/min. The wear resistance has been enhanced due to the hardness of Gr [148]. The addition of B_4C along with Gr considerably increases the wear resistance [80].

Recent studies have shown that the tribological properties of MMCs can be further enhanced by choosing the proper reinforcement, amount of reinforcement, reinforcement dispersion, and optimum tribological parameters.

5. Corrosion Properties

In this section, the authors report the key findings about the corrosion properties of MMCs as found in the literature. Yue et al. [149] examined the corrosion cracking resistance of Nd-YAG laser surface-treated Al 7075 T651 alloy prepared in air and nitrogen gas environments. Corrosion is severely attacked with intergranular cracks in the untreated specimen at the grain boundaries. In air-treated specimens, long-stress corrosion cracks and a less number of large corrosion pits are found at interdendritic boundaries. A few short-stress corrosion cracks appear on the alloy surface in the nitrogen-treated specimen. Superior corrosion resistance is achieved on the laser-melted surface due to the formation of the AlN phase, an electrical insulator. The preheated reinforcement particles with a range of 500°C produce uniformly distributed reinforced composites and reduce agglomeration when the nanoreinforcement particles' presence does not exceed 2%.

Varma and Vasquez [150] analyzed the corrosive wear characteristics of Al 7075 MMCs reinforced with Al_2O_3 particles. Pitting corrosion can occur in both alloys and composites. Al 7075/Al_2O_3 composites show better corrosive wear than the base alloy, while solutionizing composites reveals significant grain growth. Zhou et al. [151] examined the corrosion properties of Al 7075 with thin electrolyte layers in 1 M sodium sulfate solutions and a pH of 5. The oxygen reduction current of 110 μm is more significant at −1.1 V and measured from the potentiodynamic polarization. The electrochemical impedance spectroscopy results reported that the corrosion rate increases when the immersion time between 0 hr and 96 hr increases, independent of the electrolyte layer.

Karunanithi et al. [152] developed an Al 7075/TiO_2 composite by powder metallurgy route and studied the corrosion behavior of 3.5 wt.% NaCl. The corrosion potential moves in the noble-gas direction, and the corrosion current density increases with the accumulation of TiO_2 particles. The current density is determined using the TAFEL curve, with a minimum for the base alloy and a maximum for 30 vol.% TiB_2 reinforced composites. The current density values for 5 and 10 vol.% TiB_2 reinforced composites are in the same range. Increasing the reinforcement particles increases the pitting damage observed by SEM analysis. Nagaswarupa et al. [153] fabricated an Al 7075/Zr composite using stir casting, and the stress corrosion studies were done using seawater. Zr is an inert material that does not involve a galvanic effect. Therefore, the composite material is less susceptible to corrosion, mass loss, and pit formation than the base alloy. Increasing the reinforcement material improves the TS and bonding strength.

El-Amoush [154] investigated the corrosion behavior of hydrogenated Al 7075 T6 alloy in a 0.5 M NaCl solution with a pH of 3.56. Increasing the precharged hydrogen time increases the pitting and severity of the attack. Pitting is lower compared to the nonhydrogenated alloy material. Huang et al. [155] studied the electrochemical behavior of Al 7075-T73 alloy and its cooled rolled components. It is reported that the anodized, cooled, and rolled Al 7075-T73 alloys show higher corrosion resistance compared to the base alloy. Microcell approaches are viable for characterizing and understanding localized corrosion in microstructurally complex alloys.

Recent studies have shown that the corrosion properties of Al 7075 MMCs can be further enhanced by choosing the suitable reinforcement, amount of reinforcement, and reinforcement dispersion.

6. Summary and Future Direction

(i) Numerous obstacles must be optimized to increase the application of MMCs, such as reinforcement vol./wt.%, reinforcement size/shape/type, operating temperature, and development method, to develop advanced materials for a wide range of structural and frictional applications

(ii) According to the literature, it was found that hybrid nanocomposites offer a wide range of possible industrial uses

(iii) The exact composition with different manufacturing methods will lead to the development of advanced MMCs

(iv) Further studies in thermal properties and heat treatment of MMCs with different reinforcements will improve the thermal applications

(v) The secondary processing methods in MMCs are the main problem

(vi) Further advancements in research are required to combine MMCs easily, and specialized tool innovations are required for machining MMCs

7. Conclusions

An extensive literature study has been performed for various AMCs and different reinforcements. Based on the study, the following conclusions have arrived.

(i) Developing AMCs with different reinforcement particles improves the properties of the materials required in different application areas such as aerospace, automobiles, military, and general structural applications.

(ii) Most researchers use the liquid metallurgy technique for developing composite materials. This technique is cost effective, simple, and absent of size limitations, and it can be used for mass production.

(iii) The review found that adding hard reinforcement particles enhances the mechanical, tribological, and corrosion properties of MMCs compared to the base alloy.

(iv) The composite material's properties increased when the reinforcement particles increased, irrespective of the manufacturing process.

(v) Hybrid MMCs have better mechanical, tribological, corrosion, and thermal properties than single-reinforced composites and base alloys.

(vi) In the case of hybrid MMC, adding a small amount of two or more reinforcement particles provides better properties than increasing the single reinforcement in the matrix.

Nomenclature

AMCs: Aluminium matrix composites
Al_2O_3: Aluminium oxide
Al-Zn: Aluminium-zinc
BA: Bagasse ash
B_4C: Boron carbide
BHN: Brinell hardness number
CB: Carbon black
COF: Coefficient of friction
EDAX: Energy-dispersive X-ray spectroscopy
FA: Fly ash
FSP: Friction stir processing
Gr: Graphite
MML: Mechanical mixed layer
MMCs: Metal matrix composites
PM: Powder metallurgy
RRA: Retrogression and reaging
HRB: Rockwell hardness
SEM: Scanning electron microscope
SiC: Silicon carbide
TS: Tensile strength
TiC: Titanium carbide
TiB_2: Titanium diboride
TiO_2: Titanium dioxide
UTS: Ultimate tensile strength
VHN: Vickers hardness number
wt.%: Weight %
Y_2O_3: Yttrium oxide.

Conflicts of Interest

The authors declare that they have no conflicts of interest.

References

[1] T. Dursun and C. Soutis, "Recent developments in advanced aircraft aluminium alloys," *Materials & Design*, vol. 56, pp. 862–871, 2014.

[2] C. G. E. Mangin, J. A. Isaacs, and J. P. Clark, "MMCs for automotive engine applications," *Journal of Occupational Medicine*, vol. 48, no. 2, pp. 49–51, 1996.

[3] M. Sam, N. Radhika, V. Sidvilash, and T. Mohanraj, "Investigation on the mechanical and wear behaviour of Al-6082-BN-B4C-corn cob ash hybrid composites," *Tribology in Industry*, vol. 44, no. 1, pp. 294–309, 2022.

[4] K. Suganeswaran, R. Parameshwaran, T. Mohanraj, and N. Radhika, "Influence of secondary phase particles Al2O3/SiC on the microstructure and tribological characteristics of AA7075-based surface hybrid composites tailored using friction stir processing," *Proceedings of the Institution of Mechanical Engineers - Part C: Journal of Mechanical Engineering Science*, vol. 235, no. 1, pp. 161–178, 2021.

[5] S. Kangishwar, N. Radhika, A. A. Sheik, A. Chavali, and S. Hariharan, "A comprehensive review on polymer matrix composites: material selection, fabrication, and application," *Polymer Bulletin*, pp. 1–41, 2022.

[6] F. C. Campbell Jr, *Manufacturing Technology for Aerospace Structural Materials*, Elsevier, Amsterdam, Netherlands, 2011.

[7] M. K. Kulekci, "Magnesium and its alloys applications in automotive industry," *International Journal of Advanced Manufacturing Technology*, vol. 39, no. 9-10, pp. 851–865, 2008.

[8] R. Jojith, N. Radhika, and M. Govindaraju, "Reciprocating wear behavioural analysis of heat-treated aluminium ZrO2/Al7Si0. 3Mg functionally graded composite through taguchi's optimization method," *Silicon*, pp. 1–18, 2022.

[9] S. R. Lampman and T. B. Zorc, *Properties and Selection of Non-ferrous Alloys and Special Materials*, ASM handbook, Washington, DC, USA, 1998.

[10] S. Donaldson and D. Miracle, *ASM Handbook Composites*, Wyd ASM International, Washington, DC, USA, 2001.

[11] A. Adebisi, M. Maleque, and M. Rahman, "Metal matrix composite brake rotor: historical development and product life cycle analysis," *International Journal of Automotive and Mechanical Engineering*, vol. 4, pp. 471–480, 2011.

[12] A. U. Rao, V. Vasu, M. Govindaraju, and K. S. Srinadh, "Stress corrosion cracking behaviour of 7xxx aluminum alloys: a literature review," *Transactions of Nonferrous Metals Society of China*, vol. 26, no. 6, pp. 1447–1471, 2016.

[13] E. Canepa, R. Stifanese, L. Merotto, and P. Traverso, "Corrosion behaviour of aluminium alloys in deep-sea environment: a review and the KM3NeT test results," *Marine Structures*, vol. 59, pp. 271–284, 2018.

[14] A. Ramanathan, P. K. Krishnan, and R. Muraliraja, "A review on the production of metal matrix composites through stir casting–Furnace design, properties, challenges, and research opportunities," *Journal of Manufacturing Processes*, vol. 42, pp. 213–245, 2019.

[15] V. Chak, H. Chattopadhyay, and T. L. Dora, "A review on fabrication methods, reinforcements and mechanical properties of aluminum matrix composites," *Journal of Manufacturing Processes*, vol. 56, pp. 1059–1074, 2020.

[16] V. M. Kumar and C. V. Venkatesh, "A comprehensive review on material selection, processing, characterization and applications of aluminium metal matrix composites," *Materials Research Express*, vol. 6, no. 7, Article ID 072001, 2019.

[17] K. Singh, H. Singh, S. Vardhan, and S. Mohan, "Mechanical study of Al 7050 and Al 7075 based metal matrix composites: a review," *Materials Today Proceedings*, vol. 43, pp. 673–677, 2021.

[18] J. Singh and A. Chauhan, "Characterization of hybrid aluminum matrix composites for advanced applications–A review," *Journal of Materials Research and Technology*, vol. 5, no. 2, pp. 159–169, 2016.

[19] N. Idusuyi and J. I. Olayinka, "Dry sliding wear characteristics of aluminium metal matrix composites: a brief overview," *Journal of Materials Research and Technology*, vol. 8, no. 3, pp. 3338–3346, 2019.

[20] B. V. Ramnath, C. Elanchezhian, R. M. Annamalai et al., "Aluminium metal matrix composites–a review," *Reviews on Advanced Materials Science*, vol. 38, pp. 55–60, 2014.

[21] J. Hashim, L. Looney, and M. S. J. Hashmi, "Metal matrix composites: production by the stir casting method," *Journal of Materials Processing Technology*, vol. 92–93, pp. 1–7, 1999.

[22] A. Mandal, M. Chakraborty, and B. Murty, "Effect of TiB2 particles on sliding wear behaviour of Al–4Cu alloy," *Wear*, vol. 262, no. 1-2, pp. 160–166, 2007.

[23] A. Anasyida, A. Daud, and M. J. Ghazali, "Dry sliding wear behaviour of Al–12Si–4Mg alloy with cerium addition," *Materials & Design*, vol. 31, no. 1, pp. 365–374, 2010.

[24] S. Ghosh, *Engineering materials: properties and selection: by K. Budinski*, 486 pages, Elsevier, Amsterdam, Netherlands, 1986.

[25] J. Hashim, L. Looney, and M. Hashmi, "Particle distribution in cast metal matrix composites—Part I," *Journal of Materials Processing Technology*, vol. 123, no. 2, pp. 251–257, 2002.

[26] F. A. Girot, J. M. Quenisset, and R. Naslain, "Discontinuously-reinforced aluminum matrix composites," *Composites Science and Technology*, vol. 30, no. 3, pp. 155–184, 1987.

[27] A. M. Sankhla, K. M. Patel, M. A. Makhesana et al., "Effect of mixing method and particle size on hardness and compressive strength of aluminium based metal matrix composite prepared through powder metallurgy route," *Journal of Materials Research and Technology*, vol. 18, pp. 282–292, 2022.

[28] S. P. Dwivedi, A. Saxena, S. Sharma et al., "Effect of ball-milling process parameters on mechanical properties of Al/Al2O3/collagen powder composite using statistical approach," *Journal of Materials Research and Technology*, vol. 15, pp. 2918–2932, 2021.

[29] A. Ercetin and D. Y. Pimenov, "Microstructure, mechanical, and corrosion behavior of Al2O3 reinforced Mg2Zn matrix magnesium composites," *Materials*, vol. 14, no. 17, 4819 pages, 2021.

[30] P. K. Swamy, S. Mylaraiah, M. P. Gowdru Chandrashekarappa et al., "Corrosion behaviour of high-strength Al 7005 alloy and its composites reinforced with industrial waste-based fly ash and glass fibre: comparison of stir cast and extrusion conditions," *Materials*, vol. 14, 3929 pages, 2021.

[31] S. Sharma, J. Singh, M. K. Gupta et al., "Investigation on mechanical, tribological and microstructural properties of Al–Mg–Si–T6/SiC/muscovite-hybrid metal-matrix composites for high strength applications," *Journal of Materials Research and Technology*, vol. 12, pp. 1564–1581, 2021.

[32] E. Salur, A. Aslan, M. Kuntoğlu, and M. Acarer, "Effect of ball milling time on the structural characteristics and mechanical properties of nano-sized Y2O3 particle reinforced aluminum matrix composites produced by powder metallurgy route," *Advanced Powder Technology*, vol. 32, no. 10, pp. 3826–3844, 2021.

[33] K. Doğan, M. İ Özgün, H. Sübütay et al., "Dispersion mechanism-induced variations in microstructural and mechanical behavior of CNT-reinforced aluminum nanocomposites," *Archives of Civil and Mechanical Engineering*, vol. 22, pp. 55–17, 2022.

[34] M. R. Rosenberger, E. Forlerer, and C. E. Schvezov, "Wear behavior of AA1060 reinforced with alumina under different loads," *Wear*, vol. 266, no. 1-2, pp. 356–359, 2009.

[35] M. Alizadeh, M. Paydar, and F. Sharifian Jazi, "Structural evaluation and mechanical properties of nanostructured Al/B4C composite fabricated by ARB process," *Composites Part B: Engineering*, vol. 44, no. 1, pp. 339–343, 2013.

[36] K. L. Tee, L. Lu, and M. O. Lai, "In situ processing of Al–TiB2 composite by the stir-casting technique," *Journal of Materials Processing Technology*, vol. 89–90, pp. 513–519, 1999.

[37] T. M. Yue, Y. X. Wu, and H. C. Man, "On the role of CuAl2 precipitates in pitting corrosion of aluminium 2009/SiCW metal matrix composite," *Journal of Materials Science Letters*, vol. 19, no. 11, pp. 1003–1006, 2000.

[38] Y. Sahin and M. Acılar, "Production and properties of SiCp-reinforced aluminium alloy composites," *Composites Part A: Applied Science and Manufacturing*, vol. 34, no. 8, pp. 709–718, 2003.

[39] Y. Liu, S. Lim, S. Ray, and P. Rohatgi, "Friction and wear of aluminium-graphite composites: the smearing process of graphite during sliding," *Wear*, vol. 159, no. 2, pp. 201–205, 1992.

[40] A. Mazahery and M. O. Shabani, "Microstructural and abrasive wear properties of SiC reinforced aluminum-based composite produced by compocasting," *Transactions of Nonferrous Metals Society of China*, vol. 23, no. 7, pp. 1905–1914, 2013.

[41] M. Kök and K. Özdin, "Wear resistance of aluminium alloy and its composites reinforced by Al2O3 particles," *Journal of Materials Processing Technology*, vol. 183, no. 2-3, pp. 301–309, 2007.

[42] Z.-Y. Xiu, G.-Q. Chen, G.-H. Wu, W.-S. Yang, and Y.-M. Liu, "Effect of volume fraction on microstructure and mechanical properties of Si3N4/Al composites," *Transactions of Nonferrous Metals Society of China*, vol. 21, pp. s285–s289, 2011.

[43] F. Akhlaghi and A. Zare-Bidaki, "Influence of graphite content on the dry sliding and oil impregnated sliding wear behavior of Al 2024–graphite composites produced by in situ powder metallurgy method," *Wear*, vol. 266, no. 1-2, pp. 37–45, 2009.

[44] M. Kok, "Production and mechanical properties of Al2O3 particle-reinforced 2024 aluminium alloy composites," *Journal of Materials Processing Technology*, vol. 161, no. 3, pp. 381–387, 2005.

[45] T. S. Srivatsan, "The low-cycle fatigue behaviour of an aluminium-alloy-ceramic-particle composite," *International Journal of Fatigue*, vol. 14, no. 3, pp. 173–182, 1992.

[46] S. Basavarajappa, G. Chandramohan, S. Ramanathan, and A. Chandrasekar, *Dry Sliding Wear Behaviour of Al 2219/SiC Metal Matrix Composites*, Materials Science-Wroclaw, vol. 24, no. 2/1, pp. 357–366, 2006.

[47] H. Mindivan, E. S. Kayali, and H. Cimenoglu, "Dry Sliding Wear Behaviour of SiC Particle Reinforced AA2618 Composites," *International Conference on Tribology*, pp. 1–6, 2006.

[48] O. Yılmaz and S. Buytoz, "Abrasive wear of Al2O3-reinforced aluminium-based MMCs," *Composites Science and Technology*, vol. 61, no. 16, pp. 2381–2392, 2001.

[49] A. A. Daniel, S. Murugesan, S. Sukkasamy, and S. Sukkasamy, "Dry sliding wear behaviour of aluminium 5059/SiC/MoS2 hybrid metal matrix composites," *Materials Research*, vol. 20, no. 6, pp. 1697–1706, 2017.

[50] S. Suresh, N. Shenbaga Vinayaga Moorthi, S. Vettivel, and N. Selvakumar, "Mechanical behavior and wear prediction of stir cast Al–TiB2 composites using response surface methodology," *Materials & Design*, vol. 59, pp. 383–396, 2014.

[51] P. Zhang, Y. Li, W. Wang, Z. Gao, and B. Wang, "The design, fabrication and properties of B4C/Al neutron absorbers," *Journal of Nuclear Materials*, vol. 437, no. 1-3, pp. 350–358, 2013.

[52] C. Ramesh and A. Ahamed, "Friction and wear behaviour of cast Al 6063 based in situ metal matrix composites," *Wear*, vol. 271, no. 9-10, pp. 1928–1939, 2011.

[53] G. Naveen Kumar, R. Narayanasamy, S. Natarajan, S. Kumaresh Babu, K. Sivaprasad, and S. Sivasankaran, "Dry sliding wear behaviour of AA 6351-ZrB2 in situ composite at room temperature," *Materials & Design*, vol. 31, no. 3, pp. 1526–1532, 2010.

[54] L. Ceschini, G. Minak, and A. Morri, "Tensile and fatigue properties of the AA6061/20 vol% Al2O3p and AA7005/10 vol% Al2O3p composites," *Composites Science and Technology*, vol. 66, no. 2, pp. 333–342, 2006.

[55] T. S. Srivatsan, S. Anand, S. Sriram, and V. K. Vasudevan, "The high-cycle fatigue and fracture behavior of aluminum alloy 7055," *Materials Science and Engineering A*, vol. 281, no. 1-2, pp. 292–304, 2000.

[56] H. B. Michael Rajan, S. Ramabalan, I. Dinaharan, and S. J. Vijay, "Synthesis and characterization of in situ formed titanium diboride particulate reinforced AA7075 aluminum alloy cast composites," *Materials & Design*, vol. 44, pp. 438–445, 2013.

[57] A. Baradeswaran and A. E. Perumal, "Wear and mechanical characteristics of Al 7075/graphite composites," *Composites Part B: Engineering*, vol. 56, pp. 472–476, 2014.

[58] T. G. D. Río, A. Rico, M. Garrido, P. Poza, and J. Rodríguez, "Temperature and velocity transitions in dry sliding wear of Al–Li/SiC composites," *Wear*, vol. 268, no. 5-6, pp. 700–707, 2010.

[59] A. Jha, S. Prasad, and G. Upadhyaya, "Dry sliding wear of sintered 6061 aluminium alloy—graphite particle composites," *Tribology International*, vol. 22, no. 5, pp. 321–327, 1989.

[60] S. Lim, M. Gupta, L. Ren, and J. Kwok, "The tribological properties of Al–Cu/SiCp metal–matrix composites fabricated using the rheocasting technique," *Journal of Materials Processing Technology*, vol. 89-90, pp. 591–596, 1999.

[61] A. Sato and R. Mehrabian, "Aluminum matrix composites: fabrication and properties," *Metallurgical Transactions A B*, vol. 7, no. 3, pp. 443–451, 1976.

[62] F. Chen, Z. Chen, F. Mao, T. Wang, and Z. Cao, "TiB2 reinforced aluminum based in situ composites fabricated by stir casting," *Materials Science and Engineering A*, vol. 625, pp. 357–368, 2015.

[63] M. Khakbiz and F. Akhlaghi, "Synthesis and structural characterization of Al–B4C nano-composite powders by mechanical alloying," *Journal of Alloys and Compounds*, vol. 479, no. 1-2, pp. 334–341, 2009.

[64] A. R. Kennedy and S. M. Wyatt, "The effect of processing on the mechanical properties and interfacial strength of aluminium/TiC MMCs," *Composites Science and Technology*, vol. 60, no. 2, pp. 307–314, 2000.

[65] P. Rohatgi, B. Schultz, A. Daoud, and W. Zhang, "Tribological performance of A206 aluminum alloy containing silica sand particles," *Tribology International*, vol. 43, no. 1-2, pp. 455–466, 2010.

[66] S. Basavaraju, K. Arasukumar, C. Bendigeri, and C. Umesh, "Studies on mechanical properties and tribological characteristics of LM25-graphite-silicon carbide and LM25-flyash-silicon carbide-hybrid MMCs," *International Journal Of Innovative Research in Science Engineering And Technology*, vol. 1, pp. 107–112, 2012.

[67] M. Singh, B. Prasad, D. Mondal, and A. Jha, "Dry sliding wear behaviour of an aluminium alloy–granite particle composite," *Tribology International*, vol. 34, no. 8, pp. 557–567, 2001.

[68] S. K. Chaudhury, C. S. Sivaramakrishnan, and S. C. Panigrahi, "A new spray forming technique for the preparation of aluminium rutile (TiO2) ex situ particle composite," *Journal of Materials Processing Technology*, vol. 145, no. 3, pp. 385–390, 2004.

[69] R. Kumar and S. Dhiman, "A study of sliding wear behaviors of Al-7075 alloy and Al-7075 hybrid composite by response surface methodology analysis," *Materials & Design*, vol. 50, pp. 351–359, 2013.

[70] H. Ahlatci, T. Kocer, E. Candan, and H. Çimenoğlu, "Wear behaviour of Al/(Al2O3p+ SiCp) hybrid composites," *Tribology International*, vol. 39, no. 3, pp. 213–220, 2006.

[71] S. Alidokht, A. Abdollah-Zadeh, S. Soleymani, and H. Assadi, "Microstructure and tribological performance of an aluminium alloy based hybrid composite produced by friction stir processing," *Materials & Design*, vol. 32, no. 5, pp. 2727–2733, 2011.

[72] K. Mahendra and K. Radhakrishna, "Characterization of stir cast Al—Cu—(fly ash+ SiC) hybrid metal matrix composites," *Journal of Composite Materials*, vol. 44, no. 8, pp. 989–1005, 2010.

[73] G. Elango and B. Raghunath, "Tribological behavior of hybrid (LM25Al+ SiC+ TiO2) metal matrix composites," *Procedia Engineering*, vol. 64, pp. 671–680, 2013.

[74] M. Uthayakumar, S. Aravindan, and K. Rajkumar, "Wear performance of Al–SiC–B4C hybrid composites under dry sliding conditions," *Materials & Design*, vol. 47, pp. 456–464, 2013.

[75] K. K. Alaneme, T. M. Adewale, and P. A. Olubambi, "Corrosion and wear behaviour of Al–Mg–Si alloy matrix hybrid composites reinforced with rice husk ash and silicon carbide," *Journal of Materials Research and Technology*, vol. 3, no. 1, pp. 9–16, 2014.

[76] A. Baradeswaran and A. E. Perumal, "Study on mechanical and wear properties of Al 7075/Al2O3/graphite hybrid composites," *Composites Part B: Engineering*, vol. 56, pp. 464–471, 2014.

[77] B. Vijaya Ramnath, C. Elanchezhian, M. Jaivignesh, S. Rajesh, C. Parswajinan, and A. Siddique Ahmed Ghias, "Evaluation of mechanical properties of aluminium alloy–alumina–boron carbide metal matrix composites," *Materials & Design*, vol. 58, pp. 332–338, 2014.

[78] K. Kanayo Alaneme and P. Apata Olubambi, "Corrosion and wear behaviour of rice husk ash—alumina reinforced Al–Mg–Si alloy matrix hybrid composites," *Journal of Materials Research and Technology*, vol. 2, pp. 188–194, 2013.

[79] Y. Mazaheri, M. Meratian, R. Emadi, and A. Najarian, "Comparison of microstructural and mechanical properties of Al–TiC, Al–B4C and Al–TiC–B4C composites prepared by casting techniques," *Materials Science and Engineering A*, vol. 560, pp. 278–287, 2013.

[80] A. Baradeswaran, S. Vettivel, A. Elaya Perumal, N. Selvakumar, and R. Franklin Issac, "Experimental investigation on mechanical behaviour, modelling and optimization of wear parameters of B4C and graphite reinforced aluminium hybrid composites," *Materials & Design*, vol. 63, pp. 620–632, 2014.

[81] S. Suresh, N. Shenbaga Vinayaga Moorthi, S. Vettivel, N. Selvakumar, and G. Jinu, "Effect of graphite addition on mechanical behavior of Al6061/TiB2 hybrid composite using acoustic emission," *Materials Science and Engineering A*, vol. 612, pp. 16–27, 2014.

[82] D. S. Pradeep, R. Ganesh, and T. Senthilvelan, "On the mechanical properties of hybrid aluminium 7075 matrix composite material reinforced with SiC and TiC produced by

powder metallurgy method," *Indian Journal of Materials Science*, vol. 2017, Article ID 3067257, 6 pages, 2017.

[83] A. Kalkanlı and S. Yılmaz, "Synthesis and characterization of aluminum alloy 7075 reinforced with silicon carbide particulates," *Materials & Design*, vol. 29, no. 4, pp. 775–780, 2008.

[84] R. K. Bhushan, S. Kumar, and S. Das, "Fabrication and characterization of 7075 Al alloy reinforced with SiC particulates," *International Journal of Advanced Manufacturing Technology*, vol. 65, no. 5-8, pp. 611–624, 2013.

[85] T. B. Rao, "An experimental investigation on mechanical and wear properties of Al7075/SiCp composites: effect of SiC content and particle size," *Journal of Tribology*, vol. 140, no. 3, Article ID 031601, 2018.

[86] M. Ayyanar Raja, V. Manikandan, P. Amuthakkannan, S. Rajesh, and I. Balasubramanian, "Wear resistance of basalt particulate-reinforced stir-cast Al7075 metal matrix composites," *Journal of the Australian Ceramic Society*, vol. 54, no. 1, pp. 119–128, 2018.

[87] C. Y. Liu, Q. Wang, Y. Z. Jia et al., "Evaluation of mechanical properties of 1060-Al reinforced with WC particles via warm accumulative roll bonding process," *Materials & Design*, vol. 43, pp. 367–372, 2013.

[88] S. A. Sajjadi, H. R. Ezatpour, and M. Torabi Parizi, "Comparison of microstructure and mechanical properties of A356 aluminum alloy/Al2O3 composites fabricated by stir and compo-casting processes," *Materials & Design*, vol. 34, pp. 106–111, 2012.

[89] H. Zhang, Y. He, and L. Li, "Tensile deformation and fracture behavior of spray-deposition 7075/15SiCp aluminum matrix composite sheet at elevated temperatures," *Materials Characterization*, vol. 59, no. 8, pp. 1078–1082, 2008.

[90] J. E. Allison and G. S. Cole, "Metal-matrix composites in the automotive industry: opportunities and challenges," *Journal of Occupational Medicine*, vol. 45, no. 1, pp. 19–24, 1993.

[91] K. S. Al-Rubaie, H. Goldenstein, and J. D. Biasoli de Mello, "Three-body abrasion of Al–SiC composites," *Wear*, vol. 225-229, pp. 163–173, 1999.

[92] L. R. Deaquino, E. Gutiérrez-Castañeda, I. Estrada-Guel et al., "Structural characterization of Aluminum alloy 7075-graphite composites fabricated by mechanical alloying and hot extrusion," *Materials & Design*, 2013.

[93] Ł Rogal, J. Dutkiewicz, H. V. Atkinson, L. Lityńska-Dobrzyńska, T. Czeppe, and M. Modigell, "Characterization of semisolid processing of aluminium alloy 7075 with Sc and Zr additions," *Materials Science and Engineering A*, vol. 580, pp. 362–373, 2013.

[94] Y.-D. Qu, R.-M. Su, J.-H. You, and R. D. Li, "Study on microstructure, mechanical properties and corrosion behavior of spray formed 7075 alloy," *Materials Today Communications*, vol. 4, pp. 109–115, 2015.

[95] T. Senthilvelan, S. Gopalakannan, S. Vishnuvarthan, and K. Keerthivaran, "Fabrication and characterization of SiC, Al2O3 and B4C reinforced Al-Zn-Mg-Cu alloy (AA 7075) metal matrix composites: a study," *Advanced Materials Research*, vol. 622-623, pp. 1295–1299, 2013.

[96] R. Clark Jr, B. Coughran, I. Traina et al., "On the correlation of mechanical and physical properties of 7075-T6 Al alloy," *Engineering Failure Analysis*, vol. 12, no. 4, pp. 520–526, 2005.

[97] Y. Reda, R. Abdel-Karim, and I. Elmahallawi, "Improvements in mechanical and stress corrosion cracking properties in Al-alloy 7075 via retrogression and reaging," *Materials Science and Engineering A*, vol. 485, no. 1-2, pp. 468–475, 2008.

[98] S. W. Kim, D. Y. Kim, W. G. Kim, and K. D. Woo, "The study on characteristics of heat treatment of the direct squeeze cast 7075 wrought Al alloy," *Materials Science and Engineering A*, vol. 304–306, pp. 721–726, 2001.

[99] K. B. Lee and H. Kwon, "Strength of Al-Zn-Mg-Cu matrix composite reinforced with SiC particles," *Metallurgical and Materials Transactions A*, vol. 33, no. 2, pp. 455–465, 2002.

[100] W. Chen, Y. Liu, C. Yang, D. Zhu, and Y. Li, "(SiCp+Ti)/7075Al hybrid composites with high strength and large plasticity fabricated by squeeze casting," *Materials Science and Engineering A*, vol. 609, pp. 250–254, 2014.

[101] C. Kannan and R. Ramanujam, "Comparative study on the mechanical and microstructural characterisation of AA 7075 nano and hybrid nanocomposites produced by stir and squeeze casting," *Journal of Advanced Research*, vol. 8, no. 4, pp. 309–319, 2017.

[102] T. Lu, W. Chen, P. Wang, M. Mao, Y. Liu, and Z. Fu, "Enhanced mechanical properties and thermo-physical properties of 7075Al hybrid composites reinforced by the mixture of Cr particles and SiCp," *Journal of Alloys and Compounds*, vol. 735, pp. 1137–1144, 2018.

[103] R. Deaquino-Lara, E. Gutiérrez-Castañeda, I. Estrada-Guel et al., "Structural characterization of aluminium alloy 7075–graphite composites fabricated by mechanical alloying and hot extrusion," *Materials & Design*, vol. 53, pp. 1104–1111, 2014.

[104] B. Subramaniam, B. Natarajan, B. Kaliyaperumal, and S. J. S. Chelladurai, "Investigation on mechanical properties of aluminium 7075-boron carbide-coconut shell fly ash reinforced hybrid metal matrix composites," *China Foundry*, vol. 15, no. 6, pp. 449–456, 2018.

[105] A. Gajakosh, R. Keshavamurthy, G. Ugrasen, and H. Adarsh, "Investigation on mechanical behavior of hot rolled Al7075-TiB2 in-situ metal matrix composite," *Materials Today Proceedings*, vol. 5, no. 11, Article ID 25605, 2018.

[106] B. T. Chandra, H. S. Shankar, and H. Shiva Shankar, "Effect of heat treatment on dry sand abrasive wear behavior of Al7075-Albite particulate composites," *Materials Today Proceedings*, vol. 5, no. 2, pp. 5968–5975, 2018.

[107] D. R. Kumar, P. Asha, P. Asha, and C. P. Rao, "Influence of percent filler on tensile strength, impact strength and wear properties of the Al7075-cenosphere composite," *Materials Today Proceedings*, vol. 5, Article ID 11697, 2018.

[108] R. Rajesh, S. Sharma, and M. C. Gowrishankar, "Influence of solutionising and aging treatments on mechanical behavior of stir-cast eutectoid steel powder reinforced Al 7075 metal matrix composites," *International Journal of Automotive and Mechanical Engineering*, vol. 15, no. 3, pp. 5583–5591, 2018.

[109] S. Suresh GhgaMDK, "Experimental Investigation on Mechanical Properties of Al 7075/Al2O3/Mg NMMC's by Stir Casting Technique," *Sadhana-indian Academy of scinece*, vol. 44, 2019.

[110] G. B. V. Kumar, C. S. P. Rao, N. Selvaraj, and M. S. Bhagyashekar, "Studies on Al6061-SiC and Al7075-Al₂O₃ Metal Matrix Composites," *Journal of Minerals and Materials Characterization and Engineering*, vol. 09, no. 01, pp. 43–55, 2010.

[111] P. Roy, S. Singh, and K. Pal, "Enhancement of mechanical and tribological properties of SiC-and CB-reinforced aluminium 7075 hybrid composites through friction stir

processing," *Advanced Composite Materials*, vol. 28, pp. 1–18, 2017.

[112] A. Atrian, G. Majzoobi, S. Nourbakhsh, S. Galehdari, and R. Masoudi Nejad, "Evaluation of tensile strength of Al7075-SiC nanocomposite compacted by gas gun using spherical indentation test and neural networks," *Advanced Powder Technology*, vol. 27, no. 4, pp. 1821–1827, 2016.

[113] V. Balaji, N. Sateesh, and M. M. Hussain, "Manufacture of aluminium metal matrix composite (Al7075-SiC) by stir casting technique," *Materials Today Proceedings*, vol. 2, no. 4-5, pp. 3403–3408, 2015.

[114] T. B. Rao and A. G. Krishna, "Selection of optimal process parameters in WEDM while machining Al7075/SiCp metal matrix composites," *International Journal of Advanced Manufacturing Technology*, vol. 73, no. 1-4, pp. 299–314, 2014.

[115] R. Kumar and S. Chauhan, "Study on surface roughness measurement for turning of Al 7075/10/SiCp and Al 7075 hybrid composites by using response surface methodology (RSM) and artificial neural networking (ANN)," *Measurement*, vol. 65, pp. 166–180, 2015.

[116] M. Sambathkumar, P. Navaneethakrishnan, K. Ponappa, and K. Sasikumar, "Mechanical and corrosion behavior of Al7075 (hybrid) metal matrix composites by two step stir casting process," *Latin American Journal of Solids and Structures*, vol. 14, no. 2, pp. 243–255, 2017.

[117] A. Azimi, A. Shokuhfar, and O. Nejadseyfi, "Mechanically alloyed Al7075–TiC nanocomposite: powder processing, consolidation and mechanical strength," *Materials & Design*, vol. 66, pp. 137–141, 2015.

[118] M. Imran, A. A. Khan, S. Megeri, and S. Sadik, "Study of hardness and tensile strength of Aluminium-7075 percentage varying reinforced with graphite and bagasse-ash composites," *Resource-Efficient Technologies*, vol. 2, pp. 81–88, 2016.

[119] A. Javdani and A. Daei-Sorkhabi, "Microstructural and mechanical behavior of blended powder semisolid formed Al7075/B4C composites under different experimental conditions," *Transactions of Nonferrous Metals Society of China*, vol. 28, no. 7, pp. 1298–1310, 2018.

[120] M. Matuszewski, T. Mikolajczyk, D. Y. Pimenov, and M. Styp-Rekowski, "Influence of structure isotropy of machined surface on the wear process," *International Journal of Advanced Manufacturing Technology*, vol. 88, no. 9-12, pp. 2477–2483, 2017.

[121] S. Prasad, P. Rohatgi, and T. Kosel, "Mechanisms of material removal during low stress and high stress abrasion of aluminum alloy-zircon particle composites," *Materials Science and Engineering*, vol. 80, no. 2, pp. 213–220, 1986.

[122] D. R. Askeland and P. Webster, *The Science and Engineering of Materials*, Springer, Berlin, Germany, 1996.

[123] L. Huei-Long, L. Wun-Hwa, and S. L.-I. Chan, "Abrasive wear of powder metallurgy Al alloy 6061-SiC particle composites," *Wear*, vol. 159, no. 2, pp. 223–231, 1992.

[124] R. Uyyuru, M. Surappa, and S. Brusethaug, "Tribological behavior of Al–Si–SiCp composites/automobile brake pad system under dry sliding conditions," *Tribology International*, vol. 40, no. 2, pp. 365–373, 2007.

[125] I. A. Ibrahim, F. A. Mohamed, and E. J. Lavernia, "Particulate reinforced metal matrix composites—a review," *Journal of Materials Science*, vol. 26, no. 5, pp. 1137–1156, 1991.

[126] I. Sinclair and P. J. Gregson, "Structural performance of discontinuous metal matrix composites," *Materials Science and Technology*, vol. 13, no. 9, pp. 709–726, 1997.

[127] S. Das, "The influence of matrix microstructure and particle reinforcement on the two-body abrasive wear of an Al-Si alloy," *Journal of Materials Science Letters*, vol. 16, no. 21, pp. 1757–1760, 1997.

[128] B. S. Ünlü, "Investigation of tribological and mechanical properties Al2O3–SiC reinforced Al composites manufactured by casting or P/M method," *Materials & Design*, vol. 29, no. 10, pp. 2002–2008, 2008.

[129] O. Modi, B. Prasad, A. Yegneswaran, and M. Vaidya, "Dry sliding wear behaviour of squeeze cast aluminium alloy-silicon carbide composites," *Materials Science and Engineering A*, vol. 151, no. 2, pp. 235–245, 1992.

[130] H. Zhu, H. Wang, and L. Ge, "Wear properties of the composites fabricated by exothermic dispersion reaction synthesis in an Al–TiO2–B2O3 system," *Wear*, vol. 264, no. 11-12, pp. 967–972, 2008.

[131] Z. Ma, Y. Liang, Y. Lu, and J. Bi, "Effect of Matrix Strengthening on Sliding Wear Properties of SiCp/2024Al Composites", *Transactions of Nonferrous Metals Society of China*, vol. 8, no. 4, pp. 556–561, 1998.

[132] J. Zhang, R. Perez, and E. Lavernia, "Effect of SiC and graphite particulates on the damping behavior of metal matrix composites," *Acta Metallurgica et Materialia*, vol. 42, no. 2, pp. 395–409, 1994.

[133] B. Venkataraman and G. Sundararajan, "Correlation between the characteristics of the mechanically mixed layer and wear behaviour of aluminium, Al-7075 alloy and Al-MMCs," *Wear*, vol. 245, no. 1-2, pp. 22–38, 2000.

[134] A. Daoud, M. A. El-Khair, and A. Abdel-Azim, "Effect of Al_2O_3 particles on the microstructure and sliding wear of 7075 Al alloy manufactured by squeeze casting method," *Journal of Materials Engineering and Performance*, vol. 13, no. 2, pp. 135–143, 2004.

[135] R. H. B. Michael, S. Ramabalan, I. Dinaharan, and S. J. Vijay, "Effect of TiB2 content and temperature on sliding wear behavior of AA7075/TiB2 in situ aluminum cast composites," *Archives of Civil and Mechanical Engineering*, vol. 14, no. 1, pp. 72–79, 2014.

[136] A. Baradeswaran and A. E. Perumal, "Influence of B4C on the tribological and mechanical properties of Al 7075–B4C composites," *Composites Part B: Engineering*, vol. 54, pp. 146–152, 2013.

[137] M. Baydoğan, H. Çimenoğlu, and E. Sabri Kayalı, "A study on sliding wear of a 7075 aluminum alloy," *Wear*, vol. 257, no. 7-8, pp. 852–861, 2004.

[138] R. Dasgupta and H. Meenai, "SiC particulate dispersed composites of an Al–Zn–Mg–Cu alloy: property comparison with parent alloy," *Materials Characterization*, vol. 54, no. 4-5, pp. 438–445, 2005.

[139] J. Lakshmipathy and B. Kulendran, "Reciprocating wear behavior of 7075Al/SiC in comparison with 6061Al/Al2O3 composites," *International Journal of Refractory Metals and Hard Materials*, vol. 46, pp. 137–144, 2014.

[140] Y. Liu, Z. Zheng, C. Yang, D. Zhu, and W. Chen, "Effects of unreacted Ti particles on the dry sliding tribological behavior of squeeze-cast (SiCp+ Ti)/7075Al hybrid composites under different applied loads," *Tribology Letters*, vol. 65, no. 2, p. 39, 2017.

[141] A. Raturi, K. Mer, and P. Kumar Pant, "Synthesis and characterization of mechanical, tribological and micro structural behaviour of Al 7075 matrix reinforced with nano Al2O3 particles," *Materials Today Proceedings*, vol. 4, no. 2, pp. 2645–2658, 2017.

[142] T. Ram Prabhu, M. Murugan, B. P. Chiranth et al., "Effects of dual-phase reinforcement particles (fly Ash+ Al 2 O 3) on the wear and tensile properties of the AA 7075 Al alloy based composites," *Journal of The Institution of Engineers (India): Series D,* vol. 100, no. 1, pp. 29–35, 2019.

[143] S. Suresh, G. H. Gowd, and M. L. S. D. Kumar, "Mechanical and wear behavior of Al 7075/Al 2 O 3/SiC/mg metal matrix nanocomposite by liquid state process," *Advanced Composites and Hybrid Materials*, vol. 2, no. 3, pp. 530–539, 2019.

[144] G. Majzoobi, A. Atrian, and M. Enayati, "Tribological properties of Al7075-SiC nanocomposite prepared by hot dynamic compaction," *Composite Interfaces*, vol. 22, no. 7, pp. 579–593, 2015.

[145] H. Rana, V. Badheka, and A. Kumar, "Fabrication of Al7075/B4C surface composite by novel Friction Stir Processing (FSP) and investigation on wear properties," *Procedia Technology*, vol. 23, pp. 519–528, 2016.

[146] T. R. Prabhu, "Processing and properties evaluation of functionally continuous graded 7075 Al alloy/SiC composites," *Archives of Civil and Mechanical Engineering*, vol. 17, no. 1, pp. 20–31, 2017.

[147] R. R. Veeravalli, R. Nallu, and S. Mohammed Moulana Mohiuddin, "Mechanical and tribological properties of AA7075–TiC metal matrix composites under heat treated (T6) and cast conditions," *Journal of Materials Research and Technology*, vol. 5, no. 4, pp. 377–383, 2016.

[148] S. P. Kumarasamy, K. Vijayananth, T. Thankachan, and G. Pudhupalayam Muthukutti, "Investigations on mechanical and machinability behavior of aluminum/flyash cenosphere/Gr hybrid composites processed through compocasting," *Journal of Applied Research and Technology*, vol. 15, no. 5, pp. 430–441, 2017.

[149] T. M. Yue, L. J. Yan, and C. P. Chan, "Stress corrosion cracking behavior of Nd:YAG laser-treated aluminum alloy 7075," *Applied Surface Science*, vol. 252, no. 14, pp. 5026–5034, 2006.

[150] S. Varma and G. Vasquez, "Corrosive Wear Behavior of 7075 Aluminum Alloy and its Composite Containing Al_2O_3 Particles," *Journal of Materials Engineering and Performance*, vol. 12, no. 1, pp. 99–105, 2003.

[151] H. Zhou, X. Li, J. Ma, C. Dong, and Y. Huang, "Dependence of the corrosion behavior of aluminum alloy 7075 on the thin electrolyte layers," *Materials Science and Engineering: B*, vol. 162, pp. 1–8, 2009.

[152] R. Karunanithi, S. Bera, and K. Ghosh, "Electrochemical behaviour of TiO2 reinforced Al 7075 composite," *Materials Science and Engineering: B*, vol. 190, pp. 133–143, 2014.

[153] H. Nagaswarupa, H. Bheemanna, and G. Banuprakash, "Electrochemical studies of Al 7075/zircon metal matrix composites in natural sea water," *Journal of Ultra Chemistry*, vol. 8, pp. 319–328, 2012.

[154] A. S. El-Amoush, "Investigation of corrosion behaviour of hydrogenated 7075-T6 aluminum alloy," *Journal of Alloys and Compounds*, vol. 443, no. 1-2, pp. 171–177, 2007.

[155] Y.-S. Huang, T.-S. Shih, and J.-H. Chou, "Electrochemical behavior of anodized AA7075-T73 alloys as affected by the matrix structure," *Applied Surface Science*, vol. 283, pp. 249–257, 2013.

Hindawi
Advances in Materials Science and Engineering
Volume 2022, Article ID 9539790, 11 pages
https://doi.org/10.1155/2022/9539790

Research Article

Influence of Coated Electrode in Nanopowder Mixed EDM of Al–Zn–Mg–Si_3N_4 Composite

G. Anbuchezhiyan,[1] **R. Saravanan**,[1] **R. Pugazhenthi**,[2] **Kumaran Palani**,[3] **and Vamsi Krishna Mamidi**[4]

[1]*Department of Mechanical Engineering, Saveetha School of Engineering, Saveetha Institute of Medical and Technical Sciences, Chennai 602105, Tamil Nadu, India*
[2]*Department of Mechanical Engineering, Vels Institute of Science Technology and Advanced Studies, Chennai 600117, Kancheepuram, Tamil Nadu, India*
[3]*Department of Mechanical Engineering, College of Engineering, Wolaita Sodo University, Wolaita Sodo, P.O. Box 138, Ethiopia*
[4]*Department of Mechanical Engineering, Sri Venkateshwara College of Engineering, Tirupathi 517507, Andhra Pradesh, India*

Correspondence should be addressed to G. Anbuchezhiyan; tsgaaa1981@gmail.com and Kumaran Palani; pkumaran2003et@gmail.com

Received 24 August 2022; Revised 11 September 2022; Accepted 17 September 2022; Published 15 October 2022

Academic Editor: R. Thanigaivelan

Machinability investigation of new material is one of the mandatory investigations to complete the purpose of creation of it. Electrical discharge machining (EDM) is one of the promising unconventional machining processes for highly accurate machining performance in difficult-to-cut material even machining complicated profiles. The powder-mixed EDM and nanopowder-mixed EDM are the improved versions of the EDM. The Al–Zn–Mg composite is reinforced with Si_3N_4 (9 wt. %) for meeting automotive and marine applications. The aluminium nanoparticles enhanced deionised water was used in NPMEDM. The nickel-coated brass and uncoated brass tube electrode were considered for the investigation. Pulse on time (μs), voltage (V), input current (A), and capacitance (nF) were independent variables and varied at 3 levels. The microhole machining performance with a coated and uncoated electrode was investigated. The L18 orthogonal array involved in the experimental design, material removal rate, and electrode wear rate were analysed. The SEM analysis was employed in the surface morphological study of electrodes before and after machining. The input parameters were optimised for the coated electrode for the responses of MRR and EWR.

1. Introduction

Due to the increasing demands of the aerospace and tooling industries, EDM can be used to machine modern alloys and composites with high toughness, high strength, and high rigidity [1]. However, it has some limitations such as low machining rates and poor surface finishes, this can be addressed by various methods such as electron orbiting, rotating the tool, applying ultrasonic vibrations to the tool, and mixing conductive particles with dielectric fluid [2]. Introducing conductive particles in the dielectric fluid known as powder mixer EDM (PMEDM) is a new development that increases the gap between tools and the workpiece while providing a bridge between the electrodes, resulting in an even distribution of spark energy, which makes the process more stable and as a result, it significantly enhances the machining performance such as tool wear, surface roughness [3]. In the PMEDM process, the abrasives were uniformly mixed with dielectric fluid. It has been inferred that adding powdered particles to a dielectric medium such as copper, aluminium, iron, and carbon improved the machining rate as the concentration of the powdered particles increased [4–6]. The addition of the fine graphite powder in the range of 4 g/l improves the material

removal rate by 60% and reduced the tool wear ratio by 28% [7]. The addition of silicon carbide particles to H-13 die-steel resulted in a fine surface finish of 2 μm as well as an improvement in corrosion resistance. [8] Use a different concentration of tantalum carbide with the concentration value of 5 g/l, 10 g/l, and 15 g/l. Peak current increased both material removal rate and surface roughness. However, there is no consistency in the concentration of abrasive particles. [9] Observed microcracks and craters after using the PMEDM process. The role of abrasive particles in the dielectric medium has advantages and disadvantages based on the abrasive particles used. As a result, in this study, a thorough investigation was carried out by using aluminium nanoparticles in combination with dielectric fluid to conduct experimentation using the PMEDM process.

The length and side wear of the electrode in EDM affects the process machining accuracy [10]. The electrode wear rate can be reduced by providing coating or using composite material electrodes. [11] Investigates the coated electrode material results in reduced electrode wear and increased aspect ratio. The secondary spark can also be avoided using the coated electrode. [12] Compared commercially available brass electrode to composite tool electrode. For the manufacturing of composite electrodes, chromium and copper were used as the same material. The machining rate of the composite electrode is double that of the brass electrode, with better surface finish accuracy [13] observed that coating the copper electrode with NIP improved MRR and reduced electrode wear and overcut. Smooth and burr-free images were observed on the SEM image of the microholes. Copper electrodes were coated with zinc, chrome, and silver materials. The zinc-coated electrode had the highest rate of material removal out of the three [14].

It is clear from the literature review that coating highly conductive material over the tool electrode reduced dimensional inaccuracies, surface irregularities, and secondary spark. Hence in this study, the high electrical conductivity of nickel is coated over the brass electrode to assess the machinability of microholes in Al–Zn–Mg/Si_3N_4 composites using the PMEDM process has not been carried out for manufacturing application. Considering this as a major constraint an attempt has been made to PMEDM on Al–Zn–Mg/Si_3N_4 composites and compare its outcome with the coated and uncoated tool.

This research is unique by investigating the microhole machinability investigation of specially prepared Al–Zn–Mg/Si_3N_4 composites on the advanced machining technology of nano-PMEDM with the conventional brass electrode and nickel-coated brass electrode (by electroless plating) to suggest the best electrode for machining microholes in high material removal rate and lower electrode wear. To the best of our knowledge, this kind of investigation is not reported in the literature.

2. Experimental Methodology

The present study made use of Al–Zn–Mg composites reinforced with Si_3N_4 (9 wt. %) of a thickness of 10 mm because these composites have higher mechanical properties than Al–Zn–Mg alloys and they have been successfully used in automotive and marine applications [15]. The test was carried out on an ocean OCT-3525NA electrical discharge machine with nickel-coated brass, uncoated brass, and tube electrodes as tool materials. PMEDM was performed using deionised water as a dielectric fluid and aluminium nanoparticles in a ball mill to create a nanodielectric fluid. The process parameters used in this study are shown in Table 1 while the MRR and EWR were calculated based on equations (1) and (2) [16].

The Weight of the workpiece before and after machining was calculated by using 'OHAUS' make high precision weight balancing device. An optical microscope is used to measure the diameter of the machined hole on the workpiece. The electroless plating method was used in this work to coat the nickel of 2 μm thickness on the brass tube to evaluate the effectiveness of the coating on MRR and EWR.

$$\text{MRR} = \frac{(W_a - W_b)}{t}\left(\frac{\text{mg}}{\text{min}}\right), \tag{1}$$

$$\text{EWR} = \frac{(E_a - E_b)}{t \times \rho}\left(\frac{\text{mm}^3}{\text{min}}\right). \tag{2}$$

The chemical composition of the brass tube electrode and nickel coating material with a diameter of 14 mm is shown in Table 2.

The properties of aluminium nanoparticles and dielectric fluid is inferred in Tables 3 and 4.

In the present study, the machining parameters of micro-EDM such as current, voltage, pulse on time, and capacitance were studied. The effect of input process parameters has been evaluated by using machining time, MRR, and EWR. The experiment was carried out using an L18 orthogonal array as shown in Table 5 [17]. All process parameters were set to an equal level of three.

3. Outcome of the Experiment

3.1. Material Removal Rate (MRR). MRR is expressed as the amount of material removed from the workpiece per unit of time [18]. MRR was calculated by using equation (1). The Unit of MRR is mm^3/min. The effect of various input process parameters on MRR is shown in Figures 1(a)–1(d). It has been observed that an increase in current boosts the intensity of electrical sparks, resulting in a higher MRR, and the same results were observed with uncoated and coated electrodes for different input currents, as shown in Figure 1(a). Higher MRR was observed for the coated electrode. The MRR improved significantly when the current increased from 3 A to 9 A, but the nickel-coated electrode has better workability. When the input process parameter was set to 3 A with a coated tool, MRR increased by 74% when compared to the uncoated tool. Similarly, under current 6 A and 9 A conditions, the coated tool can enhance MRR by 28% and 38%, respectively. Figure 1(b) shows the comparison of MRR with the uncoated and coated electrodes under various voltage conditions. In this project, voltages were selected at three levels (25 V, 50 V, and 75 V). From the graph, it can be seen

Table 1: Process parameter variables.

Process variables	Description
Workpiece	Al–Zn–Mg/Si_3N_4 composites
Tool	Nickel-coated brass and uncoated brass tube electrode
Diameter of the hole	50 μm
Current (A)	3, 6, 9
Voltage (V)	25, 50, 75
Pulse on time (μs)	20, 40, 60
Capacitance (nF)	3, 6, 9

Table 2: Chemical properties of electrode.

Properties	Brass electrode	Nickel coating
Electrical conductivity (s/m)	1.67 × 107	1.43 × 107
Melting point (°C)	930	1455
Thermal conductivity (W/m°K)	159	975
Electrical resistivity (ohm-cm)	4.7 × 10−8	6.99 × 10−8
Specific heat capacity (J/g-°C)	0.38	0.444

Table 3: Properties of aluminium powder.

Properties	Aluminium
Density (g/cm^3)	3.9
Melting point (°C)	650
Electrical conductivity (s/m)	3.69×10^7
Thermal conductivity (W/m°K)	239
Electrical resistivity (ohm-cm)	2.82×10^{-8}

Table 4: Properties of dielectric fluid.

Properties	Kerosene oil
Dielectric constant, K	1.8
Electrical conductivity (s/m)	1.6×10^{-14}
Mobility, m^2/Vs	2.2×10^{-8}
Electric field, MV/m	16.6
Mass density, kg/m^3	728

Table 5: Experimental run order.

Exp run	Material of electrode	Current (A)	Voltage (V)	Pulse on time (μs)	Capacitance (nF)
1	Brass	3	25	20	3
2	Brass	3	50	40	6
3	Brass	3	75	60	9
4	Brass	6	25	20	6
5	Brass	6	50	40	9
6	Brass	6	75	60	3
7	Brass	9	25	40	3
8	Brass	9	50	60	6
9	Brass	9	75	20	9
10	Nickel-coated brass	3	25	60	9
11	Nickel-coated brass	3	50	20	3
12	Nickel-coated brass	3	75	40	6
13	Nickel-coated brass	6	25	40	9
14	Nickel-coated brass	6	50	60	3
15	Nickel-coated brass	6	75	20	6
16	Nickel-coated brass	9	25	60	6
17	Nickel-coated brass	9	50	20	9
18	Nickel-coated brass	9	75	40	3

that the MRR decreases with increasing voltage. But the MRR of the coated tool was quite high, compared with the uncoated tool. MRR can be improved drastically with the coated tool by about 49%. In this condition, the machine tool was operated under 75 V. MRR can be improved up to 39% and 34% by the coated tool, under the machining conditions of 25 V and 50 V. The comparison of MRR with the uncoated and coated electrodes under various pulses on time is shown in Figure 1(c). Abnormality was observed in this graph. When the machine tool was run at a pulse on time of 40 μs, it gave a low MRR compare to the other two levels. But normally, the MRR of the coated tool is high compared to that of the uncoated tool. Here, MRR can be improved up to 46% with this machine tool operating on a pulse on time of 60 μs. MRR can be improved by 31% and 35% by the coated tool, under the pulse on time of 20 μs and 40 μs.

Figure 1(d) shows the comparison of MRR with the uncoated and coated electrodes under various capacitance conditions. From the graph, it can be seen that coated electrode gives a high MRR, compared to the uncoated electrode. Normally, MRR increases with increasing the capacitance from 3 nF to 9 nF, but here, tremendous changes were produced by the coated electrode. When the machine was run at 6 nF with the coated tool, it gave a 43% improvement in MRR, compared to the uncoated tool. Similarly, MRR can be improved by 49% and 32% with the coated tool under the capacitance conditions of 3 nF and 9 nF.

The graphs in Figure 1 show that the current, voltage, and capacitance exhibited good sensitivity with MRR. The increase in Current and Capacitance improves the MRR [19]. The decrease in voltage decreases the MRR [20, 21]. So the process could be controlled by varying these parameters. The pulse on time can be used for fine-tuning the process for more accuracy. The coated electrode recorded a significant improvement in MRR [22]. The nano-PMEDM is a promising process for a better surface finish. The coated electrode supported well in higher material removal rate. This result is supported by previous investigations. The ANOVA results (Table 6) helped to rank the influence of factors on the MRR. A lower p value indicates a higher influence. Hence factor current is rank 1 (As $p = 0.001$), voltage Rank 2 (current is rank 1 (As $p = 0.0364$), and finally, rank 4 for pulse on time. The same could be ensured by observing the F value in that Table 6. The Higher F value is indicated as a more influencing input parameter.

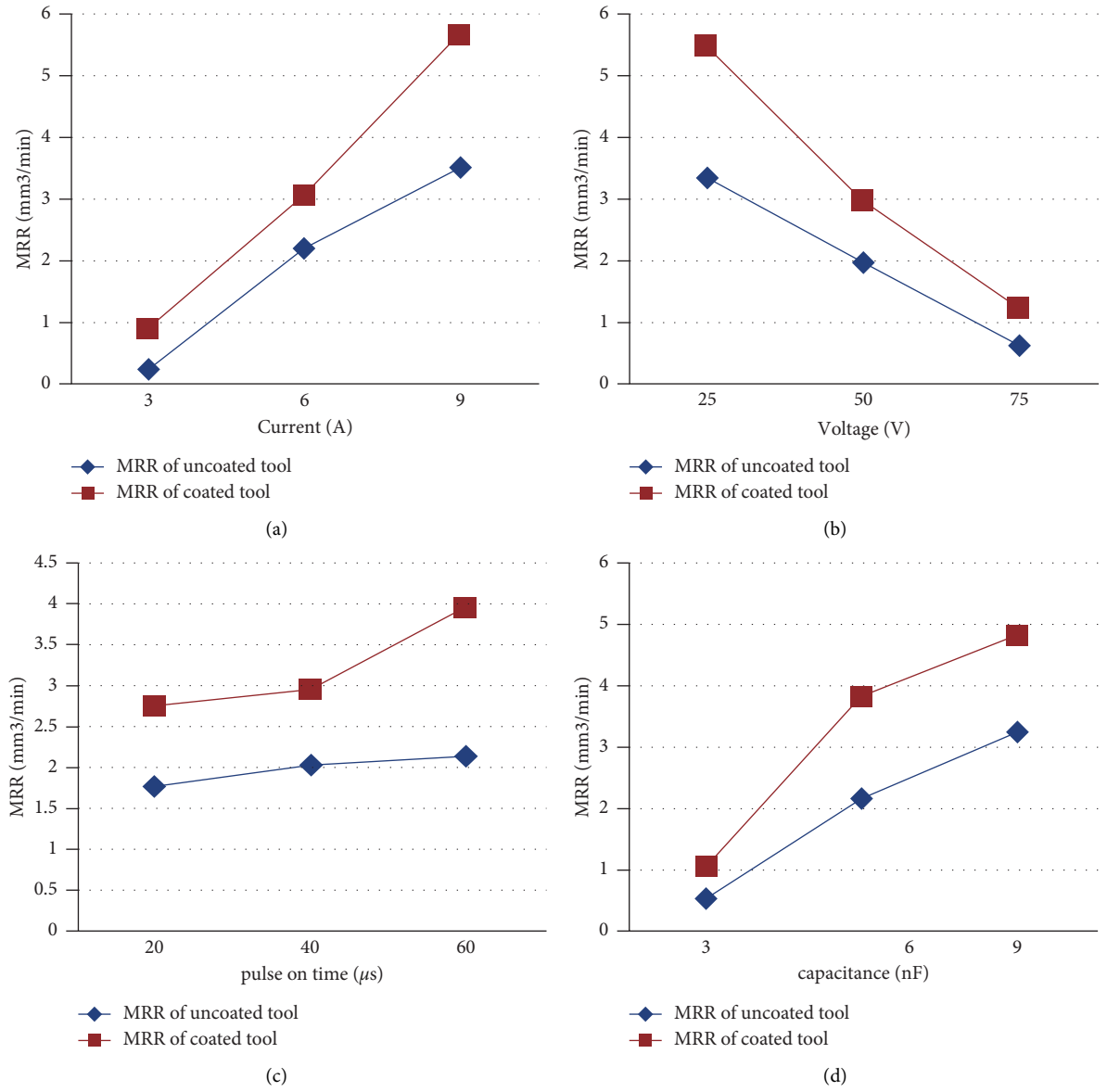

Figure 1: The MRR response with the variation of (a) input current, (b) voltage, (c) pulse on time, and (d) capacitance.

Table 6: ANOVA of MRR.

Source	DF	Adj SS	Adj MS	F value	p value
Electrode	1	0.095048	0.095048	35.37	0.001
Current (A)	2	0.217744	0.108872	40.51	0.001
Voltage (V)	2	0.008565	0.004283	1.59	0.0261
Pulse on time (μs)	2	0.001269	0.000635	0.24	0.0495
Capacitance (nF)	2	0.002887	0.001443	0.54	0.0364
Error	8	0.021499	0.002687		
Total	17	0.347013			

3.2. Analysis of Machining Time. Machining a microhole on the aluminium composites with the coated tool takes less time compared to the uncoated tool. Figure 2 represents the machining times of a coated and uncoated tool; the graph shows that the machining time of the coated tool is minimal. The machining time changed significantly in the first three experiments. Machining nine holes with an uncoated tool took 50 minutes and 88 seconds, but machining those same nine holes with a coated tool takes only 18 minutes and 11 seconds. In the remaining experiments, slight time

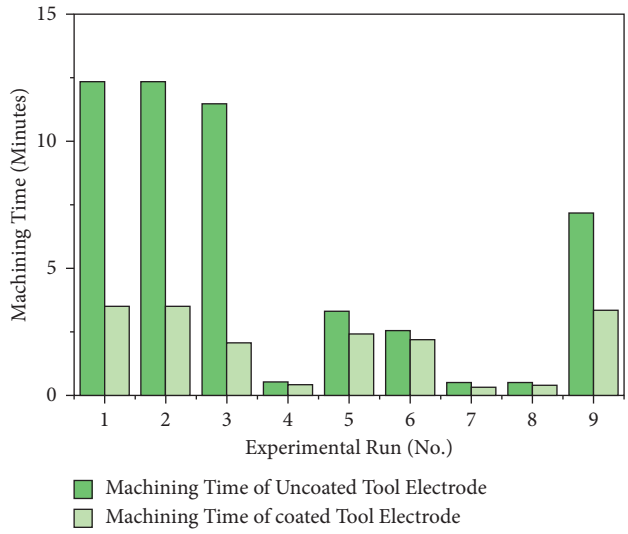

Figure 2: Machining time of composites.

variations were observed. The coated tool can reduce machining time by 64% in this particular scenario.

3.3. Electrode Wear Rate (EWR). One of the most important characteristics of an electrode to be used in EDM is higher material removal with lower electrode wear. The amount of material removed from the electrode material per unit of time is expressed as EWR. It is a major factor that contributes to achieving better productivity. The primary goal of this project is to reduce electrode wear rate to increase productivity. In this study, two kinds of electrodes were used: coated electrodes and uncoated electrodes. This pioneering investigation shows that the coated electrode has a higher EWR than the uncoated electrode. The unit of EWR is mm^3/min.

Figure 3(a) shows the comparison of EWR in the uncoated electrode and coated electrode under various current conditions. The graph shows that the coated electrode has a lower EWR than the uncoated electrode for the increase in current from 3 A to 9 A. When the current was set to 3 A with the coated tool, EWR improved by 63% when compared to the uncoated tool. Similarly, under current conditions of 6 A and 9 A, the coated tool can improve EWR by 5% and 29%. The main reason for the lower EWR in nickel-coated electrodes is that they are exposed to a higher energy electric spark for a shorter period than uncoated electrodes. Figure 3(b) shows the comparison of EWR with the uncoated and coated electrodes for various voltage conditions. In this study, voltages were selected at three levels, namely, 25 V, 50 V, and 75 V. [23] Observed that increasing gap voltage causes the formation of larger craters, which reduces the EWR linearly. The graph clearly shows that EWR decreases with increasing voltage, and the EWR of coated tool resulted in less wear than the uncoated tool. EWR has been reduced by approximately 76% with the coated tool for a voltage of 75 V, but by 26% and 32% for 25 V and 50 V, respectively.

The comparison of EWR with the uncoated and coated electrodes for various pulses on time is shown in Figure 3(c). Higher spark energy was produced with the increase in pulse on time, resulting in a higher EWR. For the pulse on time of 60 μs, the EWR of the nickel-coated tool has been improved to 38%. EWR has been improved by 24% and 7% with the coated tool under the machining conditions of pulse on time of 20 μs and 40 μs. Moreover, the comparison of EWR with the uncoated electrode and coated electrode for various capacitance conditions. As the capacitance value increases, the discharge energy of this spark increases linearly. As a result of the increased material removal, EWR begins to increase. From the graph, it can be seen that the coated electrode gives a high EWR compared to the uncoated electrode. Normally, EWR increases with increasing capacitance from 3 nF to 9 nF, a significant improvement was observed with the coated electrode. When the machine tool was run at 6 nF with the coated tool, it gave a 36% of improvement in EWR compared to the uncoated tool. Similarly, EWR has been improved by 27% and 15% by coated electrodes under the capacitance conditions of 3 nF and 9 nF.

3.4. Volume of Electrode Saved by Coated Tool. The volume of material removed from the electrode was used to calculate the amount of material electrode consumed by both uncoated and coated tools for machining with various process parameters, as shown in Figure 4. The uncoated tool consumed a large amount of material to make the 50 μm holes on Al–Zn–Mg/Si_3N_4 composites under various machining conditions, whereas the coated tool consumed a small amount of tool material to make the 50 μm holes. The uncoated tool used 7.527 mm^3 of material to make the nine holes in the Al–Zn–Mg/Si_3N_4 composites whereas the coated tool used less material (5.75 mm^3). Eventually, the coating process saved 24% of the material volume in the tool/electrode.

4. Analysis of Variance (ANOVA)

Analysis of variance (ANOVA) of the response can be used to investigate the significance of the process parameter [24]. ANOVA of MRR revealed that the electrode (coated and nickel-coated) and current were the most significant parameters, followed by voltage and capacitance as shown in Table 6.

The pulse-on-time process parameter is the least significant for MRR. The most important process parameter for EWR is an electrode (coated and nickel-coated) followed by pulse on time, voltage, and capacitance which is found to be the least significant as shown in Table 7. The linear regression model can be used to develop the relationship between input and output process parameters. In this study, Minitab software is used to create the linear regression model. Equations (3) and (4) show the relationship between the input parameter and the response of MRR. Equations (5) and (6) show the relationship between inputs and response of EWR. Both models were accurate and followed normality based on the residual plot of MRR and EWR as shown in

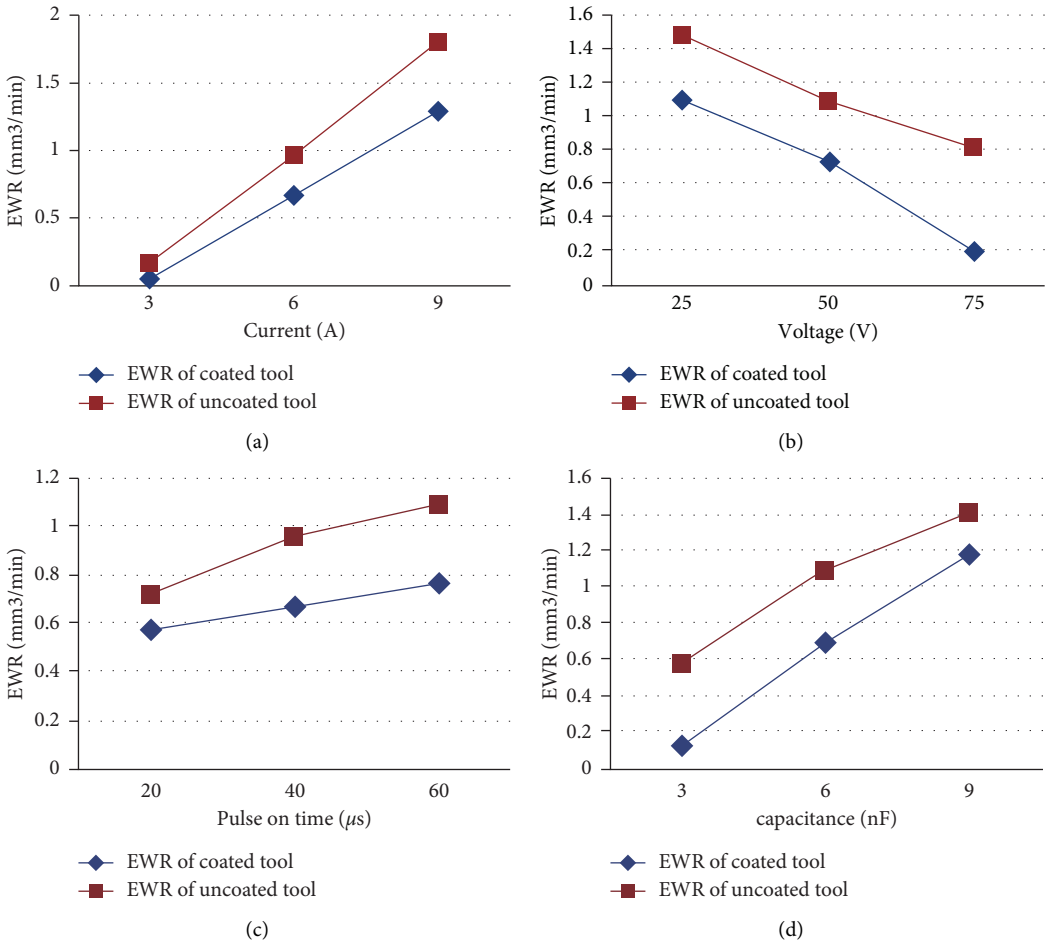

Figure 3: Effect of input process parameters on EWR.

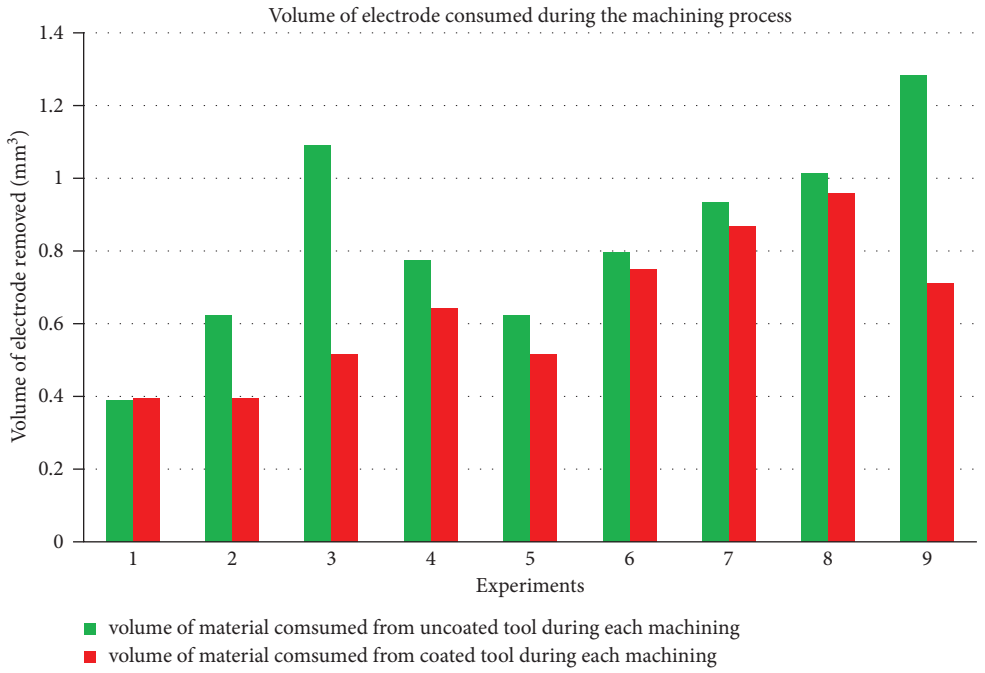

Figure 4: The volume of electrodes removed by coated and uncoated electrodes.

Table 7: ANOVA of EWR.

Source	DF	Adj SS	Adj MS	F value	p value
Electrode	1	0.042491	0.042491	3.5	0.0098
Current (A)	2	0.033721	0.016861	1.39	0.0304
Voltage (V)	2	0.02381	0.011905	0.98	0.0416
Pulse on time (μs)	2	0.036301	0.018151	1.49	0.0281
Capacitance (nF)	2	0.00286	0.00143	0.12	0.0389
Error	8	0.097155	0.012144		
Total	17	0.236339			

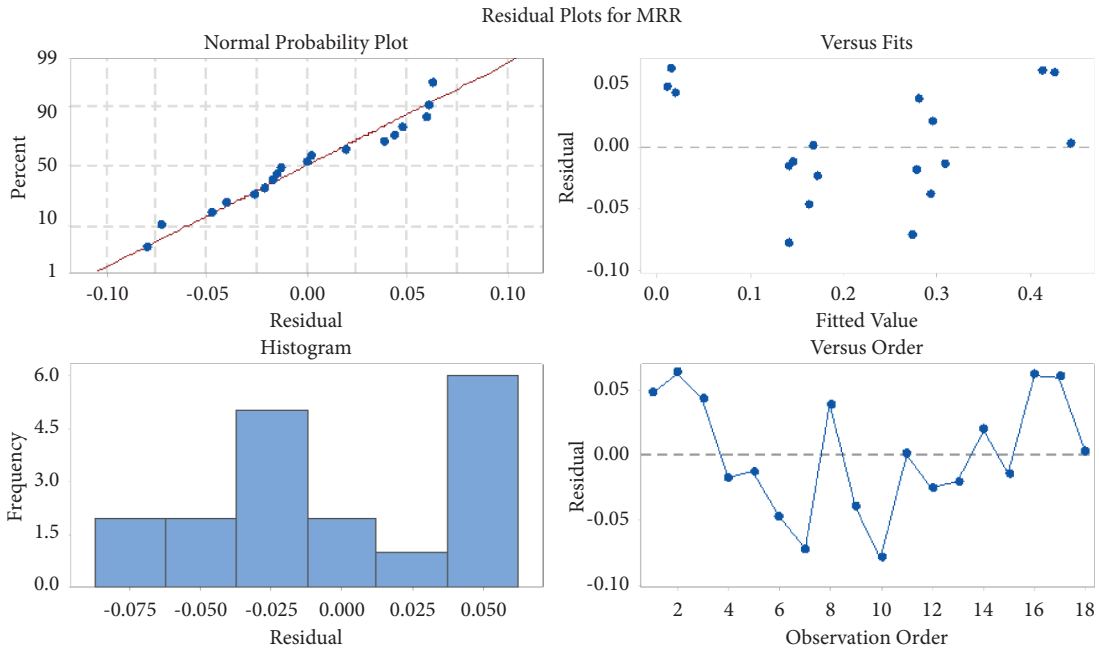

Figure 5: Residual plots for MRR.

Figures 5 and 6. In addition, no deviations or improper patterns were observed.

$$\text{MRR with Brass electrode} = -0.1298 + 0.04467\ \text{Current (A)} + 0.000477\ \text{Voltage (V)} - 0.000146\ \text{Pulse on Time}\ (\mu\text{s}) - 0.00136\ \text{Capacitance (nF)}, \tag{3}$$

$$\text{MRR with Nickel Coated Brass electrode} = 0.0156 + 0.04467\ \text{Current (A)} + 0.000477\ \text{Voltage (V)} - 0.000146\ \text{Pulse on Time}\ (\mu\text{s}) - 0.00136\ \text{Capacitance (nF)}, \tag{4}$$

$$\text{EWR with Brass electrode} = 0.157 + 0.0173\ \text{Current}\ (A) - 0.00164\ \text{Voltage (V)}0.00063\ \text{Pulse on Time}\ (\mu\text{s}) - 0.0025\ \text{Capacitance (nF)}, \tag{5}$$

$$\text{EWR with Nickel Coated Brass electrode} = 0.060 + 0.0173\ \text{Current (A)} - 0.00164\ \text{Voltage (V)} - 0.00063\ \text{Pulse on Time}\ (\mu\text{s}) - 0.0025\ \text{Capacitance (nF)}. \tag{6}$$

5. Tool Morphology

5.1. Analysis of the Surface of the Uncoated Tool by Scanning Electron Microscope (SEM). The surface of the uncoated and coated tools was scrutinised using a scanning electron microscope (SEM). Following the machining process, erosion occurred on the brass tube, resulting in a small crater on the tool surface in both coated and uncoated electrodes as shown

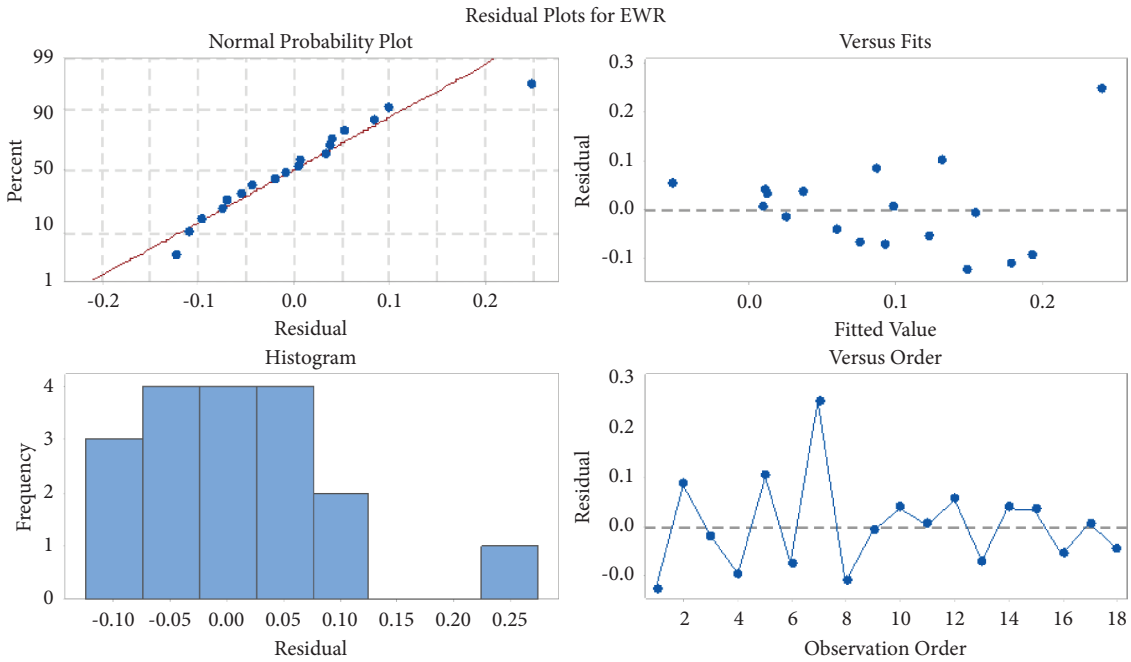

Figure 6: Residual plot for EWR.

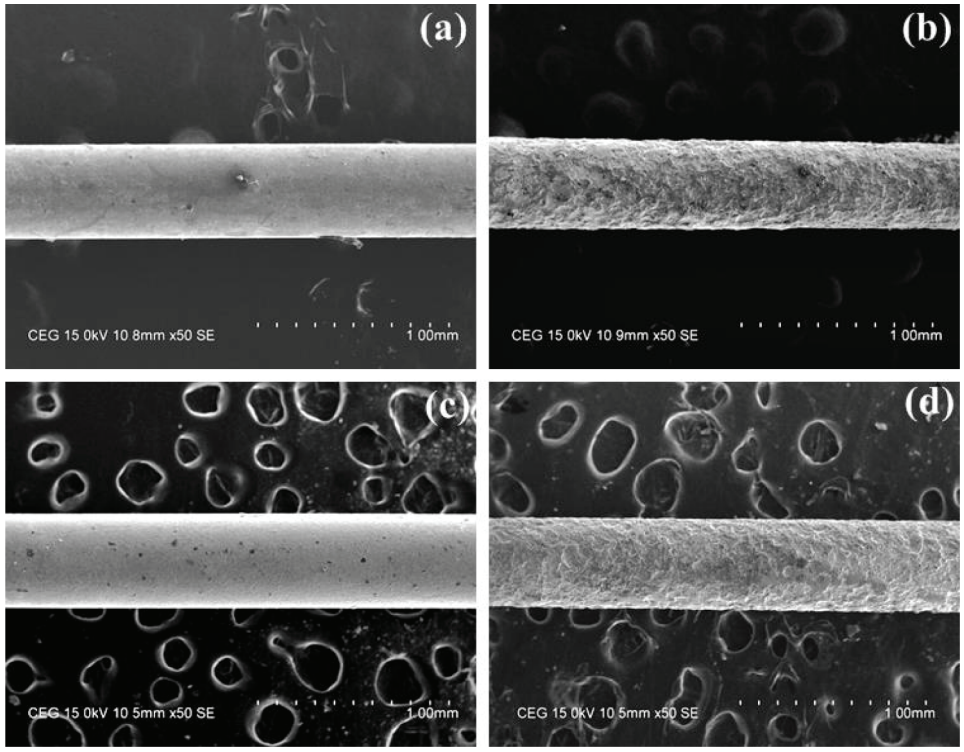

Figure 7: (a) Uncoated electrode before machining; (b) uncoated electrode after machining; (c) coated electrode before machining; (d) coated electrode after machining.

in Figures 7(a)–7(d). The Size of the crater is more with the uncoated electrode, which affected the life of the electrode as shown in Figure 7(b). From the SEM image, electrode wear in the coated tool has been reduced, with the ragged surface being the least in the case of coated tool electrode when compared to the uncoated electrode, as shown in Figures 7(b) and 7(d). The coated and uncoated electrodes effects are similar to those used for the machining of the D2 steel [25].

5.2. Analysis of the Edge of the Tool. Initially, the edge of the brass tube is the taper section that is shown in Figure 8(a) with small dust particles seen on the tool surface. After the

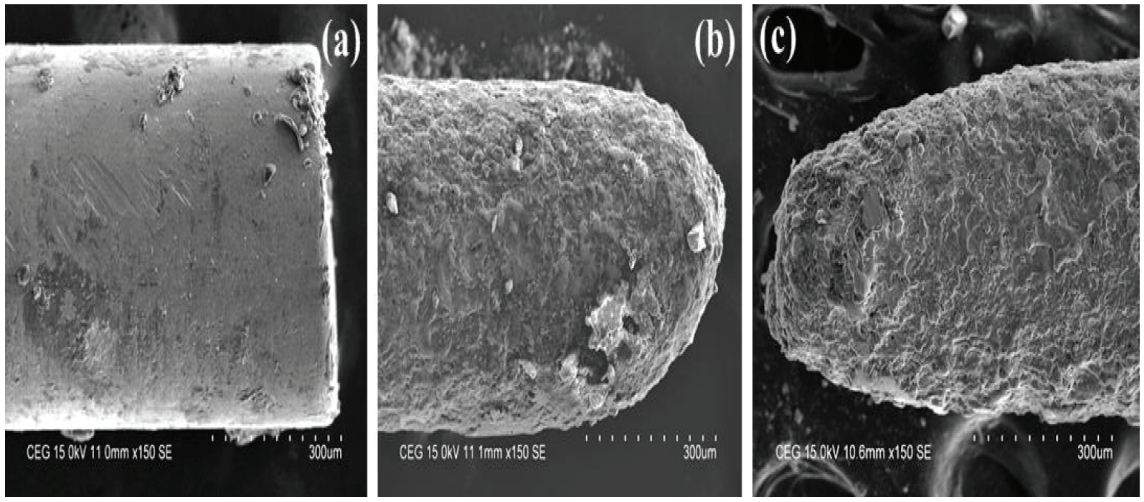

Figure 8: (a) Electrode before machining, (b) uncoated electrode edge after machining, and (c) coated electrode edge after machining.

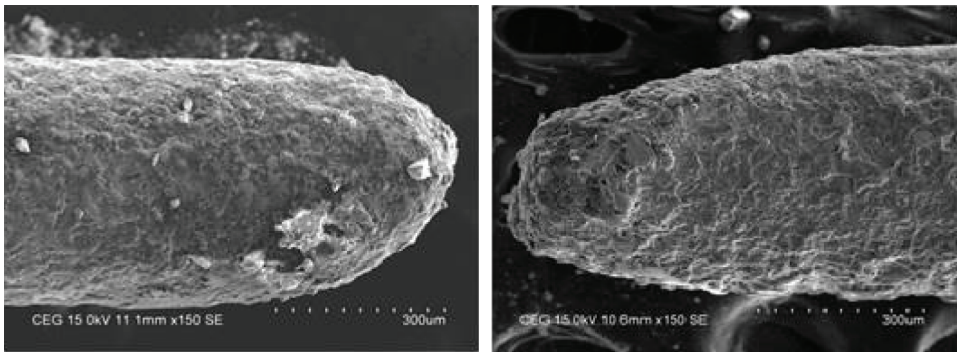

Figure 9: Uncoated (parabola section) and coated tools (elliptical section) were used for Al–Zn–Mg/Si_3N_4 composites.

machining process, erosion takes place on the tool surface, so a conical section was observed on the edge of the tool as shown in Figures 8(b) and 8(c). From the SEM image, EWR is more on the bottom section of the brass tube. The effects have good agreement with the machining of D2 steel [25].

5.3. Surface Analysis of the Coated Tool. Nickel is coated on the brass tube with a thickness of 2 microns as shown in Figure 8(c). Nickel particles look like small bubbles on the brass tube's substrate material. SEM analysis shows that nickel is uniformly distributed on the tool surface during the coating process. During the metal removal process, the nickel particles were eroded. Craters were observed on the machined tool surface as shown in Figure 8(c). When compared to an uncoated electrode, the size of the crater is smaller in the coated tool, indicating that the tool life is increased. The result supported for justification as it was used for machining D2 steel [25].

5.4. Comparison of the Coated Tool and Uncoated Tools. Figure 9 portrays that more metal removal occurs on the side wall of the uncoated tool. This causes a secondary reaction during machining, preventing the uncoated tool from providing the necessary spark energy. This results in a low MRR for the uncoated electrode, but because the coated tool provides concentrated spark energy during machining, more material was removed, as evident from the coated electrode edge. The coated electrode showed an elliptical section, but the uncoated tool showed a parabola section due to the secondary reaction as it was used for machining the D2 steel [25].

6. Conclusions

Powder-mixed micro-EDM experiments on Al–Zn–Mg/Si_3N_4 composites were carried out with a nickel-coated brass electrode and an uncoated brass electrode. The coated tool has increased tool life additionally, the coated tool provides more benefits than the uncoated electrode which are as follows: the electroless plating on the brass electrode coated with nickel reduced the machining time by 63.86%. The volume of material removal from the electrode has been reduced from 7.6227 to 5.39 mm^3 for the coated electrode. In comparison to an uncoated tool, a nickel-coated brass electrode improves MRR by 48.34%. High MRR was achieved due to more concentrated spark energy during machining with the nickel-coated electrode. The coated tool improves electrode life by 23.26% when compared to the uncoated tool. The superior properties of the nickel-coated

electrodes provided high thermal stability during the machining process. This extends the life of the electrode. The electrode wear rate was minimised by using nickel-coated electrodes to about 21.92%. From ANOVA tables, the electrode material is an important factor in maximising MRR and minimising EWR. The investigation shall be extended by optimising the nanoparticles variety, effects of hybrid nanoparticles, and optimising the size of nanoparticles for improving the machinability.

Data Availability

The data used to support the findings of this study are included in the article. Should further data or information be required, these are available from the corresponding author upon request.

Conflicts of Interest

The authors declare that they have no conflicts of interest.

References

[1] S. S. Sidhu, A. Batish, and S. Kumar, "Study of surface properties in particulate-reinforced metal matrix composites (MMCs) using powder-mixed electrical discharge machining (EDM)," *Materials and Manufacturing Processes*, vol. 29, no. 1, pp. 46–52, 2014.

[2] S. Mohanty and B. C. Routara, "A review on machining of metal matrix composites using nanoparticle mixed dielectric in electro-discharge machining," *International Journal of Automotive and Mechanical Engineering*, vol. 13, no. 2, pp. 3518–3539, 2016.

[3] S. G. Iyyappan, R. Sudhakarapandian, and M. Sakthivel, "Influence of silicon carbide mixed used engine oil dielectric fluid on EDM characteristics of AA7075/SiCp/B4Cp hybrid composites," *Materials Research Express*, vol. 8, no. 8, Article ID 086514, 2021.

[4] M. S. Surya and S. K. Gugulothu, "Investigations on powder mixed electrical discharge machining of aluminum alloy 7075–4 wt.% TiC in-situ metal matrix composite," *International Journal on Interactive Design and Manufacturing*, pp. 1–7, 2022.

[5] S. S. Thakur, B. Patel, R. K. Upadhyay, D. K. Bagal, and A. Barua, "Machining characteristics of metal matrix composite in powder-mixed electrical discharge machining–A review," *Australian Journal of Mechanical Engineering*, pp. 1–23, 2022.

[6] V. Tao Le, "The influence of additive powder on machinability and surface integrity of SKD61 steel by EDM process," *Materials and Manufacturing Processes*, vol. 36, no. 9, pp. 1084–1098, 2021.

[7] S. Singh, B. Patel, R. K. Upadhyay, and N. K. Singh, "Improvement of process performance of powder mixed electrical discharge machining by optimisation-A Review," *Advances in Materials and Processing Technologies*, pp. 1–31, 2021.

[8] J. Khajuria, N. Nagabhooshanam, P. Sharma et al., "Effect of SiC particle incorporated dielectric medium on electrical discharge machining behavior of AA6061/B4Cp/SiCp AMCs," *Advances in Materials Science and Engineering*, pp. 1–9, 2022.

[9] K. G. Sagar, P. K. Anjani, M. S. Raman et al., "Improving sustainability of EDM sector by implementing unconventional competitive manufacturing approach," *Advances in Materials Science and Engineering*, pp. 1–10, 2022.

[10] R. S. Barot, J. B. Valaki, A. H. Makwana, and H. Beravala, "Experimental investigation and machinability study of Ni–Cr-based super alloy using powder mixed EDM," in *Technology Innovation in Mechanical Engineering*, pp. 673–683, Springer, Singapore, 2022.

[11] S. Srivastava, M. Vishnoi, M. T. Gangadhar, and V. Kukshal, "An insight on powder mixed electric discharge machining: a state of the art review," *Proceedings of the Institution of Mechanical Engineers - Part B: Journal of Engineering Manufacture*, Article ID 095440542211118, 2022.

[12] N. Kaliappan, M. Balaji, T. Ch Anil Kumar et al., "Machining performance of aa2024/5Al2O3/5gr hybrid composites under Al2O3 mixed dielectric medium," *International Journal of Chemical Engineering*, pp. 1–10, 2022.

[13] G. Karthik Pandiyan, T. Prabaharan, D. Jafrey Daniel James, and V. Sivalingam, "Machinability analysis and optimization of electrical discharge machining in AA6061-T6/15wt.% SiC composite by the multi-criteria decision-making approach," *Journal of Materials Engineering and Performance*, vol. 31, no. 5, pp. 3741–3752, 2022.

[14] S. S. Thakur, S. K. Pradhan, S. Sehgal, and K. K. Saxena, "Experimental investigations on silicon carbide mixed electric discharge machining," *Silicon*, pp. 1–19, 2022.

[15] R. K. Shastri, C. P. Mohanty, S. Dash, K. M. P. Gopal, A. R. Annamalai, and C. P. Jen, "Reviewing performance measures of the die-sinking electrical discharge machining process: challenges and future scopes," *Nanomaterials*, vol. 12, no. 3, p. 384, 2022.

[16] V. Kumar, C. Prakash, A. Babbar, S. Choudhary, A. Sharma, and A. S. Uppal, "Additive manufacturing in biomedical engineering: present and future applications," in *Additive Manufacturing Processes in Biomedical Engineering*, pp. 143–164, CRC Press, Boca Raton, Florida, United States, 2017.

[17] B. K. Baroi, P. K. Patowari, and P. K. Patowari, "A review on sustainability, health, and safety issues of electrical discharge machining," *Journal of the Brazilian Society of Mechanical Sciences and Engineering*, vol. 44, no. 2, pp. 59–38, 2022.

[18] D. P. Singh, S. Mishra, S. K. S. Yadav, R. K. Porwal, and V. Singh, "Comparative analysis and optimization of thermoelectric machining of alumina and silicon carbide reinforced aluminum metal matrix composites using different electrodes," *Journal of Advanced Manufacturing Systems*, pp. 1–29, 2022.

[19] B. Xu, M. Q. Lian, S. G. Chen et al., "Combining PMEDM with the tool electrode sloshing to reduce recast layer of titanium alloy generated from EDM," *International Journal of Advanced Manufacturing Technology*, vol. 117, no. 5-6, pp. 1535–1545, 2021.

[20] T. Muthuramalingam and N. H. Phan, "Experimental investigation of white layer formation on machining silicon steel in PMEDM process," *Silicon*, vol. 13, no. 7, pp. 2257–2263, 2021.

[21] N. Huu-Phan, B. Tien-Long, L. Quang-Dung, N. Duc-Toan, and T. Muthuramalingam, "Multi-criteria decision making using preferential selection index in titanium based die-sinking PMEDM," *Journal of the Korean Society for Precision Engineering*, vol. 36, no. 9, pp. 793–802, 2019.

[22] K. Karunakaran and M. Chandrasekaran, "Influence of process parameters in n-PMEDM of Inconel 800 with electrode and coated electrodes," in *MATEC web of conferences*, vol. 95, Les Ulis, France, EDP Sciences, Article ID 02002, 2017.

[23] D. Sundaresan, L. Marappan, K. Thangavelu, and V. Venkatraman, "Machinability of nimonic alloy 90 in μ-titanium carbide mixed electrical discharge machining," *Arabian Journal for Science and Engineering*, pp. 1–21, 2022.

[24] S. Kumar, S. Kumar, R. Sharma, P. Bishnoi, M. Singh, and R. Singh, "To evaluate the effect of boron carbide (B4C) powder mixed EDM on the machining characteristics of INCONEL-600," *Materials Today Proceedings*, vol. 56, pp. 2794–2799, 2022.

[25] M. Siva, N. Arunkumar, M. Subramanian, and R. Elakkiyadasan, "Influence of micro-electrical discharge machining parameters on the surface morphology of the nickel-coated electrode," *Materials and Manufacturing Processes*, pp. 1–16, 2022.

Hindawi
Advances in Materials Science and Engineering
Volume 2022, Article ID 7584482, 8 pages
https://doi.org/10.1155/2022/7584482

Research Article

The Effect of GTAW Variants on Tensile and Microstructural Properties of AZ31B Magnesium Alloy Joints

V. Subravel,[1] G. Padmanaban,[2] T. V. Rajamurugan,[3] M. Seeman,[4] V. Chandrasekaran,[5] C. Rajaganapathy,[3] and Haiter A. Lenin[6]

[1]*Government College of Engineering, Sengipatti, Thanjavur, Tamil Nadu, India*
[2]*Mechanical Engineering, Thanthai Periyar Government Institute of Technology, Vellore, Tamil Nadu, India*
[3]*Government College of Engineering Srirangam, Trichy 620012, Tamil Nadu, India*
[4]*Department of Manufacturing Engineering, Annamalai University, Chidambaram, Tamil Nadu, India*
[5]*Government Polytechnic College, Papanasam 614205, Tamil Nadu, India*
[6]*Department of Mechanical Engineering, WOLLO University, Kombolcha Institute of Technology, Post Box No: 208, Kombolcha, Ethiopia*

Correspondence should be addressed to Haiter A. Lenin; haiterlenina@gmail.com

Received 12 August 2022; Accepted 19 September 2022; Published 3 October 2022

Academic Editor: Sengottuvelu Ramesh

In this investigation, an attempt is made to study the tensile and microstructural impact of different gas tungsten arc (GTA) welding processes of pulsed current, constant current, and magnetic arc oscillation welded AZ31B magnesium metal joints. These techniques were chosen because they have the potential to produce welds with high tensile strength and excellent microstructural integrity. Five joints were produced using each approach, each one employing a unique combination of parameters. According to the findings of this experiment, the joints that were manufactured utilising a welding process called magnetic arc oscillation yielded superior tensile qualities when compared to the properties of other joints. The improved tensile characteristics of these joints can be ascribed in a large part to the creation of smaller grains and surface hardness in the transition region, as well as uniformly dispersed precipitates.

1. Introduction

The realm of materials science is becoming increasingly interested in magnesium alloys as a result of their advantageous properties, which include low density, high damping qualities, machinability, dimensional stability, and inexpensive casting expenses [1, 2]. High stiffness-to-weight ratios make magnesium alloys useful in many applications. Automotive, industrial, materials handling, and aircraft all require improved composites [3, 4]. Magnesium alloys with additions of aluminium and zinc have high strength properties coupled with quite low density, which makes them very appealing as building components in applications where minimising weight is of utmost importance. These alloys can be made by adding aluminium and zinc to magnesium. Welding is an essential industrial process that is inextricably linked to the structural uses of magnesium alloys. Welding can be accomplished with relative ease on the vast majority of magnesium alloys by employing methods such as gas tungsten arc welding (GTAW), gas metal arc welding, electron beam, and laser beam welding [5]. The GTAW is a material joining procedure that is utilised extensively. Because of the reliability, clearance, and strength of the weld, GTA welds are considered to be of a higher quality than those produced by any of the arc-welding methods. However, the physical features of magnesium may readily produce several processing issues and welding flaws such as oxide coatings, fractures, and porosity. High thermal conductivity, melting and boiling temperatures, high solidification shrinkage, low viscosity, and good hydrogen solubility are just a few of magnesium's unique qualities [6]. It also has a strong

Table 1: AZ31B magnesium alloy chemical composition.

Zn	Al	Ni	Mn	Cr	Cu	Mg
0.67	2.60	0.012	0.27	0.008	0.017	Bal

tendency to oxidise and has low melting and boiling temperatures.

Many weld flaws are less severe when the solidification pattern is improved [7]. In the fusion zone of welds, one method for fine-tuning grain structure is magnetic arc oscillation (MAO). The MAO method uses a two-pole magnetic probe to oscillate the arc column in the opposite direction of welding. Weld fusion zone dendritic columns are broken down mechanically by arc oscillation. The microstructure is refined as the fractured dendrites act as forming sites and boost the cooling rate [8, 9]. Inside the pulsed current method, the welding pulse is cycled amongst two levels. The arc is stable because the ambient current (Ib) is insufficient to melt the metal surface. In a small area, the peak current (Ip) melts the base plate, and the adjoining base material acts as a chill, causing the spot to cool more quickly. The weld pool is agitated and the cooling rate is increased by a series of pulses delivered at a precise frequency. This results in a continuous weld bead. This technique has been studied extensively, and the purported benefits include greater bead contour, high acceptance to heat sink changes, inferior heat input needs, minimum residual stresses, and distortions. Many studies have shown that pulsed current welding progresses the quality of the weld by reducing the grain size and microstructure. Grain structure in weld fusion regions and an increase in weld powered characteristics have been achieved using current pulsing.

The impression of magnetic arc oscillation on fusion zone grain growth and tensile behaviour in aluminium alloy welds were investigated by Janaki Ram et al. [10]. Sivaprasad and Raman investigated the microstructure and hot temperatures tensile stress of the 718 alloy TIG welded joints influenced by magnetic arc oscillations and current pulsing [11]. Mahajan et al. [12] investigated the impact of MAC of the grain boundary. An aluminium alloy GTA weld with magnetically agitated GTA welds was the subject of research by Rao et al. [13]. Magnetic arc oscillation has received a relatively small number of studies despite the fact that it has a number of advantages. Nevertheless, there is no evidence available on the effect of constant current, pulsed current, and magnetic arc oscillation on magnesium alloys. Keeping this in mind, a study was conducted to determine the inspiration of continuous, pulsed, and MAO welding procedures on the tensile and microstructural properties of AZ31B magnesium alloys joints; the findings are obtainable in this article.

2. Experimental Work

The thickness of the AZ31B magnesium alloy plates was trimmed to the specified measurements. Table1 presents the chemical composition as well as mechanical characteristics of the base metal. The joints were manufactured using a square butt joint arrangement. The axis of welding was parallel to the direction of rolling. Autogenous arc welding procedures (without filler metal) such as continuous current gas tungsten arc welding, pulse current gas tungsten arc welding, and magnetic arc oscillations were utilised to construct square butt joints. The MAO equipment is equipped and circumscribed with GTAW torch. In addition, it is interfaced with a microcontroller, which controls the arc oscillations frequency and amplitude. The experimental setup and MAO equipment is shown in Figure 1. Dimensions of tensile samples are exposed in Figure 2. The pictures of fabricated joints are revealed in Figure 3 steady flow rate of 20 l/min, argon gas has been used as a gasification agent.

Input heat is an important factor that determines weld quality, Table 2 mechanical qualities, and metallurgical properties. As a result, heat input was calculated and included in this analysis. Heat input is proportional to voltage and amperage and inversely to welding speed for each unit length.

The welded joints were cut and then finished to the necessary dimensions in accordance with the ASTM E8M-04 standards for sheet-type materials (50 mm × 12.5 mm). For evaluating the transverse tensile characteristics of the welded joints, two distinct tensile samples were constructed. For the purpose of measuring yield point, tensile strength, and joint elongation, smooth tensile specimens were created. A 100 kN electromechanically driven universal testing machine was used to conduct the tensile test. The 0.2% offset yield strength was calculated using the load-displacement diagram. The proportion of elongation was also assessed, and the results are reported in Table 3. Using a light optical microscope equipped with image-analysing software, microstructural examination was performed (metal vision).

3. Results

3.1. Tensile Properties. At its maximum load, a notched specimen's tensile strength (NTS) is compared to the UTS of an unnotched sample. Table 3 give the average of the three test findings for each condition, which were conducted on a total of three samples. Figure 4 depicts the tensile curves of the materials. In comparison to CCGTAW and PCGTAW, MAO welding produced better tensile characteristics. This type of joint has yield strength of approximately 192 MPa and tensile strength of approximately 153 MPa, 165 MPa, and 214 MPa, and these are the PCGTAW joints yield and tensile strengths. The MAO joints have yield and tensile strengths of 192 MPa and 248 MPa. MAO joints when compared to CCGTAW and PCGTAW, the MAO-fabricated joints have the highest values of the three types of welded junctions.

3.2. Macrostructure Study. The macrostructure image of the joints made with CCGTAW, PCGTAW, and MAO welding process at optimized conditions are presented in Figure 5. The joint fabricated using the different welding parameters from this various condition in every process only defect free joint with full penetration which are presented in Figure 5.

Figure 1: Photographs of MAO unit.

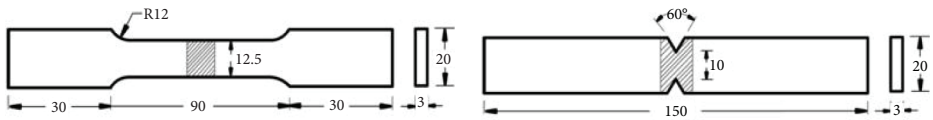

(a) (b)

Figure 2: Dimensions of tensile specimen. (a) Unnotched tensile specimen. (b) Notched tensile specimen.

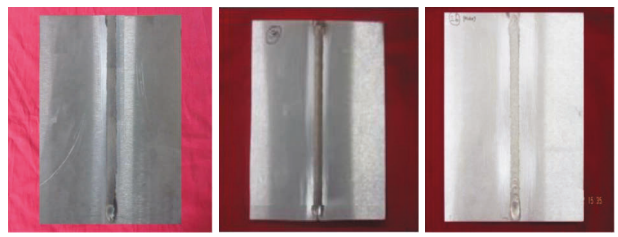

CC PC MAO

Figure 3: Photographs of MAO joints.

Table 2: AZ31B magnesium alloy mechanical properties.

Yield strength (MPa)	Ultimate tensile strength (MPa)	Elongation in 50 mm gauge length (%)	Cross section area reduction (%)	Notch tensile strength (MPa)	Hardness (hv)	Notch strength ratio
161	274	14.70	14.30	253	69	0.92

Table 3: Process parameters.

Process	Current (amp)	Voltage (V)	Welding speed (mm/min)	Pulse frequency (Hz)	Pulse on time (50%)	Oscillation frequency (Hz)	Arc amplitude (mm)
CCGTAW	80	18	125	—	4	—	—
PCGTAW	115	19	135	5	50	2	0.6
MAO	75	18	125	—	7	—	—

3.3. Microstructure. Autogenous arc weld optical micrographs are revealed in Figure 6. The grain size of the weld metal sections can be discerned from the micrographs. As a result, an effort was made to determine the normal weld metal grain diameter for all of the joints captured by the picture analysing software. CCGTAW joints have a mean grain diameter of 42 microns, whereas PCGTAW joints have a mean grain diameter of 30 microns. Pulsed current welding reduced the grain diameter by 12microns, according to this data. The mean grain diameter of MAO joints is 26

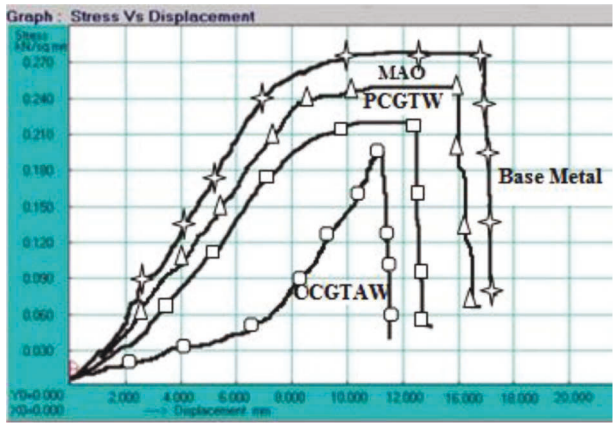

Figure 4: Load Displacement curves recorded during the tensile test.

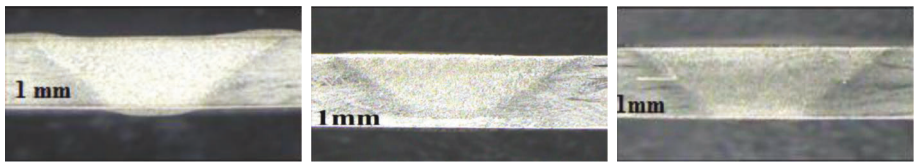

CCGTAW PCGTAW MAO

Figure 5: effect of CCGTAW, PCGTAW, and MAO on the fusion zone macrostructure.

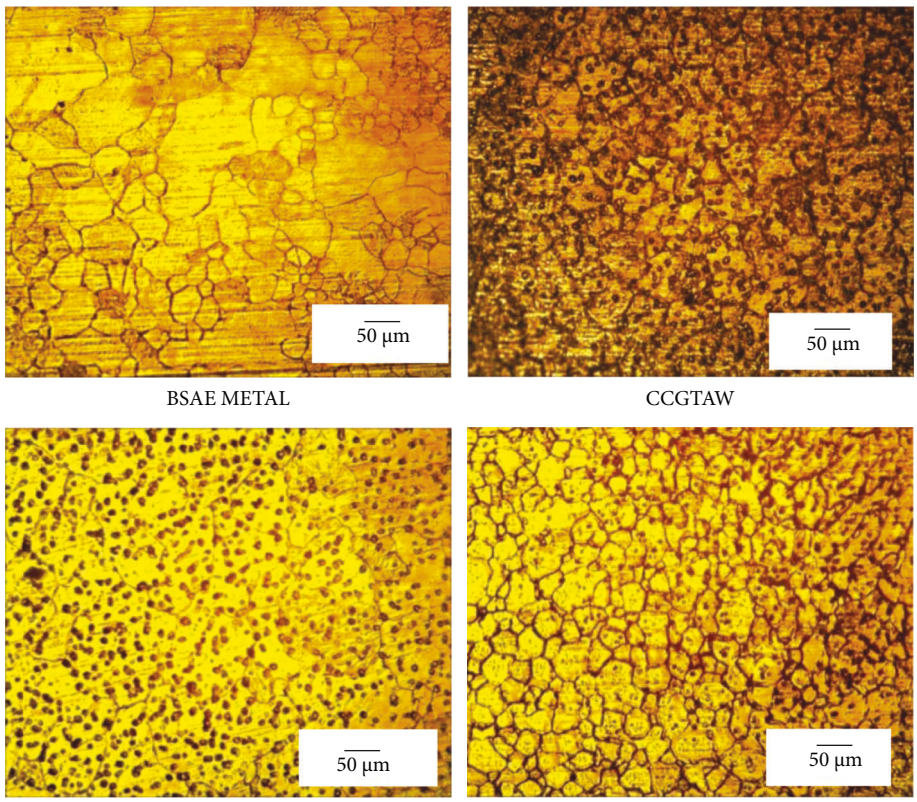

BSAE METAL CCGTAW

PCGTAW MAO

Figure 6: Fusion zone microstructures of autogenous welds.

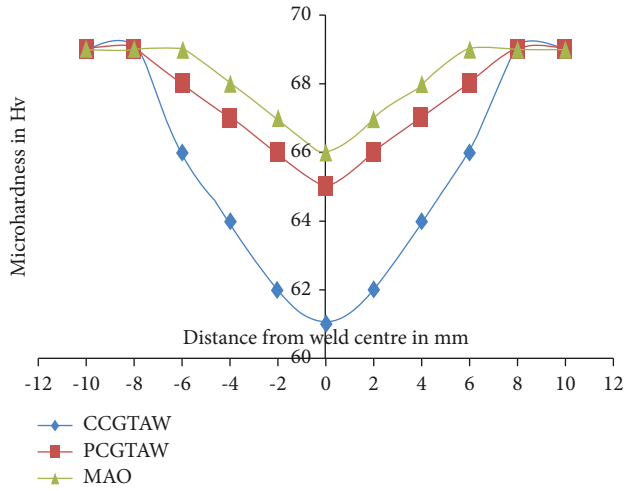

Figure 7: Fusion zone microhardness of the GTA weld.

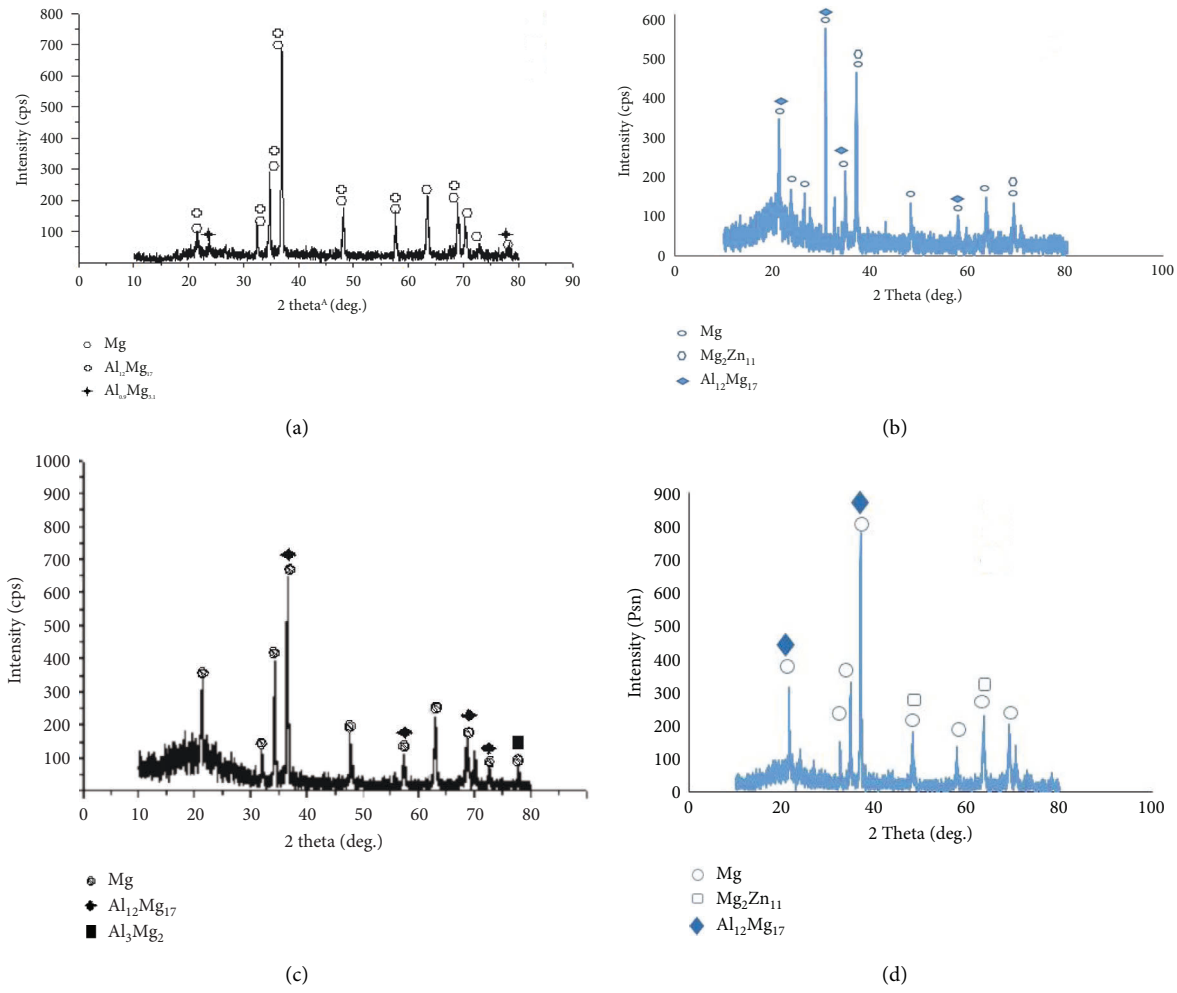

Figure 8: XRD results. (a) Base metal. (b) CCGTAW. (c) PCGTAW. (d) MAO.

microns, which implies that the grain diameter is reduced by 16 microns as a result of the MAO process. The MAO process has the smallest grain in the weld metal associated to the CCGTAW and PCGTAW methods.

3.4. Microhardness. There was a microhardness study conducted from the welded zone to the base metal [14]. Based on differences in microstructure, the areas marked on Figure 7 are the areas of base metal, the heat impacted

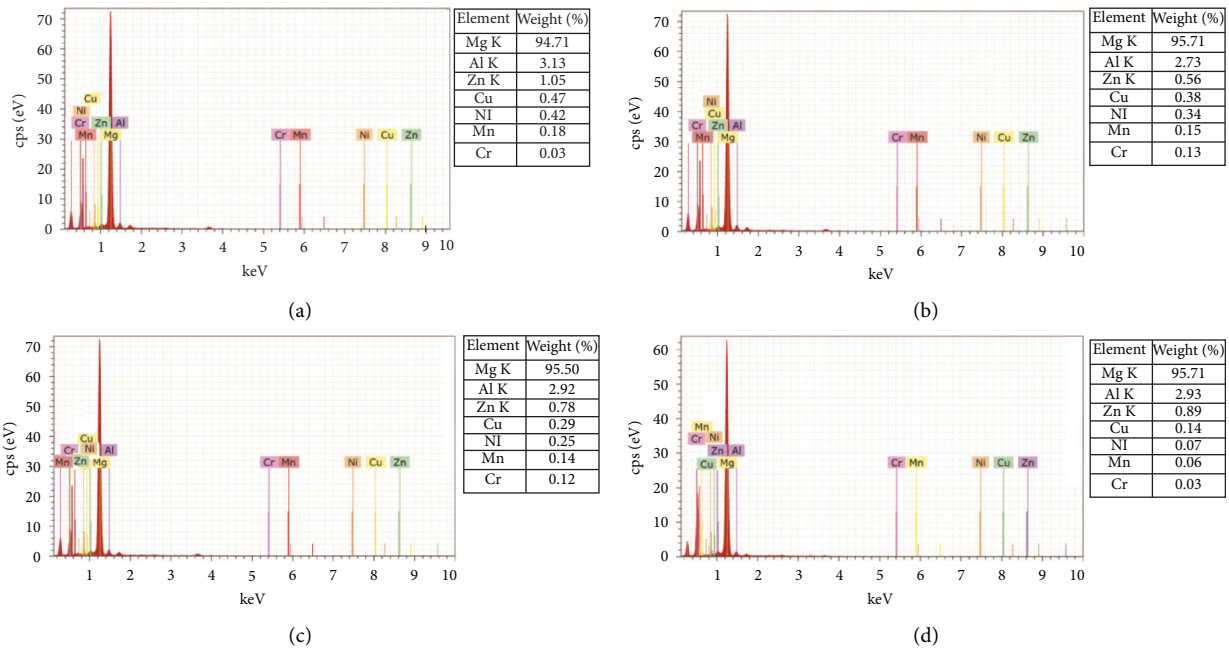

Figure 9: EDS results. (a) Base metal. (b) CCGTAW. (c) PCGTAW. (d) MAO.

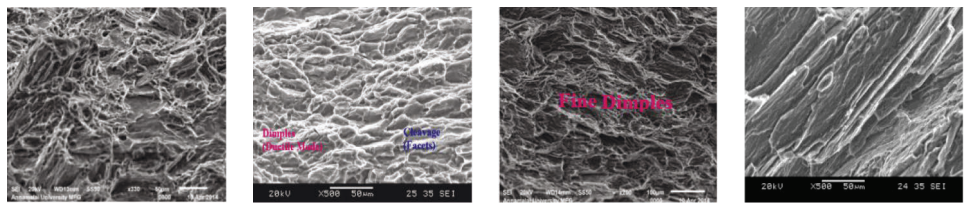

Figure 10: SEM fractograph of unnotched tensile specimen. (a) CCGTAW. (b) PCGTAW. (c) MAO. (d) BASE METAL.

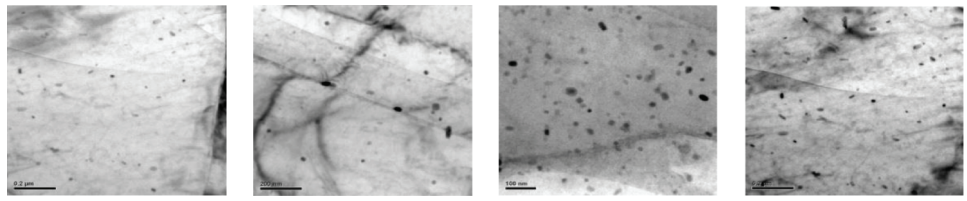

Figure 11: TEM micrographs (size distribution of the precipitates). (a) Base metal. (b) CCGTAW. (c) PCGTAW. (d) MAO.

region, and the fusion region. In the weld metal region, the CCGTAW and PCGTAW joints have hardness values of HV 61 and HV 66. In contrast, the weld metal hardness of MAO joints is HV 68, which is higher than that of CCGTAW and PCGTAW joints.

3.5. XRD and EDS Analysis. Analysis of the chemical components of the weld area and the base metal was done using the XRD. $Al_{12}Mg_{17}$ precipitates are shown in Figure 8 XRD data, as well as traces of Mg_2Zn_{11} and Al_3Mg_2. The matrix's composition was also determined using energy dispersive spectroscopy (EDS). Figure 9 shows the EDS data, which reveal that magnesium and aluminium components dominate the matrix composition. Due of the increased peak temperature achieved by the weld area, zinc evaporation is also present in all the joints.

4. Discussion

Compared to CCGTAW and PCGTAW weld joints, MAO joints are stronger in terms of yield and tensile strength.

Weld thermal cycles, or more specifically, the heat input provided by the welding process, have an effect on this. The CCGTAW technique creates coarser grains in autogenous arc welds than the PCGTAW and MAO procedures (Table 3). The CCGTAW method has a larger heat input than the PCGTAW and MAO procedures (Table 3). The MAO method has a lower heat input than the PCGTAW and CCGTAW processes do. The microstructural features and toughness qualities of the weld are affected by these fluctuations in heat input during welding procedures. It is a version of the GTAW process that cycles the welding current between high and low levels at a predetermined frequency. The PCGTAW method peak current values are frequently selected to offer appropriate penetration and beading contour, while background current levels are controlled at a suitable level to keep a constant arc [11]."Because the base material is melted only when the maximum peak pulses for short durations, the heat dissipates into the raw product rather than being trapped in the weld pool" [10].

Grain refinement can be achieved through the usage of current pulsing and arc fluctuation in combination with their simultaneous application in the MAO process, which is an extension of the GTAW process. As can be perceived in Figure 9, the autogenous arc manipulation approaches produced fine grained microstructures, as well as the columnar grained structure that is typical of CCGTA weld metals. The satisfactory equiaxed grains in the welding process are the consequence of a variety of oscillation and pulse conditions. There is a strong correlation between oscillation/pulsing frequency and the equiaxed grain formation. When compared to CCGTAW and PCGTAW joints, MAO welds were shown to have a higher toughness (68VHN) (Figure 10). "Microhardness in fusion can be traced to a rapid cooling point due to steeper thermal gradients, which results in a microstructure with finer grain size" [15, 16]. The tensile characteristics of the fusion zone were improved as a result of grain refining. The junction created by welding MAO joints reached its maximum tensile strength. The higher tensile strength of the junction is also due to the weld metal's spreading of higher hardness [17, 18]. "In the weld, very fine grains were produced as a result of enhanced cooling rates near the weld center in comparison to the fusion boundary" [19].

The employment of arc manipulation techniques and arc oscillation provides motorized agitation in the weld transition region and breaks down the developing dendritic supports created during weld solidifying, according to the results of the tensile tests performed on the welded joints. Dendrites that have been shattered can serve as new nucleation points, resulting to a more refined grain structure. The tensile characteristics of welded joints should be affected by the development of grain structure in the fusion zone [20].

The SEM fractograph of base metal CCGTAW, PCGTAW, and MAO are revealed in Figures 10(a)–11(d), respectively. The fracture surface of the base metal shown in Figure 10(a) shows shear mode of failure with secondary cracking which is attributed to the high tensile strength. The fracture surface of CCGTAW joint shown in Figure 10(b) represents required mode failure with flat regions indicates the brittle mode of failure which is associated with the reduced ductility of the joints. The fracture surface of PCGTAW joint shown in Figure 10(c) reveals greater number of dimples than that of the CCGTAW joint which indicates the improvement in the ductility of the PCGATW in comparison to the CCGTAW joint. The fracture surface of the MAO weld joint (Figure 10(d)) consists of fine and large number of dimples with no flat featureless region indicating the ductile mode of failure in the joint in comparison to other weld joints [23, 24].

The TEM micrograph of the base metal is displayed in Figure 11(a) reveals $Al_{12}Mg_{17}$ precipitates dispersed in the Mg matrix. The TEM micrograph of CCGTAW shown in Figure 11(b) reveals the coarsening of precipitates during welding and even some clustering was observed. The TEM micrograph of the PCGTAW joint shown in Figure 11(c) reveals lesser and finer precipitates involved the PCGTAW joint than that of the CCGTAW joint. The precipitates tend to coarsen and aligned in the grain boundaries. The TEM micrograph of the MAO joint shown in Figure 11(d) reveals higher precipitates of finer size precipitates due to the disorder created in the weld pool of the MAO joint, by the stirring action of the arc [21, 22].

5. Conclusions

The influence of GTAW variants on the tensile and mechanical characteristics of AZ31B magnesium alloy joints was considered. Important findings from this examination are as follows:

(i) Associated to the CCGTAW and PCGTAW joints, the tensile strength of the MAO-fabricated joints was enhanced by 24 and 16 percent, respectively.

(ii) MAO joints may have superior tensile properties compared to the CCGTAW as well as PCGTAW joints because of their lower heat input, thinner weld zone grain diameter, and greater fusion zone hardness.

(iii) The strength difference of weld joints has mainly attributed to size and dispersal of precipitates in the MAO than the PCGTAW and CCGTAW joints.

Data Availability

There is no data availability statement.

Conflicts of Interest

The authors declare that they have no conflicts of interest.

References

[1] G. Mahendran, V. Balasubramanian, and T. Senthilvelan, "Developing diffusion bonding windows for joining AZ31B magnesium and copper alloys," *International Journal of*

Advanced Manufacturing Technology, vol. 42, no. 7-8, pp. 689–695, 2009.

[2] M. Seeman, P. Sivaraj, R. Seetharaman, and I. Ashok Kumar, "Analysis and optimization of machining parameter during turning of A356/10%SiCp MMC using response surface methodology approach," *IOP Conference Series: Materials Science and Engineering*, vol. 961, no. 1, Article ID 012014, 2020.

[3] J. Veerasundaram, K. Kani, S. Murugesan, and R. Nallamuthu, "Effect of extrusion ratio and die angle on the microstructure of an AA6063/SiC composite," *Materials Testing*, vol. 64, no. 6, pp. 874–883, 2022.

[4] W. B. Ding, H. Y. Jiang, X. Q. Zeng, D. H. Li, and S. S. Yao, "The surface modified composite layer formation with boron carbide particles on magnesium alloy surfaces through pulse gas tungsten arc treatment," *Applied Surface Science*, vol. 253, no. 8, pp. 3877–3883, 2007.

[5] R. Manti, D. Dwivedi, and A. Agarwal, "Pulse TIG welding of two Al-Mg-Si alloys," *Journal of Materials Engineering and Performance*, vol. 17, no. 5, pp. 667–673, 2008.

[6] S. Prakash, C. S. Abdul Favas, I. Ameeth Basha et al., "Investigation of mechanical and tribological characteristics of medical grade Ti6al4v titanium alloy in addition with corrosion study for wire EDM process," *Advances in Materials Science and Engineering*, vol. 2022, Article ID 5133610, 10 pages, 2022.

[7] S. P. Jani, A. S. Jose, C. Rajaganapathy, and M. A. Khan, "A polymer resin matrix modified by coconut filler and its effect on structural behavior of glass fiber-reinforced polymer composites," *Iranian Polymer Journal (English Edition)*, vol. 31, no. 7, pp. 857–867, 2022.

[8] N. Kishore Babu and C. E. Cross, "Grain refinement of AZ31 magnesium alloy weldments by AC pulsing technique," *Metallurgical and Materials Transactions A*, vol. 43, no. 11, pp. 4145–4154, 2012.

[9] T. Ramkumar, A. Haiter Lenin, M. Selva kumar, M. Mohanraj, S. C. Ezhil Singh, and M. Muruganandam, "Influence of rotation speeds on microstructure and mechanical properties of welded joints of friction stir welded AA2014-T6/AA6061- T6 alloys," in *Proceedings of the Institution of Mechanical Engineers - Part E: Journal of Process Mechanical Engineering*, vol. 9, Article ID 095440892210776, 2016.

[10] G. D. Janaki Ram, R. Murugesan, and S. Sundaresan, "Fusion zone grain refinement in aluminum alloy welds through magnetic arc oscillation and its effect on tensile behavior," *Journal of Materials Engineering and Performance*, vol. 8, no. 5, pp. 513–520, 1999.

[11] K. Sivaprasad and S. G. S. Raman, "Influence of magnetic arc oscillation and current pulsing on fatigue behavior of alloy 718 TIG weldments," *Materials Science and Engineering*, vol. 448, no. 1-2, pp. 120–127, 2007.

[12] S. Mahajan, N. S. Biradar, R. Raman, and S. Mishra, "Effect of mechanical arc oscillation on the grain structure of mild steel weld metal," *Transactions of the Indian Institute of Metals*, vol. 65, no. 2, pp. 171–177, 2012.

[13] S. R. K. Rao, G. M. Reddy, M. Kamaraj, and K. P. Rao, "Grain refinement through arc manipulation techniques in Al–Cu alloy GTA welds," *Materials Science and Engineering*, vol. 404, no. 1-2, pp. 227–234, 2005.

[14] P. Sivaraj, M. Seeman, D. Kanagarajan, and R. Seetharaman, "Influence of welding parameter on mechanical properties and microstructural features of resistance spot welded dual phase steel sheets joint," *Materials Today Proceedings*, vol. 22, pp. 558–562, 2020.

[15] C. Pandey, M. M. Mahapatra, P. Kumar, F. Daniel, and B. Adhithan, "Softening mechanism of P91 steel weldments using heat treatments," *Archives of Civil and Mechanical Engineering*, vol. 19, no. 2, pp. 297–310, 2019.

[16] G. Padmanaban and V. Balasubramanian, "Influences of pulsed current parameters on mechanical and metallurgical properties of gas tungsten arc welded AZ31B magnesium alloy," *Metals and Materials International*, vol. 17, no. 4, pp. 679–687, 2011.

[17] S. Vijayananth, V. Jayaseelan, and G. Shivasubbramanian, "Formability analysis of AA6061 sheet in T6 condition," *Applied Mechanics and Materials*, vol. 766, pp. 416–421, 2015.

[18] K. Sivaprasad, S. Ganesh Sundara Raman, P. Mastanaiah, and G. Madhusudhan Reddy, "Influence of magnetic arc oscillation and current pulsing on microstructure and high temperature tensile strength of alloy 718 TIG weldments," *Materials Science and Engineering*, vol. 428, no. 1-2, pp. 327–331, 2006.

[19] N. S. Biradar and R. Raman, "Grain refinement in Al-Mg-Si alloy TIG welds using transverse mechanical arc oscillation," *Journal of Materials Engineering and Performance*, vol. 21, no. 11, pp. 2495–2502, 2012.

[20] N. S. Biradar and R. Raman, "Investigation of hot cracking behavior in transverse mechanically arc oscillated autogenous AA2014 T6 TIG welds," *Metallurgical and Materials Transactions A*, vol. 43, no. 9, pp. 3179–3191, 2012.

[21] F. Rubino, H. Parmar, V. Esperto, and P. Carlone, "Ultrasonic welding of magnesium alloys: a review," *Materials and Manufacturing Processes*, vol. 35, no. 10, pp. 1051–1068, 2020.

[22] S. P. Kumar, M. Vigneshwar, S. T. Selvamani, and P. Hariprasath, "The comparative analysis on friction stir welded and gas tungsten arc welded AZ91 grade magnesium alloy butt joints," *Materials Today Proceedings*, vol. 4, no. 6, pp. 6688–6696, 2017.

[23] P. Kumar, J. Victor, R. Arunachalam et al., "Production of aluminium alloy-based metal matrix composites using scrap aluminium alloy and waste materials," *Jornal of Alloys and Compounds: Influence on microstructure and mechanical properties*, vol. 324, p. 567, 2019.

[24] P. K. Krishnan, R. Arunachalam, A. Husain, and M. Al-Maharbi, "Studies on the influence of stirrer blade design on the microstructure and mechanical properties of a novel aluminum metal matrix composite," *Journal of Manufacturing Science and Engineering*, vol. 143, no. 2, pp. 1–25, 2020.

Hindawi
Advances in Materials Science and Engineering
Volume 2022, Article ID 8330144, 8 pages
https://doi.org/10.1155/2022/8330144

Research Article

Extreme Gradient Boosting Regressor Solution for Defy in Drilling of Materials

Sangeetha Elango,[1] **Elango Natarajan**,[2] **Kaviarasan Varadaraju**,[3] **Ezra Morris Abraham Gnanamuthu**,[1] **R. Durairaj**,[1] **Karthikeyan Mohanraj**,[4] **and M. A. Osman**[5]

[1]*Lee Kong Chian Faculty of Engineering and Science, Universiti Tunku Abdul Rahman (UTAR), Sungai Long, Malaysia*
[2]*Faculty of Engineering, Technology and Built Environment, UCSI University, Kuala Lumpur, Malaysia*
[3]*Mechanical Engineering, Sona College of Technology, Salem, Tamilnadu, India*
[4]*PACE Enterprise Pte Ltd., 20A Tg Pagar Road, Singapore*
[5]*Sudan University of Science and Technology, Khartoum, Sudan*

Correspondence should be addressed to M. A. Osman; m.osman62m@gmail.com

Received 24 June 2022; Accepted 29 August 2022; Published 27 September 2022

Academic Editor: R. Thanigaivelan

Drilling is a quite common operation being performed in the manufacturing of components. Instrumental response in drilling is geometrical accuracy and surface integrity of the drilled parts. For the application where geometrical tolerance is very small, an operation is to be carried out very carefully. If not, rejection of drilled samples will be higher and consequently production loss will be higher. The use of prediction model in this scenario is much more appropriate and cost-effective. This research aimed to apply extreme gradient boosting (XGBoost) regressor to develop a drilling prediction model. Drilling experiments were conducted after developing design of experiments with twenty-seven unique sets. Experimental data analysis was then carried out on experimental data sets that have features such as speed, feed, angle, hole length, and surface roughness. After correlation analysis, the k-fold cross validation method was applied for parameterisation. Hyperparameters estimated from the k-fold cross validation were then applied to train and test the XGBoost regressor-based machine learning (ML) model. It is concluded from the model evaluation metric (R^2) that the XGBoost regressor model has resulted 0.89 before tuning and 0.94 after tuning of the model, which is higher than the polynomial regressor and support vector regressor.

1. Introduction

Polyether ether ketone (PEEK) is a biomaterial that is preferred in the medical application including tissue engineering, dentistry spine surgery, and maxilla facial surgery. PEEK is semicrystalline material that contains both amorphous and crystalline regions. This two-phase semicrystalline polymer has repeating units of single ketone bond and double ether bonds in the main chain. It has become an important material in the dental application. Many research publications and review articles have been published in the suitability of PEEK in the dental application. Different types of functionalization have been attempted to improve their osteoinductive and antimicrobial capabilities. A review article published by Paratelli et al. [1] reports that the PEEK was applied in implant-supported fixed dental prosthesis (IFDP) frameworks, prosthetic implant abutments, implant abutment screws, and retention clips on implant bars. The PEEK exhibits a glass transition temperature (Tg) of around 289°F and, hence, can be used in high-temperature environment. Due to its electrical properties, it is widely used for electrical components including semiconductor test sockets and electrical connectors. It is resistant to steam and, hence, suitable for reusable medical components subject to repeating autoclave cycles. The PEEK has gained widespread popularity in downhole oil and gas applications due to its

resistance to harsh chemicals including H_2S. Due to its flame-retardant characteristic and ability to hold UL 94 V-0 flammability ratings from thin cross-sections, it can be applied in electric vehicles too.

Verma [2] reported that designed PEEK costal cartilage prostheses have mechanical properties almost the same as natural costal cartilages. It assists in improved breathing as for the patient going through chest wall reconstruction. It has been applied in replacing the rib cartilage, total knee, and many implants. Davani et al. [3] investigated the structural integrity of PEEK material for a bone application and reported that it is a suitable alternative to stainless steel material. He et al. [4] and Wang [5] reported bio inertness of virgin PEEK hinders its practical application in bone repair application and, hence, modification is required for the PEEK to suit it in the bone application. Kumar et al. [6] also reported in their study on the application of PEEK for spine application that PEEK is a highly suitable material and alternative to titanium alloy. These results are augmented by research conducted by Tan et al. [7]. They investigated different polymeric materials through simulations for bone plating application and reported that modified PEEK is better for this application. The use of the PEEK material in the dental application was discussed in [8].

As the potentiality of PEEK and PEEK composites take them to more versatile material in biomedical and industrial applications, drilling of these materials with high geometrical accuracy is highly appreciated. In general, burrs are produced at the exit of the holes and, hence, the surface finish of the hole is affected. Ranjan et al. [9] used artificial intelligence to predict the hole quality (roundness) in microdrilling (0.4 mm). Kayaroganam et al. [10] used metaheuristic algorithm to optimize the drilling parameters of mica reinforced composite. Parasuraman et al. [11] analyzed the drilling of TiB2 reinforced composite and reported that cutting force was increased according to the filler content. Kaviarasan et al. [12] used artificial intelligence to predict the surface roughness of drilled hole in the Delrin material. Elango et al. [13] recently reported in their study on drilling of PTFE material that use of ANFIS and RSM together for modeling has given more accurate results. Nguyen et al. [14] developed a machine learning (ML) model using Bayesian optimization for polycarbonate material. Support vector regressor (SVR) was applied to develop prediction models for carbon fiber reinforced polymer (CFRP) [15] and Delrin [16]. In [15], Xu et al. attempted SVR for drilling of CFRP and predicting the cutting force. In [16], Elango et al. attempted polynomial and SVR models for turning of Delrin material and concluded that SVR performs better than polynomials. In the case of machining of PEEK material, no research has been conducted so far, despite it is considered as a significant material.

This research is aimed at developing a prediction model for drilling of the PEEK material. The experiments were conducted in CNC machine, and 27 unique datasets were collected. Firstly, exploratory data analysis (EDA) was conducted to understand the correlation between input parameters and response variable. Later, extreme gradient boosting regressor (EGDR) was applied to train the machine learning (ML) model. At this end, the paper is organized as follows: Section 2 describes the material and experimentation. Section 3 presents the model development, while section 4 presents the results and validation.

2. Material and Experimentation

2.1. Material. In this research, a biomaterial known as polyether ether ketone (PEEK) was considered. This biomaterial has superior modulus and strength even at elevated temperature. Its wear properties and durability give it a special consideration in biomedical applications and some industrial applications where high frictional stress is involved. The glass transition temperature (T_g) is about 143°C to 250°C and, hence, it is preferred in valves, bearings, pistons, seals manufacturing, and implants. It is seen as a viable alternative material for stainless steel and titanium alloys for the reason of avoiding stress shielding [17].

Industrial grade PEEK granules were purchased from local supplier in India. Injection molding (Mathman Plastics Molding Machine, China, Model: MPR750R2) was employed in the preparation of PEEK samples. Preheated PEEK granules at 80°C were filled into the injection tube and then heated to 200°C to ensure perfect melting of the raw material. The molten material at 235°C was then passed through the nozzle to mold plate. The plate was allowed to cool at room temperature for 24 h, followed by 30 min in a hot oven at 50°C. Injection molded sheet was in the dimensions of $300 \times 300 \times 2.5$ mm. Dumb bell samples according to ASTM D412/ISO 37 standard were then cut from the injection molded sheet. Tensile tests were conducted using an Instron universal testing machine (Instron 5582, USA) that has 250 mm extensometer and a pneumatic gripper. Three samples were tested at a strain rate of 25 ms^{-1} until they fracture. Figure 1 shows dumb bell samples which were used in tensile testing and a sample load-displacement graph obtained from the test. The stiffness of PEEK material is 1.52 GPa and tensile strength is 99.48 MPa. These data are commonly used data in design of parts.

2.2. Drilling Experimentation. For drilling experimentation, the PEEK rod of 20 mm in diameter and 1000 mm in length was prepared and used. Drilling experiments were conducted in a CNC machine using Taguchi L27 design of experiments (DoE). Three levels of control parameters, viz., speed, feed, angle, and hole length were used in DoE. Solid TiN coated carbide drill bit (code DIN6537) of 10 mm diameter was used in all experiments. Surface roughness of the drilled holes was measured with surf tester (Model Mitutoya Surftest SJ-210). The surface roughness values were measured in three different locations and the average of measurements was considered. Figure 2 shows the experimental setup and drilled samples, while Table 1 lists input parameters used in the experiments and the respective surface roughness of the drilled samples. In general, large number of datasets are used in machine learning model development, because higher the datasets, higher the possibility to fit the model. But getting the experimental data is a cost consuming

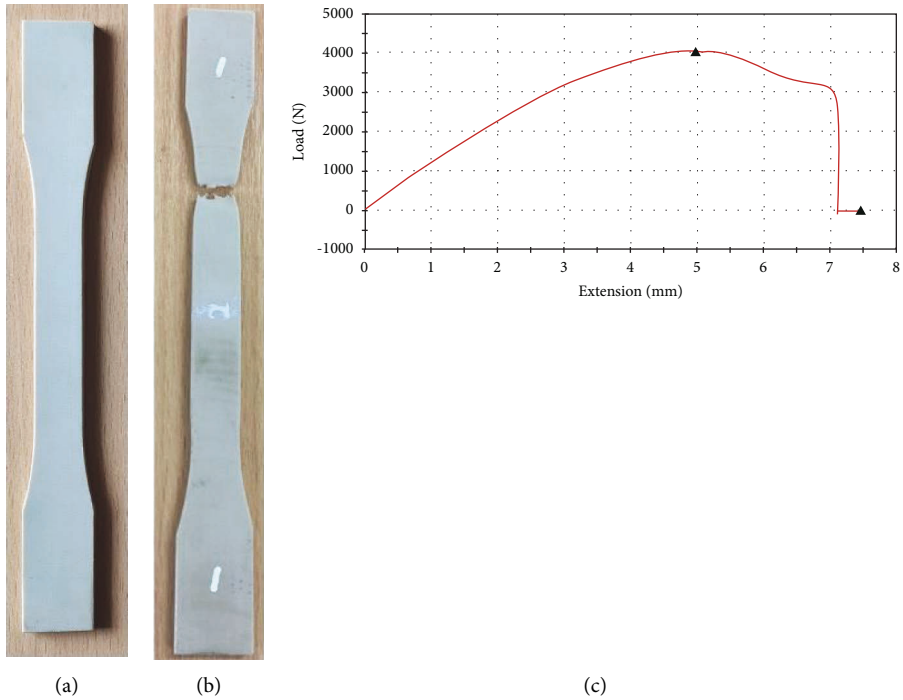

Figure 1: (a) PEEK sample; (b) broken sample; (c) load-displacement diagram.

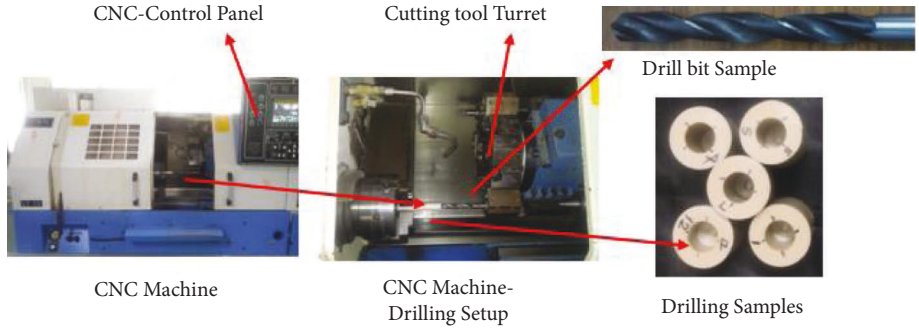

Figure 2: Experimental setup and drilled samples.

process. Hence, it was planned to use minimal number of data (27 datasets) to fit the ML model.

3. Machine Model Development

The reason for developing machine learning model or prediction model is to avoid wastages in the machining and also to know the response beforehand [18]. Decision tree approach is a simple and easier method of modeling that interprets the features and concludes the response of the subject. This method has been used in statistics, data mining, and machine learning. The accuracy of decision tree is dependent upon the size of datasets, greater the amount of data available, higher the accuracy. Gradient boosting algorithm is a machine learning technique that can be used both in regression and classification problems. The term boosting refers to a family of algorithms that convert weak learners in the datasets into strong learners. It could understand that weak learners are slightly better than a random choice, while strong learners are perfect in performance. This approach can produce an ensemble predictive model from weak predictive models. In gradient boosting algorithm, gradient descent in function space is stage-wise used to construct the ensemble. The final model is a function taking input parameters as a vector of attributes $x \in R^n$ to get $F(x) \in R$. In $F_i(x) = F_{i-1}(x) + \gamma_i h_i(x)$, h_i is a function that models a single tree, and $\gamma_i \in R$ is the weight associated with i^{th} tree. The two terms, function h_i and weight γ^i, are learned during the training phase. Gradient boosting algorithm is more reliable and easier when compared to other machine learning algorithms. Algorithm such as linear regression has its number of degrees of freedom scaling with the number of features $O(M)$. It means that its ability to learn from the data plateau in the regime $N \gg M$, where N is the number of samples and M is number of features. The linear regression algorithm results in low variance, but high bias. In the $N < M$ regime, L_1 regularization becomes necessary to learn the relevant features and zero-out the noise. A tree, in its

Table 1: The results obtained from the experiments.

Expt. No.	Speed (rpm)	Feed (mm/min)	Angle (degree)	Hole length (mm)	Ra (μm)
1.	600	0.1	80	10	0.80
2.	600	0.1	100	20	0.88
3.	600	0.1	120	30	0.98
4.	600	0.15	80	20	0.90
5.	600	0.15	100	30	1.02
6.	600	0.15	120	10	1.25
7.	600	0.2	80	30	1.14
8.	600	0.2	100	10	1.30
9.	600	0.2	120	20	1.47
10.	1200	0.1	80	10	0.84
11.	1200	0.1	100	20	0.92
12.	1200	0.1	120	30	0.80
13.	1200	0.15	80	20	1.00
14.	1200	0.15	100	30	1.03
15.	1200	0.15	120	10	1.09
16.	1200	0.2	80	30	1.37
17.	1200	0.2	100	10	1.44
18.	1200	0.2	120	20	1.53
19.	1800	0.1	80	10	0.97
20.	1800	0.1	100	20	0.89
21.	1800	0.1	120	30	0.85
22.	1800	0.15	80	20	1.31
23.	1800	0.15	100	30	1.26
24.	1800	0.15	120	10	1.24
25.	1800	0.2	80	30	1.80
26.	1800	0.2	100	10	1.79
27.	1800	0.2	120	20	1.80

Table 2: Descriptive statistics of features used in the model.

Feature parameters	Number of count	Mean $\bar{x}$	Standard deviation (σ)	Minimum	25%	50%	75%	Maximum
Speed	27	1200	499.2302	600	600	1200	1800	1800
Feed	27	0.15	0.041603	0.1	0.1	0.15	0.2	0.2
Angle	27	100	16.64101	80	80	100	120	120
Ra	27	1.172	0.31032	0.8	0.91	1.09	1.34	1.8

unregularized form, has a low bias which can over fit the data to extreme, with the depth of field scaling as $O(N)$, but it has a high variance (i.e., deep trees do not generalize well). But, because a tree can reduce its complexity as much as needed, it can work in the regime $N < M$ by simply selecting the necessary features. A random forest is a low bias algorithm and the ensemble averages away the variance (but deeper trees call for more trees), and it does not over fit on the number of trees, so it is a lower variance algorithm. The homogenous learning is that the trees tend to be similar and tend to limit its ability to learn more on much data. Flores and Keith [19] used gradient booster algorithm to predict the surface roughness in high-speed milling of a metal.

3.1. Exploratory Data Analysis (EDA). Data in Table 1 are analyzed to identify general patterns in the data, which perhaps include outliers of the data to be capped. Table 2 shows the descriptive statistics of basic features of the data used. It shows the "center" of distribution values (mean) and dispersion (standard deviation) for each variable. Outlier has greatly exaggerated the range and decile distribution for data with 4 intervals of 25%, 50%, 75%, and 100% (Max).

Understanding the correlation among variables is more important during model development. Correlation analysis is a method for measuring the covariance of two random variables X and Y in a matched dataset. The correlation coefficient is a unitless number that varies from −1 to +1. The magnitude of the correlation coefficient is the standardized degree of association between X and Y. The sign is the direction of the association, which can be positive or negative. Figure 3 is drawn to comprehend data statistically from predictive features and their relationship. It is evident that each parameter involved in drilling is independent, and there is no correlation between them.

3.2. Extreme Gradient Boosting (XGBoost) Regressor. Extreme gradient boosting (XGBoost) is one of the tree algorithms to mathematically formalize regularization in a tree. It is adapted to large data scales, as it has a low bias and high variance (due to the boosting mechanism). It is a

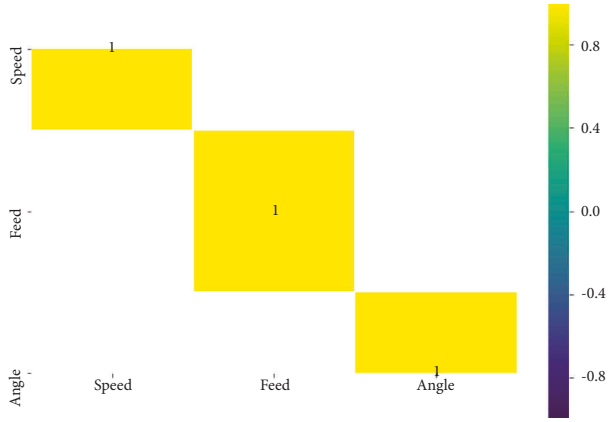

Figure 3: Univariate analysis of the feature parameters.

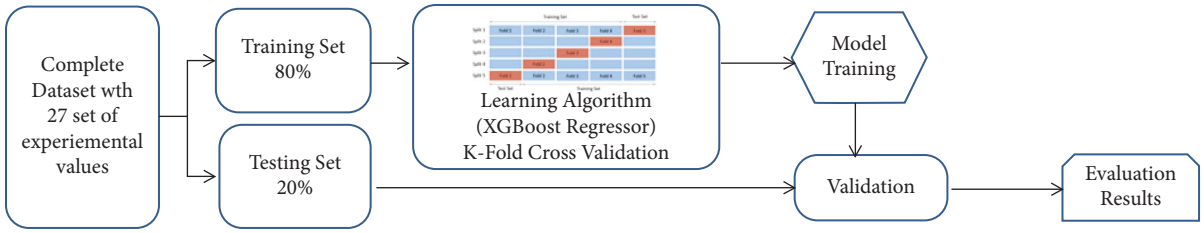

Figure 4: Workflow implemented for ML model development.

parallelized and carefully optimized version of the gradient boosting algorithm. It has improved the training time by parallelizing the whole boosting process.

Pseudocode for XGBoost algorithm is as follows:

(1) Input: training set $\{X_i, Y_i\}$, a differentiate loss function $L(Y, F(x))$, and number of iterations M

(2) Initiate model with a constant value: F_0 = γ (i.e., fits to actual value)

(3) Compute so-called pseudoresiduals and fit a base learner (e.g., tree) to pseudoresiduals. That is, training it using the train set $\{X_i, Y_i\}$

(4) Compute multiplier by solving the one-dimensional problem and followed by that update model

(5) Output of model $F_m(X)$

As explained above, gradient boosting takes the training set and a loss function as inputs, and the final trained model is gotten at the end of the algorithm by output $F_m(X)$. The workflow of the model development is shown in Figure 4.

The split of training and testing data sets for machine model development was done using the k-fold cross validation approach. It was used to split the experimental data into k subsets, since it is small size data. Below steps were followed in 5-fold cross validation:

(1) Training model using k-1 folds

(2) Validating model on the remaining fold that is not used for training

(3) Repeating above two steps for each combination of folds and averaging the model results, while the optimal results (5-fold) are not obtained

Figure 5 depicts the model parameterisation applied in the current problem. In the process of cross validation, the dataset was split into 80% for training and 20% for testing. Hyperparameterization was processed using training data set of 80% in order to comprehend imbalanced accuracy in training. The optimal hyperparameters and their accuracy are shown in Table 3. It is evident that accuracy of grid search is increased when a number of trees are increased. Among three different cases considered, M1 set (200 trees) has resulted in the accuracy of 98% and 93% for training and testing, respectively. When number of trees is increased from 200 to 300, the accuracy of training data is of course increased to 99%, but accuracy of test data is decreased to 88%. This is because of high variance resulted by higher number of trees.

After cross validation, the XGBoost prediction model was tuned iteratively to achieve the maximum performance. In order to determine the fitness of the XGBoost regression model, a statistical validation technique of residual sum of square (RSS, also known as the sum of squared errors of prediction) was used to identify the dispersion of data as well as how well the data fit the trained ML model. Generally, a lower residual sum of squares indicates that the regression model can better explain the data, while a higher residual sum of squares indicates that the model poorly explains the data.

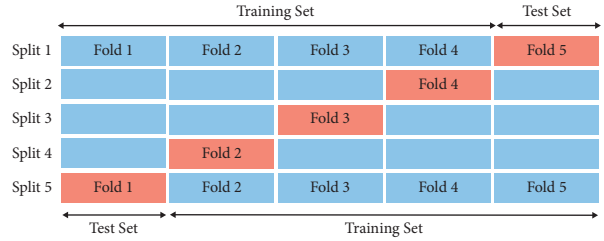

Figure 5: Five-fold cross validation method applied in the parameterisation.

Table 3: List of hyper-parameters used for model building using XGBoost regressor.

Experiment	No of trees	Max depth	Accuracy grid search	Test set
M1 set	200	6	0.98	0.93
M2 set	300	7	0.99	0.88
M3 set	400	8	0.99	0.79

Table 4: Performance evaluation of three different regression models.

Regressor algorithm	Ssr (R^2)	
	Before tuning	After tuning
Polynomial regressor	0.68	0.72
Support vector regressor	0.76	0.80
XGBoost regressor	0.89	0.94

Table 5: XGBoost regressor predicted values and actual values.

S. No.	Speed	Feed	Angle	Prediction output surface roughness in micron	Experimental output (from validation experiments) surface roughness in micron	Deviation between predicted data and experimental data
1	500	0.1	70	0.791179121	0.79	0.001
2	500	0.15	90	1.014292955	1.0	0.014
3	500	0.2	110	1.540123343	1.52	0.02
4	500	0.25	120	1.540123343	1.52	0.02
5	700	0.1	70	0.791179121	0.80	0.009
6	700	0.15	90	1.014292955	1.0	0.014
7	700	0.2	110	1.540123343	1.53	0.01
8	700	0.25	120	1.540123343	1.53	0.01
9	1000	0.1	70	0.828593671	0.82	0.009
10	1000	0.15	90	1.044688106	1.1	0.055
11	1000	0.2	110	1.50600183	1.5	0.006
12	1000	0.25	120	1.50600183	1.5	0.006
13	1400	0.1	70	0.82450515	0.83	0.005
14	1400	0.15	90	1.044688106	1.0	0.045
15	1400	0.2	110	1.517023683	1.49	0.027
16	1400	0.25	120	1.517023683	1.52	0.003
17	1600	0.1	70	0.985206783	0.98	0.005
18	1600	0.15	90	1.259504914	1.1	0.16
19	1600	0.2	110	1.803998828	1.8	0.004
20	1600	0.25	120	1.803998828	1.8	0.004
Mean deviation in 20 data sets = 0.0214 micron						

$$RSS = \sum_{i=1}^{n} \left(y^i - f\left(X_i\right)\right)^2, \quad (1)$$

where y^i is the i^{th} value of the variable to be predicted, $f(X_i)$ is the predicted value of y^i, and n is the upper limit of summation.

4. Results and Validation of XGBoost Regressor Model

The prediction model was evaluated by computing R^2 value in each iteration. The coefficient of determination (R^2) is a measure of performance of the model. Tuning of model by changing its hyper-parameters has improved R^2 value of the

model. After several attempts of tuning of the model, it is found that $R^2 = 0.89$ for training data and $R^2 = 0.94$ for testing datasets.

To compare the XGBoost model with other regressors that have been used in the literature, polynomial model and SVR model were developed with the same data. In order to have a fair comparison, the optimal parametrization for each one of the compared algorithms was carried out using the same strategy as before. Overall performance of XGBoost model and other selected models (polynomial and SVR) is shown in Table 4.

Evaluating these three regressor models, XGBoost stands highest in the performance, followed by the SVR model. It is found higher than other two models in any iteration before tuning and after tuning as well.

4.1. Experimental Validation of the XGBoost Model. It is obvious that ML model is performed to predict the responses for unseen independent features. For example, the current XGBoost model can predict the surface roughness of PEEK material, if anonymously selected speed, feed, and angle values are given. To validate the developed model, twenty random input values were given into the model, and the respective predicted parameters were observed. Later, the validation experiments were conducted for the same input values, and actual results and predicted results are compared as tabulated in Table 5.

5. Conclusion

This research was focused on to develop a machine learning model for drilling of PEEK material. Development of the model was started with collecting the experimental data from L_{27} DoE. Considering speed, feed, and drill tool angle, surface roughness of the drilled PEEK rod was measured. Collected experimental data were then applied to XGBoost regressor to develop a machine learning model. Exploratory data analysis revealed that these three independent variables have significance in the surface roughness of the drilled material, particularly combination of speed and feed has more influence in the output. The XGBoost regression model is better than polynomial and SVR regression models. Besides, after testing the ML model, twenty unique data were predicted and further validated. The validation results confirm the effectiveness of the predicted model.

Data Availability

Data associated with this research are available on request from the corresponding author.

Conflicts of Interest

The authors declare that there are no conflicts of interest.

References

[1] A. Paratelli, G. Perrone, R. Ortega, and M. Gómez-Polo, "Polyetheretherketone in implant prosthodontics: a scoping review," *The International Journal of Prosthodontics*, vol. 33, no. 6, pp. 671–679, 2020.

[2] S. Verma, N. Sharma, S. Kango, and S. Sharma, "Developments of PEEK (Polyetheretherketone) as a biomedical material: a focused review," *European Polymer Journal*, vol. 147, Article ID 110295, 2021.

[3] K. Davani, M. P. Navid, E. Natarajan, B. R. Hanumandarao, and S. Paramasivam, "Mechanical integrity of PEEK bone plate in internal fixation of femur: experimental and finite element analysis towards performance measurement," *International Journal of Enterprise Network Management*, vol. 12, no. 1, pp. 17–31, 2021.

[4] M. He, Y. Huang, H. Xu et al., "Modification of polyetheretherketone implants: from enhancing bone integration to enabling multi-modal therapeutics," *Acta Biomaterialia*, vol. 129, pp. 18–32, 2021.

[5] W. Wang, C. J. Luo, J. Huang, and M. Edirisinghe, "PEEK surface modification by fast ambient-temperature sulfonation for bone implant applications," *Journal of The Royal Society Interface*, vol. 16, no. 152, Article ID 20180955, 2019.

[6] N. Kumar, S. A. Ramakrishnan, K. G. Lopez et al., "Can polyether ether ketone dethrone Titanium as the choice implant material for metastatic spine tumor surgery?" *World Neurosurgery*, vol. 148, pp. 94–109, 2021.

[7] J. H. Tan, E. Natarajan, W. Lim et al., "Effects of bone-plate materials on the healing process of fractured tibia bone under time-varying conditions: a finite element analysis," *Materials Research Express*, vol. 8, no. 9, Article ID 095308, 2021.

[8] L. Bathala, V. Majeti, N. Rachuri, N. Singh, and S. Gedela, "The role of polyether ether ketone (peek) in dentistry - a review," *Journal of medicine and life*, vol. 12, no. 1, pp. 5–9, 2019.

[9] J. Ranjan, K. Patra, T. Szalay et al., "Artificial intelligence-based hole quality prediction in micro-drilling using multiple sensors," *Sensors*, vol. 20, no. 3, p. 885, 2020.

[10] P. Kayaroganam, V. Krishnan, E. Natarajan, S. Natarajan, and K. Muthusamy, "Drilling parameters analysis on in-situ Al/B4C/mica hybrid composite and an integrated optimization approach using fuzzy model and non-dominated sorting genetic algorithm," *Metals*, vol. 11, no. 12, p. 2060, 2021.

[11] S. Parasuraman, I. Elamvazuthi, G. Kanagaraj, E. Natarajan, and A. Pugazhenthi, "Assessments of process parameters on cutting force and surface roughness during drilling of AA7075/TiB2 in situ composite," *Materials*, vol. 14, no. 7, p. 1726, 2021.

[12] V. Kaviarasan, R. Venkatesan, and E. Natarajan, "Prediction of surface quality and optimization of process parameters in drilling of Delrin using neural network," *Progress in Rubber, Plastics and Recycling Technology*, vol. 35, no. 3, pp. 149–169, 2019.

[13] S. Elango, K. Varadaraju, E. Natarajan, E. M. A. Gnanamuthu, R. Durairaj, and P. Mariappan, "PTFE in wet and dry drilling: two-tier modeling and optimization through ANFIS," *Mathematical Problems in Engineering*, vol. 2022, Article ID 4812470, 2022.

[14] V. H. Nguyen, T. T. Le, H. S. Truong et al., "Applying bayesian optimization for machine learning models in predicting the surface roughness in single-point diamond turning

polycarbonate," *Mathematical Problems in Engineering*, vol. 202116 pages, 2021.

[15] C. Xu, S. Yao, G. Wang, Y. Wang, and J. Xu, "A prediction model of drilling force in CFRP internal chip removal hole drilling based on support vector regression," *International Journal of Advanced Manufacturing Technology*, vol. 117, no. 5-6, pp. 1505–1516, 2021.

[16] S. Elango, E. M. A. Gnanamuthu, R. Durairaj, and K. Mohanraj, "Machine learning model for discrete, nonlinear datasets from machining operation: an industrial need to have high quality," *Multiscale and Multidiscip. Model. Exp. and Des.*vol. 5, no. 3, pp. 279–291, 2022.

[17] S. Paramasivam, N. M. Davani K, E. Natarajan, and B. R. Hanumandarao, "Mechanical integrity of PEEK bone plate in internal fixation of femur: experimental and finite element analysis towards performance measurement," *International Journal of Enterprise Network Management*, vol. 12, no. 1, pp. 17–31, 2021.

[18] E. Natarajan, V. Kaviarasan, K. M. Ang, W. H. Lim, S. Elango, and S. S. Tiang, "Production wastage avoidance using modified multi-objective teaching learning based optimization embedded with refined learning scheme," *IEEE Access*, vol. 10, Article ID 19186, 2022.

[19] V. Flores and B. Keith, "Gradient boosted trees predictive models for surface roughness in high-speed milling in the steel and aluminum metalworking industry," *Complexity*, vol. 2019, Article ID 1536716, 15 pages, 2019.

Hindawi
Advances in Materials Science and Engineering
Volume 2022, Article ID 4174210, 10 pages
https://doi.org/10.1155/2022/4174210

Research Article

Experimental Investigation of AA6063 Welded Joints Using FSW

T. Rajkumar,[1] **K. Radhakrishnan**,[1] **C. Rajaganapathy**,[2] **S. P. Jani**,[3] **and Nowshadth Ummal Salmaan**[4]

[1]*Department of Mechanical Engineering, K. Ramakrishnan College of Technology, Samayapuram, Trichy 621 112, Tamil Nadu, India*
[2]*Department of Mechanical Engineering, Government College of Engineering Srirangam, Trichy 620012, India*
[3]*Department of Mechanical Engineering, Marri Laxman Reddy Institute of Technology and Management, Hyderabad 500043, India*
[4]*Aksum University, Aksum, Ethiopia*

Correspondence should be addressed to S. P. Jani; spjani10@gmail.com and Nowshadth Ummal Salmaan; ummalsalmaan90@gmail.com

Received 25 May 2022; Accepted 5 August 2022; Published 19 September 2022

Academic Editor: Sengottuvelu Ramesh

The AA6063 aluminium alloy has gained widespread use in manufacturing the light-weighted structures which requires a high strength to weight ratio, and it possesses an excellent corrosive resistance in T6 heat-treated (solution heat treated and artificially aged) condition. The process of friction stir welding (FSW) is an emerging joining process of solid state that does not melt and recast the material being welded, as opposed in various other fusion welding processes, which are extensively utilized for combining the structural alloys of aluminium. The process of connecting separate components with external heat has resulted in induced stress on metals. The stir welding using friction was introduced in order to reduce the formation in residual stress during the joining process. The aluminium alloy AA6063 plates were fused utilising the friction stir welding procedure in this study. The studies were carried out using various combinations of speed in rotary condition, speed in transverse condition, and stress in axial condition. The generated joints that are welded was analysed mechanically and microstructurally. The maximum hardness of the mechanical joints produced is 93.25 HV, and the maximum tensile strength is 286.15 N/mm^2. According to the results of the response surface analysis, transverse and rotary velocities possess a notable impact in hardness and durability, respectively.

1. Introduction

Friction stir welding (FSW) is a solid phase welding technology that capacitate for welding of a wide range of parts and geometries of various structural alloys such as Al-alloys, Cu-alloys, and steel [4–8]. FSW is a late approach which uses an incombustible rotary tool for welding to produce heat by friction and plasticity in the fusing area, influencing junction formation much as the substance is still solid. The weld, on average, reduces the thickness of the parent metal by 3–6 percent [1,2]. The stir action is provided by the revolving tool, which plasticizes metal within a restricted zone while moving metal from the pin's leading face to the trailing edges. The tool and the work piece to be connected are moved in relation to each other to the point where the tool tracks along the weld interface. The weld cools as the tool passes over it, cementing the two plates [3].

This procedure can locally wipe out the defects that usually arise in fusion welding of Al-alloys such as porosity formation [9–13] accordingly improvising the physical strength and malleability, enhancing resistive property to corrosive and fatigue of the substance, and upgrading malleability along with enhancing different possessions. The goal of this research is to optimise the parameters which can be listed as the rotating speed (RS), velocity in welding (WS), and the angle of tool tilt (TTA) in order to achieve superior mechanical properties such as strength in tensile property and firmness of the friction stir welding joint on alloys of aluminium (AA6063).The investigations are devised by the Taguchi design concept. Three-factor and three-level design

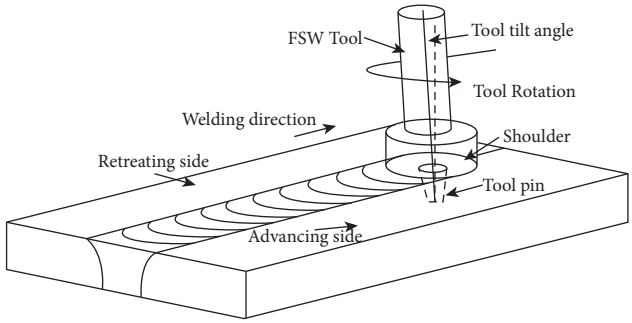

Figure 1: General arrangement of FSW.

Table 1: Taguchi L9 orthogonal array.

Trial no.	Taguchi L9 (parameters = 3 and levels = 3)		
	Rotational speed	Welding speed	Tool tilt angle
1	560	60	0
2	560	80	1
3	560	100	2
4	730	60	1
5	730	80	2
6	730	100	0
7	900	60	2
8	900	80	0
9	900	100	1

matrices have been developed by using MINITAB 17 software package.

The tool is not consumed in the FSW process when mixing and joining the workpiece materials. As a result, it is referred to as nonconsumable tool. The tool with the pin in the shoulder is introduced to the neighbouring edges of the plate and moved in a line until it reaches the conclusion of the process [14–21]. Because of its energy efficiency and economic considerations, it is a cutting-edge approach in the metal joining process. The general arrangement of solid-state joining techniques is depicted in Figure 1.

2. Methodology

2.1. Needs of DOE. DOE, or design of experiments, is used in a variety of industries, such as in the improvement and optimization of manufacturing processes. The fabrication of wafers in the electronics business, the manufacturing of engines in the auto industry, and the blending of substances in the pharmaceutical sector are all common examples.

2.1.1. Taguchi Orthogonal Array. Orthogonal arrays are a type of conventional experimental design that only takes a minimal number of trials to determine the primary elements that influence output, as shown in Table 1. The 9-run array is preferable (if cost and time allow) because each level of any one parameter gets evaluated along with all three levels of the other parameters. Of course, either array here is less expensive to perform than a full factorial analysis, because a full factorial analysis requires $N = L^P = 3^3 = 27$ runs.

Table 2: Chemical composition of AA 6063.

Elements	Si	Fe	Cu	Mn	Mg	Cr	Zn	Ti	Al
Percentage	0.2–0.6	0.35	0.1	0.1	0.45–0.9	0.1	0.1	0.1	Rem

Variables are assigned to columns based on the primary factor, as specified by the orthogonal array.

3. Experimental Work

The materials utilized in this experiment were 6 mm thick aluminium alloy AA6063-T6 plates. For friction stir welding, the rolled plates were cut and machined into the appropriate shapes of 120 mm long and 100 mm broad. Welding was done on an FSW machine, which uses a tool with a design that fits the job. Table 2 shows chemical composition of AA6063.

Tool RS, tool TS, and TTA are the process parameters. FSW was performed using a cylindrical tool that is made of high-speed steel (HSS) with a threaded pin along a 16 mm shoulder diameter, 5.7 mm length in pin, and 6 mm diameter in pin (Figure 2). The pin was positioned in the joint line's middle. Figure 3 shows FSW arrangements.

3.1. Procedure Parameters and Its Levels. The experiments were designed using Taguchi's method [22, 23]. Throughout three different parameters and three different levels, an orthogonal array of L9 was employed. The range of parameters was determined based on multiple experimental trials [24–30]. The independently variable major process parameters that govern aspect ratio were discovered. The Taguchi orthogonal array selector for the parameters and its levels are given in Table 3.

4. Results and Analysis

4.1. Tensile Test. Each welded plate was made to tensile test specimens in line with ASTM E8M-04 specifications. The proportions of the testing specimen in tensile property are shown in Figure 4. Tensile test specimens are described in Figure 4 which were made with a wire cut EDM. Tensile specimens in transverse section with a length of gauge having 57 mm and a width of 13 mm were made from the weld samples (overall length: 136 mm). Nine illustrative specimens were tensile-tested at a nominal ambient room temperature with a universal tensile testing machine. Figure 5 shows the ASTM standard tensile specimen.

The tensile test findings for the experiment are shown in Table 4 and Figure 6.

4.2. Hardness Test. The Vickers microhardness testing machine was assessed to assess microfirmness values along the welded zone of samples. Vickers microhardness testing technique IS: 1501 was used to take hardness measurements at various places with an applied load of 100 gm. A square-based pyramid diamond intender with an angle of apex about 136° is utilized in Vickers test. The indenter is pressed through the surface of the specimen for 10 to 15 seconds

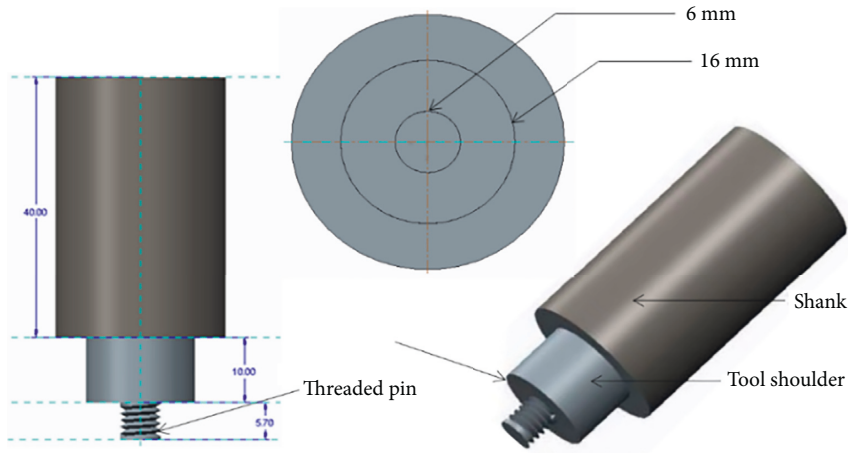

Figure 2: Geometry of the FSW tool.

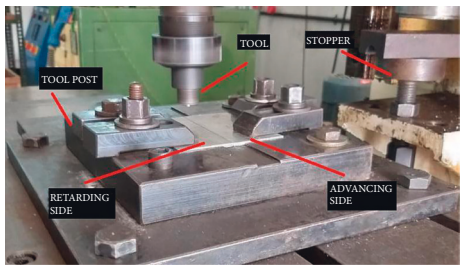

Figure 3: General arrangement of FSW.

Table 3: Process parameters and design levels.

S. no.	Parameters	Levels		
		1	2	3
1	RS (rpm)	560	730	900
2	WS (mm/min)	60	80	100
3	TTA (degree)	0	1	2

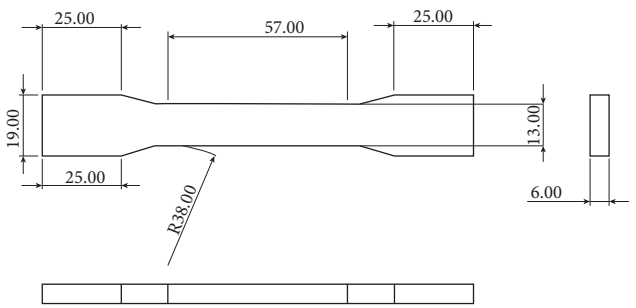

Figure 4: Dimensions of the tensile specimen.

Figure 5: Tensile specimen.

under force. The indentation diagonals d (mm^2) are measured following the load provided, and the indenter is withdrawn. The hardness number of Vickers HV is obtained

Table 4: Tensile test results obtained for various tensile specimens.

Trial no.	RS (rpm)	WS (mm/min)	TTA (degree)	Ultimate tensile strength (N/mm^2)
1	560	60	0	286.15
2	560	80	1	235.89
3	560	100	2	120.57
4	730	60	1	205
5	730	80	2	107.69
6	730	100	0	151.28
7	900	60	2	130
8	900	80	0	133.33
9	900	100	1	233.33

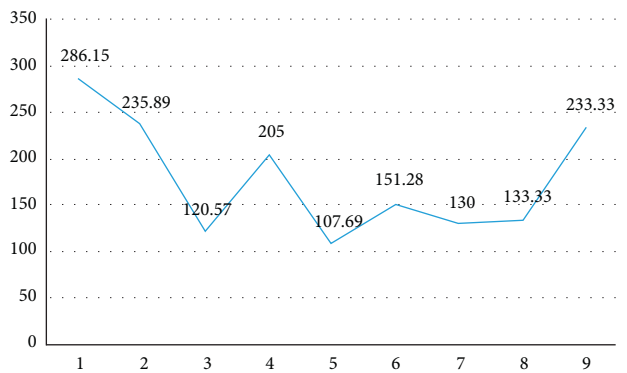

Figure 6: Graph of tensile strength.

by splitting the applied load F (kgf) by the exterior surface area A of the indentation (mm). As a result, the HV is given in Table 5 and Figure 7.

4.3. Analysis of S/N Ratio.

$$\frac{S}{N} = -10\log_{10}\left(\frac{1}{n}\sum_{i=1}^{n}\frac{1}{Y_i^2}\right). \quad (1)$$

Table 5: Hardness test results.

Trial no.	Rotational speed (rpm)	Welding speed (mm/min)	Tool tilt angle (degree)	Hardness (HV)
1	560	60	0	86.12
2	560	80	1	93.25
3	560	100	2	81.45
4	730	60	1	86.12
5	730	80	2	89.02
6	730	100	0	84.12
7	900	60	2	80.25
8	900	80	0	85.35
9	900	100	1	87.35

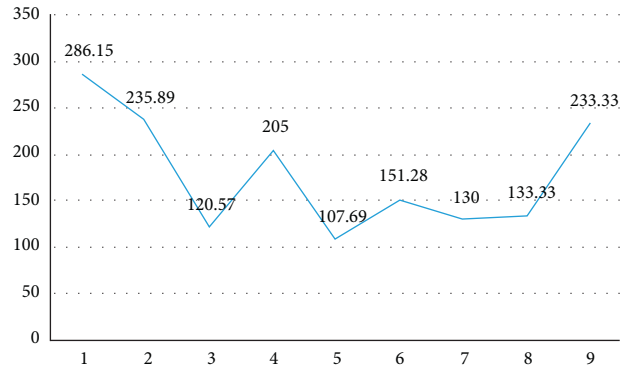

Figure 7: Graph of hardness.

Table 6: Response values and S/N ratio values for experiments.

Exp. no.	Rotational speed (RPM)	Welding speed (mm/min)	Tool tilt angle (degree)	Tensile strength (MPa)	Hardness (HV)	S/N ratio
1	560	60	0	286.15	86	41.3247
2	560	80	1	235.89	93	41.7525
3	560	100	2	120.51	81	39.561
4	730	60	1	205	86	40.9962
5	730	80	2	107.69	89	39.7372
6	730	100	0	151.28	84	40.3288
7	900	60	2	130	80	39.6774
8	900	80	0	133.33	85	40.1175
9	900	100	1	233.33	87	41.2353

Table 7: Response table for signal to noise ratios.

Levels	RS (rpm)	WS (mm/min)	TTA (degree)
1	40.88	40.67	40.59
2	40.35	40.54	41.33
3	40.34	40.38	39.66
Delta	0.54	0.29	1.67
Rank	2	3	1
Larger is better			

Taking the first trial, $-10\ \log10\ [1/2 \times ((1/286.152) + (1/862))] = 41.32$ dB.

Table 6 shows response values and S/N ratio outcomes for experiments. A high S/N number corresponds to better performance regardless of the performance characteristic category. Table 7 shows the outcomes of creating a response table for RS, WS, and TTA in an integrated way.

The most significant factor, according to the delta values from Table 6, is angle, of tool tilt following the rotary velocity, and finally welding speed. The main effect plots displayed in Figures 8–10 were created using MINITAB 17 software and the answer statistics and ratio of s/n values from Table 6.

The larger-the-better criterion was used to calculate S/N ratio values. In a major effect plot, if the line's inclination is higher, the corresponding parameters are more significant, and if the line's inclination is lower, the impacts of the corresponding factor are lower. The major effect graphs at the highest S/N ratio values of response variables corresponding to each factor can be used to determine the best parametric setting. The best condition is $A1$, $B1$, and $C2$ (i.e., rotary speed (A) = 560 RPM, speed of welding (B) = 60 mm/min, and angle of tool tilt (C) = 1 degree).

4.4. Analysis of Variance (ANOVA). The F value is utilized to trail the importance of an element in the ANOVA (Table 8) by set side-by-side model variance along with the variance of residual (derived by splitting the model's mean square through the mean square of residue) [31–33]. If the difference in the value is close in proximity to one another, the ratio obtained would be close to one, and any of the factors will be less likely to have a substantial impact on the response. A higher value of F for a limiting factor indicates that the limiting factor has a larger consequence on the characteristics. The maximum value of F in the operation is obtained through a tool tilt angle of 9.22, as shown in Table 8. Table 9 and Figure 11 show the optimum condition and percentage contribution of parameters.

$$\text{Percentage contribution}\,(P) = \left(\frac{SS'A}{SST}\right) \times 100. \tag{2}$$

Rotational speed (rpm) = 0.5634/5.3458 × 100 = 10.5%.
Welding speed (mm/min) = 0.1276/5.3458 × 100 = 2.3%.
Tool tilt angle (degree) = 4.1996/5.3458 × 100 = 78.5%.
Error (E) = 0.4553/5.3458 × 100 = 8.5%.

4.5. Regression Model Analysis. Regression equations for output response, respectively, as shown in Tables 10 and 11, give actual and predicted value of tensile and hardness.

Tensile strength (MPa) = 395 − 0.143 RS (RPM) − 0.97 WS (mm/min) − 35.4 tool tilt angle (degree).

Hardness (HV) = 92.2 − 0.0078 RS (RPM) + 0.0000 WS (mm/min) − 0.83 tool tilt angle (degree).

Taking the first trail, tensile strength (MPa) = 395 − 0.143 (560) − 0.97 (60) − 35.4 (0) = 256.75 MPA.

Hardness (HV) = 92.2 − 0.0078 (560) + 0.000 (60) − 0.83 (0) = 87.83 = 88 Hv.

In a coordinate plane, the graph plot shows ordered pairs of X and Y variables. It provides a clear visual representation of the relationship between the two variables and aids in regression model interpretation. The experimental and

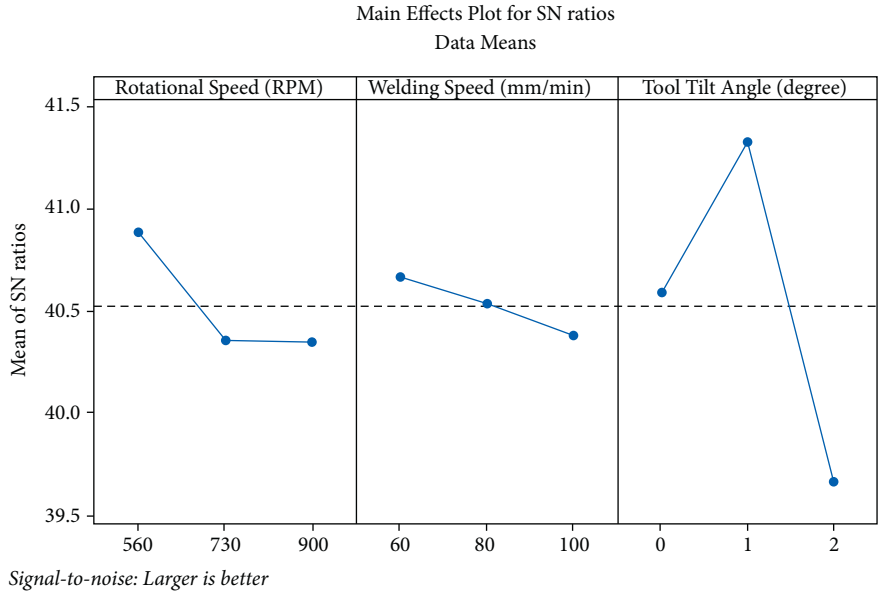

Figure 8: The main effect plots for SN ratios.

Table 8: Analysis of variance for S/N ratios.

Sources	DF	Adj SS	Adj MS	*F*	*P*
Rotational speed (RPM)	2	0.5634	0.28168	1.24	0.447
Welding speed (mm/min)	2	0.1276	0.06378	0.28	0.781
Tool tilt angle (degree)	2	4.1996	2.0998	9.22	0.098
Residual error	2	0.4553	0.22765		
Total	8	5.3458			

Table 9: Optimum condition and percentage contribution of parameters.

S. no.	Factors	Level description	Rank	Contribution (%)
1	Rotational speed (rpm)	560	2	10.50
2	Welding speed (mm/min)	60	3	2.30
3	Tool tilt angle (degree)	1	1	78.50

anticipated weld strength and hardness values obtained from the regression models are plotted and are practically identical in Figures 12 and 13, indicating that the constructed regression models are well-fitted.

5. Interaction Effects of Process Variables

Figures 12 and 13 show the interaction effects of the specified process factors on tensile strength. Tensile strength is less affected by RS and WS. Tensile strength is mostly affected by RS and tool tilt angle.

The impact of rotating speed and welding speed on hardness is reduced, as shown in Figures 14 and 15. The impact of rotary velocity and angle of tool tilt on hardness is greater.

Table 10: Actual values and predicted values of tensile strength.

Exp. no.	Tensile strength (MPa)	
	Actual value	Predicted value
1	286.15	256.72
2	235.89	201.92
3	120.57	147.12
4	205	197.01
5	107.69	142.21
6	151.28	193.61
7	130	137.3
8	133.33	188.7
9	233.33	133.9

Table 11: Actual values and predicted values of hardness.

Exp. no.	Hardness values	
Actual value	Predicted value	
1	86	88
2	93	87
3	81	86
4	86	85
5	89	85
6	84	86
7	80	83
8	85	85
9	87	84

6. Metallographic Observations

The distinct zones in microstructure of the welded samples are studied using metallographic inspection of transverse cross sections [34–37]. Due to differences in grain size and orientation, various microstructural zones listed as stir zone (SZ), heat-affected zone (HAZ), and thermo-mechanically

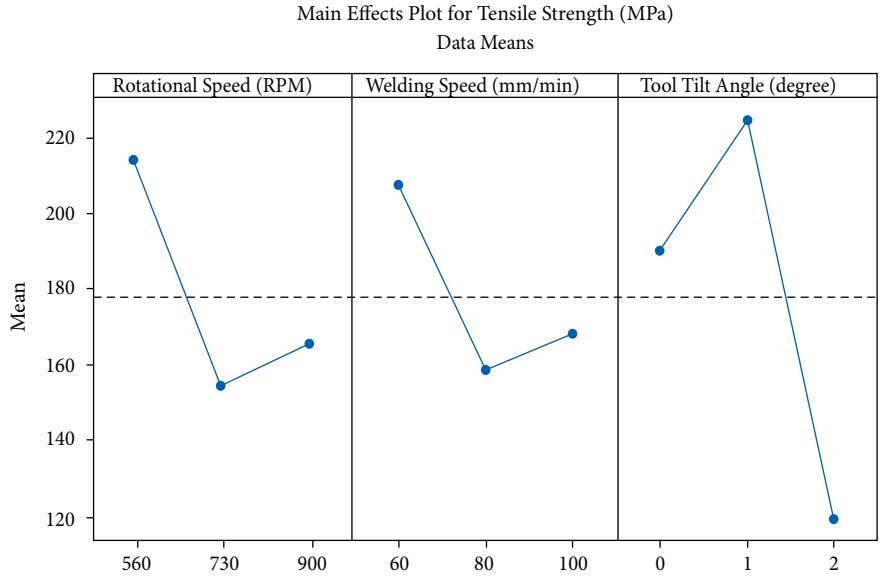

Figure 9: The main effect plots for tensile strength (MPa).

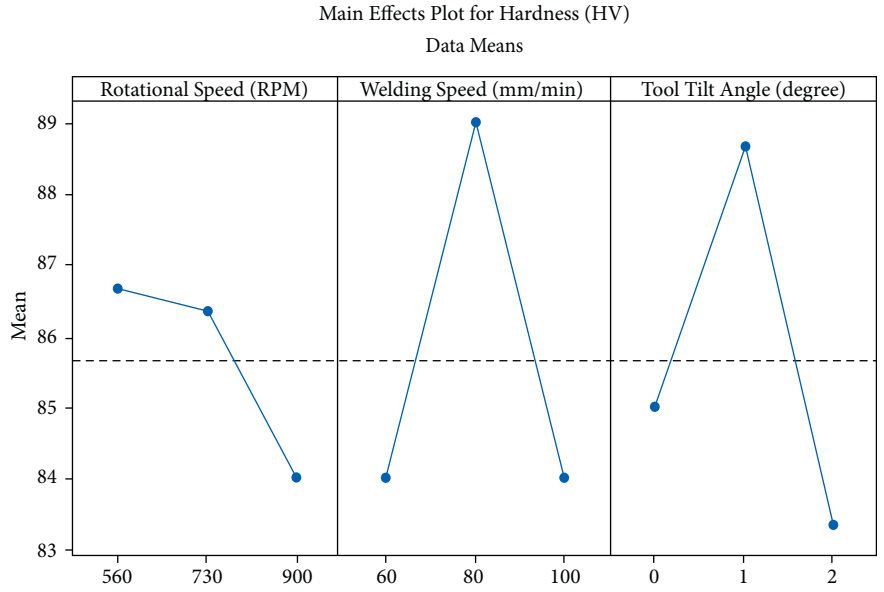

Figure 10: The main effect plots for hardness (HV).

affected zone (TMAZ) of comparable FS welded joints have been found using scanning electron microscopy (SEM). There is a distinct interaction between the HAZ, TMAZ, and SZ regions of the FSW joint (Figure 16).

According to ASTM E-2142, the microstructural study was done in the transverse (YZ) plane. The material was segmented in the proper direction, installed, and cleaned to remove any remaining cutting damage. It was enough to finish the polishing procedure with a quick chemical polish in the OPS solution before etching in a solution of 4 ml HF, 4 ml H2SO4, and 2 g CrO3 in 90 ml water for optical microscopy. Electro polishing the sample in 30 percent nitric acid/methanol for 20–30 seconds was required for the more demanding requirements of scanning electron microscopy (SEM). A Philips XL30 FEGSEM, interfaced to a HKL channel EBSD system, was used to generate SEM pictures and electron backscatter diffraction (EBSD) patterns at 15–30 kV and a current of roughly 4 nA.

Figure 17 indicates that the grains in the stir region are fine and equiaxed, whereas the other regions have higher mechanical strength and ductility. During the FSW process, TMAZ is exposed to both temperature and deformation. Due to insufficient heating, recrystallization did not occur in this zone, albeit, it did undergo some plastic deformation.

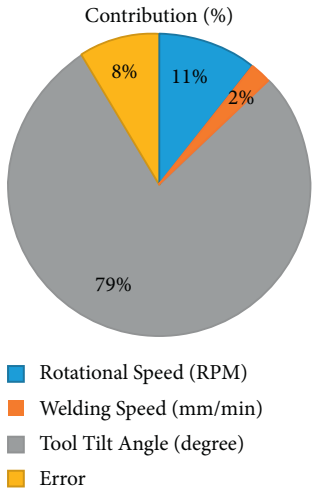

Figure 11: Contribution of process parameters.

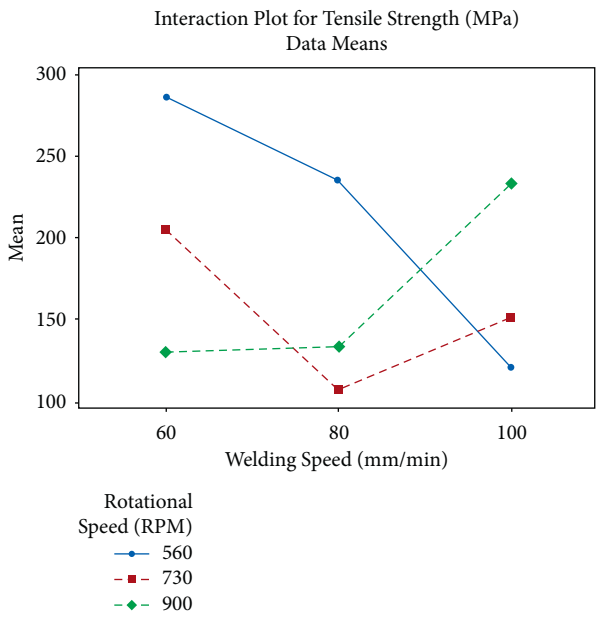

Figure 12: Interaction effects of rotational speed and welding speed on tensile strength.

Mechanical processes have no influence on the HAZ, and there is no plastic deformation in the HAZ [38].

The number of tunnels and pores grows as welding speed increases and flaws travel upright to the aluminium weld nugget [39]. Due to the tool's lesser time to plasticize and reframe the substances around the pin, and as the highest temperature of the weld drops, the flow stress of the materials rises, resulting in nonsufficient deformation in plasticity of the material at the welding area [40]. In this case, the tool is unable to complete the line of weld and consolidate materials in the zone of welding, resulting in the formation of a tunnel.

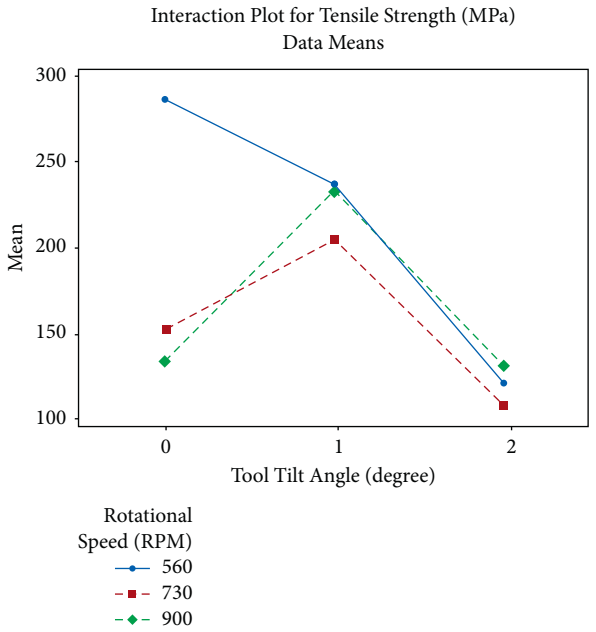

Figure 13: Interaction effects of rotational speed and tool tilt angle on tensile strength.

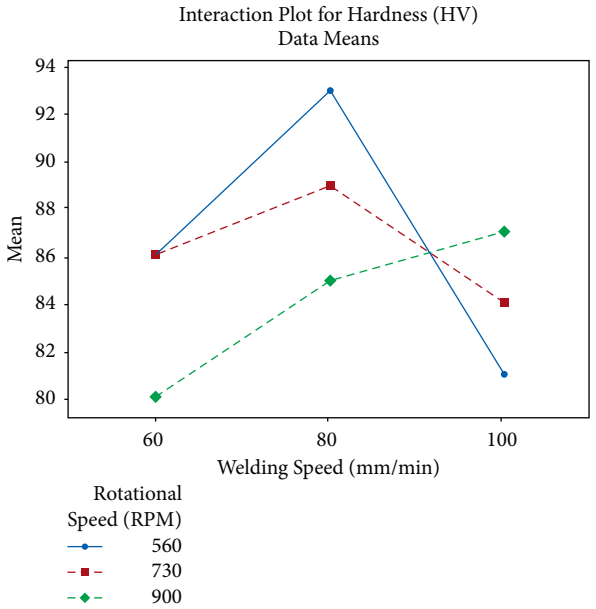

Figure 14: Interaction effects of rotational speed and welding speed on hardness.

The analysis of elements or chemical characteristics of a substance is carried out using energy dispersive X-ray analysis (EDXA). It is relied on an interactivity between an X-ray source and a sample. The fundamental conception is that each element possesses a distinctive atomic structure, allowing for a unique set of peaks on its electromagnetic emission spectrum, is predicted to play a large role in its

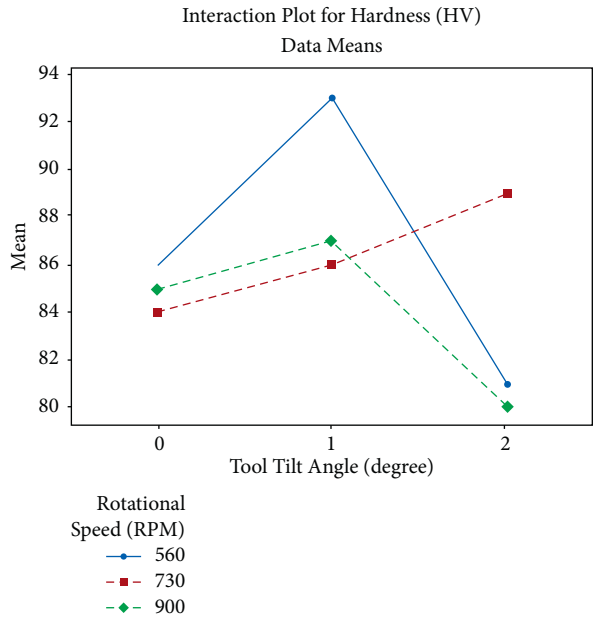

Figure 15: Interaction effects of rotational speed and tool tilt angle on hardness.

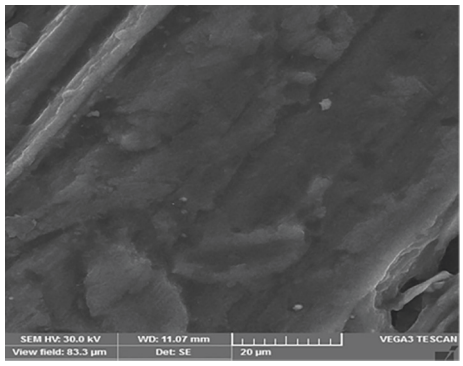

Figure 16: Microstructures of HAZ + TMAZ of the FS welded joint.

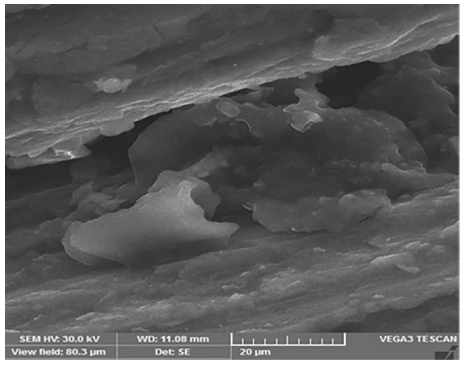

Figure 17: Microstructures of TMAZ + HAZ of the FS welded joint.

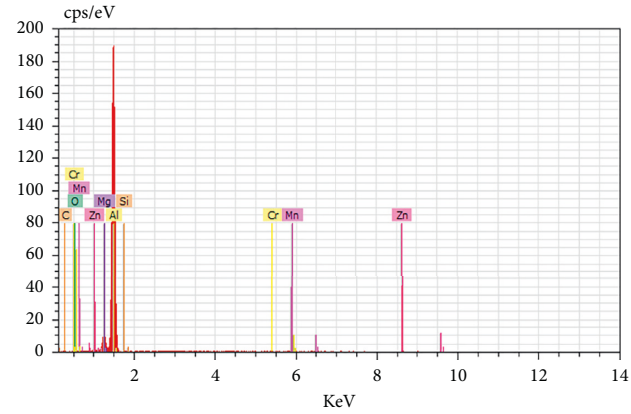

Figure 18: EDX mappings of the FS welded joint.

portrayal capabilities. The EDX (Figure 18) analysis is effective for identifying materials and impurities, as well as determining their relative concentrations on the specimen's surface.

7. Conclusion

With experimental analysis and outcomes, a thorough experimental inquiry is processed to assess the effect of major FSW processive parameters. The Taguchi L9 orthogonal planned experiments have been offered as a method of determining the FSW parameters for welded aluminium alloy (6063) joints. The ANOVA table and main effect charts reveal that tool tilt angle and rotary velocity have a notable impact on tensile strength and hardness. Welding speed has a smaller impact.

The processive parameters were tuned for maximum tensile strength and hardness of the welded connection, with 560 rpm, 60 mm/min, and 1 degree as the best levels of tool rotating velocity, speed of welding, and angle of tool tilt, respectively. In addition, the predictions generated by regression analysis are very similar to the comparison results.

Data Availability

All data generated or analysed during this study are included in this article.

Conflicts of Interest

The authors declare that they have no conflicts of interest.

References

[1] R. Arun Kumar, S. Ramesh, E. Kedarvignesh, M. Aravind Arulchelvam, and S Anjunath, "Review of friction stir processing of magnesium alloys," *Materials Today Proceedings*, vol. 16, pp. 1320–1324, 2019.

[2] J. W Choi, H. Liu, and H. Fujii, "Dissimilar friction stir welding of pure Ti and pure Al," *Materials Science and Engineering A*, vol. 730, pp. 168–176, 2018.

[3] J. Li, M. Su, W. Qi et al., "Mechanical property and characterization of 7A04-T6 aluminum alloys bonded by friction stir welding," *Journal of Manufacturing Processes*, vol. 52,

pp. 263–269, 2020, https://doi.org/10.1016/j.jmapro.2020.02.018.

[4] G. Çam, V. Javaheri, and A. Heidarzadeh, "Advances in FSW and FSSW of dissimilar Al-alloy plates," *Journal of Adhesion Science and Technology*, 2022.

[5] G. Çam and G. Ipekoglu, "Recent developments in joining of aluminum alloys," *International Journal of Advanced Manufacturing Technology*, vol. 91, no. 5-8, pp. 1851–1866, 2017.

[6] N. Kashaev, V. Ventzke, and G. Çam, "Prospects of laser beam welding and friction stir welding processes for aluminum airframe structural applications," *Journal of Manufacturing Processes*, vol. 36, pp. 571–600, 2018.

[7] G. Çam, G. Ipekoglu, and H. Tarık Serindağ, "Effects of use of higher strength interlayer and external cooling on properties of friction stir welded AA6061-T6 joints," *Science and Technology of Welding & Joining*, vol. 19, no. 8, pp. 715–720, 2014.

[8] T. Kucukomeroglu, S. M. Aktarer, G. Ipekoglu, and G. Çam, "Mechanical properties of friction stir welded St 37 and St 44 steel joints," *Materials Testing*, vol. 60, no. 12, pp. 1163–1170, 2018a.

[9] G. Çam, V. Ventzke, J. F. dos Santos, M. Koçak, G. Jennequin, and P. Gonthier-Maurin, "Characterisation of electron beam welded aluminium alloys," *Science and Technology of Welding & Joining*, vol. 4, no. 5, pp. 317–323, 1999.

[10] G. Çam and M. Koçak, "Microstructural and mechanical characterization of electron beam welded Al-alloy 7020," *Journal of Materials Science*, vol. 42, no. 17, pp. 7154–7161, 2007.

[11] G. Ipekoğlu and G. Çam, "Formation of weld defects in cold metal transfer arc welded 7075-T6 plates and its effect on joint performance," *IOP Conference Series: Materials Science and Engineering*, vol. 629, no. 1, Article ID 012007, 2019.

[12] D. M. Rodrigues, C. Leitão, R. Louro, H. Gouveia, and A. Loureiro, "High speed friction stir welding of Aluminium alloys," *Science and Technology of Welding & Joining*, vol. 15, 2010.

[13] E. Paduan Alves, F. Piorino Neto, and Y. An Chen, "Welding of AA1050 aluminum with AISI 304 stainless steel by rotary friction welding process," *J. Aerosp.Technol. Manag., São José dos Campos*, vol. 2, no. 3, 2010.

[14] A. Heidarzadeh, A. Chabok, and Y. Pei, "Friction stir welding of monel alloy at different heat input conditions: microstructural mechanisms and tensile behavior," *Materials Letters*, vol. 245, pp. 94–97, 2019.

[15] S. P. Jani, A. S. Jose, C. Rajaganapathy, and M. A. Khan, "A polymer resin matrix modified by coconut filler and its effect on structural behavior of glass fiber-reinforced polymer composites," *Iranian Polymer Journal (English Edition)*, vol. 31, no. 7, pp. 857–867, 2022.

[16] M. Kumar, A. Das, and R. Ballav, "Influence of interlayer on microstructure and mechanical properties of friction stir welded dissimilar joints: a review," *Materials Today Proceedings*, vol. 26, pp. 2123–2129, 2020.

[17] K. P. Mehta, P. Carlone, A. Astarita, F. Scherillo, F. Rubino, and P. Vora, "Conventional and cooling assisted friction stir welding of AA6061 and AZ31B alloys," *Materials Science*, vol. 759, 2019.

[18] M. Vural, A. Ogur, G. Cam, and C. Ozarpa, "On the friction stir welding of Aluminium alloys EN AW 2024-0 and EN AW 5754-H22," *Archives of Materials Science and Engineering*, vol. 28, no. Issue 1, January 2007.

[19] M. Prasad, V. R. Durga, and K. Kumar Namala, "Process parameters optimization in friction stir welding by ANOVA," in *Materials Today: Proceedings*, pp. 4824–4831, Elsevier, Amsterdam, Netherlands, 2018.

[20] P. Sathiya, S. Aravindan, and A. Noorul Haq, "Friction welding of austenitic stainless steel and optimization of weld quality," *International Symposium of Research Students on Materials Science and Engineering December*, 2004.

[21] S. G. Arul, S. F. Miller, G. H. Kruger, T.-Y. Pan, P. K. Mallick, and A. J. Shih, "Experimental study of joint performance in spot friction welding of 6111-T4 Aluminium alloy," *Science and Technology of Welding & Joining*, vol. 13, no. 7, pp. 629–637, 2008.

[22] D. Muruganandam, K. S. Sreenivasan, S. Ravi Kumar, S. Das, and V Seshagiri Rao, "Study of process parameters in friction stir welding of dissimilar Aluminium alloys," in *Proceedings of the International 26 Conference on Industrial Engineering and Operations Management Kuala Lumpur*, Malaysia, January 2011.

[23] M. Merzoug, M. Mazari, L. Berrahal, and A. Imad, "Parametric studies of the process of friction spot stir welding of Aluminium 6060-T5 alloys," *Materials & Design*, vol. 31, no. 6, pp. 3023–3028, 2010.

[24] G. Ipekoglu, S. Erim, and G. Çam, "Investigation into the influence of post-weld heat treatment on the friction stir welded AA6061 Al-alloy plates with different temper conditions," *Metallurgical and Materials Transactions A*, vol. 45, no. 2, pp. 864–877, 2014a.

[25] G. Çam, H. T. Serindag, A. Çakan, S. Mistikoglu, and H. Yavuz, "The effect of weld parameters on friction stir welding of brass plates," *Mat.-wiss. u. Werkstofftech*, vol. 39, no. 6, pp. 394–399, 2008.

[26] T. Rajkumar, A. Godwin Antony, P. Parameswaran, S. Dinesh, and K. Rajaguru, "Influence of tool Geometry in microstructure and mechanical properties of AA2024 alloy," *Friction Stir Welding" Test Engineering and Management*, vol. 83, pp. 25551–25556, 2020.

[27] R. Abrahams, J. Mikhail, and P. Fasihi, "Effect of friction stir process parameters on the mechanical properties of 5005-H34 and 7075-T651 Aluminium Alloys," *Materials Science and Engineering*, vol. 751, pp. 363–373, 2019.

[28] K. E. Ahmed, Bm. Nagesh, B. S. Raju, and D. N. Drakshayani, "Studies on the effect of welding parameters for friction stir welded AA6082 reinforced with aluminium oxide," in *Materials Today: Proceedings*, pp. 108–119, Elsevier, Amsterdam, Netherlands, 2020.

[29] K. A. Babu, P. Venkataramaiah, P. Dileep, and P. Dileep, "AHP-DENG'S similarity based optimization of WEDM process parameters of Al/SiCp composite," *American Journal of Materials Science and Technology*, vol. 6, no. 1, pp. 1–14, 2017.

[30] C. Chanakyan, S. Sivasankar, M. Meignanamoorthy, M. Ravichandran, and M. Muralidharan, "Experimental investigation on influence of process parameter on friction stir processing of AA6082 using response surface methodology," in *Materials Today: Proceedings*, pp. 231–236, Elsevier, Amsterdam, Netherlands, 2020.

[31] S. Rajeshkannan, M. Vigneshkumar, V. Gopal, and S. Ramesh, "Optimization and mechanical characterization of AA5083 and AA7075 dissimilar aluminium alloy joints produced by friction stir welding," *International Journal of Vehicle Structures & Systems*, vol. 13, no. 3, pp. 335–340, 2021.

[32] A. Kumar, "Optimization of process parameter for AA6061 alloy during friction stir processing," *Materials Today Proceedings*, vol. 46, pp. 9164–9167, 2021.

[33] M. M. Asif, K. A. Shrikrishna, and P. Sathiya, "Optimization of process parameters of friction welding of UNS S31803 duplex stainless steels joints," *Advances in Manufacturing*, vol. 4, no. 1, pp. 55–65, 2016.

[34] T. Kucukomeroglu, S. M. Aktarer, G. Ipekoglu, and G. Çam, "Microstructure and mechanical properties of friction stir welded St52 steel joints," *International Journal of Minerals, Metallurgy and Materials*, vol. 25, no. 12, pp. 1457–1464, 2018b.

[35] G. Ipekoglu, S. Erim, and G. Çam, "Effects of temper condition and post weld heat treatment on the microstructure and mechanical properties of friction stir butt welded AA7075 Al-alloy plates," *International Journal of Advanced Manufacturing Technology*, vol. 70, no. 1-4, pp. 201–213, 2014b.

[36] G. Çam, S. Mistikoglu, and M. Pakdil, "Microstructural and mechanical characterization of friction stir butt joint welded 63%Cu-37%Zn brass plate," *Welding Journal*, vol. 88, no. 11, pp. 225s–232s, 2009.

[37] T. Rajkumar, K. Raja, K. Lingadurai, S. D. Vetrivel, and A. G. Antony, "Interfacial microstructure analysis of AA2024 welded joints by friction stir welding," *Journal of New Materials for Electrochemical Systems*, vol. 23, no. 2, pp. 123–132, 2020.

[38] R. Nandan, T. Debroy, and H. Bhadeshia, "Recent advances in friction stir welding – process, weldment structure and properties," *Progress in Materials Science*, vol. 53, no. 6, pp. 980–1023, 2008.

[39] S. K. Dewangan, M. K. Tripathi, and M. K. Manoj, "Effect of welding speeds on microstructure and mechanical properties of dissimilar friction stir welding of AA7075 and AA5083 alloy," *Materials Today Proceedings*, vol. 27, pp. 2713–2717, 2020.

[40] J. Adamowski, C. Gambaro, E. Lertora, M. Ponte, and M. Szkodo, "Analysis of FSW welds made of Aluminium alloy AW 6082-T6," *Archives of Materials Science and Engineering*, vol. 28, no. Issue 8, August 2007.

Hindawi
Advances in Materials Science and Engineering
Volume 2022, Article ID 3608984, 8 pages
https://doi.org/10.1155/2022/3608984

Research Article

Improvement of Mechanical Behavior of FSW Dissimilar Aluminum Alloys by Postweld Heat Treatments

S. Prabhu,[1] **M. Naga Swapna Sri**,[2] **P. Anusha**,[2] **G. Saravanan**,[3] **K. Kannan**,[4] **and Selvaraj Manickam**[5]

[1]*Department of Electrical & Electronics Engineering, Sree Vidyanikethan Engineering College, Tirupati, India*
[2]*Department of Mechanical Engineering, P V P Siddhartha Institute of Technology, Vijayawada, India*
[3]*Department of Mechanical Engineering, Kongunadu College of Engineering and Technology, Tamilnadu, India*
[4]*Department of Physics, M.Kumarasamy College of Engineering, Karur, Tamilnadu 639 113, India*
[5]*Department of Mechanical Engineering, Bule Hora University, Ethiopia*

Correspondence should be addressed to Selvaraj Manickam; selva83selva@gmail.com

Received 28 July 2022; Revised 1 September 2022; Accepted 3 September 2022; Published 16 September 2022

Academic Editor: R. Thanigaivelan

AA6262 and AA5456 alloys are welded through friction stir weld (FSW) with process parameters of tool speed of 1200 rpm, welding speed of 25 mm/min, and tool angle of 3 degree. A cylindrical shape HSS-13 tool is used to perform the welding process To improve mechanical properties of tensile strength (TS), yield strength (YS), elongation%, hardness, and wear behavior, postweld heat treatment was conducted on the FSW sample at different temperatures from 300°C to 500°C. The influence of heat treatment (HT) changes the material characteristics. It is observed that the maximum TS (209 MPa) and YS (178 MPa) are identified when maintaining temperature 350°C on the FSW sample. The reduction in elongation of as-welded joints is entirely improved by HT, and the elongation percentage is almost increased to 5% when increasing temperature on the heat treatment process, and hardness test results exhibited that the increased hardness value (120Hv) is found at HT-300°C nugget zone distance of 0 to 5 mm range.

1. Introduction

Al6xxx and Al5xxx series are frequently used in a variety of fields, including the automobile, aviation, and aeronautical sectors because they have enough strength and corrosion resistance, producing fusion welding with enhanced mechanical characteristics and strong corrosion resistance on Al alloys, which is currently a major industry challenge. Several techniques such as liquid casting, powder metallurgy, and the FSW process are often used to create Al-based composites. The researchers have chosen an appropriate procedure among the above depending on the materials, material-reinforcement size, weight-ratio of the matrix, and purposes [1]. Fundamentally, FSW is a thermo-mechanical process that mixes the materials mechanically and thermally at the same time [2]. It was developed at TWI in the early 1990s, and it has already shown significant promise in combining materials that are typically thought of as difficult or impossible to weld [3]. Even though many of the welding techniques such as arc welding, gas welding, MIG, and TIG welding are available to join the dissimilar metals, many academicians and engineers from various businesses have focused on FSW dissimilar materials amongst Al alloys because the FSW process prevents joints from fusion defects and provides better strength than other welding techniques. The dissimilar joint properties primarily depend on the characteristics of the materials and input variables of tool and weld speed and locations of the joint, inequity of temperature, and material flow between the advancing and retreating sides [4, 5]. Ravikumar et al. selected three different shapeable tools (square, cylinder, and thread) to perform the FSW process on AA6061/AA7075 [6]. Trimble et al. have chosen a mixture of chosen parameters to generate welds and endurance at greater speeds using a T6 heat treatment experiment; various rotating speeds and tool speeds were employed in AA 2024-T3 research, and the

outcomes were better when the tool geometry had a scrolling shoulder and a tri-flute form for the pin [7]. Four-blade stirrers blade designs in CFD mostly improve tensile strength and hardness, as per Krishnan et al.'s [8] study on the effect of the design of stirrer blade on the mechanical behavior of AMCs. Delijaicov et al. identified the rotational speed and flowing rate as the most important variables that determine the heat input and material flow [9]. It has been established that changing the welding and rotating speeds reduces the hardness value in the stir zone between AA7075 and AA2024 by increasing rotational speed and reducing welding speed [10]. Hua-Bin Chen and colleagues investigated the FSW of 5456 Al under various circumstances. The plastic material was not flowing adequately and drives down nearby the pin end due to tool's small tilt angle (less than 1.5). Weld flash produced where the plastic material is being retreated, and no sufficient of plastic metal fill-up in a nugget zone was observed due to an increase in the tilt angle greater than 4.5° angle [11]. As per Goebel et al. investigation, HAZ and the border of TMAZ/SZ are extra prone to fail the thermal cyclesand give a partial precipitation in the HAZ, which is why it is weak, while residual stress causes weak bonding at the SZ/TMAZ contact [12]. Reddy et al. [13] analyzed FSW of AA7475-T761 plates, the welding centers, which has the finest microstructure, and exhibits the highest hardness value. Furthermore, according to their observations, the primary particles frequently generated in the SZ of AA7475 were MgZn2, Al2Cu, and Al2CuMg. Under various welding conditions, creation of the dissimilar welded junction of Al5083–Al 6061(T6) was done; however, due to the dissolution of precipitation-hardening segments in the weld zone as well as the impact of the postweld heat treatment technique on the improvement of the mechanical properties of the dissimilar welded Al5083–Al6061 and leading abnormal grain evolution through various factors, softening behavior developed in the weld samples [14]. Baghdadi et al. directed to enhance the mechanical characteristics of Al-Mg-Si alloy through postweld heat treatment, the potential for regulating aberrant grain growth by adjusting welding conditions. The decomposition of precipitation hardening particles in the HAZ was shown to have reduced the strength of the FSW samples in evaluation to that of the base material [15]. The UTS of AA6061-AA1100 and AA6061-AA5083 is 93 MPA and 113 MPa, respectively, after two types of dissimilar joints of these two alloys were joined using the FSW technique. In comparison to AA6061 base metal, the joint efficiency of AA6061-AA1100 and AA6061-AA5083 was 80% and 97%, respectively [16]. The FSW of AA6061 and AA1100 were studied by Jurnal Kejuruteraan et al. Welded samples were then cold rolled to various thickness reductions percentages of 10, 20, and 40%. Both the as-welded joints and the rolled specimens had no internal flaws visible from a microscopic examination of the sample's cross section [17]. Addition of small amounts of powders B4C/CeO2 to the Al matrix was done in order to increase the weld ability of the AA2XXX and AA7XXX joints [18]. However, the most popular method for enhancing the strength and formability of the FSW sheets to the necessary level is solution treatment, and aging (SA) could rise the hardness and tensile strength due to precipitation hardening [19, 20]. After studying above literature articles, it was witnessed that few articles were discussed for the influence of various FSW parameters of weld speed and tool geometry to join dissimilar Al alloys for improving mechanical characteristics. Usually, weld strength depends on the heat generated and metal mixing during the FSW process [21, 22]. Even though the weld strength and mechanical properties are dependent on FSW parameters, but after welding, internal stresses on plates will affect the strength and properties of the joint heat treatment (HT) which is one important consideration to increase joint strength. So, in this research part, we introduced different heat treatment processes by variation of temperature which change hardness, tensile strength, and also wear rate, and this effort benefits to study the effect of heat treatment on FSW AA6262 and AA5456 alloys. The dissimilar welds of AA6262/5456 are useful in many application products such as hinge pins, marine fittings, screw machine products, pressure vessels, and storage tanks.

2. Material Selection and Experimental Procedure

AA 6xxx and 5xxx series alloys such as AA6262 and AA5456 plates are chosen to join with the FSW approach, and a plate size of $120*55*4\,mm^3$ was preferred in the work. The compositions of each alloy are exposed in Table 1. The FSW process is carried out with the HSS 13 tool and possesses shoulder length* pin-length*pin size of $20*3.5*3\,mm^3$. Three variables of tool rotational speed (FTR-1200 rpm), welding speed (FWS-25 mm/min), and tool tilt angle (FTA-3 degree) are maintained. To perform welding operations, milling machine/FSW tools are fixed together, and the process of FSW schematic image is shown in Figure 1. The advancing and retreating sides are clearly mentioned in the FSW process figure. The plates 6262 and 5456 have grooves formed at their edges and are put over milling table with a clamp before operation begins. The specimens are gently penetrated with the spinning tool until the shoulder is 0.5 mm into specimen. The stated spot is fixed for 60 to 90 seconds in order to generate the required heat for the operation. Due to the production of heat at the weld location and the stirring caused by tool movement, the material enters the plastic phase, permitting the combination of the two metals. After the weld is finished, the machine setup is removed. The friction welded sample of both alloys 6262 & 5456 is shown in Figure 2. Once the FSW process is completed, the sample will go under various tests such as tensile, hardness, and wear test at different annealing temperatures or heat treatment (HT). In this work, total six HT conditions are preferred to check the weld strength and mechanical properties.

3. Mechanical Properties' Test

3.1. Tensile Test. The unwelded AA 6262 exhibited YS and TS of 230 MPa and 285 MPa, whereas YS and TS values of AA5456 are 245 MPa and 320 MPa, respectively. Universal

Table 1: AA6262 and AA5456 alloy compositions.

Chemical elements	AA6262 in %	AA5456 in %
Mn	0.15–0.20	1.2–1.5
Fe	0.7–0.9	0.45–.5
Mg	1.3–1.5	5.5–6.0
Si	0.8–1.0	0.3–0.5
Zn	0.25–0.30	0.15–0.25
Ti	0.15–0.32	0.5–0.75
Cr	0.15–0.35	0.25–0.45
Cu	0.10–0.15	0.15–0.20
Bi	0.4–0.5	-
Pb	0.8–1.5	-
Al	Balance	Balance

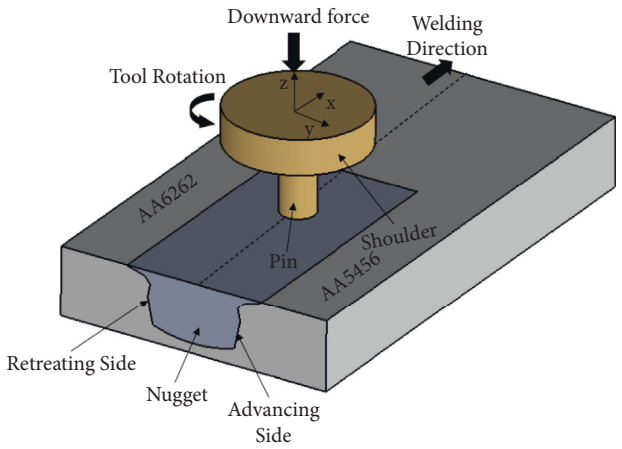

Figure 1: Schematic diagram of the friction stir welding process.

testing machine (UTM) is utilized to carry out the tensile test at room temperature. Before this particular test, we need to remove the sample from welded materials according to the standard size of ASTM-E08 in Figure 3. An extensometer (A50 grade) is attached with specimen through the help of screw mechanism for calculating elongation after applying load on the specimen. This device is able to extend the length from 10 to 60 mm; the overall tensile properties results are displayed in Table 2. The fractured specimens for tensile test are exposed in Figure 4.

3.2. Hardness Test. A material's resistance to a persistent indentation or marking by scratches is referred to as its hardness. Hardness is a value assigned to a material as a consequence of empirical testing and not a quality of the material itself. The majority of hardness tests involves the use of equipment that identifies the material while exerting a predefined force or loading. The hardness of welded composites can be found by making an impression of 1/16 indenter with 50 kg load on the surface of composites at different places on unwelded and welded areas. These experiments have been conducted on the hardness tester. The experimental works of hardness which are done by the hardness tester.

3.3. Wear Test. Wear test is performed as per standard ASTM - G99by pin on disc device to find out the wear rate or

Figure 2: Friction welded joint on AA6262 and AA5456.

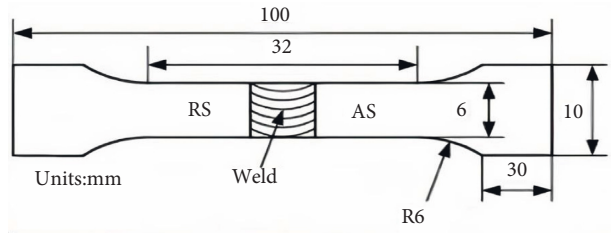

Figure 3: Tensile specimen standard dimension.

wear amount of composites at different T6 heat treatments. Welded specimens were machined as pin shapes, and it was contacted on rotating steel by applying the load of 30N; sliding speed and distance are fixed as constant values of 2.25 m/s and 50 m, respectively. Before the start of the experiment, the composite's sample weight is measured. During the process, the material is removed due to friction between the rotating disc and sample and the difference in weight after completion of an experiment which was used to calculate the wear rate for different temperatures of HT-0 to 500°C.

4. Results and Discussion

4.1. Tensile Properties. Tensile properties such as tensile strength (TS), yield Strength (YS), and elongation(%) of AA6262/5456 sample are prepared by FSW procedure. Annealing or Heat treatment (HT) is carried out on a removed sample from welded plates and mechanical properties are analyzed on welded portions of AA6262/5456 plates by a variation of temperature (300–500°C) in HT process. The result of tensile properties in Figure 5 showed that the highest TS & YS (209 MPa and 178 Mpa) are obtained while heating the sample at 350°C, when maintaining HT at 300°C and 500°C which leads to reduce the TS and YS values; the elongation of the joint is 11.25%, which displays 35% reduction in elongation compared with base metals, and after HT, elongation has developed expressively due to changes in HT temperature in Figure 6. The maximum elongation is obtained as16.21% at HT-500°C, followed by 15.25% at HT-300°C, 14.25% at HT-350°C, and the least elongation is observed in the welded section without the involvement of HT around 10.25%. However, TS values at various HT are almost near to base metals due to presence of molecules dispersed, steady precipitates that increasing tensile strength by restraining grain boundaries andinterfering of dislocation motion [23]. The relative sliding of

Table 2: Tensile properties of FSW joints at the heat treatment method.

Heat treatment on samples	Tensile strength, TS (MPa)	Yield strength, YS (MPa)	Elongation (%)
HT-0°C	201.45	162.38	10.25
HT-300°C	199.58	152.38	15.25
HT-350°C	208.26	178	14.25
HT-400°C	200.53	158	12.34
HT-450°C	197.99	167	12.99
HT-500°C	195.36	153	16.21

Figure 4: Fractured tensile specimens.

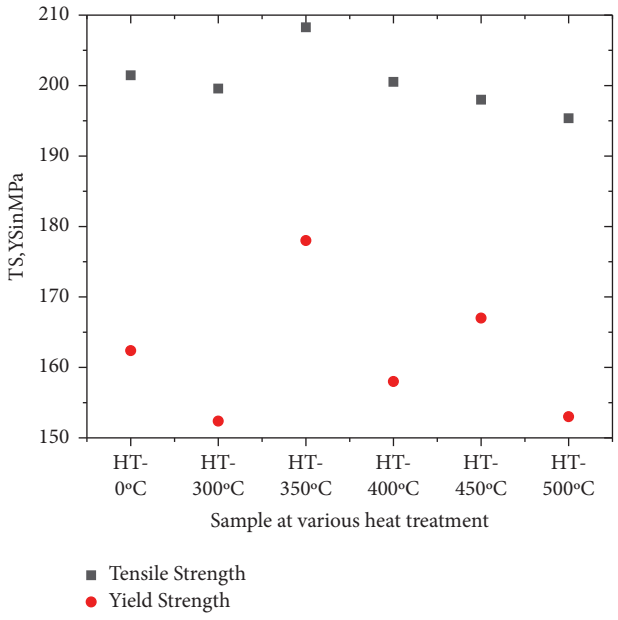

Figure 5: Tensile and yield strength values at different HT.

ordered atomic planes occurs concurrently with plastic deformation in crystalline materials. Each atom normally moves along with the slip plane by the same integral atomic distances, but the crystal's orientation does not change. The nearby packed planes and the highest atomic density are often the slip planes, and they considerably give to the complete extent of a tensile sample [24].

4.2. Fractured Surfaces. Analyzing fractured surfaces of tensile samples can reveal important details about the impact of the joints' inherent microstructural characteristics on their strength and ductility [25, 26]. The fractured surfaces of

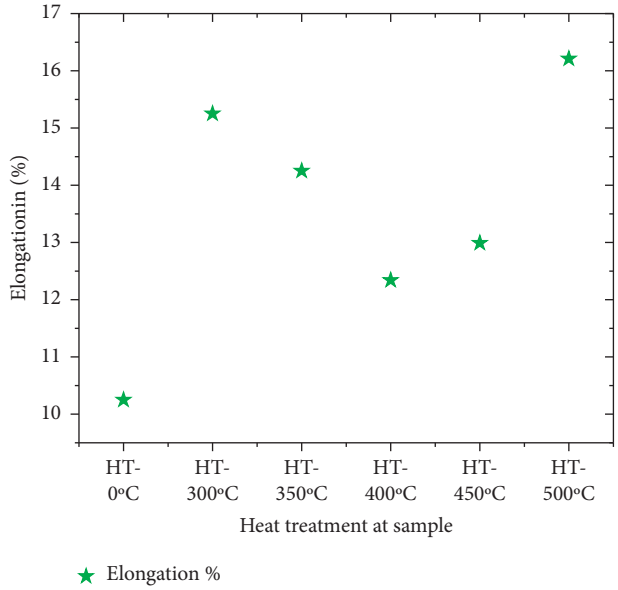

Figure 6: Elongation reading at various HT processes.

the tensile test samples at different heat treatments are analyzed using SEM. The SEM photographs of three HT processes are presented in Figures 7(a)–7(c). The random adequate microscopic cracks and more voids of size variation and shape are disseminated on the fractured surface of HT-0 joint in Figure 7(a) The cracked second-phase particles and shallow dimples are found in the fracture region shown in Figure 7(b). However, The depth and width of the observed dimples are more in the fractured face of the HT-500 joint as shown in Figure 7(c). The main factor that leads to the fracture is overload, and the coalescence of microvoids controls failure. The regions near second phase particles inclusions, the structure of grain, and displacement pileups are where the voids may form. Therefore, as the strain increases during the tensile test, the microgaps expand, combine, and ultimately create a continuous fractured surface [27]. The formation of spaced b-Mg2Si particles in the HAZ at the joint might sometimes generate dimples because more severe precipitated coarsening occurred during FSW.

4.3. Wear Test. POD is a device used to execute the wear test to estimate the wear rate (WR) of welded composites at HT (0 to 500°C). Figure 8 showed the wear rate at different HT processes and noticed that WR differs from 0.0178 to 0.0258 mm^3/Nm. Minimum intensity of WR was found at

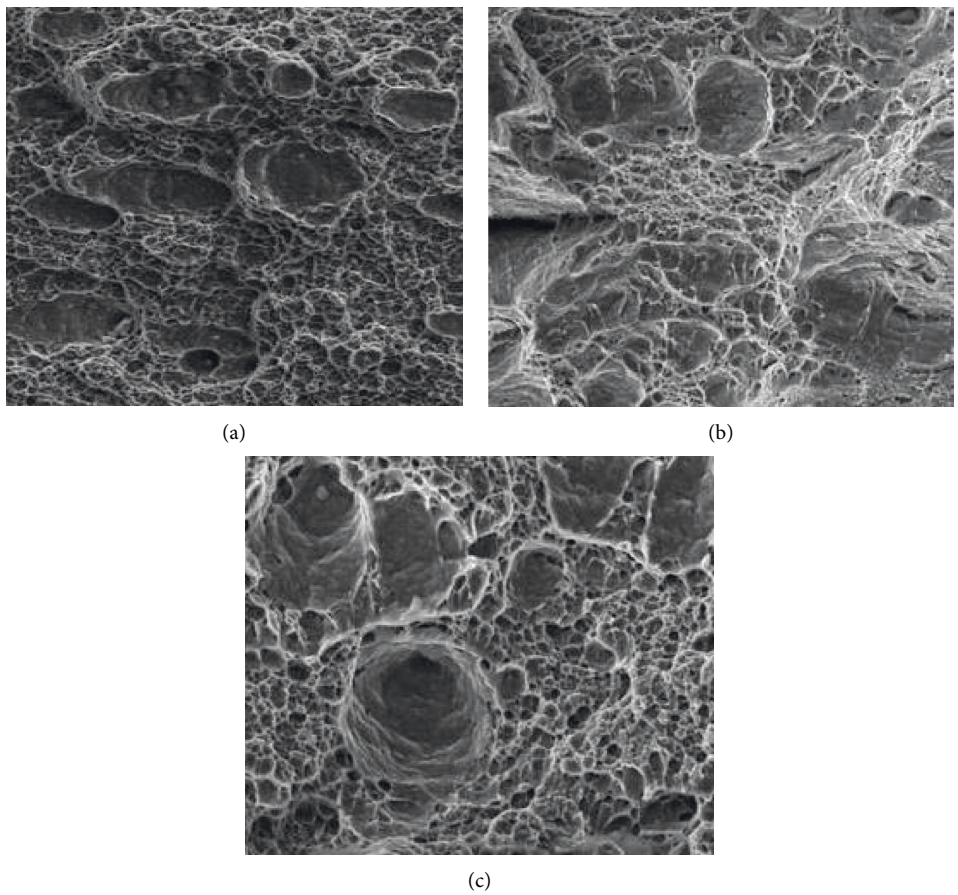

Figure 7: SEM image of the fractured surface at different joints. (a) HT-0 weld joint. (b) HT-350 weld joint. (c) HT-500 weld joint.

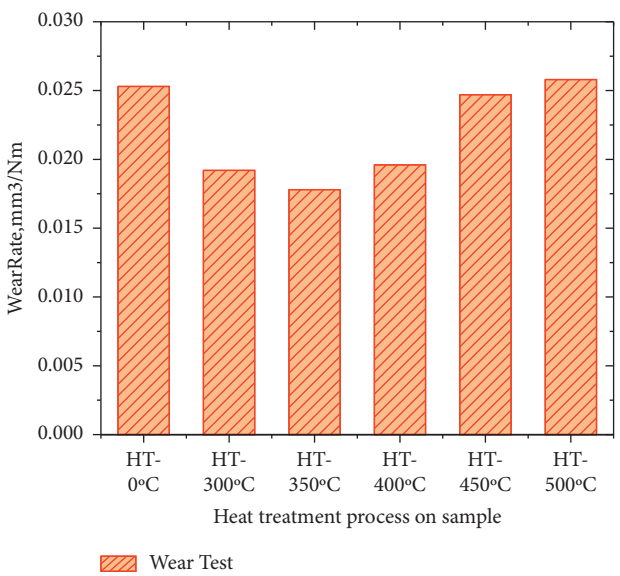

Figure 8: Wear test at sample heat treatment.

HT-350°C, and maximum WR was acknowledged at HT-500°C and HT 0°C. The increments of HT (up to 350°C) reduce the wear rate value, but after above 350°C , wear rate is increasing gradually. It was discovered that the wear rate was lessened or remained constant between the heat treatment (0 to 400°C) condition. This may be connected to compensation between the softening of joints, the loss of more material, and the hardening brought on by the transformation of a soft part into hard and the precipitation of carbides. The improvement in the wear rate seen for the test piece after heat treatment under the conditions of 400 to 500°C heat treatment could be attributed to this precipitation.

4.4. Hardness Test. Hardness (BHN) of the sample across the joint varyies depending on temperature variations in HT. The overall length of the sample from -20 mm to 20 mm is selected to conduct a hardness test in Figure 9. The maximum BHN (120Hv) is found at HT-300°C nugget zone distance of 0-5 mm range. The minimum value attained at HT-500°C in the distance of 10–15 mm. It is observed that the BHN value is two times more than that of base metals up to 350°C. The primary reason for this is the coarsening, dissolving, and reprecipitation of stronger precipitates brought on through the welding thermal cycle. Even though grain structure refinement might make a small benefit [2]. The loss of Guinier–Preston zones and the coarsening of strengthening precipitates, which is comparable to an over-aging process in HAZ, are responsible for the slightly decreased hardness. Due to a similar outcome of the solution treatment in TMAZ, considerable coarsening and potential

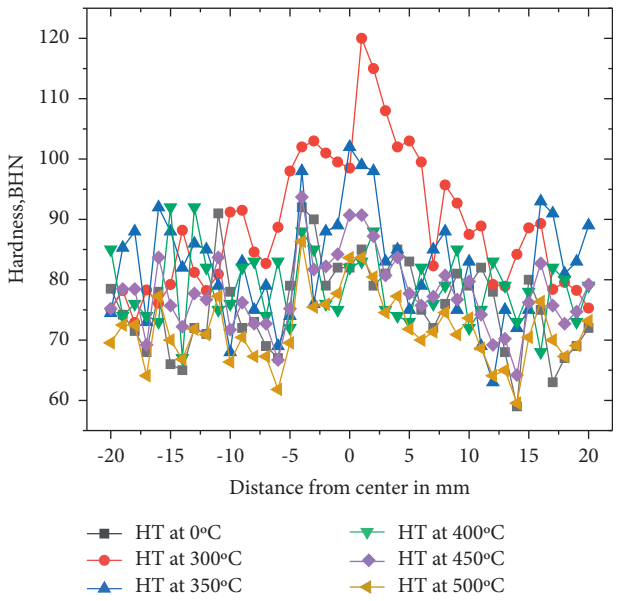

Figure 9: Hardness test result.

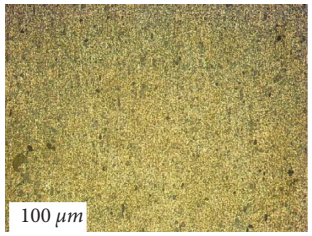

Figure 10: Optical microscope image of AA5456 alloy.

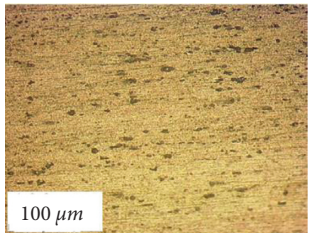

Figure 11: Optical microscope image of AA6262 alloy.

full precipitate dissolution occurred. Since the material experienced higher temperature in the nugget region, some reprecipitation after full dissolving may have occurred.

4.5. Microstructure Analysis. Figure 10 illustrates the optical microscope image of base alloy AA5456 which has a homogeneous grain size of 100 μm. Figure 11 shows a microscope image of AA6262 alloy which has a considerable amount of Mg2Si particles distributed nonhomogeneously in the grain boundaries [28]. Figure 12 showed the HT-350 condition of the microstructure image at different welding zones for AA6262 plate that make up the FSW such as the stir zone (SZ), thermomechanically affected zone (TMAZ), and heat-affected zone (HAZ and noticed that the grain size of SZ is greater than TMAZ and HAZ due to the more plastic

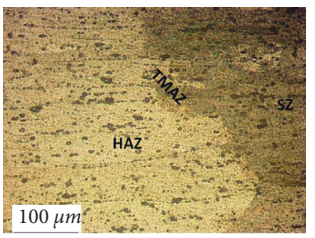

Figure 12: Optical microscope image of AA6262 at heat treatment -350°C.

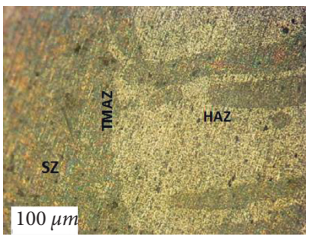

Figure 13: Optical microscope image of AA5456 at heat treatment -350°C.

deformation and moderate frictional heat input enforced on the particular areas as a result of the tool shoulder and tool pin). Figure 13 exposed the microstructure of three weld zones for AA5456plate after the HT-350 process and found that SZ grains exhibited are smaller than HAZ and TMAZ zones due to uniform distribution of particles by maintainence of the rotational speed of the pin.

5. Conclusion

In this work, the influence of heat treatment on the mechanical behavior for AA6262 and AA5456 joints was examined, and the conclusions are attained as follows:

(1) The developments of Al composites are done by the friction stir welding process. The three considerations are selected to perform welding operation such as 1200 rpm of tool rotational speed, 25 mm/min of weld speed, and 3° of tool tilt angle.

(2) The maximum tensile strength of 209 MPa was acquired when maintaining temperature (HT-350°C); similarly, supreme yield strength of the composite sample is attained at the same HT-350°C, whereas the lowest TS and YS are attained at HT-500°C and HT-300°C, respectively.

(3) The maximum values of elongation are measured at HT-500°C, followed by HT-300°C (15.25%) and HT-350°C (14.25%), respectively. The welded segment without the use of HT exhibits the least elongation, which is roughly 10.25%.

(4) The sample's hardness (BHN) varies across the joint depending on temperature fluctuation in HT. At HT-300°C (nugget zone distances of 0–5 mm range), the greatest BHN (120Hv) is discovered. The lowest BHN value was obtained at HT-500°C across a distance of 10–15 mm.

(5) POD is a tool used to carry out wear tests and calculate the wear rate of welded composites at high temperatures (0 to 500°C) WR which varied from 0.0178 to 0.0258 mm3/Nm. Maximum WR is recognized at HT-0 C & 500°C, whereas the minimum intensity of WR was discovered at HT-350°C.

Data Availability

The data used to support the findings of this study are included within the article. If further data or information arerequired, these are available from the corresponding author upon request.

Conflicts of Interest

The authors declare that there are no conflicts of interest regarding the publication of this paper.

Acknowledgments

The authors appreciate the technical assistance to complete this experimental work from the Department of Mechanical Engineering, Bule Hora University, Ethiopia. The author thanks P V P Siddhartha Institute of Technology and Sree Vidyanikethan Engineering College, Andhra Pradesh, for the support of draft writing. It was performed as a part of the Employment Bule Hora University, Ethiopia.

References

[1] J. W. Kaczmar, K. Pietrzak, and W. Włosiński, "The production and application of metal matrix composite materials," *Journal of Materials Processing Technology*, vol. 106, no. 1–3, pp. 58–67, 2000.

[2] Y. S. Sato, H. Kokawa, M. Enomoto, and S. Jogan, "Microstructural evolution of 6063 aluminum during friction-stir welding," *Metallurgical and Materials Transactions A*, vol. 30, no. 9, pp. 2429–2437, 1999.

[3] W. M. Thomas, E. D. Nicholas, J. C. Needham, M. G. Murch, P. Templesmith, and C. J. Dawes, *Friction-stir butt welding*, Vol. 8, G.B. Patent 9125978, UK, 1991.

[4] K. Kumar and S. V Kailas, "Positional dependence of material flow in friction stir welding: analysis of joint line remnant and its relevance to dissimilar metal welding," *Science and Technology of Welding & Joining*, vol. 15, no. 4, pp. 305–311, 2010.

[5] J. F. Guo, H. C. Chen, C. N. Sun, G. Bi, Z. Sun, and J. Wei, "Friction stir welding of dissimilar materials between AA6061 and AA7075 Al alloys effects of process parameters," *Materials and Design*, vol. 56, pp. 185–192, 2014.

[6] S. Ravikumar and V. S. Rao, "Pranesh RV Effect of process parameters on mechanical properties of friction stir welded dissimilar materials between AA6061-T651 and AA7075-T651 alloys," *International Journal of Advanced Mechanical Engineering*, vol. 4, no. 1, pp. 101–114, 2014.

[7] D. Trimble, G. O'Donnell, and J. Monaghan, "Characterisation of tool shape and rotational speed for increased speed during friction stir welding of AA 2024-T3," *Journal of Manufacturing Processes*, vol. 17, pp. 141–150, 2015.

[8] P. K. Krishnan, R. Arunachalam, A. Husain, and M. Al-Maharbi, "Studies on the influence of stirrer blade design on the microstructure and mechanical properties of a novel aluminum metal matrix composite," *Journal of Manufacturing Science and Engineering*, vol. 143, no. 2, pp. 1–13, 2021.

[9] S. Delijaicov, P. AdO. Silva, H. B. Resende, and M. H. F. Batalha, "Effect of weld parameters on residual stress, hardness and microstructure of dissimilar aa2024-T3 and aa7475-t761 friction stir welded joints," *Materials Research*, vol. 21, no. 6, 2018.

[10] P. Bahemmat, M. Haghpanahi, M. K. Besharati Givi, and K. Reshad Seighalani, "Study on dissimilar friction stir butt welding of AA7075-O and AA2024-T4 considering the manufacturing limitation," *International Journal of Advanced Manufacturing Technology*, vol. 59, no. 9–12, pp. 939–953, 2012.

[11] H.-B. Chen, K. Yan, T. Lin, S.-B. Chen, C.-Y. Jiang, and Y. Zhao, "The investigation of typical welding defects for 5456 aluminum alloy friction stir welds," *Materials Science and Engineering*, vol. 433, no. 1–2, pp. 64–69, 2006.

[12] J. Goebel, M. Reimann, and N. A. J. F. Dos Santos, "Semi-stationary shoulder bobbin tool friction stir welding of AA2198-T851," *Journal of Materials Processing Technology*, vol. 245, p. 37, 2017.

[13] S. A. Nithin Joseph Reddy, R. Sathiskumar, K. Gokul Kumar et al., "Friction based joining process for high strength aerospace aluminium alloy," *Materials Research Express*, vol. 6, no. 8, Article ID 0865a3, 2019.

[14] A. H. Baghdadi, Z. Sajuri, A. Keshtgar, N. Mohd Sharif, and A. Rajabi, "Mechanical property improvement in dissimilar friction stir welded Al5083/Al6061 joints: effects of post-weld heat treatment and abnormal grain growth," *Materials*, vol. 15, no. 1, p. 288, 2021.

[15] A. H. Baghdadi, Z. Sajuri, M. Z. Omar, and A. Rajabi, "Friction stir welding parameters: impact of abnormal grain growth during post-weld heat treatment on mechanical properties of Al–Mg–Si welded joints," *Metals*, vol. 10, no. 12, p. 1607, 2020.

[16] N. F. Mohd Selamat, A. H. Baghdadi, Z. Sajuri, and A. H. Kokabi, "Weldability and mechanical properties of dissimilar Al-mgsi to pure aluminium and Al-mg using friction stir welding process," *Jurnal Teknologi*, vol. 81, no. 1, 2018.

[17] J. Kejuruteraan, N. Mohd Selamata, A. Baghdadi, and Z. Sajuria, "Effect of rolling on strength of friction stir welded joint of aluminium alloys," *J Kejuruter*, vol. 1, pp. 9–15, 2018.

[18] T. Senthilnathan and K. Balachandar, "Friction stir welding of AA7475 HYBRID COMPOSITES," *Technology*, vol. 9, pp. 582–588, 2018.

[19] G. İpekoğlu and G. Cam, "Effects of initial temper condition and postweld heat treatment on the properties of dissimilar friction-stir-welded joints between AA7075 and AA6061 aluminum alloys," *Metallurgical and Materials Transactions A*, vol. 45, no. 7, pp. 3074–3087, 2014.

[20] X. Tao, Y. Chang, Y. Guo, W. Li, and M. Li, "Microstructure and mechanical properties of friction stir welded oxide dispersion strengthened AA6063 aluminum matrix composites enhanced by post-weld heat treatment," *Materials Science and Engineering*, vol. 725, pp. 19–27, 2018.

[21] A. Rodriguez, A. Calleja, L. N. Lopez de Lacalle et al., "Burnishing of FSW aluminum Al–Cu–Li components," *Metals*, vol. 9, no. 2, p. 260, 2019.

[22] H. Sidhar, R. S. Mishra, A. P. Reynolds, and J. A. Baumann, "Impact of thermal management on post weld heat treatment

efficacy in friction stir welded 2050-T3 alloy," *Journal of Alloys and Compounds*, vol. 722, pp. 330–338, 2017.

[23] M. J. Starink, A. Deschamps, and S. C. Wang, "The strength of friction stir welded and friction stir processed aluminium alloys," *Scripta Materialia*, vol. 58, no. 5, pp. 377–382, 2008.

[24] A. D Cubillos, E. R. Parra, B. S. Giraldo, Y. C. Arango, and D. F. A. Mateus, "Study of TiN and Ti/TiN coatings produced by pulsed-arc discharge," *Surface and Coatings Technology*, vol. 190, pp. 83–89, 2005.

[25] H. Aydın, A. Bayram, and I. Durgun, "The effect of post-weld heat treatment on the mechanical properties of 2024-T4 friction stir-welded joints," *Materials and Design*, vol. 31, no. 5, pp. 2568–2577, 2010.

[26] T. S. Srivatsan, S. Vasudevan, and L. Park, "The tensile deformation and fracture behavior of friction stir welded aluminum alloy 2024," *Materials Science and Engineering*, vol. 466, no. 1-2, pp. 235–245, 2007.

[27] V. Kerlins, "Modes of fracture," in *ASM Handbook Committee Editors Fractography Materials Park, OH*, ASM, International, 1991.

[28] A. H. Baghdadi, A. Rajabi, N. F. M. Selamat, Z. Sajuri, and M. Z. Omar, "Effect of post-weld heat treatment on the mechanical behavior and dislocation density of friction stir welded Al6061," *Materials Science and Engineering*, vol. 754, pp. 728–734, 2019.

Hindawi
Advances in Materials Science and Engineering
Volume 2022, Article ID 5692298, 11 pages
https://doi.org/10.1155/2022/5692298

Research Article

Numerical Modelling, Simulation, and Analysis of the End-Milling Process Using DEFORM-3D with Experimental Validation

B. Deepanraj,[1] **N. Senthilkumar**,[2] **G. Hariharan**,[3] **T. Tamizharasan**,[4] **and Tesfaye Tefera Bezabih**[5]

[1]*Department of Mechanical Engineering, Prince Mohammad Bin Fahd University, Al-Khobar, 31952, Saudi Arabia*
[2]*Saveetha School of Engineering, Saveetha Institute of Medical and Technical Sciences, Chennai 602105, Tamil Nadu, India*
[3]*University College of Engineering (Anna University), Kancheepuram 631552, Tamil Nadu, India*
[4]*SRM Technologies, Infotech, Chennai 600017, Tamil Nadu, India*
[5]*Department of Mechanical Engineering, Ambo University, Ambo, Ethiopia*

Correspondence should be addressed to N. Senthilkumar; nskmfg@gmail.com and Tesfaye Tefera Bezabih; tesfaye.tefera@ambou.edu.et

Received 21 July 2022; Revised 16 August 2022; Accepted 25 August 2022; Published 13 September 2022

Academic Editor: R. Thanigaivelan

In this present work, finite element analysis (FEA)-based simulation of end-milling of AISI1045 steel using tungsten carbide tool was performed using DEFORM-3D simulation software. Usui tool wear model, Johnson-cook material model and adaptive remeshing are considered during machining simulation. The impact of machining variables rate of feed, tool speed, and depth of cut was investigated, and the best integration of variables was distinguished for lower cutting temperature, principal stress, cutting forces, effective stresses, tool wear, and effective strain. The obtained results were correlated using experimentation in a vertical machining center attached with a Kistler tool dynamometer with data acquisition setup for capturing the cutting forces, and an infrared (IR) thermometer was used to measure the cutting temperature, and a comparison was done. Results showed a good correlation. There is a relationship between experimental and numerical results, and simulation findings can be utilised for interpreting the influence of machining parameters.

1. Introduction

The development of several computational strategies for tackling engineering problems has resulted from the revolution in computer technology over the last few decades. Mathematical modelling has become an important part of engineering problem analysis, and several numerical methods were created, including the finite element method (FEM), the finite difference method (FDM), the boundary element method (BEM), and the finite volume method (FVM) [1]. FEM is one of the most adaptable and versatile engineering problem-solving techniques. To gain information, simulation is the recreation of dynamic procedures in a model that may be applied in real life. Cutting forces, morphology of chips, stresses, strains, and temperatures can all be determined using simulation earlier than actual machining using a cutting tool. Modelling and experiments also contribute to a better understanding of fundamental problems in machining theory [2]. Mechanics of milling includes the shearing between the workpiece and the edge of the cutting tool, the effect of friction between the chip and the rake face of the tool, and ploughing action between the machined surface and the cleared surface. Cutting forces are generated by the cumulative impact of the three components, which can induce deflection in cutting and can cause additional damage to the machined part surface quality [3].

Jing et al. [4] performed simulation studies on microend-milling for developing an ideal cutting force mechanics model and found the momentary thickness of uncut chip by taking the runout of the tool, least chip thickness, the trajectory of the tool, and the elastic recovery rate of the workpiece and discovered that the forces of cutting were affected by the elastic recovery rate. Pragadish et al. [5] considered the Johnson–Cook materials model for cutting

force prediction of Ti–6Al–4V microend milling through a hybrid approach. Cutting force coefficients were extracted from the undeformed chip thickness using simulation model and the numerical results are validated in comparison with experimental results. Vishwakarma and Sharma [6] adopted DEFORM-3D software for simulating the end-milling process to compare the experimental surface roughness values with the simulated values during machining aluminium, and considering the Johnson-Cook material model, it was found that the higher surface roughness was due to chatter of unstable tool. Shi et al. [7] analyzed acoustic emission signals during microcutting experiments to investigate formability in Inconel 718 microend milling and noticed that cutting material properties and tool geometry influences the minimum uncut chip thickness, providing a theoretical basis for surface quality evaluation and optimal cutting parameter selection. Senthilkumar and Tamizharasan [8] used Taguchi's technique to investigate the cutting tool inserts with variable tool geometry while simultaneously addressing numerous responses and verifying them using FEM analysis. Venkata Rao [9] suggested an optimization method to reduce power consumption by improving process variables and minimising machining forces through teaching-learning-based optimization in combination with FEM analysis, with roughness and vibration amplitude as constraints.

Davoudinejad et al. [10] performed 3D-FEM analysis on Al6061-T6 by varying helix angle and cutting-edge radius for predicting burr formation, chip flow, and cutting forces and concluded that the size of a burr at the entrance and top was exaggerated by the rate of feed and that both FEM and experimental cutting force profiles in feed and transverse directions match. Gao et al. [11] used the Eulerian–Lagrangian (EL) FEM model in Abaqus/Explicit for Al6061-T6 to simulate end-milling operations and accurately predicted cutting forces and chip geometry for shoulder and slot milling with up and down milling configurations. Yang et al. [12] investigated the effect of a blunt round edge tool radius and microtexture characteristics on milling cutting forces and observed that the radius of a blunt round edge has the greatest effect, trailed by the tool diameter, cutting edge distance, spacing, and depth. A cutting force estimation framework centred on FEM and nonrational basis splines (NURBS) for a single blade is suggested [13], in which the cutting force estimation technique is more productive than the FEM and NURBS methods because it is established by simulation data, which may not necessitate the use of cutting force information from experiments. Fairly forecasting force is critical for improving machining performance and life of the tool [14], and all coefficients of force frequently vary with the angle of rotation in milling, and a good prediction is possible with FEM as it agrees with the experimental data. Tamizharasan and Senthilkumar [15] performed turning simulation studies in AISI 1045 with dissimilar cutting tool profiles and optimized the geometrical parameters over cutting force and machining temperature and compared the obtained values with experimental results.

From the performed literature, it is concluded that 3D-FEM simulation of end-milling process quality characteristics depends on the selected material, parameters of tool geometry, and machining parameters along with the material model. Correlation of simulation studies with experimental results is carried out widely, but 3D-FEM analysis of end-milling cutter is scary in literature. Numerical simulation of AISI 1045 steel under end-milling conditions is conducted in this work, which was not considered previously by researchers as per our knowledge. Moreover, measurement of the interface temperature and cutting forces experimentally and its correlation with simulation studies are limitedly reported by various researchers for different conditions of machining. Hence, an attempt has been made to perform the simulation of the end-milling process for different machining conditions and to determine the cutting forces acting during machining and machining temperature. 3D simulation of the end-milling process is not studied widely by researchers, and hence, it is performed, which is the novelty of the present study for a commonly used steel material in the industry. Finally, the simulation results were compared with experimental results for further studies and implementation.

2. Material Selection and Methodology

The workpiece considered for the simulation of the plane-strain machining condition is a medium carbon AISI 1045 steel, with a Brinell hardness of 181HB and is a low carbon alloy with acceptable stiffness and strength for applications of construction and engineering [16]. There are shafts, bolts, pins, gears, cold drawings, forgings, and extrusion parts made from AISI 1045 steel. It is considered for the analysis because it is a low-cost steel that is used in many areas of the economy [17]. The end-milling tool considered in this work is made up of tungsten carbide (WC). Figure 1 shows the nomenclature of the end-milling tool. End-milling cutters produce two workpiece surfaces simultaneously, with cutting edges on both the end face and the cutter body's periphery. They are the most flexible milling tools and are commonly used in facing, profiling, slotting, shouldering, slabbing, and plunging operations [19, 20]. The diameter, corner radius, length of the flute, and length of the end-mill must always complement the measurements of the machined pocket. The stiffness of an end mill is determined by its flute number, the diameter of its core, and the spacing of its flutes [21].

The specifications of the end-milling tool considered in this work are as follows: no. of the flute is 4, cutting diameter is 8 mm, cutting length is 20 mm, shank diameter is 8 mm, overall length is 50 mm, the tool material is tungsten carbide of grade KC633M, the helix angle is 30, straight cylindrical shank, shank length is 36 mm, and corner chamfer angle is 45°. DEFORM-3D is an extensive simulation of processes for analysing complex metal forming procedures in three-dimensional(3D) flow. DEFORM-3D is a useful and effective technique for predicting the flow of materials in a cost-effective way in forming operations in industries and time

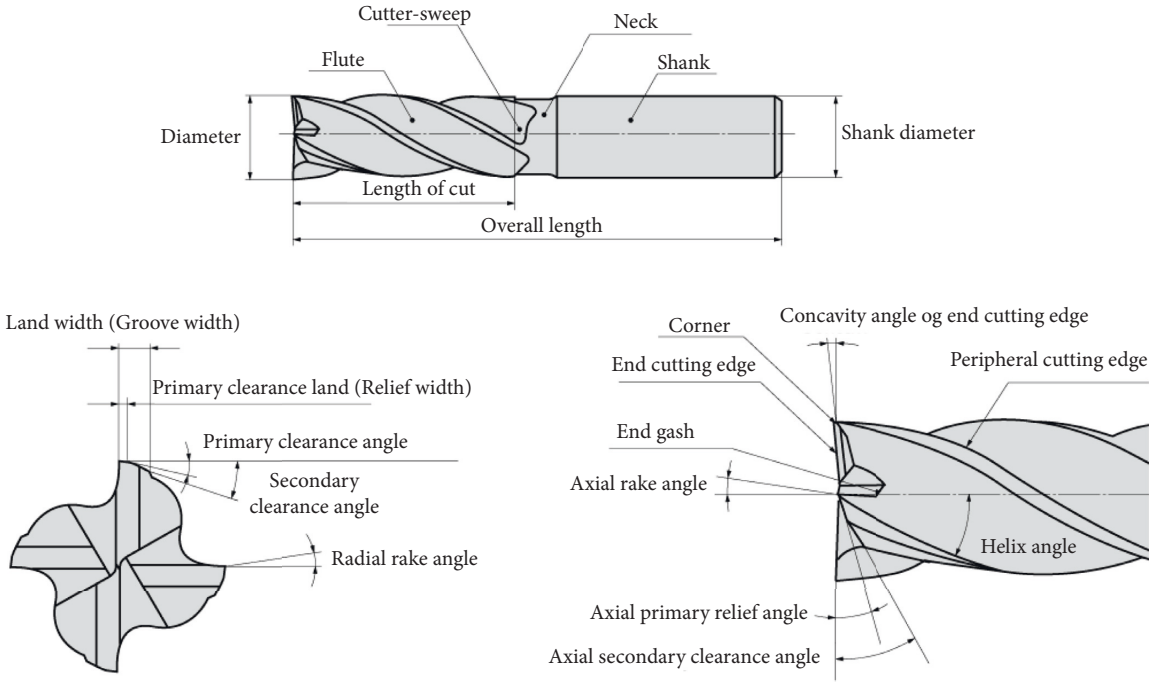

Figure 1: Nomenclature of the end-milling tool [18].

delays associated with shop trials [22, 23]. Open die forging, closed die forging, extrusion, rolling, cogging, drawing, machining, compaction, extrusion, and upsetting are all common applications.

Figure 2 shows the modeled milling cutter and workpiece using DEFORM-3D. Initially, the cutter is modeled for a diameter of 8 mm, length of 20 mm, and a helix angle of 45°. Then, the workpiece is generated with a 50 mm diameter, with a starting angle of 0° and an arc angle of 30°. The relative mesh technique is adopted for workpiece and tool meshing [24], and simulation has been performed with 25000 elements which are sufficient to give an accurate model of the cutter. The edges of the workpiece are fixed in all directions [25, 26]. For the end-milling tool, the surface mesh is generated with 5482 polygons and 2743 points, and the solid mesh is generated with 21383 elements and 5170 nodes with dynamic zooming. For the workpiece, the solid mesh is generated with 20365 elements and 4886 nodes with dynamic zooming.

The region between the workpiece and the tip of the tool where the contact is made has a finer mesh. Initially, the Lagrangian incremental methodology is used to solve the problem, and then steady-state machining is performed. The workpiece is considered a thermo-viscoplastic deformable body with isotropic behaviour. The Johnson–Cook material model was considered which is a temperature and strain rate dependent model that describes thermo-mechanical behaviour of material flow over the entire range of strain rate and temperature as given in the equation for equivalent flow stress [27, 28].

$$\sigma = \left(A + B\varepsilon^{n}\right)\left(1 + C\ln\frac{\dot{\varepsilon}}{\dot{\varepsilon}_0}\right)\left[1 - \left(\frac{T - T_r}{T_m - T_r}\right)^{m}\right], \quad (1)$$

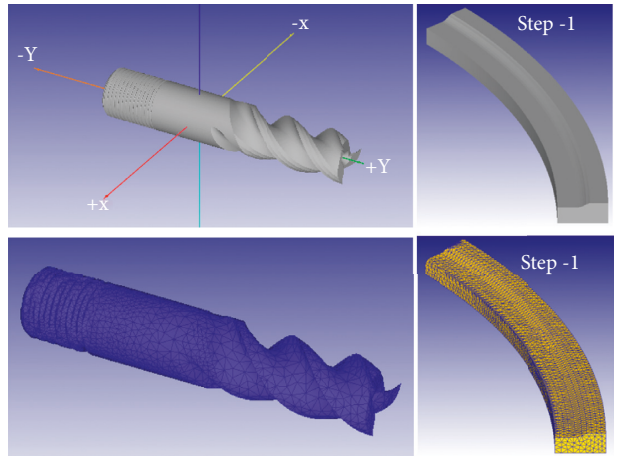

Figure 2: Modelled tool and workpiece with the meshed condition.

where $T, \sigma, \dot{\varepsilon}, \wedge \varepsilon$ indicate equivalent temperature, flow stress, rate of plastic strain, and plastic strain. The yield stress at the initial condition is A, the hardening modulus is B, the exponent of strain hardening is n, and the sensitivity coefficient of strain rate is C. T_r is the reference temperature which is equal to 20°C, and T_m is the melting temperature which is equal to 1520°C. The Cockcroft–Latham fracture criterion was employed in this chip separation study [6], which is the total damage calculated with the equivalent strain and maximum principal stress, as shown in the equation. To represent the quantity of ductile damage, only one material constant is required. As a result, the material constant can only be ascertained by experimental investigation [29, 30].

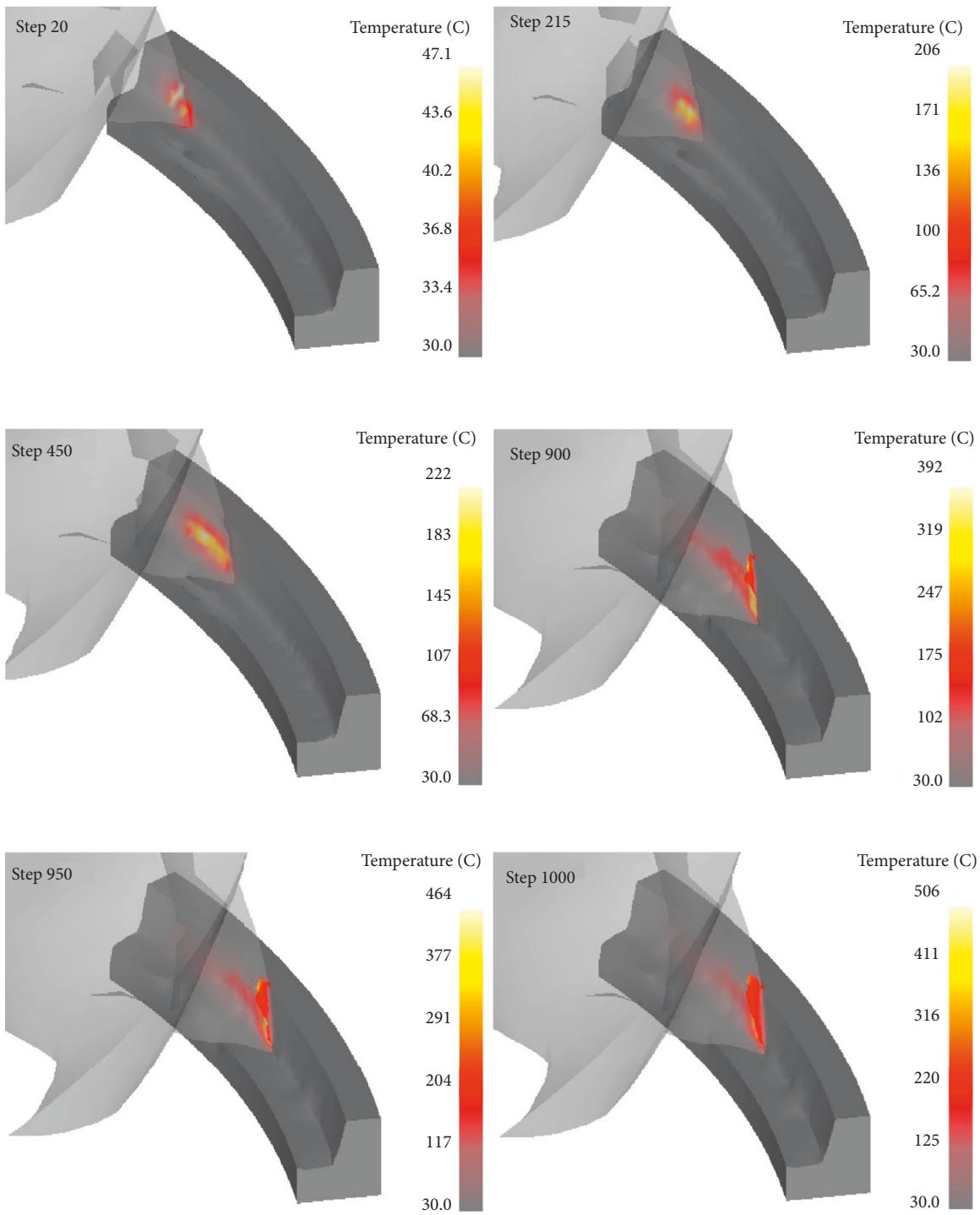

Figure 3: Simulation results of the end-milling process.

$$\int_0^{\bar{\varepsilon}_f} \sigma_{\max} d\bar{\varepsilon} = C_1, \tag{2}$$

where $\sigma_{\max}$ is the maximum principal stress, $\bar{\varepsilon}$ is the equivalent strain, $\bar{\varepsilon}_f$ is the equivalent strain at which the fracture occurs, and C_1 is the material constant for ductile damage. Adaptive meshing is a remesh technique in which an old deformed mesh is replaced with a new one. Smoothing shifts nodes to produce more standard element configurations, whereas refinement enhances the density of mesh by decreasing the size of mesh [31, 32]. Adaptive meshing enhances simulation accuracy. The wear rate at the contact surface is determined by relative velocity, constant pressure, and absolute temperature in Usui's model of tool wear as given in the following equation:

$$\frac{dw}{dt} = A\sigma_u V_s e^{(-B/T)}. \tag{3}$$

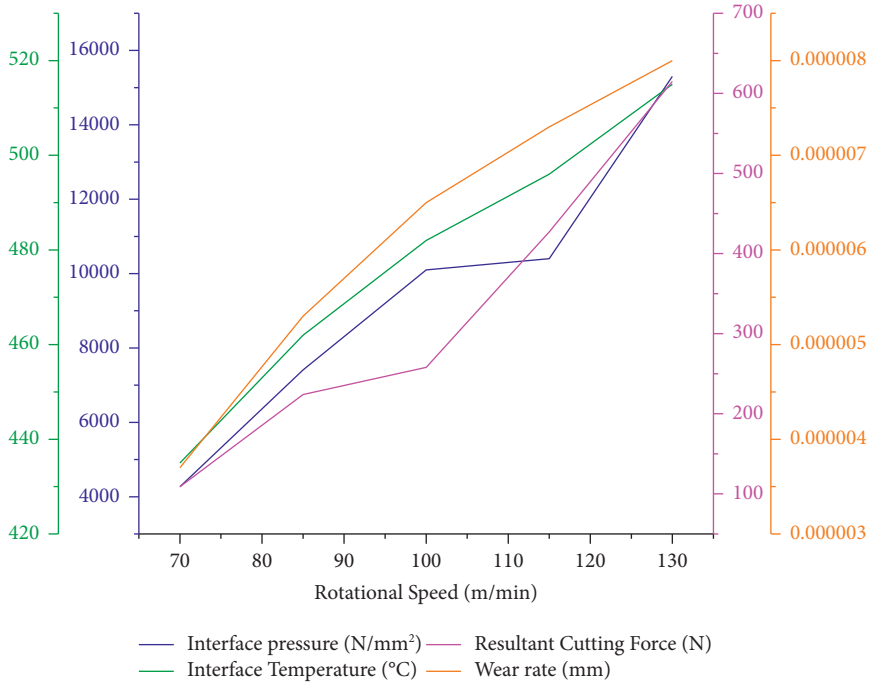

Figure 4: Influence of rotational speed on machining outputs.

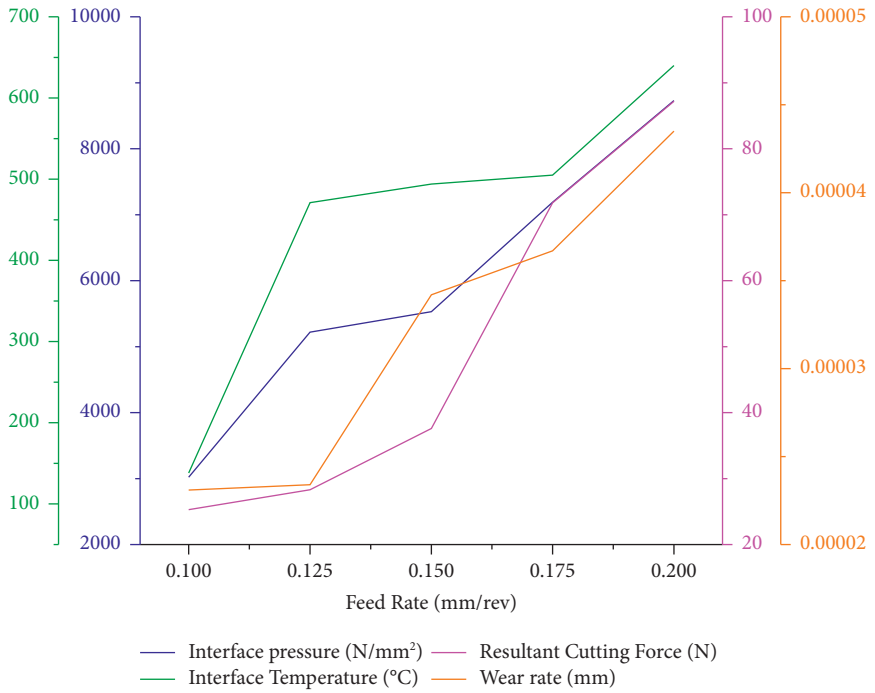

Figure 5: Influence of the feed rate on machining outputs.

The wear rate simulation constants are $A = 0.0000000078$ and $B = 5302$ [33].

3. Results and Discussions

For performing simulation of the end-milling process, spindle speeds are varied as 70, 85, 100, 115, and 130 m/min, feed rates are varied as 0.1, 0.125, 0.15, 0.175, and 0.2 mm/rev, and the depths of cut are varied as 0.5, 0.75, 1.0, 1.25, and 1.5 mm, and the machining process is analyzed numerically. During the simulation of the end-milling process, the environment temperature is defined as 30°C. The heat exchange is usually very small because the cutter process happens very quickly (<1sec). The tool-workpiece interface parameters such as the

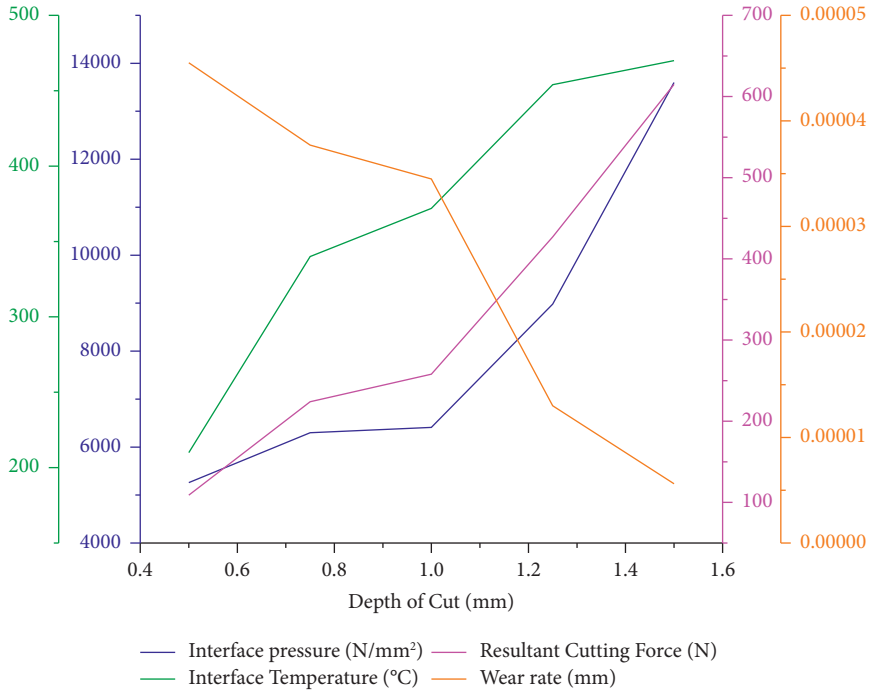

Figure 6: Influence of the depth of cut on machining outputs.

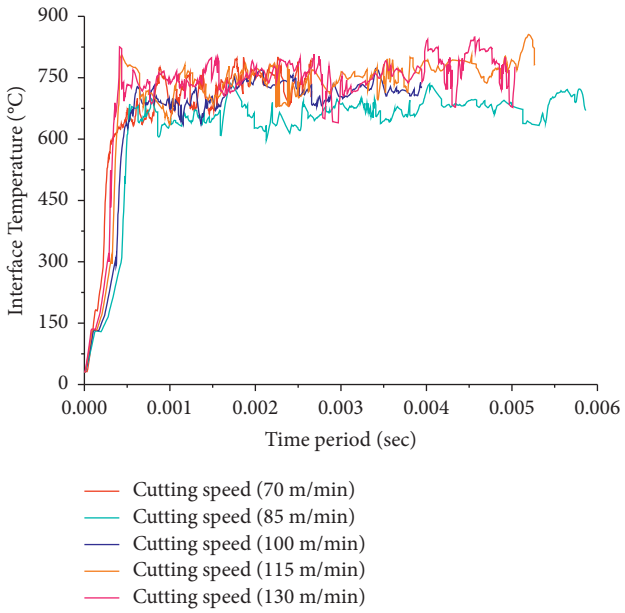

Figure 7: Fluctuation in cutting temperature for various speeds during milling.

shear friction factor and heat transfer coefficient are not varied or not considered during the analysis. Initially, simulation is performed for transient conditions, and after the required steps are completed, steady-state machining is performed, and the outputs are measured [34]. After the end of the simulation, the values of the parameters such as mean stress, effective stress, effective strain, maximum principal stress, and temperature are taken from it, and the graphs are developed on a timely basis. Figure 3 displays the various stages captured during the simulation of the end-milling process, temperature rising during machining along with the contact of the milling tool with the workpiece, and the formation of the chip from the workpiece.

After performing simulation in a transient condition, and after the required length is cut, machining is carried out in a steady-state condition [35]. The output responses such as interface pressure, interface temperature, resultant cutting forces, and wear rate were

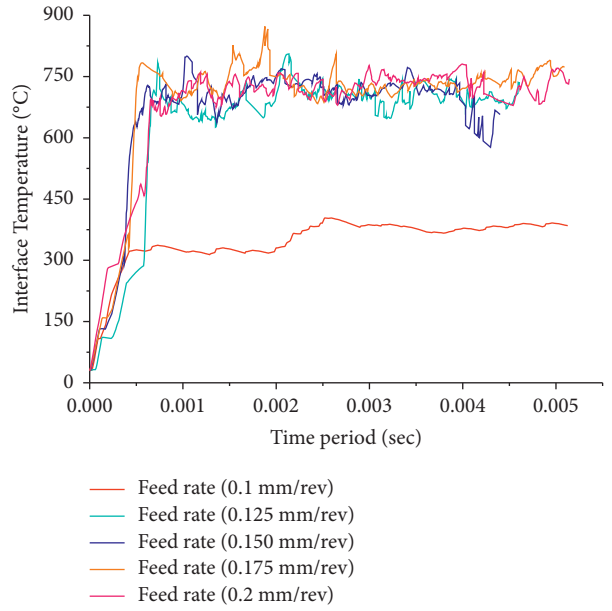

Figure 8: Variation of cutting temperature for different feed rates.

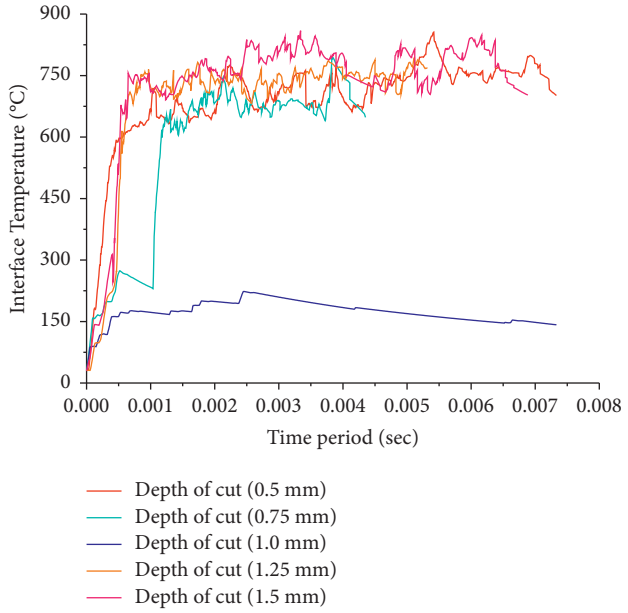

Figure 9: Variation of cutting temperature for different depths of cuts.

measured, and a comparison was performed. Figure 4 presents the comparison of output responses for different conditions of rotational speed. It is observed that a linear increase in output conditions was seen, with an increase in rotation speed, due to the higher material removal and friction that exists between the tool and the workpiece.

The change in output values for different feed rates of the end-milling tool during simulation is presented in Figure 5. With increase in feed rate values from 0.1 mm/rev to 0.2 mm/rev, output values also tend to increase. Initially, with a change in feed rate value from 0.1 to 0.125 mm/rev, an abrupt increase in the interface temperature is visualized, followed by interface pressure due to the higher load acting on the tool, which obviously increases the pressure and friction between the tool and the workpiece. Similarly, milling forces tend to increase with the increase in the feed rate [36–38].

Figure 6 displays the variation of interface pressure, interface temperature, resultant cutting force, and wear rate obtained with a variation in the depth of cut. An increase in interface temperature, interface pressure, and resultant

Figure 10: Photographic view of VMC used for machining.

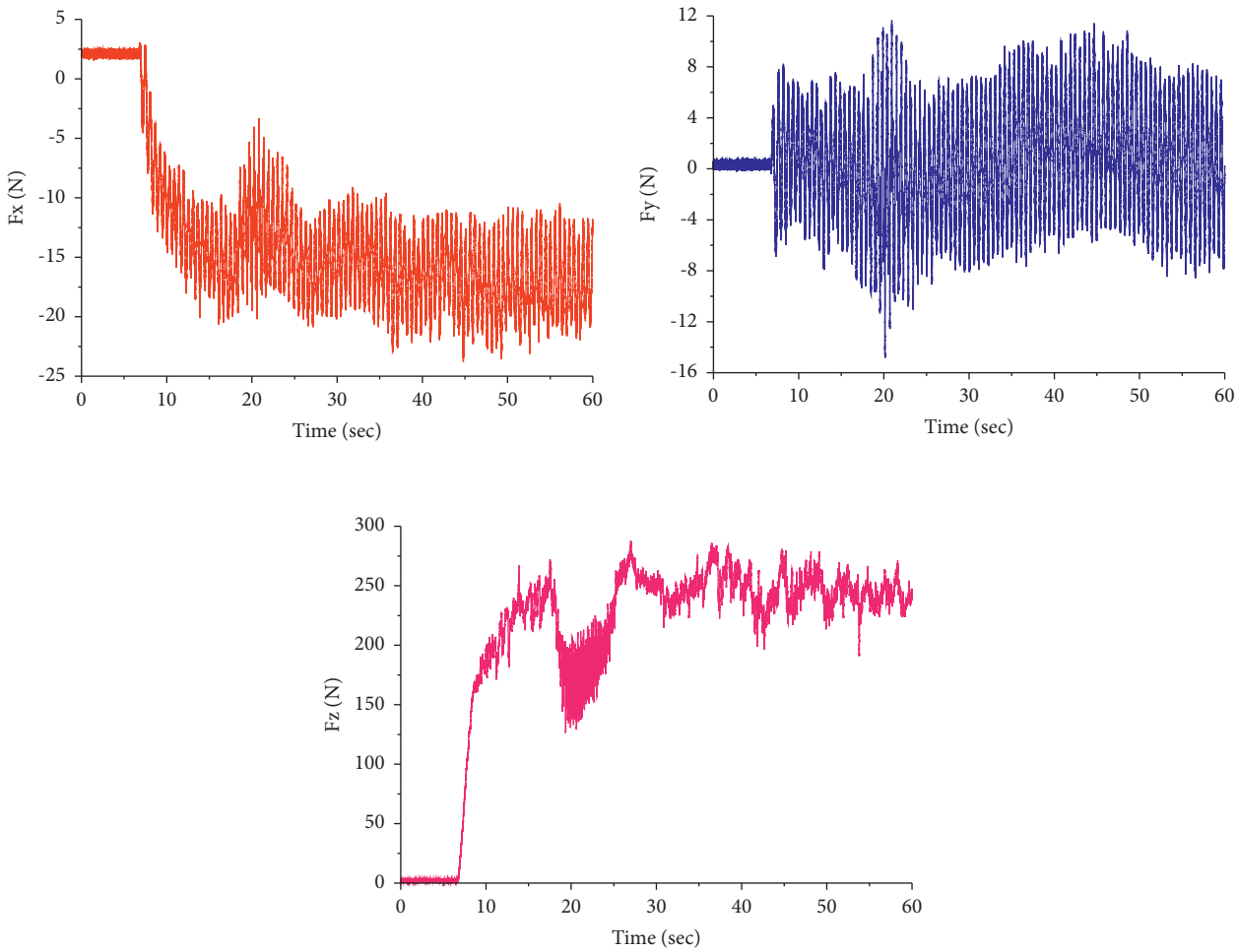

Figure 11: Experimental cutting force.

cutting force is observed, and simultaneously a reduction in the wear rate is obtained with an increase in the depth of cut values [39–42].

The variation of cutting temperature during the simulation process for different rotational speeds is shown in Figure 7. It is visualized that at initial conditions of milling, a steep increase in temperature takes place during the extreme friction between the cutting tool and the workpiece arising from the shearing action of the tool on the workpiece [43]. The trend of different rotational speeds is similar. Similarly, for change in the feed rate as presented in Figure 8, the cutting temperature is similar except for a feed rate of 0.1 mm/rev. With a lower feed rate, the pressure between the workpiece and the tool gets lowered, and hence, a lower cutting temperature is sensed. But with higher feed rates, pressure tends to increase which subsequently increases the cutting temperature [44]. A similar trend is also observed for change in depth of cut in Figure 9, the cutting temperature is lower for 0.5 mm of depth of cut, and for other depths of cut, it is higher.

For validating the results obtained from simulation studies, a set of experiments are performed with 100 m/min of

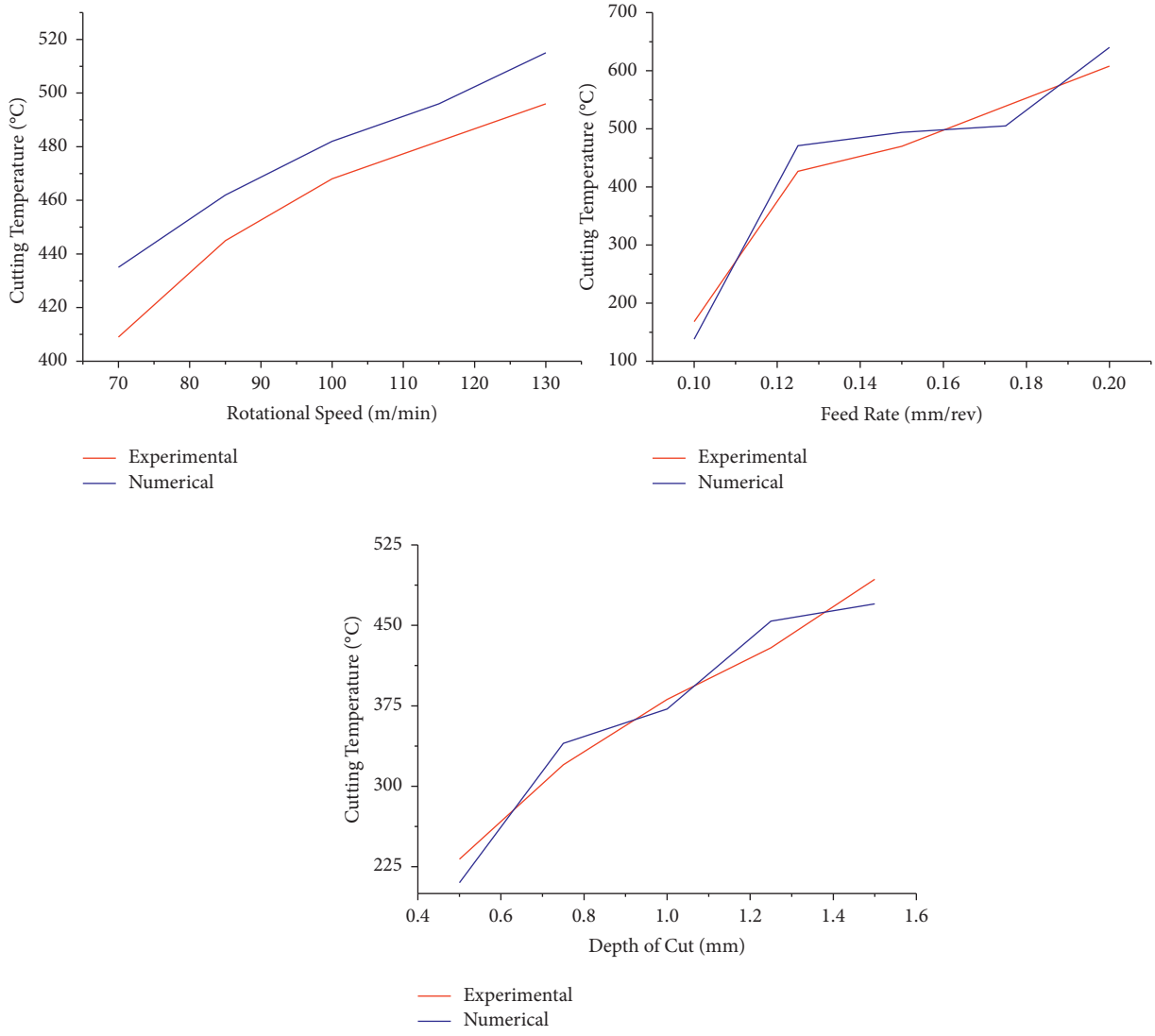

Figure 12: Comparison of experimental and numerical cutting temperature.

tool rotation, 1 mm of the depth of cut, and 0.15 mm/rev of the rate of feed. The experiment is performed with the WC end-milling tool in a vertical machining center (VMC) attached with a cutting force dynamometer integrated with a data acquisition system connected with a personal computer, which is shown in Figure 10. Cutting forces are measured using a piezoelectric type Kistler dynamometer (9257B type) having ranges of Fx, Fy, and Fz between −5 kN and +5 kN with a threshold value of <0.01 N, a natural frequency of *fn* (*x*, *y*, *z*) kHz≈3, 5, and an operating temperature ranging from 0°C to 70°C with a clamping area of 100 × 170 mm [45]. The METRAVI MT-9 IR thermometer with dual laser is utilised to determine the milling temperature that has a measuring range of −50°C to 1000°C, 0 to 50°C working temperature, and a response time of 150 ms [46].

Figure 11 shows the components of cutting force obtained during the machining process. At the initial stages of machining, cutting forces tend to increase abruptly, after which it tends to stabilize around a specific value [47].

The temperature obtained during milling from the experimental and numerical methods is compared as presented in Figure 12, and it was found that a close correlation exists between them for variation in considered milling parameters [28, 48]. Experimental results show that with the increasing rotational speed of the end-milling cutter, the interface temperature tends to rise due to the higher friction that exists between the carbide cutter and the workpiece as no lubrication is added during machining. Similarly, an increase in the feed rate obviously increases the cutting temperature sharply. A drastic rise in cutting temperature is observed with higher feed rates [49]. Increasing the depth of cut of machining increases the friction as more material is removed through shearing action which eventually increases the cutting temperature as illustrated in Figure 12.

4. Conclusion

In this work, milling process simulation is performed to study the behavior of the milling cutter using Deform-3D.

The temperature distribution, effective stress, and maximum effective stress in the cutter, workpiece, and chip are studied and analyzed. The simulation result helps to analyze the performance of AISI 1045 steel during end-milling process with tungsten carbide tool. With the change in the feed rate, an increase in the interface temperature and interface pressure is observed due to the higher load acting on the tool, which obviously increases the pressure and friction between the tool and the workpiece. Similarly, milling forces tend to rise with a higher rate of feed. Higher pressure and temperature at the interface with increased resultant force are observed, and simultaneously, a reduction in the wear rate is obtained with an increase in the depth of cut values.

At initial conditions of milling, a steep increase in temperature takes place during extreme friction between the cutting tool and the workpiece arising from the shearing action of the tool on the workpiece. With a lower feed rate, the pressure between the workpiece and the tool gets lowered, and hence, a lower cutting temperature is sensed. But with higher feed rates, pressure tends to increase which subsequently increases the cutting temperature.

The comparison of cutting temperature between the experimental and numerical analyses has a close correlation between variation in the rate of feed, speed of milling cutter, and depth of cut.

Data Availability

The data used to support the findings of this study are included within the article and are available from the corresponding author upon reasonable request.

Conflicts of Interest

The authors declare that they have no conflicts of interest.

References

[1] A. P. Markopoulos, *Finite Element Method in Machining Processes*, Springer, London, U.K, 2012.

[2] A. P. Markopoulos and J. P. Davim, *Advanced Machining Processes: Innovative Modeling Techniques*, CRC Press, London, U.K, 2017.

[3] M. Wan and W. Zhang, *Milling Simulation: Metal Milling Mechanics, Dynamics and Clamping Principles*, Wiley, Germany, 2016.

[4] X. Jing, R. Lv, Y. Chen, Y. Tian, and H. Li, "Modelling and experimental analysis of the effects of run out, minimum chip thickness and elastic recovery on the cutting force in micro-end-milling," *International Journal of Mechanical Sciences*, vol. 176, Article ID 105540, 2020.

[5] N. Pragadish, S. Kaliappan, M. Subramanian et al., "Optimization of cardanol oil dielectric-activated EDM process parameters in machining of silicon steel," *Biomass Conversion and Biorefinery*, vol. 32, pp. 1–10, 2022.

[6] P. Vishwakarma and A. Sharma, "3D Finite Element Analysis of milling process for non-ferrous metal using deform-3D," *Materials Today Proceedings*, vol. 26, no. 2, pp. 525–528, 2020.

[7] Z. Shi, Y. Li, Z. Liu, and Y. Qiao, "Determination of minimum uncut chip thickness during micro-end milling Inconel 718 with acoustic emission signals and FEM simulation," *International Journal of Advanced Manufacturing Technology*, vol. 98, no. 1-4, pp. 37–45, 2018.

[8] N. Senthilkumar and T. Tamizharasan, "Effect of tool geometry in Turning AISI 1045 steel: experimental investigation and FEM analysis," *Arabian Journal for Science and Engineering*, vol. 39, no. 6, pp. 4963–4975, 2014.

[9] K. Venkata Rao, "Power consumption optimization strategy in micro ball-end milling of D2 steel via TLBO coupled with 3D FEM simulation," *Measurement*, vol. 132, pp. 68–78, 2019.

[10] A. Davoudinejad, P. Parenti, and M. Annoni, "3D finite element prediction of chip flow, burr formation, and cutting forces in micro end-milling of aluminum 6061-T6," *Frontiers of Mechanical Engineering*, vol. 12, no. 2, pp. 203–214, 2017.

[11] Y. Gao, J. H. Ko, and H. P. Lee, "3D coupled Eulerian-Lagrangian finite element analysis of end milling," *International Journal of Advanced Manufacturing Technology*, vol. 98, no. 1-4, pp. 849–857, 2018.

[12] S. Yang, W. Ren, T. Wang, and S. Su, "Parameter optimization of a micro-textured ball-end milling cutter with blunt round edge," *International Journal of Advanced Manufacturing Technology*, vol. 106, no. 1-2, pp. 577–588, 2020.

[13] M. Karthick, P. Anand, M. Meikandan, S. Sekar, L. Natrayan, and K. Bobe, "Optimization of plasma arc cutting parameters on machining of Inconel 718 superalloy," *Journal of Nanomaterials*, vol. 2022, Article ID 7181075, pp. 1-13, 2022.

[14] F. Su, J. Yuan, F. Sun, Z. Wang, and Z. Deng, "Modeling and simulation of milling forces in milling plain woven carbon fiber-reinforced plastics," *International Journal of Advanced Manufacturing Technology*, vol. 95, no. 9-12, pp. 4141–4152, 2018.

[15] T. Tamizharasan and N. Senthilkumar, "Optimization of cutting inserts geometry using DEFORM-3D: numerical simulation and experimental validation," *International Journal of Simulation Modelling*, vol. 11, no. 2, pp. 65–76, 2012.

[16] A. T. Abbas, A. E. Ragab, F. Benyahia, and M. S. Soliman, "Taguchi robust design for optimizing surface roughness of turned AISI 1045 steel considering the tool nose radius and coolant as noise factors," *Advances in Materials Science and Engineering*, vol. 2018, Article ID 2560253, 9 pages, 2018.

[17] M. Shnfir, O. A. Olufayo, W. Jomaa, and V. Songmene, "Machinability study of hardened 1045 steel when milling with ceramic cutting inserts," *Materials*, vol. 12, no. 23, p. 3974, 2019.

[18] Z. Huda, *Machining Processes and Machines: Fundamentals, Analysis, and Calculations*, CRC Press, London, U.K, 2020.

[19] S. S. Bhogal, C. Sindhu, S. S. Dhami, and B. S. Pabla, "Minimization of surface roughness and tool vibration in CNC milling operation," *Journal of Optimization*, vol. 2015, Article ID 192030, 13 pages, 2015.

[20] J. Ji, Q. Yang, P. Chen, K. Lu, and Y. Wu, "An improved mathematical model of cutting temperature in end milling Al7050 based on the influence of tool geometry parameters and milling parameters," *Mathematical Problems in Engineering*, vol. 2021, Article ID 5705091, 10 pages, 2021.

[21] P. Sureshkumar, T. Jagadeesha, L. Natrayan, M. Ravichandran, D. Veeman, and S. Muthu, "Electrochemical corrosion and tribological behaviour of AA6063/Si3N4/Cu (NO3)2 composite processed using single-pass ECAPA route with 120 die angle," *Journal of Materials Research and Technology*, vol. 16, pp. 715–733, 2022.

[22] N. Senthilkumar, A. Pon, and T. Tamizharasan, "A finite element simulation study on effects of variation in machining

and geometrical parameters in turning," *Applied Mechanics and Materials*, vol. 592-594, pp. 3–7, 2014.

[23] A. Mathivanan, G. Swaminathan, P. Sivaprakasam, R. Suthan, V. Jayaseelan, and M. Nagaraj, "DEFORM 3D simulations and Taguchi analysis in dry turning of 35CND16 steel," *Advances in Materials Science and Engineering*, vol. 2022, Article ID 7765343, 10 pages, 2022.

[24] V. Kumar, A. Eakambaram, and A. Arivazhagan, "FEM analysis to optimally design end mill cutters for milling of Ti-6Al-4V," *Procedia Engineering*, vol. 97, pp. 1237–1246, 2014.

[25] L. Yang and M. L. Zheng, "Simulation and analysis of ball-end milling of panel moulds based on DEFORM-3D," *International Journal of Simulation Modelling*, vol. 16, no. 2, pp. 343–356, 2017.

[26] L. Zhu, C. Zhu, J. Pei, X. Li, and W. Wang, "Prediction of three-dimensional milling forces based on finite element," *Advances in Materials Science and Engineering*, vol. 2014, Article ID 918906, 7 pages, 2014.

[27] T. Bergs, M. Hardt, and D. Schraknepper, "Determination of Johnson-Cook material model parameters for AISI 1045 from orthogonal cutting tests using the Downhill-Simplex algorithm," *Procedia Manufacturing*, vol. 48, pp. 541–552, 2020.

[28] Z. L. Wang, Y. J. Hu, and D. Zhu, "DEFORM-3D based on machining simulation during metal milling," *Key Engineering Materials*, vol. 579–580, pp. 197–201, 2013.

[29] S. Stebunov, A. Vlasov, and N. Biba, "Prediction of fracture in cold forging with modified Cockcroft-Latham criterion," *Procedia Manufacturing*, vol. 15, pp. 519–526, 2018.

[30] T. Kvačkaj, J. Tiža, J. Bacsó et al., "Cockcroft-latham ductile fracture criteria for non-ferrous materials," *Materials Science Forum*, vol. 782, pp. 373–378, 2014.

[31] B. Zeramdini, C. Robert, G. Germain, and T. Pottier, "Simulation of metal forming processes with a 3D adaptive remeshing procedure," *AIP Conference Proceedings*, vol. 1769, 2016.

[32] H. Luo, J. Fu, T. Wu, N. Chen, and H. Li, "Numerical simulation and experimental study on the drilling process of 7075-t6 aerospace aluminum alloy," *Materials*, vol. 14, no. 3, p. 553, 2021.

[33] Y.-C. Yen, J. Sohner, B. Lilly, and T. Altan, "Estimation of tool wear in orthogonal cutting using the finite element analysis," *Journal of Materials Processing Technology*, vol. 146, no. 1, pp. 82–91, 2004.

[34] T. Tamizharasan and N. Senthilkumar, "Numerical simulation of effects of machining parameters and tool geometry using DEFORM-3D: optimization and experimental validation," *World Journal of Modelling and Simulation*, vol. 10, no. 1, pp. 49–59, 2014.

[35] W. Grzesik, "Chapter nine - heat in metal cutting," *Wit Grzesik, Advanced Machining Processes of Metallic Materials*, Elsevier, Netherlands, pp. 163–182, 2017.

[36] S. Tamura and T. Matsumura, "Cutting force simulation in milling of tapered wall with barrel end mill," *Procedia Manufacturing*, vol. 47, pp. 466–471, 2020.

[37] V. Bajpai, I. Lee, and H. W. Park, "Finite element modeling of three-dimensional milling process of Ti–6Al–4V," *Materials and Manufacturing Processes*, vol. 29, no. 5, pp. 564–571, 2014.

[38] I. A. Daniyan, I. Tlhabadira, O. O. Daramola, S. N. Phokobye, M. Siviwe, and K. Mpofu, "Measurement and optimization of cutting forces during M200 TS milling process using the response surface methodology and dynamometer," *Procedia CIRP*, vol. 88, pp. 288–293, 2020.

[39] Z. Ping, X. Yue, H. Shuangfeng, S. Ailing, L. Baoshun, and Y. Xiao, "Experiment and simulation on the high-speed milling mechanism of aluminum alloy 7050-T7451," *Vacuum*, vol. 182, Article ID 109778, 2020.

[40] Y. Sun, J. Sun, G. Wang, J. Du, and P. Zhang, "A modified analytical cutting force prediction model under the tool crater wear effect in end milling Ti6Al4V with solid carbide tool," *International Journal of Advanced Manufacturing Technology*, vol. 108, no. 11-12, pp. 3475–3490, 2020.

[41] B. S. Wang, J. M. Zuo, M. L. Wang, and J. M. Hou, "Prediction of milling force based on numerical simulation of oblique cutting," *Materials and Manufacturing Processes*, vol. 27, no. 10, pp. 1011–1016, 2012.

[42] L. Zhou, B. Deng, F. Peng, R. Yan, Y. Minghui, and H. Sun, "Analytical modelling and experimental validation of micro-ball-end milling forces with progressive tool flank wear," *International Journal of Advanced Manufacturing Technology*, vol. 108, no. 9-10, pp. 3335–3349, 2020.

[43] P. K. Parsi, R. S. Kotha, T. Routhu, S. Pandey, and M. Dwivedy, "Machinability evaluation of coated carbide inserts in turning of super-duplex stainless steel," *SN Applied Sciences*, vol. 2, no. 11, 2020.

[44] W. Zhang, C. Cheng, X. Du, and X. Chen, "Experiment and simulation of milling temperature field on hardened steel die with sinusoidal surface," *International Journal on Interactive Design and Manufacturing*, vol. 12, no. 1, pp. 345–353, 2018.

[45] K. Gajalakshmi, N. Senthilkumar, and K. Palanikumar, "Experimental analysis and optimization on machining of coated carbon fiber and nanoclay reinforced aluminum hybrid composites," *Carbon Letters*, vol. 32, no. 3, pp. 815–833, 2022.

[46] N. S. Kumar and T. Tamizharasan, "Impact of interface temperature over flank wear in hard turning using carbide inserts," *Procedia Engineering*, vol. 38, pp. 613–621, 2012.

[47] Z. Lei, X. Lin, G. Wu, and L. Sun, "Cutting force modeling and experimental study for ball-end milling of free-form surfaces," *Mathematical Problems in Engineering*, vol. 2021, Article ID 3344889, 18 pages, 2021.

[48] T. Dewen, P. Cong, and Z. Jiayu, "Finite element simulation of high-speed finish milling of SKD11 hardened steel based on modified constitutive equation," *Cogent Engineering*, vol. 5, Article ID 1482589, 2018.

[49] Z. Ren, X. Zhang, Y. Wang, Z. Li, and Z. Liu, "Finite element analysis of the milling of Ti6Al4V titanium alloy laser additive manufacturing parts," *Applied Sciences*, vol. 11, no. 11, p. 4813, 2021.

Hindawi
Advances in Materials Science and Engineering
Volume 2022, Article ID 3180442, 9 pages
https://doi.org/10.1155/2022/3180442

Research Article

Optimization of Stir-Squeeze Casting Parameters to Analyze the Mechanical Properties of Al7475/B4C/Al_2O_3/TiB2 Hybrid Composites by the Taguchi Method

Bhiksha Gugulothu,[1] **P. Anusha**,[2] **M. Naga Swapna Sri**,[3] **S. Vijayakumar**,[4] **R. Periyasamy**,[5] **and Suresh Seetharaman**[6]

[1]*Department of Mechanical Engineering, Bule Hora University, Bule Hora, Ethiopia*
[2]*Department of Mechanical Engineering, P V P Siddhartha Institute of Technology, Vijayawada, India*
[3]*Department of Mechanical Engineering, P V P Siddhartha Institute of Technology, Vijayawada, India*
[4]*Department of Mechanical Engineering, BVC Engineering College (Autonomous), Odalarevu 533210, Andhra Pradesh, India*
[5]*Department of Mechanical Engineering, Kongunadu College of Engineering and Technology, Trichy, Tamil Nadu, India*
[6]*Department of Electrical and Electronics Engineering, KIT-Kalaignar Karunanidhi Institute of Technology, Coimbatore, India*

Correspondence should be addressed to Bhiksha Gugulothu; bhikshamg@gmail.com

Received 5 August 2022; Revised 23 August 2022; Accepted 3 September 2022; Published 12 September 2022

Academic Editor: Thanigaivelan R

Stir-squeeze casting (SSC) is the appropriate and inexpensive technique for producing aluminum hybrid matrix composites as it creates a uniform distribution of reinforcements in the composite with finer grains. Al7475 is a lightweight castable alloy that possesses enough hardness and strength with applications in automotive and aerospace. This research work examines the effect of process parameters for Al7475/Al_2O_3/B_4C/TiB_2 hybrid matrix composites produced by the stir-squeeze casting methodology. As per Taguchi design L16, four parameters with four levels were selected in the optimization process of SSC are stir speed (SD) of 300-450 rpm, melting temperature (ME) of 750–900°C, squeeze pressure (SE) of 50-125 MPa, and reinforcement (RT) of 2-8 wt%. The mechanical properties such as tensile strength (TS) and hardness (HN) are studied by the variation of each process parameters levels. The optimization results on TS and HN are predicted by Minitab-17 Software. It is observed that maximum TS of 325 MPa and HN of 130.6 Hv are attained at experiments L1 and L7, respectively. From the SN ratio result, the TS value is improved at the parameter level of RT2-SE4-ME2-SD4. The ANOVA result exposed that reinforcement is the most significant factor for enhancing tensile strength which contributes 38.9%, followed by squeeze pressure of 28.4%, stir speed of 13.6%, and melting temperature of 12.16%.

1. Introduction

Metal matrix composites are formed by combining two or more materials, and custom qualities are created by carefully combining the constituent parts. Specific combinations of features in composites, such as fatigue strength, hardness, damping property, coefficient of friction, wear resistance, and coefficient of thermal expansion, are made possible by systematic designs and synthesis techniques. Because of their superior physical and mechanical characteristics, aluminum-matrix composites reinforced with discontinuous supports have been used more frequently in the automotive, aerospace, and electrical industries [1]. Al7000's superior strength is by far its most significant advantage. Its tolerance of stress/strain makes it extremely valuable in aircraft applications, where it allows for weight savings over steel, even if it does not have a similar level of corrosion opposition or weldability as other alloys do. Stir-squeeze casting is a flexible method for making the composite cheaply. The components' sizes typically vary from small to large and have elaborate designs. Melt and solidification are crucial phases in the casting processes. [2] The effect of the cast feature is based on a number of factors,

Table 1: AA7475 chemical compositions.

Compositions	Cr	Cu	Fe	Mg	Mn	Si	Ti	Zn	Al
Weight in%	0.20	1.8	0.12	1.9	0.05	0.12	0.07	5.6	Balance

combined with the effect of limited automation [3]. Segregation, center-line cracking, and porosity are the uncontrollable process characteristics in casting that show poor mechanical characteristics. Squeeze casting could be able to solve these issues. This process combines closed die forging with gravity die casting. High squeeze pressure crystallization of liquid metal results in better microstructure and mechanical properties [5]. B4C/SiC-strengthened AA7075 composites with various compositions were effectively produced by utilizing the stir and squeeze casting methods to study mechanical properties. SEM and optical microstructure analysis revealed a uniform dispersion in the A7075 matrix strengthened with 1% wt of both B_4C and SiC. The A7075 alloy's hardness values were also raised by the addition of 1.5 wt% of boron carbide and 1%of tiny SiC particles. [6] To clarify the impact of extra additive particles on the mechanical properties of the produced composites, the hardness and elongation behaviors of AA7039 strengthened with particular particles of alumina, boron carbide, and also silicon carbide were investigated. Utilizing powder metallurgy and the hot-extrusion technique, AA7039 along with three composite specimens reinforced Al_2O_3,B_4C, and SiC (10 wt.%) were effectively created. The findings showed that all reinforcement particles were dispersed properly in the matrix and a strong interfacial bond between reinforcements and matrix components had been achieved. The specimen with the highest hardness and elongation among the other samples was 10 wt.% Al_2O_3 with Al alloy. Compared to the B_4C- and SiC-reinforced composites, the Al_2O_3-reinforced composite demonstrated improved interfacial bonding [7]. According to the study of Zheng et al., secondary phases are produced quickly in the melt as a result of the reaction between molten aluminum and B_4C, which leads to the formation of the Al_3BC and AlB_2 phases [8]. Rajan et al. looked into how various stir casting processes such as (i) compo casting and modified compo casting and squeeze casting routes affected the microstructure and characteristics of small fly ash/Al-7Si-0.35 Mg composites. There have been reports of $MgAl_2O_4$ being formed by the reaction of aluminum with SiO_2 and Al_2O_3 [9]. The evaluation of mechanical and wear properties were done after stir casting a 6061 Al–Al_2O_3 metal matrix composite. The melt stirring process, which combines three stages of mixing with preheat reinforcement, was successfully used to create composites including 6061Al with 6–12wt% of Al_2O_3. The alumina particle in the 6061Al metal matrix is distributed pretty uniformly in the optical micrographs of stir-cast composites [10]. Tiwen Lu and colleagues examined into the impact of Zr/Fe particle modifications on the microstructure and mechanical performance of 7075Al-based composites reinforced with 40 wt.% SiC. The created composite has the highest UTS and fracture strain with a measurement of 564 MPa and 1.12%, respectively. It also displays a mixed ductile and brittle fracture feature, with Zr elements being infrequently found in the fracture due to strong interface bonding. The majority of the iron particles in the broken AMC/Fe composite, however, show interfacial debonding from the Al matrix [11]. Ni/Ti particles of the same size were added to SiCp/7075Al composites using squeeze casting. Ti particle-added composites had better tensile strength and plasticity with values of 573 MPa and 0.65%, respectively. The more desirable interfacial structure that would guarantee the strengthening effects of metal particles is the interdiffusion metallurgical bonding. [12] The literature survey revealed that the AA7xxx series has received very little attention. In various industries, especially in the automotive and aerospace sectors, the improvement of reinforced 7475 composites with high strength and light weight is essential. Many researchers have attempted to produce composites using combined stir-squeeze casting. However, little effort has been put into optimizing the stir-squeeze casting process parameters (SSC). The novelty of this work is to produce AA7475/Al_2O_3/B_4C/TiB_2 hybrid composites by the stir-squeeze method and determine the mechanical properties of the prepared composites. The primary goals of this research are to identify the most appropriate SSC parameters and the contribution of reinforcements to enhance tensile strength (TS) and hardness (HN). With the help of the Taguchi method and Minitab software, we were to find the optimized parameters of stirrer speed (SD), melting temperature (ME), squeeze pressure (SE), and also reinforcement (RT).

2. Materials and Methodology

AA7475 is used as the main material and Al_2O_3/B_4C/TiB_2 with 50 μm powder as the reinforcement. A strong substance with excellent strength and high wear resistance at high temperatures is titanium diboride (TiB_2). It has high stability and wettability in liquid metals like zinc and aluminum and is unaffected by the majority of chemical reagents. Boron carbide powder acts as an abrasive material for polishing purposes, especially in grinding and water jet cutting applications due to its high hardness. Additionally, it is employed for treating diamond tooling. Aluminum oxide (Al_2O_3), a commonly used ceramic reinforcing material, has shown to exhibit good compressive strength, wear resistance [13], and high machinability. The base alloy 7475 chemical elements contributions are exposed in Table 1.

Four SSC process parameters with four levels were selected for the present experiment. Each level's on parameters are presented in Table.2. The selected reinforcements (Al_2O_3/B_4C/TiB_2) are equally added with AA7475 as per Table 2 values during the casting process. As per the full factorial method, a total 256 experimental samples have to be created. Enhancing the response variables of HN and TS using a factorial design could be more time consuming and very costly. Hence, to minimize the number of experiments, the

Table 2: SSC parameters and levels.

SSC parameter	Unit	Levels			
		1	2	3	4
Stir speed (SD)	Rpm	300	350	400	450
Melting temperature (ME)	°C	750	800	850	900
Squeeze pressure (SE)	MPa	50	75	100	125
Reinforcements (RT)	wt%.	2	4	6	8

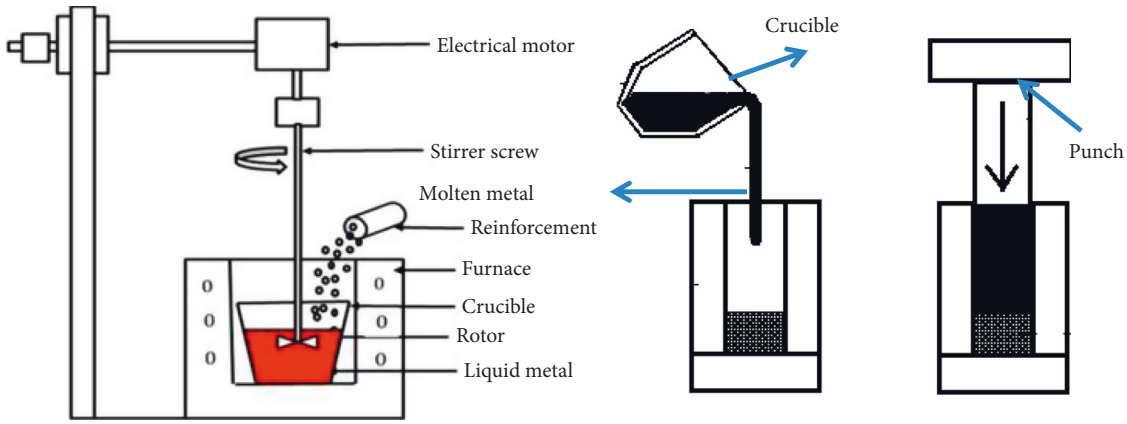

Figure 1: Stir-squeeze casting setup.

Taguchi methodology was employed using different orthogonal arrays to offer reduced variance and less number of experiments. The Taguchi method resulted in sixteen experimental arrangements (L1–L16) with parameters disseminated at four levels. AA7475 was melted in a heating furnace with the stirrer. Ages, melted 7475 was mixed with $Al_2O_3/B_4C/TiB_2$ at various weight percentages in the casting to produce a hybrid composite.5–10 g of Na_3AlF_6 were further added to the furnace throughout the melting process in order to reduce the production of slag and increase casting effectiveness. The SSC complete setup is given in Figure 1. The lifting mechanism facilitated the travel of the stirrer into contact with the mix's constituent elements. Al alloy was kept inside a crucible and melted at around 750°C in an electric furnace. 2w.t% of $Al_2O_3/B_4C/TiB_2$ mixed powder burned at 280°C in another furnace. 7475 alloy and reinforcements were blended and heated. To create Al-based composites, the prepared melted particles were placed into the required mold after being continuously stirred by a stirrer connected to the motor for 5-10 min; then, the plunger was used to apply the pressure (50 MPa) from the top of the die, and holding that plunger for 1-2 minutes and then removing the solidified part from the preferred die [14–17]. This process is to be continued for the remaining parameter levels to create several specimens by adjusting the casting parameters.

3. Result and Discussion

The fabricated specimens underwent a tensile test in accordance with the ASTM B557 M Standard. The entire samples were cleaned and polished using an abrasive paper to remove any slag from the surface prior to applying a load of 6 KN. Using a 1/16-inch ball indenter and a 250 kg weight, the Brinell hardness machine conducts hardness tests at room temperature. Each specimen is subjected to three different trails which are then averaged. TS and HN readings from the experiment and signal to noise ratio are displayed in Table 3. It was comprehended that the highest and lowest optimum groupings of parameters for tensile strength were acknowledged at SD1-ME1-SE1-RT1 (300 rpm, 750°C, 50 MPa, and 2wt%) and SD4-ME1-SE4-RT2 (450 rpm, 750°C, 125 MPa, and 4wt%), respectively. The best and least for the HN value were also discovered at SD2-ME3-SE4-RT1 (350 rpm, 850°C, 125 MPa & 2wt%) and SD4-ME3-SE2-RT4 (450 rpm, 850°C, 75MPa & 8wt%). S/N ratio response table and main plots help to find the suitable level of each parameter in the mechanical properties (TS and HN) (TS and HN). From Table 4 and Figure 2, it can be seen that the second level of RT was the first rank to develop tensile strength, followed by the fourth level of SE, second level of ME, and fourth level of SD parameters. The smallest is considered as a significant value. Similarly, from Table 5 and Figure 3, it was noticed that HN values were improved by SD4 as the first influencing parameter level, trailed by SE1, RT4, and ME3.Table 6 and Table 7 show the percentage contribution of SSC parameters of SD, ME,SE, and RT for HN and TS properties. F value, P value, and contribution percentage acted as controllable and probability of irrepressible to achieve the maximum TS value [18]. The highest contribution of RT is 38.9% which is the most significant factor to improve TS, followed by SE 28.4%, SD13.6%, and ME 12.16%. Similarly, in the case of hardness (HN), SE is the

Table 3: Hardness and tensile strength results from experiment and Minitab.

Experiment No	*SSC parameters*				*Observational result*		*S/N ratio*	
	SD (Rpm)	ME (°C)	SE (MPa)	RT (wt%)	TS (Mpa)	HN	TS (dB)	HN (dB)
L1	300	750	50	2	325.23	95.60	−50.2438	−39.6092
L2	300	800	75	4	245.23	108.20	−47.7915	−40.6845
L3	300	850	100	6	315.26	107.80	−49.9734	−40.6524
L4	300	900	125	8	278.69	88.20	−48.9024	−38.9094
L5	350	750	75	6	322.56	95.60	−50.1722	−39.6092
L6	350	800	50	8	285.36	110.50	−49.1079	−40.8672
L7	350	850	125	2	258.69	130.60	−48.2556	−42.3189
L8	350	900	100	4	243.52	120.80	−47.7307	−41.6413
L9	400	750	100	8	312.60	95.60	−49.8998	−39.6092
L10	400	800	125	6	246.87	105.80	−47.8494	−40.4897
L11	400	850	50	4	275.23	79.25	−48.7939	−37.9800
L12	400	900	75	2	315.26	112.87	−49.9734	−41.0516
L13	450	750	125	4	215.23	128.50	−46.6581	−42.1781
L14	450	800	100	2	276.29	89.50	−48.8273	−39.0365
L15	450	850	75	8	243.88	79.20	−47.7435	−37.9745
L16	450	900	50	6	302.89	102.90	−49.6257	−40.2483

Table 4: S/N ratio response for TS.

Level	SD	ME	SE	RT
1	−49.23	−49.24	−49.44	−49.33
2	−48.82	−48.39	−48.92	−47.74
3	−49.13	−48.69	−49.11	−49.41
4	−48.21	−49.06	−47.92	−48.91
Delta	1.01	0.85	1.53	1.66
Rank	3	4	2	1

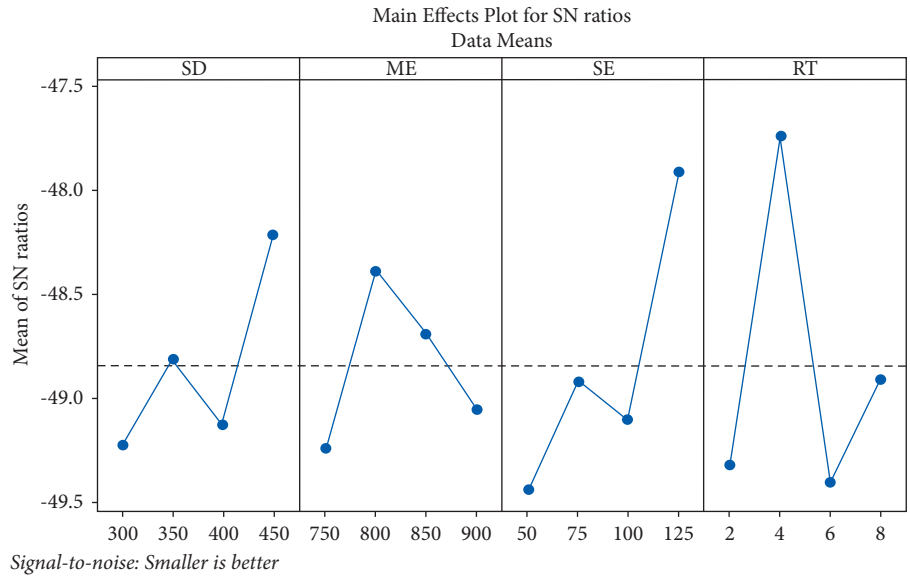

Figure 2: SN plot for TS.

Table 5: S/N ratio response for HN.

Level	SD	ME	SE	RT
1	−39.96	−40.25	−39.68	−40.50
2	−41.11	−40.27	−39.83	−40.62
3	−39.78	−39.73	−40.23	−40.25
4	−39.86	−40.46	−40.97	−39.34
Delta	1.33	0.73	1.30	1.28
Rank	1	4	2	3

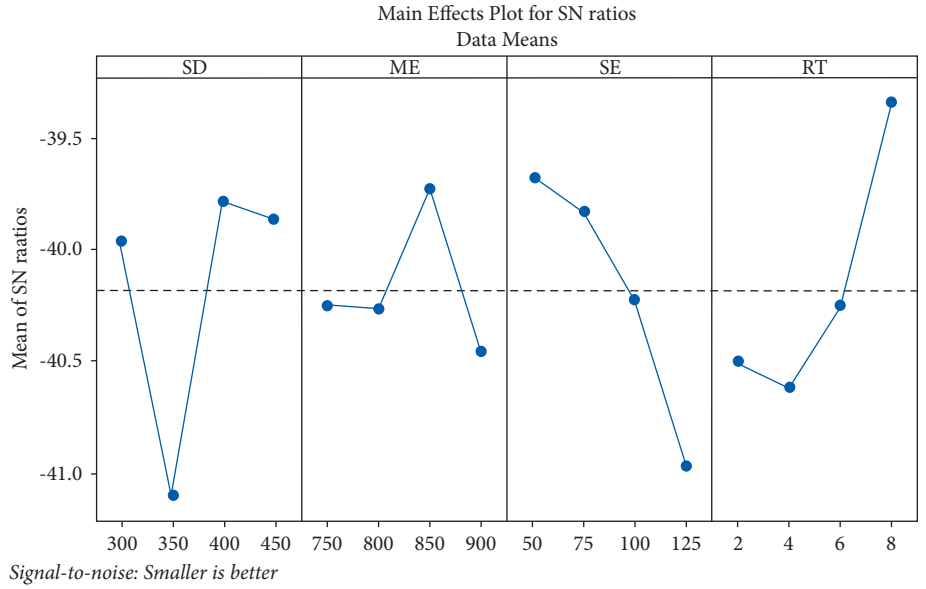

Figure 3: SN plot for HN.

Table 6: Analysis of variance-TS.

Sources	Df	Seq-SS	Adj-MS	F	*P*	Contribution (%)
SD	3	2392	797.5	12.00	0.0292	13.6
ME	3	2137	712.4	11.79	0.0323	12.16
SE	3	4996	1665.5	44.18	0.0135	28.4
RT	3	6848	2282.7	55.73	0.0093	38.9
Residual error	3	1196	398.7			6.94
Total	15	17570				

Table 7: Analysis of variance for HN.

Sources	Df	Seq-SS	Adj-MS	F	*P*	Contribution (%)
SD	3	375.0	225.01	12.50	0.457	5.71
ME	3	201.3	33.78	21.37	0.577	4.52
SE	3	1828.6	209.52	135.38	0.047	50.26
RT	3	1091.8	197.27	10.36	0.078	38.23
Residual error	3	139.3	546.42			1.28
Total	15	3636				

most influencing factor (50.26%) to develop hardness of prepared composite, trailed by RT 38.23%, SD 5.71%, and ME 4.52%.The results of tensile tests reveal the ductility and strength of materials when subjected to uniaxial tensile stresses. A metal's capacity to bear tensile loads without breaking is largely determined by its tensile strength. Brittle metals are more likely to rupture and are an important component in the metal forming process.

This test can determine whether potential materials meet the necessary strength and elongation standards for a certain product. Generally, tensile and hardness offer an opportunity to identify novel alloys, their characteristics, and potential applications in the metal of manufacturing industries. The applications of developed composites are bicycle frames, shell casings, aircraft components, and rock climbing equipment, etc.

3.1. Regression Equation. The relationship among process parameters was recognized with the aid of a regression equation and also calculate the value of HN and TS in (1) and (2), which were carried out by Minitab software.

$$\mathrm{TS} = 415 - 0.169\,\mathrm{SD} - 0.033\,\mathrm{ME} - 0.547\,\mathrm{SE} + 0.54\,\mathrm{RT}. \quad (1)$$

$$\mathrm{HN} = 103.6 - 0.0315\,\mathrm{SD} + 0.0056\,\mathrm{ME} + 0.212\,\mathrm{SE} - 2.37\,\mathrm{RT}. \quad (2)$$

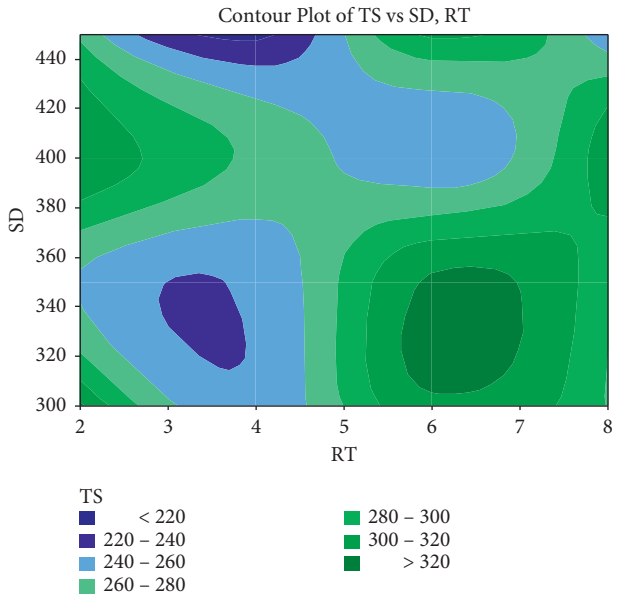

Figure 4: Contour plot-TS vs SD and RT.

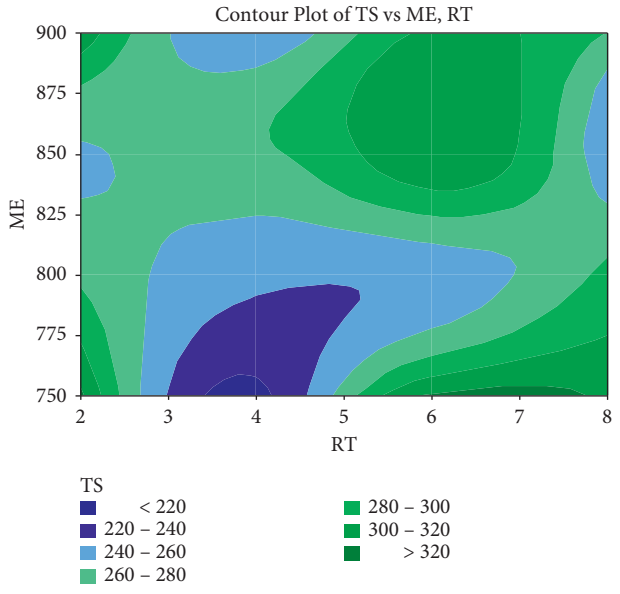

Figure 5: Contour plot-TS vs ME and RT.

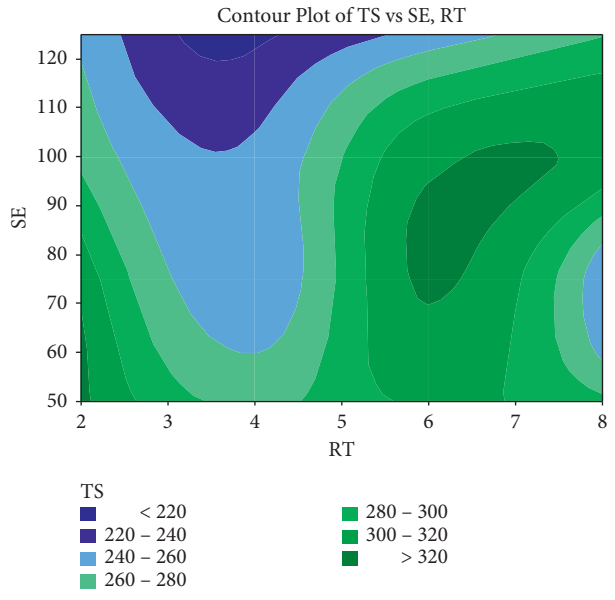

Figure 6: Contour plot-TS vs SE and RT.

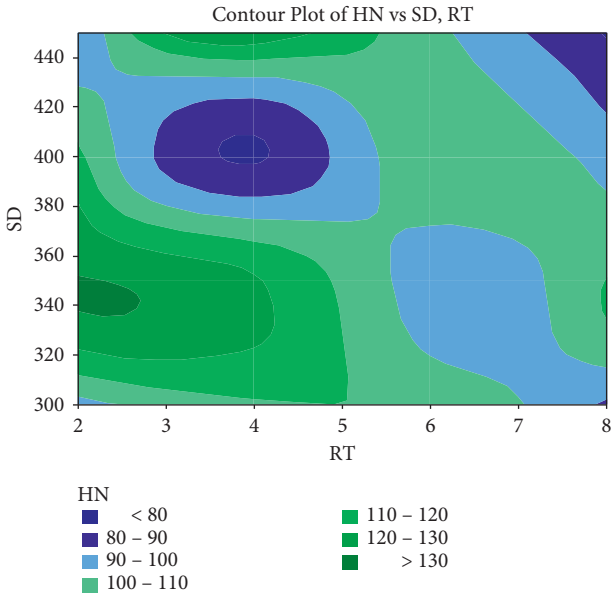

Figure 7: Contour plot-HN vs SD and RT.

3.2. Contour Plots. These plots are to illustrate the three-dimensional surface on a two-dimensional plane. It displays two parameters on the x and y axes and a response variable of TS and HN on the Z axis. Figure 4, Figure 5, and Figure 6 show the interaction between the SSC parameters on the output response of TS, and Figure 7, Figure 8 and Figure 9 show the interaction between the three parameters on HN. From graph observation, the ranges of casting factors SD(320–450Rpm), ME(800–875°C), SE (65–110 MPa), and RT (4-7wt%) were suggested for achieving high tensile strength and hardness of Al7475/Al2O3/B4C/TiB2 hybrid composites.

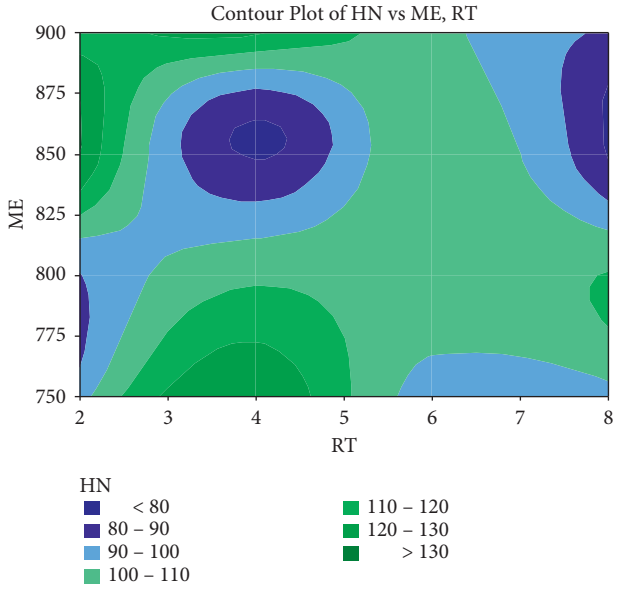

Figure 8: Contour plot-HN vs ME and RT.

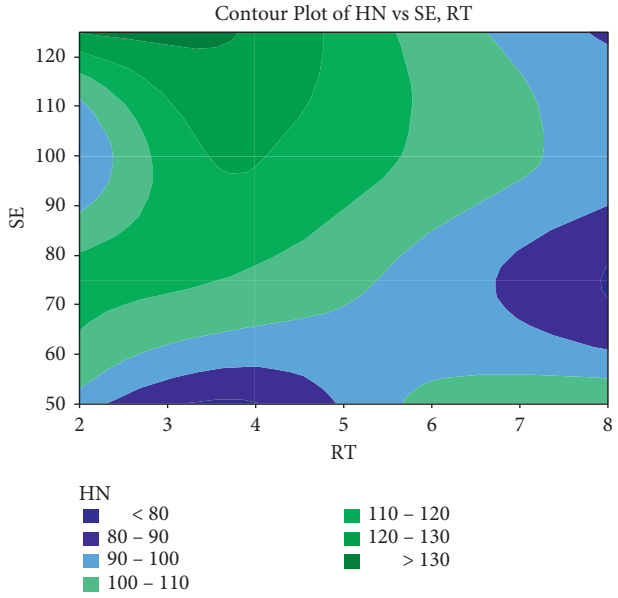

Figure 9: Contour plot-HN vs SE and RT.

3.3. Microstructure of the Composite. Figure 10(a) shows the microstructure of Al7475 alloys without the addition of any reinforcements. It is observed that all elements are evenly dispersed in 7475 Al. Figure 10(b) presents the microstructure of the L13 sample and exposed a tough to find out any major difference in dimple morphology in the sample due to the spreading of the reinforcing particles ($B_4C/Al_2O_3/TiB_2$). Figure 10(c) shows that the L7 sample and reinforcement particles are well engaged in this composite, no marked interfacial products are perceived at the boundaries between the Al7475 matrix and $B4C/Al_2O_3/TiB2$ particles. Figure 10(d) exposes the L1 sample of composites. No cracks and dimples are observed, and reinforcements are distributed uniformly.

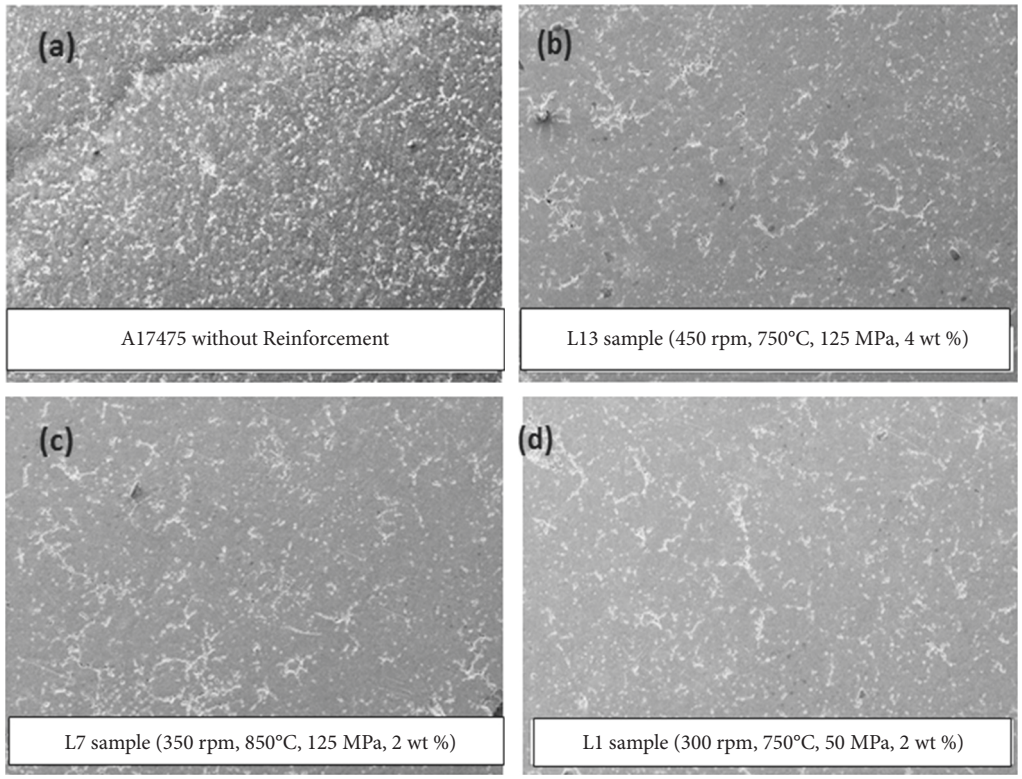

Figure 10: Microscope images of (a) Al7475 alloy, (b) L13 sample, (c) L7 sample, and (d) L1 sample.

4. Conclusion

In this research work, Al7475/Al_2O_3/B_4C/TiB_2 hybrid matrix composites were prepared by the stir-squeeze casting process. Four parameters with four levels were selected, such as stirrer speed, melt temperature, squeeze pressure, and reinforcement weight percent. The various tests were performed to analyze mechanical properties of tensile strength and hardness using L16 orthogonal array in the Taguchi methodology. From the experimental observation and optimization technique, we have made the following conclusions.

The maximum TS (325 MPa) was attained at experiment L1 with combined process parameters of a stir speed of 300 rpm, melting temperature of 750°C, squeeze pressure of 50 MPa, and reinforcements of 2wt%, whereas maximum HN (130.6 Hv) was observed by maintaining a stir speed of 350 rpm, melting temperature 850°C, squeeze pressure of 125 MPa, and reinforcements 2wt% which was in the L7 experiment.

From the S/N ratio response table, it was noticed that TS was increased at the RT2 level followed by SE4, ME2, and SD4.

ANOVA results revealed that the most important factor in enhancing tensile strength is reinforcements, which contribute 38.9%, followed by a squeeze pressure of 28.4%, stir speed 13.6%, and melting temperature of 12.16%. Similarly, when it comes to hardness (HN), SE has the greatest influence (50.26%), followed by RT (38.23%), SD (5.71%), and ME (4.52%).

Data Availability

The data used to support the findings of this study are included in the article. Should further data or information be required, these are available from the corresponding author upon request.

Disclosure

It was performed as a part of the Employment Bule Hora University, Ethiopia.

Conflicts of Interest

The authors declare that there are no conflicts of interest regarding the publication of this paper.

Acknowledgments

The authors appreciate the technical assistance to complete this experimental work from the Department of Mechanical Engineering, Bule Hora University, Ethiopia. The authors thank BVC Engineering College (Autonomous), Andhra Pradesh, for the support in writing the draft.

References

[1] C. K. Yung and S. L. I. Chan, "Tensile properties of nanometric Al2O3 particulate reinforced aluminium matrix composites," *Journal of Materials Chemistry and Physics*, vol. 85, Article ID 438443, 2004.

[2] A. Sata and B. Ravi, "Bayesian inference-based investment-casting defect analysis system for industrial application," *International Journal of Advanced Manufacturing Technology*, vol. 90, no. 9–12, pp. 3301–3315, 2016.

[3] S. Kumar, P. S. Satsangi, and D. R. Prajapati, "Optimization of process factors for controlling defects due to melt shop using Taguchi method," *International Journal of Quality & Reliability Management*, vol. 30, no. 1, pp. 4–22, 2013.

[4] M. R. Ghomashchi and A. Vikhrov, "Squeeze casting: an overview," *Journal of Materials Processing Technology*, vol. 101, no. 1–3, pp. 1–9, 2000.

[5] R. Srinivasan, A. Ramesh, and P. Senthil, "Experimental investigation on the effect of pressure on microstructure and mechanical properties of squeeze cast rectangular plate of LM6 aluminium alloy," *International Journal of Applied Engineering Research*, vol. 10, pp. 44080–44085, 2015.

[6] K. Sekar and D. V. Ananda Rao, "Investigation of hybrid composite A7075/SiC/B4C by stir and squeeze casting method," *Materials Today Proceedings*, vol. 22, pp. 1398–1408, 2020.

[7] Ş. Karabulut, U. Gökmen, and H. Çinici, "Study on the mechanical and drilling properties of AA7039 composites reinforced with Al2O3/B4C/SiC particles," *Composites Part B: Engineering*, vol. 93, pp. 43–55, 2016.

[8] J. Zheng, Q. Li, W. Liu, and G. Shu, "Microstructure evolution of 15 wt% boron carbide/aluminum composites during liquid-stirring process," *Journal of Composite Materials*, vol. 50, no. 27, pp. 3843–3852, 2016.

[9] T. P. D. Rajan, R. M. Pillai, B. C. Pai, K. G. Satyanarayana, and P. K. Rohatgi, "Fabrication and characterisation of Al–7Si–0.35Mg/fly ash metal matrix composites processed by different stir casting routes," *Composites Science and Technology*, vol. 67, no. 15–16, pp. 3369–3377, 2007.

[10] V. Bharath, M. Nagaral, V. Auradi, and S. A. Kori, "Preparation of 6061Al-Al 2 O 3 MMC's by stir casting and evaluation of mechanical and wear properties," *Procedia Materials Science*, vol. 6, pp. 1658–1667, 2014.

[11] T. Lu, W. Chen, B. Li et al., "Influence mechanisms of Zr and Fe particle additions on the microstructure and mechanical behavior of squeeze-cast 7075Al hybrid composites," *Journal of Alloys and Compounds*, vol. 798, pp. 587–596, 2019.

[12] Y. Liu, Z. Zheng, M. Mao et al., "Effects of micron heterogeneous metal particles on the microstructure and mechanical properties of 7075Al hybrid composites," *Journal of Alloys and Compounds*, vol. 808, no. 151727, Article ID 151727, 2019.

[13] R. Arunachalam, S. Piya, P. K. Krishnan et al., "Optimization of stir–squeeze casting parameters for production of metal matrix composites using a hybrid analytical hierarchy process–Taguchi-Grey approach," *Engineering Optimization*, vol. 52, no. 7, pp. 1166–1183, 2019.

[14] A. M. Jaber and P. K. Krishnan, "Development of a sustainable novel aluminum alloy from scrap car wheels through a stir-squeeze casting process," *Kovove Materialy-Metallic Materials*, vol. 60, no. 3, 2022.

[15] P. K. Krishnan, R. Arunachalam, A. Husain, and M. Al-Maharbi, "Studies on the influence of stirrer blade design on the microstructure and mechanical properties of a novel aluminum metal matrix composite," *Journal of Manufacturing Science and Engineering*, vol. 143, no. 2, pp. 1–13, 2021.

[16] P. K. Krishnan, J. V. Christy, R. Arunachalam et al., "Production of aluminum alloy-based metal matrix composites using scrap aluminum alloy and waste materials: influence on microstructure and mechanical properties," *Journal of Alloys and Compounds*, vol. 784, pp. 1047–1061, 2019.

[17] J. V. Christy, R. Arunachalam, A.-H. I. Mourad, P. K. Krishnan, S. Piya, and M. Al-Maharbi, "Processing, properties, and microstructure of Recycled aluminum alloy composites produced through an optimized stir and squeeze casting processes," *Journal of Manufacturing Processes*, vol. 59, pp. 287–301, 2020.

[18] L. Natrayan and M. Senthil Kumar, "An integrated artificial neural network and Taguchi approach to optimize the squeeze cast process parameters of AA6061/Al2O3/SiC/Gr hybrid composites prepared by novel encapsulation feeding technique," *Materials Today Communications*, vol. 25, Article ID 101586, 2020.

Hindawi
Advances in Materials Science and Engineering
Volume 2022, Article ID 2707879, 8 pages
https://doi.org/10.1155/2022/2707879

Research Article

Tensile Properties of Thermal Cycled Titanium Alloy (Ti–6Al–4V)

Putti Venkata Siva Teja,[1] **Manikandan S**,[1] **Ayyagari Kiran Kumar**,[2] **Suresh K**,[1] **and Jenifer Mahilraj**[3]

[1]*Department of Mechanical Engineering, Annamalai University, Annamalai Nagar, Chidambaram, Tamil Nadu, India*
[2]*Department of Mechanical Engineering, Dhanekula Institute of Engineering & Technology, Ganguru, Vijayawada, Andhra Pradesh, India*
[3]*Department of Computer Science and Engineering, Kebri Dehar University, Kebri Dehar, Ethiopia*

Correspondence should be addressed to Putti Venkata Siva Teja; pvsteja1990@gmail.com and Jenifer Mahilraj; jenifer2022@kdu.edu.et

Received 30 June 2022; Accepted 1 August 2022; Published 23 August 2022

Academic Editor: Thanigaivelan R

The effect of thermal cycling on tensile properties and microstructural characterization of Titanium (Ti–6Al–4V) alloy which were subjected to various types of thermomechanical treatments especially stress relief annealing and solution treated aging were studied and results presented. The specimens were thermally treated at a temperature of 427°C for up to 1500 cycles. The test setup used for thermal treatment of the specimens was a specially designed experimental setup. After thermal treatment the specimens, were prepared for a tensile test to get the desired tensile properties. It was noticed that the maximum tensile strength of the specimen was observed when reached at 250 cycles and thereafter marginally increasing up to 1000 cycles. After 1000 cycles the tensile strength of the specimen decreases. Similarly, the hardness of the specimen increases up to 1000 cycles and then decreases after 1000 cycles, while elongation increases marginally when the cycle increases. Solution-treated aged specimen attains greater strength and hardness when compared to stress relief annealed specimen. With the increased number of cycles, the strength of the specimen when treated with stress relief annealing and solution-treated aging specimen increases. It was observed that the hardness and strength values decrease after 1000 cycles. With an increasing number of cycles, the tensile elongation increased. When compared with both the treatment processes the solution-treated aged specimen shows better results after thermal cycling.

1. Introduction

Titanium alloys are recognized for their high tensile strength and toughness properties even at extreme temperatures. Usually, they are a mixture of titanium as metal and some other chemical elements. The present study, an alpha-beta titanium alloy which has high specific strength as well good corrosive resistance properties. Due to its wide range of applicable properties like lightweight in nature, high specific strength, thermally stability, and corrosion resistance; Ti–6Al–4V alloy is being used in various applications on demand in aviation and automobile industries. These days titanium and its alloys are widely used in applications like spacecraft, missiles, aircraft frames, aircraft engines, marine applications, military [1, 2], chemical [3–6], armor plate applications, metallurgic [7] sports equipment [8], automotive components [9], surgical devices, medical implants [7, 10], and petrochemical production [11]. The alloy Ti–6Al–4V is widely acceptable and viable for structural applications in aerospace or aviation vehicles. PVD coatings have been shown to improve mechanical properties, biocompatibility, osseointegration, wear, and corrosion resistance in Ti–6Al–4V and SS 316 LVM substrates [12, 13]. Out of all titanium alloys, Ti–6Al–4V is the most preferable to use in engine components, airframe, and aerospace components. Ti–6Al–4V can also be represented as Ti–6Al–4V. Ti–6Al–4V alloys are heat treated in two different forms [14] in order to get an optimum combination of machinability, and structural stability by annealing and also for an increase in strength by treating with solution and aged and also for ductility. Researchers have identified that Ti–6Al–4V will behave as superplastic material under the temperature condition

between 750°C and 950°C with a strain rate of 5×10^{-4}s- [15, 16]. Reports say that in titanium alloy after heat treatment, the α in the α-β phase-field will not transform while cooling to room temperature still the presence of α-phase affects the % of elongation of the β phase. The alloy's mechanical properties also depend on the transformation of β-phase to α' martensite and ultrafine refinement of α and β grains. This transformation is possible by solution treatment and aging process, which improves the tensile strength of alloy without reducing the ductility. This process produces a 20% increase in the strength of the annealing process [17–19]. Between the temperatures of 930°C to 980°C good refinement of α grain is notorious because of this refinement strength of the alloy increases. Above 980°C, the strength decreases due to the rapid growth in prior β grains [20, 21].

Li et al. [22] reported that when heat treated at 950°C and then cooled in the furnace increased the strength and elongation of Ti–6Al–4V alloy than the base metal. Despite this, it has resulted in a decreased hardness value than the base metal. Wang et al. [15] observed that the strength of titanium alloys was higher when tested in a condition of 950°C for 1 hour, WQ + 540°C for 4 hours followed by air cooling (AC) than when treated at 970°C for 1 hour, WQ + 540°C for 4 hours, AC. Researchers have proven that when alloys are heat-treated by thermal cycles ductile properties of the alloys could be improved. By treating an alloy with thermal cycling will result in the strengthening of mechanical properties along with improved ductility [23]. Hu et al. investigated the effect of heat treatment on microstructure and tensile properties of Ti–6Al–4V alloy. As the annealing temperature was increased, α' martensite decomposed into the $\alpha + \beta$ phase, whereas the width of the lamellae increased, resulting in an increase in ductility and a reduction in strength [24]. The influence of heat treatment on the microstructural evolution and mechanical characteristics of Ti–6Al–4V alloys produced by selective laser melting (SLM) was studied. The ductility of the as-fabricated −1133 K sample was substantially higher than that of the as-fabricated sample. This was attributed to the precipitation of micro/nanoscale and thermal phases, which was accompanied by columnar grain equiaxial transition [25]. A strong association was found between α lath width and microhardness levels. The solution air-cooled plus aged samples had the finest refinement in α-β morphology, with homogeneous equiaxed grains. The tensile characteristics of the solution air-cooled plus aged samples were comparable to those of the EBM printed samples and exceeded ASTMF1472 requirements [26]. The CCT diagram clearly shows that β transfers to α' martensite occurs in both sections of the SLM process. However, a higher energy density occurred at the surface, resulting in a greater remelt depth and a greater number of effective thermal cycles in the preceding layers. As a result, the martensite size in the SLM samples reduced from the core to the surface [27]. Hence, titanium and its alloys play a vital role in all kinds of structural applications. In the case of high fidelity applications, the material is often subjected to thermal cycling with temperature and time in various cycles. In the present work Ti–6Al–4V alloy is heat treated in two different forms and thermal cycling is carried out in specially designed equipment with different cycles ranging from 500 to 1500 cycles.

2. Concept of Thermal Cycling Testing

Thermal cycling is the process with two extreme temperatures being applied to a material in a cyclic manner of relatively high rates of change, to observe the latent defects. This test is used for modulating the temperature which is used to improve the strength and performance of a variety of materials. It is considered to be one of the most severe among environmental stress carrying a test to evaluate a material or product's behavior toward reliability. As many industries are looking towards improved material performance in typical world situations, this test determines the material withstanding capability when exposed to alternating high and low extreme temperatures. The workpiece is heated and cooled in cycles throughout this thermal cycling process until the material undergoes molecular reformation. This reorganization helps in relieving stresses, reduces particle structure, and tightens the material throughout and making the metal more uniform. Additionally, the material's properties for distributing heat and conducting energy will be improved. The steel is heated until it reaches its maximum non-magnetic state and then cooled by air until it acquires its magnetic property.

The time it takes for each metal varies, viz., for 1080 steel it takes a few seconds. In general, an instrument in continuous working condition will experience wear and tear till its performance is gradually compromised in real-time sequences. So, it may fail or require maintenance in time as needed sooner or later. When it is combined with thermal cycling it brings favorable results which contrasts to experience failure later than sooner. The applications of this type of technology are broadly used in aircraft, medicals, industries, automotive and railroad cars. The advantages of the thermal cycling process include relieving internal stress in forged or cast materials, reducing maintenance and repair costs, extending the life of surgical instrumentation.

2.1. Forced Air Cooling. In this process, warm air is pulled out rapidly which increases the effective cooling rate and thus avoids condensation also which in turn is also used as a dehumidifying effect. In this process, effective surface area will be increased. As air is a medium to cool the component/material in thermal cycling, for advanced applications forced air is blown towards the specimen to cool till it cools back to normal and the cycle is repeated for thermal cycling. Air at a pressure of 3 bars will be sprayed over the specimen to cool for 2 minutes to attain room temperature. In our case, two minutes is the dwell time. Some advantages of forced air cooling are microstructure of the metal can be improved and also increase in microhardness can be observed [28, 29].

3. Experimental Procedure

A specific approach was adopted for studying Ti–6Al–4V alloy and its tensile properties. Figure 1 shows that the flow chart of the experimentation process. At first, specimens were prepared for the heat treatment process. Later the specimens were processed with two different heat treatment methods. One for stress relieving and annealing, and the

other for Solution treating and aging (STA). In a later stage, the heat-treated specimens were subjected to thermal cycling. The results of tensile properties were compared before and after thermal cycling.

An experimental study was conducted using high-precision instrumentation to acquire accurate test values. At a room temperature, the tensile tests were carried out using the UTM machine of Model Unitek 9410. Hardness measurement was done by using the Vickers hardness testing method on Zwick 3212 on the same specimen as used for the tensile test.

3.1. Specimen Preparation. The specimen is prepared from a Ti– 6Al– 4V plate. It is machined by using a wire cut EDM machine. It is a type of metal removal process where the metal is removed using an electric spark. The spark will remove the material as the spark-erosion technique is applied in this principle. EDM is mostly used for metal components especially electrically conductive metals or heat-treated metals like high carbon steels, Inconel, Titanium alloys, and AMC [30–32]. The specimen is prepared by ASTM E8/E8M specifications. The geometry of the tensile specimen is shown in Figure 2.

3.2. Heat Treatment of the TI–6Al–4V Alloy. To study the tensile behavior, Ti–6Al–4V alloy specimens were subjected to heat treatments (Stress Relief Anneal, Solution treated, and Aged). Primarily, the specimens of stress relief anneal are heated to a temperature of 538°C for 1 hour and it is furnace-cooled to reach the atmospheric temperature as shown in Figure 3.

As part of the preparation of an alloy, annealing is used to relieve stress in the material, hence increasing its tensile strength and ductility. Then, the specimens are heated at a temperature of 950°C for 1 hour and it is quenched in water as part of the STA process. After the quenching process with a delay of 2 seconds, the aging process is performed at 524°C for 4 hours, and then it is forced to air cool outside the furnace to reach an atmospheric temperature shown in Figure 4. This process is termed as solution treatment and aging, which increases the strength and hardness of the material.

3.3. Thermal Cycling Test Setup. Thermal cycling testing is also termed as temperature cycling process. It is generally performed to determine material's resistance when exposed to extreme high and low temperatures cyclically as alternating the high and low temperatures. This is performed for checking thermal mismatch in the alloys as they can cause certain kinds of failures and damages like cracking etc.

So before performing this test, the specimen has been heat-treated. The test setup of the thermal cycling test has been shown in Figure 5. The apparatus can be controlled using the Program Logic Control (PLC) unit. Using this apparatus, the specimens are thermally cycled. For exposing the specimen to extreme temperatures rapidly. A pneumatic actuator is attached to the specimen works in a translation motion as required, in and out of the muffle furnace. The temperature of the muffle furnace has been maintained

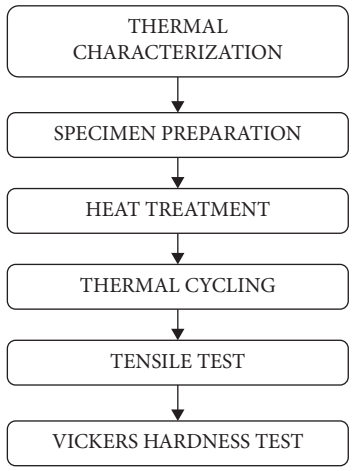

Figure 1: Flowchart of the experimentation process.

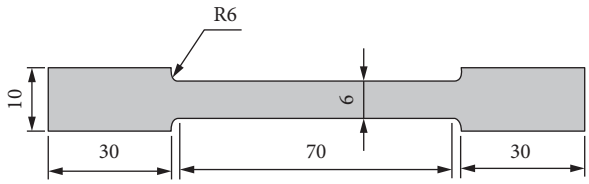

Figure 2: Geometrical shape with dimensions of the tensile specimen (All dimensions are in mm).

Figure 3: Stress relief anneal.

constantly at 427°C with a dwell time of 2 minutes. The dwell time of 2 minutes is programmed in PLC, to operate the pneumatic actuator (5).

For force cooling of the specimens, samples are exposed to air (as a medium) under 3 bars of pressure. For a proper test result, it is estimated to be 1500 cycles per test. So systematically the test specimens are exposed to 1500 cycles.

(a) (b)

Figure 4: Solution treated and aged.

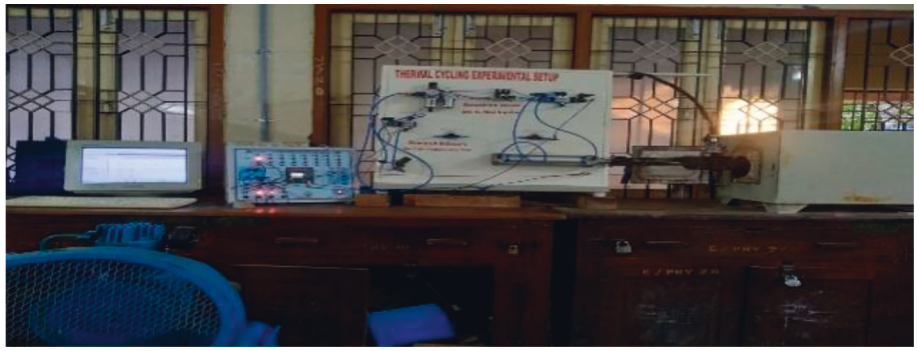

Figure 5: Thermal-cycled experimental setup.

3.4. Tensile Testing. In tensile testing of a specimen, a sample is fully loaded under controlled tension until it fails. With this test, we knew about the strength properties and ductility of the material before and after the thermal cycling test. The apparatus used for the tensile test is a UTM with the following specifications:

Model: Unitek 94100 with a Load range of 0 to 100 kN, Maximum cross head stroke of 1000 mm, Clearance between columns of 450 mm, Crosshead displacement measurement with 0.01 mm, Cross head speed of 0.25 to 250 mm/min, Power supply: 230 VAC, 50 Hz Single Phase.

The specimen with dimensions of 130 mm as length and a diameter of 10 mm has been used for testing. The specimen is shown in Figure 6. The deformations due to elongations and load applied have been recorded down at various time intervals with the help of computer. From the values observed through the experimentation, the elastic modulus (E), yield strength, % of elongation has been calculated and noted.

The specimen is inserted into the grips of the testing machine to hold the test piece, and then, the load is applied

Figure 6: The tensile specimen.

to observe the elongations through which mechanical properties can be calculated. The reading is taken frequently as yield point is approached. The universal testing machine is shown in Figure 7.

4. Results and Discussion

A titanium alloy was subjected to stress relief annealing and STA to study the thermal cycling effects on tensile properties. On UTM, tensile test was performed at room temperature with the specimens after and before heat treatment and temperature cycling. The results of the effect of with heat treatment and without heat treatment were presented in this section.

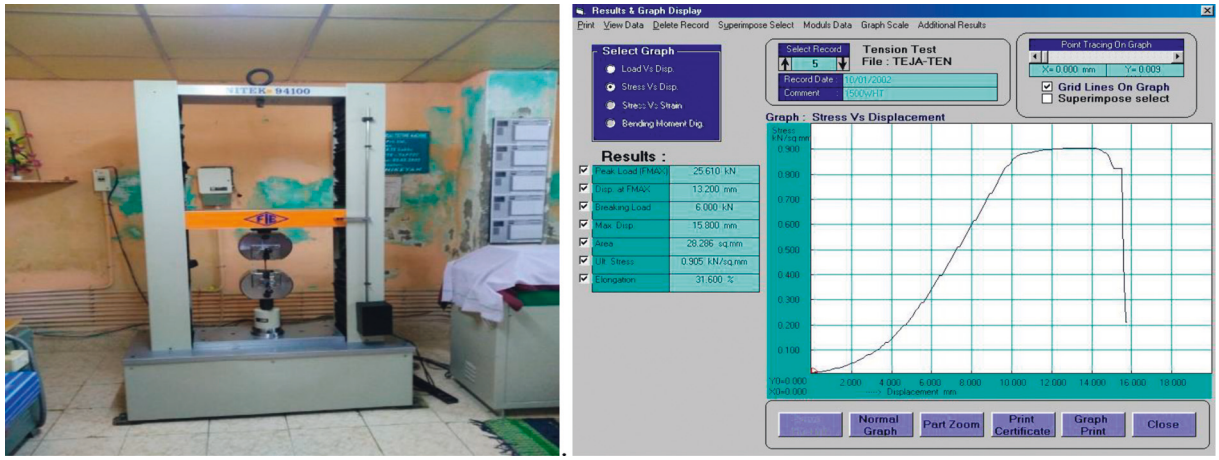

Figure 7: The universal testing machine.

4.1. Effect of Thermal Cycling on the Ti–6Al–4V Alloy without Heat Treatment (WHT). The specimens were first gone through thermal cycling without heat treatment. The test results were plotted into graphs and are presented in Figures 8 and 9. By analysis, it is observed that the tensile strength of the specimen increases with the increase in a number of cycles until 1000 thermal cycles. The maximum tensile strength has been observed at 1000 cycles. Ultimate tensile strength (UTS) of 920 mpa and yield strength (YS) of 885 MPa and elongation of 26%. After 1000 cycles, ultimate tensile strength (UTS) is observed to be in decreasing trend. As the number of cycles increases, the % of elongation of the alloy under study shows a steep decreasing trend. The hardness of specimen shows a similar trend as in the case of tensile strength is maximum at 1000 cycle and decreases after 1000 cycles as shown in Figure 10. Among the three mentioned thermal cycles, 1000 cycles showed 374.6 $HV_{0.5}$ which is the highest value among the three thermal cycle conditions. The lowest values have resulted in 500 cycles as 356 $HV_{0.5}$, and at 1500 cycles as 369 $HV_{0.5}$ respectively. The Without Heat Treated (WHT) thermal cycle process yielded a 4.9% and 1.5% increase in hardness value for 1000 cycles while comparing the 500 and 1500 cycles, respectively.

4.2. Effect of Thermal Cycling on Ti–6Al–4V Alloy Stress Relief Anneal (SRA). The specimens have been tested with thermal cycling after SRA heat treatment, for which results were presented in this section. The results have been presented in the form of plotted graphs as shown in Figures 11 and 12. By analysis, it is observed that the tensile strength of the specimen after heat treated with an annealing process for stress relief increases with the number of cycles, with a maximum tensile strength at the 1000th cycle. After 1000 cycles, ultimate tensile strength (UTS) decreases. Ultimate tensile strength (UTS) of 935 MPa and yield strength (YS) of 896 MPa and elongation of 26%. A similar trend can be observed here by the results of WHT. The % of elongation of the alloy shows an increase in ductile nature.

The maximum hardness of the specimen has been noted at the 1000th cycle after which the trend line decreases as shown in Figure 13. Among the three mentioned thermal cycles, 1000 cycles showed 381 $HV_{0.5}$ which is the highest value among the three thermal cycle conditions. The lowest values have resulted in 500 cycles as 368 $HV_{0.5}$, and at 1500 cycles as 376 $HV_{0.5}$ respectively.

The stress relief anneal (SRA) thermal cycle process yielded a 3.4% and 1.3% increase in hardness value for 1000 cycles while comparing the 500 and 1500 cycles, respectively.

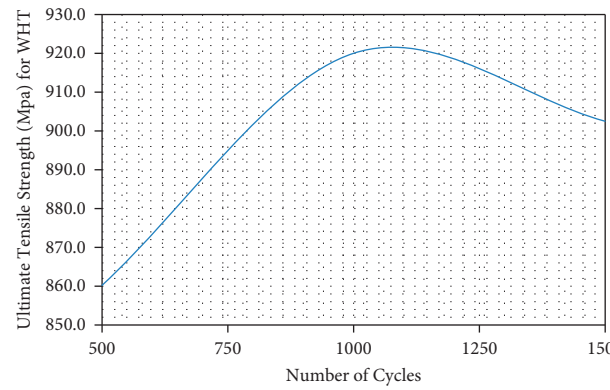

Figure 8: Ultimate tensile strength of WHT.

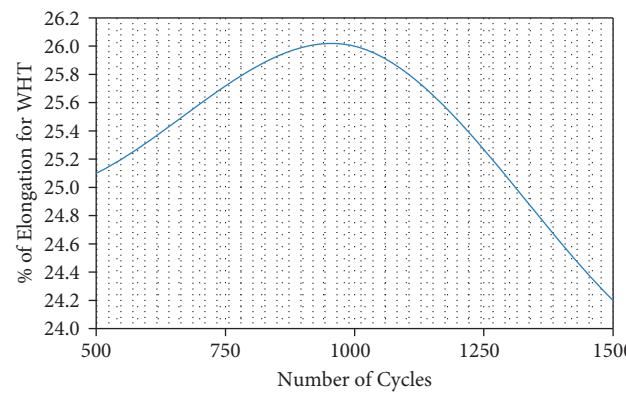

Figure 9: % of elongation of WHT.

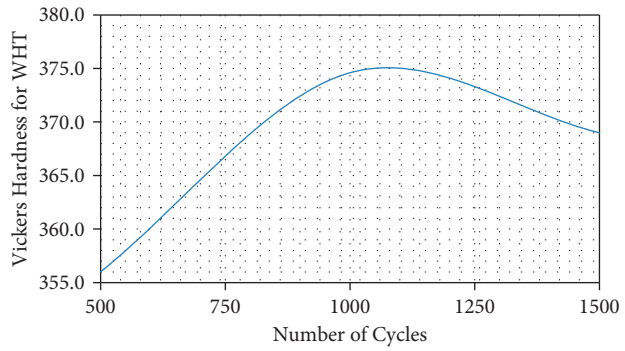

Figure 10: Vickers hardness of WHT.

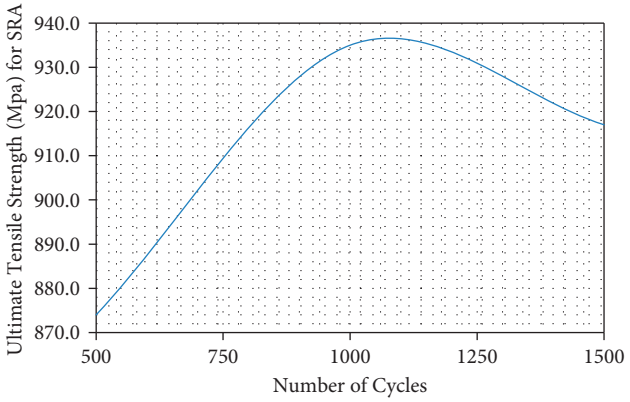

Figure 11: Ultimate tensile strength of SRA.

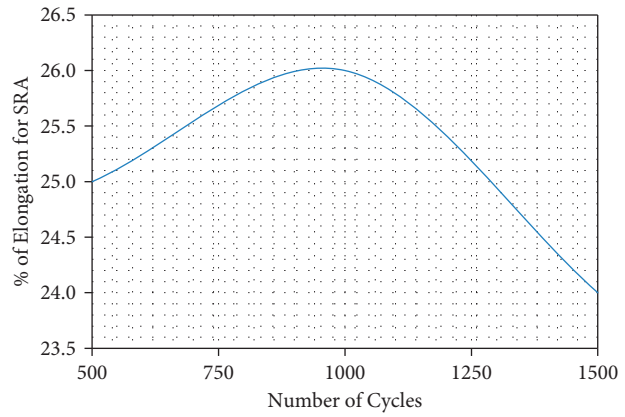

Figure 12: % of elongation of SRA.

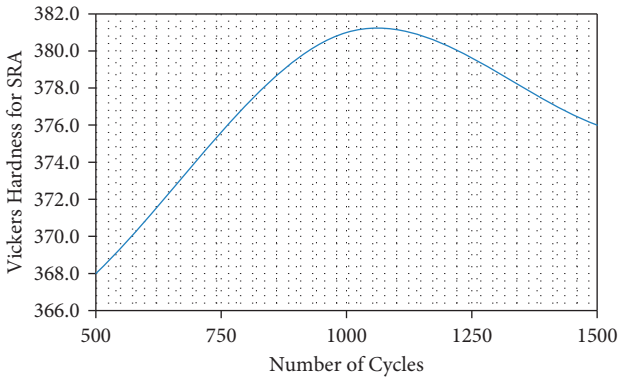

Figure 13: Vickers hardness of SRA.

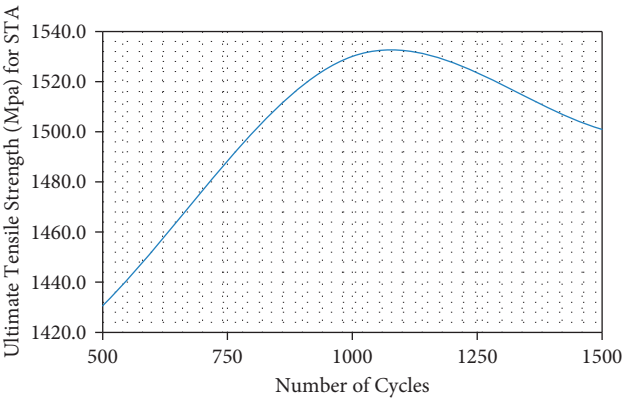

Figure 14: Ultimate tensile strength of STA.

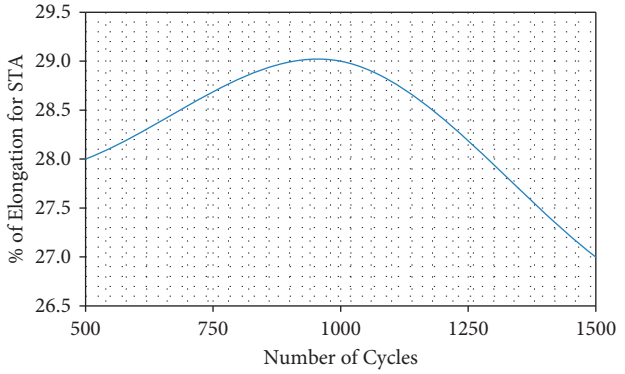

Figure 15: % of elongation of STA.

4.3. Effect of Thermal Cycling on Ti–6Al–4V Alloy after Solution Treated Aged (STA). The specimens have been tested with thermal cycling after STA heat treatment, for which results were presented in this section. The results have been presented in the form of plotted graphs as shown in Figures 14 and 15. After analyzing the results, it can be observed that an increased maximum tensile strength at 1000 cycles after which a decline of UTS can be noted. The % of elongation of the alloy decreases with an increased number of cycles but points to an increase in ductile nature. Ultimate Tensile Strength (UTS) of 1530 MPa and Yield Strength (YS) of 1420 MPa and elongation of 29%. The maximum hardness of the specimen has been noted at the 1000th cycle after which the trend line decreases as shown in Figure 16. Among the three mentioned thermal cycles, 1000 cycles showed 471 $HV_{0.5}$ which is the highest value among the three thermal cycle conditions. The lowest values have resulted in 500 cycles as 443.6 $HV_{0.5}$, and at 1500 cycles as 456.4 $HV_{0.5}$ respectively, which shows that there is an increase in the hardness when compared to WTH and SRA results. The Solution Treated Aged (STA) thermal cycle process gave a

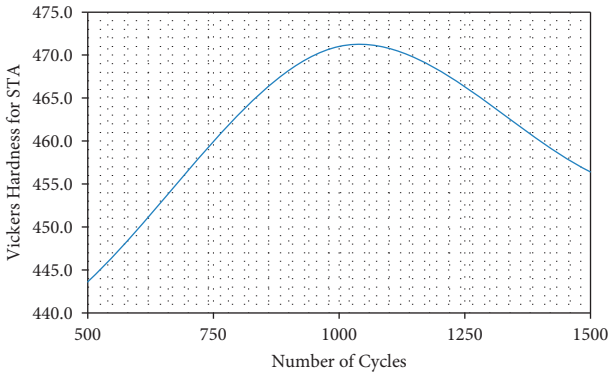

Figure 16: Vickers hardness of STA.

5.8% and 3.1% increase in hardness value for 1000 cycles while comparing the 500 and 1500 cycles, respectively.

When compared between the heat treatment processes, the STA process was shown with a 20.46% and 19.1% increase in WHT and SRA processes at 1000 cycles, respectively. The tensile test also proved that the Solution treated aged (STA) process showed a higher percentage of improvement in ultimate tensile strength (UTS) 39.86%, yield strength (YS) 37.67%, and elongation of 10% than without heat treatment (WHT). Similarly, Solution treated aged (STA) has shown ultimate tensile strength (UTS) of 39.56%, yield strength (YS) of 36.90%, and 10% of elongation, higher than the stress relief anneal (SRA) process at 1000 cycles. When comparing the results of the Solution treated aged (STA) process within its thermal cycles, 1000 cycles showed ultimate tensile strength (UTS) of 6.5%, yield strength (YS) of 2.1% with 3.4% of elongation than 500 cycles, and ultimate tensile strength (UTS) of 1.9%, yield strength (YS) of 1.4% and 6.8% of elongation than 1500 cycles.

5. Conclusions

In the present study, the Ti–6Al–4V alloy has been processed with two different kinds of heat treatment processes i.e., stress relief annealing (SRA) and solution treated aged (STA). After heat treatment, thermal cycling of 500, 1000, and 1500 cycles with two minutes dwell time was applied and carried over the specimens. After heat treatment and thermal cycling, the tensile test and hardness test were conducted at room temperature.

The following conclusions are drawn from the present study:

(i) At 1000 cycles, without heat treatment conditions recorded the higher ultimate tensile strength of 920 MPa and yield strength of 885 MPa, and the percentage of elongation is 26%.

(ii) Similar results were observed for stress relief anneal with ultimate tensile strength of 935 MPa, yield strength of 896 and percentage of elongation is 26% and solution treated aged with ultimate tensile strength of 1530 MPa and yield strength of 1420 MPa and percentage of elongation is 29% at 1000 cycles.

(iii) Solution treated aged process shown a higher percentage of strength improvement with ultimate tensile strength of 39.86%, yield strength of 37.67% and percentage of elongation 10% than without heat treatment. Similarly, solution treated aged has shown ultimate tensile strength of 39.56%, yield strength of 36.90%, and 10% of elongation higher than the stress relief anneal process at 1000 cycles.

(iv) Among all three heating conditions and displays, the solution treated aged process with higher strength and elongation.

(v) Among the three mentioned thermal cycles, 1000 cycles showed 374.6 $HV_{0.5}$, 381 $HV_{0.5}$, and 471 $HV_{0.5}$ for without heat treated, stress relief anneal, and solution treated aged, and 1000 cycles had the highest value among the three thermal cycle conditions in their heat-treatment process.

(vi) The lowest values have resulted in 500 cycles for all three heat treatment conditions. They were 356 $HV_{0.5}$, 368 $HV_{0.5}$, and 443.6 $HV_{0.5}$ for without heat treated, stress relief anneal, and solution treated aged, respectively.

(vii) Among all heat treatment conditions, the solution treated aged process showed improved hardness value when compared to the other two without heat treated and stress relief anneal processes with a percentage of 20.46% and 19.1% at 1000 cycles, respectively.

(viii) While heating, the material microstructure will have movements of dislocation density. This dislocation density movement will result in the entanglement of dislocation, which will result in the formation of high distortion energy. This energy leads to nucleation and recrystallization of grains to fine grains in titanium alloys.

(ix) These fine-grain formations have resulted in the higher hardness value of the solution treated aged process at 1000 cycles.

Data Availability

The data used to support the findings of this study are included within the article.

Conflicts of Interest

The authors declare that they have no conflicts of interest regarding the publication.

References

[1] J. S. Montgomery and M. G. H. Wells, "Titanium armor applications in combat vehicles," *Journal of the Minerals Metals & Materials Society*, vol. 53, no. 4, pp. 29–32, 2001.

[2] I. Lerner, "Titanium market recovering on commercial military aircraft," *Chemical Market Reporter*, vol. 266, no. 18, p. 17, 2004.

[3] T. Farthing, "Application of titanium in the chemical industry," *Chemical Age of India*, vol. 30, no. 2, pp. 151–166, 1979.

[4] N. H. Orr, "Industrial Application of Titanium in the Metallurgic and Chemical Industries Light Metals," in *Proceedings of the Sessions, AIME Annual Meeting*, pp. 1149–1156, Warrendale, Pennsylvania, 1982.

[5] M. M. Salama, J. Murali, and M. W. Joosten, "Titanium drilling risers-application and qualification," *Journal of Offshore Mechanics and Arctic Engineering*, vol. 122, no. 1, pp. 47–51, 2000.

[6] R. W. Schutz, C. F. Baxter, P. L. Boster, and F. H. Fores, "Applying titanium alloys in drilling and offshore production systems," *ABI/INFORM Trade & Industry*, vol. 53, no. 4, pp. 33–35, 2001.

[7] F. H. Sam Froes, "Titanium sport and medical application focus," *Materials Technology*, vol. 17, no. 1, pp. 4–7, 2002.

[8] R. Dąbrowski, "The kinetics of phase transformations during continuous cooling of the ti6al4v alloy from the single α phase β range," *Archives of Metallurgy and Materials*, vol. 56, no. 3, pp. 703–707, 2011.

[9] Y. Yamashita, I. Takayama, H. Fuji, and T. Yamazaki, "Applications and features of titanium for automotive industry," *Nippon Steel Technical Report*, vol. 85, pp. 11–14, 2002.

[10] I. S. Abdullin, A. G. Bagautdinov, and G. I. Ibragimov, "Improving surface finish for titanium alloy medical instruments," *Biomedical Engineering*, vol. 22, no. 2, pp. 48–50, 1988.

[11] L. W. Meyer, L. Krüger, K. Sommer, T. Halle, and M. Hockauf, "Dynamic strength and failure behavior of titanium alloy Ti-6Al-4V for a variation of heat treatments," *Mechanics of Time-dependent Materials*, vol. 12, no. 3, pp. 237–247, 2008.

[12] P. Sivaprakasam, A. Kirubel, G. Elias, P. Maheandera Prabu, and P. Balasubramani, "Mathematical modeling and analysis of wear behavior of AlTiN coating on titanium alloy (Ti-6Al-4V)," *Advances in Materials Science and Engineering*, vol. 2021, Article ID 1098605, 9 pages, 2021.

[13] P. Sivaprakasam, G. Elias, P. Maheandera Prabu, and P. Balasubramani, "Experimental investigations on wear properties of AlTiN coated 316LVM stainless steel," *Materials Today Proceedings*, vol. 33, pp. 3470–3474, 2020.

[14] M. Bermingham, S. McDonald, M. Dargusch, and D. St John, "Microstructure of cast titanium alloys," *Materials Forum*, vol. 31, pp. 84–89, 2007.

[15] L. Wang, H. Ma, Q. Fan et al., "Simultaneously enhancing strength and ductility of Ti-6Al-4V alloy with the hierarchical structure via a novel thermal annealing treatment," *Materials Characterization*, vol. 176, Article ID 111112, 2021.

[16] M. Vanderhasten, L. Rabet, and B. Verlinden, "Ti–6Al–4V: deformation map and modelisation of tensile behaviour," *Materials & Design*, vol. 29, no. 6, pp. 1090–1098, 2008.

[17] A. S. M. Handbook, *Heat Treating*, pp. 2054–2064, ASM International, Metals Park, OH, USA, 1991.

[18] Z. Du, S. Xiao, L. Xu, J. Tian, F. Kong, and Y. Chen, "Effect of heat treatment on microstructure and mechanical properties of a new β high strength titanium alloy," *Materials & Design*, vol. 55, pp. 183–190, 2014.

[19] R. K. Gupta, V. A. Kumar, and S. Chhangani, "Study on variants of solution treatment and aging cycle of titanium alloy Ti6Al4V," *Journal of Materials Engineering and Performance*, vol. 25, no. 4, pp. 1492–1501, 2016.

[20] Z. Liu, Z. Zhao, J. Liu et al., "Effects of solution-aging treatments on microstructure features, mechanical properties and damage behaviors of additive manufactured Ti–6Al–4V alloy," *Materials Science and Engineering A*, vol. 800, Article ID 140380, 2021.

[21] S. Shekhar, R. Sarkar, S. K. Kar, and A. Bhattacharjee, "Effect of solution treatment and aging on microstructure and tensile properties of high strength β titanium alloy, Ti-5Al-5V-5Mo-3Cr," *Materials and Design*, vol. 66, 2014.

[22] H. Li, D. Jia, Z. Yang et al., "Effect of heat treatment on microstructure evolution and mechanical properties of selective laser melted Ti–6Al–4V and TiB/Ti–6Al–4V composite: a comparative study," *Materials Science and Engineering A*, vol. 801, Article ID 140415, 2021.

[23] Q. Wang, X. Lei, M. Hu, X. Xu, R. Yang, and L. Dong, "Effect of heat treatment on microstructure and tensile property of Ti-6Al-6V-2Sn alloy," *Metals*, vol. 11, no. 4, p. 556, 2021.

[24] J. Hu, J. Zhang, Y. Wei et al., "Effect of heat treatment on microstructure and tensile properties of Ti-6Al-4V alloy produced by coaxial electron beam wire feeding additive manufacturing," *Journal of Occupational Medicine*, vol. 73, no. 7, pp. 2241–2249, 2021.

[25] J. Ju, J. Li, C. Yang, K. Wang, M. Kang, and J. Wang, "Evolution of the microstructure and optimization of the tensile properties of the Ti–6Al–4V alloy by selective laser melting and heat treatment," *Materials Science and Engineering A*, vol. 802, Article ID 140673, 2021.

[26] S. Raghavan, M. L. S. Nai, P. Wang, W. J. Sin, T. Li, and J. Wei, "Heat treatment of electron beam melted (EBM) Ti-6Al-4V: microstructure to mechanical property correlations," *Rapid Prototyping Journal*, vol. 24, no. 4, pp. 774–783, 2018.

[27] I. Drstvenšek, F. Zupanič, T. Bončina, T. Brajlih, and S. Pal, "Influence of local heat flow variations on geometrical deflections, microstructure, and tensile properties of Ti-6Al-4 V products in powder bed fusion systems," *Journal of Manufacturing Processes*, vol. 65, pp. 382–396, 2021.

[28] S. Manikandan and S. Ramanathan, "Flow behaviour of thermal cycled titanium (Ti-6AL-4V) alloy," *Int. J. Mech. Eng. & Rob. Res*, vol. 2, no. 2, 2013.

[29] V. S. T. Putti, S. Manikandan, and K. K. Ayyagari, "Effect of thermal cycling on mechanical and microstructural properties of heat-treated Ti-6Al-4V alloy," *Materials Research Express*, vol. 9, no. 1, Article ID 16512, 2022.

[30] P. Sivaprakasam and P. Hariharan, "Optimization of process parameters of micro-WEDM process on inconel super alloy through response surface methodology," *International Journal of Mechanical and Production Engineering Research and Development*, vol. 8, no. 6, pp. 1001–1012, 2018.

[31] P. Sivaprakasam, P. Hariharan, and G. Elias, "Experimental investigations on magnetic field-assisted micro-electric discharge machining of inconel alloy," *International Journal of Ambient Energy*, vol. 43, no. 1, pp. 2619–2626, 2022.

[32] A. Divya Sadhana, J. Udaya Prakash, P. Sivaprakasam, and S. Ananth, "Wear behaviour of aluminium matrix composites (LM25/Fly ash)–A Taguchi approach," *Materials Today Proceedings*, vol. 33, pp. 3093–3096, 2020.

Hindawi
Advances in Materials Science and Engineering
Volume 2022, Article ID 9151839, 12 pages
https://doi.org/10.1155/2022/9151839

Review Article

A Recent Trend on Additive Manufacturing Sustainability with Supply Chain Management Concept, Multicriteria Decision Making Techniques

Raja Subramani,[1] **S. Kaliappan**,[2] **P. V. Arul kumar**,[3] **S. Sekar**,[4] **Melvin Victor De Poures**,[5] **Pravin P. Patil**,[6] **and E. S. Esakki raj**[7]

[1]*School of Mechanical Engineering, Vellore Institute of Technology, Vellore, Tamil Nadu, India*
[2]*Department of Mechanical Engineering, Velammal Institute of Technology, Chennai 601204, Tamil Nadu, India*
[3]*Department of Mechanical Engineering, Bharath Niketan Engineering College, Aundipatti 625531, Theni, Tamil Nadu, India*
[4]*Department of Mechanical Engineering, Rajalakshmi Engineering College, Rajalakshmi Nagar, Thandalam, Chennai 602105, Tamilnadu, India*
[5]*Department of Thermal Engineering, Saveetha School of Engineering, SIMATS, Chennai 600124, Tamil Nadu, India*
[6]*Department of Mechanical Engineering, Graphic Era Deemed to be University, Bell Road, Clement Town 248002, Dehradun, Uttarakhand, India*
[7]*Department of Mechanical Engineering, Dambi Dollo University, Dambi Dollo, Ethiopia*

Correspondence should be addressed to Raja Subramani; engineerraja1995@gmail.com, S. Kaliappan; kaliappan2675@yahoo.com, Melvin Victor De Poures; melvin.victor02@gmail.com, and E. S. Esakki raj; essakkiraj@dadu.edu.et

Received 4 June 2022; Revised 6 July 2022; Accepted 19 July 2022; Published 13 August 2022

Academic Editor: R. Thanigaivelan

In the past 3 decades, the emerging technology in manufacturing sector other than conventional manufacturing is additive manufacturing (AM). The additive manufacturing principle was completely born from the research gaps of conventional manufacturing concepts such that the elimination of wastage and produce the component layer upon layer. Every new technology obtains the sustainability that may consider in the supply chain management principle of the raw material to finished products and decision-making techniques are to reach the consumer or customer as properly and periodically but these things are addressed challenges in additive manufacturing. This review paper aims to narrate the common research gaps on additive manufacturing, the structure of the supply chain management on AM, MCDM tools/techniques, AM application in different fields, challenges of selection of additive manufacturing, AM processes, and its application. The traditional method of literature review has been used for this review. The outcome of this review has helped the new researcher's decision making on the AM various problems as easily and the new researchers may give the experimental solution for explored research gaps.

1. Introduction

1.1. Additive Manufacturing. Additive manufacturing is nothing but adding the material as layer by layer to make the thing. The AM method is completely differs from the conventional method of manufacturing [1, 2]. The first edition of Gibson et al. [3] book has described the development and application of AM based on the ASTM standard. Jonathan explored the second edition of their book as main objective is teaching aid of AM that it may be developed and the author also covered the main points of current development, innovation, and fast growth of AM. In the principle and processes headlines under the chapters are reviewed. These books having interesting topics such as impact of low-cost AM, and guidelines for process selection like the main parameters for selection of AM processes are such as speed, cost, accuracy, and material property. These book authors point out the decision-making software

demand related to machine choosing that cause drawback of certain part design and capacity of machine. Kadviser system databases were developed and made use of relevant database system with extensive application numbers, materials, and machines [3]. The main challenges of decision making various users need various things from an AM machine. The following Figures 1(a) and 1(b) expressed the challenges of selection of AM machines in different categories and the main application of AM in different fields [4].

Niaki and Nonino [6] were the authors, who wrote a review about AMM and their subsequent research agenda. Their study was focused on eight major streams such as supply chain, AM technology selection, environmental aspects, manufacturing system, strategic challenges, open source innovation and business model, economics, product design, and production design model. The essential benefits of supply chain management in AM such as "agile," "mass customization," "legality," and "lean." The authors may not be more concentrated on the area of supply chain management in their paper. Bikas et al. [7] were done a critical review on the topic of AM methods and modeling approach. The process mechanisms and modeling method-based research gaps were identified. The following Figure 1(b) shows the application of additive manufacturing.

Tapia and Elwany [8] reveal the sequence of operation monitoring and control of the metal-based AM. The authors were finding out research gaps in the area of monitoring and controlling the metal-based AM. The authors are identifying the research gap in the quality of metallic AM parts not to reach the requirements or regulations. Douglas and Stanley [9] point out that in the AM process the cost of raw materials has decreased 51% from 2001 to 2011. There are some research gaps also point out in the supply chain management like searching land, time expended and labor on the manufacturing, utilization, and disposal of AM products. AM is minimized the production time and design for the customized parts. The AM spare parts receiving time is more as compared to the conventional method [10].

Mc Kinsey is the senior magazine related to organization and management theory that released the Quarterly article about AM on the name of "3D Printing Shape." This magazine narrated that the application of AM is less visible to the customer as compared to traditional conventional manufacturing. The key challenges of supply chain management in AM have not been focused by the inventory management [11].

Wohlers and Gornet [12] groups are playing a vital role in the field of additive manufacturing and they give their contribution to identifying the latest growth and trends in AM on every year. This report shows the development of AM in major equipment manufacturing gradually rised in every year. Metal-based AM methods are having more demand [12]. Knofius et al. [13] are the authors from Beta (research school for operation management and logistics), who review the sales-services after AM in supply chain management in their 515^{th} paper series. There are a lot of research gaps available on the AM after sale-services supply chain by their review such as the decision making is challenging on after sales-services in AM [13]. Khajavi et al. [14] have contributed the AM development in the field of aeronautical industry. The author proved the super hornet fighter of F-18 is used for air cooling duct purposes in aeronautical field and it is manufactured by AM technology. The authors expected output of a model, illustrates emergency requirements and cost trade-off of AM deployment. An effective supply chain management in which the following characteristics are very essential. Such as

(a) Efficient conversion an input to output

(b) Dispatching high-quality customer/consumer response and

(c) Developing the assets utilization.

The author of the paper reveals that research gaps like personnel intensiveness and the AM acquisition price are the major obstacles, and slow production rate as compared with spare part fleet, which is another research gap [14]. Hopkinson and Dickens are analysts of AM processes with comparing the layer manufacturing processes for production. Stereolithography is the form AM by using the photochemical process. The machine cost is the main drawback of rapid manufacturing. The research gap of secondary equipment cost may vary depending upon the location and it may affect the machine cost. The inkjet has a broad basement for AM and transforms someway the products are manufactured [15].

1.2. Supply Chain Management. Supply chain management is the concept of raw materials to finished products to reach the consumer. Cestana et al. [16] have referred to the single echelon supply chain with assumptions of uncountable manufacturing capacity for the inventory problem. The slow-moving is in AM and CM (conventional manufacturing) may more costly. This paper's authors consider the sole OEM with their part inventory. The following conditions were taken for performing their research such as the first condition, part make by CM, and the second condition, part make AM. Thus the result has been obtained by the Analytical Markov Chain Model [16]. Cozmei and Caloian [17] have used embryonic technology in supply chain management and considered the factors like stock flow, divergence of function, labor cost saving, and workforce productivity.

The author concludes that the design of the required product should send through the Internet and manufactured by the AM. In this way, the production is applicable and reduces the inventory and labor costs. The author notifies the research gap on the conclusion such that AM development may give the job opportunity only the skilled labor [17]. The basic supply chain management concept in AM is shown below Figure 2. The revenue and risk may share with the services provider; contractor and supply chain partners are major research gaps in AM [18].

Gosselin et al. [19] have examined the drawback of existing concrete depended on AM and describe the unique process proposal in their paper. The future work was prescribed by the authors such as the use of more than one material including the printing process in the form of

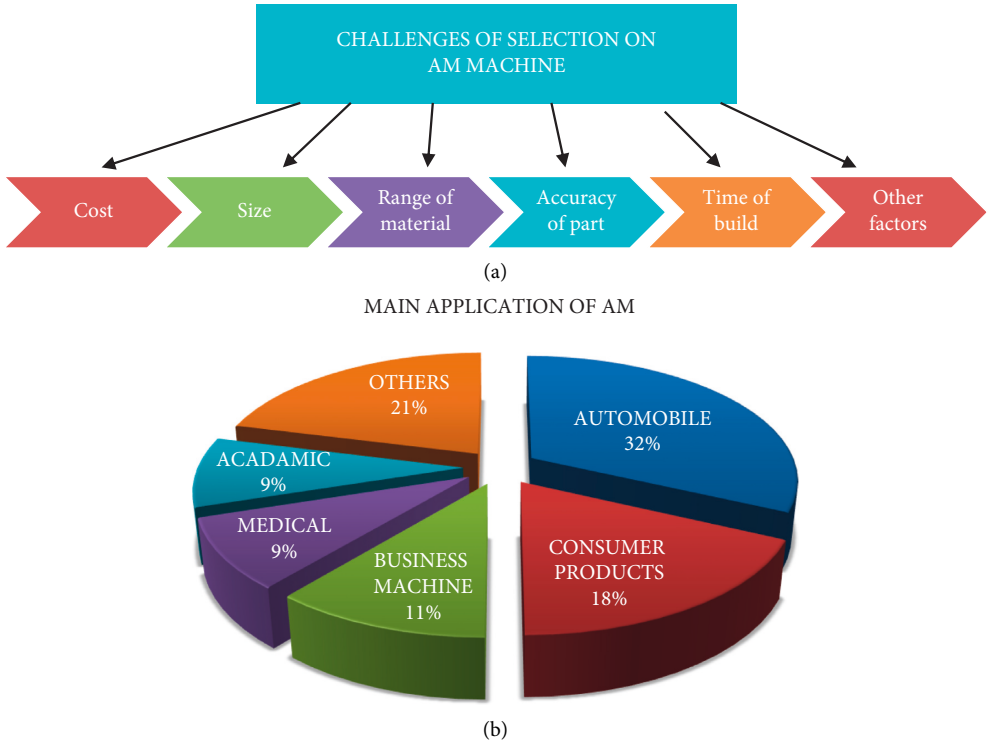

Figure 1: (a) Challenges of selection on AM Machine [3]. (b) Main application of AM in different fields [4, 5].

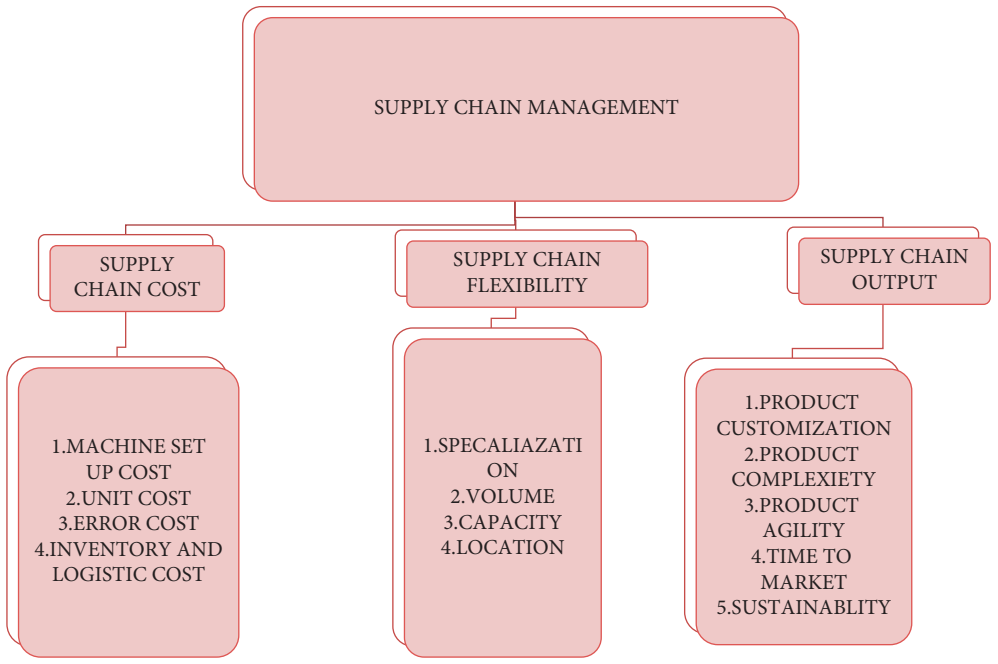

Figure 2: Supply chain management concepts [16].

gradient on material property. The author of this paper has included the mechanical properties in their abstract but they did not concentrate on thermal analysis for this paper [19]. Thierry Rayna and Striukova [20] described the AM model innovation changes that the difficulties of combining the technologies such as quick prototyping, quick tooling, digital production, and house fabrication. The novel area is very difficult to adopt the existing manufacturing model on 3D printing [20]. Jong and Bruijn [21] are from the Rotterdam School Of Management Netherlands and described the

concept of existing CM responded to the latest technique of AM. Conventional manufacturing has also withstood in the different fields of recent pieces of research like glass fiber, nanofillers, nanopowders, graphene, etc., and also the fault analysis using the IIOT. The CM can defend their business by following ways such as monitor, attack, adopt, acquire, and facilitate [21–25]. However, the main research gap prescribed that 3D printing will affect the CM in future [26]. The AM is having some folk tales revealed by Roca et al. [26]. The first folktale is that additive manufacturing easy to make components without difficulties and is economical. The second folk tale is the AM products make it local and the final folktale manufacturer can replace the bulk manufacturing bulk customization. The quality of AM is may challenge to compare the CM [27]. AM also contributes wood making industries such as furniture-making fields. Pringle et al. [27] were given the research gap such as to quantify the mechanical properties of wood polymer composite after first recycling [27]. Moreover, a lot of literature research gaps are explored in this review article. This paper has explored the structure of supply chain management concept in the AM field. This review paper is also focused on the different novelties of supply chain management and multi-choice decision-making possibilities in AM.

2. Methodology

The traditional literature survey method is used for this review paper. First of all, one hundred and three papers were taken by four different classifications as shown in Figure 3 such as additive manufacturing, supply chain management, AM application, and supply chain management application. In each classification twenty-five papers were taken from the top reputed journal publishing such as Elsevier, Springer, Taylor and Francis, Emerald publishing limited, Hindawi, MDPI, and other publishers. The search engine application used for this review is Google scholar. The keywords used for collecting this paper such as "additive manufacturing," "supply chain management," "supply chain management on additive manufacturing," "a recent review for additive manufacturing and applications of additive manufacturing with supply chain management." The following filters were applied during collecting the papers such as time-since 2022 and sorted by the relevance.

The collecting papers were sorted by the year and title in ascending order on a folder. The collecting paper was analyzed by each and every line as a more critical review point of view and essentially focused on the abstract, methodology, result, and conclusion of every paper. Finally, research gaps were identified and explored in this review paper.

3. Scenario, Material, and Operation of AM

In AM process, to ensure the heat treatment should obtain the required physical and metallurgical properties. Because AM technology has the part of challenges as huge level manufacturing to find the new way for obtaining desired metallurgy specifications exclude post processing. Kowalewski [28] has

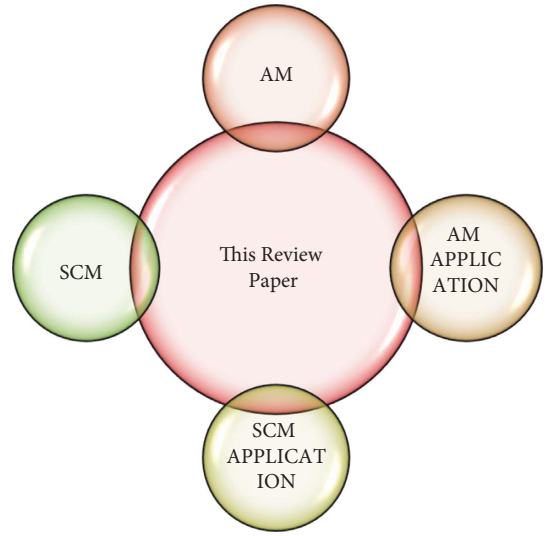

Figure 3: Methodologies.

expressed the IVD method for surface improvement and corrosion resistance and it is shown in Table 1 [28].

3.1. Adoption of AM up to 2022. Alabi et al. [29] wrote a review that the application of AM in South African universities and implement the different AM technologies in education [1, 2]. Figure 4 shows the adoption of additive manufacturing up to the year 2022. This paper author detailed cover the topic of AM but the limitations of author miss the huge content of the application on AM and the author concentrate on proposed particular PG program. The author expressed the research gap that the limited scope only for AM in education field [29]. Additive manufacturing is used on the UAV inner structure. The author highlights the research gap in physical form, altitude, weight, strength, and life of AM is less compared to CM. Carbon fiber reinforced polymer (CFRP) has been used for AM but it has short fiber and short fiber has poor mechanical property [22, 23, 30]. Kianian et al. [31] published a paper of adoption of AM in Sweden. Most of the firms applied the AM techniques for quick prototyping in Sweden and trusted that the initial investment and the SME try their innovation as basic amount on AM.

The author points out the research gap as there is no exact data for AM holding companies in the world and the comparison of different variables of AM application and implementation in different countries [31].

3.2. Various AM Application and Process. AM contributes to more different fields and different applications. Table 2 shows the different processes and different applications of AM.

The key term of supply chain management challenges on AM such as purchasing costs, developing new material, obtaining huge consistency and standardization, developing new CAD tools, educating engineers, increasing process speed, and advancing the biological [32]. In AM process such

Table 1: Different materials and operation of AM [28].

Metals/Operation	Polymer and polymer blends	Composite	Graded hybrid metal	Metal	Ceramic	Sand mold and cores	Paper
Metal extrusion	AP	NP	NP	NP	NP	AP	NP
Material jetting	NP	AP	NP	AP	NP	NP	NP
Blinder jetting	NP	AP	NP	AP	AP	AP	NP
Sheet lamination	NP	NP	AP	AP	NP	NP	AP
Powder bed fusion	NP	AP	NP	AP	AP	NP	NP
Direct energy deposition	NP	NP	AP	AP	NP	NP	NP
Vat photopolymerization	NP	AP	NP	NP	AP	NP	NP

AP, aApplicable, NP, not applicable.

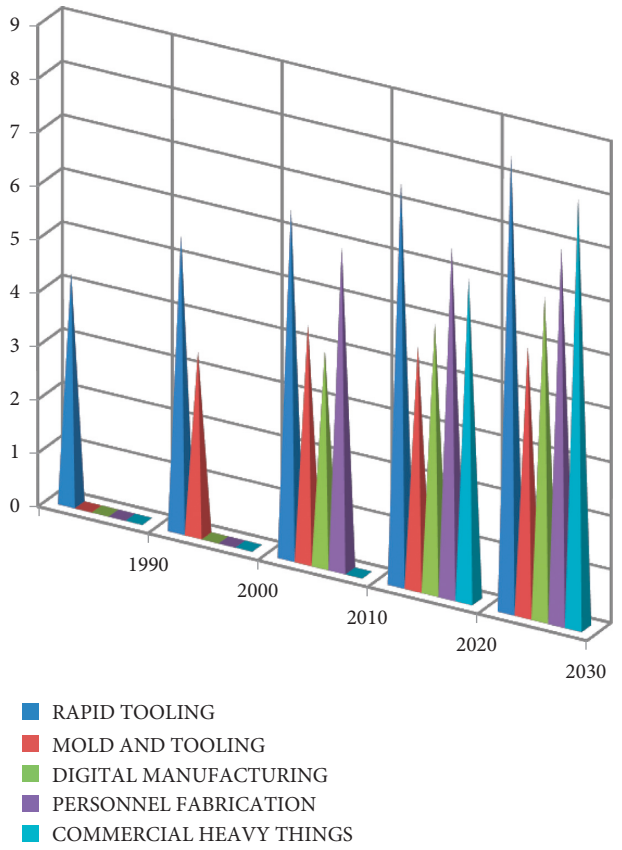

Figure 4: Adoption of AM up to 2021 [1, 2, 28, 29].

key challenges are the point out lead time, inventory, system responsiveness, and supply chain cost were minimized [33].

4. MCDM Tools/Techniques and Its Application

The MCDM is a tool or technique from the operational research area for more than critical alternatives that selected opted one. The following Table 3 describes the various MCDM tools and techniques available for the manufacturing sector.

The Stojčić et al. [5] narrate the research gaps of MCDM to find out the simpler and flexible ways for synchronous problems [5]. Table 3 shows the MCDM Tools or Techniques and their application in additive manufacturing.

The laser-based AM is having the parameters such as laser power, laser velocity, and layer thickness but it did not use a systematical approach [34]. The AM's huge components are may make of metal. Yampolskiy et al. [35] observe the research gaps on AM software and hardware having some flaws such as material on AM is commonly used polymer but the gap on metals and composite [35]. The price affordable and AM reach everyone to make different things but it is a reason for some crimes also [36]. AM is to produce the physical components in the short period by using CAD, CAE, and CAM. The process of AM is just designed and directly manufacture. The AM process is also referred layer manufacturing [37]. Conventional manufacturing is safe from cybercrime as compared to AM. A lot of AM machines is used digital data for making the component [1, 2] and it has cyber threats to weaken or destroy the component [38]. The AM process is having excellent geometrical flexibility and rapid manufacturing. But the research gap in AM process such as tooling, advantage based on only homogeneous material, and decisions making for choosing AM process [1, 2, 39]. The common key issues of the AM are, namely, occupational health, energy usage, lifecycle impact, and waste usage [40]. In the AM, only the consumer may involve in the manufacturing process to share their design ideas or concept. This concept is destroying the whole seller, retailer, customer, and consumer traditional supply chain. Hence, the product price may be more affordable to the consumer [41]. ASTM [24] F2792 committee is formed to standardize the AM process in 2015. The AM process will overcome the traditional manufacturing process as well as soon [42]. The maturity model of AM involves the technology, production support by direct tooling, part support by direct manufacturing, and its application [43]. The Bio-AM is playing a vital role in forecasting the safety and accuracy of maxillofacial surgery [44]. On FDM is to adopt the concurrent process to optimize the shape of components [45].

Table 2: Different AM processes and application.

Additive manufacturing: [1, 2, 32]					
Process					
SLS	**SLA**	**FDM**	**PMD**	**3DP**	**OTHERS**
Applications					
Arts, jewelry, visualization, aeronautical, aerospace, automotive, medical, tooling, repair, nanotechnology, consumer products, electronics, entertainment, education, energy, architecture, and others.					

Table 3: MCDM tools/techniques and its application [1, 2, 5].

MCDM tool or techniques	Application
(i) AHP [2]	(i) Location selection (ii) numerical decision support for most appropriate result (iii) Evaluate the data and select the most appropriate one. (iv) Sustainable process planning. (v) Selecting the most appropriate machine (vi) Critical decision making (vii) Measuring the sustainable level of production (viii) Priority-based problems (ix) Huge alternative problems
(ii) FAHP	(i) Various goals of mathematical program for supplier selection. (ii) Priority calculations in operation (iii) Select the optimum on alternative (iv) Improve the determination of securities performance (v) Identify the importance of SCM on the industrial performance
(iii) TOPSIS [1]	(i) Capital installation models (ii) Reducing risk models (iii) Investment and profit models (iv) Cost estimation of entire process (v) Dispatch products distribution problems (vi) Determine the sustainability of supplier (vii) Determine the fleet after dispatching products (viii) Determine the plant location (ix) Evaluate the public investor (x) Optimum the electric sources (xi) Estimate the future activity
(iv) COPRAS	(i) Numerical decision support method for multi alternatives (ii) Multi-criteria assessment on AM
(v) DEMATEL	(i) Selection of project area (ii) Evaluation and selection of alternatives (iii) Multi-criteria assessment on AM (iv) Determine the fleet after dispatching products (v) Developing the methodological system approach for workpiece selection (vi) Evaluation of pollution model (vii) Evaluating the green supplier (viii) Identify and evaluate the customer needs
(vi) ANP	(i) Select the most feasible AM construction and installation (ii) Evaluation of pollution model
(vii) WASPAS	(i) Standard estimation of waste disposal (ii) Ranking the operation or process
(viii) PROMETHEE	(i) Logistic model (ii) Fleet model (iii) Ranking the material handling models (iv) Selection of sustainable operation or process (v) Assessing the performance of alternative
(ix) WSM	(i) Fleet model
(x) LNN	(i) Selection and evaluation of power source problem
(xi) BWM	(i) Investigating the supply chain management of production companies (ii) Selection of three-phase supplier selection
(xii) MAIRCA	(i) Estimate and evaluate the performance of employees, suppliers, and operations
(xiii) ARAS	(i) Selecting the suitable alternatives in logistics of AM products (ii) Development of the methods for decision support
(xiv) VIKOR	(i) Estimate the applicability of MCDM problems (ii) Estimate and evaluation supplier selection (iii) Selection of sustainable things or factors
(xv) ASPID	(i) Estimate the quality of the AM (ii) Measure the sustainability of demand and supply

Table 3: Continued.

MCDM tool or techniques	Application
(xvi) MOORA	(i) Estimate and evaluate the risk factors for logistics (ii) Choosing the most sustainable
(xvii) ELECTRE	(i) Selection of an optimum solution (ii) Differentiate the sustainability of organization supply (iii) Identify the firm's SCM performance (iv) Evaluate the fleet's sustainable performance (v) Sustainability problems
(xviii) IFDM	(i) Estimate the performance of firm
(xix) MIVES	(i) Numerical decision support for the most appropriate result (ii) Evaluate the data and select the most appropriate one (iii) Sustainable process planning (iv) Selecting the most appropriate machine (v) Critical decision making (vi) Measuring the sustainable level of production (vii) Estimate the mechanical properties (vii) Finding the investor with strategies for prioritization
(xx) SWM	(i) Evaluate the technology.

Table 4: Supply chain concept and its application.

Supply chain concept	Application
Lean paradigm	Minimize the wastage throughout supply chain
Agile paradigm	Lead time compression and eliminate the waste
Leegility and postponement	Both lean and agile paradigm application
Mass customization	It is used to meet the customer's requirements.

4.1. Supply Chain Concept and Application. The AM is may minimize the low-wage factory workers' job opportunities [46]. The AM gives the optimized design and customized component basis of demand. The safety weight components are made by AM process [47]. The following Table 4 describes the supply chain concepts and their application to AM [48].

The AM is a multi technology combined and each technology has a separate mature stage. The AM is believed from the industrialist, researchers, and scientist point of view that the next industrial revolution may occur [49]. The supply chain management of AM estimate and evaluate the essential effects of sustainability and obtain to point out the key problem for boosting sustainability outcomes [50]. The most of cybercrime has occurred on AM processes such as a design of products copied from the top brands and the sensitive data were insecure from owners [51]. The AM process plays a vital role in hearing-aid manufacturing. The individual unit is may change multi-unit for offering economic product delivery by batch production [52]. Barz et al. [53] have observed that AM involves the two-stage supply apex such as source, production, and customer apex [53]. The industrial four-point zero is more dependent on their decision making to select the appropriate technology [54]. The AM process is commonly also known as 3D printing technology. It is especially designed for customized manufacturing. The process is opposed to the conventional manufacturing principle such as elimination of waste[55]. Additive manufacturing is developed emerged manufacturing on nowadays and the demand occurred on mass production [56]. Compare to conventional manufacturing the AM is eliminating the cost of die, scarabs, and raw material cost [57].

Zanoni et al. [58] were described the supply chain management on AM that involves to minimize the fleet cost, improve the supply chain dynamics, and minimize the delivery lead time [58]. Supply chain management is basically a consideration of supply planning, supplier selection, and contracting for the end of finished process in any manufacturing process. Similar to beginning any manufacturing the supply chain management includes material purchasing, expediting, and money settlement [59]. Sustainable development is only possible if the manufacturers satisfy the customer or consumer expectation because "the customer is the king of every business" [60]. The potential advantage of AM is followed. Such as:

(1) Not need the tooling cost.

(2) Possible to make a small batch production.

(3) Easy to select the product for function,

(4) Easy to make complex geometrics, and

(5) No need for more inventory and minimize the supply lead time [61].

The current demand for additive manufacturing is to introduce more logistics hubs and sales-services centers [62]. The lacking of reorganization and rethinking in additive manufacturing has expired in the commercial sectors [63]. The limitation of AM such as lacking the choice of products to select the customer appropriate color, material, and surface finish [64]. The input for AM machine is directly from the AUTOCAD product design converted into an STL file [65]. STEM is a teaching topic for AM in different ways of product making and it is very useful to young researchers [66]. 3D printing may play the vital role to minimize carbon

emission and the process principle of zero material waste [67]. The slow construction time and limited number of material are another drawback of AM [68]. The AM is commonly classified as rapid manufacturing (polymers, metals, ceramics, and composites), rapid tooling (polymer and metal), and rapid prototyping [69]. Risk prediction is the important term in supply chain management to be determined by two methods such as systematic literature review and bibliometric network analysis [70]. In the high temperature polymer extrusion process contains emission like dirt particles and hazardous gases on the large-format AM machine [71]. A minimal quantity of research papers that enhance the circular economy with additive manufacturing was avail and it shows the research gaps in this area to need to explore the particular topic [72]. The lot of sustainable analysis theory is may be found by literature reviews on the AM process [73]. The manufacturing supply risk can be minimized by using the different supplier strategies and supplier selection depend on the quality, not the cost [74]. Knofius et al. [75] were observed the tiny spare parts firms may the essential beneficiary by the AM process [75]. In the 3D printing manufacturing process has been possible to reuse and recycle raw materials specifically permanent magnets [76]. The AM is the part of manufacturing producers that it raising the flexibility minimizes the warehouse cost and sustains the processes as mass production [77]. The main objective of the supply chain management on additive manufacturing such as minimize the inventory cost, minimize the operation cost, develop the customer services, and rapid product dispatch to market [78]. In AM terms of rapid manufacturing and rapid tooling is only applicable to the direct production methods of components [79]. In 1996, the layer manufacturing (LM) process is now commonly known as AM. The LM (layer manufacturing) ultimate goal was to deposit the material with the varying density [80]. The AM plays a major role on the complexity geometric parameter in the field of aeronautics such as aerodynamic, reliability, manufacturing, maintainability, weight, and cost [81]. Digital data reproducible manner were easily obtained in the AM by the composite propellant grain geometric [82]. India is the second largest manufacturing hub to amend the AM processes without barriers as hugely by the "Make in India" initiative within 2016–2026 [83].

The printing magnets are obtained with good thermal performance by using magnet filament from recycled material [76]. Kalyan et al. [84] explored the AM vaccums in future applications such as in situ monitoring (online measurement), topology optimization, smart manufacturing, hybrid 3D printing, and standardization [84]. The growth of AM process increased gradually day to day. However, the research gaps may occur in different fields like thermal management, system management, and materials [85]. The metal material processes and nonmetal material processes in which comparison of the strength of manufacturing components is obtained by different processes [86]. The last five years of the most popular AM technique are observed in the polymer extrusion by Love et al. [87].

The AM process is having different printers and different accuracy parameters. Moreover, the best professional printers followed the dimensional elite that it has more accuracy and surface finish [88]. A lot of research areas are present on the materials like metals, polymer, ceramics, etc. However, the new researchers have focused on the metallic materials area as more gained [89]. The benefits of the optimization such as minimize the overall build cost, material usage, regulate the material properties, avoid the requirement of support, and manufacturing costs [90]. The AM processes are having the vaccums on the precision engineering components and validating the software tools that determine the process and effect [91]. The lithography tool in the AM process is too expensive for the SME [92]. The existing porosity measuring devices are used on AM as the part pose and laser angle but they did not use different machines [93]. The manufacturers are having the mission that barriers of cost and technology should be removed and change the manufacturing field as a sustainable portfolio [94]. The metal and thermoplastic parts are manufactured by the most suitable AM process SLS and SLM only [95]. The stainless steel is manufactured layer-wise through laser additive manufacturing technology and it is fabricated 3D parts by choosing the melting powder with a laser beam [96].

5. Discussion

Additive manufacturing is an emerging technology in the manufacturing sector. Sustainable manufacturing is a goal for the manufacturers to withstand the competitive market. To obtain the sustainability of manufacturing technologies are must focus on supply chain management, logistics, and decision-making techniques application. In the AM processes of logistic is too complicated and it is classified into three categories such as:

(a) Supply chain network

(b) Inventory management and

(c) Dispatching management [97].

The AM is the "third revolution of industries" on essential changes of the manufacturing market [98]. Compare to conventional manufacturing growth that additive manufacturing development is much slow and gradual [99]. The AM process is having socio-technology factors such as operational factor, strategy factor, and supply chain factor [100]. The solid-based metal making is most suitable process by the fusion deposition machine in the AM [101]. The topology optimization is the essential support for AM to minimize the material and sustainable processing [102]. The Cost effective of AM is the following points. Such as:

(a) Pick the most exact part that is important

(b) Pick the most exact process and material

(c) Do not prefer old spares

(d) Ensure the usage of appropriate design

(e) Apply the existing solution as more if possible

(f) Ensure the lifecycle

(g) Do not optimize the spare [103].

The triangular facet model or the polygonal meshes is used for the most common data format by agreed on most AM technology [104]. Ghadge et al. [105] explored that the AM process required more research for achieving sustainability [105]. The digital-driven operations are generally having threats that it is also applicable to AM [106]. Thus the sustainable improvement of AM with supply chain management must carefully handle the reliability, flexibility, innovation, and quality of the products at every stage [107]. The AM application plays vital role in most appropriate industries, especially prototypes [108].

6. Conclusions

Additive manufacturing is only believed the future in production field that may replace conventional manufacturing. AM is rapidly growing in the various industries sector at the previous year. However, the material was made in economic by the manufacturer but it reaches to consumers at a huge cost then there is no use for making the material. Because the "customers are the king of business" the mostly cost and quality have expected from the products. In this review, different research gaps were explored from the previous literature review. The AM has lack on supply chain management and MCDM to choose the appropriate vendors after sales/services of the machines. The mechanical properties of the AM products are also carefully considered and improved in future for the sustainable manufacturing. Thus this review paper explored a lot of research gaps and it helps the new researcher's decision making on the AM various problems as easily and the new researchers may give the experimental solution for explored research gaps in the future.

Data Availability

The data used to support the findings of this study are included in the article. Should further data or information be required, these are available from the corresponding author upon request.

Conflicts of Interest

The authors declare that they have no conflicts of interest.

Acknowledgments

The authors thank and acknowledge the management of Vellore Institute of Technology, Vellore, for their support to carry out this research work. The authors also express special thanks to DIGI-MAN Lab in charge and technician staff and Mr. R Business Corporation and Mr. R Educational Services (NGO).

References

[1] S. Raja and A. J. Rajan, "A decision-making model for selection of the suitable FDM machine using fuzzy TOPSIS," *Mathematical Problems in Engineering*, vol. 2022, p. 1, Article ID 7653292, 2022.

[2] S. Raja, A. John Rajan, V. Praveen Kumar, N. Rajeswari, and M. Girija, "Santanu modak, R. Vinoth kumar, wubishet degife mammo, "selection of additive manufacturing machine using analytical hierarchy process," *Scientific Programming, vol*, vol. 2022, Article ID 1596590, 2022.

[3] I. Gibson, D. Rosen, and B. Stucker, "Additive manufacturing technologies: 3D printing, rapid prototyping, and direct digital manufacturing," *Additive Manufacturing Technologies: 3D Printing, Rapid Prototyping, and Direct Digital Manufacturing, Second Edition*, vol. 3, pp. 1–498, 2015.

[4] O. Diegel, A. Nordin, and D. Motte, "Additive manufacturing technologies," *Springer Series in Advanced Manufacturing*, Heidelberg, Germany, 2019.

[5] M. Stojčić, E. K. Zavadskas, D. Pamučar, Ž. Stević, and A. Mardani, "Application of MCDM methods in sustainability engineering: a literature review 2008-2018," *Symmetry*, vol. 11, no. 3, p. 350, 2019.

[6] M. K. Niaki and F. Nonino, "Additive manufacturing management: a review and future research agenda. 7543," *International Journal of Production Research*, vol. 55, 2016.

[7] H. Bikas, P. Stavropoulos, and G. Chryssolouris, "Additive manufacturing methods and modelling approaches: a critical review," *International Journal of Advanced Manufacturing Technology*, vol. 83, no. 1–4, pp. 389–405, 2016.

[8] G. Tapia and A. Elwany, "A review on process monitoring and control in metal-based additive manufacturing," *Journal of Manufacturing Science and Engineering*, vol. 136, no. 6, 2014.

[9] S. Douglas and W. Stanley, "NIST special publication 1176 Costs and cost Effectiveness of additive manufacturing A literature Review and discussion," *NIST special publication*, vol. 1176, 2015.

[10] W. W. Wits, J. R. R. García, and J. M. J. Becker, "How additive manufacturing enables more sustainable end-user maintenance, repair and overhaul (MRO) strategies," *Procedia CIRP*, vol. 40, pp. 693–698, 2016.

[11] D. Cohen, M. Sargeant, and K. Somers, "3-D printing takes shape," *McKinsey Quarterly*, vol. 1, pp. 1–6, 2014.

[12] T. Wohlers and T. Gornet, "History of additive manufacturing Introduction of non-SL systems Introduction of low-cost 3D printers," *Wohlers Report*, vol. 2012, pp. 1–23, 2012.

[13] N. Knofius, M. C. Van Der Heijden, and W. H. M. Zijm, "Selecting parts for additive manufacturing in service logistics," *Journal of Manufacturing Technology Management*, vol. 27, no. 7, pp. 915–931, 2016.

[14] S. H. Khajavi, J. Partanen, and J. Holmström, "Additive manufacturing in the spare parts supply chain," *Computers in Industry*, vol. 65, no. 1, pp. 50–63, 2014.

[15] N. Hopkinson and P. Dicknes, "Analysis of rapid manufacturing - using layer manufacturing processes for production," *Proceedings of the Institution of Mechanical Engineers - Part C: Journal of Mechanical Engineering Science*, vol. 217, no. 1, pp. 31–39, 2003.

[16] A. Cestana, E. Pastore, A. Alfieri, and A. Matta, "Reducing resupply time with additive manufacturing in spare part supply chain," *IFAC-PapersOnLine*, vol. 52, no. 13, pp. 577–582, 2019.

[17] C. Cozmei and F. Caloian, "Additive manufacturing flickering at the beginning of existence," *Procedia Economics and Finance*, vol. 3, no. march 2009, pp. 457–462, 2012.

[18] H. Rogers, N. Baricz, and K. S. Pawar, "3D printing services: classification, supply chain implications and research

agenda," *International Journal of Physical Distribution & Logistics Management*, vol. 46, no. 10, pp. 886–907, 2016.

[19] C. Gosselin, R. Duballet, P. Roux, N. Gaudillière, J. Dirrenberger, and P. Morel, "Large-scale 3D printing of ultra-high performance concrete - a new processing route for architects and builders," *Materials & Design*, vol. 100, pp. 102–109, 2016.

[20] T. Rayna and L. Striukova, "From rapid prototyping to home fabrication: how 3D printing is changing business model innovation," *Technological Forecasting and Social Change*, vol. 102, pp. 214–224, 2016.

[21] J. P. J. Jong and E. Bruijn, "Innovation lessons from 3-D printing," *MIT Sloan Management Review*, vol. 52, no. 2, pp. 43–52, 2013.

[22] M. Karthick, M. Meikandan, S. Kaliappan et al., "Experimental investigation on mechanical properties of glass fiber hybridized natural fiber reinforced penta-layered hybrid polymer composite," *International Journal of Chemical Engineering*, vol. 2022, Article ID 1864446, 2022.

[23] G. Velmurugan, V. S. Shankar, S. Kaliappan et al., "Effect of Aluminium Tetrahydrate Nanofiller Addition on the Mechanical and Thermal Behaviour of Luffa Fibre-Based Polyester Composites under Cryogenic Environment," *Journal of Nanomaterials*, vol. 2022, pp. 1–10, Article ID 5970534, 2022.

[24] K. C. Sekhar, R. Surakasi, P. Roy et al., "Mechanical behavior of aluminum and graphene nanopowder-based composites," *International Journal of Chemical Engineering*, vol. 2022, Article ID 2224482, 2022.

[25] S. Venkatasubramanian, S. Raja, V. Sumanth et al., "Fault diagnosis using data fusion with ensemble deep learning technique in IIoT," *Mathematical Problems in Engineering*, vol. 2022, Article ID 1682874, 2022.

[26] J. B. Roca, P. Vaishnav, J. Mendoņa, and M. G. Morgan, "Getting past the hype about 3-D printing," *MIT Sloan Management Review*, vol. 58, no. 3, pp. 57–62, 2017.

[27] A. Pringle, M. Rudnicki, J. Pearce et al., "Wood furniture waste-based recycled 3-D printing filament to cite this version: HAL id : hal-02111355," 2019, https://core.ac.uk/download/pdf/217851407.pdf.

[28] J. Kowalewski, *Improving additive manufactured parts with aluminum ion vapor deposition improving additive manufactured parts with aluminum ion vapor deposition*, Ispen USA, 2020.

[29] M. O. Alabi, D. De Beer, and H. Wichers, "Applications of additive manufacturing at selected South African universities: promoting additive manufacturing education," *Rapid Prototyping Journal*, vol. 25, no. 4, pp. 752–764, 2019.

[30] G. D. Goh, S. Agarwala, G. L. Goh, V. Dikshit, S. L. Sing, and W. Y. Yeong, "Additive manufacturing in unmanned aerial vehicles (UAVs): challenges and potential," *Aerospace Science and Technology*, vol. 63, no. April, pp. 140–151, 2017.

[31] B. Kianian, S. Tavassoli, T. C. Larsson, and O. Diegel, "The adoption of additive manufacturing technology in Sweden," *Procedia CIRP*, vol. 40, pp. 7–12, 2016.

[32] C. L. Weber, M. K. Micali, S. A. Rood, and J. A. Scott, *The role of the national science foundation in the origin and evolution of additive manufacturing in the United States*, United State, 2013.

[33] H. Zijm, N. Knofius, and M. van der Heijden, "Additive manufacturing and its impact on the supply chain," *Operations, Logistics and Supply Chain Management*, vol. 1, pp. 521–543, 2019.

[34] A. M. Aboutaleb, L. Bian, A. Elwany, N. Shamsaei, S. M. Thompson, and G. Tapia, "Accelerated process optimization for laser-based additive manufacturing by leveraging similar prior studies," *IISE Transactions*, vol. 49, no. 1, pp. 31–44, 2017.

[35] M. Yampolskiy, W. E. King, J. Gatlin et al., "Security of additive manufacturing: attack taxonomy and survey," *Additive Manufacturing*, vol. 21, pp. 431–457, 2018.

[36] P. J. Day and S. J. Speers, "The assessment of 3D printer technology for forensic comparative analysis," *Australian Journal of Forensic Sciences*, vol. 52, no. 5, pp. 579–589, 2020.

[37] A. D. Lantada and P. L. Morgado, "Rapid prototyping for biomedical engineering: current capabilities and challenges," *Annual Review of Biomedical Engineering*, vol. 14, no. 1, pp. 73–96, 2012.

[38] M. Yampolskiy, L. Schutzle, U. Vaidya, and A. Yasinsac, "Security challenges of additive manufacturing with metals and alloys," *IFIP Advances in Information and Communication Technology*, vol. 466, pp. 169–183, 2015.

[39] D. Lehmhus, C. Aumund-Kopp, F. Petzoldt et al., "Customized smartness: a survey on links between additive manufacturing and sensor integration," *Procedia Technology*, vol. 26, pp. 284–301, 2016.

[40] E. Buranská, I. Buranský, L. Morovič, and K. Líška, "Environment and safety impacts of additive manufacturing: a review," *Research Papers Faculty of Materials Science and Technology Slovak University of Technology*, vol. 27, no. 44, pp. 9–20, 2019.

[41] C. Kapetaniou, A. Rieple, A. Pilkington, T. Frandsen, and P. Pisano, "Building the layers of a new manufacturing taxonomy: how 3D printing is creating a new landscape of production eco-systems and competitive dynamics," *Technological Forecasting and Social Change*, vol. 128, no. March, pp. 22–35, 2018.

[42] R. Jemghili, A. Ait Taleb, and K. Mansouri, "Additive manufacturing progress as a new industrial revolution," in *Proceedings of the 2020 IEEE 2nd International Conference on Electronics, Control, Optimization and Computer Science, ICECOCS 2020*, Kenitra, Morocco, 2020 January.

[43] M. Præst, "Development and test of an additive manufacturing maturity model development and test of an additive manufacturing maturity model paper prepared for the R & D management conference 2019," *The innovation challenge: Bridging research, industry & society*, vol. 12, 2021.

[44] A. Manmadhachary, Y. Ravi Kumar, and L. Krishnanand, "Finding of correction factor and dimensional error in bio-AM model by FDM technique," *Journal of the Institution of Engineers: Series C*, vol. 99, no. 3, pp. 293–300, 2018.

[45] S. Brischetto, A. Ciano, and C. G. Ferro, "A multipurpose modular drone with adjustable arms produced via the FDM additive manufacturing process," *Curved and Layered Structures*, vol. 3, no. 1, pp. 202–213, 2016.

[46] B. Berman, "3-D printing: the new industrial revolution," *Business Horizons*, vol. 55, no. 2, pp. 155–162, 2012.

[47] S. H. Huang, P. Liu, A. Mokasdar, and L. Hou, "Additive manufacturing and its societal impact: a literature review," *International Journal of Advanced Manufacturing Technology*, vol. 67, no. 5–8, pp. 1191–1203, 2013.

[48] C. Tuck, R. Hague, and N. Burns, "Rapid manufacturing: impact on supply chain methodologies and practice," *International Journal of Services and Operations Management*, vol. 3, no. 1, pp. 1–22, 2007.

[49] S. Ford, L. Mortara, and T. Minshall, "The emergence of additive manufacturing: introduction to the special issue,"

Technological Forecasting and Social Change, vol. 102, pp. 156–159, 2016.

[50] J. Holmström and T. Gutowski, "Additive manufacturing in operations and supply chain management: No sustainability benefit or virtuous knock-on opportunities?" *Journal of Industrial Ecology*, vol. 21, no. S1, pp. S21–S24, 2017.

[51] V. C. K. Ma, "3D printing and the law," *Intersec: The Stanford Journal of Science, Technology and Society*, vol. 11, 2017.

[52] K. Oettmeier and E. Hofmann, "How additive manufacturing impacts supply chain business processes and management components," *Proceedings of the 28th Annual Nordic Logistics Research Network Conferenc*, vol. 1, pp. 444–460, 2016.

[53] A. Barz, T. Buer, and H. D. Haasis, "A study on the effects of additive manufacturing on the structure of supply networks," *IFAC-PapersOnLine*, vol. 49, no. 2, pp. 72–77, 2016.

[54] S. C. Chang, H. H. Chang, and M. T. Lu, "Evaluating industry 4.0 technology application in smes: using a hybrid mcdm approach," *Mathematics*, vol. 9, no. 4, pp. 414–420, 2021.

[55] N. Komatina, M. Djapan, I. Ristić, and A. Aleksić, "Fulfilling external stakeholders' demands—enhancement workplace safety using fuzzy mcdm," *Sustainability*, vol. 13, no. 5, pp. 2892–2913, 2021.

[56] S. Mohr and O. Khan, "3D printing and supply chains of the future," *Innovations and Strategies for Logistics and Supply Chains*, vol. 1, pp. 147–174, 2015.

[57] M. Bogers, R. Hadar, and A. Bilberg, "Additive manufacturing for consumer-centric business models: implications for supply chains in consumer goods manufacturing," *Technological Forecasting and Social Change*, vol. 102, pp. 225–239, 2016.

[58] S. Zanoni, M. Ashourpour, A. Bacchetti, M. Zanardini, and M. Perona, "Supply chain implications of additive manufacturing: a holistic synopsis through a collection of case studies," *International Journal of Advanced Manufacturing Technology*, vol. 102, no. 9–12, pp. 3325–3340, 2019.

[59] P. Liu, S. H. Huang, A. Mokasdar, H. Zhou, and L. Hou, "The impact of additive manufacturing in the aircraft spare parts supply chain: supply chain operation reference (scor) model based analysis," *Production Planning & Control*, vol. 25, no. 13-14, pp. 1169–1181, 2014.

[60] S. Editors, U. Clausen, H. Robert et al., "Lecture notes in logistics operations," *logistics and supply chain management*, China, 2020.

[61] L. Natrayan and M. S. Kumar, "A potential review on influence of process parameter and effect of reinforcement on mechanical and tribological behaviour of HMMC using squeeze casting method," *Journal of Critical Reviews*, vol. 7, no. 2, pp. 1–5, 2020.

[62] K. Seeniappan, B. Venkatesan, N. N. Krishnan et al., "A comparative assessment of performance and emission characteristics of a DI diesel engine fuelled with ternary blends of two higher alcohols with lemongrass oil biodiesel and diesel fuel,," *Energy & Environment*, vol. 13, 2021.

[63] V. S. Nadh, C. Krishna, L. Natrayan et al., "Structural behavior of nanocoated oil palm shell as coarse aggregate in lightweight concrete," *Journal of Nanomaterials*, vol. 2021, pp. 1–7, Article ID 4741296, 2021.

[64] G. Choubey, W. Huang, L. Yan, H. Babazadeh, and K. Pandey, "Hydrogen fuel in scramjet engines - a brief review," *International Journal of Hydrogen Energy*, vol. 45, no. 33, pp. 16799–16815, 2020.

[65] L. Natrayan, M. Senthil Kumar, and M. Chaudhari, "Optimization of squeeze casting process parameters to investigate the mechanical properties of AA6061/Al 2 O 3/SiC hybrid metal matrix composites by taguchi and anova approach," *Advanced Engineering Optimization through Intelligent Techniques*, pp. 393–406, Springer, Singapore, 2020.

[66] S. Kaliappan, M. D. Raj Kamal, S. Mohanamurugan, and P. K. Nagarajan, "Analysis of an innovative connecting rod by using finite element method," *Taga Journal Of Graphic Technology*, vol. 14, pp. 1147–1152, 2018.

[67] S. Yogeshwaran, L. Natrayan, S. Rajaraman, S. Parthasarathi, and S. Nestro, "Experimental investigation on mechanical properties of Epoxy/graphene/fish scale and fermented spinach hybrid bio composite by hand lay-up technique," *Materials Today Proceedings*, vol. 37, pp. 1578–1583, 2021.

[68] S. Justin Abraham Baby, S. Suresh Babu, and Y. Devarajan, "Performance study of neat biodiesel-gas fuelled diesel engine," *International Journal of Ambient Energy*, vol. 42, no. 3, pp. 269–273, 2018.

[69] L. Natrayan, S. Yogeshwaran, L. Yuvaraj, and M. S. Kumar, "Effect of graphene reinforcement on mechanical and microstructure behavior of AA8030/graphene composites fabricated by stir casting technique," *AIP Conference Proceedings*, vol. 2166, 2019 1, Article ID 020012.

[70] Y. Devarajan, G. Choubey, and K. Mehar, "Ignition analysis on neat alcohols and biodiesel blends propelled research compression ignition engine," *Energy Sources, Part A: Recovery, Utilization, and Environmental Effects*, vol. 42, no. 23, pp. 2911–2922, 2019.

[71] L. Natrayan, V. Sivaprakash, and M. S. Santhosh, ""Mechanical, microstructure and wear behavior of the material AA6061 reinforced SiC with different leaf ashes using advanced stir casting method."," *International Journal of Engineering and Advanced Technology*, vol. 8, pp. 366–371, 2018.

[72] L. Natrayan and A. Merneedi, "Experimental investigation on wear behaviour of bio-waste reinforced fusion fiber composite laminate under various conditions," *Materials Today Proceedings*, vol. 37, pp. 1486–1490, 2021.

[73] V. Balaji, S. Kaliappan, D. M. Madhuvanesan, D. S. Ezhumalai, S. Boopathi, and S. Mani, "Combustion analysis of biodiesel-powered propeller engine for least environmental concerns in aviation industry," *Aircraft Engineering and Aerospace Technology*, vol. 94, pp. 760–769, 2020.

[74] L. Natrayan, P. S. S. Sundaram, and J. Elumalai, "Analyzing the uterine physiological with MMG signals using SVM," *International journal of pharmaceutical research*, vol. 11, pp. 165–170, 2019, 2.

[75] N. Knofius, M. C. van der Heijden, A. Sleptchenko, and W. H. M. Zijm, "Improving effectiveness of spare parts supply by additive manufacturing as dual sourcing option," *In OR Spectrum*, vol. 43, no. 1, 2021.

[76] T. Pham, P. Kwon, and S. Foster, "Additive manufacturing and topology optimization of magnetic materials for electrical machines—a review," *Energies*, vol. 14, no. 2, 2021.

[77] C. Achillas, D. Tzetzis, and M. O. Raimondo, "Alternative production strategies based on the comparison of additive and traditional manufacturing technologies," *International Journal of Production Research*, vol. 55, no. 12, pp. 3497–3509, 2017.

[78] S. Bhattacharya, "Supply chain management in Indian automotive industry: complexities, challenges and way ahead,"

International Journal of Managing Value and Supply Chains, vol. 5, no. 2, pp. 49–62, 2014.

[79] G. N. Levy, R. Schindel, and J. P. Kruth, "Rapid manufacturing and rapid tooling with layer manufacturing (LM) technologies, state of the art and future perspectives," *CIRP Annals*, vol. 52, no. 2, pp. 589–609, 2003.

[80] V. Kumar and D. Dutta, "An assessment of data formats for layered manufacturing," *Advances in Engineering Software*, vol. 28, no. 3, pp. 151–164, 1997.

[81] S. Singamneni, Y. Lv, A. Hewitt, R. Chalk, W. Thomas, and D. Jordison, "Additive manufacturing for the aircraft industry: a review," *Journal of Aeronautics & Aerospace Engineering*, vol. 08, no. 01, 2019.

[82] R. A. Chandru, N. Balasubramanian, C. Oommen, and B. N. Raghunandan, "Additive manufacturing of solid rocket propellant grains," *Journal of Propulsion and Power*, vol. 34, no. 4, pp. 1090–1093, 2018.

[83] G. Dwivedi, S. K. Srivastava, and R. K. Srivastava, "Analysis of barriers to implement additive manufacturing technology in the Indian automotive sector," *International Journal of Physical Distribution & Logistics Management*, vol. 47, no. 10, pp. 972–991, 2017.

[84] M. V. D. S. Kalyan, H. Kumar, and L. Nagdeve, "Latest trends in Additive manufacturing," , 2021.

[85] P. S. Ghahfarokhi, A. Podgornovs, A. Kallaste et al., "Opportunities and challenges of utilizing additive manufacturing approaches in thermal management of electrical machines," *IEEE Access*, vol. 9, pp. 36368–36381, 2021.

[86] K. V. Wong and A. Hernandez, "A review of additive manufacturing," *ISRN Mechanical Engineering*, vol. 2012, pp. 1–10, Article ID 208760, 2012.

[87] L. J. Love, V. Kunc, O. Rios et al., "The importance of carbon fiber to polymer additive manufacturing," *Journal of Materials Research*, vol. 29, no. 17, pp. 1893–1898, 2014.

[88] K. Hemalatha, C. James, L. Natrayan, and V. Swamynadh, "Analysis of RCC T-beam and prestressed concrete box girder bridges super structure under different span conditions," *Materials Today Proceedings*, vol. 37, pp. 1507–1516, 2021.

[89] V. Paranthaman, K. S. Sundaram, and L. Natrayan, ""Influence of SiC particles on mechanical and microstructural properties of modified interlock friction stir weld lap joint for automotive grade aluminium alloy."," *Silicon*, vol. 14, pp. 1617–1627, 2022.

[90] M. Vijayaragavan, B. Subramanian, S. Sudhakar, and L. Natrayan, *"Effect of induction on exhaust gas recirculation and hydrogen gas in compression ignition engine with simarouba oil in dual fuel mode, " International Journal of Hydrogen Energy*, vol. 47, pp. 1–13, 2021.

[91] D. Veeman, M. S. Sai, P. Sureshkumar et al., "Additive manufacturing of biopolymers for tissue engineering and regenerative medicine: an overview, potential applications, advancements, and trends," *International Journal of Polymer Science*, vol. 2021, pp. 1–20, Article ID 4907027, 2021.

[92] R. Suryanarayanan, V. G. Sridhar, L. Natrayan et al., "Improvement on mechanical properties of submerged friction stir joining of dissimilar tailor welded aluminum blanks," *Advances in Materials Science and Engineering*, vol. 2021, p. 1, Article ID 3355692, 2021.

[93] R. Liu, S. Liu, and X. Zhang, "A physics-informed machine learning model for porosity analysis in laser powder bed fusion additive manufacturing," *International Journal of Advanced Manufacturing Technology*, vol. 113, no. 7–8, pp. 1943–1958, 2021.

[94] D. Vidosav, "Manufacturing innovation and horizon 2020–developing and implement "new manufacturing"," *Proceedings in Manufacturing Systems*, vol. 9, no. 1, pp. 3–8, 2014.

[95] C. Klahn, B. Leutenecker, and M. Meboldt, "Design for additive manufacturing - supporting the substitution of components in series products," *Procedia CIRP*, vol. 21, pp. 138–143, 2014.

[96] J. P. Järvinen, V. Matilainen, X. Li et al., "Characterization of effect of support structures in laser additive manufacturing of stainless steel," *Physics Procedia*, vol. 56, no. C, pp. 72–81, 2014.

[97] P. Szymczyk, I. Smolina, M. Rusińska, A. Woźna, A. Tomassetti, and E. Chlebus, "Logistical aspects of transition from traditional to additive manufacturing," *Advances in Intelligent Systems and Computing*, vol. 835, no. August, pp. 752–760, 2019.

[98] M. Piazza, S. Alexander, and A. Serena, "EngagedScholarship," *dditive Manufacturing: A Summary of the Literature Repository Citation*, vol. 1, 2015.

[99] M. Seifi, A. Salem, J. Beuth, O. Harrysson, and J. J. Lewandowski, "Overview of materials qualification needs for metal additive manufacturing," *Journal of Occupational Medicine*, vol. 68, no. 3, pp. 747–764, 2016.

[100] I. Flores Ituarte, J. Partanen, and S. H. Khajavi, "Challenges to implementing additive manufacturing in globalised production environments," *International Journal of Collaborative Enterprise*, vol. 5, no. 3/4, 2016.

[101] M. Khorram Niaki and F. Nonino, "Impact of additive manufacturing on business competitiveness: a multiple case study," *Journal of Manufacturing Technology Management*, vol. 28, no. 1, pp. 56–74, 2017.

[102] J. Jiang, X. Xu, and J. Stringer, "Support structures for additive manufacturing: a review," *Journal of Manufacturing and Materials Processing*, vol. 2, no. 4, 2018.

[103] B. Maiti, "済無No title No title," *Journal of Chemical Information and Modeling*, vol. 53, no. 9, pp. 1689–1699, 1981.

[104] G. H. Loh, E. Pei, D. Harrison, and M. D. Monzón, "An overview of functionally graded additive manufacturing," *Additive Manufacturing*, vol. 23, no. c, pp. 34–44, 2018.

[105] A. Ghadge, G. Karantoni, A. Chaudhuri, and A. Srinivasan, "Impact of additive manufacturing on aircraft supply chain performance: a system dynamics approach," *Journal of Manufacturing Technology Management*, vol. 29, no. 5, pp. 846–865, 2018.

[106] J. Butt, "Exploring the interrelationship between additive manufacturing and industry 4.0," *Design*, vol. 4, no. 2, pp. 13–33, 2020.

[107] V. Verboeket and H. Krikke, "Additive manufacturing: a game changer in supply chain design," *Logistics*, vol. 3, no. 2, 2019.

[108] J. P. Kruth, M. C. Leu, and T. Nakagawa, "Progress in additive manufacturing and rapid prototyping," *CIRP Annals*, vol. 47, no. 2, pp. 525–540, 1998.

Hindawi
Advances in Materials Science and Engineering
Volume 2022, Article ID 4120145, 8 pages
https://doi.org/10.1155/2022/4120145

Research Article

Wear Investigation of Aluminum Alloy Surface Layers Fabricated through Friction Stir Welding Method

S. Vijayakumar,[1] **S. Anitha**,[2] **R. Arivazhagan**,[3] **Ashebir Dingeto Hailu**,[4] **T. V. Janardhana Rao**,[5] **and Hari Prasadarao Pydi**[6]

[1]*Department of Mechanical Engineering, BVC Engineering College (Autonomous), Odalarevu-533210, Andhrapradesh, India*
[2]*Department of Physics, Arulmigu Palaniandavar College of Arts and Culture, Palani, Tamilnadu, India*
[3]*Department of Mechanical Engineering, Kongunadu College of Engineering and Technology, Tamilnadu, India*
[4]*Department of Mechanical Engineering, Bule Hora University (BHU), P. O. Box 144, Ethiopia*
[5]*Department of Electronics and Communications Engineering, BVC Engineering College (Autonomous), Odalarevu 533210, Andhra Pradesh, India*
[6]*Department of Mechanical Engineering, Bule Hora University, Bule Hora, Ethiopia*

Correspondence should be addressed to Hari Prasadarao Pydi; haripydi609@gmail.com

Received 22 June 2022; Revised 11 July 2022; Accepted 16 July 2022; Published 9 August 2022

Academic Editor: R. Thanigaivelan

In this research paper, an effort was made to investigate the dry sliding wear rate of friction stir welded AA6262/AA5456 composite performed by the Taguchi approach. Wear experiments are carried out by selecting suitable process parameters such as load (LD), sliding speed (SS), and sliding distance (SE) to recognize the individual and combination effects of parameters. Orthogonal array L27 mode is applied to make numbers of experiments to find the extreme and minimum wear amount. The experimental works are conducted on Pin on Disc (POD) apparatus and measured the weight of samples before and after test for calculating wear rate (WR) and then various analyses are performed such as ANOVA, interaction plot between parameters, and regression model with support of MINITAB software. The results revealed that maximum wear rate is found as 0.01215 mm^3/Nm at LD of 50 N, SE of 600 m, and SS of 4 m/s, whereas minimum 0.00414 mm^3/Nm at the grouping process parameters which are LD of 30 N, SE of 400 m, and SS of 6 m/s. From the observation of ANOVA, the most significant factor is identified as load, followed by sliding distance, sliding speed, and combination of each parameter. The load is considered as main parameter which contributes about 83.75% to achieve the maximum wear rate of developed AA6262/5456 composites. The contribution of sliding distance and speed are 3.75% and 1.85%, respectively.

1. Introduction

Aluminum alloy's importance in the automotive and construction sectors may be attributed to their low density and high rigidity. AA6XXX rated components have better physical qualities and strength, making them desirable in applications such as missiles, weapons, and automobiles [1]. AA6262/5456 is a higher-grade alloy with a higher amount of magnesium, silicon, and iron components, all of which have been carefully regulated to improve resistance to oxidation and mechanical characteristics [2]. Different techniques including stir casting [3], squeeze-casting, metallurgy method, and friction stir process (FSP) are used to create aluminum matrix composites based on size of particles, volume fraction, and shape of reinforcing components [4]. Friction stir welding (FSW) is a production method for combining metals, steels, and aluminum alloys [5–7]. It is really energy-efficient and perfect example of create composites from two metallic phases as per several researchers point of view [8, 9]. FSW factors of Al 6061/7075 alloys were examined by Ravikumar's team. They chose three distinct pin tools in the shapes of square, cylinder, and square thread shapes [10]. According to the study conducted by Bhushan and Gupta, wear is caused by friction between two comparable or different metals when they come into contact [11]. Singla et al. exposed AA6061/SiC composite made using the

Table 1: Mechanical properties of Al6262 and Al5456.

Material	Tensile strength, TS (MPa)	Yield strength, YS (MPa)	Elongation, δ (%)	Hardness (HV)
Al6262	260	206	12	85
Al5456	305	244	15	110

Figure 1: Friction stir welding process.

Figure 2: POD apparatus.

Table 2: Wear test parameter levels.

Parameters	Level		
	1	2	3
LD (N)	30	40	50
SE (m)	400	500	600
SS (m/s)	2	4	6

SC process with modifications in silicon carbide volume %, and the wear examination was conducted via a POD device [12]. Sesharao et al. studied on the effect of sliding distance on the response of wear rate for Al6066/HSS-Cu produced by the heat treated casting method [13]. The maximum wear resistance is attained in 24 hrs milling powder method performed by Guler and team. They compared the ZA27/B4C/graphite composites with and without milled process and found corrosion resistance is more in milling powder technique [14]. Singh et al. studied about wear and friction performance of panama oil lubricants at various levels of sliding speed, and the results conclude that this kind of biolubricant mainly applicable in automobile enterprise [15]. Natarajan et al. studied wear rate of Al 2014/flyash on the brake pads. When they compared with grey cast iron, Al-based composite provides superior wear resistance [16]. Panneerselvam et al. used the Taguchi approach to examine wear performance of Al-HMMC by employing input variables of load, slide speed, and MoS_2 particles. The influence factor was identified through the ANOVA technique [17]. Hemanth Reddy and Perumal used compression moulding to prepare samples of (C3H6)n/Nylon/Honeycomb Al-based composite and preferred Taguchi-L9 orthogonal array on wear experiments [18]. To conduct the wear experiment on POD device, AA5052/ZrO2/Al2O3 specimens are made as according to ASTM standards using the stir process. The MINITAB software was used to examine the design of experiments for wear parameters [19, 20]. From other research works, many scholars selected almost 3 to 5 input factors such as load, sliding speed, time, distance, and reinforcement percentage to perform wear examination. "The wear rate of Al 7075-SiC-graphite reinforced matrix is lower in the composite than in the nonreinforced alloy, according to a parametric investigation (load, speed, and sliding distance). With the exception of sliding velocity, where a transitional velocity was seen, the wear rate was shown to rise with the increase in process parameters [21]. The wear behaviour of B4C particles reinforced with aluminium that were manufactured using the friction stir procedure is revealed by Mehta et al. A variety of specimen passes were tested. One advantage of reverse pass is that the base metal is well-reinforced uniformly [22]. Wu et al. assessed the wear rate (WR) and friction coefficient (FC), finding that WR values was improved when Nd was at 0.5% of weight and subsequently dropped when Nd was at 1.0 w.t%, when a load was applied from 30 to 160 N [23]. In the absence of reinforcement particles, the composite hardness reduced in contrast to the basic metal, according to Barmouz et al.'s study, who generated Cu/SiC composites by dispersing 5 mm and 30 nanometers SiCp into the surface of pure Cu using FSP [24]. Trimble's team used a postweld experiment and monitoring force to pick a combination of welding

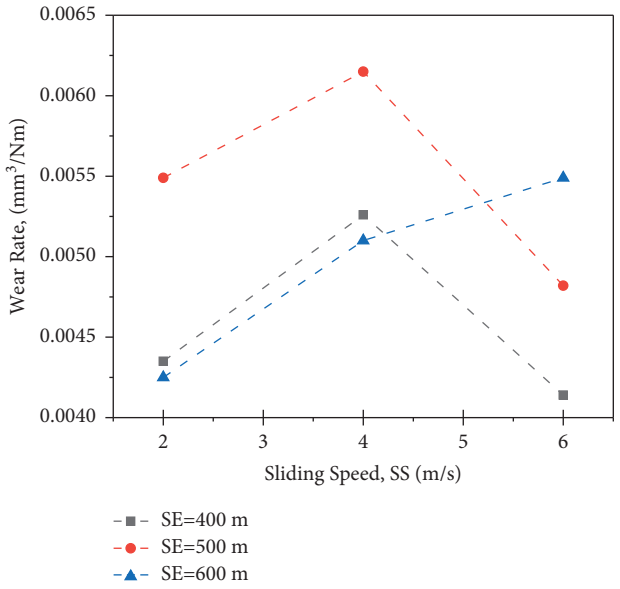

Figure 3: Interaction between SS and SE levels at LD = 30 N.

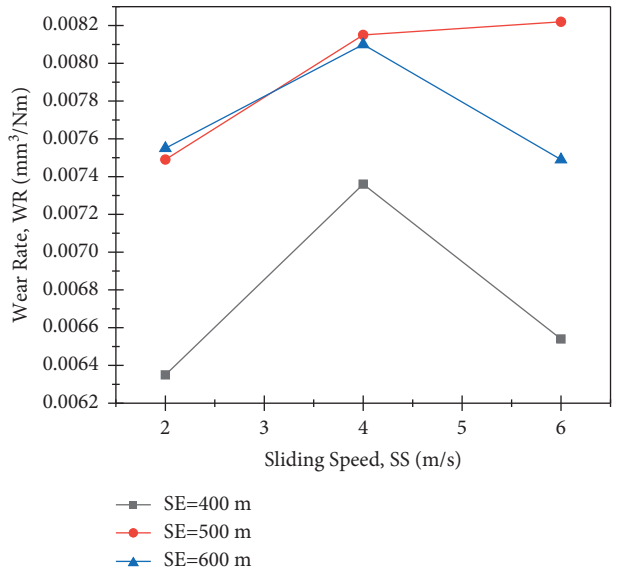

Figure 4: Interaction between SS and SE levels at LD = 40 N.

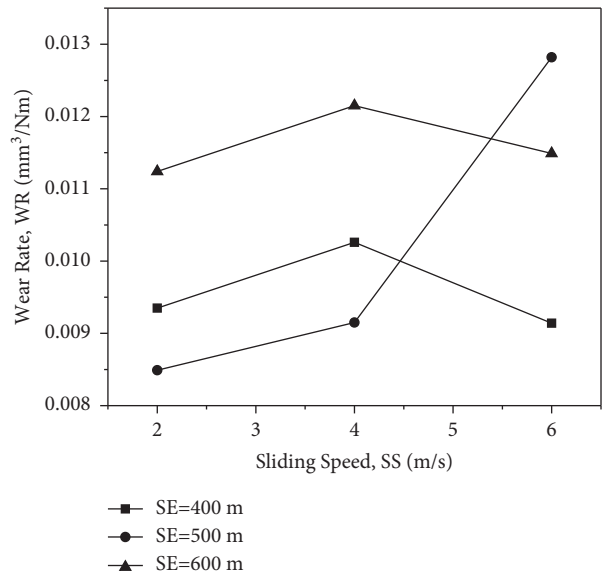

Figure 5: Interaction between SS and SE levels at LD = 50 N.

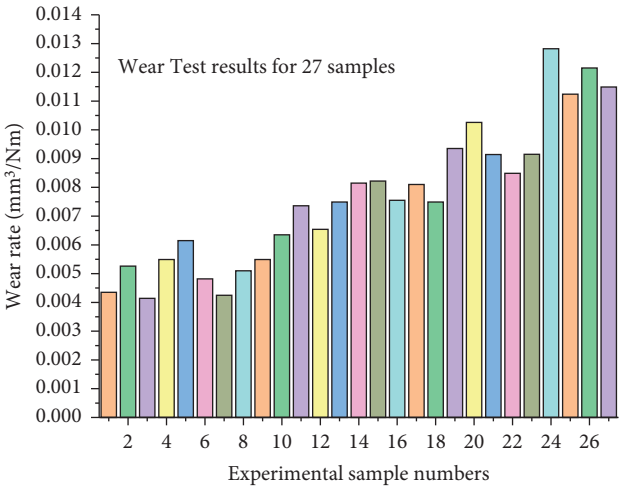

Figure 6: Wear test results for overall specimens.

process parameters for producing sound welds and strength at higher speeds. Variations of rotating speeds and tool speed were used in the AA 2024-T3 research. However, they discovered that tool geometry with a scrolling shoulder and a triflute shape for the pin produced superior results [25]. Prado et al. investigated the influence of rotational speed on tool wear in FSW of AA6061-20% alumina and discovered that tool wear was not linear [26]. Lee et al. compared WR of AZ91-10% wt of SiC with base composite to that of FSW and discovered a reduction in the wear rate. However, he was not trying to attempt to link the influence of FSW parameters on wear amount [27]. Krishnan et al. [28] studied the effect of stirrer blade design on mechanical properties of AMCs and performed simulation through the CFD method. The result revealed that four blade stirrers give more tensile strength and hardness amongst 5 different blades. Krishnan and team [29] prepared different aluminum matrix composites by stir-squeeze casting. Microstructural investigations such as optical microscopy, XRD, and EDS were carried out, and mechanical proprieties exposed that UTS around 126 MPa was obtained at scrap Al/Alumina composites. Rayapandi Thevar et al. [30] used the Taguchi approach with L9 orthogonal array to conduct experimental study of Al–Al_2O_3 composites. Based on various literature articles, the effects of weld speed and tool tilt angle while joining different Al-based alloys were found and explored. As the tool rotating speed (TRS), tilt angle (TA), and weld speed (WS) are the

Table 3: ANOVA wear rate.

Considerations	Dof	SS	MS	F	*P* value	Contribution level (%)
LD	2	0.000134	0.000067	72.02	0.000	83.75
SE	2	0.000006	0.000003	3.40	0.085	3.75
SS	2	0.000003	0.000002	1.68	0.246	1.85
LD ∗ SE	4	0.000004	0.000001	1.08	0.428	2.12
LD ∗ SS	4	0.000002	0.000001	0.55	0.704	1.25
SE ∗ SS	4	0.000003	0.000001	0.79	0.563	1.85
Residual error	8	0.000007	0.000001			5.43
Total	26	0.000160				

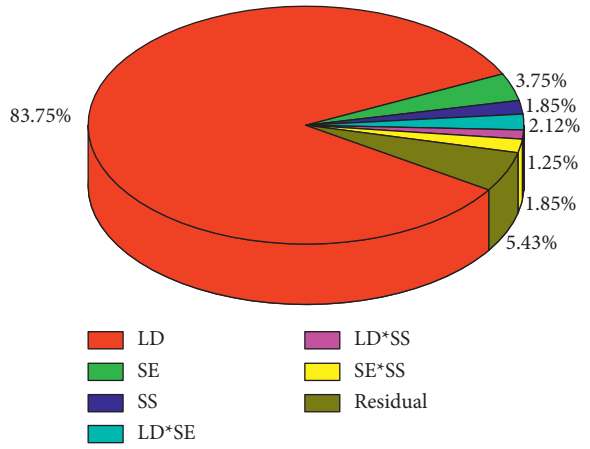

Figure 7: Contribution of WR parameters.

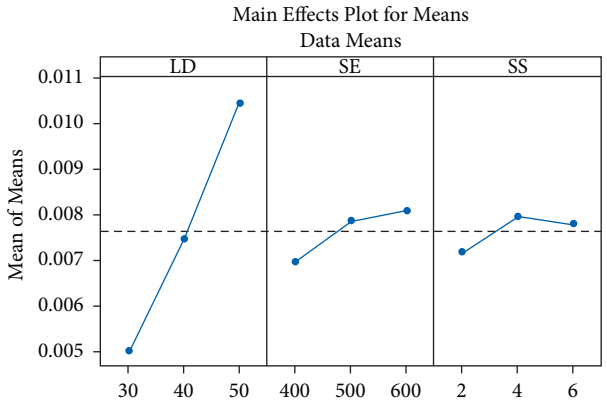

Figure 8: Effects of plot on WR.

Table 4: Response output for WR.

Level	LD	SE	SS
1	0.005006	0.006972	0.007173
2	0.007472	0.007864	0.007964
3	0.010454	0.008096	0.007794
Delta	0.005449	0.001123	0.000791
Rank	1	2	3

primary sources of heat generation, the weld strength and quality typically depend on the heat generated and material mixing during welding. Our objective is to create AA6262/AA5456 composites with help of these parameters (TRS, TA, and WS) in the FSW method and prepared 27 specimens for conducting the wear test. With the support of the Taguchi technique and MINITAB software [31], significant parameter was identified to increase the wear rate. The fabrication of pressure vessels, screw machine products, nuts, oil line fittings, and valve components are applied for the development of FSW of Al5456/6262 composites.

2. Materials and Methodology

The plates of AA6262 and AA5456 are preferred to make a joint via friction stir welding (FSW). 6262 alloy which possess 91–92% of aluminum along with some other elements such as 5.2–5.7% of magnesium, 0.4–0.5% of iron, 1.5–1.75% manganese, 2.08–0.35 of copper, 0.2–0.4% of silicon [32]. Similarly, 5456 alloy has 95.5% of Al and other chemical contents such as Mg-1.2%, Mn-0.15%, and Si-0.9% [33]. The mechanical properties of base metal AA5456 and AA6262 alloys are shown in Table.1. Vertical milling machine and H13 pin were used as machine and welding tool to complete the FSW process as shown in Figure 1. Al plates with a dimension of 100 ∗, ∗ 50 ∗ 6 mm^3 are connected by inserting pin tool with 25 mm of shoulder diameter and 4 mm length. Figure 2 shows Pin on Disc (POD) unit which utilized to conduct dry sliding wear test size of specimens Ø12 mm ∗ 35 mm length (ASTM-G99) was removed from the FSW sample. Before the carryout experiment, we cleaned the specific sample by acetone and then measure its weight through electronic digital device. After that, the specimen is placed in pin, then make sample to touch on rotating disc of diameter 75 mm. The wear test is performed by varying parameter of load (30N), slide distance (400m), and slide speed (2 m/s). The load is applied on the arm to make contact with revolving disc till the sample surface is wear off. Due to movement of arm with disc which creates wear on composite. Afterward, the experiment is completed, and take out specimen and calculate weight loss by measuring weight of the specimen. In this dry wear examination, we did not use any lubricants. This procedure is followed for the remaining 26 parameter levels on the wear test. Design of Experiments (DOE) is frequently used to examine the input process variables or parameters with their stages to attain objectives. The conduction of experiments was performed with the aid of parametric combinations and their levels. The number of experiments is to be established according to the Taguchi design [34, 35]. In this task, we have selected three parameters of LD, SS, and SE at 3 levels as shown in Table.2. The optimization software MINITAB

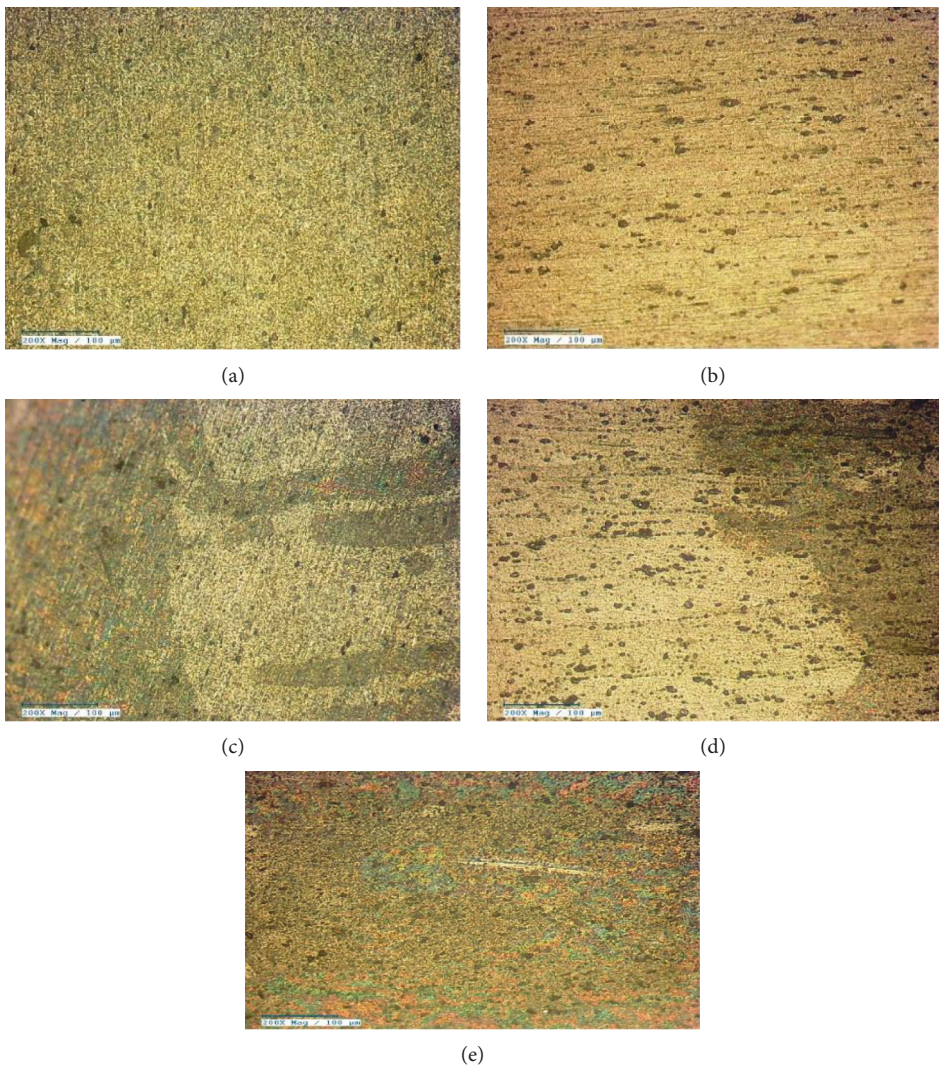

(a) (b) (c) (d) (e)

Figure 9: Optical microstructure image. (a) Al5456 base metal, (b) Al6262 base metal, (c) HAZ in Al5456, (d) HAZ in Al6262, and (e) weld nugget.

helped to generate the combination of three factors as per L27 OA, and it allows to establishing and understanding a significance of the process variables on output response of the wear rate. DOE examination, ANOVA [36], regression model, response of SN ratio, and plots were examined after collection of experimental results from the wear test which performed on POD apparatus.

3. Result and Discussion

3.1. Influence of FSW Parameters. The equipment is called pin disc which assisted to perform the wear behavior test on friction stir welded (FSW) samples of AA6262/AA5456 composites. For joining both the surfaces of chosen materials, we utilized steel pin tool and maintained the tool rotational speed of 1400 rpm, weld speed of 30 mm/min, and tool angle of 2° to carry out FSW joints. Wear rates (WR) have been measured by variation of three important process parameters such as application of load (LD), sliding speed (SS), and sliding distance (SE). Totally, 27 experiments are conducted with change of LD, SS, and SE factors. 1 to 9 experiments are performed by kept LD (30 N) and variation of SE (400–600 m) and SS (2–6 m/s), respectively. Figure 3 shows that the lowest wear rate (0.00414 mm^3/Nm) was achieved at SE (400 m) and SS (6 m/s) whereas the maximum WR was attained at 0.00615 mm^3/Nm at SE (500 m) and SS (4 m/s). 10–18 wear tests were conducted by increasing the applied load from 30 to 40 N. The wear rate varies from 0.00635 to 0.00822 mm^3/Nm as shown in Figure 4. Low intensity of WR is at SE of 400 m SS of 2 m/s and highest wear intensity is acknowledged at SE (500 m) and SS (6 m/s). The final (19–27) tests are carried out by increasing LD as 50N. As mentioned in Figure 5, minimum (0.00849 mm^3/Nm) and maximum (0.01282 mm^3/Nm) WR were accomplished at SE (500 m) and SS (2 m/s) and SE (500 m) and SS (6 m/s), respectively. The overall wear results are declared in Figure 6 and noticed that among 27 experimental outcome, the highest (0.01215 mm^3/Nm) and lowest (0.00414 mm^3/Nm)

wear rate are acknowledged at specimen 27 and specimen 3 that the combination of process parameters levels are LD3-SE3-SS2 (50 N, 600 m, and 4 m/s) and LD1-SE1-SS3 (30 N, 400 m, and 6 m/s), respectively. The outcomes revealed that WR is almost directly proportional to applied load and sliding distance. When the load and sliding distance are increased, the wear rate also is improved more.

3.2. Analysis of Variance. The Taguchi-GRA method was used to identify the optimize process parameters [37]. ANOVA is one of the essential steps in the optimization process which is to investigate an effect of individual parameters of LD, SS, SE, and influence of combined factors such as LD ∗ SS, LD ∗ SE, and SS ∗ SE on wear quantity. Table.3 shows the contribution of each input variables, representing their influence level on outcome of the wear amount. The AA6262/5456 surface layer is subjected to rubbing under altered loads, slide speeds, and slide distances. From Figure 7, it is observed that the load is the most influencing factor contributing 83.75%, second significant is to be considered as sliding distance of 3.75% to improve wear rates and remaining individual (SS) and joint factors are involved as negligible or low significant factors on the wear performance. Residual error is obtained as 5.43% due to machine and operational mistakes.

The influenced input parameters are being analyzed by generating effect of plots through optimal software. Figure 8 and Table.4 exhibited that the sliding distance is moderate at 600 m compared to other two factors of load and sliding speed. At the same time, load is major contributor in wear rate increment. The maximum WR is seen at LD of 50N. The optimal significance of each wear parameters have been identified as per Taguchi analysis. LD3 is the most influenced factor when increasing wear rate of 0.010454 mm^3/Nm trailed by 0.008096 mm^3/Nm and 0.007964 mm^3/Nm at SE3 and SS2, respectively.

The mathematical equation or regression model is established with the aid of regression design as showed in (1) in order to know the relation between input variables and output response of WR and also it helps to find the approximate reading of the wear rate by submitting process factors of load, sliding speed, and distance.

$$WearRate = 0.00668 + 0.000272LD + 0.000006SE + 0.000155SS. \quad (1)$$

3.3. Optical Microscope Investigation. The optical microscopic images of base metals, heat affected zone (HAZ), and weld nugget in specimen L24 are shown in Figure 9. It is noticed that the large number of dark spots and occurrence of massive quantity of strengthening precipitates in Figure 9(a). The grains of Al6262 are oriented along the rolling direction of the plates in Figure 9(b), and it is evident that the grains have become rougher in the HAZ region compared to the base metal of Al5456 in Figure 9(c). From Figure 9(d), we observed that the grain growth and Mg2Si precipitates magnitude in the HAZ-Al6262 are decreased. Figure 9(e) shows the grains are broken down into finer grain size in weld nugget due to mixing of two dissimilar Al alloys.

4. Conclusion

In the present work, wear rate of FSW 6262 and 5456 Al alloys are examined by the Taguchi L27 method, and analysis of variance, regression equation, and plots between selected variables are carried out by using the MINITAB software. This research work is to identify the highest and lowest wear rate of FSW composites. According to effects of plots and interaction between parameters graph, increasing of load and sliding distance increase dry wear rate. However, the WR reduces when increasing the sliding speed. The maximum quantity of wear is reached in LD of 50 N, SE of 600 m, and SS of 4 m/s and minimum at LD of 30 N, SE of 400 m, and SS of 6 m/s. ANOVA result concluded that apply load on the sample is the most significant parameter which contributes around 83.75% to achieve maximum wear rate, followed by sliding distance of 3.75%, sliding speed of 1.85%, and remaining percentage are contributed by combined parameters.

Data Availability

The data used to support the findings of this study are included in the article. Should further data or information be required, these are available from the corresponding author upon request.

Conflicts of Interest

The authors declare that they have no conflicts of interest.

References

[1] M. Bakkiyaraj, P. Palanisamy, N. Pk, and Balasubramanian, "Effect of post weld heat treatment on tensile strength and microstructure characteristics in dissimilar friction welded (AA6061 – AA7075-T6) joints," *Materials Research Express*, vol. 6, no. 12, p. 1265, 2020.

[2] P. V. Reddy, P. R. Prasad, D. M. Krishnudu, and E. V. Goud, "An investigation on mechanical and wear characteristics of Al 6063/TiC metal matrix composites using RSM," *Journal of Bio- and Tribo-corrosion*, vol. 5, no. 4, 90 pages, 2019.

[3] B. Gugulothu, N. Nagarajan, A. Pradeep, G. Saravanan, S. Vijayakumar, and J. Rao, "Analysis of mechanical properties for Al-MMC fabricated through an optimized stir casting process," *Journal of Nanomaterials*, vol. 2022, pp. 1–7, 2022.

[4] J. W. Kaczmar, K. Pietrzak, and W. Włosiński, "The production and application of metal matrix composite materials," *Journal of Materials Processing Technology*, vol. 106, no. 1–3, pp. 58–67, 2000.

[5] A. Prakash Pasupulla, H. Abebe Agisho, S. Seetharaman, and S. Vijayakumar, "Characterization and analysis of TIG welded stainless steel 304 alloy plates using radiography and destructive testing techniques," *Materials Today Proceedings*, vol. 51, pp. 935–938, 2022.

[6] H. P. Pydi, A. P. Pasupulla, S. Vijayakumar, and H. A. Agisho, "Study on microstructure, behavior and AlO3 content flux

A-TIG weldment of SS-316L steel," *Materials Today Proceedings*, vol. 51, pp. 728–734, 2022.

[7] H. P. Pydi, A. Pradeep, S. Vijayakumar, and R. Srinivasan, "Examination of various weld process parameters in MIG welding of carbon steel on weld quality using radiography & magnetic particle testing," *Materials Today Proceedings*, vol. 62, pp. 1909–1912, 2022.

[8] A. L. Etter, T. Baudin, N. Fredj, and R. Penelle, "Recrystallization mechanisms in 5251 H14 and 5251 O aluminum friction stir welds," *Materials Science and Engineering A*, vol. 445–446, pp. 94–99, 2007.

[9] A. K. Srivastava, N. K. Maurya, A. R. Dixit, S. P. Dwivedi, A. Saxena, and M. Maurya, "Experimental investigations of A359/Si3N4 surface composite produced by multi-pass friction stir processing," *Materials Chemistry and Physics*, vol. 257, Article ID 123717, 2021.

[10] S. Ravikumar, V. S. Rao, and R. V. Pranesh, "Effect of process parameters on mechanical properties of friction stir welded dissimilar materials between AA6061-T651 andAA7075-T651 alloys," *International Journal of Advanced Mechanical Engineering*, vol. 4, no. 1, pp. 101–114, 2014.

[11] B. Bhushan and B. K. Gupta, *Handbook of Tribology: Materials, Coatings, and Surface Treatments*, McGraw-Hill, New York, NY, USA, 1991.

[12] M. Singla, L. Singh, and V. Chawla, "Study of wear properties of Al-SiC composites," *Journal of Minerals and Materials Characterization and Engineering*, vol. 08, no. 10, pp. 813–821, 2009.

[13] Y. Sesharao, T. Sathish, K. Palani et al., "Optimization on operation parameters in reinforced metal matrix of AA6066 composite with HSS and Cu," *Advances in Materials Science and Engineering*, vol. 2021, Article ID 1609769, 12 pages, 2021.

[14] O. Guler, M. Celebı, R. Dalmıs, A. Canakci, and H. Cuvalci, "Novel ZA27/B4C/graphite hybrid Nano composite-bearing materials with enhanced wear and corrosion resistance," *Metallurgical and Materials Transactions A*, vol. 51, no. 9, pp. 4632–4646, 2020.

[15] Y. Singh, R. Garg, and A. Kumar, "Energy sources," *Particle Accelerators: Recovery,Utilization, and Environmental Effects*, vol. 38, pp. 2406–2412, 2016.

[16] N. Natarajan, S. Vijayarangan, and I Rajendran, "Wear behaviour of A356/25SiCp aluminium matrix composites sliding against automobile friction material," *Wear*, vol. 261, no. 7-8, pp. 812–822, 2006.

[17] K. Panneerselvam, K. Lokesh, D. Chandresh, and T. N. S. Ramakrishna, "Optimization of tribological properties of aluminium honeycomb reinforced polymeric composites using grey based fuzzy algorithm," *Mech., Mater. Sci. Eng*, vol. 4, 2016.

[18] B. Hemanth Reddy and S. Perumal, "Optimization of tribology properties of A356 aluminium matrix composites using grey relational analysis," *SSRG Int. J. Mech. Eng. (Special Issue)*, vol. 12, pp. 16–20, 2017.

[19] B. Gugulothu, S. L. Sankar, S. Vijayakumar et al., "Analysis of wear behaviour of AA5052 alloy composites by addition alumina with zirconium dioxide using the Taguchi-grey relational method," *Advances in Materials Science and Engineering*, vol. 20227 pages, 2022.

[20] S. Manickam, A. Pradeep, S. Vijayakumar, and E. Mosisa, "Optimization of arc welding process parameters for joining dissimilar metals," *Materials Today Proceedings*, 2022.

[21] R. Deaquino-Lara, N. Soltani, A. Bahrami, E. Gutiérrez-Castañeda, E. García-Sánchez, and M. A. L. Hernandez-Rodríguez, "Tribological characterization of Al7075–graphite composites fabricated by mechanical alloying and hot extrusion," *Materials & Design*, vol. 67, pp. 224–231, 2015.

[22] K. M. Mehta and V. J. Badheka, "Wear Behavior of boron-carbide Reinforced Aluminum Surface Composites Fabricated by Friction Stir Processing," *Wear*, vol. 426, pp. 975–980, 2019.

[23] X.-F. Wu, G.-G. Zhang, and F.-F. Wu, "Microstructure and dry sliding wear behavior of cast Al–Mg2Si in-situ metal matrix composite modified by Nd," *Rare Metals*, vol. 32, no. 3, pp. 284–289, 2013.

[24] M. Barmouz, P. Asadi, M. K. B. Givi, and M. Taherishargh, "Innvestigation of mechanical properties of Cu/SiC composite fabricated by FSP effect of SiC particles size and volume friction," *Materials Science and Engineering A*, vol. 528, pp. 1740–1749, 2011.

[25] D. Trimble, G. E. O' Donnell, and J. Monaghan, "Characterisation of tool shape and rotational speed for increased speed during friction stir welding of AA 2024-T3," *Journal of Manufacturing Processes*, vol. 17, pp. 141–150, 2015.

[26] R. A. Prado, L. E. Murr, D. J. Shindo, and K. F. Soto, "Tool wear in the friction-stir welding of aluminum alloy 6061+20% Al2O3: a preliminary study," *Scripta Materialia*, vol. 45, no. 1, pp. 75–80, 2001.

[27] W. B. Lee, C. Y. Lee, M. K. Kim et al., *Composites Science and Technology*, vol. 66, pp. 1513–1520, 2006.

[28] P. K. Krishnan, R. Arunachalam, A. Husain, and M. Al-Maharbi, "Studies on the influence of stirrer blade design on the microstructure and mechanical properties of a novel aluminum metal matrix composite," *Journal of Manufacturing Science and Engineering*, vol. 143, no. 2, pp. 1–13, 2021.

[29] P. K. Krishnan, J. V. Christy, R. Arunachalam et al., "Production of aluminum alloy-based metal matrix composites using scrap aluminum alloy and waste materials: influence on microstructure and mechanical properties," *Journal of Alloys and Compounds*, vol. 784, pp. 1047–1061, 2019.

[30] T. Rayapandi Thevar, P. K. Krishnan, T. R, and R. Arunachalam, "A novel approach for the production and characterisation of aluminium–alumina hybrid metal matrix composites," *Materials Research Express*, vol. 7, no. 4, Article ID 046512, 2020.

[31] B. Gugulothu, P. S. Satheesh Kumar, B. Srinivas, A. Ramakrishna, and S. Vijayakumar, "Investigating the material removal rate parameters in ECM for Al 5086 alloy-reinforced silicon carbide/flyash hybrid composites by using Minitab-18," *Advances in Materials Science and Engineering*, vol. 2021, pp. 1–6, 2021.

[32] P. Paramasivam and S. Vijayakumar, "Mechanical characterization of aluminium alloy 6063 using destructive and non-destructive testing," *Materials Today Proceedings*, 2021.

[33] D. Pal, S. Vijayakumar, T. J. Rao, and R. S. R. Babu, "An examination of the tensile strength, hardness and SEM analysis of Al 5456 alloy by addition of different percentage of SiC/flyash," *Materials Today Proceedings*, vol. 62, pp. 1995–1999, 2022.

[34] A. Pradeep, N. Kavitha, T. V. Janardhana Rao, and S. Vijayakumar, "Influence of nano alumina/vegetable oil based cutting fluid on MQL turning of stainless steel 304," *Materials Today Proceedings*, 2022.

[35] H. P. Pydi, A. P. Pasupulla, S. Vijayakumar, and K. P. Indira, "Defect analysis and evaluation of mechanical properties of tig welded chrome alloy steel joints for high temperature applications," *AIP Conference Proceedings*, vol. 2473, 2022.

[36] B. Gugulothu, S. Seetharaman, S. Vijayakumar, and D. Jenila Rani, "Process parameter optimization for tensile strength and Hardness of Al-MMC using RSM technique," *Materials Today Proceedings*, vol. 62, pp. 2115–2118, 2022.

[37] J. V. Christy, R. Arunachalam, A.-H. I. Mourad, P. K. Krishnan, S. Piya, and M. Al-Maharbi, "Processing, properties, and microstructure of recycled aluminum alloy composites produced through an optimized stir and squeeze casting processes," *Journal of Manufacturing Processes*, vol. 59, pp. 287–301, 2020.

Hindawi
Advances in Materials Science and Engineering
Volume 2022, Article ID 8259804, 8 pages
https://doi.org/10.1155/2022/8259804

Research Article

Polymer Filament Process Parameter Optimization with Mechanical Test and Morphology Analysis

Raja Subramani,[1] **S. Kaliappan**,[2] **S. Sekar**,[3] **Pravin P. Patil**,[4] **R. Usha**,[5] **Narapareddi Manasa**,[6] **and E. S. Esakkiraj**[7]

[1]*School of Mechanical Engineering, Vellore Institute of Technology, Vellore, Tamil Nadu, India*
[2]*Department of Mechanical Engineering, Velammal Institute of Technology, Chenna 601204, Tamil Nadu, India*
[3]*Department of Mechanical Engineering, Rajalakshmi Engineering College Rajalakshmi Nagar Thandalam, Chennai 602105, Tamilnadu, India*
[4]*Department of Mechanical Engineering, Graphic Era Deemed to be University, Bell Road Clement Town 248002, Dehradun, Uttarakhand, India*
[5]*Department of Physics, Saveetha School of Engineering, SIMATS, Chennai 600124, Tamil Nadu, India*
[6]*Department of Civil Engineering, Aditya College of Engineering, Surampalem, Affiliated to JNTU Kakinada, Andhra Pradesh 533437, India*
[7]*Department of Mechanical Engineering, Dambi Dollo University, Dambi dolo, Ethiopia*

Correspondence should be addressed to Raja Subramani; raja.s2020@vitstudent.ac.in and E. S. Esakkiraj; essakkiraj@dadu.edu.et

Received 15 May 2022; Revised 5 July 2022; Accepted 12 July 2022; Published 3 August 2022

Academic Editor: R. Thanigaivelan

3D printing is one of the emerging technologies in the manufacturing sector, and polymer materials play a vital role in the raw material of the additive manufacturing sector. This research explores reducing the production time by testing and analyzing the microstructure of the different polylactic acid (PLA) filament polymer samples. For this purpose, 15 pieces of ASTM (American society for testing and materials) D638 tensile samples with polylactic acid (PLA) filaments have been used exclusively with five different sets of modified process parameters in slicing software of 3D printing technology. The results of this research reveal the best PLA filament FDM production method in terms of time, mechanical strength, and FESEM analysis comparing all the results.

1. Introduction

Additive manufacturing plays a very important role in the manufacturing sector to make products with geometrical complex designs [1]. Additive manufacturing does not require huge production costs compared to conventional manufacturing, and the use of additive manufacturing in many fields is increasing day by day. An earlier literature has classified additive manufacturing into seven categories. These include vat photo polymerization, binder jetting, material jetting, material extrusion, powder bed fusion, sheet lamination, and direct energy deposition [2–4]. This allows the product to be created with multiple raw materials, especially metals, plastics, resins, etc. [5]. This research paper explores the cheapest [6] and the most widely [7] used FDM method in additive manufacturing. In particular, the PLA filament that can be used in the FDM system and how it can be used to produce better output products are explored. The FDM method is part of the extrusion process [8]. Continuous heating of a plastic filament (polylactic acid) produces a substance that is to be produced layer by layer as a thin solid-liquid form [9, 10]. Many previous researchers have studied the different filaments that can be used in FDM. Ning et al. [11] studied the mechanical properties of short carbon fiber, tensile strength, and Young's modulus. Polyamides (PA) are made up of many nanofibers including microsphere and

glass [12]. Jorge Manuel Mercado et al. explored the PLA compression uniaxial properties [13]. Fuda Ning et al. [14] and Aleksandar B Stefaniak et al. [15] explored in the carbon reinforced and nanopolymer particles. Xing Guan Zhao et al. [16] demonstrated the recycling of PLA filament with polydopamine coated.

No studies can be found on the set of printing/process parameters selected with microstructure analysis and mechanical properties analysis in the PLA material. Therefore, this paper aims at analyzing the effect of manual optimization on the set of parameters in slicing software with five ASTM D638 tensile specimens of PLA filament material and carries out the tensile test and microstructure analysis. The research paper includes the following upcoming section to obtain the main research objective. The basics of material, printing process and the entire optimization, fabrication, testing, and analysis are explored by the fabrication and testing part. At the fabrication stage, the making time of each piece has been calculated. Then, based on fabrication and time of fabrication, the result is discussed. Finally, the whole research summary and the direction of future works are detailed in the conclusion.

2. Fabrication and Testing

PLA (polylactic acid) filament material is used in this research. Generally, PLA is derived from hydroxyl acids and is considered as compostable and biodegradable. The PLA has thermoplastic properties with very high strength and high modulation, and also the thermal degradation of PLA is above 200°C [17]. It is available in the Indian market in the form of an FDM filament to INR 800 at least and is tailored to the selector in many colors. Hence, in this research, we explore 15 pieces of ASTM D638 tensile specimens made with PLA filament which is optimized by 5 different sets of printing parameters in slicing software.

This research specifically modifies the optimization parameters such as infill, printing speed, and making temperature to produce a homogeneous sample of fifteen ASTM D638 tensile specimens. Also, the production time of those fifteen fabricated specimens is calculated. This identifies the selection of which one set of parameters of the FDM is required to produce an object in the best way and in the shortest time. The famous Botzlab's Wanhao Duplicator 4S was used to fabricate these fifteen specimens. This machine can be able to use materials that have a temperature degradation of 230–250 C. Therefore, a maximum of 219°C making temperature has been used in this research paper. Also, only room temperature is used as the minimum bed/platform temperature.

2.1. Design and Optimization Parameters. This research paper explores the tensile specimen ASTM D638 and is the standard used by previous researchers, especially for polymer materials [18, 19]. Then, type 5 in particular has been used in this research. Its basic geometrical shape is shown in Figure 1. Its design is as follows: overall length (lo) is 63.5 mm, distance (d) between grip is 25.4 mm, length of the narrow section is 9.53 mm, width (Wn) of the narrow section is 3.18 mm, and width (Wo) of the narrow section is 19 mm [20]. Also, in this research paper, the ASTM D638 design.STL (Standard Triangle Language) file is sliced by flash print Magic 5.0 slicing software. Of these, 7 fabrication parameters of each set like extruder temperature, layer height, printing speed [21], travel speed, and infill (density/pattern) [22] were modified and production started separately. Table 1 describes all the modified set of printing parameters. The image taken during production can be seen in Figure 2. Moreover, the product make time of each specimen is calculated during production. The time of the calculated specimen can be seen in Table 2. Also, the optimized .STL (standard triangle language) file is converted to G-code and fabrication started.

2.2. Tensile Test. The breaking point, tensile strain, tensile stress, Young's modulus, and elongation of the presently manufactured specimen are calculated one after the other by the Instron 8801 testing system. An experiment's gauge length, width, and weakness are 7.62 mm, 3.18 mm, and 3 mm, respectively. During the process, a constant load was applied automatically for fitting both the gripper parts of the specimen to the tensile testing piston. Then, the initial area of cross section and the load helps to estimate the nominal stress (S). Similarly, other specimens were tested, and we found the breaking point, tensile strain, tensile stress, Young's modulus, and elongation of the fifteen pieces of the modified parameters specimens produced by the PLA filament. In previous literature, only the composite and one or two optimization parameters were modified and tested. The most notable aspect of this research is the infill parameters. All of the significant infill percentages and infill parameters in the slicing software have been tested in this research. All these can be seen in Table 2.

2.3. Field Emission Scanning Electron Microscope (FESEM). The slicing parameters of each specimen produced in this research are of different types. In particular, the infill parameter is specified in Section 2.2. Infill patterns such as line, hexagonal, triangle 45°, infill 3D, and triangle 65° are used in this research. During production, the 3D printer produces specimen according to the infill pattern method mentioned above. Also, the tensile specimen produced in this way has different braking points and production times. Therefore, the tensile fracture surface of the five specimens being produced and the surface of the other specimen was detected by Quanta™ 250 FEG machine with the help of high magnification topography. Prior to this test, the sputter coating was applied to each specimen. Polishing is not mandatory as it comes in the form of PLA polymer and plastic [24]. Moreover, below are the FESEM images of all the found specimens.

3. Results and Discussion

3.1. Fabrication Time. Table 1 describes the modified set of parameters and the production time required. The extruder temperature used is a minimum of 195°C for specimen I

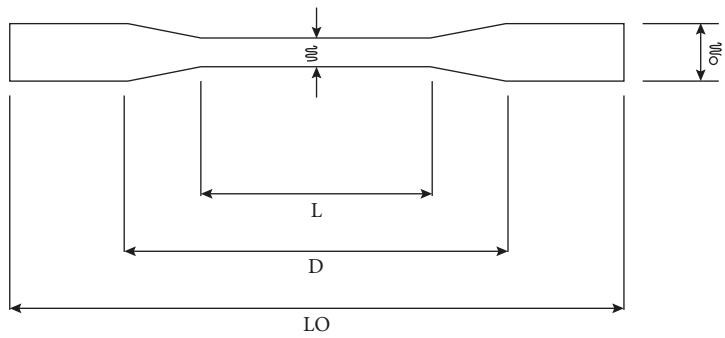

ASTM D638
TYPE-V

LO	63.5 mm
D	25.4 mm
L	9.53 mm
Wo	19 mm
Wn	3.18 mm

Figure 1: Geometrical parameters of the specimen.

Table 1: Optimization parameters of specimens.

Parameters/specimens	Specimen I	Specimen II	Specimen III	Specimen IV	Specimen V
Printing speed	70 mm/s	35 mm/s	75 mm/s	80 mm/s	55 mm/s
Travel speed	80 mm/s	60 mm/s	85 mm/s	75 mm/s	70 mm/s
Layer height	0.12 mm	0.18 mm	0.17 mm	0.19 mm	0.21 mm
Extruder temperature	195°C	210°C	215°C	217°C	220°C
Infill (Density/pattern)	15% hexagonal pattern	15% line pattern	30% triangle 45° pattern	20% 3D infill pattern	35% triangle 65° pattern
Shell count	3	2	3	2	2
Bed temperature	50°C	40°C	30°C	35°C	0°C
Time taken for fabrication	10 minutes	17 minutes	11 minutes	9 minutes	10 minutes

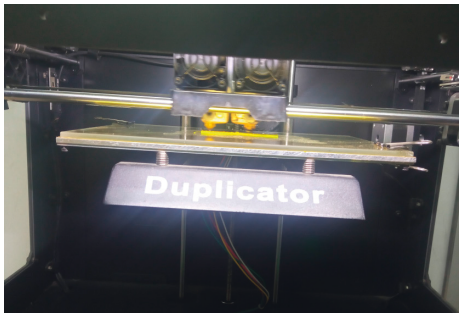

Figure 2: Fabrication: final photo of the specimen.

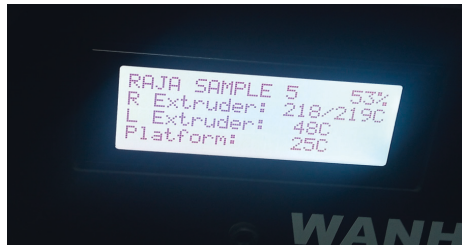

Figure 3: Fabrication temperature of the final specimen.

Figure 4: Common fabricated samples after the tensile test.

Table 2: Breaking load and extension of specimens.

Specimens	Load at breaking (KN)	Extension (mm)
1	0.72	0.23206
2	0.66	0.22772
3	0.28	0.09042
4	0.24	0.16210
5	0.33	0.14127

and a maximum of 220°C for specimen V. Similarly, the bed/platform temperature used is a minimum of 0°C and a maximum of 50°C, where 0°C is the base bed/platform temperature at which specimen is produced. Instead, the fabricating machine will automatically use room temperature as bed temperature. The layer height is known as the first form of an initial outline of a specimen that can be produced [25]. The minimum first layer of specimen I is 0.12 mm, and the maximum specimen V is 0.21 mm. The printing speed is used to produce specimen at a minimum speed of 35 mm/s in specimen II and a maximum of

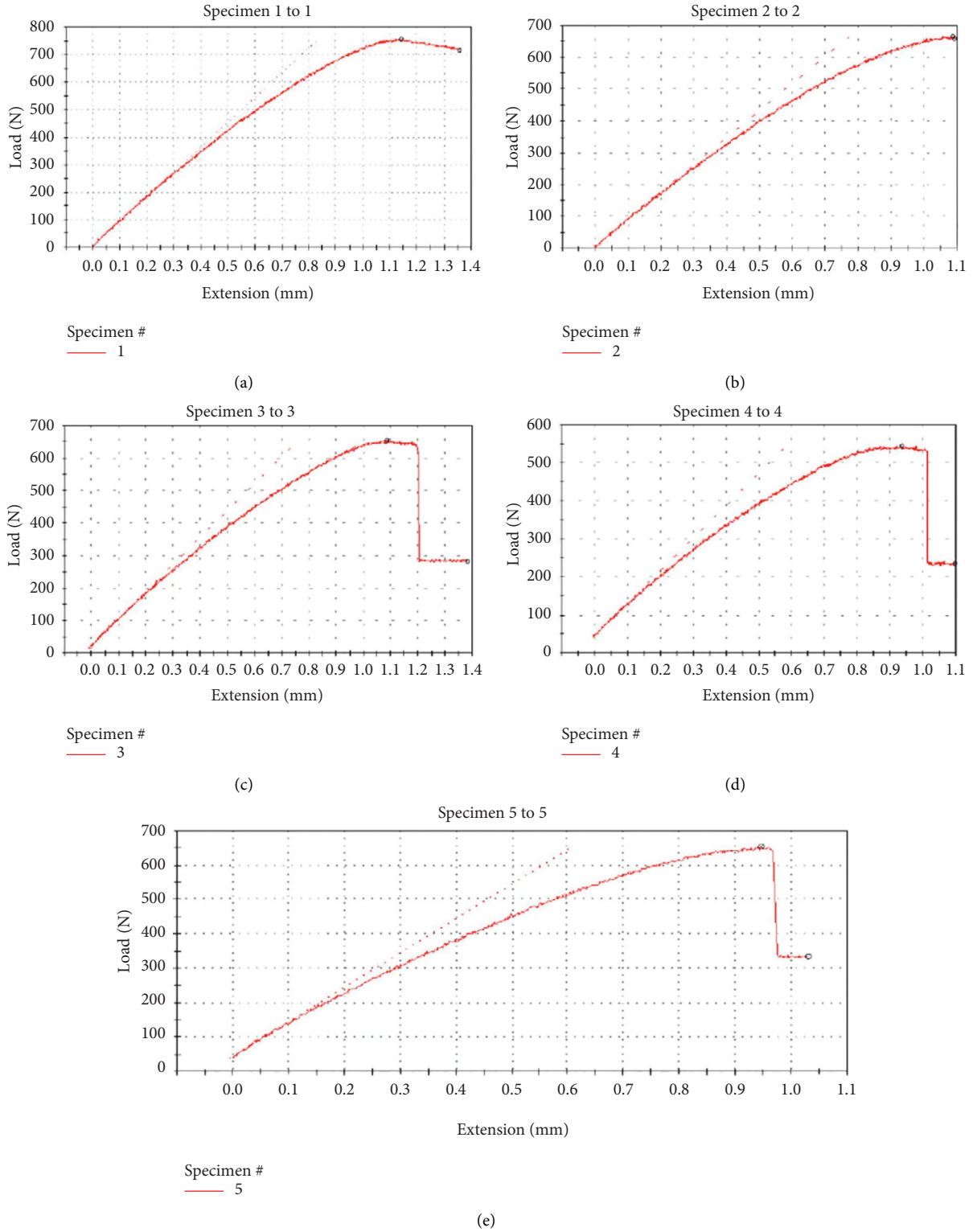

Figure 5: Load vs. extension curve of the specimen.

80 mm/s in specimen IV. Then, the travel speed is the interval between producing one layer and producing the next layer [26]. A minimum speed of 60 mm/s in specimen II and a maximum speed of 85 mm/s in specimen III are applied in this research

Moreover, infill is known as "how the filament fills and how much it fills" when the material is produced. The most common infill parameters are hexagonal line, triangle, and 3D infill pattern [27]. It also has many angles on the line and triangle patterns. Of these, triangle 45° and triangle 65° of

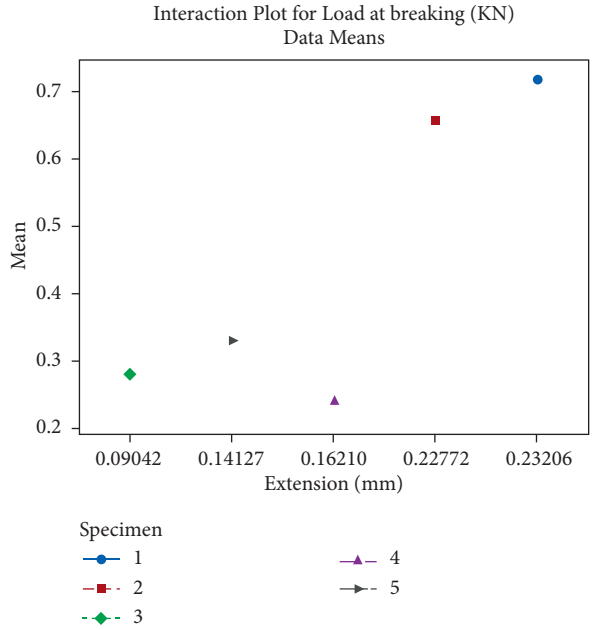

Figure 6: ANOVA interaction plot for load at breaking (KN) through Minitab.

specimens III and V were used to produce the tensile specimen in this research [28].

Finally, the shell count is used as a minimum of 2 and a maximum of 3. Thus, when optimization is perfectly fabricated, the production time of specimen I is 10 minutes, the production time of specimen II is 17 minutes, the production time of specimen III is 11 minutes, the production time of specimen IV is 9 minutes, and the production time of specimen V is estimated at 10 minutes. In terms of time, specimen IV is rated at a minimum of 8 minutes and specimen II at a maximum of 18 minutes [29]. Nevertheless, this research provides an excellent PLA FDM production technique based on tensile test and field emission scanning electron microscope results [30]. Moreover, Figure 1 illustrates the geometrical parameter of the specimen. Similarly, Figures 2 and 3 illustrate photos taken during production [31]. Figure 4 shows a photograph taken after a tensile test of the main types of modified specimen is produced.

3.2. Tensile Test. Figures 5(a)–5(e) show the load versus extension of specimen I to specimen V plotted, and each specimen has a separate load withstand and extension. Figure 5(a) shows the 730 N load and 0.23206 mm extension of specimen I. Figure 5(b) shows the 660 N load and 0.22772 mm extension of specimen II [32]. Figure 5(c) shows the 280 N load withstand and 0.0904 2 mm extension of specimen III. Similarly, Figures 5(d) and 5(e) illustrate the 240 N load withstand and 0.16210 mm extension of specimen IV and 330 N load and 0.14127 mm extension of specimen V. All these can be seen in Table 2.

Optimum tensile test results were found in the ANOVA interaction plot using Minitab software [33]. This is because each specimen has different load and extension. Figure 6 illustrates the ANOVA interaction plot. The high load-bearing specimen I can be seen in blue. Thus, the parameters of specimen I are considered as the best set of parameters, that is, the extrusion temperature is 200°C, the bed temperature is 50°C, the layer height is 0.18 mm, the printing speed is 60 mm/s, the travel speed is 80 mm/s, and the tensile density is 15%, and the hexagonal pattern and shell count 2 are the best PLA manufacturing printing parameters.

However, the purpose of this research paper is to reach a final conclusion based on the microstructure results and production time also. Hence, the FESEM test and the final results are as follows [34].

3.3. Field Emission Scanning Electron Microscope. The microstructure of each specimen can be seen in Figure 7. Figure 7(a) illustrates the microstructure of specimen I, and it detects distances between the two layers ranging from 441.6 μm to 468.4 μm, and also, some subtle cracks can be seen. However, the closed microstructure can be also found.

Figure 7(b) illustrates the microstructure of specimen II. Layer distance spacing was found from 821.8 μm to 826.0 μm in Figure 7(b). Figure 7(c) illustrates the microstructure of specimen III. The spacing of the inbetween layers is estimated to be 606.1 μm to 623.6 μm. Figure 7(d) illustrates the microstructure of specimen V. It is calculated in the range of 536.3 μm to 558.3 μm. The research did not reveal the microstructure of specimen IV. This is because in the slicing parameter of specimen IV the 3D infill is used. Thus, higher density and moisture are found in specimen IV. The microstructure could not be detected due to high moisture and density.

This research paper also reveals that when an object is manufactured using the 3D infill pattern, its internal structure cannot be found out. Specimen I includes slightly more optimized parameters than other specimens in terms

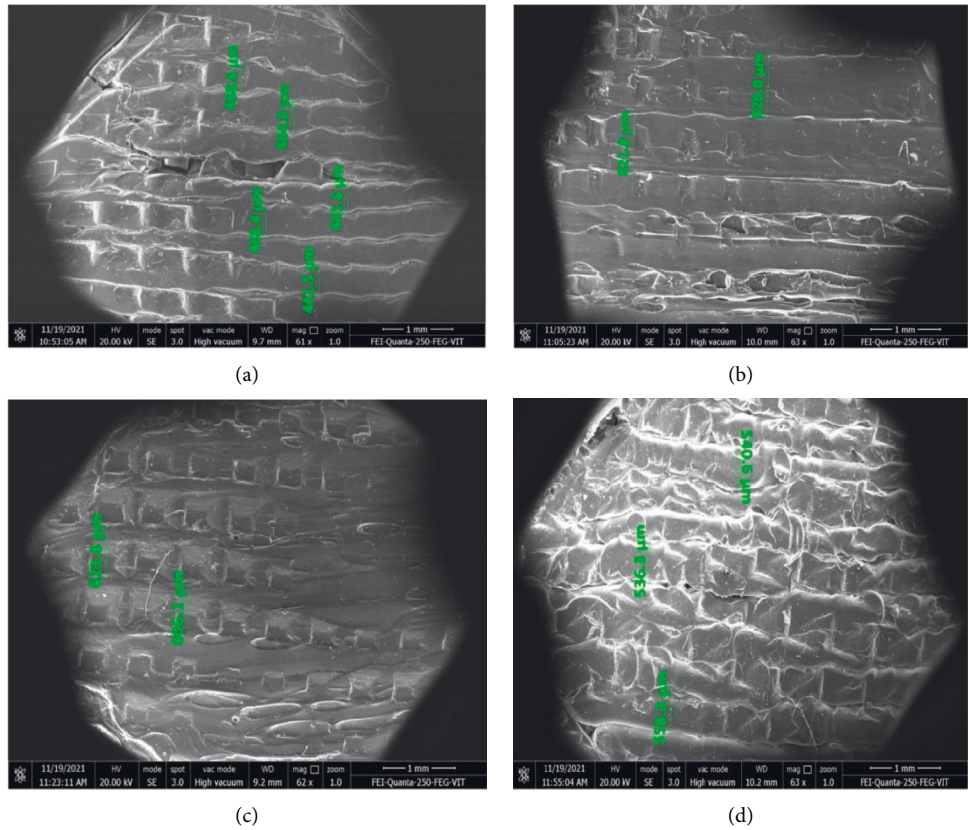

(a) (b) (c) (d)

Figure 7: Microstructure of different optimized specimens.

of time and available data. Also, FESEM-based specimen I has a very close microstructure compared to other specimens. Therefore, the results of FESEM also ensured the slicing parameters of specimen I have the most optimum.

In terms of time, specimen IV, specimen I, specimen V, and specimen III, have the shortest time. However, there is one minute time difference for specimen IV and specimen I. Therefore, specimen I set of parameters is the best production parameters for PLA.

4. Conclusion

In this research, the main objective is selecting the optimum set of process parameters for PLA filament in the FDM fabrication method. For this, five types of ASTM D638 tensile specimens were produced by modifying the seven set of process parameters. The tensile test and FESEM analysis were performed on all 15 specimens being produced. Based on the results obtained, the process parameters of specimen I were found to be the best. Specimen I withstands high load and extension based on the tensile test, and it also has a very close microstructure in terms of FESEM. Furthermore, the process parameters of specimen I are considered as the best production parameters for PLA filament as they are close to the average production time in terms of total production time. An additional novelty of this research is that the microstructure cannot be detected using the 3D infill pattern from that modern slicing software infill options. This research ensures the quality of the product with less time with modifying set of printing parameters for the manufacturers who want high productivity.[23].

Data Availability

The data used to support the findings of this study are included in the article. Further data or information required are available from the corresponding author upon request.

Conflicts of Interest

The authors declare that there have no conflicts of interest regarding the publication of this paper.

Acknowledgments

The authors thank and acknowledge the management of Vellore Institute of Technology, Vellore, for their support to carry out this research work, and they specially thank Additive Manufacturing Laboratory **(DIGI-MAN)** incharge and technician staff. The authors also express their sincere thanks to Tensile and FESEM laboratories staffs.

References

[1] S. Raja, A. J. Rajan, V. P. Kumar et al., "Selection of Additive Manufacturing Machine Using Analytical Hierarchy Process," *Scientific Programming*, 2022.

[2] I. Gibson, D. W. Rosen, B. Stucker, I. Gibson, D. W. Rosen, and B. Stucker, *Introduction and Basic Principles, Additive*

Manufacturing Technologies, pp. 20–35, Springer, Berlin, 2010.

[3] I. Gibson, D. W. Rosen, and B. Stucker, *Additive Manufacturing Technologies: Rapid Prototyping to Direct Digital Manufacturing, Additive Manufacturing Technologies: Rapid Prototyping to Direct Digital Manufacturing*, Springer, Berlin, 2010.

[4] A. Wojcieszynski, "Special issue focus: additive manufacturing," *Journal of Materials Engineering and Performance*, vol. 28, no. 2, p. 593, 2019.

[5] M. S. Hossain and H. Taheri, "In situ process monitoring for additive manufacturing through acoustic techniques," *Journal of Materials Engineering and Performance*, vol. 29, no. 10, pp. 6249–6262, 2020.

[6] V. K. Srivastava, P. K. Jain, P. Kumar, A. Pegoretti, and C. R. Bowen, "Smart manufacturing process of carbon-based low-dimensional structures and fiber-reinforced polymer composites for engineering applications," *Journal of Materials Engineering and Performance*, vol. 29, no. 7, pp. 4162–4186, 2020.

[7] P. K. Penumakala, J. Santo, and A. Thomas, "A critical review on the fused deposition modeling of thermoplastic polymer composites," *Composites Part B: Engineering*, vol. 201, Article ID 108336, 2020.

[8] K. Hemalatha, C. James, L. Natrayan, and V. Swamynadh, "Analysis of RCC T-beam and prestressed concrete box girder bridges super structure under different span conditions," *Materials Today Proceedings*, vol. 37, pp. 1507–1516, 2021.

[9] P. Parandoush and D. Lin, "A review on additive manufacturing of polymer-fiber composites," *Composite Structures*, vol. 182, pp. 36–53, 2017.

[10] B. Brenken, E. Barocio, A. Favaloro, V. Kunc, and R. B. Pipes, "FusedFilament fabrication of fiber-reinforced polymers: a review," *Additive Manufacturing*, vol. 21, pp. 1–16, 2018.

[11] F. Ning, W. Cong, J. Qiu, J. Wei, and S. Wang, "Additive manufacturing of carbon fiber reinforced thermoplastic composites using fused deposition modeling," *Composites Part B: Engineering*, vol. 80, pp. 369–378, 2015.

[12] C. Capela, J. M. Ferreira, J. M. Costa, and N. Mendes, "Mechanical properties of injection-molded glass microsphere-reinforced polyamide," *Journal of Materials Engineering and Performance*, vol. 25, no. 10, pp. 4256–4265, 2016.

[13] J. M. Mercado-Colmenero, M. A. Rubio-Paramio, M. D. la Rubia-Garcia, D. Lozano-Arjona, and C. Martin-Doñate, "A numerical and experimental study of the compression uniaxial properties of PLA manufactured with FDM technology based on product specifications," *International Journal of Advanced Manufacturing Technology*, vol. 103, no. 5–8, pp. 1893–1909, 2019.

[14] F. Ning, W. Cong, Y. Hu, and H. Wang, "Additive manufacturing of carbon fiber-reinforced plastic composites using fused deposition modeling: effects of process parameters on tensile properties," *Journal of Composite Materials*, vol. 51, no. 4, pp. 451–462, 2017.

[15] A. B. Stefaniak, L. N. Bowers, A. K. Knepp et al., "Three-dimensional printing with nano-enabled filaments releases polymer particles containing carbon nanotubes into air," *Indoor Air*, vol. 28, no. 6, pp. 840–851, 2018.

[16] X. G. Zhao, K. J. Hwang, D. Lee, T. Kim, and N. Kim, "Enhanced mechanical properties of self-polymerized polydopamine-coated recycled PLA filament used in 3D printing," *Applied Surface Science*, vol. 441, pp. 381–387, 2018.

[17] D. Garlotta, "A literature review of poly (lactic acid)," *Journal of Polymers and the Environment*, vol. 9, no. 2, pp. 63–84, 2001.

[18] H. L. Tekinalp, V. Kunc, G. M. Velez-Garcia et al., "Highly oriented carbon fiber- polymer composites via additive manufacturing," *Composites Science and Technology*, vol. 105, pp. 144–150, 2014.

[19] K. C. Sekhar, R. Surakasi, P. Roy et al., *Mechanical Behavior of Aluminum and Graphene Nanopowder-Based Composites*, 2022.

[20] A. Hassan, N. A. Rahman, and R. Yahya, "Moisture absorption effect on thermal, dynamic mechanical and mechanical properties of injection-molded short glass-fiber/polyamide 6, 6 composites," *Fibers and Polymers*, vol. 13, no. 7, pp. 899–906, 2012.

[21] H. N. Dhakal, Z. Y. Zhang, and M. O. W. Richardson, "Effect of water absorption on the mechanical properties of hemp fibre reinforced unsaturated polyester composites," *Composites Science and Technology*, vol. 67, no. 7–8, pp. 1674–1683, 2007.

[22] D. Hala´pi, S. E. Kova´cs, Z. Bodna´r, A. B. Palota´s, and L. Varga, "Tensile analysis of 3D printer filaments, Multi-Science-XXXII," in *Proceedings of the microCAD International Multidisciplinary Scientific Conference*, Hungary, September 2018.

[23] T. Letcher and M. Waytashek, "Material property testing of 3D-printed specimen in PLA on an entry-level 3D printer," *Volume 2A: Advanced Manufacturing*, 2014.

[24] G. Velmurugan, V. S. Shankar, S. Kaliappan et al., "Effect of Aluminium Tetrahydrate Nanofiller Addition on the Mechanical and Thermal Behaviour of Luffa Fibre-Based Polyester Composites under Cryogenic Environment," *Journal of Nanomaterials*, vol. 2022, Article ID 5970534, 10 pages, 2022.

[25] L. Natrayan, M. Senthil Kumar, and M. Chaudhari, *Optimization of squeeze casting process parameters to investigate the mechanical properties of AA6061/Al 2 O 3/SiC hybrid metal matrix composites by taguchi and anova approach*, pp. 393–406, Springer, Singapore, 2020.

[26] K. Seeniappan, B. Venkatesan, N. N. Krishnan et al., "A comparative assessment of performance and emission characteristics of a DI diesel engine fuelled with ternary blends of two higher alcohols with lemongrass oil biodiesel and diesel fuel," *Energy & Environment*, vol. 13, Article ID 0958305X2110513, 2021.

[27] G. Choubey, Y. Devarajan, W. Huang, L. Yan, H. Babazadeh, and K. Pandey, "Hydrogen fuel in scramjet engines - a brief review," *International Journal of Hydrogen Energy*, vol. 45, no. 33, pp. 16799–16815, 2020.

[28] L. Natrayan and A. Merneedi, "Experimental investigation on wear behaviour of bio-waste reinforced fusion fiber composite laminate under various conditions," *Materials Today Proceedings*, vol. 37, pp. 1486–1490, 2021.

[29] S. Kaliappan, M. D. Raj Kamal, S. Mohanamurugan, and P. K. Nagarajan, "Analysis of an innovative connecting rod by using finite element method," *Taga Journal Of Graphic Technology*, vol. 14, pp. 1147–1152, 2018.

[30] D. Veeman, M. S. Sai, P. Sureshkumar et al., "Additive manufacturing of biopolymers for tissue engineering and regenerative medicine: an overview, potential applications, advancements, and trends," *International Journal of Polymer Science*, vol. 2021, Article ID 4907027, 20 pages, 2021.

[31] S. Justin Abraham Baby, S. Suresh Babu, and Y. Devarajan, "Performance study of neat biodiesel-gas fuelled diesel

engine," *International Journal of Ambient Energy*, vol. 42, no. 3, pp. 269–273, 2018.

[32] Y. Devarajan, G. Choubey, and K. Mehar, "Ignition analysis on neat alcohols and biodiesel blends propelled research compression ignition engine," *Energy Sources, Part A: Recovery, Utilization, and Environmental Effects*, vol. 42, no. 23, pp. 2911–2922, 2019.

[33] V. Balaji, S. Kaliappan, M. D m et al., "Combustion analysis of biodiesel-powered propeller engine for least environmental concerns in aviation industry," *Aircraft Engineering & Aerospace Technology*, vol. 94, no. 5, pp. 760–769, 2022.

[34] V. S. Nadh, C. Krishna, L. Natrayan et al., "Structural behavior of nanocoated oil palm shell as coarse aggregate in lightweight concrete," *Journal of Nanomaterials*, p. 1, Article ID 4741296, 2021.

Hindawi
Advances in Materials Science and Engineering
Volume 2022, Article ID 3057829, 6 pages
https://doi.org/10.1155/2022/3057829

Research Article

Effect of Ceramic Nano Fillers in Jute Fibre Composites

A. Padma Rao,[1] Ananda Mohan Vemula,[2] M. Prakash Babu,[2] P. Senthil Kumar,[1] V. Murali Krishna,[1] and Perumalla Janaki Ramulu[3]

[1]*Department of Mechanical Engineering, B. V. Raju Institute of Technology, Narsapur, Medak, Telangana 502313, India*
[2]*Department of Mechanical Engineering, Guru Nanak Institutions Technical Campus, Hyderabad, Telangana, India*
[3]*Department of Mechanical Engineering and Centre of Excellence for Advanced Manufacturing Engineering, Adama Science and Technology University, Adama, Post Box 1888, Oromia, Ethiopia*

Correspondence should be addressed to Perumalla Janaki Ramulu; perumalla.janaki@astu.edu.et

Received 23 April 2022; Revised 27 May 2022; Accepted 20 June 2022; Published 5 July 2022

Academic Editor: Sengottuvelu Ramesh

The demand and applications of bolstered plastics such as natural, attainable, biodegradable, and fibres were developing worldwide in industries beginning from home utilities to aerospace applications. The high cost and weight of synthetic fibres were bolstered by a multitude of concerns. Subsequently, it is far vital to create a natural fibre combination with a matrix to accumulate the most efficient common presentation. In this present study, a composite is made of a natural fibre (jute) reinforced with vinyl ester resin with and without a filler (SiO_2). Untreated jute fibres are utilised as reinforcement, while filler materials were used to increase the characteristics of jute fibre and analyse the impact of filler material in the composite. The produced composite was tested for tensile strength, compressive strength, flexural strength, and hardness. The SEM study of the fracture surface was also evaluated in the present study. Filler-mixed composites have a 50 percent higher tensile strength than those without fillers, and the remaining attributes have enhanced by at least 5 to 10%. From analysis, filler-mixed composites hold a good mechanical property due to fibre-filler bonding with the help of vinyl ester resin.

1. Introduction

In many tenders, natural fibre reinforced composites have a lot of potential as a replacement for different substances. Environmentally friendly materials are employed due to qualities such as reduced weight, low cost, biodegradability, and better strength. Composites are also replacing metals and nonmetals used previously due to their greater strength-to-weight ratio, less weight, and good durability. In this context, the jute fiber has contained comprised cells and spiral fibrils together [1].

It has good bonding among cells due to high modulus and high strength. The shape of the jute fibre is created based on their physical and chemical properties.

Rezaur Rahman et al. [2] described the impact of benzene diazonium salt in an alkaline medium as a chemical treatment. Jute fibre was treated with alkaline media and o-hydroxybenzene diazonium salt. The uncooked and changed jute fiber had been used to put together with the composites. The combination was made by mixing polypropylene with a volume fraction of 20.25%, 30%, and 35%. The mechanical properties, besides extension of harm, are dealt with the jute fibre PP composite.

Safiee et al. [3] stated that the strengthened composite with 70% fiber material had effectively organized PJFRC specimen and exhibited less compression and flexural results. The fibre compressive failure and shear failure is possible from matrix local microbuckling. Yadav et al. [4] prepared and tested the polymer nano composite with and without SiO_2. It has been determined that adding 2.5 percent SiO_2 to S-glass fibre results in improved mechanical houses. Nabila et al. [5] stated that the fibre and matrix bonded well due to the increase in tensile strength. The load is spread out properly in the entire part of the matrix. Also, the terrible bonding surface was formed because of improper wet conditions.

Das et al. [6] Jute/polypropylene composites are successfully fabricated to the growth of jute fibre loading through

weight. Mechanical houses were stepped forward substantially. The mechanical qualities of the fibre were increased by 50%, but after that, it began to deteriorate. The appropriate optimization of this method's parameter could result in a higher or possibly composite answer for household shipments that include fences, chairs, and other items. Khalid et al. [7] The natural fibre evolved composite reveals better mechanical overall performance in terms of tensile and flexural conduct compared to warmness. Epoxy/jute and polyester/jute composites are expected to be 58.23 MPa and 63.31 MPa, respectively. In comparison to zero, an epoxy/jute composite with a maximum flexural modulus of 3.30 GPa was discovered. Polyester/jute has a tensile strength of 9176 GPa. Subrahmanyam et al. [8] prepared short jute fiber reinforced polyester composites by varying the fiber loading (0–40 wt.%). The experimental thermal conductivity results were validated with the results obtained by analytical methods and met as per the standards. Recently evolved quick mixtures are mild, within your means, and possess desirable thermal insulating residences. So, automobile interior components, building additives, and digital composites use those composites. Aranno et al. [9] investigated the jute fibre composites and described higher mechanical homes of jute composites that had been acquired for the usage of woven jute fibre mats with the aid of handloom procedures. Shahinur et al. [10] found that the quantitative analysis of thermal tests of the final residue at a higher temperature changed the range for RT, WT, and uncooked jute fibres into a similar range but that there is 40% more residue determined at temperatures above 400 in toes treated jute fibres than in uncooked jute fibres. Chubuike et al. [11] Chemical treatments on the jute fibre are crucial because they allow you to improve the characteristics of the exposed floor. After the alkaline and permanganate treatments, it was discovered that the load of the handled fibre was reduced to a large volume in comparison to the untreated fibre. The moisture level of the fibre was reduced, resulting in an increase in electricity. Chemical treatments remove hemicelluloses, lignin, pectin, wax, and oil concealing compounds in small amounts. [12, 13].

According to the literature review, there is no credible research on the use of 5% SiO_2 as a filler material. To generate natural fibre composites with and without SiO_2, a natural fibre-jute and matrix-vinyl ester resin were employed in this work. The research reveals that there are several papers on jute fibre-reinforced composite materials with varied mechanical property evaluations available but just a few articles on ceramic filled natural fibre composite materials and methodology.

1.1. Jute Fibre. Jute has an appealing herbal fibre used as a reinforcement in the composite due to its low price, renewable nature, and mass lower strength requirement for processing. The mechanical strengths of jute fibre are as follows in Table 1.

1.1.1. Filler Material. In this present work, Silicon dioxide (SiO_2) is used as a filler material. This powder was purchased from the local market of Hyderabad, India. The purity of the powder is 99%. These filler materials act as a nanofiller. Figure1 shows the SEM image of SiO_2. The properties of SiO_2 powder are available in Table 1.

1.1.2. Matrix Material. The matrix substance used in this work is vinyl ester. This material was purchased from the local market of Hyderabad, India.

1.2. Fabrication of the Composite. The 10:1 ratio of the hardener and vinyl ester resin was used for preparing the composite material. These matrix materials are blended for 5–10 min by using a mechanical stirrer, and also various steps are involved in fabrication of the composite material as shown in Figure 2. Before starting the fabrication procedure, the hand layup method was used to prepare the composite in the present study. Dimensions are in 300 mm length × 300 mm width × 4 mm thickness [14, 15]. For easy removal purpose of specimens, the plastic cover and wax were used to clean the mold both sides (front and back). In this present study, two different types of samples were prepared. The material composition of both specimens is listed in Table 2.

1.3. Testing Procedure. The hardness, compression, tensile, and density characteristics of the specimens were studied. The tensile specimen was prepared and measured by using the ASTM D638-10 on an KIC-2-1000-C universal testing machine (3 mm/min crosshead speed). The composite specimens were prepared, and their hardness was tested using the Rockwell hardness tester as per ASTM D 2583 [16]. The SEM (scanning electron microscope) images are used to identify the fracture surface of failure samples.

2. Results and Discussion

2.1. Filler Material Effect on Tensile Strength. Figure 3 indicates that the filler-filled composite retains more tensile strength and has tensile values nearly twice as high as the fabric composite without a filler [17]. The tensile strength for fibre loading in a jute-vinyl ester resin composite is shown in Figure 3, indicating that when the number of sheets in the composite increases from two to a few, then four, the tensile strength increases. Jute fibre is the most important load-bearing element in a jute-vinyl ester resin composite. As a result, increasing the fibre weight fraction and filler enhances the composite's tensile strength [18]. It is clear that a composite made up of four layers of woven jute with a vinyl ester resin matrix had a high tensile strength in a number of the tests carried out.

2.2. Effect of the Filler Material on Compressive Strength. The compression specimen was made as per the ASTM D1621 standard. A compression check entails mounting the specimen in a machine and subjecting it to compression. The compression technique involves the specimen in the checking out device and puts on compression for fractures. The compressing pressure is recorded as a feature of

Table 1: Several mechanical properties of present study materials.

Material	Density (g/cm^3)	Modulus of rigidity (GPa)	Tensile strength (MPa)	Percentage of elongation
Jute-fiber	1.31	26.52	393–778	1.5–1.82
SiO2 powder	2.52	66.9	36.2	—
Matrix material	2.52	2.9–3.2	68–80	5–7

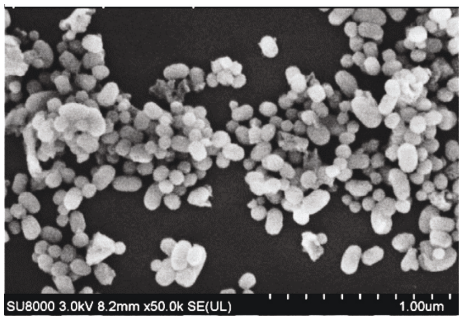

Figure 1: The SEM view of SiO_2.

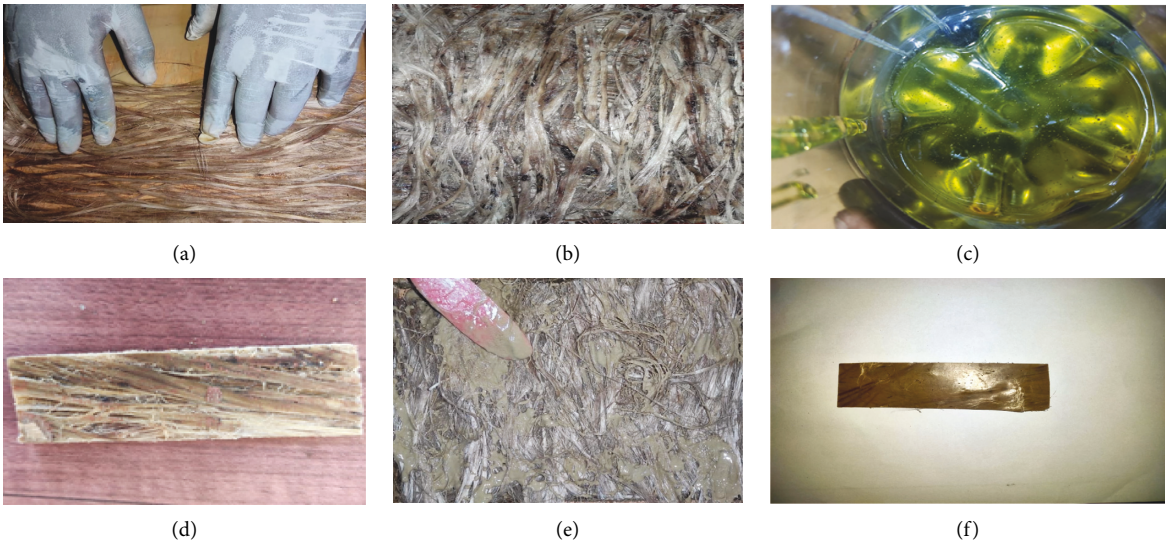

Figure 2: Various steps involved in natural composite preparation. (a) Alignment of jute in the mould frame (b) Jute vinyl ester resin in the mould frame. (c) Mixture of vinyl ester resin and hardener. (d) Jute vinyl ester resin specimen. (e) Jute ceramic vinyl ester resin in the mould frame. (f) Jute ceramic specimen.

Table 2: Different composition prepared samples.

Sample no.	Jute fibre (wt. %)	Epoxy (wt. %)	Ceramic powder (wt. %)
SP-1	45	55	—
SP-2	45	50	5

displacement. At some stage in the application of compression, the extension of the specimen is noted towards implemented pressure [19]. From Figure 4, the ceramic filled composite material has more compression strength compared to without a filler material composite. From this analysis, a filler gives good compressive strength to jute fibre.

2.3. Effect of the Filler Material on Flexural Strength. The specimen is tested on the UTM system. The reason for this end result may be without troubles positioned by means of assembling the two damaged component surfaces. They shape simply the best particular element without any lines of neck formation, as in ductile materials. The SiO_2 crammed

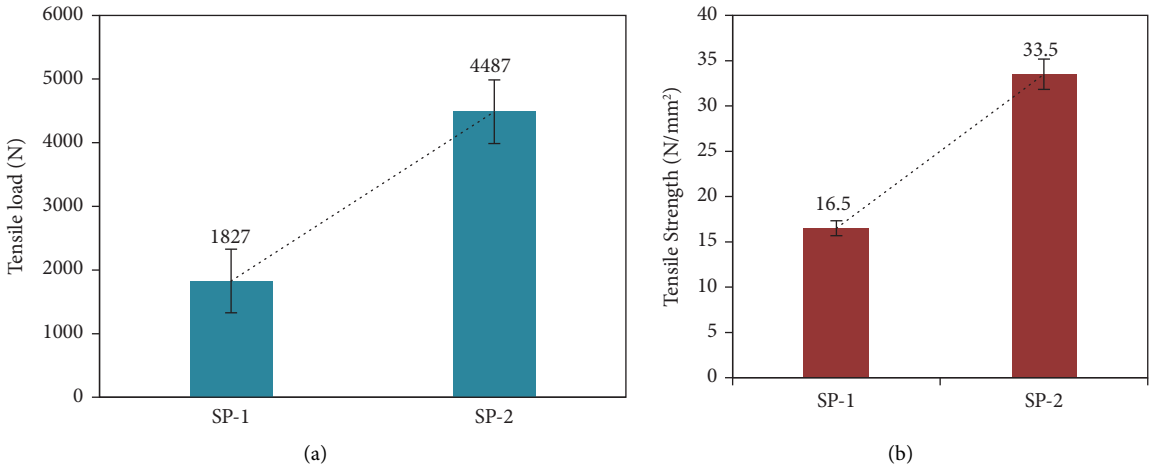

Figure 3: The effect of a filler material in the composite. (a) Tensile load. (b) Tensile strength.

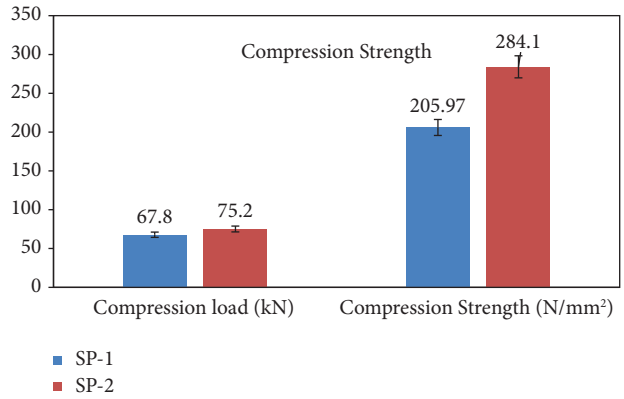

Figure 4: The effect of filler material in compressive strength.

jute vinyl ester resin showed higher flexural electricity than the jute epoxy composite (parent Figure 5). Filler stuffed with jute and vinyl ester resin to have higher electric conductivity and strain to failure during the assessment. The satisfactory flexural load to failure showed ductile conduct. However, the adhesive and stiffness belongings of the resin are important. The location of the resin is to keep the fibres as instant columns and to save them from bending. In homogenous substances, flexural energy could be the same as that of tensile strength of the material; however, all of the materials could have some defects due to different values. At the same time while doing the flexural check, the fibres at the intense will make more extreme pressure.

2.4. Effect of the Filler Material on Hardness. The hardness test has been located in 3 different places in the same specimen, and the average values have been plotted in Figure 6. The discount fibre composite was provided with a good rockwell hardness value, but compared to this result, the filler added natural fibre composite holds a larger hardness value, and the development in hardness with the incorporation of fillers can be explained as follows: below the motion of compressive pressure, the filler-matrix interface is prone to debonding relying on the interfacial bond between the matrix and the fibre, and this will cause spoil within the composite. So, the polymeric matrix segment and the stable filler segment would be pressed collectively and touch each other extra tightly. From the result, the interface can switch pressure more efficaciously, although the interfacial bond may be negative. This could have ended in the enhancement of hardness.

2.5. Fracture Analysis of the Composite. The microstructures had been taken at 2000 magnification for the jute ceramic through the use of scanning electron microscopy which is proven in Figures 7(a) and 7(b). SEM snap shots of the fractured surface of vinyl ester resin–jute fibre composites provide direct proof of fiber-matrix interplay adhesion development. As, there is no companionable bonding on a few of the fibers and the matrix, although a small quantity of vinyl ester resin entered into the interface vicinity. Fiber-matrix debonding is the cause

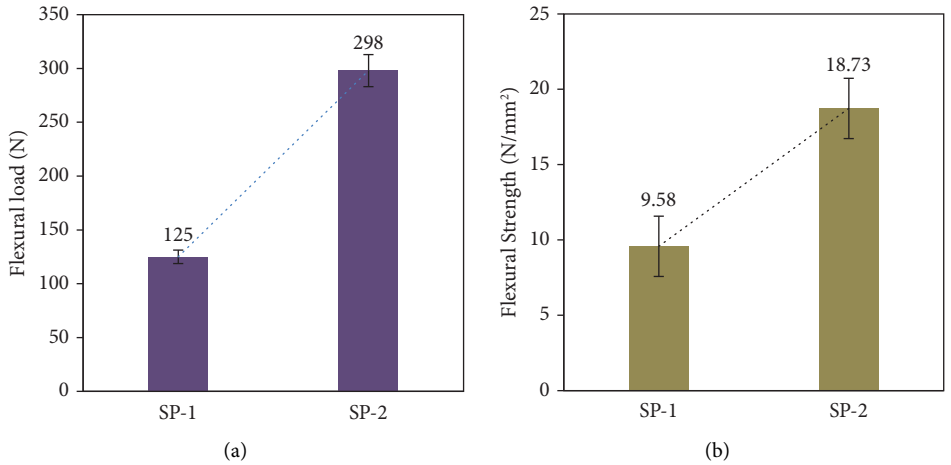

Figure 5: The effect of filler materials in the composite. (a) Flexural load. (b) Flexural strength.

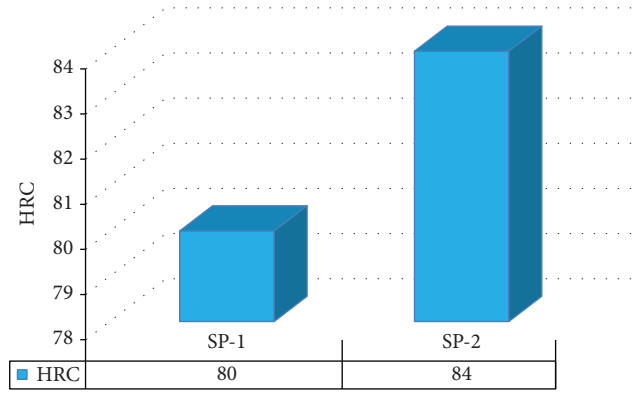

Figure 6: Effect of filler material in hardness.

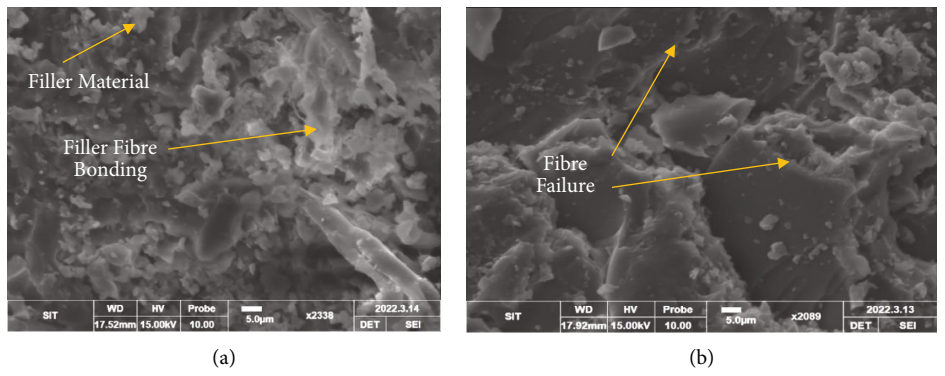

Figure 7: Fracture surface analysis of tested. (a) Jute-vinyl ester resin-ceramic composite. (b) Jute-vinyl ester resin composite.

of composite delamination failure. This demonstrates that some jute fibres and the vinyl ester resin were not enchanted, confirming the need to improve the fibre/vinyl ester resin interface [21]. After the remedy, the adhesion interfaces a number of jute fibres, and the vinyl ester resin is stepped forward. This can be seen via the disappearance of boundary gaps. The improvement can be defined with the aid of a sturdy interfacial interplay after the treatment of the jute fibre [22].

3. Conclusions

In this present investigation, the mechanical properties were studied with and without the ceramic filler jute fibre.

(i) When compared to natural fibre composites without a filler material, there is a significant improvement in tensile character and tensile load. According to the findings of this investigation, the

tensile strength of the filler material composite improves by more than twofold.

(ii) The jute-ceramic vinyl ester resin-reinforced composites regarded an improved compressive property (284 N/mm^2) than the jute epoxy composite.

(iii) The jute-ceramic vinyl ester resin-filler composite has a fairly extra flexural property than the jute vinyl ester resin natural fibre composite. Also, hardness increased more in the SiO_2 filled jute/vinyl ester resin natural fibre composite.

(iv) From SEM analysis, the SiO_2 filled composite gives more bonding strength to the natural fibre composite and also spread evenly in matrix and reinforcement.

Data Availability

All data generated or analyzed during this study are included within this published article.

Conflicts of Interest

The authors declare that they have no conflicts of interest.

References

[1] S. P. Jani, A. S. Kumar, M. A. Khan, and M. U. Kumar, "Machinablity of hybrid natural fiber composite with and without filler as reinforcement," *Materials and Manufacturing Processes*, vol. 31, no. 10, pp. 1393–1399, 2016.

[2] M. Rezaur Rahman, M. Hasan, M. Monimul Huque, and M. Nazrul Islam, "Physico-mechanical properties of jute fiber reinforced polypropylene composites," *Journal of Reinforced Plastics and Composites*, vol. 29, no. 3, pp. 445–455, 2010.

[3] S. Safiee, H. M. Akil, A. A. M. Mazuki, Z. A. M. Ishak, and A. A. Bakar, "Properties of pultruded jute fiber reinforced unsaturated polyester composites," *Advanced Composite Materials*, vol. 20, no. 3, pp. 231–244, 2011.

[4] P. S. Yadav, R. Purohit, and A. Kothari, "The effect of nano SiO2 on the mechanical and tribological properties of hybrid polymer matrix composites: a review," *Advanced Materials Manufacturing & Characterization*, vol. 7, no. 2, pp. 101–110, 2017.

[5] S. Nabila, A. L. Juwono, and S. Roseno, "Effect of weight fractions of jute fiber on tensile strength and deflection temperature of jute fiber/polypropylene composites," *IOP Conference Series: Materials Science and Engineering*, vol. 196, no. 1, Article ID 012029, 2017, May.

[6] S. C. Das, D. Paul, M. M. Fahad, M. K. Das, G. S. Rahman, and M. A. Khan, "Effect of fiber loading on the mechanical properties of jute fiber reinforced polypropylene composites," *Advances in Chemical Engineering and Science*, vol. 8, no. 4, pp. 215–224, 2018.

[7] M. Y. Khalid, Z. U. Arif, M. F. Sheikh, and M. A. Nasir, "Mechanical characterization of glass and jute fiber-based hybrid composites fabricated through compression molding technique," *International Journal of Material Forming*, vol. 14, no. 5, pp. 1085–1095, 2021.

[8] B. V. Subrahmanyam, S. G. Gopala Krishna, R. J. Jithedra Kumar, and S. B. R. Devireddy, "Experimental and micro-mechanical ThermalCharacteristics of jute fiber reinforced polyester composites," *Materials Today Proceedings*, vol. 18, pp. 350–356, 2019.

[9] T. M. Aranno, S. Mia, M. S. U. Khan et al., "Fabrication, experimental investigation of jute fiber reinforced epoxy composites and hybrid composites," in *IOP Conference Series: Materials Science and Engineering*, vol. 628, no. No. 1, IOP Publishing, Article ID 012011, 2019, September.

[10] S. Shahinur, M. Hasan, Q. Ahsan, and J. Haider, "Effect of chemical treatment on thermal properties of jute fiber used in polymer composites," *Journal of Composites Science*, vol. 4, no. 3, p. 132, 2020.

[11] E. Chubuike, C. Ebele, E. Ifeanyi, E. Okwuchukwu, and O. Festus, "Study on chemical treatments of jute fiber for application in natural fiber reinforced composites (NFRPC)," *International Journal of Advanced Engineering Research and Science*, vol. 4, no. 2, pp. 21–26, 2017.

[12] E. A. Elbadry, M. S. Aly-Hassan, and H. Hamada, "Mechanical properties of natural jute fabric/jute mat fiber reinforced polymer matrix hybrid composites," *Advances in Mechanical Engineering*, vol. 4, Article ID 354547, 2012.

[13] M. Ramesh, K. Palanikumar, and K. H. Reddy, "Plant fibre based bio-composites: sustainable and renewable green materials," *Renewable and Sustainable Energy Reviews*, vol. 79, pp. 558–584, 2017.

[14] S. P. Jani, A. S. Kumar, M. A. Khan, S. Sajith, and A. Saravanan, "Influence of natural filler on mechanical properties of hemp/kevlar hybrid green composite and analysis of change in material behavior using acoustic emission," *Journal of Natural Fibers*, vol. 18, no. 11, pp. 1580–1591, 2021.

[15] M. Ramesh, C. Deepa, L. R. Kumar, M. R. Sanjay, and S. Siengchin, "Life-cycle and environmental impact assessments on processing of plant fibres and its bio-composites: a critical review," *Journal of Industrial Textiles*, vol. 1528083720924730, 2020.

[16] R. Vimal, K. H. H. Subramanian, C. Aswin, V. Logeswaran, and M. Ramesh, "Comparisonal study of succinylation and phthalicylation of jute fibres: study of mechanical properties of modified fibre reinforced epoxy composites," *Materials Today Proceedings*, vol. 2, no. 4-5, pp. 2918–2927, 2015.

[17] S. P. Jani, S. Sajith, C. Rajaganapathy, and M. A. Adam Khan, "Mechanical and thermal insulation properties of surface-modified Agave Americana/carbon fibre hybrid reinforced epoxy composites," *Materials Today Proceedings*, vol. 37, pp. 1648–1653, 2021.

[18] M. K. Gupta, M. Ramesh, and S. Thomas, "Effect of hybridization on properties of natural and synthetic fiber-reinforced polymer composites (2001-2020): a review," *Polymer Composites*, vol. 42, no. 10, pp. 4981–5010, 2021.

[19] L. P. J. Lal, S. Ramesh, and E. Natarajan, "Study on the repeatability of manufacturing nano-silica (SiO2) reinforced composite laminates," *IOP Conference Series: materials Science and Engineering*, vol. 346, no. 1, Article ID 012083, 2018.

[20] V. Subramani, B. Jayavel, R. Sengottuvelu, and P. J. L. Lazar, "Assessment of microstructure and mechanical properties of stir zone seam of friction stir welded magnesium AZ31B through nano-SiC," *Materials*, vol. 12, no. 7, p. 1044, 2019.

[21] P. J. L. Lazar, R. Sengottuvelu, and E. Natarajan, "Assessments of secondary reinforcement of epoxy matrix-glass fibre composite laminates through nanosilica (SiO2)," *Materials*, vol. 11, no. 11, p. 2186, 2018.

[22] S. P. Jani, A. S. Jose, C. Rajaganapathy, and M. A. Khan, "A polymer resin matrix modified by coconut filler and its effect on structural behavior of glass fiber-reinforced polymer composites," *Iranian Polymer Journal (English Edition)*, pp. 1–11, 2022.

Hindawi
Advances in Materials Science and Engineering
Volume 2022, Article ID 3072663, 14 pages
https://doi.org/10.1155/2022/3072663

Research Article

Gorilla Troops Optimizer Combined with ANFIS for Wire Cut EDM of Aluminum Alloy

Elango Natarajan,[1] **V. Kaviarasan**,[2] **Wei Hong Lim**,[1] **S. Ramesh**,[3] **K. Palanikumar**,[4] **T. Sekar**,[5] **and V. H. Mok**[1]

[1]*Faculty of Engineering, Technology and Built Environment, UCSI University, Kuala Lumpur, Malaysia*
[2]*Department of Mechanical Engineering, Sona College of Technology, Salem, India*
[3]*Department of Mechanical Engineering, Jerusalem College of Engineering, Chennai, India*
[4]*Department of Mechanical Engineering, Sri Sairam Institute of Technology, Chennai, India*
[5]*Department of Mechanical Engineering, Government College of Technology, Coimbatore, India*

Correspondence should be addressed to S. Ramesh; ramesh1968in@gmail.com

Received 6 April 2022; Revised 19 May 2022; Accepted 10 June 2022; Published 29 June 2022

Academic Editor: Tadeusz Mikolajczyk

Wire cut EDM is a quite regularly used machining process in mechanical and electronic industries. This research has attempted to machine aluminum alloy for which experimental design was prepared using Box-Behnken design. Different combinational options of pulse-on time (P_1), pulse-off time (P_2), servo wire feed (WF), and current (I) were investigated and surface roughness after machining was observed. Collected 27 datasets were further used in Adaptive Neuro Fuzzy Inference System (ANFIS) to produce about 500 datasets. These 500 datasets are approximated data derived from experimental datasets, known as synthetic data. Data model was further developed and used in Gorilla Troops Optimizer (GTO) to locate the optimum machining parameters. With the excellent three search operators: move towards other gorillas, migrate towards unknown places, and migrate towards known places, GTO has produced the lowest surface roughness value of 0.500953 μm when the machining parameters of pulse-on time, pulse-off time, wire feed, and current values were set as 121 μs, 52 μs, 3 m/min, and 166A, respectively. To ensure the accuracy of the synthetic data-based model and optimality, verification and validation were conducted. Wilcoxon signed rank test was conducted for the pairwise comparison of GTO with each of its competing algorithms at the significance level of $\sigma = 0.05$. Friedman test was conducted to calculate the average ranking of each algorithm and to detect the global differences between all compared algorithms. Outperforming performance by GTO algorithm in machining of the selected material is found.

1. Introduction

Among unconventional machining processes available, wire cut electric discharge machining (WEDM) is much effective process to prepare intricate shapes and delicate objects. This thermal erosion method uses the localized thermal energy to remove the material from the substrate metal. The supply of current and voltage to electrode produces plasma between the substrate metal and tool. A small amount of heat is transferred to the substrate metal to melt and evaporate. Besides, the electrolyte used in the process removes the machined metals away from the machine. Swift toggling of pulse-on time (P_1) and pulse-off time (P_2) causes fast heating and cooling effects over the surface. This advantage of WEDM has attracted this process to use for supper alloys, hard-cutting metals, and conductive materials. Khan et al. [1] investigated machining of ASTM A572-grade 50 steel, where grey rational analysis (GRA) was used to locate the optimal machining condition. Abbasi et al. [2] also attempted the same material and analyzed it to report that pulse-on time is the predominant parameter for surface finish. Takayama et al. [3] developed a high precision rotary table with many sensors to detect wire breakage, water leakage, and machining quality. The erosion of metal

destabilizes at some depth of cutting due to accumulation of debris and it affects the process time. Ayesta et al. [4] used camera vision system to monitor the debris removal. They reported that debris removal is affected by the process parameters and hence optimal process parameters must be used not only to have high surface finish, but also to have high debris removal rate. Since electrolyte is important in this process, kerosene oil, EDM oil, and distilled water were also evaluated by hazard and operability analysis [5]. They revealed that aerosol concentration and dielectric consumption affect the environment and hence new dielectric fluid must be invented. Liu et al. [6] developed a pulse power source to avoid back-off error, which occurs in WEDM of semiconductors as discharge of silicon affects the servo controller. Newly developed power source has stabilized the discharge probability. Significant research contributions [7–25] in the recent years are reviewed and listed in Table 1.

Alam et al. [26] recently reviewed optimization of WEDM parameters, in which they detailed the past published research using GRA and RSM methods. Abidi et al. [27] used MOGA-II algorithm to optimize the parameters to machine nickel-titanium-based shape memory alloy. At this end, it is acknowledged that only minimal research has been conducted in finding the best machining condition using optimization algorithm.

Metaheuristic algorithms are more efficient in locating the optimal solutions for single or multiobjective problems [28, 29] and hence Gorilla Troops Optimizer (GTO) is attempted in this research to search for optimal solution in machining of Al alloy. In a brief of method of research, experiments were conducted using L_{27} orthogonal array. Surface roughness of machined samples and their respective cutting parameters were used to develop an Adaptive Neuro Fuzzy Inference System (ANFIS) from which about 500 synthetic data were further generated. Response surface model (RSM) was developed with these data and applied to GTO algorithm to locate the optimal process parameters. At this end, the paper is organized as below; Section 2 presents the material, experimentation, ANFIS model, and GTO algorithm, while Section 3 presents and discusses the results, while conclusion of current research is presented in Section 4.

2. Materials and Methods

2.1. Materials. Aluminum 7075 alloy was the material investigated in this research, as this material is the most suitable material for structural application including transport, aerospace, marine, and defence. Aluminum alloys are famous for their mechanical properties and weight-strength ratio. Machining this alloy using a conventional machining process does not result in the dimensional accuracy every time. Besides, rejection of parts is also there due to no align with near net shape. WEDM is one of the unconventional machining processes that perfectly suits this scenario and gives better surface finish. Mechanical properties and chemical properties of Al7075 alloy are listed in Tables 2 and 3, respectively.

2.2. Experimentation. Al7075 alloy plate in 200 mm × 150 mm × 10 mm and WEDM SPRINTCUT model with CNC control was used for experimentation. Brass wire electrode of 0.25 mm diameter was used as cathode and deionised water was used as the dielectric fluid. Initially, the plate was machined using arbitrary chosen parameter setting to identify the sparking condition and wire breakage. After conducting a few preliminary experiments, the parameter setting range was fixed for pulse-on time (P_1), pulse-off time (P_2), servo wire feed (WF), and current (I) as shown in Table 4. Box-Behnken design (BBD) is the best method for threelevel design [25] and hence design of experiments (L_{27} DoE) was prepared using BBD. The machining was carried out as per DoE and surface roughness was measured in three different locations using surface roughness tester (Mitutoyo make Surftest 211). Figure 1 shows the machining and machined samples, while Table 5 reports the experimental results.

ANOVA, a statistical tool, was used to find the goodness of fit of the experimental data. The two-way ANOVA with 95% confidence level was carried out as the value of probability <5% is considered significant. Table 6 shows the results from ANOVA. Each parameter and cross product of parameters are found significant. The model is significant with $R^2 = 99.41\%$ and standard deviation = 0.0201349.

2.3. Adaptive Neurofuzzy Inference System (ANFIS). ANFIS is a soft computing technique that utilizes artificial neural network (ANN) and fuzzy logic theory to predict the data samples. It is a simple and accurate adaptive technique to build a prediction model. The reason for using ANFIS in this research is that we wanted to generate as many datasets as possible from a small size of experimental data (27 datasets). Two-tier approach of using ANFIS and RSM was tested and reported as a better method [30]. Optimal searching was more accurate when data population was large. Hence, the above tabulated twenty-seven datasets were used in ANFIS for training the Neurofuzzy Interference System, which could result in plentiful datasets.

ANFIS has different types of membership function (MF) such as triangular shaped membership function (trimf), trapezoidal-shaped membership function (trapmf), generalized bell-shaped membership function (gbellmf), Gaussian curve membership function (gaussmf), Gaussian combination membership function (gauss2mf), P-shaped membership function (pimf), difference between two sigmoidal membership functions (dsigmf), and product of two sigmoid membership functions (psigmf). We attempted all these MFs to build predictive models and finally selected generalized bell-shaped membership function (gbellmf) based on minimum root mean square error (RMSE). This MF is Sugeno type IF-THEN rules to predict the outcomes. RMSE value observed in each model is listed as Trimf model = 1.1394, Trapmf model = 1.1696, Gbelmf model = 0.9605, Gausmf model = 0.9701, Gaus2mf model = 1.1677, Sigmf model = 0.832, Dsigmf model = 1.1672, Psigmf model = 1.1666, Pimf model = 1.7280, Smf model = 1.1728, and Zmf model = 1.1728.

Training of model was done with 27 experimental data. Six additional experiments were conducted with arbitrarily

Table 1: Significant published articles on WEDM in recent years.

Reference	Material used	Contribution
[7]	Al6061/SiC/graphite	Brass wire, zinc coated wire, and diffused coated wires were investigated based on the speed. They reported that diffused coated wire is the best of these wire materials.
[8]	Carbon steel 1017 and aluminum alloy 6060	Wire feed rate (3, 5 and 7 mm/minute) was investigated and it was reported that low feed rate is the best to improve the surface finish.
[9]	High speed steel (HSS) M2 grade	Material removal rate, surface roughness, and width of kerf were analyzed using GRA. They used tool makers' microscope to measure the amount of material wasted during machining, known as kerf width.
[10]	Titanium alloy	Cause of wire rupture which subsequently affects the production and productivity was investigated. They reported that stay of debris caused by low flushing pressure and high wire tension caused by instantaneous high temperature during the machining are two major reasons for wire rupture.
[11]	Friction stir welded 5754 aluminum alloy	RSM was used to optimize the process variables in machining friction stir welded 5754 aluminum alloy.
[12]		Dry cutting, cryogenic cutting, minimum quantity lubrication (MQL), nanocutting fluids, and MQL nanofluids were investigated and it was reported that MQL nanofluid and cryogenic machining showed the best sustainable strategies.
[13]	LM13 aluminum alloy	Slotted copper tool was used to drill aluminum alloy and it was reported that modified tool design has given higher surface finish and material removal rate.
[14]	AISI 304 stainless steel	The influence of various parameters was investigated and it was reported than wire tension influences greatly the surface finish, removal rate, and microhardness of the material. It does not influence the kerf width.
[15]	High carbon high chromium steel	Zirconium powder mixed dielectric fluid was used and it was reported that it has improved the performance of the machining.
[16]	Pure titanium	Multiresponse optimization was conducted using integrated approach of RSM and GRA. They reported the optimal parameters are $T_{on} = 6\mu s$, $T_{off} = 4\mu s$, and discharge current = 6A.
[17]	LM13 Al alloy/10ZrB2/5TiC hybrid composite	Multiresponse optimization was conducted using RSM and GRA. Their aim was to investigate the effect of process parameters on material removal rate (MRR), electrode wear rate (EWR), and overcut (OC). They finally reported that current is the highly influencing parameter on these responses.
[18]	AZ61 magnesium alloy /B_4C/SiC hybrid composite	The influencing parameter among percentage of filler reinforcement, stirring speed, time of stirring, and process temperature.
[19]	Al-Si12/B4C/Fly ash hybrid composite	Material removal rate was investigated and it was reported that it highly depends on pulse-on time and fly ash reinforcement.
[20]	AA1050/5 wt.% SiC composite	Zinc coated copper wire was used to machine SiC reinforced aluminum composite and it was reported that open voltage is the significant parameter.
[21]	Monel K-500, a nickel–copper based alloy	WEDM was applied to super alloy machining. Pulse-on time and pulse-off time affect cutting rate proportionally and inverse proportionally, respectively. Spark gap decreases the cutting rate and surface roughness.
[22]	Inconel-800 superalloy	Trapezoidal interval type-2 fuzzy numbers were applied for handling the uncertainties associated with the subjective assessment of the criteria. The integration of T2FS with additive ratio assessment (ARAS) method resulted in the best WEDM process parameters.
[23]	Cemented carbide	This research attempted to compare edges made using WEDM techniques and conventional edges made in the grinding process.
[24]	Ti6Al4V alloy	This work combines integrated fuzzy analytic hierarchy process (AHP) and fuzzy technique for order preference by similarity to ideal situation (TOPSIS) to optimize the WEDM process.
[25]	AZ31 alloy	They used Box-Behnken design (BBD) to conduct experiments and multiobjective particle swarm optimization (MOPSO) to optimize cutting rate and recast layer.

selected input parameters and these data as shown in Table 7 were used for testing the ANFIS model. Once training and testing of ANFIS model were completed, about 500 datasets were generated from the ANFIS model. These 500 datasets were used to build a response surface methodology (RSM) model shown below.

$$\begin{aligned} R_a = {} & -190.05 + 2.037P_1 + 2.595P_2 - 3.699WF - 0.0353I \\ & - 0.006571P_1^2 - 0.06374P_2^2 + 0.22117WF^2 - 0.005201I^2 \\ & - 0.006053P_1 \times P_2 + 0.02109P_1 \times WF - 0.000594P_1 \\ & \times I - 0.00083\,P_2 \times WF + 0.03226P_2 \times I. \end{aligned} \quad (1)$$

Table 2: Mechanical properties of aluminum 7075 alloy.

Property	Value
Density	2.81 g/cc
Ultimate tensile strength	572 MPa
Modulus of elasticity	71.7 GPa
Brinell hardness	150
Fatigue strength	159 MPa
Machinability	70%
Thermal conductivity	130 W/m-k
Melting point	477–635°C
Electrical resistivity	5.15×10^{-006} ohm-cm

Table 3: Chemical composition of aluminum 7075 alloy (as received from the supplier).

Al	Si	Fe	Cu	Mn	Mg	Cr	Zn	Ti	Others
86.77	0.4	0.5	2.0	0.3	2.9	0.28	6.1	0.2	0.15

All values mentioned in wt%.

Table 4: Machining parameters and fixed levels.

Machining parameter	Levels		
	I	II	III
Pulse-on time (P_1 in μs)	120	125	130
Pulse-off time (P_2 in μs)	50	55	60
Servo wire feed (WF in m/min)	1	2	3
Current (I in ampere)	150	160	170

2.4. Gorilla Troops Optimizer (GTO). Gorilla Troops Optimizer (GTO) is one of the emerging metaheuristic search algorithms proposed by Abdollahzadeh et al. [31] in 2021 to solve global optimization problems, where its search mechanisms are essentially inspired by the collective behavior and social intelligence of gorilla life in nature. Similar to other species of apes, gorillas live in the troops consisting of an adult male gorilla known as silverback, multiple female and male gorillas, and offspring. Silverback refers to the strongest gorilla with unique silver-colored hair on its back and it is considered as troop leader that is responsible for decision making and conflict resolution, as well as spearheading other troop activities such as food searching and strategic retreat for troop safety. On the contrary, other male gorillas that do not have silver-colored hair on their back are relatively weaker and hence affiliated to silverback as the backup defenders of troops. Five typical behaviors are generally observed from gorilla troops to enable the formulation of search operators with different exploration and exploitation strengths. These behaviors include the moving to other gorillas, migration to unknown areas, migration to the surrounding of known areas, staying in original troop to follow silverback, and competition to mate with female gorillas upon the decease of silverback. Similar to other metaheuristic search algorithms, the optimization process using GTO can be expressed in three main stages, i.e., population initialization, exploration phase, and exploitation phase as explained in next subsections.

2.4.1. Population Initialization. Suppose that a group of gorillas with population size of N is used to solve a given optimization problem with dimensional size of D. The position of each i-th gorilla in solution space at any t-th iteration is considered as a potential solution and expressed as $X_i(t) = [x_{i,1}(t), \ldots, x_{i,d}(t), \ldots, x_{i,D}(t)]$, where $i = 1, \ldots, N$ and $d = 1, \ldots, D$ represent the population index of gorilla and dimensional index of problem, respectively. Let LB and UB be the lower and upper boundary limits of solution, respectively. At $t = 0$, the position value of every i-th gorilla, i.e., $X_i(0)$, can be initialized as

$$X_i(0) = LB + r_1 \times (UB - LB), \tag{2}$$

where $r_1 \in [0, 1]$ is a real-valued number randomly generated from uniform distribution.

2.4.2. Exploration Phase. From the perspective of metaheuristic search algorithms, an exploration process is essential in early stage of optimization to enable the population for discovering the unvisited regions in solution space. For the exploration phase of GTO, three search operators are incorporated by emulating different behaviors of gorilla troops, i.e., move towards other gorillas, migrate towards unknown places, and migrate towards known places.

Define $p \in [0, 1]$ as a constant parameter used to indicate the likelihood of i-th gorilla to migrate towards unknown places and $rand \in [0, 1]$ as a real-valued number randomly generated from uniform distribution. If $rand < p$, the i-th gorilla chooses migration towards an unknown region to further enhance the exploration strength of GTO. For the scenario of $rand \geq 0.5$, the i-th gorilla tends to move towards a randomly selected gorilla denoted as $X_r(t)$ to attain good balancing of exploration and exploitation searches. Finally, the i-th gorilla chooses migration towards a known region to maintain good population diversity when $rand < 0.5$. Let $GX_r(t)$ be candidate position of a randomly selected gorilla created in the t-th iteration, whereas $GX_i(t+1)$ refers to the candidate position of each i-th gorilla created in the next $(t+1)$-th iteration. Define $r_2, r_3 \in [0, 1]$ as two real-valued numbers randomly generated from uniform distribution; then

$$GX_i(t+1) = \begin{cases} r_1 \times (UB - LB) + LB, rand < p, \\ (r_2 - C) \times X_r(t) + L \times Z \times X_i(t), rand \geq 0.5, \\ X_i(t) - L \times \{L \times [X_i(t) - GX_r(t)] + r_3 \times [X_i(t) - GX_r(t)]\}, rand < 0.5. \end{cases} \tag{3}$$

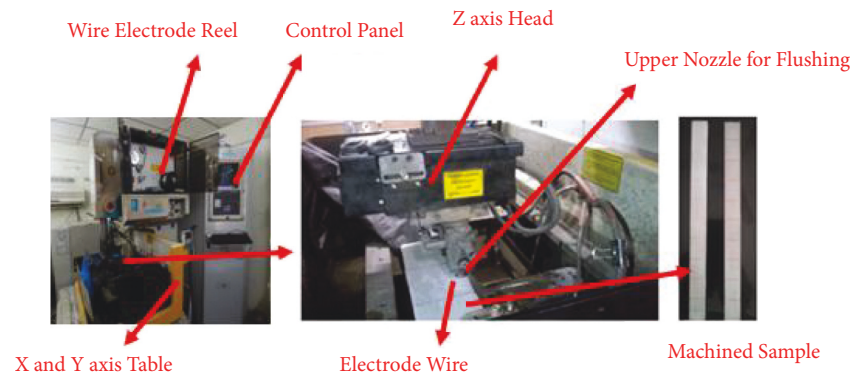

Figure 1: WEDM machining and machined sample.

Table 5: Experimental results.

Expt. No	Pulse-on time, P_1 (μs)	Pulse-off time, P_2 (μs)	Servo wire feed, WF (m/min)	Current, I (A)	Surface roughness, R_a (μm)
1	120	50	1	150	1.92
2	120	50	2	160	1.77
3	120	50	3	170	1.56
4	120	55	1	160	1.85
5	120	55	2	170	1.77
6	120	55	3	150	1.47
7	120	60	1	170	2.06
8	120	60	2	150	1.99
9	120	60	3	160	1.76
10	125	50	1	150	2.22
11	125	50	2	160	2.09
12	125	50	3	170	1.82
13	125	55	1	160	1.97
14	125	55	2	170	1.90
15	125	55	3	150	1.78
16	125	60	1	170	1.98
17	125	60	2	150	2.13
18	125	60	3	160	1.92
19	130	50	1	150	2.21
20	130	50	2	160	2.10
21	130	50	3	170	1.78
22	130	55	1	160	1.77
23	130	55	2	170	1.73
24	130	55	3	150	1.85
25	130	60	1	170	1.64
26	130	60	2	150	1.96
27	130	60	3	160	1.77

The parameters of C, L, and Z presented in equation (3) can be calculated as follows:

$$C = \left[\cos\left(2 \times r_4\right) + 1\right] \times \left(1 - \frac{t}{T_{\max}}\right), \tag{4}$$

$$L = C \times l, \tag{5}$$

$$Z \in [-C, C], \tag{6}$$

where $\cos(.)$ is a cosine operator; $T_{\max}$ is the maximum iteration numbers set for GTO; $r_4 \in [0, 1]$ and $l \in [-1, 1]$ are the real-valued numbers randomly generated from uniform distribution. Equation (4) is used to simulate the tendency of GTO to perform searching with larger interval of changes in the earlier stage of optimization process and these search ranges are gradually reduced in later stage. Meanwhile, equation (5) is designed to emulate the variation of silverback's leadership throughout the optimization process.

Upon the completion of exploration phase, the candidate position of each i-th gorilla is obtained as $GX_i(t+1)$ and its fitness value is evaluated as $F[GX_i(t+1)]$. The current fitness value of each i-th gorilla, i.e.,$F[X_i(t)]$, is then compared with $F[GX_i(t+1)]$. The new candidate position $GX_i(t+1)$ is used to update the current position $X_i(t)$ if the former solution has more superior fitness. Otherwise, the

Table 6: Results from ANOVA.

Source	Degrees of freedom (DF)	Adj SS	Adj MS	F-value	P-value	Remarks
Model	13	0.885626	0.068125	168.04	0.000	Significant
Linear	4	0.191479	0.047870	118.08	0.000	
P_1	1	0.024200	0.024200	59.69	0.000	
P_2	1	0.003756	0.003756	9.26	0.009	
WF	1	0.111111	0.111111	274.07	0.000	
I	1	0.019136	0.019136	47.20	0.000	
Square	4	0.278777	0.069694	171.91	0.000	
$P_1 \times P_1$	1	0.131030	0.131030	323.20	0.000	
$P_2 \times P_2$	1	0.115741	0.115741	285.49	0.000	
WF × WF	1	0.029606	0.029606	73.03	0.000	
I × I	1	0.000735	0.000735	1.81	0.201	
2-Way	5	0.270307	0.054061	133.35	0.000	
$P_1 \times P_2$	1	0.136533	0.136533	336.78	0.000	
$P_1 \times$ WF	1	0.056033	0.056033	138.21	0.000	
$P_1 \times$ I	1	0.064533	0.064533	159.18	0.000	
$P_2 \times$ WF	1	0.011756	0.011756	29.00	0.000	
$P_2 \times$ I	1	0.000450	0.000450	1.11	0.311	
Error	13	0.005270	0.000405			
Total	26	0.890896				

Standard deviation = 0.0201349 $R^2 = 99.41\%$, R^2(adj) = 98.82%, R^2(pred) = 96.67%.

Table 7: Test datasets used in ANFIS model.

Expt. No Units	Puls-on P_1 (μs)	Pulse-off P_2 (μs)	Wire feed rate WF (m/min)	Current I (A)	Surface roughness R_a (μm)
1.	122	52	1	155	2.06
2.	122	52	2	165	1.66
3.	124	54	3	165	1.98
4.	124	54	1	155	2.01
5.	126	56	2	165	1.69
6.	126	56	3	155	1.88

solution $GX_i(t+1)$ is discarded if it has more inferior fitness. Similar mechanism is used to update the position of silverback $X_{\text{silverback}}(t)$ by comparing its fitness value of $F[X_{\text{silverback}}(t)]$ with that of $F[GX_i(t+1)]$.

2.4.3. Exploitation Phase. On the contrary to exploration, exploitation has crucial role in the later stage of optimization process because it can further refine the solutions found in promising regions of search space. For the exploitation phase of GTO, two search operators are designed by simulating the behaviors of gorilla troops to follow the silverback for food searching and to compete for mating with the adult female gorillas.

Suppose that W is a parameter used to determine the behavior of each i-th gorilla in exploitation phase and C is a parameter obtained from equation (4). When $C \geq W$, the i-th gorilla chooses to obey the instructions of silverback in exploitation phase and its candidate position at the next $(t+1)$-th iteration; i.e., $GX_i(t+1)$, is updated as follows:

$$GX_i(t+1) = L \times M \times [X_i(t) - X_{\text{silverback}}(t)] + X_i(t), \quad (7)$$

where L is a parameter obtained from equation (5); $X_{\text{silverback}}(t)$ refers to the position of silverback at the t-th iteration. Meanwhile, the parameter M in equation (7) is calculated as

$$M = \left(\left| \frac{1}{N} \sum_{i=1}^{N} GX_i(t) \right|^{2^L} \right)^{1/2^L}, \quad (8)$$

where N refers to population size of GTO; $GX_i(t)$ represents the candidate position of each i-th gorilla at the current t-th iteration.

On the contrary, the i-th gorilla tends to compete with other male gorillas for mating with the adult female gorillas during exploitation phase if $C < W$. The mathematical models used to simulate this behavior are formulated as

$$GX_i(t+1) = X_{silverback}(t) - [X_{silverback}(t) \times Q - X_i(t) \times Q] + A, \quad (9)$$

where Q represents the impact force; A is a vector used to indicate the degree of violence encountered in competition. Both of Q and A can be computed as

$$Q = 2 \times r_5 - 1, \quad (10)$$

$$A = \beta \times E, \quad (11)$$

$$E = \begin{cases} N_1, r_6 \geq 0.5 \\ N_2, r_6 < 0.5 \end{cases}, \quad (12)$$

where $r_5, r_6 \in [0, 1]$ are two real-valued numbers randomly generated from uniform distribution; β is a constant; E is used to simulate the violence effect on each dimension of solution based on two normal distributions of N_1 and N_2. If$r_6 \geq 0.5$, E is assigned as an array with size of$1 \times D$, where N_1 is used to randomly generate different values for each dimension. On the other hand, only a single random number is generated by N_2 and assigned to E when $r_6 < 0.5$.

Similar with exploration phase, the fitness value of each i-th gorilla's candidate position $GX_i(t+1)$ is evaluated as $F[GX_i(t+1)]$ and then compared with the current fitness $F[X_i(t)]$. If $GX_i(t+1)$ has more superior fitness than $X_i(t)$, the latter solution will be replaced by the former one. Otherwise, $GX_i(t+1)$ will be discarded due to its inferior fitness. Similar mechanism is also used to update the position of silverback $X_{\text{silverback}}(t)$ by comparing its fitness value of $F[X_{\text{silverback}}(t)]$ with that of $F[GX_i(t+1)]$.

2.4.4. Overall Search Mechanisms of GTO. The overall search mechanisms of GTO are presented in Figure 2. Initially, the population of GTO is randomly generated by using uniform distribution. Both of the exploration and exploitation phases are switched alternately during the optimization process of GTO. For exploration phase, three different search operators can be used to determine the candidate position of every i-th gorilla. Meanwhile, two different search operators are devised in exploitation phase to update the candidate position of every i-th gorilla. It is notable that greedy selection is used to update the current position of each i-th gorilla and position of silverback for both exploration and exploitation phases. The iterative search processes of GTO in exploration and exploitation phases are repeated until the predefined termination condition, i.e., current iteration exceeding maximum iteration ($t > T_{\max}$), is satisfied. At the end of optimization process, the silverback's position, i.e., $X_{\text{silverback}}(T_{\max})$, is returned as the best solution to solve given problem. Due to the promising optimization performance of GTO, it has been applied to solve some real-world optimization problems such as feature selection [32], image segmentation [33], and parameter estimation of fuel cell [34] and solar panel [35]. To the best of authors' knowledge, the feasibility of GTO to solve machining optimization problem is one of the areas that remains unexplored.

3. Performance Evaluation of Proposed WEDM Machining Optimization Problem

3.1. Simulation Settings of All Compared Algorithms. Extensive simulation studies are conducted to evaluate the performance of GTO in solving the proposed WEDM machining optimization problem. The simulation results produced by GTO are then compared with another six metaheuristic search algorithms known as particle swarm optimization (PSO) [36], differential evolution (DE) [37], teaching learning-based optimization (TLBO) [28], grey wolf optimizer (GWO) [38], sine cosine algorithm (SCA) [39], and arithmetic optimization algorithm (AOA) [40]. The optimal parameter settings of all compared algorithms are determined based on the recommendations in their respective literature as shown in Table 8 and original source codes are obtained from their authors to ensure fair comparison. The same population size of $N = 10$ and maximum iteration numbers of $T_{\max} = 100$ are also set to ensure all seven metaheuristic algorithms are compared in fair manner. When solving real-world optimization problem such as WEDM machining considered in current study, it is essential to achieve proper tradeoff between the solution accuracy and computational overhead of algorithm. Although it is more likely for metaheuristic search algorithm such as GTO to obtain the solutions with better accuracy when larger population size is set, the computational complexity of algorithm is estimated as $O(N \times (1 + T_{\max} + T_{\max} D) \times 2)$ [31] using Big-O notation that tends to increase with population size, where N, $T_{\max}$, and D refer to the population size, maximum iteration numbers, and total dimensional size of problems, respectively. The increasing computational complexity of GTO is undesirable and not computationally feasible for real-world optimization problems. Furthermore, our simulation studies indicate that GTO can solve the WEDM machining optimization problems with better accuracy than other competing algorithms when the population size of $N = 10$ is set. This is a crucial finding to reveal the competitive optimization performances of GTO when solving real-world optimization problems. In order to alleviate the random discrepancy issue, all compared algorithms are simulated independently for 20 runs under the same simulation environment of Matlab (R2021a) installed in a personal computer with Intel® Core™ i5-7400 CPU processor with 24.0 GB RAM when solving the proposed WEDM machining optimization problems.

3.2. Simulation Results and Discussion. The optimal machining parameters (i.e., pulse-on time, pulse-off time, wire feed, and current values) obtained by GTO and their corresponding response variable of surface roughness (R_a) when solving the proposed WEDM machining optimization problems for 20 consecutive times are presented in Table 9. The number of iteration numbers T_{best} consumed by GTO to achieve the best machining result in every simulation run is also recorded in Table 9. Accordingly, GTO is able to consistently search for the optimal values of pulse-on time, pulse-off time, wire feed, and current that lead to the low values of surface roughness. It is also noteworthy that GTO has consumed an average iteration number of 24 to find the optimal machining parameters in these 20 simulations runs, implying the promising search efficiency of this algorithm. From Table 9, it is observed that GTO has produced the lowest surface roughness value of 0.500953 μm when the machining parameters of pulse-on time, pulse-off time, wire feed, and current values are set as 121 μs, 52μs, 3 m/min, and 166 A, respectively, at the 18th simulation run with 8 iterations and 19th simulation run with 15 iterations. These optimal machining parameters are further validated by measuring the experimental value of surface roughness as 0.500μm, i.e., only 0.2% of deviation from the predicted

Algorithm 1: GTO

Inputs: N, D, T_{max}, LB, UB, p, W, β

Initialize $t = 0$, $X_{silverback}(0) \leftarrow \emptyset$, $F[X_{silverback}(t)\,] \leftarrow \infty$;
for each i-th gorilla **do** /*Population Initialization*/
  Randomly generate $X_i(0)$ using Eq. (2);
  Evaluate the fitness of $X_i(0)$ as $F[X_i(0)]$;
  $GX_i(0) \leftarrow X_i(0)$, $F[GX_i(0)] \leftarrow F[X_i(0)]$
  if $F[GX_i(0)]$ *is superior to* $F[X_{silverback}(0)]$ **then**
    $X_{silverback}(0) \leftarrow GX_i(0)$, $F[X_{silverback}(t)\,] \leftarrow F[GX_i(0)]$;
  end if
end for
while $t \le T_{max}$ **do** /*Main Loop*/
  Update C, L and Z using Eqs. (4), (5) and (6), respectively;
  for each i-th gorilla **do** /*Exploration*/
    Update $GX_i(t+1)$ using Eq. (3);
    Evaluate the fitness of $GX_i(t+1)$ as $F[GX_i(t+1)]$;
    if $F[GX_i(t+1)]$ *is superior to* $F[X_i(t)]$ **then**
      $X_i(t+1) \leftarrow GX_i(t+1)$, $F[X_i(t+1)] \leftarrow F[GX_i(t+1)]$
      if $F[GX_i(t+1)]$ *is superior to* $F[X_{silverback}(t)]$ **then**
        $X_{silverback}(t+1) \leftarrow GX_i(t+1)$, $F[X_{silverback}(t+1)\,] \leftarrow F[GX_i(t+1)]$;
      end if
    end if
  end for
  for each i-th gorilla **do** /*Exploitation*/
    if $C \ge W$ **then**
      Update $GX_i(t+1)$ using Eqs. (7) and (8);
    else
      Update $GX_i(t+1)$ using Eqs. (9) to (12);
    end if
    Evaluate the fitness of $GX_i(t+1)$ as $F[GX_i(t+1)]$;
    if $F[GX_i(t+1)]$ *is superior to* $F[X_i(t)]$ **then**
      $X_i(t+1) \leftarrow GX_i(t+1)$, $F[X_i(t+1)] \leftarrow F[GX_i(t+1)]$
      if $F[GX_i(t+1)]$ *is superior to* $F[X_{silverback}(t)]$ **then**
        $X_{silverback}(t+1) \leftarrow GX_i(t+1)$, $F[X_{silverback}(t+1)\,] \leftarrow F[GX_i(t+1)]$;
      end if
    end if
  end for
  $t \leftarrow t+1$;
end while

Outputs: $X_{silverback}(T_{max})$, $F[X_{silverback}(T_{max})\,]$

Figure 2: Pseudocode of GTO.

value of surface roughness. Given the small performance difference, it can be concluded that there is good consistency between the simulated and actual results.

Table 10 presents the best, worst, mean, and standard deviation (SD) values of surface roughness obtained by all compared seven metaheuristic search algorithms when solving the proposed WEDM machining optimization problems for 20 consecutive times. The best (i.e., lowest) surface roughness values produced by each algorithm are highlighted in bold. Although there are four algorithms (i.e., PSO, DE, TLBO, and GTO) that are able to produce the lowest values, GTO is the only algorithm that can solve the proposed WEDM machining optimization problems with the lowest values of worst and mean surface roughness. The promising performance of GTO to consistently solve the WEDM machining problem with low surface roughness value is also reflected from the lowest SD value. On the contrary, the optimization performances of algorithms such as PSO, DE, TLBO, and AOA are observed to be inconsistent as revealed by the inferior values of worst surface roughness and SD. These findings imply the high tendencies of PSO, DE, TLBO, and AOA to be trapped into local optima and suffer with premature convergence issues in certain trials of simulations. Although GWO and SCA can deliver more consistent performances when dealing with the proposed WEDM machining optimization problem, the overall surface roughness values obtained by these two competing algorithms are generally more inferior than those of GTO.

Figure 3 depicts the convergence curves obtained by all metaheuristic search algorithms when solving the proposed WEDM machining problem to further analyze their optimization performances in real-world application. Accordingly, each compared algorithm has exhibited different accuracy and efficiency in searching for the best combinations of machining parameters (i.e., pulse-on time, pulse-off time, wire feed, and current) that aim to minimize the surface roughness value. Among all compared metaheuristic search algorithms, AOA is identified to have worst performance because it has very slow convergence speed during the early stage of search process and its population only starts to converge towards the promising solution regions at the middle stage of optimization. The poor convergence characteristic of AOA is considered as a main contributing factor that prohibits its population to locate the global optimum in earlier stage, hence resulting in its inferior performance to solve the proposed WEDM machining problems with undesirably large surface roughness value. Although both PSO and DE have started the optimization processes with relatively lower surface roughness values, these two algorithms are observed to suffer with

Table 8: Parameter settings of all compared metaheuristic search algorithms used to solve WEDM machining optimization problems.

Algorithm	Parameter settings
PSO	Inertia weight ω: 0.9 $\longrightarrow$ 0.2, acceleration coefficients $c_1 = c_2 = 2.0$
DE	Scaling factor $F = 0.5$, crossover rate $CR = 0.9$
TLBO	Teaching factor $T_f \in \{1, 2\}$
GWO	Convergence coefficient a: 2.0 $\longrightarrow$ 0.0
SCA	Constant used to balance exploration and exploitation, $A_{SCA} = 2$
AOA	Control parameter used to adjust search process $\mu = 0.5$, control parameter used to define exploitation accuracy over iterations $\alpha = 5$
GTO	Constant parameter used to multiply with violence effect $\beta = 3$, constant parameter used to determine the behavior of gorilla in exploitation phase $W = 0.8$, constant parameter used to indicate the likelihood of gorilla to migrate towards unknown places $p = 0.03$

Table 9: Optimal machining parameters and the corresponding response variables produced by GTO in 20 consecutive simulation runs.

Run	Pulse-on time, P_1 (μs)	Pulse-off time, P_2 (μs)	Wire feed, WF (m/min)	Current, I (A)	Surface roughness, R_a (μm)	Iteration numbers to achieve best result, T_{best}
1	121	54,	3	173	0.520676	3
2	120	52	2	166	0.503164	7
3	130	50	4	164	0.501744	37
4	127	52	3	168	0.504061	35
5	121	53	1	173	0.512619	38
6	121	54	3	173	0.520676	8
7	128	53	1	173	0.500999	23
8	128	53	1	173	0.500999	45
9	120	53	3	169	0.508859	29
10	121	52	3	166	0.500953	24
11	120	53	3	169	0.508859	24
12	128	59	4	154	0.507776	12
13	120	53	3	169	0.508859	43
14	120	53	3	169	0.508859	50
15	130	50	4	164	0.501744	31
16	120	53	3	169	0.508859	12
17	120	53	3	169	0.508859	16
18	121	52	3	166	0.500953	8
19	121	52	3	166	0.500953	15
20	120	53	3	169	0.508859	19

premature convergence issues as demonstrated by the plateau regions of their convergence curves in early stage of optimization, i.e., before 20th iteration. The high tendency of PSO and DE populations to be trapped into the local optima regions can be justified by their relatively simple search mechanisms that are unable to achieve good balancing of exploration and exploitation when dealing with fitness landscapes of real-world optimization problems. The inferior performances of PSO and DE to avoid misleading information of local optima regions tend to prevent these two algorithms consistently solving the proposed WEDM machining problems with lower surface roughness values. The remaining algorithms such as TLBO, GWO, SCA, and GTO have better robustness to handle premature convergence issues as demonstrated by their convergence curves with more promising convergence characteristics and lower surface roughness values. Among these four algorithms, GTO is proven as the best performing algorithm to solve the proposed WEDM machining optimization problem because it shows fastest convergence rate and is able to locate the solution that is nearest to the global optimum. The competitive optimization performances demonstrated by GTO against TLBO, GWO, and SCA can be justified by its inherent mechanisms used to achieve proper balancing of exploration and exploitation searches of algorithm. As compared to the latter three algorithms equipped with lesser numbers of search operators, GTO is designed to have two optimization phases (i.e., exploration and exploitation) with five search operators with different exploration and exploitation strengths. Depending on the optimization stage and location of each individual solution in search space, one of the embedded search operators can be triggered and play dominant role to guide the individual solution searching towards the promising regions of search space. The excellent capability of GTO in balancing its exploration and exploitation searches enables its population to locate the global optimum of WEDM machining optimization problem rapidly without requiring large numbers of population size for effective searching.

Different nonparametric statistical procedures [41, 42] are further used for performance evaluation of all competing metaheuristic search algorithms by referring to their surface

Table 10: The best, worst, mean, and standard deviation (*SD*) values of surface roughness produced by all compared algorithms.

Algorithm	Surface roughness, R_a			
	Best	Worst	Mean	SD
PSO	**0.500953**	1.210000	0.58860	0.1672400
DE	**0.500953**	1.006769	0.53508	0.1113500
TLBO	**0.500953**	1.151530	0.53999	0.1440400
GWO	0.501744	0.570686	0.52383	0.0187180
SCA	0.501744	0.586320	0.52038	0.0195790
AOA	0.501744	0.790220	0.59673	0.0666010
GTO	**0.500953**	**0.520676**	**0.50697**	**0.0060295**

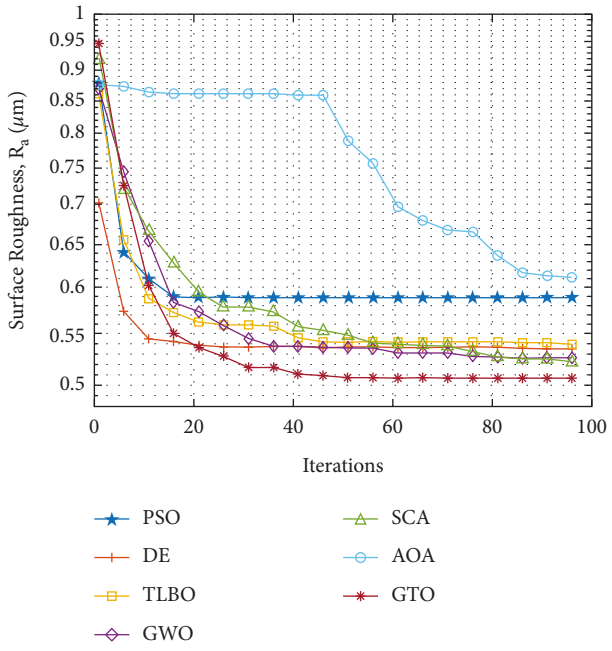

Figure 3: Convergence curves produced by all compared meta-heuristic search algorithms.

roughness values obtained. Wilcoxon signed rank test [41, 42] is employed for the pairwise comparison of GTO with each of its competing algorithms at the significance level of $\sigma = 0.05$. The results of Wilcoxon signed rank test are reported in terms of the sum of rank (i.e., R^+ anR^- d) and the associated p-values. R^+ and R^- shown in Table 11 indicate the sum of rank for GTO to perform better and perform worse than a given competing algorithm, respectively. Meanwhile, p-value is the minimum level of significance for detecting performance differences between algorithms. If $p < \sigma$, it implies the existence of strong evidence to reject null hypothesis and the best results achieved by better performing algorithms are statistically significant. The pairwise comparison results reported in Table 12 show that GTO can perform significantly better than PSO, GWO, SCA, and AOA because their corresponding p-values are all smaller than the threshold significance value of $\sigma = 0.05$. In other words, the competitive performances of GTO against PSO, GWO, SCA, and AOA are evident and not achieved by any random chances. On the other hand, there are no significance performance differences detected between GTO and

Table 11: Wilcoxon signed rank test for the pairwise comparison between GTO and its peer algorithms.

Algorithm compared with GTO	R^+	R^-	p-value
PSO	177.0	13.0	0.000900
DE	127.5	62.5	0.173118
TLBO	117.0	93.0	0.637602
GWO	185.5	24.5	0.002060
SCA	171.5	18.5	0.001844
AOA	208.0	2.0	0.000104

DE as well as GTO and TLBO as indicated by their relatively large p-values. This implies that the poor performances of DE and TLBO might only happen in certain simulation runs. GTO is still considered as a better performing algorithm due to excellent consistency to solve the proposed WEDM machining optimization problem with low surface roughness values.

Multiple comparison analyses [41, 42] are also conducted for more thorough evaluations of GTO and its competing algorithms. Friedman test was first employed to calculate the average ranking of each algorithm and detect the global differences between all compared algorithms. As reported in Table 12, GTO with lowest average rank value emerges as the best performing algorithm to solve the proposed WEDM problem with lowest surface roughness values. The remaining compared algorithms are ranked as follows: TLBO, DE, SCA, GWO, PSO, and AOA. The p-value presented in Table 12 also detects the significant global differences between all compared algorithms because $p < \sigma$, where $\sigma = 0.05$ is defined as the threshold significance level. Referring to the findings from Friedman test, another three post hoc analyses known as Bonferroni-Dunn, Holm, and Hochberg methods are employed to further compare the performance differences between GTO and each peer algorithm [41, 42]. Table 13 presents the results of each post hoc analysis in terms of z values, unadjusted p-values, and adjusted p-values. It is observed that all post hoc analyses have validated that GTO can outperform AOA and PSO significantly in terms of surface roughness value because all adjusted p-values obtained are smaller than $\sigma = 0.05$. If the threshold significance level is adjusted to $\sigma = 0.10$, GTO is verified by all post hoc analyses to perform significantly better than GWO. Finally, both of Holm and Hochberg analyses can verify the significant performance of GTO against SCA when $\sigma = 0.10$.

Table 12: Friedman test for the multiple comparison between GTO and its peer algorithms.

Algorithm compared with GTO	Ranking	Chi-square statistic	p-value
PSO	4.825		
DE	3.225		
TLBO	2.775		
GWO	4.325	$3.99E+01$	$0.00E+00$
SCA	4.1		
AOA	6.125		
GTO	2.625		

Table 13: Post hoc analyses for the multiple comparison between GTO and its peer algorithms.

Algorithm compared with GTO	Unadjusted p	Bonferroni-Dunn p	Holm p	Hochberg p
AOA	0.000000	0.000002	0.000002	0.000002
PSO	0.001280	0.007679	0.006399	0.006399
GWO	0.012827	0.076960	0.051307	0.051307
SCA	0.030836	0.185018	0.092509	0.092509
DE	0.379775	2.278653	0.759551	0.759551
TLBO	0.826200	4.957201	0.826200	0.826200

4. Conclusion

This research was aimed at using an emerging metaheuristic algorithm known as Gorilla Troops Optimizer (GTO) to solve WEDM machining problem by searching for the optimal machining parameters that can lead to the best (i.e., lowest) surface finish.

The machining of aluminum alloy was done with brass wire as a cathode tool and deionised water as a dielectric medium. ANFIS was used to generate about 500 datasets from 27 experimental datasets. On the contrary to many existing metaheuristic search algorithms, GTO has two different optimization phases with five search operators. It was able to search for the optimal machining parameters in solution space effectively and efficiently without having large population number. At the end of optimization processes, the optimal machining parameters as stored in silverback solution of GTO were pulse-on time = 121 μs, pulse-off time = 52 μs, wire feed = 3 m/min, and current value = 166 A. These parameters are the best process parameters to achieve the minimum surface roughness of 0.500953 microns.

The current metaheuristic algorithm was able to solve WEDM machining problem in 20 independent simulation runs with small standard deviation value of $SD = 0.0060295$, implying the high consistency of the algorithm to search for the optimal machining parameters. Various statistical analyses such as Wilcoxon signed rank test, Friedman test, and post hoc analyses were also performed to verify the significant performance gain of GTO against other metaheuristic search algorithms when solving the current machining problem. To ensure the practicability of optimization results produced by GTO, validation experiments were also performed and found deviation of $\Delta = 0.2\%$ between the predicted and measured surface roughness values. The negligible error value implies the feasibility of GTO to solve real-world WEDM machining optimization problems.

Nomenclature

ANFIS: Adaptive Neurofuzzy Inference System
WEDM: Wire cut electric discharge machining
GRA: Grey rational analysis
HSS: High speed steel
MQL: Minimum quantity lubrication
MRR: Material removal rate
EWR: Electrode wear rate
OC: Overcut
RSM: Response surface model
ARAS: Additive ratio assessment
AHP: Analytic hierarchy process
TOPSIS: Technique for order preference by similarity to ideal situation
BBD: Box-Behnken design
MOPSO: Multiobjective particle swarm optimization
GTO: Gorilla Troops Optimizer
DoE: Design of experiment
ANN: Artificial neural network
MF: Membership function
trimf: Triangular shaped membership function
trapmf: Trapezoidal-shaped membership function
gbellmf: Generalized bell-shaped membership function
gaussmf: Gaussian curve membership function
gauss2mf: Gaussian combination membership function
pimf: P-shaped membership function
dsigmf: Difference between two sigmoidal membership functions
psigmf: Product of two sigmoid membership functions
gbellmf: Generalized bell-shaped membership function
RMSE: Root mean square error
PSO: Particle swarm optimization
DE: Differential evolution
TLBO: Teaching learning-based optimization
GWO: Grey wolf optimizer
SCA: Sine cosine algorithm
AOA: Arithmetic optimization algorithm

Indices

i: Population index of gorilla in GTO
d: Dimension index
t: Iteration index
$\cos(\bullet)$: Cosine operator
$F[\bullet]$: Operator used to calculate the fitness value of a given position value
$O(\bullet)$: Complexity of algorithm estimated using Big-O notation

Parameter and Variables

P_1: Pulse-on time
P_2: Pulse-off time
WF: Servo wire feed
I: Current
R_a: Surface roughness
D: Total dimension size of optimization problem
N: Population size
$X_i(t)$: Position value of ith gorilla at the tth iteration
$x_{i,d}(t)$: Position value of ith gorilla in dth dimension at the tth iteration
r_1, r_2, r_3, r_4, r_5, r_6, rand: Real-valued number within [0, 1] randomly generated from uniform distribution
l: Real-valued number within [-1, 1] randomly generated from uniform distribution.
LB: Lower boundary limits
UB: Upper boundary limits
p: Constant parameter within [0, 1] used to indicate the likelihood of gorilla to migrate towards unknown places
$X_r(t)$: Position value of a randomly selected gorilla at the tth iteration
$GX_r(t)$: Candidate position value of a randomly selected gorilla at the tth iteration
$GX_i(t)$: Candidate position value of ith gorilla at the tth iteration
C: Search range of gorilla
L: Variation of silverback's leadership
T_{max}: Maximum iteration numbers
W: Parameter used to determine the behavior of gorilla in exploitation phase
M: Mean position of gorilla population
Q: Impact force
A: Degree of violence encountered by gorilla in competition
β: Constant parameter used to determine violence effect of gorilla
E: Parameter used to simulate the violence effect on each dimension of solution
N_1, N_2: Normal distributions used to model the violence effect
ω: Inertia weight of particle swarm optimization
c_1, c_2: Acceleration coefficient of particle swarm optimization
F: Scaling factor of differential evolution
CR: Crossover rate of differential evolution
T_f: Teaching factor of teaching learning based optimization
a: Convergence coefficient of grey wolf optimizer
A_{SCA}: Constant used to balance exploration and exploitation of sine cosine algorithm
μ: Control parameter used to adjust the search process of arithmetic optimization algorithm
α: Control parameter used to define exploitation accuracy of arithmetic optimization algorithm over iterations
T_{best}: Iteration number consumed by an algorithm to achieve best result
SD: Standard deviation
σ: Significant level of nonparametric statistical procedures
R^+: Sum of rank for GTO to perform better than a given competing algorithm
R^-: Sum of rank for GTO to perform worse than a given competing algorithm.

Data Availability

The data associated with this research can be obtained from the corresponding author upon request.

Conflicts of Interest

The authors declare that there are no conflicts of interest.

References

[1] N. Z. Khan, Z. A. Khan, A. N. Siddiquee, and A. K. Chanda, "Investigations on the effect of wire EDM process parameters on surface integrity of HSLA: a multi-performance characteristics optimization," *Production & Manufacturing Research*, vol. 2, no. 1, pp. 501–518, 2014.

[2] J. A. Abbasi, M. Jahanzaib, M. Azam, S. Hussain, A. Wasim, and M. Abbas, "Effects of wire-cut EDM process parameters on surface roughness of HSLA steel," *International Journal of Advanced Manufacturing Technology*, vol. 91, no. 5-8, pp. 1867–1878, 2017.

[3] Y. Takayama, Y. Makino, Y. Niu, and H. Uchida, "The latest technology of wire-cut EDM," *Procedia CIRP*, vol. 42, pp. 623–626, 2016.

[4] I. Ayesta, O. Flaño, B. Izquierdo, J. A. Sanchez, and S. Plaza, "Experimental study on debris evacuation during slot EDMing," *Procedia CIRP*, vol. 42, pp. 6–11, 2016.

[5] J. Singh and R. K. Sharma, "Assessing the effects of different dielectrics on environmentally conscious powder-mixed EDM of difficult-to-machine material (WC-Co)," *Frontiers of Mechanical Engineering*, vol. 11, no. 4, pp. 374–387, 2016.

[6] L. Liu, M. Qiu, C. Shao, M. Zhang, and J. Zhao, "Research on wire-cut electrical discharge machining constant discharge probability pulse power source for silicon crystals,"

International Journal of Advanced Manufacturing Technology, vol. 100, no. 5-8, pp. 1815–1824, 2019.

[7] A. Muniappan, C. Thiagarajan, P. V. Senthiil, V. Jayakumar, and T. Shaafi, "Effect of wire-EDM process parameters on cutting speed of AL6061 hybrid composite," *International Journal of Mechanical Engineering & Technology*, vol. 8, no. 10, pp. 185–189, 2017.

[8] M. S. Alsoufi and D. K. Suker, "Experimental investigation of wire-EDM process parameters for surface roughness in the machining of carbon steel 1017 and aluminum alloy 6060," *American Journal of Mechanical Engineering*, vol. 6, no. 3, pp. 132–147, 2018.

[9] A. Kumar, T. Soota, and J. Kumar, "Optimisation of wire-cut EDM process parameter by Grey-based response surface methodology," *Journal of Industrial Engineering International*, vol. 14, no. 4, pp. 821–829, 2018.

[10] A. Pramanik and A. K. Basak, "Sustainability in wire electrical discharge machining of titanium alloy: understanding wire rupture," *Journal of Cleaner Production*, vol. 198, pp. 472–479, 2018.

[11] S. K. Shihab, "Optimization of WEDM process parameters for machining of friction-stir-welded 5754 aluminum alloy using Box–Behnken design of RSM," *Arabian Journal for Science and Engineering*, vol. 43, no. 9, pp. 5017–5027, 2018.

[12] H. Hegab, H. A. Kishawy, and B. Darras, "Sustainable cooling and lubrication strategies in machining processes: a comparative study," *Procedia Manufacturing*, vol. 33, pp. 786–793, 2019.

[13] P. Nagarajan, P. K. Murugesan, and E. Natarajan, "Optimum control parameters during machining of LM13 aluminum alloy under dry electrical discharge machining (EDM) with a modified tool design," *Materials Science*, vol. 25, no. 4, pp. 407–412, 2019.

[14] T. Chaudhary, A. N. Siddiquee, and A. K. Chanda, "Effect of wire tension on different output responses during wire electric discharge machining on AISI 304 stainless steel," *Defence Technology*, vol. 15, no. 4, pp. 541–544, 2019.

[15] S. Ramesh, N. Vijayakumar, and E. Natarajan, "Electrical discharge machining analysis of zirconium powder mixed dielectric on performance of high carbon high chromium steel," *Journal of the Balkan Tribological Association*, vol. 26, no. 1, pp. 165–192, 2020.

[16] R. Chaudhari, J. Vora, D. M. Parikh, V. Wankhede, and S. Khanna, "Multi-response optimization of WEDM parameters using an integrated approach of RSM–GRA analysis for pure titanium," *Journal of the Institution of Engineers*, Series D, vol. 101, pp. 117–126, 2020.

[17] A. Ramaswamy, A. V. Perumal, and A. V. Perumal, "Multi-objective optimization of drilling EDM process parameters of LM13 al alloy–10ZrB2–5TiC hybrid composite using RSM," *Journal of the Brazilian Society of Mechanical Sciences and Engineering*, vol. 42, no. 8, p. 432, 2020.

[18] T. Sathish, V. Mohanavel, K. Ansari et al., "Synthesis and characterization of mechanical properties and wire cut EDM process parameters analysis in AZ61 magnesium alloy + B4C + SiC," *Materials*, vol. 14, no. 13, p. 3689, 2021.

[19] J. U. Prakash, P. Sivaprakasam, I. Garip et al., "Wire electrical discharge machining (WEDM) of hybrid composites (Al-Si12/B_4C/Fly Ash)," *Journal of Nanomaterials*, vol. 2021, pp. 1–10, 2021.

[20] N. R. J. Hynes, D. S. S. P. Kumar, M. V. Prabhu, M. A. Ali, M. H. Raza, and C. I. Pruncu, "Investigating the parametric effects on wire electric discharge machining performance in processing AA1050-5 wt.% SiC composite with zinc-coated brass wire," *Journal of the Brazilian Society of Mechanical Sciences and Engineering*, vol. 44, no. 4, p. 127, 2022.

[21] V. Aggarwal, C. I. Pruncu, J. Singh, S. Sharma, and D. Y. Pimenov, "Empirical investigations during WEDM of Ni-27Cu-3.15Al-2Fe-1.5Mn based superalloy for high temperature corrosion resistance applications," *Materials*, vol. 13, no. 16, p. 3470, 2020.

[22] B. Sen, S. A. I. Hussain, A. D. Gupta, M. K. Gupta, D. Y. Pimenov, and T. Mikołajczyk, "Application of type-2 fuzzy AHP-ARAS for selecting optimal WEDM parameters," *Metals*, vol. 11, no. 1, p. 42, 2020.

[23] T. Mikolajczyk, "Analyse of possibility of form tools manufacturing using wire cutting EDM," *Applied Mechanics and Materials*, vol. 656, pp. 200–205, 2014.

[24] K. Fuse, A. Dalsaniya, D. Modi et al., "Integration of fuzzy AHP and fuzzy TOPSIS methods for wire electric discharge machining of titanium (Ti6Al4V) alloy using RSM," *Materials*, vol. 14, no. 23, p. 7408, 2021.

[25] K. K. Goyal, N. Sharma, R. Dev Gupta et al., "A soft computing-based analysis of cutting rate and recast layer thickness for AZ31 alloy on WEDM using RSM-MOPSO," *Materials*, vol. 15, no. 2, p. 635, 2022.

[26] M. N. Alam, A. N. Siddiquee, Z. A. Khan, and N. Z. Khan, "A comprehensive review on wire EDM performance evaluation," *Proceedings of the Institution of Mechanical Engineers - Part E: Journal of Process Mechanical Engineering*, Article ID 095440892210748, 2022.

[27] M. H. Abidi, A. M. Al-Ahmari, U. Umer, and M. S. Rasheed, "Multi-objective optimization of micro-electrical discharge machining of nickel-titanium-based shape memory alloy using MOGA-II," *Measurement*, vol. 125, pp. 336–349, 2018.

[28] S. Suresh, N. Elango, K. Venkatesan, W. H. Lim, K. Palanikumar, and S. Rajesh, "Sustainable friction stir spot welding of 6061-T6 aluminium alloy using improved non-dominated sorting teaching learning algorithm," *Journal of Materials Research and Technology*, vol. 9, no. 5, pp. 11650–11674, 2020.

[29] P. Kayaroganam, V. Krishnan, E. Natarajan, S. Natarajan, and K. Muthusamy, "Drilling parameters analysis on in-situ al/b4 c/mica hybrid composite and an integrated optimization approach using fuzzy model and non-dominated sorting genetic algorithm," *Metals*, vol. 11, no. 12, p. 2060, 2021.

[30] S. Elango, K. Varadaraju, E. Natarajan, E. M. Abraham Gnanamuthu, R. Durairaj, and P. Mariappan, "PTFE in wet and dry drilling: two-tier modeling and optimization through ANFIS," *Mathematical Problems in Engineering*, vol. 2022, pp. 1–10, 2022.

[31] B. Abdollahzadeh, F. Soleimanian Gharehchopogh, and S. Mirjalili, "Artificial gorilla troops optimizer: a new nature-inspired metaheuristic algorithm for global optimization problems," *International Journal of Intelligent Systems*, vol. 36, no. 10, pp. 5887–5958, 2021.

[32] I. Ahmed, A. Dahou, S. A. Chelloug, M. A. A. Al-Qaness, and M. A. Elaziz, "Feature selection model based on gorilla troops optimizer for intrusion detection systems," *Journal of Sensors*, vol. 2022, Article ID 6131463, 12 pages, 2022.

[33] G. I. Sayad and A. E. Hassanien, "A novel chaotic artificial gorilla troops optimizer and its application for fundus images segmentation," in *Proceedings of the International Conference on Advanced Intelligent Systems and Informatics 2021. AISI 2021. Lecture Notes on Data Engineering and Communications Technologies*, A. E. Hassanien, V. Snášel, KC. Chang, A. Darwish, and T. Gaber, Eds., vol. 100, 2022.

[34] A. H. Yakout, H. Kotb, K. M. AboRas, and H. M. Hasanien, "Comparison among different recent metaheuristic algorithms for parameters estimation of solid oxide fuel cell: steady-state and dynamic models," *Alexandria Engineering Journal*, vol. 61, no. 11, pp. 8507–8523, 2022.

[35] A. Ginidi, S. M. Ghoneim, A. Elsayed, R. El-Sehiemy, A. Shaheen, and A. El-Fergany, "Gorilla troops optimizer for electrically based single and double-diode models of solar photovoltaic systems," *Sustainability*, vol. 13, no. 16, p. 9459, 2021.

[36] J. Kennedy and R. Eberhart, "Particle swarm optimization," in *Proceedings of ICNN'95 - International Conference on Neural Networks*, Perth, WA, Australia, December 1995.

[37] R. Storn and K. Price, "Differential evolution – a simple and efficient heuristic for global optimization over continuous spaces," *Journal of Global Optimization*, vol. 11, no. 4, pp. 341–359, 1997.

[38] S. Mirjalili, S. M. Mirjalili, and A. Lewis, "Grey wolf optimizer," *Advances in Engineering Software*, vol. 69, pp. 46–61, 2014.

[39] S. Mirjalili, "SCA: a Sine Cosine Algorithm for solving optimization problems," *Knowledge-Based Systems*, vol. 96, pp. 120–133, 2016.

[40] L. Abualigah, A. Diabat, S. Mirjalili, M. Abd Elaziz, and A. H. Gandomi, "The arithmetic optimization algorithm," *Computer Methods in Applied Mechanics and Engineering*, vol. 376, Article ID 113609, 2021.

[41] S. García, D. Molina, M. Lozano, and F. Herrera, "A study on the use of non-parametric tests for analyzing the evolutionary algorithms' behaviour: a case study on the CEC'2005 Special Session on Real Parameter Optimization," *Journal of Heuristics*, vol. 15, no. 6, pp. 617–644, 2009.

[42] J. Derrac, S. García, D. Molina, and F. Herrera, "A practical tutorial on the use of nonparametric statistical tests as a methodology for comparing evolutionary and swarm intelligence algorithms," *Swarm and Evolutionary Computation*, vol. 1, no. 1, pp. 3–18, 2011.

Hindawi
Advances in Materials Science and Engineering
Volume 2022, Article ID 4160276, 11 pages
https://doi.org/10.1155/2022/4160276

Research Article

Experimental Investigation of Heat-Treated Tool on Wire Electric Discharge Machining of Titanium Alloy (Ti-6Al-4V)

R. Manoj Samson,[1] **Ashvin Sridhar**,[2] **R. Ranjith**,[3] **Solomon Jenoris Muthiya**,[4] **Joshuva Arockia Dhanraj**,[5] **Murgayya S. Basavankattimath**,[6] **and Agegnehu Shara Shata**[7]

[1]*Department of Mechanical Engineering, SRM Institute of Science and Technology, Kattankulathur, Chengalpattu, Tamil Nadu 603203, India*
[2]*Department of Industrial Engineering, University of Illinois, Chicago, IL 60607, USA*
[3]*Department of Industrial Engineering, University of Texas, Arlington, TX 76019, USA*
[4]*Department of Automobile Engineering, Dayananda Sagar College of Engineering, Bengaluru 560078, India*
[5]*Centre for Automation and Robotics (ANRO), Department of Mechanical Engineering, Hindustan Institute of Technology and Science, Padur, Chennai 603103, India*
[6]*Department of Mechanical Engineering, KLS Vishwanathrao Deshpande Institute of Technology, Haliyal 58 1329, India*
[7]*Faculty of Mechanical Engineering, Arba Minch Institute of Technology, Arba Minch University, P.O. Box 21, Arba Minch, Ethiopia*

Correspondence should be addressed to R. Manoj Samson; manoj.sam6@gmail.com

Received 18 February 2022; Revised 19 May 2022; Accepted 3 June 2022; Published 27 June 2022

Academic Editor: Sengottuvelu Ramesh

Ti-6Al-4V is known for its lightweight, high tensile strength, exceptional corrosion resistance, and low thermal coefficient of expansion due to which it finds its application in precision surgical instruments and aeronautical and marine engine parts. In this study, Ti-6Al-4V has been machined using wire EDM machine with two different wire materials. The wire thickness of 0.25 mm heat-treated brass and zinc-coated brass tool and super cool oil as dielectric fluid were utilized for the machining process. Taguchi *L*9 orthogonal array was used. T_{on} (Pulse ON time), T_{off} (Pulse OFF time), wire feed, and I_p (Current) were the input parameters, and the response parameters such as surface roughness (*Ra*), material removal rate (MRR), tool wear rate (TWR), and recast layer thickness were optimized by TOPSIS optimization. From the results, higher tool wear rate was observed in brass tool. The titanium percentage after machining was found to be 55.05% for zinc-coated brass wire, whereas it was 51.58% for brass wire. Better productivity and surface integrity were observed in zinc-coated brass tool compared to heat-treated brass. MRR increased to 54.93%, surface roughness decreased to 2.40%, recast layer thickness increased to 3.44%, and tool wear rate was increased to 47.96%.

1. Introduction

Titanium alloy is one of the hardest materials that exhibits minimum weight ratio, exceptional corrosion resistance, low density, high strength, low thermal coefficient of expansion, and excellent properties at elevated temperature [1]. Its applications are mainly in manufacturing precision surgical instruments and aeronautical and marine engine components [2]. Ti-6Al-4V is considered to be one of the most difficult-to-be machined materials. To machine harder materials, nonconventional machining techniques are preferred over the conventional machining techniques, like lathe, CNC, drilling, milling, and so on. Nonconventional machining techniques are often preferred for harder materials and to improve the tool life. Ti-6Al-4V finds extensive use in manufacturing aeronautical parts the surface integrity of the machine work

piece should be at par excellence to avoid fatigue and cracks which lead to major failures. Considering Ti-6Al-4V's exceptional physical and chemical properties, a nonconventional method of wire EDM is being carried out. WEDM is a machining process that uses spark-generated electrical current to make the desired shape that helps in maintaining the surface integrity. Material removal from the work piece is done by a series of electrical discharges that are rapidly recurring between the two electrodes [3]. There are many advantages; for example, machining complex shapes easily, tool life is increased, precise cutting leaves very fewer burrs on its surface, and so on follows when WEDM is chosen. The cons include consumption of higher energy levels, very expensive than conventional machining, and the ability to machine only conductive materials. Hence, EDM wire cut machining is used. Jadam et al. [4] elucidated that the selection of tools for the manufacturing process includes many choices like copper (Cu), brass, zinc, molybdenum, and coated wires. The zinc-coated brass wire and brass wire of 0.25 mm thickness are chosen over Cu wires that are predominantly used. The reason for choosing brass over Cu is that, even though the conductivity of Cu is high, it possesses a high melting point, low vapor pressure rating, and low tensile strength, whereas brass, which is an alloy of copper, possesses a low melting point, high vapor pressure rating, and high tensile strength, which makes it the best choice in the selection criteria. The second tool chosen for comparison was a zinc-coated brass wire of the same thickness. When a material is given a zinc coating, its properties are enhanced. Since the brass wire was coated with zinc, it exhibited excellent improvement in the time of machining, good discharge characteristics, and better surface finish when compared with that of brass wire. The zinc coating helps to increase the tool life. To bring clarity to the work done, Pramanik and Basak [5] have identified the optimizing parameters for the fatigue life of Ti-6Al-4V. Using the technique, they have claimed that the propagation of the fatigue cracks does not influence the machined finished surface. Palanikumar et al. [6] have shown that the continuous generation of chips is caused by the cutting zone's high temperature. There is evidence of shear localization, which is a frequent occurrence when titanium is machined. At the tip of the chips, we saw some undeformed elements. The increased temperature would affect the tool life and finish of machined items. When the temperature is lower, short chips also emerge. Akkuş and Yaka [7] investigated that low values for Ra, tool wear, and energy consumption are sought, the target has been set to minimal after conducting various optimizations. Predictions for Ra, tool wear, and energy consumption were produced with an accuracy of 89.1%, 58.33%, and 96.75%, respectively. The reason for the significant error rate in tool wear prediction due to multiple optimizations is that, although feed rate is the effective parameter for Ra and energy consumption, cutting speed is the effective parameter for tool wear. Aydın [8] investigated that both computational and experimental tests revealed that plastic deformation occurred inside the PSZ around the tooltip. It was discovered that at considerably higher cutting speeds, serration of chips was begun by extensive periodic fracturing in the PSZ and progressed to the chip. Rao and Selvaraj [9] have conducted the optimization of the parameters such as servo voltage, servo feed, feed current, pulse on, wire tension, pulse off and concluded that the pulse off, pulse on, and peak current are widely remarkable. Kumar et al. [10] have analyzed the influence of EDM on wire to enhance the productivity of the surface finish of titanium alloy which develops a tolerable refinement on its surface finish. Pramanik et al. [11] have examined the process parameters on multilayered recast layers, identifying the presence of traces of wire electrode on its surface, holes, and cracks on Ti-6Al-4V. Chalisgaonkar et al. [12] have carried out the two different techniques for material removal rate and surface roughness for the characteristics of the machined surface using the principle of WEDM on the titanium alloy. Amorim et al. [13] concluded that the zinc-coated wire produced a better material removal rate and surface integrity at a higher wire feed rate when compared to the brass tool. Srinivasan et al. [14] have concluded that TOPSIS optimization is one of the best multicriterion decision-making criteria. TOPSIS optimization technique is considered to be one the finest methods of optimization when multiple criteria decision analysis is considered [15]. After the machining process, the response parameters were optimized using the TOPSIS optimization technique. The metallurgical aspects were studied using FESEM and EDS. R_a, MRR, TWR, and recast layer thickness were found to be higher in the zinc-coated brass wire when compared to those of heat-treated brass wire. A proper set of input parameters should be chosen to obtain better surface integrity. An improved situation was found when a heat-treated zinc-coated brass wire was used. Upon the extensive literature survey conducted, a very less number of works were performed on comparing heat-treated brass and zinc-coated brass as a tool in the wire EDM process.

2. Materials and Methods

Ti-6Al-4V is chosen because of its extensive physical and chemical properties. This metal exhibits excellent cryogenic properties. This work is a comparative study of the response parameters obtained by machining the workpiece with two different wires of 0.25 mm thickness utilized. The heat-treated brass wire and the zinc-coated brass wire was used as tool in wire EDM machine. The titanium (Ti-6Al-4V) workpiece was machined into rectangular shape of dimensions 10×20 mm using wire EDM machine. From the literature survey [16,17], it was finalized that the input parameters were Wire Feed, Ipeak, Pulse OFF time, and Pulse ON time. Similarly, response parameters were recast layer thickness, tool wear rate (TWR), surface roughness (*Ra*), and material removal rate (MRR). The recast layer thickness is measured using Machine Vision OLM, which uses VMS3.1 software. FESEM is conducted on the wire EDM machined sample of 10×20 mm to delineate the surface integrity of the machined surface. The specimen was first cleansed with acetone solution. To remove the impurities found on the surface, later the specimen was mounted onto a vacuumed chamber, which was then monitored under greater magnification. The SEM photograph was taken with two different magnifications of 300x and 600x.

Energy Dispersion Spectroscopy (EDS) is used to find the change in the material composition of the workpiece. The EDS results were obtained from the same equipment. The EDS conducted on the machined surface of the workpiece to find the change in the composition of Ti-6Al-4V.

2.1. Design of Experiments (DOE). The DOE was created by using Taguchi Analysis in Minitab 2018. The level was fixed to be three, and four parameters were entered. Tables 1 and 2 were formulated by Minitab. L9 was chosen in consideration of the material cost. The machined parts with brass wire as a tool are mentioned in Figure 1.

2.2. Experimental Work for Brass and Zinc-Coated Brass Wire as a Tool. The wire is wound around the wire drum, and it is aligned in such a position to machine the required surface. After fixing the constants of the input parameters, the start command is activated. In accordance with the feed rate given, the wire drum spins, and the machining starts with the given *Ip*, Pulse ON, and Pulse OFF. In case if the wire is cut during the machining process, the entire reel on the wire drum should be unwounded and reeled again. After each machining process, the workpiece is weighed, and the material loss is calculated. Similarly, the tool wear is also found by weighing it before and after machining process. The time required for a specimen to be machined is noted down. After the workpiece is machined to the desired shape, its surface roughness is studied using the Surf com apparatus and the recast layer is found using the Machine Vision OLM.

2.2.1. Material Removal Rate. MRR can be delineated by the difference between before weight (*Wa*) and after weight (*Wb*) of the machining process by the time taken (*t*). An increased material removal rate will have an upper hand in the machining process by improving the productivity rate.

2.2.2. Surface Roughness. The irregularities that regulate the surface finish are called surface roughness. To regulate a better surface finish and a good accuracy in the micromilling operation, it is very essential to cut the low chip feed. The feed per tooth should always be kept minimal at 1 μm. The machine that is being used to calculate the surface roughness is Surf com. To get the final *Ra* value, we need to calculate the surface roughness of all of its sides and then find the average *Ra*. The unit is μm [18].

2.2.3. Recast Layer Thickness. The recast layer is a thin layer formed on the machined surface after the solidification. Machine Vision OLM was utilized to measure the recast layer thickness. Recast Layer thickness is measured to find change in chemical composition of the machined surface.

2.2.4. Tool Wear Rate. The Tool wear rate is the ratio of difference of weight before machining and after weight after machining to time taken. TWR is inversely proportional to the tool life.

Table 1: Levels of DOE.

Level	T_{on} (μsec)	T_{off} (μsec)	I_p (A)	Wire feed (m/min)
I	40	6	2	80
II	60	10	3	90
III	80	14	4	100

Table 2: Design of experiments.

Exp.	T_{on} (μsec)	T_{off} (μsec)	I_p (A)	Wire feed (m/min)
*L*1	40	6	2	80
*L*2	40	10	3	90
*L*3	40	14	4	100
*L*4	60	6	3	100
*L*5	60	10	4	80
*L*6	60	14	2	90
*L*7	80	6	4	90
*L*8	80	10	2	100
*L*9	80	14	3	80

Figure 1: Wire EDM machined samples.

3. Results and Discussion

3.1. WEDM Influence on MRR, R_a, Recast Layer, and Tool Wear Rate. From the results obtained, MRR was found to be higher. While using zinc-coated brass wire, the best MRR was found in *L*6 experiment with the process parameters such as 60 μs of T_{on}, 14 μs of T_{off}, 2 A of I_p, and 90 m/min of wire feed. Similarly, for the surface finish, the least value is to be chosen to ensure the best surface integrity. For the zinc-coated brass wire, the least value of 3.99 μm was found for *L*1experiment. Likewise for the recast layer thickness and the tool wear rate, the least results are chosen to be the best results. For recast layer thickness, the best one was from *L*2 experiment, which gave a satisfying value of 0.18029 mm and for the tool wear rate, it was from *L*6, giving a convincing value of 1.0353 g/min. Apparently, *L*6 gave the best MRR value too. Similar kind of trend was observed in results of MRR, Ra, recast layer thickness, and tool wear rate in the previously conducted research on wire EDM process [18–23].

3.2. TOPSIS Optimization. The technique of order of preference by similarity to the ideal solution is the common technique that is being used to comprehend the problems in decision making. This technique enables us to form a comparison between all the alternatives that are included in the comparison. This method is highly useful in large-scale industries, like automobile and aeronautical industries [24–26].

Table 3: Design of experiments using brass wire as a tool.

Exp.	T_{on} (μs)	T_{off} (μs)	I_p (A)	Wire feed (m/min)	Material removal rate (g/min)	R_a (μm)	Recast layer thickness (mm)	Tool wear rate (g/min)
*L*1	40	6	2	80	0.554×10^{-1}	5.0444	0.2214	4.1250
*L*2	40	10	3	90	2.297×10^{-1}	6.3780	0.2923	3.0982
*L*3	40	14	4	100	1.575×10^{-1}	5.3010	0.3277	2.1325
*L*4	60	6	3	100	2.307×10^{-1}	5.1350	0.1742	3.9872
*L*5	60	10	4	80	1.758×10^{-1}	5.4437	0.2982	3.5280
*L*6	60	14	2	90	1.060×10^{-1}	4.0937	0.4669	2.9682
*L*7	80	6	4	90	2.666×10^{-1}	6.8372	0.2337	5.6324
*L*8	80	10	2	100	1.083×10^{-1}	4.6398	0.5074	2.5554
*L*9	80	14	3	80	1.097×10^{-1}	5.2216	0.5280	1.9895

Table 4: Determination of performance matrix.

Exp.	MRR	TWR	R_a	Recast layer thickness
*L*1	0.0554	4.125	5.0444	0.2214
*L*2	0.2297	3.0982	6.378	0.2923
*L*3	0.1575	2.1325	5.301	0.3277
*L*4	0.2307	3.9872	5.135	0.1742
*L*5	0.1758	3.5280	5.4437	0.2982
*L*6	0.1060	2.9682	4.0937	0.4669
*L*7	0.2666	5.6324	6.8372	0.2337
*L*8	0.1083	2.5554	4.6398	0.5074
*L*9	0.1097	1.9895	5.2216	0.5280
SOS	0.27084017	110.5288927	262.5260852	1.16996348

Table 5: Normalized decision matrix.

Exp.	MRR	TWR	R_a	Recast layer thickness
*L*1	0.106451853	0.39236119	0.311331659	0.204687567
*L*2	0.441371672	0.294694167	0.393639149	0.270235663
*L*3	0.302638391	0.202838846	0.327168568	0.302963486
*L*4	0.443293186	0.379253948	0.316923335	0.16105047
*L*5	0.33780209	0.335575825	0.335975766	0.2756903
*L*6	0.203680441	0.282328845	0.252656096	0.43165594
*L*7	0.512275524	0.535741859	0.42198018	0.216059098
*L*8	0.208099922	0.24306419	0.286360445	0.469098787
*L*9	0.210790041	0.189236991	0.322268137	0.488143791

3.2.1. TOPSIS Optimization for Brass Wire

Stage 1. Determination of a Performance Matrix

To calculate the performance matrix, first, we need to calculate the sum of squares for R_a, TWR, MRR, and thickness of the recast layer as shown in Table 3. The performance matrix is shown in Table 4.

Stage 2. Calculation of the Normalized Decision Matrix

The formula for calculating normalized decision matrix is denoted in equation (1). Table 5 depicts the normalized decision matrix table.

$$z_{ij} = \frac{x_{ij}}{\sqrt{\left(\sum x_{ij}^2\right)}}. \quad (1)$$

Stage 3. Calculation of Weighted Normalized Decision Matrix

Weights are being allocated based the importance of the attributes. All response parameters are considered as beneficial attributes. Hence, the weights of equal percentage of 0.25 are allotted for all the response parameters. Based on the importance of the attributes, any value can be chosen by the decision maker, but the total weights must be equal to one [14,15]. Weights of attributes are shown in Table 6. The weighted normalized matrix is shown in Table 7.

Table 6: Weights of the response parameters.

MRR	TWR	R_a	Recast layer thickness
0.25	0.25	0.25	0.25

The weighted normalized matrix can be calculated by using

$$A_{ij} = W_{ij} \times Z_{ij}. \quad (2)$$

Stage 4. Determination of the Ideal (B_i^+) and (B_i^-)

The ideal best and worst are given in Table 8:

Table 7: Weighted normalized matrix.

Exp.	MRR	TWR	R_a	Recast layer thickness
*L*1	0.026612963	0.098090298	0.077832915	0.051171892
*L*2	0.110342918	0.073673542	0.098409787	0.067558916
*L*3	0.075659598	0.050709711	0.081792142	0.075740871
*L*4	0.110823296	0.094813487	0.079230834	0.040262618
*L*5	0.084450522	0.083893956	0.083993941	0.068922575
*L*6	0.05092011	0.070582211	0.063164024	0.107913985
*L*7	0.128068881	0.133935465	0.105495045	0.054014775
*L*8	0.052024981	0.060766048	0.071590111	0.117274697
*L*9	0.05269751	0.047309248	0.080567034	0.122035948

Table 8: Determination of ideal (B_i^+) and ideal (B_i^-).

	MRR	TWR	R_a	Recast layer thickness
B_i^+	0.128068881	0.047309248	0.063164024	0.040262618
B_i^-	0.026612963	0.133935465	0.105495045	0.122035948

Table 9: Euclidian distance between ideal (B_i^+) and ideal (B_i^-).

Exp.	K_i^+	K_i^-
*L*1	0.114918262	0.084093899
*L*2	0.054741552	0.116876655
*L*3	0.066060649	0.109713992
*L*4	0.053030230	0.126485555
*L*5	0.067054312	0.095564971
*L*6	0.105215356	0.081214637
*L*7	0.097391676	0.122148202
*L*8	0.109387474	0.158989338
*L*9	0.112563697	0.162477728

(1) Ideal positive solu. = V_j^+ (min or max)

(2) Ideal negative solu. = Vj^- (min or max)

Stage 5. Calculate the Euclidian distance between ideal (B_i^+) and ideal (B_i^-) using equations (3) and (4). The calculated Euclidian distance is shown in Table 9.

$$K_i^+ = \left[\sum \left(B_i^+ - A_{ij}\right)^2\right]^{0.5}, \quad (3)$$

$$K_i^- = \left[\sum \left(B_i^- - A_{jj}\right)^2\right]^{0.5}. \quad (4)$$

Stage 6. Determine the relative performance closeness to the ideal solu. using equation (5).

Table 10 shows the relative performance closeness.

$$P_i = \frac{K_i^-}{k_i^+ + k_i^-}. \quad (5)$$

Stage 7. Ranking of the Performance Matrix

$0 < P_i < 1$, closest to 1 is preferred. Table 11 shows the rank of the performance matrix.

Figure 2 shows the graph of P_i versus rank for heat-treated brass as tool.

Table 10: Relative performance closeness.

Exp.	P_i
*L*1	0.422556586
*L*2	0.681027133
*L*3	0.624174177
*L*4	0.704592941
*L*5	0.587660758
*L*6	0.435630747
*L*7	0.556382753
*L*8	0.592410860
*L*9	0.590739116

Table 11: Ranking of the performance matrix.

Exp.	P_i	Rank
*L*1	0.422556586	9
*L*2	0.681027133	2
*L*3	0.624174177	3
*L*4	0.704592941	1
*L*5	0.587660758	4
*L*6	0.435630747	8
*L*7	0.556382753	7
*L*8	0.592410860	5
*L*9	0.590739116	6

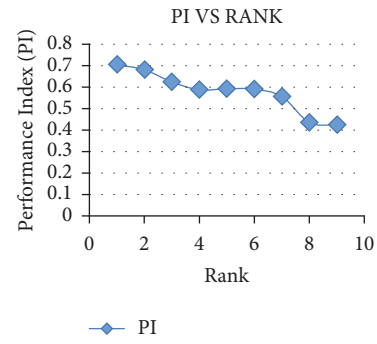

Figure 2: P_i versus rank for heat-treated brass wire as tool.

3.2.2. TOPSIS Optimization for Zinc-Coated Brass Wire

Stage 8. Determination of Performance Matrix

To calculate the performance matrix, first, we need to calculate the sum of squares for R_a, TWR, MRR, and the thickness of the recast layer shown in Table 12. The performance matrix is shown in Table 13.

Table 12: Design of experiments using zinc-coated brass wire as a tool.

Exp.	T_{on} (μs)	T_{off} (μs)	I_p (A)	Wire feed (m/min)	Material removal rate (g/min)	R_a (μm)	Recast layer thickness (mm)	Tool wear rate (g/min)
*L*1	40	6	2	80	2.222×10^{-1}	3.9952	0.3327	3.0555
*L*2	40	10	3	90	1.946×10^{-1}	4.4327	0.1802	2.8224
*L*3	40	14	4	100	1.509×10^{-1}	6.0951	0.1963	1.8868
*L*4	60	6	3	100	4.441×10^{-1}	4.6747	0.3235	3.8490
*L*5	60	10	4	80	3.303×10^{-1}	4.6796	0.3627	3.0238
*L*6	60	14	2	90	5.915×10^{-1}	4.9992	0.2880	1.0353
*L*7	80	6	4	90	5.333×10^{-1}	4.7921	0.4032	4.9777
*L*8	80	10	2	100	1.439×10^{-1}	4.1095	0.2954	1.3087
*L*9	80	14	3	80	1.363×10^{-1}	6.6128	0.3452	1.4366

Table 13: Determination of performance matrix.

Exp.	MRR	TWR	R_a	Recast layer thickness
*L*1	0.222	3.0555	3.9952	0.3327
*L*2	0.1946	2.8224	4.4327	0.1802
*L*3	0.1509	1.8868	6.0951	0.1963
*L*4	0.4441	3.849	4.6747	0.3235
*L*5	0.3303	3.0238	4.6796	0.3627
*L*6	0.5915	1.0353	4.9992	0.288
*L*7	0.5333	4.9777	4.7921	0.4032
*L*8	0.1439	1.3087	4.1095	0.2954
*L*9	0.1363	1.4366	6.6128	0.3452
SOS	1.08981291	74.44606232	225.0855097	0.869837

Table 14: Normalized decision matrix.

Exp.	MRR	TWR	R_a	Recast layer thickness
*L*1	0.212655686	0.354128942	0.266296069	0.356725259
*L*2	0.186408994	0.327112920	0.295457195	0.193212779
*L*3	0.144548392	0.218677954	0.406262809	0.210475408
*L*4	0.425407164	0.446094681	0.311587464	0.346860900
*L*5	0.316397177	0.350454949	0.311914069	0.388891649
*L*6	0.566602876	0.119990081	0.333216688	0.308797339
*L*7	0.510852602	0.576909716	0.319412644	0.432316275
*L*8	0.137843033	0.151676828	0.273914622	0.316731715
*L*9	0.130562928	0.166500291	0.440769586	0.370127922

Stage 9. Calculation of Normalized Decision Matrix

The formula for calculating normalized decision matrix is denoted as follows. Table 14 depicts the normalized decision matrix table.

$$z_{ij} = \frac{x_{ij}}{\sqrt{\left(\sum x_{ij}^2\right)}}. \tag{6}$$

Stage 10. Calculation of Weighted Normalized Decision Matrix

Weights are being allocated based the importance of the attributes. All response parameters are considered as beneficial attributes. So, the weights of equal percentage of 0.25 are allotted for all the response parameters [14,15]. The weights of attributes are presented in Table 15. The weighted normalized matrix is shown in Table 16.

We can calculate the weighted normalized matrix using

Table 15: Weights of the response parameters.

MRR	TWR	R_a	Recast layer thickness
0.25	0.25	0.25	0.25

$$A_{ij} = W_{ij} \times Z_{ij}. \tag{7}$$

Stage 11. Determination of the Ideal (B_i^+) and (B_i^-)

The ideal best and worst are given in Table 17:

(1)Ideal positive solu. = V_j^+ (min or max).

(2) Ideal negative solu. = Vj^- (min or max).

Stage 12. Calculate the Euclidian distance between ideal (B_i^+) and ideal (B_i^-) using equations (8) and (9). The calculated Euclidian distance is shown in Table 18.

Table 16: Weighted normalized matrix.

Exp.	MRR	TWR	R_a	Recast layer thickness
*L*1	0.053163922	0.088532236	0.066574017	0.089181315
*L*2	0.046602248	0.08177823	0.073864299	0.048303195
*L*3	0.036137098	0.054669488	0.101565702	0.052618852
*L*4	0.106351791	0.11152367	0.077896866	0.086715225
*L*5	0.079099294	0.087613737	0.077978517	0.097222912
*L*6	0.141650719	0.02999752	0.083304172	0.077199335
*L*7	0.127713150	0.144227429	0.079853161	0.108079069
*L*8	0.034460758	0.037919207	0.068478655	0.079182929
*L*9	0.032640732	0.041625073	0.110192396	0.092531980

Table 17: Determination of the ideal (B_i^+) and ideal (B_i^-).

	MRR	TWR	R_a	Recast layer thickness
B_i^+	0.141650719	0.02999752	0.066574017	0.048303195
B_i^-	0.032640732	0.144227429	0.110192396	0.108079069

Table 18: Euclidian distance between the ideal (B_i^+) and ideal (B_i^-).

Exp.	K_i^+	K_i^-
*L*1	0.113698051	0.076045013
*L*2	0.108483187	0.094803545
*L*3	0.113951187	0.105750200
*L*4	0.097448542	0.089455414
*L*5	0.098769988	0.080740933
*L*6	0.033389893	0.163120152
*L*7	0.130354204	0.099795962
*L*8	0.111846441	0.117812451
*L*9	0.126004467	0.103773578

$$K_i^+ = \left[\sum \left(B_i^+ - A_{ij}\right)^2\right]^{0.5}, \tag{8}$$

$$K_i^- = \left[\sum \left(B_i^- - A_{jj}\right)^2\right]^{0.5}. \tag{9}$$

Stage 13. Determine the relative performance closeness to the ideal solu. using equation (10).

Table 19 shows the relative performance closeness.

$$P_i = \frac{K_i^-}{k_i^+ + k_i^-}. \tag{10}$$

Stage 14. Rank the performance matrix.

$0 < P_i < 1$, closest to 1 is preferred. Table 20 shows the rank of the performance matrix.

Figure 3 shows the graph of P_i versus rank for zinc-coated wire as a tool.

3.3. Field Emission Scanning Electron Microscopy (FESEM) Analysis. The machined surfaces of Ti-6Al-4V machined using heat-treated brass and zinc-coated brass tool were undergone with SEM analysis. The surface cracks were not noticed on the machined surfaces. The SEM photographs of machined surface using heat-treated brass tool are shown in Figures 4–7. The machined surface was with overlapping craters, cavities, pile of debris, and rippled surface. This is due to the applied stress, melting, and solidification of the machined surface. Zinc-coated brass tool machined surface had lesser craters, cavities, and rippled surface. The absence of dimples and river marking on the machined surface

Table 19: Relative performance closeness to the ideal solu.

Exp.	P_i
*L*1	0.400778880
*L*2	0.466353825
*L*3	0.481336058
*L*4	0.478617017
*L*5	0.449782846
*L*6	0.830085565
*L*7	0.433612382
*L*8	0.512988850
*L*9	0.451625297

Table 20: Rank of the performance matrix.

Exp.	P_i	Rank
*L*1	0.40077888	9
*L*2	0.466353825	5
*L*3	0.481336058	3
*L*4	0.478617017	4
*L*5	0.449782846	7
*L*6	0.830085565	1
*L*7	0.433612382	8
*L*8	0.512988850	2
*L*9	0.451625297	6

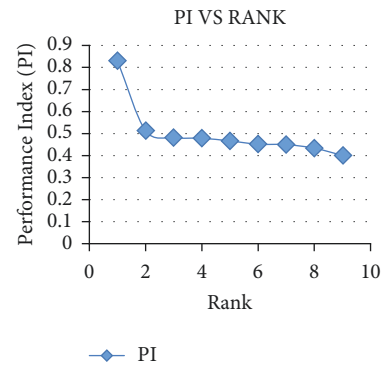

Figure 3: P_i versus rank for zinc-coated wire as a tool.

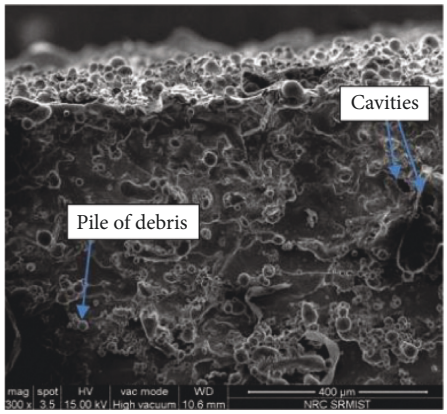

Figure 4: Machined surface using heat-treated brass tool with 300x magnification.

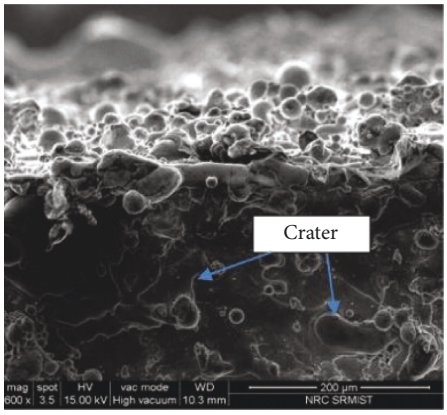

Figure 5: Machined surface using heat-treated brass tool with 600x magnification.

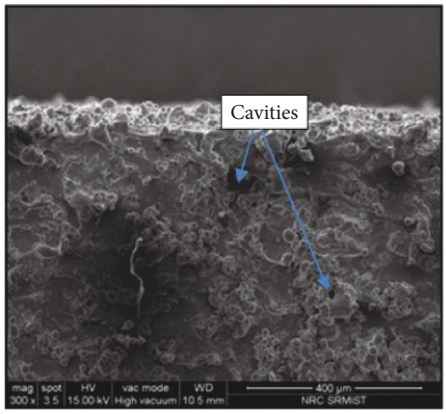

Figure 6: Machined surface using zinc-coated tool with 300x magnification.

confirms the absence of surface cracks. The formation of surface cracks was due to high fluctuating stresses applied during the process of machining. Similar kind of observation was reported on wire EDM machine surfaces [27–31].

3.4. Energy Dispersion Spectroscopy (EDS). Energy Dispersion Spectroscopy is a methodology used to find changes in

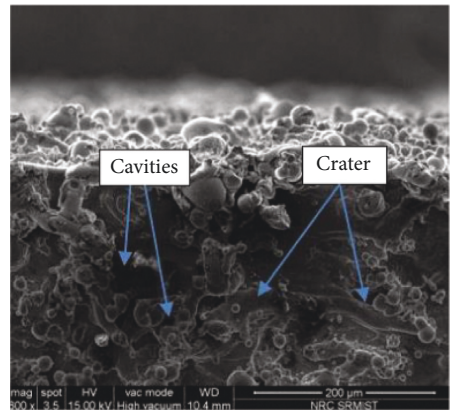

Figure 7: Machined surface using zinc-coated tool with 600x magnification.

the material composition of the workpiece. The EDS results were obtained from the same equipment that was used for getting the SEM results. The EDS conducted at the machined edge of the workpiece revealed certain changes in the composition of the material. Carbon and oxygen deposits were found at the edges. Traces of metals like sodium (Na), barium (Ba), and zinc (Zn) were found. Based on these, certain assumptions can be made about these depositions. They are assumed to be deposited on the workpiece from the electrolyte used.

The EDS analysis is taken based on TOPSIS optimization of the performance closeness. For brass wire, *L*4 (Figure 8) is being ranked first based on performance closeness and hence the EDS analysis is conducted on that particular specimen and the same for zinc-coated brass wire, *L*6 (Figure 9) is being ranked first based on performance closeness and hence EDS analysis is conducted on that particular specimen. The titanium percentage after machining was found to be 55.05% for zinc-coated brass wire whereas it was 51.58% for brass wire, from which it can be inferred that there has been no change in the property when the zinc-coated brass wire was used, whereas the aluminum composition dropped from 5.992% to 3.33% for zinc-coated brass wire. Due to WEDM process, some amount of oxidation has taken place, which results in the presence of oxygen and carbon deposits. The change in composition of the machined surface was due to the melting and solidification of the machined surface. Similar kind of change in composition of the workpiece was observed in previously undergone research work in wire EDM process [29,31].

3.5. Response Value Table Using Closeness Value. To narrow down to the best possible combinations of the input parameters, the response table has been formulated using the Minitab 17 software. The process parameters such as $\boldsymbol{T_{on}}$, $\boldsymbol{T_{off}}$, $\boldsymbol{I_p}$, and Wire-feed are represented as **A**, **B**, **C**, and **D**, respectively.

From Table 21 and Figure 10, it is found that the optimized combination of the input parameters is $\mathbf{A_3B_2C_2D_3}$. It denotes that the results obtained from the above combination get the best in class output. The output parameters

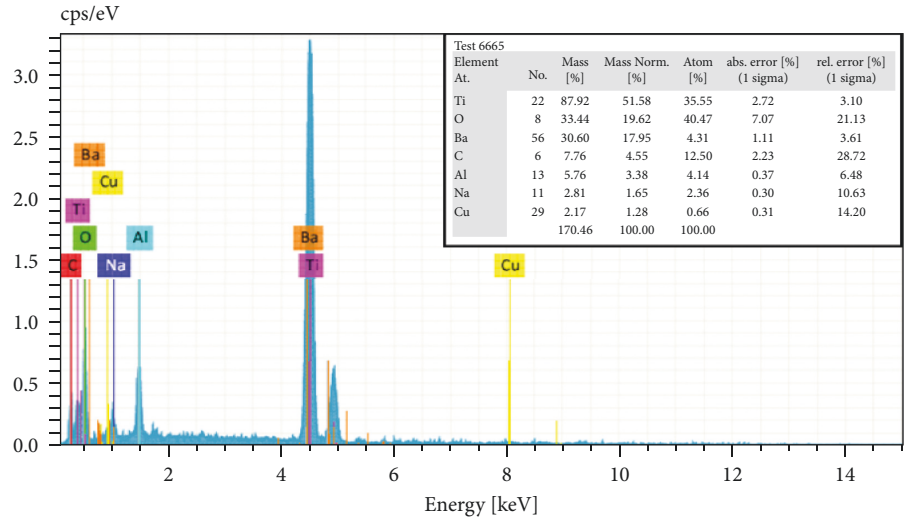

Figure 8: EDS analysis for *L*4 workpiece using brass wire as a tool.

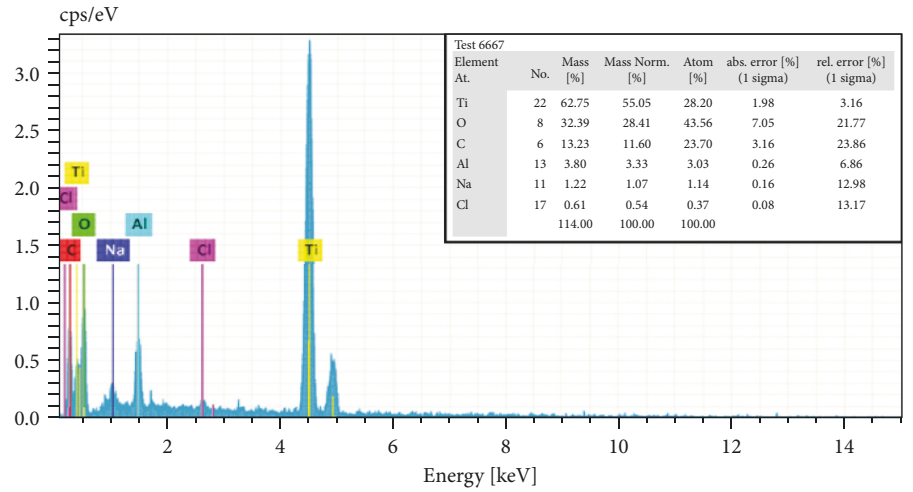

Figure 9: EDS analysis for *L*6 workpiece using zinc-coated brass wire as a tool.

Table 21: Response table for brass wire.

Level	T_{on}	T_{off}	I_p	Wire feed
1	0.5759	0.5612	0.4835	0.5337
2	0.576	0.6204	0.6588	0.5577
3	0.5798	0.5502	0.5894	0.6404
Rank	3	2	2	3

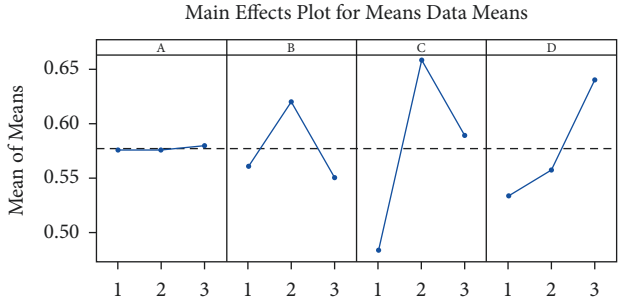

Figure 10: Main effects plot for means for brass wire.

having the following values as $T_{on} = 40\,\mu$ sec, $T_{off} = 10\,\mu$ sec, $I_p = 3$ A, and wire feed = 100 m/min deliver the best outcome.

Similarly, from Table 22 and Figure 11 above, it is found that the optimized combination of the input parameters is $\mathbf{A_2B_3C_1D_2}$. It denotes that the results obtained from the above combination get the best in class output. The output parameters having the following values as $T_{on} = 40\,\mu$s, $T_{off} = 14\,\mu$s, $I_p = 2$ A, and wire feed = 90 m/min deliver the best outcome. Thus, from the above two response tables and graphs of the main effects plot for means, we can conclude that zinc-coated brass wire had a better response to the closeness value.

3.6. Confirmation Test. The confirmation has been carried out to check the repeatability of the machine used. The highly ranked specimens have been considered, such as *L*4 and *L*6 for brass and zinc-coated brass wire, respectively. The value obtained for specimen *L*4 for MRR, TWR, Ra, and recast layer thickness were 0.2237, 3.821, 4.9210, and 0.1675,

Table 22: Response table for zinc-coated brass wire.

Level	T_{on}	T_{off}	I_p	Wire feed
1	0.4495	0.4377	0.5813	0.4341
2	0.5862	0.4764	0.4655	0.5767
3	0.4661	0.5877	0.4549	0.491
Rank	2	3	1	2

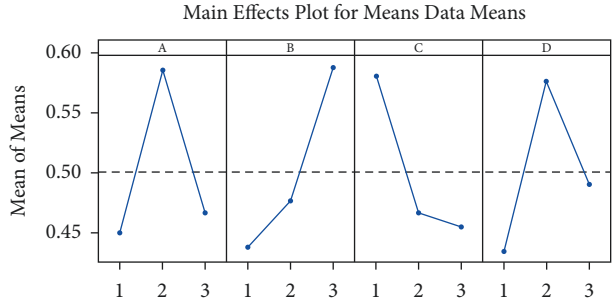

Figure 11: Main effects plot for means for zinc-coated brass wire.

respectively. Similarly, for specimen *L6*, the values obtained were 0.5723, 0.9891, 4.8442, and 0.2791, respectively. From this, it can be concluded that the values produced by the confirmation test are having an error percentage below 5%, which proves that the repeatability factor of the machine is good.

4. Conclusion

Ti-6Al-4V is successfully machined using heat-treated brass and zinc-coated brass tool. The following results were obtained:

(i) Zinc-coated brass tool produced better productivity and surface quality compared to the heat-treated brass tool.

(ii) Zinc-coated brass tool produced lesser recast layer compared to heat-treated brass tool.

(iii) Lower tool wear rate was observed in zinc-coated tool compared to heat-treated brass.

(iv) From TOPSIS optimization, *L4* is ranked first based on the performance score for brass wire and *L6* is ranked first based on the performance score for zinc-coated brass wire.

(v) The SEM of machined surface showed the presence of overlapping craters, cavities, pile of debris, and rippled surface.

(vi) The 6.30% decrease in titanium content in Ti-6Al-4V was observed in heat-treated brass tool when compared to zinc-coated brass tool.

(vii) From this experimental investigation, there were 54.93% increase in MRR, 2.40% decrease in surface roughness, and 3.44% increase in recast layer and 47.96% decrease in tool wear rate was observed in zinc-coated tool compared to heat-treated brass tool. The zinc coating has improved the productivity, surface quality with minimal change in the composition of Ti-6Al-4V.

Data Availability

The data used to support the findings of this study are included in the article.

Conflicts of Interest

The authors declare that they have no conflicts of interest regarding the publication of this paper.

References

[1] Arikatla, S. Prasad, K. Tamil Mannan, A. Krishnaiah, and Ch V. Krishna Rao, "Surface integrity of wire electrical discharge machined surface of titanium alloy,".

[2] A. Vs Ram Prasad, K. Ramji, and B. Raghu Kumar, "Study of wire-electrical discharge machining parameters of titanium alloy by using Taguchi method," *International Journal of Engineering & Technology*, vol. 7, pp. 10–12, 2018.

[3] S. A. Sonawane and M. L. Kulkarni, "Multi-response optimization of wire electrical discharge machining for titanium grade-5 by weighted principal component analysis," *International Journal of Engineering and Technology Innovation*, vol. 8, no. 2, p. 133, 2018.

[4] T. Jadam, S. Datta, and M. Masanta, "Study of surface integrity and machining performance during main/rough cut and trim/finish cut mode of WEDM on Ti–6Al–4V: effects of wire material," *Journal of the Brazilian Society of Mechanical Sciences and Engineering*, vol. 41, no. 3, pp. 1–23, 2019.

[5] A. Pramanik and A. K. Basak, "Effect of wire electric discharge machining (EDM) parameters on fatigue life of Ti-6Al-4V alloy," *International Journal of Fatigue*, vol. 128, p. 105186, 2019.

[6] K. Palanikumar, S. B. Boppana, and E. Natarajan, "Analysis of chip formation and temperature measurement in machining of titanium alloy (Ti-6Al-4V)," *Experimental Techniques*, pp. 1–13, 2022.

[7] H. Akkuş and H. Yaka, "Optimization of cutting parameters in turning of titanium alloy (grade 5) by analysing surface roughness, tool wear and energy consumption," *Experimental Techniques*, pp. 1–12, 2021.

[8] M. Aydın, "Numerical study of chip formation and cutting force in high-speed machining of Ti-6Al-4V bases on finite element modeling with ductile fracture criterion," *International Journal of Material Forming*, vol. 14, no. 5, pp. 1005–1018, 2021.

[9] L. Rao and N. Selvaraj, "Optimization of WEDM process parameters on titanium alloy using Taguchi method," *International Journal of Modern Engineering Research (IJMER)*, vol. 3, no. 4, pp. 2281–2286, 2013.

[10] S. Kumar, S. Dhanabalan, and C. S. Narayanan, "Application of ANFIS and GRA for multi-objective optimization of optimal wire-EDM parameters while machining Ti–6Al–4V alloy," *SN Applied Sciences*, vol. 1, no. 4, pp. 1–12, 2019.

[11] A. Pramanik, A. K. Basak, and C. Prakash, "Understanding the wire electrical discharge machining of Ti6Al4V alloy," *Heliyon*, vol. 5, no. 4, 4 pages, Article ID e01473, 2019.

[12] R. Chalisgaonkar, J. Kumar, and P. Pant, "Prediction of machining characteristics of finish cut WEDM process for pure titanium using feed forward back propagation neural

network," *Materials Today Proceedings*, vol. 25, pp. 592–601, 2020.

[13] F. L. Amorim, R. Diego Torres, C. A. Henning Laurindo, and L. Watanabe Reolon, "Performance and surface integrity of wire electrical discharge machining of thin Ti6Al4V plate using coated and uncoated wires," *Materials Research*, vol. 22, 2019.

[14] L. Srinivasan, K. Mohammad Chand, T. Deepan Bharathi Kannan, P. Sathiya, and S. Biju, "Application of GRA and TOPSIS optimization techniques in GTA welding of 15CDV6 aerospace material," *Transactions of the Indian Institute of Metals*, vol. 71, no. 2, pp. 373–382, 2018.

[15] V. S. Gadakh, "Parametric optimization of wire electrical discharge machining using TOPSIS method," *Advances in Production Engineering & Management*, vol. 7, no. 3, pp. 157–164, 2012.

[16] S. Senkathir, R. Aravind, R. Manoj Samson, and A. C. Arun Raj, "Optimization of machining parameters of Inconel 718 by WEDM using Response surface methodology," in *Advances in Manufacturing Processes*, pp. 383–392, Springer, Singapore, 2019.

[17] S. Senkathir, A. C. Arun Raj, and M. S. R. Vaddi Thulasikanth, "Performance analysis of process parameters on machining of Inconel 718 using electrical discharge machining with brass electrode,".

[18] S. Ramesh, L. Karunamoorthy, and K. Palanikumar, "Surface roughness analysis in machining of titanium alloy," *Materials and Manufacturing Processes*, vol. 23, no. 2, pp. 174–181, 2008.

[19] A. Pramanik and A. K. Basak, "Sustainability in wire electrical discharge machining of titanium alloy: understanding wire rupture," *Journal of Cleaner Production*, vol. 198, pp. 472–479, 2018.

[20] M. Mahalingam and R. Varahamoorthi, "Investigation on tool wear rate of brass tool during machining of Monel 400 alloy using electric discharge machine," *Materials Today Proceedings*, vol. 26, pp. 1213–1220, 2020.

[21] G. Singh, A. S. Bhui, and L. Singh, "On the assessment of material removal rate and surface characteristics of Ti-6Al-4V processed by WEDM," *Engineering Research Express*, vol. 1, Article ID 015038, 2019.

[22] D. Devarasiddappa, M. Chandrasekaran, and R. Arunachalam, "Experimental investigation and parametric optimization for minimizing surface roughness during WEDM of Ti6Al4V alloy using modified TLBO algorithm," *Journal of the Brazilian Society of Mechanical Sciences and Engineering*, vol. 42, no. 3, pp. 1–18, 2020.

[23] T. Muthuramalingam, A. Ramamurthy, K. Sridharan, and S. Ashwin, "Analysis of surface performance measures on WEDM processed titanium alloy with coated electrodes," *Materials Research Express*, vol. 5, no. 12, Article ID 126503, 2018.

[24] D. Welling, "Results of surface integrity and fatigue study of wire-EDM compared to broaching and grinding for demanding jet engine components made of Inconel 718," *Procedia CIRP*, vol. 13, pp. 339–344, 2014.

[25] N. Musa, J. B. Saedon, and M. S. Adenan, "An investigation on the surface integrity of grade 5 titanium alloy proceeding the wire electro-discharge machining (WEDM) process," in *Applied Mechanics and Materials*vol. 899, , pp. 144–155, Trans Tech Publications Ltd, 2020.

[26] S. Malik and V. Singla, "Experimental investigation of surface integrity and machining characteristics of Ti-6Al-4V alloy machined by wire-EDM process," in *Advances in Materials Processing*, pp. 139–152, Springer, Singapore, 2020.

[27] S. K. Sahoo, A. Bara, A. K. Sahu et al., "Analysis and optimization of wire EDM process of titanium by using GRA methodology," in *Materials Science Forum*vol. 969, , pp. 678–684, Trans Tech Publications Ltd, 2019.

[28] S. Pradhan, M. Priyadarshini, and S. K. Mohapatra, "Multi-objective optimization of process parameter during dry turning of grade 5 titanium alloy with carbide inserts: hybrid fuzzy-TOPSIS approach," in *Advances in Intelligent Manufacturing*, pp. 51–58, Springer, Singapore, 2020.

[29] P. P. Das, S. Chakraborty, and S. Chakraborty, "A grey correlation-based TOPSIS approach for optimization of surface roughness and micro hardness of Nitinol during WEDM operation," *Materials Today Proceedings*, vol. 28, pp. 568–573, 2020.

[30] V. Manoharan, S. Tamilperuvalathan, E. Natarajan, and P. Ponnusamy, "Experimental investigation on electrochemical discharge machining of zirconia," in *Recent Advances in Manufacturing, Automation, Design and Energy Technologies*, pp. 27–34, Springer, Singapore, 2022.

[31] P. Nagarajan, P. K. Murugesan, and E. Natarajan, "Optimum control parameters during machining of LM13 aluminum alloy under dry electrical discharge machining (EDM) with a modified tool design," *Materials Science*, vol. 25, no. 4, pp. 407–412, 2019.

Hindawi
Advances in Materials Science and Engineering
Volume 2022, Article ID 3166547, 6 pages
https://doi.org/10.1155/2022/3166547

Research Article

Analysis of the Thermal Effects on the Behaviour of Steel Connection Beam Section

Seelam Srikanth,[1] **Sai Nitesh KJN**,[2] **Chunchu Bala Rama Krishna**,[1] **Vasugi K**,[3] **Cheerla Prabhu Teja**,[4] **Sesha Rao Y**,[5] **Sanjeev Kumar**,[6] **and Dumesa Gudissa Lemu**[7]

[1]*School of Civil Engineering, REVA University, Bengaluru, Karnataka 560064, India*
[2]*Department of Civil Engineering, Anurag Group of Institutions, Hyderabad, Telangana 500038, India*
[3]*School of Civil Engineering, VIT University, Chennai 600127, Tamil Nadu, India*
[4]*Department of Civil Engineering, Aditya College of Engineering, Surampalem, Andhra Pradesh, India*
[5]*Department of Mechanical Engineering, QIS College of Engineering and Technology, Ongole, Andhra Pradesh, India*
[6]*Department of Civil Engineering, Graphic Era Deemed to be University, Bell Road Clement Town 248002, Dehradun, Uttarakhand, India*
[7]*Department of Civil Engineering, Ambo Institute of Technology-19, Ambo University, Ambo, Ethiopia*

Correspondence should be addressed to Seelam Srikanth; srikanths.reddy@reva.edu.in and Dumesa Gudissa Lemu; dumessa.gudissa@ambou.edu.et

Received 3 March 2022; Revised 12 May 2022; Accepted 23 May 2022; Published 21 June 2022

Academic Editor: Thanigaivelan R

Steel connection is utilized to link the beam and column. It moves the plastic hinge structure away at a predetermined distance from the face of the column. To lower the cross-sectional area of the beam flanges, several shape cuts (uniform, radius, taper, and straight cut) are available, and a piece of the beam flanges at the column face is purposefully intended to yield and plastic hinge. The use of a lowered beam section connection reduces stress absorption since the criteria for a strong column–weak beam are met. The ANSYS 14.5 software was used to model four types of reduced beam sections by decreasing the beam flange. In various patterns, fatigue behaviour was studied. The objective of this project is to evaluate the deformations, stresses and transient temperatures deformations, and stresses of the reduced beam section at static structural analysis. In comparison to other connections, steel connection reduced beam section ductile and dissipated energy more. A nonlinear finite element software was used, along with a static study of exhaustion responsiveness transient temperatures. The analysis is carried out to identify the thermal effects on the behaviour of material properties in the elastic and plastic regions. The members with cuts have performed superior in comparison with members without cuts.

1. Introduction

In and near the heat-affected zones, the bolted web-welded flange moment connections in steel moment-resisting frames had unanticipated brittle failures [1]. The Northridge earthquake [2] caused a great deal of damage to people and property. Many industrial steel structures suffered significant damage [3]. Following the Northridge earthquake, many changes have been proposed for new building and steel moment. Many of the suggestions in FEMA 350 [4] have now been incorporated into the Provisions for Structural Steel Buildings of the American Institute of Steel Construction (AISC Seismic) [5]. The welded junction between the bottom flange of a girder and the supporting flange of a column was the most commonly damaged region. All of the steel moment-resisting frames connections that were approved in combined advancements in welding with details caused the beam plastic hinge to form a short distance away from the beam-to-column interface in order for the beam plastic hinge to form a short distance away from the beam-to-column interface. Strengthening details and decreased beam section detailing are the two primary forms of detailing that relocate

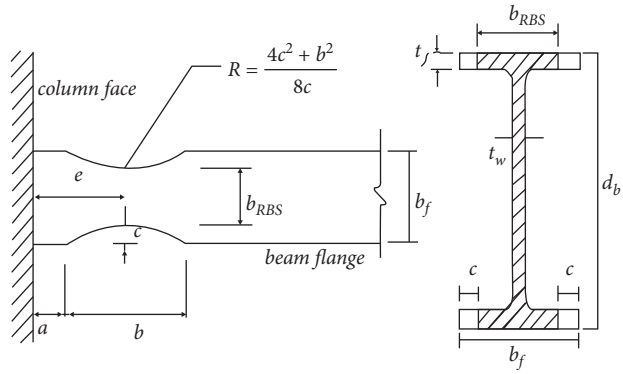

Figure 1: Geometrical details of reduced beam section.

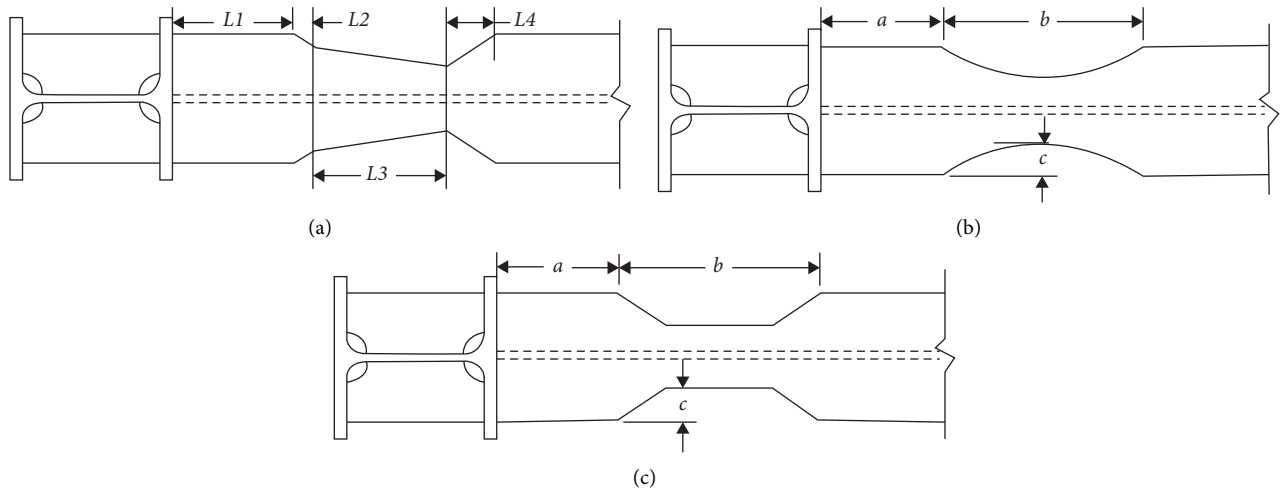

Figure 2: Geometrical details of the reduced beam section model.

the plastic hinges away from the connection region [6]. Connections provide a lot of advantages in design practice [7]. When compared to reinforced connections, they do not require continuity plates, panel zone reinforcement, or strong column–weak beam criteria. Due to the poor performance of pre-Northridge moment connections, researchers began to examine the reasons of failure and create new connections for repair, restoration, and new construction [8]. The current investigation could reduce the failure at beam–column connection.

The use of moment-resistant connections in steel constructions has been recommended as a solution by the Federal Emergency Management Agency (FEMA) 350, 351 [9]. Some other reasons why we use RBS is that it reduces stresses and deformation and we can reduce the cost in that particular area of cross-section. Other objective is to construct a connection which is cost-effective. This study helps in the investigation of suitable location of reduced beam section in buildings. The scope is to analyze the steel structure with RBS to that of steel structure without RBS [10]. First, the model is implemented into known computer software ANSYS 14.5 without RBS, and then, it is analyzed by introducing RBS in the model for the investigation of total von Mises stresses, total deformations, and nonlinear finite element software used, along with a static study of exhaustion responsiveness transient temperatures [11]. The analysis is carried out to identify the thermal effects on the behaviour of material properties in the elastic and plastic regions. In addition, severe nonlinear deformation was studied.

Table 1: Material properties of steel section.

"Density	7.85e−006 kg·mm^{-3}
Coefficient of thermal expansion	1.2e−005 C^{-1}
Specific heat	4.34e + 005 m·J·kg^{-1}C^{-1}
Thermal conductivity	6.05e−002 Wmm^{-1}C^{-1}
Resistivity	1.7e−004 ohm mm"

2. Geometrical Details of Reduced Beam Section Models

In the structural steel used for this investigation, grades were taken into account. Connections without RBS were labelled as "WRBS," while connections with RBS were labelled as "RRBS." The TRBS-to-SRBS connection was built in accordance with AISC and FEMA standards [12]. Geometrical detail of reduced beam section is shown in Figure 1. For both

Table 2: Geometrical properties of sections.

FEMA350-2000 (IMF, SMF)	EC8, part 3	AISC 358-05
a = (0.5–0.75) bf	$a = 0.6$ bf	$A = (0.5–0.75)$ bf
b =(0.65–0.85) db	$b = 0.75$ db	$b = (0.65–0.85)$ db
C ≤ 0.25bf	$g = c \leq 0.25$ bf	0.1 bf ≤ $c \leq 0.25$ bf
$s = a + b/2$	$s = a + b/2$	—
$r = (4c^2 + b^2)/8c$	$r = (4g^2 + b^2)/8g$	—

Table 3: Beam section cut details.

W 30 × 283	Radius	Taper	Straight
z (in^3)	278.82	278.82	278.82
Z (in^3)	433.64	433.64	433.64
Zf (in^3)	309.64	309.64	309.64
1-r	0.5	0.5	0.5
a (in)	6.5	6.5	6.5
((1−r) × bf)/2 (in)	2.64	2.64	2.64
e (in)	17	17	17 + 5.8

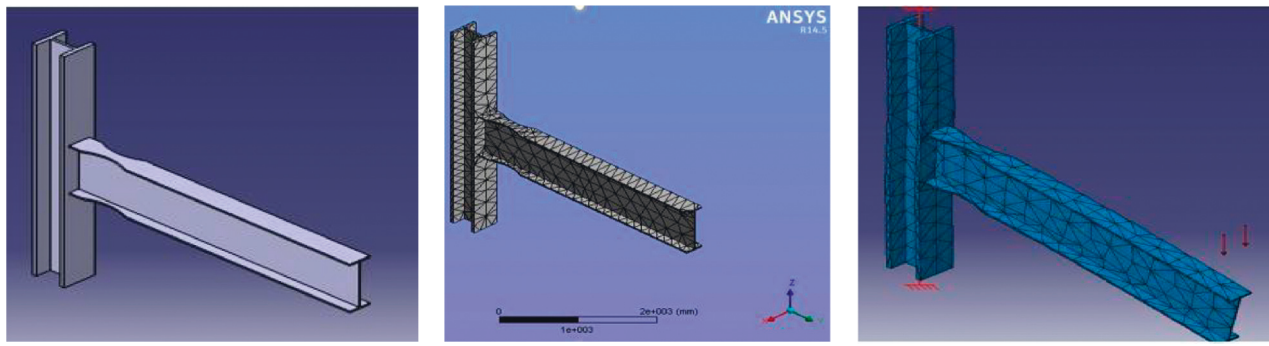

(a) (b) (c)

Figure 3: 3D meshed model of the steel beam. (a) CAD model. (b) Meshed model. (c) Boundary conditions.

panel zones and continuity plates, the design shear strength, required shear strength, and column web/flange thickness limitations were examined. From the outside, the link was a strong-axis connection [13]. Figure 2 shows the geometrical details of the reduced beam section model. Table 1 provides the material properties of steel section. The column's height was 194 inches, while the beam's length from the column's centre was 156 inches. Table 2 provides the list of the other geometrical details. Table 3 provides that doublers plates and continuity plates are not required when the connection strength is computed using the AISC/FEMA formula.

3. Results and Discussion

Figure 3 shows the meshed model for the W30 × 283 as a beam and W14 × 283 as a column connection. Figure 3(a) shows the CAD model of steel beam. Figure 3(b) shows RRBS meshing, and the model was constructed with C3D8T field-variable-dependent conductivity elements. Near the junction, the mesh was fine-tuned. For each of the three model instances, a sensitivity analysis was conducted on the mesh size [14]. The final mesh size was 5 mm, which is course meshing. The column was assumed and boundary conditions as both ends are fixed attached, and the joint beam-to-column element connection is totally restrained in Figure 3(c) [15]. Each subassembly is loaded in the displacement control at the beam free end, as detailed in the preceding portion of the analysis research. W14 283 is used as a column and W30 283 is used as a beam in this study. Specimens are taken into account to be free of continuity plates for this research. Figure 4 shows the static structural analysis at 0.05 rad. TRBS static structural, fatigue, and transient thermal analysis is carried out by importing the (Figure 4(a)) CAD model of TRBS utilized in FEM analysis ANSYS 14.5 workbench. From that, the effectiveness of the results on these models is given [16]. The top and bottom of the beam flange reduction of 50% is applied to all connections. Specimens are considered to be free of continuity plates for this research [1]. This was achieved by putting a 100 kN cyclic load on the beam's flange at a distance and the distance from the support is 147.63 inches [17]. After that, ANSYS was used to execute the static-coupled temperature displacement model by measuring temperatures at various locations of the joint and beam as a function of time [18]. The

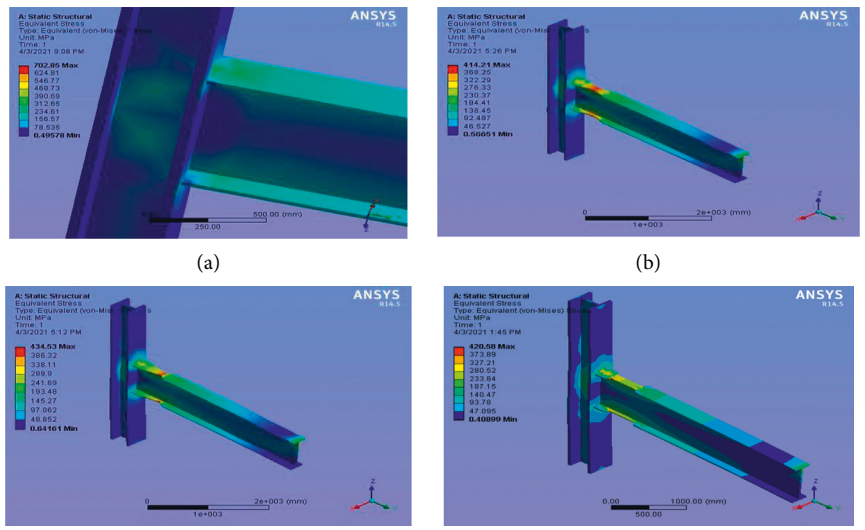

Figure 4: Static structural analysis at 0.05 rad. (a) WRBS. (b) RRBS. (c) TRBS. (d) SRBS.

column's base was thought to be fixed and joined at both ends [19]. The three cuts performed better compared to other cuts as per literature in seismic analysis.

This project is to learn about and compare the behaviour of various cut profiles. The von Mises stress diagrams for all connections between 414 MPa (Figure 4(b)) and 703 MPa (Figure 4(c)) are under static structural conditions [20]. For all connections, the stress intensity in the panel zone ranges from 140 MPa to 235 MPa due to flange reduction of 50% applied to all connections, due to flange reduction of area is 55.38 in^2. Figure 5 shows the static structural von Mises stress distribution at 0.05 rad. Compared to other RBS, WRBS is the most overall static structural von Mises stress equivalent stress distribution at a static.

The maximum static structural total deformations for all connections are between 29.83 mm and 26.238 mm under static structural conditions shown in Figure 6. Flange reduction of 50% is applied to all connections. Flange reduction of area is 55.38 in^2. At a static structural level, in comparison to other RBS, WRBS has the most overall deformations [21]. The value that is displayed next to each colour is static structural total deformations region which is depicted by that particular colour in the model. The blue colour in the model represents the lowest value of the total deformations [22]. Whereas, red colour denotes that the maximum value of the total deformations is 29.83 mm due to flange reduction of 50%. At a static structural level, in comparison to other RBS, WRBS has the most overall deformations.

The value at the temperature 100 centigrade then produces stress distribution. Static structural thermal equivalent (von Mises) stress distribution in TRBS is shown in Figure 7(a) and 810.2 MPa in Figure 7(b). Static structural thermal von Mises stress in SRBS, as shown in Figure 7(c), due to flange reduction of 50%, is applied to all connections due to flange reduction of area is 55.38 in^2. The maximum von Mises stress intensity for all connections is 810.2 MPa, as

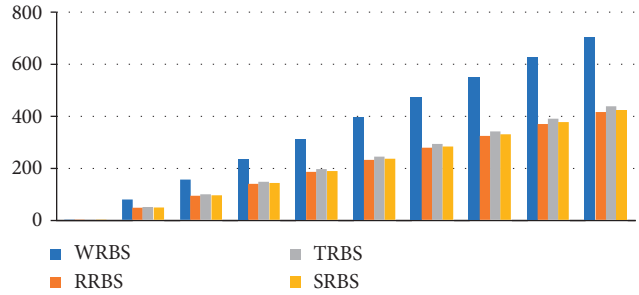

Figure 5: Static structural von Mises stress distribution at 0.05 rad.

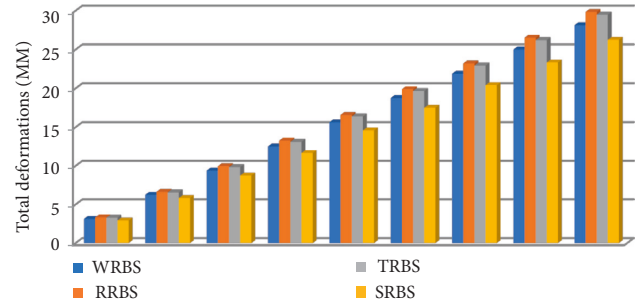

Figure 6: Static structural total deformations at 0.05 rad.

shown in Figure 7(d). Static structural thermal total deformations at 0.05 rad are shown in Figure 8.

The value at the temperature 100 centigrade then produces the value displayed static structural thermal total deformations region depicted by that particular colour in the model. The blue colour in the model represents the lowest value of the total deformations [23]. Static structural transient thermal maximum total deformation for all connections is 97.028 mm, as shown in Figure 9. Static structural thermal incremental deformations in WRBS and 92.66 mm. Static structural transient thermal total deformations, due to

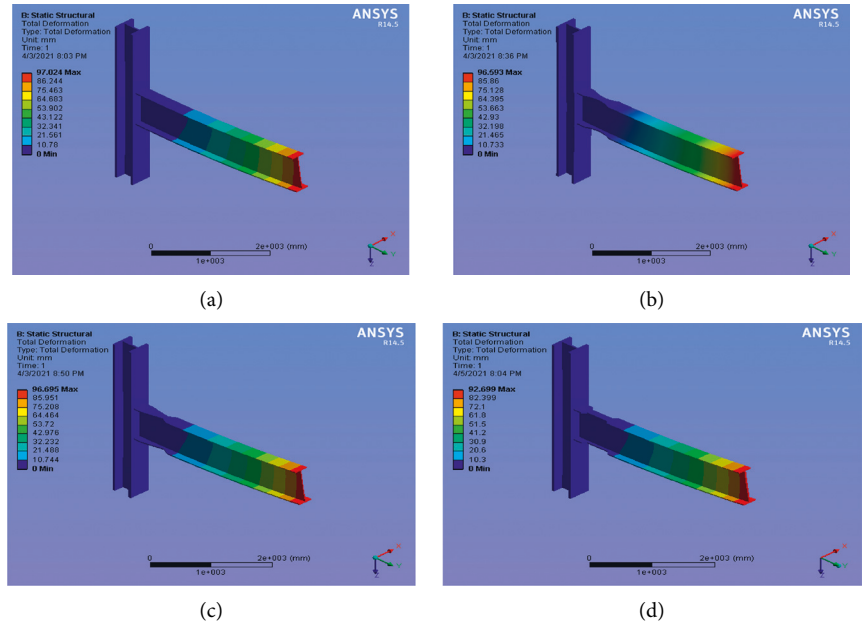

Figure 7: Thermal analysis at 0.05 rad. (a) WRBS. (b) RRBS. (c) TRBS. (d) SRBS.

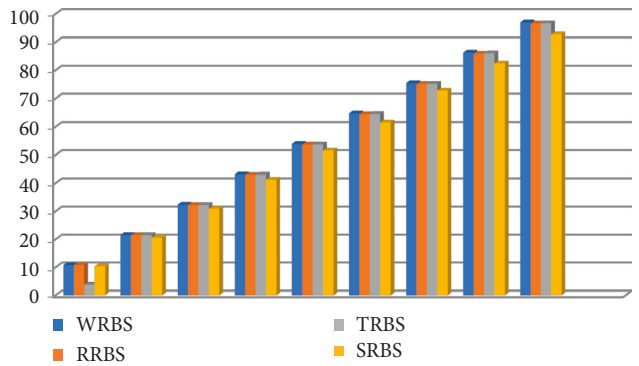

Figure 8: Static structural thermal total deformations at 0.05 rad.

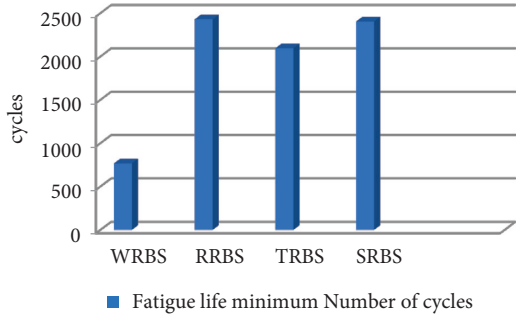

Figure 9: Fatigue life span.

flange reduction of 50%, are applied to all connections, due to flange reduction of area is 55.38 in^2.

4. Conclusions

(i) For all connections, the stress intensity in the panel zone ranges from 234.36 MPa to 319.48 MPa at static structural thermal equivalent von Mises stress distribution

(ii) At a static structural level, in comparison to other RBS, WRBS has the most overall von Mises stress intensity

(iii) The maximum at static structural total deformation for all connections is between 29.83 mm and 26.238 mm under static structural conditions

(iv) Static structural transient thermal maximum total deformation for all connections is between 97.028 mm and 92.66 mm

(v) For the radius cut RBS, the stress contours are uniform. Stress concentration is seen at the reentrant corners of trapezoidal and straight cut RBS connections, which may ultimately lead to beam flange fracture

(vi) For the radius cut RBS, the stress contours are uniform. Stress concentration is seen at the reentrant corners of trapezoidal and straight cut RBS connections, which may ultimately lead to beam flange fracture

Data Availability

The data used to support the findings of this study are included within the article and are available from the corresponding author upon request.

Conflicts of Interest

The authors declare that there are no conflicts of interest.

Acknowledgments

The authors thank and acknowledge the management of REVA University, Bengaluru, for their support to carry out this research work.

References

[1] A. K. Swati and V. Gaurang, "Study of steel moment connection with and without reduced beam section," *Case Studies in Structural Engineering*, vol. 1, pp. 26–31, 2014.

[2] K. S. Ajay and V. Gaurang, "A study of reduced beam section profiles using finite element analysis," *Journal of Mechanical and Civil Engineering*, vol. 6, pp. 01–06, 2013.

[3] R. Rahnavard, A. Hassanipour, and N. Siahpolo, "Analytical study on new types of reduced beam section moment connections affecting cyclic behavior," *Case Studies in Structural Engineering*, vol. 3, pp. 33–51, 2015.

[4] P Asha, L Natrayan, B. T Geetha et al., "IoT enabled environmental toxicology for air pollution monitoring using AI techniques," *Environmental Research*, vol. 205, Article ID 112574, 2022.

[5] C. E. Sofias and D. T. Pachoumis, "Assessment of reduced beam section (RBS) moment connections subjected to cyclic loading," *Journal of Constructional Steel Research*, vol. 171, Article ID 106151, 2020.

[6] K. Hemalatha, C. James, L. Natrayan, and V. Swamynadh, "Analysis of RCC T-beam and prestressed concrete box girder bridges super structure under different span conditions," *Materials Today Proceedings*, vol. 37, pp. 1507–1516, 2021.

[7] S. L. Jones, G. T. Fry, and M. D. Engelhardt, "Experimental evaluation of cyclically loaded reduced beam section moment connections," *Journal of Structural Engineering*, vol. 128, no. 4, pp. 441–451, 2002.

[8] L. Natrayan, V. Dhinakaran, P. P. Pravin, V. Swamy Nadh, P. Balamurugan, and M. D. Chewaka, "Surface state treatment of carbon dots using sulphur dioxide isotherm," *Adsorption Science and Technology*, vol. 2022, Article ID 7387409, 9 pages, 2022.

[9] M. Memari, H. Mahmoud, and B. Ellingwood, "Post-earthquake fire performance of moment resisting frames with reduced beam section connections," *Journal of Constructional Steel Research*, vol. 103, pp. 215–229, 2014.

[10] N. K. Berde, U. R. Awari, and S. A. Kulkarni, "The behavior of reduced beam section moment connection with varying thickness of continuity plate," *International Journal of Sustainable Construction Engineering and Technology*, vol. 8, no. 1, pp. 77–83, 2017.

[11] L. Natrayan, V. Sivaprakash, and M. S. Santhosh, "Mechanical, microstructure and wear behavior of the material AA6061 reinforced SiC with different leaf ashes using advanced stir casting method," *International Journal of Engineering and Advanced Technology*, vol. 8, pp. 366–371, 2018.

[12] R. Rahnavard and R. J. Thomas, "Numerical evaluation of the effects of fire on steel connections; Part 1: simulation techniques," *Case Studies in Thermal Engineering*, vol. 12, pp. 445–453, 2018.

[13] S. J. Venture and Guidelines Development Committee, *Recommended Seismic Design Criteria for New Steel Moment-Frame Buildings*, Federal Emergency Management Agency, Washington, DC, USA, 2000.

[14] D K R C. Naga, L. Natrayan, and D M. Wubishet, "Seismic fragility and life cycle cost analysis of reinforced concrete structures with a hybrid damper," *Advances in Civil Engineering*, vol. 2021, Article ID 4195161, 17 pages, 2021.

[15] P S. Sundaram, N H. Basker, and L. Natrayan, "Smart clothes with bio-sensors for ECG monitoring," *International Journal of Innovative Technology and Exploring Engineering*, vol. 8, no. 4, pp. 298–330, 2019.

[16] M. S. K. Sharma, S. Umadevi, Y. Sai Sampath et al., "Mechanical behavior of silica fume concrete filled with steel tubular composite column," *Advances in Materials Science and Engineering*, vol. 2021, Article ID 3632991, 9 pages, 2021.

[17] J. Malley, C. Carter, J. Hajjar, D. Lignos, C. Roeder, and M. Saunders, "Research Plan for the Study of Seismic Behavior and Design of Deep," *Slender Wide Flange Structural Steel Beam-Column Members*, Grant/Contract Reports (NISTGCR), Maryland, MD, USA, 2011.

[18] L. Natrayan, M. Senthil Kumar, and M. Chaudhari, "Optimization of squeeze casting process parameters to investigate the mechanical properties of AA6061/Al2O3/SiC hybrid metal matrix composites by taguchi and anova approach," in *Advanced Engineering Optimization through Intelligent Techniques*, pp. 393–406, Springer, Springer, Singapore, 2020.

[19] R. Goswami, J. N. Arlekar, and C. V. R. Murthy, "Limitations of available Indian hot-rolled I-section for use in seismic steel MRFs," Report nicee, IIT Kanpur, Kanpur, Uttar Pradesh, India, 2006.

[20] S. Magesh, V R. Niveditha, P S. Rajakumar, R S. Radha, and L. Natrayan, "Pervasive computing in the context of COVID-19 prediction with AI-based algorithms," *International Journal of Pervasive Computing and Communications*, vol. 16, no. 5, pp. 477–487, 2020.

[21] S. J. Venture, *SAC.Protocol for Fabrication, Inspection, Testing, and Documentation of Beam-Column Connection Test and Other Experimental Specimens*, SAC Joint Venture, CA, USA, 1997.

[22] L. Natrayan and M. K. Senthil, "Influence of silicon carbide on tribological behaviour of AA2024/Al2O3/SiC/Gr hybrid metal matrix squeeze cast composite using Taguchi technique," *Materials Research Express*, vol. 6, no. 12, Article ID 1265f9, 2020.

[23] S. Yogeshwaran, L. Natrayan, S. Rajaraman, S. Parthasarathi, and S. Nestro, "Experimental investigation on mechanical properties of epoxy/graphene/fish scale and fermented spinach hybrid bio composite by hand lay-up technique," *Materials Today Proceedings*, vol. 37, pp. 1578–1583, 2021.

Hindawi
Advances in Materials Science and Engineering
Volume 2022, Article ID 5406570, 21 pages
https://doi.org/10.1155/2022/5406570

Research Article

Multiobjective Optimization of Surface Roughness and Tool Wear in High-Speed Milling of AA6061 by Machine Learning and NSGA-II

Anh-Tu Nguyen,[1] **Van-Hai Nguyen**,[2,3] **Tien-Thinh Le**,[2,3] **and Nhu-Tung Nguyen**[4]

[1]*Faculty of Mechanical Engineering, Hanoi University of Industry, 298 Cau Dien Str., Bac Tu Liem District, Hanoi, Vietnam*
[2]*Faculty of Mechanical Engineering and Mechatronics, Phenikaa University, Yen Nghia, Ha Dong, Hanoi 12116, Vietnam*
[3]*PHENIKAA Research and Technology Institute (PRATI), A&A Green Phoenix Group JSC, No. 167 Hoang Ngan, Trung Hoa, Cau Giay, Hanoi 11313, Vietnam*
[4]*HaUI Institute of Technology, Hanoi University of Industry, Hanoi, Vietnam*

Correspondence should be addressed to Van-Hai Nguyen; hai.nguyenvan1@phenikaa-uni.edu.vn

Received 15 February 2022; Revised 30 April 2022; Accepted 5 May 2022; Published 27 May 2022

Academic Editor: Sengottuvelu Ramesh

This work addresses the prediction and optimization of average surface roughness (Ra) and maximum flank wear (Vbmax) of 6061 aluminum alloy during high-speed milling. The investigation was done using a DMU 50 CNC 5-axis machine with Ultracut FX 6090 fluid. Four factors were examined: the table feed rate, cutting speed, depth of cut, and cutting length. Three levels of each factor were examined to conduct 81 experiment runs. The response parameters in these experiments were measurements of Ra and Vbmax. We applied a two-pronged approach that combines machine learning (ML) and a Nondominated Sorting Genetic Algorithm (NSGA-II) to model and optimize Ra and Vbmax. Four ML models were used to predict Ra and Vbmax: linear regression (LIN), support vector machine regression (SVR), a gradient boosting tree (GBR), and an artificial neural network (ANN). The input variables were the significant factors that affect the surface quality and tool wear: the feed rate, depth of cut, cutting speed, and cutting time. Several quality metrics were employed to quantify the performance of the models, such as the root mean squared error (RMSE), mean absolute error (MAE), and coefficient of determination (R2). As a result, SVR and ANN were found to have the best predictive performance for Ra and Vbmax. These models and the NSGA-II-based approach were then employed for multiobjective optimization of cutting parameters during high-speed milling of aluminum 6061. Fifty Pareto solutions were found with Ra in the range of 0.257 to 0.308 μm and Vbmax in the range of 136.198 to 137.133 μm. Experimental validations were then conducted to confirm that the optimum solution was within an acceptable error range. More precisely, the absolute percentage errors for Ra and Vbmax were 2.5% and 1.5%, respectively. This work proposes an effective strategy for efficiently combining machine learning techniques and the NSGA-II multiobjective optimization algorithm. The experimental validations have reflected the potential for applying this strategy in various machining-optimization problems.

1. Introduction

Aluminum alloys have been widely employed in various areas of engineering, such as the automotive and aerospace industries. For instance, various automotive components are made out of aluminum alloys, including wheels, panels, structures, pistons, brake drums, and piston sleeves, while aluminum alloy aircraft parts include fittings, gears, and shafts. [1]. One of the main advantages of this material is that it exhibits a tremendous strength-to-weight ratio in comparison to steel and cast iron. Therefore, it can be used as a favorable alternative to these materials in manufacturing.

Aluminum alloys are often used in traditional machining processes with typical cutting conditions. However, traditional machining is considered to have low efficiency, especially from the perspectives of machining cost and surface

quality. As an alternative, high-speed milling can provide surface quality and gloss comparable to those obtained with a grinding method [2]. Moreover, high-speed milling allows us to obtain a better surface-roughness finish and better geometric accuracy than traditional machining methods. Furthermore, surface roughness also decreases during high-speed drilling as the cutting speed increases, as observed experimentally by Kannan et al. [3].

High-speed machining can also avoid the effects of ductility and built-up edges on the surface finish of aluminum alloys. In other words, high-speed machining can result in better roughness, longer tool life, and a higher material removal rate. Thus, this technique significantly helps to increase productivity, and studies on high-speed milling are being done to improve the cost and time of machining processes.

Parameter selection for a high-speed milling process is crucial because the parameters directly affect the manufacturing process. The average surface roughness Ra is one of the most critical performance criteria in such a process and is required to ensure the products' desired aesthetics, corrosion resistance, fatigue strength, and tribology characteristics. Various experimental studies have pointed out that Ra is affected by the feed rate, cutting speed, depth of cut, tool geometry, tool wear, temperature, and built-up edge formation [4]. Tool wear affects the finished surface and dimension tolerance of the product, as well as the stability of the machining operation [5]. Pimenov et al. [6] used Grey relational analysis (GRA) to find optimal cutting parameters for face milling AISI 1045 steel. In order to implement multiobjective optimization by GRA, multilayer regression analysis was used to determine a model of the surface roughness, material removal rate, sliding distance, and tool life based on feed per tooth, cutting speed, and flank wear. The wear of the cutting tool affects the surface roughness of the part in the finishing mill. Therefore, it is necessary to determine the correlation between wear and roughness to improve the machining efficiency [7, 8]. Therefore, more in-depth studies on the process parameters are needed to achieve the desired characteristics.

Recently, several studies have been conducted on the prediction of surface roughness using numerical techniques, such as machine learning [9]. Various ML techniques have also been used to predict surface roughness, such as random forest, regression trees, radial basis regression [10], gradient boosting trees [11], decision trees [12], support vector machine [13], and artificial neural network methods [14, 15]. The input parameters used in these studies include the spindle speed, feed rate, depth of cut, vibration along axes, cutting fluids, and cutting forces. The results indicated that ANN models have more potential for predicting Ra than traditional regression techniques [16].

The prediction of tool wear also plays a crucial role in the industry because it allows us to obtain proper planning and control of machining parameters, as well as optimized cutting conditions. Machining must be carefully monitored to predict wear over time. Different ML algorithms have been widely applied to predict tool wear, including ANNs [17], random forest [18], SVMs [19], decision trees, and feedforward BpNN [20]. According to the literature, various variables affect the prediction of tool wear, including the feed rate, depth of cut, cutting speed, and cutting force. Because of the multivariable and nonlinear correlations between the control and the performance variables, it is difficult to establish an accurate processing model to determine optimal machining conditions.

Interestingly, combinations of ML models and optimization algorithms have not been widely investigated, especially for the problem of high-speed machining. Recently, studies have integrated ANNs with genetic algorithms to optimize cutting parameters with minimum surface roughness in a milling process [21]. Metaheuristic algorithms can effectively deal with multiobjective optimization in engineering problems [22]. Moreover, these algorithms can efficiently optimize multiple objectives simultaneously [23]. Multiobjective methodologies have been successfully implemented in cutting-parameter optimization [24]. Unune et al. combined NSGA-II and an ANN to model and optimize the material removal rate (MRR) and Ra in grinding [25]. Kayaroganam et al. [26] combined a fuzzy model and the NSGA-II technique to determine the optimal drilling conditions for the minimum thrust force and torque in reinforcing AA6061 aluminum alloy drilling.

When machining AISI 6061 aluminum alloy, the surface roughness and tool wear depend on various cutting parameters and involve complex nonlinear problems. Therefore, defining performance parameters is challenging. Although experimental studies have given different formulas for determining Ra and tool wear values, it is difficult to define general formulas. Therefore, the use of machine learning and optimization techniques can help uncover nonlinear relationships between desired goals and problem inputs, especially the depth of cut, speed feed, cutting speed, cutting time, and tool type. Without solving complicated mechanical equations, the proposed machine learning model can effectively predict and analyze the surface roughness and tool wear when machining Al 6061.

Interestingly, the NSGA-II multiobjective optimization technique allows for the optimization of surface roughness and tool wear simultaneously. Lastly, the proposed optimization strategy has been validated using empirical tests. The information obtained could help to assess instrument surface roughness and wear quickly while reducing the required number of costly and time-consuming laboratory experiments.

Recent studies on high-speed milling have commonly been based on mathematical models and single-objective optimization [2, 27, 28]. However, to our knowledge, research on multiobjective optimization in high-speed milling 6061 aluminum alloy is rare, especially with a combination of machine learning and multiobjective optimization algorithms. Therefore, the aim of this work is to find the optimum solution to minimize Ra and Vbmax simultaneously in the high-speed milling of 6061 aluminum alloy.

Four predictive modeling algorithms were analyzed: LIN, SVR, GBR, and ANN. The results were compared using the following metrics: RMSE, MAE, and R2. Then, the two best predictive models were then optimized using NSGA-II

to find the optimum combination of input variables to achieve the optimization goals. Finally, the optimal values of cutting parameters were validated by five experiments.

2. Research Significance

The surface roughness and tool wear of 6061 aluminum alloy during high-speed milling are complex nonlinear problems that are influenced by a variety of cutting parameters, making estimation difficult. Although a number of experimental investigations have been conducted to address this issue, it is difficult to derive a generalized formulation that takes into account all of the influential variables. Machine learning and optimization techniques could be used to investigate nonlinear correlations between desired targets and problem inputs, such as the feed rate, cutting speed, depth of cut, and cutting length.

For the first time, a hybrid machine learning and NSGA-II optimization technique was created and trained to assess surface roughness and tool wear of 6061 aluminum alloy during high-speed milling in this study. The model was trained and verified using experimental data gathered from the available literature. The approach was able to predict and analyze the surface roughness and tool wear without having to solve difficult mechanical equations. Notably, the multiobjective NSGA-II optimization technique allowed for simultaneous optimization of the surface roughness and tool wear. Lastly, the proposed optimization approach was tested in experiments. The results could be used for quick measurements of surface roughness and tool wear and reduce the need for costly and time-consuming laboratory studies.

3. Materials and Methods

3.1. Methodology. A combination of multiobjective optimization techniques, NSGA-II and ML, was used to find optimal solutions. Four predictive machine learning algorithms were first used to predict Ra and Vbmax: LIN, SVR, GRB, and ANN. The two best models were then identified and combined with the NSGA-II algorithm to define the optimal machining parameters. The processing conditions in wet machining include the table feed rate, cutting speed, depth of cut, and cutting length, which were considered as input parameters for the problem.

The flowchart in Figure 1 illustrates the study methodology. The methodology involved the collection of experimental data, dataset extraction, feature selection, and data normalization to predict Ra and Vbmax using the four predictive modeling methods. The figure also illustrates how to find the best hyperparameters by using the GridSearchCV technique. The final model was selected to predict Ra and tool wear based on the smallest value of RMSE for the test dataset. Then, the optimal solutions were identified on the Pareto front according to the constraints and minimum Ra and Vbmax. Five verification experiments were then conducted to validate the optimal values of Ra and Vbmax found by the numerical model.

3.2. Machine Learning Techniques

3.2.1. Linear Regression. The main objective of linear regression is to find the relationship between the input data and the target variable. When there is only one input variable, the method is called simple linear regression, and when there are several input variables, it is called multiple linear regression. Linear regression is a powerful statistical method for finding the relation between input and output variables. Therefore, it has been employed for many applications. For example, linear regression has been used for face recognition. Other applications in fields such as mechanical and civil engineering can also be found [29]. However, the technique is only suitable for linear problems.

3.2.2. SVM Regression. The SVM method can be used for classification and regression problems and is one of the classical machine learning techniques. The method was first proposed by Vapnik et al. [30]. Many applications have been proposed using SVMs as prediction models, and they have been found to perform well. For example, Byvatov and Schneider used an SVM in a data-driven method for bioinformatic applications [31]. An SVM can also be employed in hydrology, biology, and many other applications [32].

Mainly based on statistical learning, the main idea of the SVM is to divide a given input dataset into two main categories that are distinguished by a hyperplane. The SVM then maps the input data to points in space with the aim of maximizing the gap between the two subsets of data. The points closest in space to the hyperplane are called support vectors. One of the main advantages of the SVM method is the ability to work with a multidimensional input space, which is beneficial in terms of computer memory. However, it lacks the ability to work with large datasets, and the noise from the input data needs to be filtered before being input to the model.

3.2.3. Gradient Boosted Trees. The Gradient Boosted Tree (GBR) method is a supervised learning algorithm introduced in 2015 to provide accurate predictive models [33]. The main features of GBR are its computation time, predictive accuracy, and scalability compared to other machine learning models. In view of these advantages, GBR has been applied to many scientific fields. For example, in one study [34], GBR was employed for the prediction of miRNA disease. In banking, GBR has been used to predict a US banking meltdown. In mechanical machining, GBR is also considered an excellent approach for predicting the mechanical properties of machines [33]. GBR is a gradient tree boosting algorithm where overfitting is avoided by introducing regulation terms.

3.2.4. ANN Regression. ANNs are machine learning models that are inspired by the biological neural networks of human brains [35]. The main idea of an ANN is to learn by detecting patterns and relations between components in input data. In other words, it can be said that an ANN is constructed

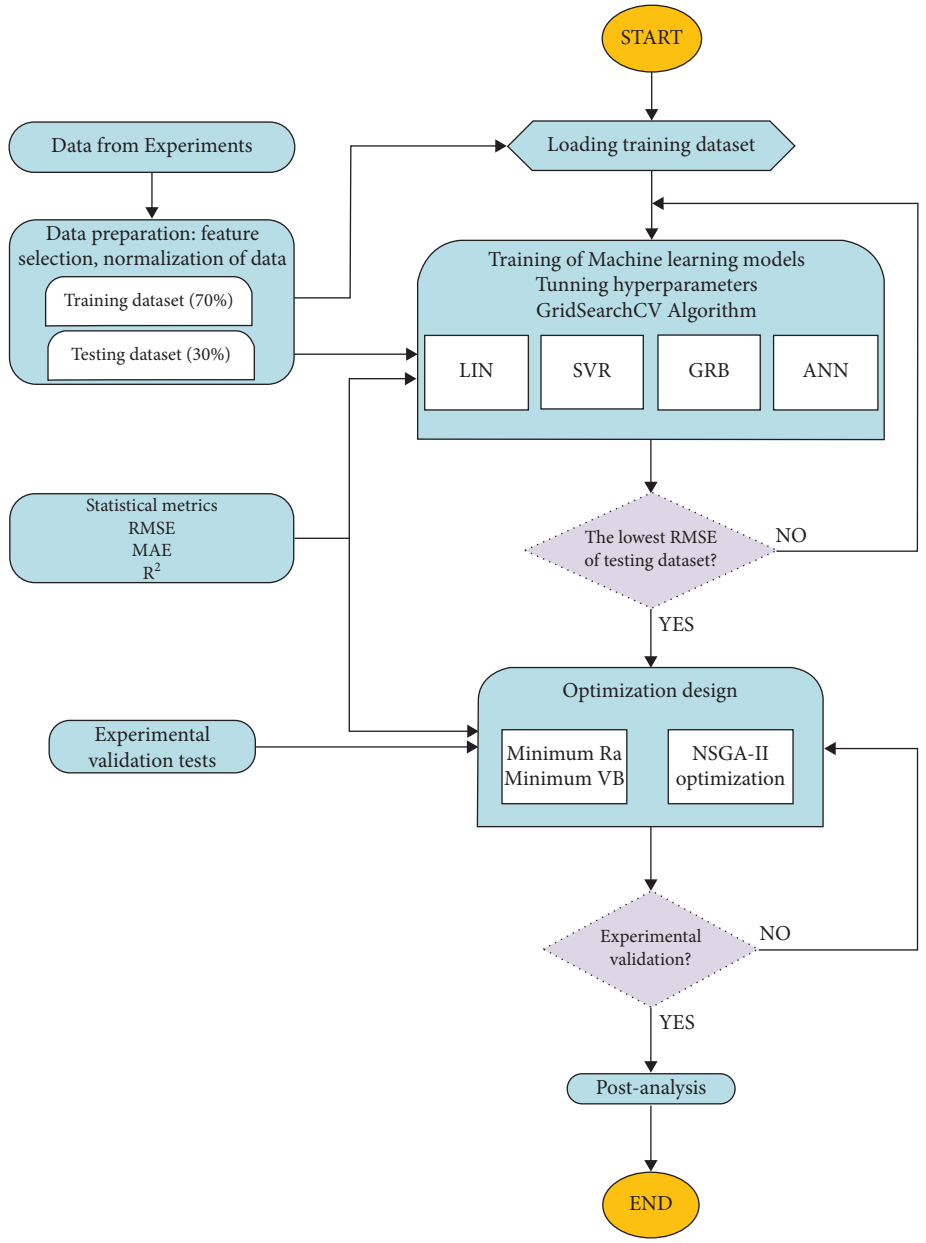

Figure 1: Flowchart of the study methodology.

through experience, not programming. There are several types of ANNs, such as backpropagation neural networks [36], probabilistic neural networks [37], convolutional neural networks [38], time-recurrent neural networks [39], and long- and short-term memory networks [40]. ANNs consist of several artificial neurons (or computing nodes) that send and receive signals to and from one another.

The performance of an ANN model depends heavily on the way in which the neurons are connected to each other. In general, ANN models have three main layers: (i) an input layer where the input data are entered, (ii) hidden layers where the model is trained and tested using the input data from the previous layer, and (iii) an output layer where the results are exported. An advantage of an ANN model is that it will work with any type of data [41], which is highly useful for problems where data are collected from multiple sources and contain much noise. Another advantage is its suitability for parallel computing, which can help it to process large datasets within reasonable processing time.

However, there are some drawbacks to this approach. For example, the information in an ANN is stored across the entire network, so it consumes a great deal of memory, especially with large datasets. In addition, a large number of trials are often required to improve the control of the behavior of the network.

3.2.5. Significance of Models Used. The following are some of the benefits of using the GBR approach. First, the model has unrivaled prediction accuracy. Second, multiple loss

functions and hyperparameter tuning options can be used to optimize the model. No data preprocessing is necessary prior to the training of the model, and the approach is frequently effective with both categorical and numerical data. Finally, GBR can deal with missing data points effectively.

The advantages of the support vector regression method are the following. When there is an understandable margin of dissociation between classes, the support vector machine works similarly well. In high-dimensional spaces, it is more productive, and when the number of dimensions exceeds the number of specimens, this method works well.

The following are some of the benefits of using the artificial neural network method. The capacity to solve complicated problems with nonlinear input-output relationships is the first advantage of an ANN model. Another advantage of the ANN technique is that it eliminates the need for assumptions and preconstraints during simulation. The method can examine complex nonlinear relationships and analyze data with a large number of dimensions. Because of its structure, which is made up of multiple nodes, an ANN is capable of solving high-dimensional complicated problems with good performance.

There are several disadvantages of fuzzy logic in artificial intelligence and machine learning. Because these systems rely on erroneous data and inputs, their accuracy is jeopardized. There is no one-size-fits-all strategy for applying fuzzy logic to address an issue. As a result, several solutions to a single problem emerge, causing confusion. Usually, they are not widely recognized due to the inaccuracy of the results. The fact that fuzzy logic control systems are fully reliant on human knowledge and expertise is a big disadvantage. A fuzzy logic control system's rules must be updated on a regular basis. Machine learning and neural networks are not recognized by these platforms. Validation and verification of the systems necessitate extensive testing.

3.2.6. Performance Assessment. In this study, RMSE, MAE, and R2 were employed as quality metrics to construct efficient ML models [42]:

$$\begin{aligned} \text{RMSE} &= \sqrt{\frac{\sum_{i=1}^{N} \left(\widehat{y}_i - y_i\right)^2}{N}}, \\ \text{MAE} &= \frac{1}{N} \sum_{i=1}^{N} \left|\widehat{y}_i - y_i\right|, \\ R^2 &= 1 - \frac{\sum_{i=1}^{N} \left(\widehat{y}_i - y_i\right)^2}{\sum_{i=1}^{N} \left(\widehat{y}_i - \overline{y}\right)^2}, \end{aligned} \tag{1}$$

where y_i and $\widehat{y}_i$ are actual and predicted values, respectively. N is the total number of observations. These metrics are the most popular in regression problems. A better model is indicated by higher values of R^2 and lower values of RMSE and MAE.

The coefficient of determination (R^2) is a good assessment metric for determining how well a model fits the input variables. However, this coefficient does not allow for the detection of overfitting problems. RMSE and MAE are assessment metrics for the goodness of fit. When evaluating the value of these metrics for a given model, RMSE is prioritized because it has distinct advantages over MAE and R^2 [43]. Unlike MAE, RMSE does not use an absolute value, which is highly undesirable in many mathematical calculations. Therefore, when comparing the predictive accuracy of different regression models, RMSE is the first choice.

3.3. Multiobjective Optimization. The NSGA-II algorithm was utilized according to the steps reported by Deb et al. [44]. The algorithm is employed by setting an initial population according to a nondominant criterion. Then, the initial population or set of individuals is changed iteratively for the optimization process. After an assessment, the individuals with better fitness are selected as parents and evolve according to the principle of natural selection using crossover, mutation, and selection to produce a new generation of offspring. This process is repeated until a stopping criterion is met. The mathematical-style pseudocode of NSGA-II is described in Figure 2.

There is a need to optimize the machining productivity and production cost in manufacturing processes. Achieving this consists of finding the optimal configuration to avoid wastage of material, labor cost, energy, time, cutting tool, and expenses while maintaining the output requirements of the product. Therefore, cutting parameters have to be optimized [46]. One of the critical technical problems in machining is simultaneously achieving two criteria: minimum Ra and minimum tool wear. To address this issue, NSGA-II was utilized to obtain Pareto-optimal solutions.

Recently, studies have integrated ANNs with genetic algorithms to optimize cutting parameters with minimum surface roughness in milling processes [47]. Metaheuristic algorithms can effectively deal with multiobjective optimization in engineering problems [28, 48]. Moreover, these algorithms can efficiently optimize multiple objectives simultaneously [23]. Multiobjective methodologies have been successfully implemented in cutting-parameter optimization [49]. Unune et al. combined NSGA-II and an ANN to model and optimize the material removal rate (MRR) and Ra in grinding [25]. Kayaroganam et al. [26] used a fuzzy model and NSGA-II to determine the optimal drilling conditions for the minimum thrust force and torque in reinforcing AA6061 aluminum alloy drilling.

The advantages of NSGA-II are as follows. First, it employs nondominated sorting approaches to obtain a solution that is as close to the Pareto-optimal as possible. Second, it employs crowding distance approaches to promote solution diversity. Finally, it employs elitist approaches to maintain an existing population's best solution for the following generation. Therefore, the NSGA-II technique for multiobjective optimization was selected in the present work.

4. Experimental Setup

4.1. Experimental Design. Experiments were performed on a DMU 50 CNC milling 5-axis machine with a maximum spindle speed of 14,000 rpm and a maximum feed rate of

NSGA-II procedure

Input: N, T, $F_k(X) \triangleright N$ members evolved T generations to solve Min $f_k(X)$

Initialize Population P_0 size N randomly;
for $t = 1$ to T do
Generate next offspring population Q_t size N by:
    Binary Tournament Selection;
    Crossover and Mutation;
Combine current Parents P_t and new offspring Q_t to form R_t;
Calculate objective values for R_t;
Assign Rank (level) for R_t based on Pareto fronts F_k (non-dominated solutions);
Calculate Crowding distance (CD) for each solution in R_t;
Initialize next Parent population P_{t+1} by the following loop:
    Add solutions in lowest rank Pareto fronts with priority for a greater CD until getting N individuals are obtained;
End

Figure 2: Pseudocode of NSGA-II [45].

30,000 mm/min. The workpiece material was 6061 aluminum alloy with a length, width, and height of 150 mm, 15 mm, and 150 mm, respectively (Figure 3). The long edge of the workpiece was traced parallel to the X-direction of the machine. Finally, the workpiece was clamped firmly in the milling vise. The chemical content of 6061 aluminum alloy is indicated in Table 1 according to the manufacturer.

The insert tool used in this study followed the American National Standards Institute (ANSI) code APMT1135PDER-M2. According to the manufacturer, the insert tool geometry has a corner radius of 0.8 mm, a major clearance angle of 11°, and an insert-included angle of 85°. Two indexable parallelogram carbide inserts were mounted on a tool shank (300R C20-20-150 2 T, Sumitomo, Japan). The length of the tool shank was 150 mm, and the diameter was 20 mm. The geometric parameters of the cutter can be found at https://www.mitsubishicarbide.net/.

The inserts' nose radius was 0.8 mm. The basic machining parameters for high-speed milling included the cutting speed (Vc), table feed rate (V_f), and axial depth of cut (a) under fluid overflow lubrication (Ultracut FX 6090). The process parameters are shown in Table 2. Experiments were conducted using the setup in Figure 4. In this study, the full factorial technique was applied to design the experimental matrix. This technique shows significant advantages compared to a fractional factorial method. Factorial designs are substantially more efficient than fractional factorial designs and can deliver more information at a similar or lower cost. They can also aid in the faster discovery of optimal conditions than fractional factorial studies. Additional components can be investigated using a factorial design without incurring additional costs. The factorial design can be used to quantify the effects of a component at several levels of other factors, which can lead to results that are applicable to a wide range of experimental settings. Therefore, a complete factorial design was selected to conduct 81 experiments.

Cutting speed is an important parameter that is commonly used to define high-speed milling [50]. For example, Ming et al. [51] performed a milling experiment for aluminum alloy using cutting speeds of 2,500 to 15,000 rpm and table feed rates of 250 to 1,500 mm/min. In another study, Zaghbani et al. [52] varied the cutting speed from 2,926 to 7,523 rpm and the table feed rate from 292 to 1,400 mm/min. Based on a literature review and the characteristics of the available equipment, an experiment was performed with the cutting-parameter ranges indicated in Table 2.

4.2. Acquisition of Data. Ra was calculated according to the ISO 1997 standard (the measurement range was 4 mm). The value was displayed through the software SurfTest SJ USB Communication Tool Ver 5.007, which was connected with a measurement device (MITUTOYO-Surftest SJ-210 Portable Surface Roughness Tester). The final Ra value of each experiment was determined by the average value of three measurements along the toolpath. The instruments used for the measurement of surface roughness and tool wear are shown in Figure 5.

The cutting tool's flank wear was measured by a LEICA DM750 M Microscope system, and the values were displayed through LAS EZ software. In each experiment, Vbmax was measured for two inserts per cut, and the average value was recorded as the final tool wear, as shown in Table 3 (see also Figure 6). In the procedure for the whole experiment, 81 experimental runs were carried out for 10, 30, and 50 machining strokes. A machining stroke was a length of 150 mm. The measurement process was conducted in standard laboratory conditions at room temperature. Each experiment was repeated three times. Therefore, the machining time can be calculated based on the cutting length [53]:

$$T_c = \frac{60 \times L \times \pi \times \mathrm{DC}}{f_z \times z \times V_c \times 1,000}, \quad (2)$$

where L is the cutting length, which is calculated by multiplying the number of machining strokes and the length of a stroke (150 mm). The numbers of machining strokes during

Figure 3: AISI 6061 aluminum alloy workpieces for experiments (with permission from [2] (open access)).

Table 1: Chemical composition of AISI 6061 aluminum.

Element	Al	Cr	Cu	Fe	Mg	Mn	Si	Ti	Zn
%	98	≤0.3	≤0.4	≤0.7	≤1.2	≤0.15	≤0.8	≤0.15	≤0.25

Table 2: Process parameters for milling 6061 aluminum alloy.

Cutting factor	Unit	Data levels
Table feed rate (V_f)	mm/min	2,700–3,577–4,050
Cutting speed (V_c)	mm/rev	10,345–11,937–13,528
Depth of cut (a)	mm	0.2–0.4–0.6
Cutting stroke (L)	mm	10–30–50
Tool type (T)		APMT1135PDER-M2 VP15 TF
Humidity (H)		Overflow lubrication - FX 6090 fluid

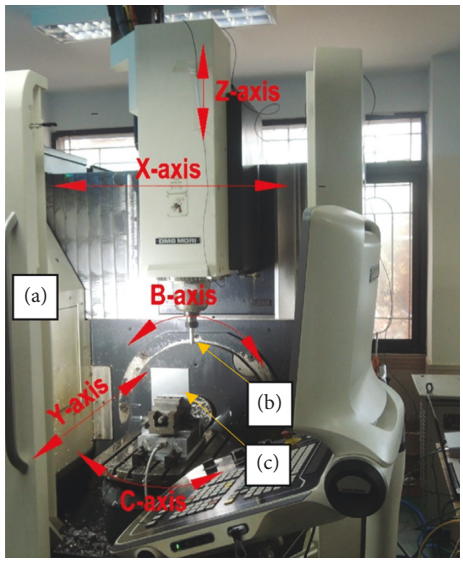

Figure 4: Experimental setup: a: DMU 50 CNC milling 5-axis machine; b: tool; c: workpiece (with permission from [2] (open access)).

the experiments were 10, 30, and 50, which correspond to cutting lengths of 1500, 4500, and 7500 mm, respectively. z is the number of teeth, V_c is the cutting speed, DC is the nominal diameter of the cutting tool, and f_z is the feed rate per tooth (mm/t), which can be calculated as [53]

$$\mathbf{f_z} = \frac{\mathbf{v_f} \times \boldsymbol{\pi} \times \mathbf{DC}}{\mathbf{z} \times \mathbf{V_c} \times 1,000}, \tag{3}$$

where V_f is the table feed rate (mm/min). The cutting time for each experimental run was calculated and is shown in Table 3.

5. Results and Discussion

5.1. Effect of Cutting Parameters on Surface Roughness and Tool Wear. Figures 7(a) and 7(b) show the effect of cutting parameters on the surface roughness and tool wear, respectively. Generally, as Figure 7(a) indicates, higher cut depth leads to reduced surface roughness. A higher table rate, cutting speed, and stroke (i.e., cutting length or cutting time) increase the surface roughness. However, the outcome does not follow this rule for some parameters. At $a = 0.2$ mm, $V_f = 2{,}700$ mm/min, and $V_c = 10{,}345$ rev/min, the surface roughness is reduced when increasing the cutting time. For $V_c = 13{,}528$ rev/min, Ra is reduced when increasing cutting time at $V_f = 3{,}557$ mm/min and $a = 0.2$ mm, at $V_f = 4{,}050$ mm/min and $a = 0.4$ mm, and at $V_f = 2{,}700$ mm/min and $a = 0.6$ mm.

The surface quality in milling aluminum alloy is affected by the production of built-up edges. A higher speed of chip flow increases the friction with the blade and tool wear, improves the blade surface finish, and can reduce the friction resistance [54]. As Figure 7(b) indicates, higher V_f, V_c, a, and the number of strokes lead to increased tool wear. The minimum of tool wear reaches 133.420 at $V_f = 2{,}700$ mm/min, Vc = 10,345 rev/min, $a = 0.2$ mm, and 10 strokes. Thus, the value of Ra changes irregularly according to cutting parameters. Therefore, it is necessary to determine the optimal value of the cutting parameters such that Ra and Vbmax are minimized together.

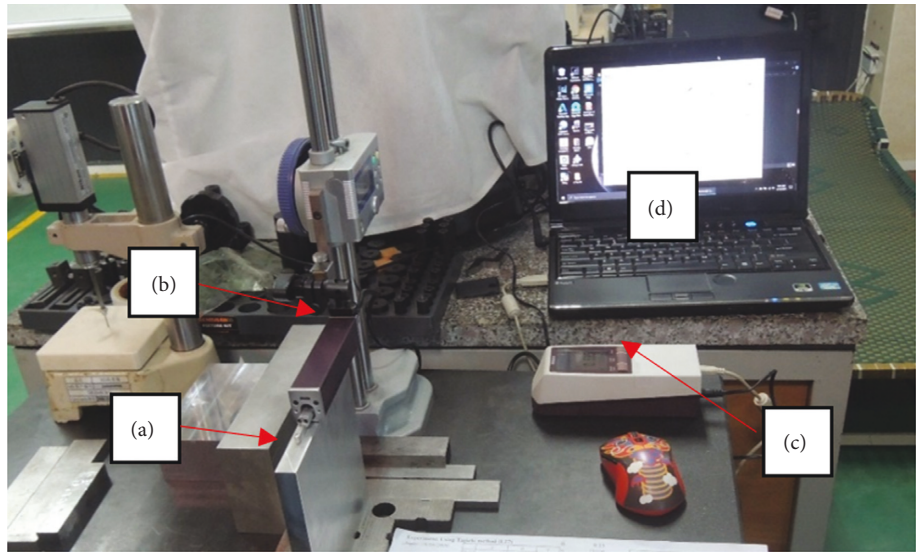

Figure 5: Surface-roughness measurement setup: a: workpiece; b: surface roughness sensor; c: data processing; d: PC and software.

5.2. Hyperparameter Tuning of Machine Learning Models. Optimization of the model is the biggest challenge in obtaining a machine learning solution. Optimization of hyperparameters is done to find the model parameters that achieve the best performance measured on the validation set for a given machine learning algorithm. Hyperparameters control the learning process and impact predictive performance. Moreover, a suitable selection of hyperparameters can avoid the overfitting and underfitting of the model and enhance the predictive accuracy.

There are many common strategies for the optimization of hyperparameters, such as manual hyperparameter tuning, grid search, random search, Bayesian optimization, Gradient-based optimization, and evolution optimization [55]. This study used grid search (GS), which is a traditional technique for hyperparameter tuning. This approach allows us to find the optimal hyperparameters by using a grid of combinations in some order [56]. The GS technique is easy to use and implement, but it is less efficient when there is a large number of parameters [57]. To solve this problem, Zöller et al. [58] proposed a procedure to determine the global optimums. It starts with ample space, then the search space is narrowed, and this step is repeated multiple times. Accordingly, this work used GS to find the hyperparameters for all considered ML models. All the simulations were done using *Python* on a Dell Vostro with12 GB of RAM and an Intel® Core™ i5-9400 CPU @ 2.90 GHz. The optimal grid values found for the models are indicated in Table 3.

Among the four machine learning models employed in this study, the LIN model does not have any hyperparameters. However, the remaining models have many sensitive hyperparameters. As shown in Table 4, the set of hyperparameter values used for SVR, GRB, and ANN are generally the kernel, C (regularization parameter), degree, and gamma for SVR [59]; n_estimators, learning_rate, max_depth, and subsample for GBR; and batch_size, epochs, optimizer, and hidden layers for an ANN [60]. RMSE on the test dataset was employed as a principal error metric to determine optimal values.

5.3. Predictive Performance of Models

5.3.1. Predictive Performance for Ra. Table 5 shows the performance of the four ML models for the prediction of Ra as indicated for the training and testing datasets. On the training dataset, the GBR model exhibits the best predictive performance. This model obtained the lowest value of RMSE and the highest value of R^2. In contrast, on the testing dataset, the predictive performance of the SVR exhibits the lowest values of RMSE and MAE and the highest value of R^2. According to all error metrics on the testing dataset, the predictive performance is best with GBR, followed by ANN, LIN, and SVR. Finally, Figures 8 and 9 show the line and scatter plots of predictive and measured values of Ra for the training and testing datasets.

5.3.2. Predictive Performance for Tool Wear. Table 6 exhibits the accuracy metrics of the four ML models for predicting Vbmax for the training and testing datasets. On the training dataset, GBR shows the best predictive performance based on the smallest values of RMSE and MAE and the highest value of R^2. However, this is not exhibited in the testing dataset: values of RMSE and MAE are larger than those of the ANN. The ANN model also shows the highest value of R^2. According to all error metrics on the testing dataset, the predictive performance of models is best with SVR, followed by LIN, GBR, and ANN.

Moreover, the R2 values are 0.998 and 0.994 when using the training and testing datasets, respectively. This evaluation shows that the ANN model is the most efficient in predicting tool wear. Finally, Figures 10 and 11 show the line and scatter plots of predictive and measured values for the training and testing datasets.

Table 3: Machining parameters employed in the experiment, including training and testing datasets for the training of machine learning models.

Runs	V_f (mm/min)	V_c (Rev/min)	a (mm)	Stroke (-)	Tc (s)	Ra (μm)	Vbmax (μm)	Dataset
1	2,700	10,345	0.2	50	166.67	0.382	182.635	
2	3,577	13,528	0.4	10	25.16	0.4479	144.305	
3	3,577	11,937	0.2	30	75.48	0.352	158.570	
4	2,700	10,345	0.6	50	166.67	0.3039	182.341	
5	4,050	13,528	0.6	50	111.11	0.4582	180.535	
6	2,700	13,528	0.4	10	33.33	0.3617	145.285	
7	4,050	11,937	0.6	30	66.67	0.4118	152.145	
8	4,050	13,528	0.6	30	66.67	0.4443	159.105	
9	4,050	10,345	0.4	10	22.22	0.329	135.745	
10	3,577	11,937	0.2	50	125.80	0.5102	182.325	
11	4,050	13,528	0.4	10	22.22	0.494	144.765	
12	3,577	13,528	0.6	30	75.48	0.4002	160.941	
13	3,577	11,937	0.4	10	25.16	0.4154	139.085	
14	4,050	11,937	0.6	50	111.11	0.4257	173.905	
15	2,700	11,937	0.2	10	33.33	0.3946	140.540	
16	3,577	13,528	0.6	10	25.16	0.3831	146.165	
17	3,577	10,345	0.6	30	75.48	0.3376	148.315	
18	2,700	13,528	0.6	10	33.33	0.2587	144.755	
19	3,577	10,345	0.6	50	125.80	0.3513	170.955	
20	2,700	13,528	0.2	10	33.33	0.4271	150.575	
21	3,577	10,345	0.2	30	75.48	0.4619	147.695	
22	4,050	10,345	0.2	50	111.11	0.5198	166.635	
23	2,700	11,937	0.4	50	166.67	0.334	191.125	
24	4,050	10,345	0.4	30	66.67	0.4426	144.765	
25	4,050	13,528	0.4	50	111.11	0.49	178.730	
26	3,577	13,528	0.2	10	25.16	0.5083	147.670	
27	2,700	10,345	0.2	30	100.00	0.41	158.990	Training dataset
28	3,577	11,937	0.6	30	75.48	0.3657	154.265	
29	4,050	13,528	0.6	10	22.22	0.4304	145.935	
30	4,050	11,937	0.2	30	66.67	0.62	147.865	
31	4,050	13,528	0.2	10	22.22	0.557	146.352	
32	3,577	13,528	0.4	30	75.48	0.4636	161.518	
33	4,050	13,528	0.2	50	111.11	0.5848	186.905	
34	2,700	11,937	0.2	50	166.67	0.4363	196.625	
35	3,577	10,345	0.6	10	25.16	0.3263	138.175	
36	2,700	11,937	0.6	30	100.00	0.3023	160.245	
37	4,050	11,937	0.4	50	111.11	0.489	174.075	
38	2,700	11,937	0.6	50	166.67	0.3175	189.335	
39	3,577	10,345	0.2	50	125.80	0.4777	171.965	
40	3,577	13,528	0.2	50	125.80	0.532	197.465	
41	3,577	10,345	0.4	30	75.48	0.436	145.420	
42	2,700	10,345	0.6	30	100.00	0.2982	154.195	
43	2,700	10,345	0.4	10	33.33	0.3029	136.755	
44	4,050	13,528	0.4	30	66.67	0.5797	159.665	
45	4,050	11,937	0.2	10	22.22	0.545	138.350	
46	2,700	10,345	0.6	10	33.33	0.2961	138.230	
47	4,050	11,937	0.6	10	22.22	0.3979	141.445	
48	4,050	11,937	0.2	50	111.11	0.527	178.710	
49	4,050	10,345	0.6	50	111.11	0.424	170.860	
50	4,050	10,345	0.6	10	22.22	0.3659	137.645	
51	2,700	13,528	0.2	50	166.67	0.4688	207.675	
52	3,577	13,528	0.6	50	125.80	0.4161	184.845	
53	3,577	11,937	0.6	10	25.16	0.2817	143.330	
54	4,050	13,528	0.2	30	66.67	0.5709	163.295	

Table 3: Continued.

Runs	V_f (mm/min)	V_c (Rev/min)	a (mm)	Stroke (-)	Tc (s)	Ra (μm)	Vbmax (μm)	Dataset
55	2,700	11,937	0.2	30	100.00	0.4155	166.245	
56	2,700	10,345	0.2	10	33.33	0.422	136.435	
57	4,050	11,937	0.4	10	22.22	0.4612	138.775	
58	2,700	11,937	0.4	30	100.00	0.3937	163.010	
59	4,050	10,345	0.2	10	22.22	0.492	136.870	
60	2,700	10,345	0.4	30	100.00	0.3185	154.895	
61	3,577	10,345	0.4	10	25.16	0.33	136.735	
62	3,577	13,528	0.4	50	125.80	0.4794	187.145	
63	2,700	11,937	0.4	10	33.33	0.364	141.910	
64	3,577	11,937	0.2	10	25.16	0.4787	137.605	
65	4,050	11,937	0.4	30	66.67	0.4751	151.665	
66	2,700	13,528	0.2	30	100.00	0.448	176.795	
67	3,577	11,937	0.4	50	125.80	0.4469	179.085	
68	2,700	13,528	0.6	30	100.00	0.3603	166.390	Testing dataset
69	3,577	11,937	0.6	50	125.80	0.409	178.695	
70	4,050	10,345	0.2	30	66.67	0.5059	144.598	
71	4,050	10,345	0.4	50	111.11	0.4565	166.880	
72	2,700	13,528	0.4	50	166.67	0.4055	201.065	
73	2,700	10,345	0.4	50	166.67	0.3389	183.305	
74	3,577	11,937	0.4	30	75.48	0.4311	154.575	
75	3,577	10,345	0.2	10	25.16	0.4462	137.475	
76	3,577	10,345	0.4	50	125.80	0.431	168.230	
77	2,700	11,937	0.6	10	33.33	0.298	141.835	
78	4,050	10,345	0.6	30	66.67	0.4263	145.085	
79	2,700	13,528	0.4	30	100.00	0.3843	169.595	
80	2,700	13,528	0.6	50	166.67	0.294	197.140	
81	3,577	13,528	0.2	30	75.48	0.5637	165.785	

V_f: table feed, V_c: cutting speed, a: depth of cut, T_c: cutting time.

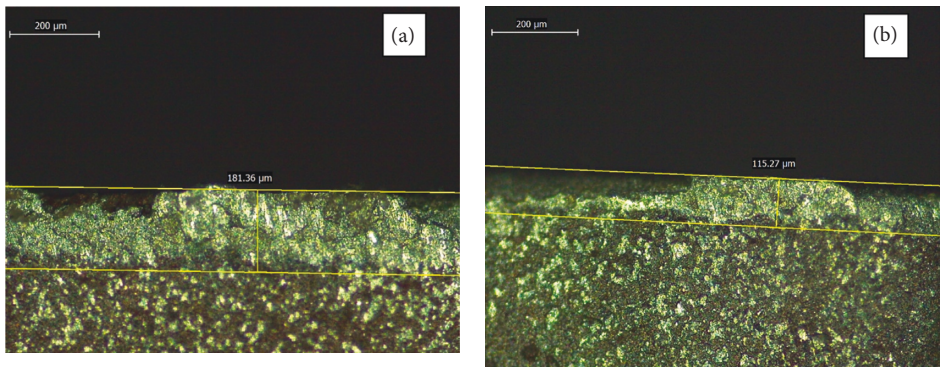

(a) (b)

Figure 6: Leica DM570 M microscope showing two-insert flank wear (Vbmax) for experiment number 17: (a) the first insert; (b) the second insert.

The performance was compared when using different activation functions, such as *relu*, *softmax*, *sigmoid*, *softplus*, *softsign*, *tanh*, *selu*, *elu*, and exponential functions. Other parameters of the model remained fixed. Table 7 shows the effects of the different activation functions on the assessment criteria.

As shown in Table 7, the relu activation function exhibits the best performance when considering all error metrics. The results for the training dataset were RMSE = 0.923, MAE = 0.637, and $R^2 = 0.998$, while those for the testing dataset were RMSE = 1.506, MAE = 1.090, and $R^2 = 0.994$. This model yields the highest value of R2 and the smallest values of RMSE and MAE. Lastly, it should be noted that the parametric study was only conducted on activation functions in the present study. Erkan et al. [61] provide a more complete parametric study on an artificial neural network model (including the learning algorithm, and the number of neurons).

5.3.3. Multiobjective Optimization by NSGA-II. Surface roughness and tool wear must be as low as possible in

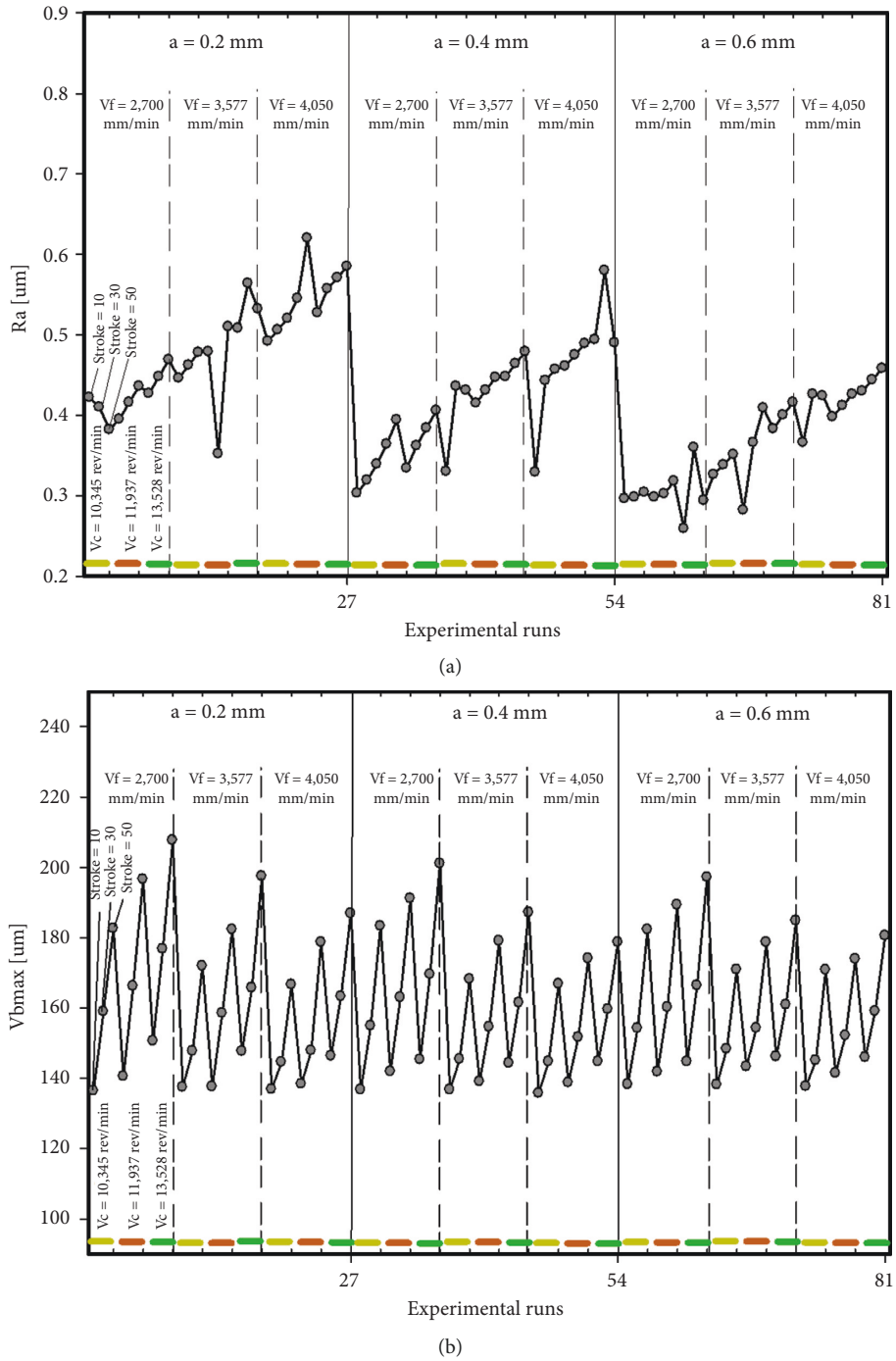

Figure 7: The effect of cutting parameters on the (a) surface roughness and (b) tool wear.

machining. Therefore, a formulation defining the multi-objective problem is expressed in the following, where SVR_reg_Ra and ANN_reg_Vbmax are models predicting Ra and Vbmax, respectively. As deduced previously, the best choices of ML models in the prediction of Ra and Vbmax are SVR and ANN, respectively (using optimal hyperparameters indicated in Table 4). The problem constraints are shown as follows:

Table 4: Hyperparameters for machine learning models.

Model	Hyperparameters tuned	Predictive Ra (Ra)		Predictive tool wear (vbmax)	
		Grid space	Results	Grid space	Results
SVR	Kernel	['rbf', 'sigmoid']	'rbf'	['rbf', 'sigmoid', 'poly']	'rbf'
	C	[30, 40, 50, 60]	40	[80, 100, 120, 150]	100
	degree	[5e-6, 1e-4, 5e-4, 5e-3]	5e-6	[1e-6, 1e-5, 1e-4, 1e-3, 5e-3]	1e-6
	Gamma	[1e-4, 2e-4, 5e-4, 1e-3, 2e-3]	5e-3	[0.02, 0.04, 0.05, 0.06]	0.05
GBR	n_estimators	[100, 500, 1000, 1500]	500	[100, 500, 1000, 1500]	500
	learning_rate	[0.01, 0.02, 0.02, 0.04]	0.02	[0.01, 0.02, 0.02, 0.04]	0.04
	max_depth	[4, 6, 8, 10]	6	[6, 8, 10, 12]	10
	Subsample	[0.1, 0.2, 0.5, 0.9]	0.2	[0.1, 0.2, 0.5, 0.9]	0.2
ANN	batch_size	[80, 90, 100]	100	[10, 15, 20]	15
	Epochs	[200, 300, 350]	300	[50, 100, 200]	200
	Optimizer	['adam', 'rmsprop']	'adam'	['adam', 'rmsprop']	'adam'
	units1	[80, 70]	80	[80, 64]	80
	units2	[36, 32, 28]	32	[64, 48]	48
	units3	[16, 8]	16	[16, 8]	16

Table 5: Performance of ML models for Ra prediction on the training and testing datasets.

Models	Training dataset			Testing dataset		
	RMSE	MAE	R2	RMSE	MAE	R2
LIN	0.034	0.018	0.850	0.026	0.018	0.854
SVR	0.026	0.015	0.911	0.014	0.012	0.973
GBR	0.021	0.016	0.942	0.032	0.027	0.807
ANN	0.032	0.017	0.866	0.029	0.020	0.849

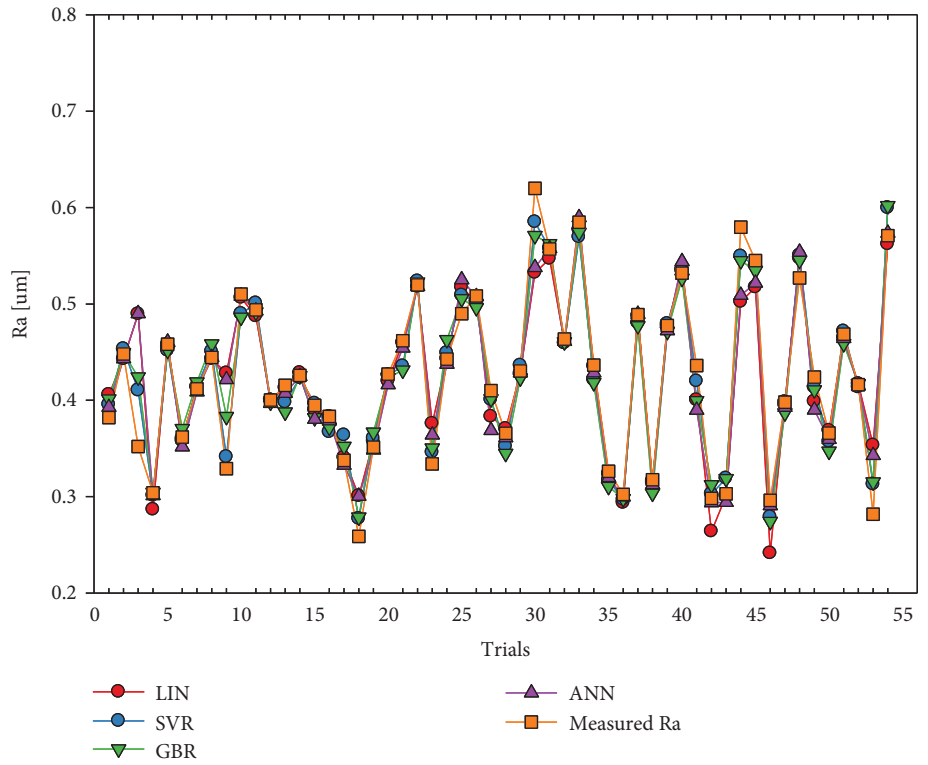

Figure 8: Comparison of experimental measurement and prediction of Ra on the training dataset.

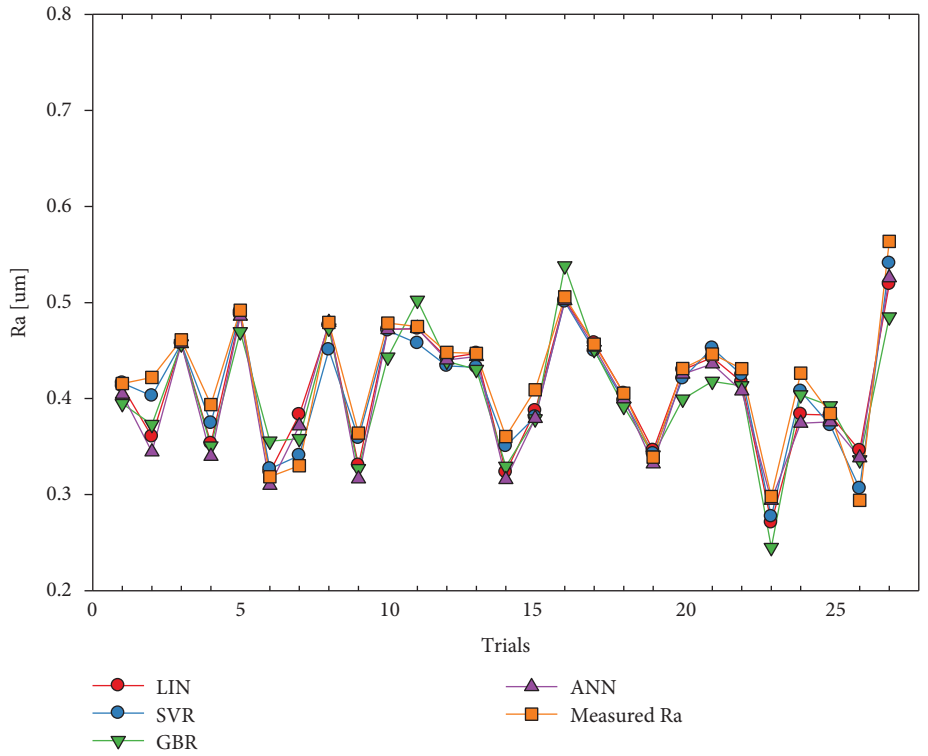

Figure 9: Comparison of experimental measurement and prediction of Ra on the testing dataset.

Table 6: Performance of ML models for Vbmax prediction on the training and testing datasets.

Model	Training dataset			Testing dataset		
	RMSE	MAE	R^2	RMSE	MAE	R^2
LIN	3.901	3.094	0.957	3.136	2.718	0.976
SVR	4.455	3.785	0.944	3.846	2.921	0.969
GRB	0.738	0.580	0.998	1.822	1.486	0.992
ANN	0.923	0.637	0.998	1.506	1.090	0.994

Objectives:

$$\begin{aligned} &\text{Minimize } Ra = SVR\_\text{reg}\_Ra\,(a, V, f, L, T), \\ &\text{Minimize } Vb\text{max} = ANN\_\text{reg}\_Vb\text{max}\,(a, V, f, L, T). \end{aligned} \tag{4}$$

subject to constraints

$$\begin{aligned} 2,700 \le V_f \le 4,050, \\ 10,345 \le V_c \le 13,528, \\ 0.2 \le a \le 0.6, \\ 22.23 \le T \le 166.67. \end{aligned} \tag{5}$$

The NSGA-II algorithm was implemented in *Python*. Control parameters were selected to operate the algorithm, such as population size, the maximum number of generations, crossover rate, mutation rate, and selection rate [62]. Table 8 shows the control parameters used in the present work. "Population size" is the initial set of solutions corresponding to each generation. A small "population size" limits the ability of the exploration of the search space and crossover operations, but a large population size can be computationally complex.

"Maximum generations" indicate the number of iterations until the end of the algorithm. "Crossover" represents the frequency with which crossovers are performed. The value of "crossover" impacts the convergence speed: a high value results in fast convergence, and a low value results in slow convergence. Finally, "mutation probability" represents how often parts of an individual solution undergo random perturbations. The "selection rate" indicates a designated probability to produce offspring for parents and applying crossover and mutation [63]. In this study, a reasonable convergence rate was obtained with a population size of 50, maximum generator of 100, crossover rate of 0.85, mutation rate of 0.25, and selection rate of 0.2.

After the NSGA-II algorithm parameters were assigned, the algorithm converged successfully after 250 function evaluations. The Pareto curve is shown in Figure 12. Pareto solutions are marked in red. The first performance objective, Ra, was found to lie between 0.257 and 0.308 μm, and the second performance objective, the tool wear (Vbmax), was found to be between 136.198 and 137.133 μm in the 50 Pareto solutions. As shown in Figure 12, the values of the optimization objective function conform to the Pareto curve, and the curve is continuous.

The optimal configuration is shown in Table 9. It is recommended that the table feed rate be between 2,700 and 2,707.411 mm/min, while the cutting speed should be between 10,345 and 10,345.08 m/min, the depth of cut should

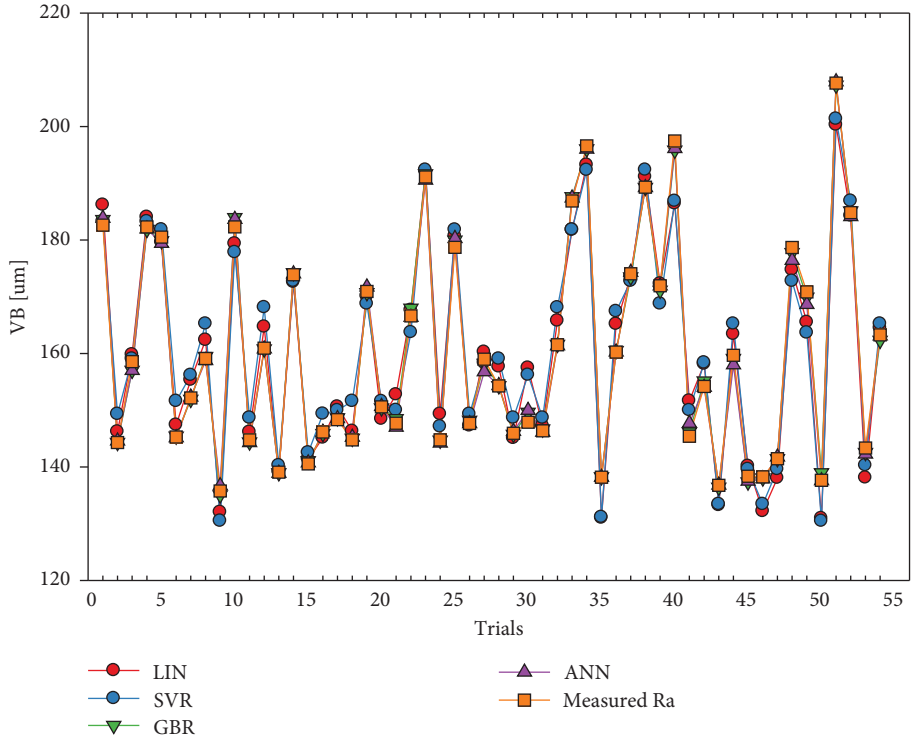

Figure 10: Comparison of experimental measurement and prediction of VB on the training dataset.

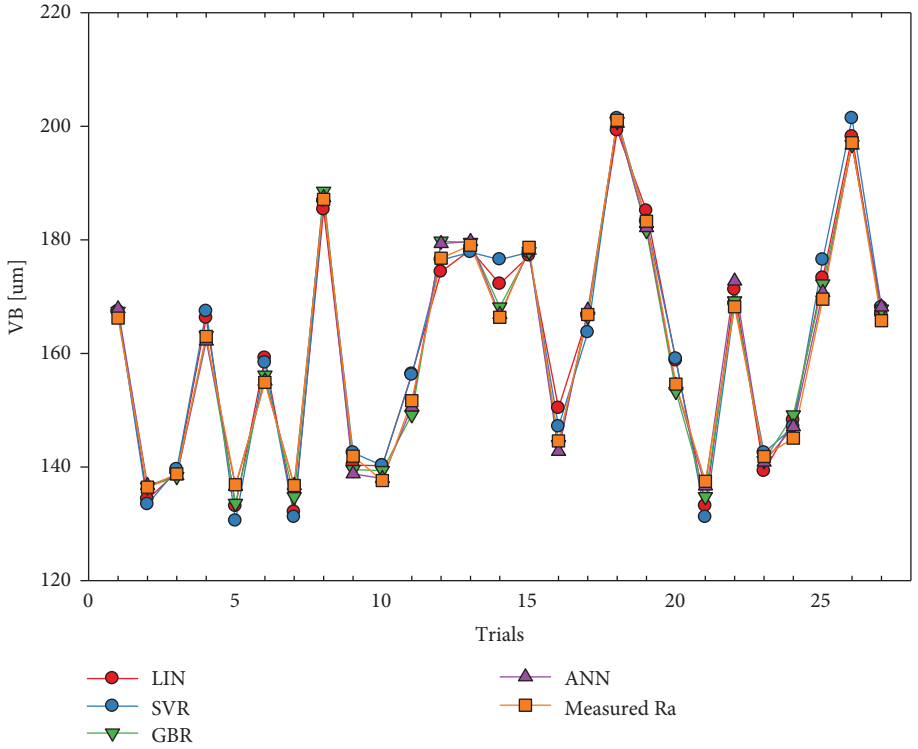

Figure 11: Comparison of experimental measurement and prediction of VB on the testing dataset.

be between 0.435 and 0.600 mm, and the cutting time should be approximately 33.33 seconds. The values of the Pareto solution set are shown in Table 10.

5.4. Validation of Predicted Results. To verify the Pareto solution results, confirmatory experiments were performed. The cutting parameters of optimal solution numbers 1, 2, 22,

Table 7: Comparison of performance using different activation functions for Vbmax prediction on the training and testing dataset.

Activation functions	Training dataset			Testing dataset		
	RMSE	MAE	R^2	RMSE	MAE	R^2
Relu	0.923	0.637	0.998	1.506	1.090	0.994
Softmax	51.045	47.495	0.000	51.145	47.385	0.000
Sigmoid	1.246	0.875	0.996	1.633	1.297	0.995
Softplus	3.596	2.741	0.969	3.200	2.613	0.974
Softsign	5.720	3.988	0.921	7.091	5.763	0.872
Tanh	5.689	4.259	0.911	5.114	4.272	0.930
Selu	1.783	1.270	0.991	1.994	1.576	0.991
elu	3.488	2.757	0.965	2.909	2.550	0.980
Exponential	4.424	3.533	0.971	3.011	2.315	0.982

Table 8: NSGA-II controlled parameters.

Parameter	Parameter value
Population size	50
Maximum generations	100
Crossover rate	0.85
Mutation rate	0.2
Selection rate	0.25

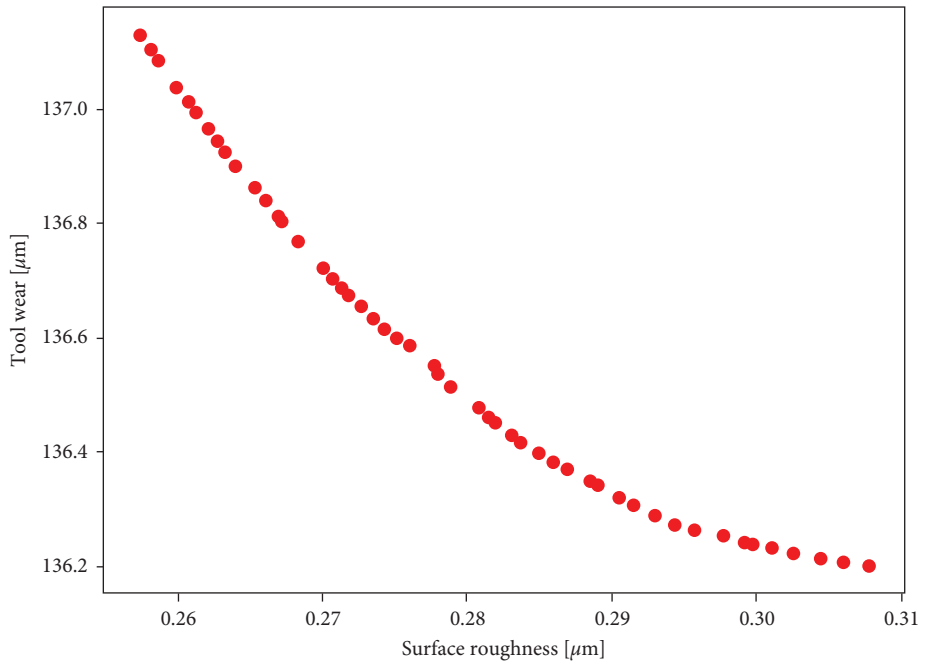

Figure 12: Pareto front of nondominated results.

Table 9: Range of values in Pareto solutions generated by multiobjective NSGA-II.

Range	Table feed (mm/min)	Cutting speed (m/min)	Depth of cut (mm)	Cutting time (s)	Ra (μm)	Vbmax (μm)
Minimum	2,700	10,345	0.435	33.33	0.257	137.133
Maximum	2,707.411	10,345.08	0.600	33.33	0.308	136.198

26, and 48 have been randomly selected from Table 10. The results are compared in Table 11. As indicated in the table, the test results are near the predicted values found through optimization using NSGA-II. The highest absolute percentage errors of Ra and Vbmax are 2.5% and 1.5%. Therefore, the combination of NSGA-II and ML can be used to obtain the desired Ra and Vbmax in high-speed milling operations.

Table 10: Performance statistics obtained by 50 Pareto solutions.

Solutions	Table feed (mm/min)	Cutting speed (m/min)	Depth of cut (mm)	Cutting time (s)	Ra (μm)	Vbmax (μm)
1	2,700.00	10,345.00	0.435	33.33	0.308	136.198
2	2,700.00	10,345.00	0.600	33.33	0.257	137.133
3	2,700.00	10,345.00	0.529	33.33	0.279	136.514
4	2,700.00	10,345.00	0.559	33.33	0.270	136.721
5	2,700.00	10,345.00	0.523	33.33	0.281	136.475
6	2,700.00	10,345.00	0.574	33.33	0.265	136.863
7	2,705.27	10,345.00	0.540	33.27	0.276	136.587
8	2,700.01	10,345.02	0.592	33.33	0.260	137.041
9	2,705.27	10,345.00	0.535	33.27	0.278	136.550
10	2,700.00	10,345.00	0.503	33.33	0.287	136.369
11	2,700.11	10,345.00	0.564	33.33	0.268	136.770
12	2,700.00	10,345.00	0.446	33.33	0.304	136.211
13	2,700.00	10,345.00	0.488	33.33	0.291	136.306
14	2,700.00	10,345.00	0.572	33.33	0.266	136.841
15	2,700.00	10,345.00	0.491	33.33	0.290	136.319
16	2,700.00	10,345.05	0.585	33.33	0.262	136.966
17	2,700.01	10,345.00	0.578	33.33	0.264	136.903
18	2,700.04	10,345.03	0.441	33.33	0.306	136.204
19	2,700.01	10,345.03	0.479	33.33	0.294	136.272
20	2,700.00	10,345.08	0.596	33.33	0.259	137.088
21	2,700.00	10,345.00	0.510	33.33	0.285	136.397
22	2,700.00	10,345.00	0.550	33.33	0.273	136.656
23	2,700.00	10,345.00	0.587	33.33	0.261	136.996
24	2,700.00	10,345.00	0.498	33.33	0.289	136.346
25	2,700.00	10,345.03	0.516	33.33	0.283	136.428
26	2,700.00	10,345.00	0.506	33.33	0.286	136.382
27	2,700.00	10,345.01	0.520	33.33	0.282	136.452
28	2,700.00	10,345.00	0.496	33.33	0.289	136.339
29	2,700.01	10,345.01	0.583	33.33	0.263	136.946
30	2,700.00	10,345.00	0.542	33.33	0.275	136.599
31	2,707.41	10,345.00	0.470	33.24	0.298	136.251
32	2,700.00	10,345.00	0.533	33.33	0.278	136.536
33	2,700.00	10,345.00	0.553	33.33	0.272	136.675
34	2,700.01	10,345.01	0.569	33.33	0.267	136.814
35	2,700.00	10,345.00	0.547	33.33	0.273	136.634
36	2,700.00	10,345.00	0.452	33.33	0.303	136.220
37	2,700.00	10,345.00	0.556	33.33	0.271	136.705
38	2,700.00	10,345.00	0.463	33.33	0.299	136.240
39	2,700.00	10,345.00	0.598	33.33	0.258	137.106
40	2,700.00	10,345.00	0.554	33.33	0.271	136.688
41	2,700.00	10,345.00	0.581	33.33	0.263	136.927
42	2,700.00	10,345.02	0.483	33.33	0.293	136.286
43	2,700.00	10,345.00	0.457	33.33	0.301	136.229
44	2,700.00	10,345.01	0.461	33.33	0.300	136.236
45	2,700.00	10,345.00	0.474	33.33	0.296	136.261
46	2,700.00	10,345.00	0.544	33.33	0.274	136.616
47	2,700.00	10,345.00	0.589	33.33	0.261	137.014
48	2,700.00	10,345.00	0.521	33.33	0.281	136.462
49	2,700.00	10,345.01	0.513	33.33	0.284	136.416
50	2,700.00	10,345.06	0.568	33.33	0.267	136.805

Table 11: Validation of predicted results.

No.	Pareto solution no.	Table feed (mm/min)	Spindle speed (rev/min)	Depth of cut (mm)	Cutting time (s)	Optimal		Experimental		Absolute percentage error	
						Ra (μm)	VB (μm)	Ra (μm)	VB (μm)	Ra (μm)	VB (μm)
1	1	2,700	10,345	0.435	33.33	0.308	136.198	0.311	136.235	0.96%	0.17%
2	2	2,700	10,345	0.600	33.33	0.257	137.133	0.255	139.215	0.78%	1.50%
3	22	2,700	10,345	0.550	33.33	0.273	136.656	0.280	137.775	2.50%	0.81%
4	26	2,700	10,345	0.506	33.33	0.286	136.382	0.284	136.025	0.70%	0.26%
5	48	2,700	10,345	0.521	33.33	0.281	136.462	0.285	137.115	1.40%	0.48%

Table 12: Values of variables in the normalized space.

Nr Unit	V_f (mm/min)	V_c (rev/min)	a (mm)	T_c (s)	R_a (μm)	VB (μm)	Dataset
1	0.0000	0.0000	0.0000	0.0769	0.4515	0.0368	
2	0.0000	0.5002	0.5000	0.0769	0.2909	0.0999	
3	0.0000	1.0000	1.0000	0.0769	0.0000	0.1460	
4	0.6496	0.0000	0.5000	0.0204	0.1967	0.0160	
5	0.6496	0.5002	1.0000	0.0204	0.0637	0.1229	
6	0.6496	1.0000	0.0000	0.0204	0.6898	0.1932	
7	1.0000	0.0000	0.5000	0.0000	0.1939	0.0000	
8	1.0000	0.5002	0.0000	0.0000	0.7922	0.0422	
9	1.0000	1.0000	0.5000	0.0000	0.6510	0.1461	
10	0.0000	0.0000	0.0000	0.5385	0.4183	0.3766	
11	0.0000	0.5002	0.5000	0.5385	0.3740	0.4418	
12	0.0000	1.0000	1.0000	0.5385	0.2798	0.4965	
13	0.6496	0.0000	0.5000	0.3687	0.4903	0.1568	
14	0.6496	0.5002	0.0000	0.3687	0.2576	0.3698	
15	0.6496	1.0000	0.0000	0.3687	0.8449	0.4867	
16	1.0000	0.0000	1.0000	0.3077	0.4626	0.1513	
17	1.0000	0.5002	0.0000	0.3077	1.0000	0.1964	
18	1.0000	1.0000	0.5000	0.3077	0.8892	0.3876	
19	0.0000	0.0000	0.0000	1.0000	0.3407	0.7597	
20	0.0000	0.5002	0.5000	1.0000	0.2078	0.8973	
21	0.0000	1.0000	1.0000	1.0000	0.0970	0.9947	
22	0.6496	0.0000	0.5000	0.7171	0.4765	0.5263	
23	0.6496	0.5002	1.0000	0.7171	0.4155	0.6959	
24	0.6496	1.0000	0.0000	0.7171	0.7562	1.0000	
25	1.0000	0.0000	1.0000	0.6154	0.4571	0.5689	
26	1.0000	0.5002	0.0000	0.6154	0.7424	0.6961	
27	1.0000	1.0000	0.5000	0.6154	0.6399	0.6965	
28	0.0000	0.0000	0.5000	0.0769	0.1773	0.0713	Training dataset
29	0.0000	0.0000	1.0000	0.0769	0.3767	0.1013	
30	0.0000	0.5002	0.0000	0.0769	0.1413	0.1144	
31	0.0000	0.5002	1.0000	0.0769	0.4986	0.1627	
32	0.0000	1.0000	0.0000	0.0769	0.3296	0.1487	
33	0.0000	1.0000	0.5000	0.0769	0.3795	0.0488	
34	0.6496	0.0000	0.0000	0.0204	0.1579	0.0659	
35	0.6496	0.0000	1.0000	0.0204	0.4294	0.1339	
36	0.6496	0.5002	0.0000	0.0204	0.2881	0.1000	
37	0.6496	0.5002	0.5000	0.0204	0.4792	0.1622	
38	0.6496	1.0000	0.5000	0.0204	0.2604	0.1562	
39	0.6496	1.0000	1.0000	0.0204	0.5125	0.0203	
40	1.0000	0.0000	0.0000	0.0000	0.2909	0.0626	
41	1.0000	0.0000	1.0000	0.0000	0.5623	0.0599	
42	1.0000	0.5002	0.5000	0.0000	0.4432	0.0940	
43	1.0000	0.5002	1.0000	0.0000	0.7479	0.1488	
44	1.0000	1.0000	0.0000	0.0000	0.4848	0.1451	
45	1.0000	1.0000	1.0000	0.0000	0.3934	0.3985	
46	0.0000	0.0000	0.5000	0.5385	0.3380	0.3991	
47	0.0000	0.0000	1.0000	0.5385	0.3850	0.4161	
48	0.0000	0.5002	0.0000	0.5385	0.3075	0.4345	
49	0.0000	0.5002	1.0000	0.5385	0.5623	0.4760	
50	0.0000	1.0000	0.0000	0.5385	0.4155	0.4838	
51	0.0000	1.0000	0.5000	0.5385	0.4432	0.2468	
52	0.6496	0.0000	0.0000	0.3687	0.3989	0.1544	
53	0.6496	0.0000	1.0000	0.3687	0.4183	0.2797	
54	0.6496	0.5002	0.5000	0.3687	0.3712	0.2517	

Table 12: Continued.

Nr Unit	V_f (mm/min)	V_c (rev/min)	a (mm)	T_c (s)	R_a (μm)	VB (μm)	Dataset
55	0.6496	0.5002	1.0000	0.3687	0.6399	0.4461	
56	0.6496	1.0000	0.5000	0.3687	0.4709	0.4514	
57	0.6496	1.0000	1.0000	0.3687	0.6150	0.1573	
58	1.0000	0.0000	0.0000	0.3077	0.4875	0.1508	
59	1.0000	0.0000	0.5000	0.3077	0.7258	0.1915	
60	1.0000	0.5002	0.5000	0.3077	0.6150	0.1666	
61	1.0000	0.5002	1.0000	0.3077	0.9003	0.3894	
62	1.0000	1.0000	0.0000	0.3077	0.6537	0.3591	
63	1.0000	1.0000	1.0000	0.3077	0.3075	0.7641	
64	0.0000	0.0000	0.5000	1.0000	0.2521	0.7750	
65	0.0000	0.0000	1.0000	1.0000	0.3407	0.8521	
66	0.0000	0.5002	0.0000	1.0000	0.2161	0.9006	
67	0.0000	0.5002	1.0000	1.0000	0.5042	0.9448	
68	0.0000	1.0000	0.0000	1.0000	0.3241	0.9621	Testing dataset
69	0.0000	1.0000	0.5000	1.0000	0.4626	0.6171	
70	0.6496	0.0000	0.0000	0.7171	0.4238	0.5649	
71	0.6496	0.0000	1.0000	0.7171	0.4598	0.7463	
72	0.6496	0.5002	0.0000	0.7171	0.4321	0.6756	
73	0.6496	0.5002	0.5000	0.7171	0.6011	0.8812	
74	0.6496	1.0000	0.5000	0.7171	0.4598	0.8710	
75	0.6496	1.0000	1.0000	0.7171	0.5596	0.6009	
76	1.0000	0.0000	0.0000	0.6154	0.4709	0.5548	
77	1.0000	0.0000	0.5000	0.6154	0.6260	0.6722	
78	1.0000	0.5002	0.5000	0.6154	0.5568	0.6628	
79	1.0000	0.5002	1.0000	0.6154	0.7396	0.7541	
80	1.0000	1.0000	0.0000	0.6154	0.5734	0.6888	
81	1.0000	1.0000	1.0000	0.6154	0.2521	0.2141	

6. Conclusion

This work has modeled and optimized the process of high-speed milling of 6061 aluminum alloy. The present study has used the ML models to predict the performance characteristics of Ra and Vbmax more robustly and accurately than the traditional approach. Moreover, a hybridization between ML models and a multiobjective optimization algorithm provided some optimal solutions. Any solution that still achieves the minimum values of Ra and Vbmax simultaneously can then be chosen. The main conclusions of this work are summarized as follows [64, 65]:

(i) 81 experiment runs were performed to determine the surface roughness and tool wear. To avoid underfitting and overfitting and to enhance the predictive accuracy, hyperparameters of models were tuned using the GridSearchCV technique. The results showed that SVR and ANN performed better than the rest of the models in the prediction of Ra and Vbmax when considering RMSE, MAE, and R2. Regarding the predictive performance of Ra, the values of RMSE, MAE, and R^2 were 0.014, 0.012, and 0.973, respectively, which are smaller than those of the other models. Regarding the predictive performance of Vbmax, the values of RMSE, MAE, and R^2 were 1.506, 1.090, and 0.994, respectively, which are again the lowest values when compared with LIN, SVR, and ANN.

(ii) After applying the NSGA-II technique, the average surface roughness (Ra) ranged between 0.257 and 0.308 μm, and the Vbmax ranged between 136.198 and 137.133 μm in the 50 Pareto solutions. The feed rate ranged between 2,700 and 2,707.411 mm/min, the cutting speed ranged between 10,345 and 10,345.08 m/min, the depth of cut ranged between 0.435 and 0.600 mm, and the cutting time was approximately 33.33 seconds.

(iii) The experimental verification results showed that absolute percentage errors of Ra and Vbmax were 2.5% and 1.5%, respectively.

Thus, this work confirmed that the multiobjective optimization approach provided good performance regarding the quality metrics for Ra and Vbmax. Nevertheless, more studies are needed to develop an intelligent system using NSGA-II as a decision-making tool to integrate user preferences. In further studies, the cutting forces should be measured and analyzed for a better understanding of the mechanical process.

Abbreviations

Ra: Average surface roughness
Vbmax: Maximum flank wear wear
NSGA-II: Nondominated Sorting Genetic Algorithm
LIN: Linear regression
SVR: Support vector machine regression

GBR: Gradient boosting tree
ANN: Artificial neural network
RMSE: Root mean squared error
MAE: Mean absolute error
R^2: Coefficient of determination
V_f: Table feed rate
V_c: Cutting speed
a: Depth of cut
T_c: Cutting time
L: Cutting length.

Appendix

A. Experimental Data

In this work, the experimental data points were scaled to a range of [0; 1], as is common in machine learning for minimizing the bias between variables. The procedure for scaling a variable x is shown in Equation (A.1), which consists of two parameters, ϕ and ψ. It should be noted that ψ is the minimum of the considered variable x, and ϕ is its maximum. Finally, a reverse transformation can also be deduced from Eq. (A.1) for converting data from the scaling space to the original one (Table 12).

$$x^{\text{scaled}} = \frac{x^{\text{original}} - \psi}{\phi - \psi}. \tag{A.1}$$

Data Availability

The excel data used to support the findings of this study are available from the corresponding author upon request.

Conflicts of Interest

The authors declare that there are no conflicts of interest regarding the publication of this paper.

References

[1] C. K. Ng, S. N. Melkote, M. Rahman, and A. Senthil Kumar, "Experimental study of micro-and nano-scale cutting of aluminum 7075-T6," *International Journal of Machine Tools and Manufacture*, vol. 46, no. 9, pp. 929–936, 2006.

[2] N.-T. Nguyen, D. H. Tien, N. T. Tung, and N. D. Luan, "Analysis of tool wear and surface roughness in high-speed milling process of aluminum alloy Al6061," *Eureka*, vol. 3, pp. 71–84, 2021.

[3] S. Parasuraman, I. Elamvazuthi, G. Kanagaraj, E. Natarajan, and A. Pugazhenthi, "Assessments of process parameters on cutting force and surface roughness during drilling of AA7075/TiB2 in situ composite," *Materials*, vol. 14, no. 7, p. 1726, 2021.

[4] A. Gómez-Parra, M. Álvarez-Alcón, J. Salguero, M. Batista, and M. Marcos, "Analysis of the evolution of the Built-Up Edge and Built-Up Layer formation mechanisms in the dry turning of aeronautical aluminium alloys," *Wear*, vol. 302, no. 1-2, pp. 1209–1218, 2013.

[5] Z. A. Zoya and R. Krishnamurthy, "The performance of CBN tools in the machining of titanium alloys," *Journal of Materials Processing Technology*, vol. 100, no. 1-3, pp. 80–86, 2000.

[6] D. Y. Pimenov, A. T. Abbas, M. K. Gupta, I. N. Erdakov, M. S. Soliman, and M. M. El Rayes, "Investigations of surface quality and energy consumption associated with costs and material removal rate during face milling of AISI 1045 steel," *International Journal of Advanced Manufacturing Technology*, vol. 107, no. 7-8, pp. 3511–3525, 2020.

[7] D. Y. Pimenov, "Experimental research of face mill wear effect to flat surface roughness," *Journal of Friction and Wear*, vol. 35, no. 3, pp. 250–254, 2014.

[8] D. Chuchala, M. Dobrzynski, D. Y. Pimenov, K. A. Orlowski, G. Krolczyk, and K. Giasin, "Surface roughness evaluation in thin EN AW-6086-T6 alloy plates after face milling process with different strategies," *Materials*, vol. 14, no. 11, p. 3036, 2021.

[9] V.-H. Nguyen and T.-T. Le, *Developing geometric error compensation software for five-Axis CNC machine tool on NC program based on artificial neural network*, N. V. Khang, N. Q. Hoang, and M. Ceccarelli, Eds., Springer International Publishing, Cham, pp. 541–548, 2022.

[10] D. Y. Pimenov, A. Bustillo, and T. Mikolajczyk, "Artificial intelligence for automatic prediction of required surface roughness by monitoring wear on face mill teeth," *Journal of Intelligent Manufacturing*, vol. 29, no. 5, pp. 1045–1061, 2018.

[11] V.-H. Nguyen, T.-T. Le, H.-S. Truong et al., "Applying bayesian optimization for machine learning models in predicting the surface roughness in single-point diamond turning polycarbonate," *Mathematical Problems in Engineering*, vol. 2021, Article ID 6815802, 16 pages, 2021.

[12] V. Flores and B. Keith, "Gradient boosted trees predictive models for surface roughness in high-speed milling in the steel and aluminum metalworking industry," *Complexity*, vol. 2019, Article ID 1536716, 15 pages, 2019.

[13] R. M. C. Karthik, R. L. Malghan, F. Kara, A. Shettigar, S. S. Rao, and M. A. Herbert, "Influence of support vector regression (SVR) on cryogenic face milling," *Advances in Materials Science and Engineering*, vol. 2021, Article ID 9984369, 18 pages, 2021.

[14] I. V. Manoj, H. Soni, S. Narendranath, P. M. Mashinini, and F. Kara, "Examination of machining parameters and prediction of cutting velocity and surface roughness using RSM and ANN using WEDM of altemp HX," *Advances in Materials Science and Engineering*, vol. 2022, Article ID e5192981, 9 pages, 2022.

[15] A. Eser, E. Aşkar Ayyıldız, M. Ayyıldız, and F. Kara, "Artificial intelligence-based surface roughness estimation modelling for milling of AA6061 alloy," *Advances in Materials Science and Engineering*, vol. 2021, Article ID 5576600, 10 pages, 2021.

[16] F. Kara, M. Karabatak, M. Ayyıldız, and E. Nas, "Effect of machinability, microstructure and hardness of deep cryogenic treatment in hard turning of AISI D2 steel with ceramic cutting," *Journal of Materials Research and Technology*, vol. 9, no. 1, pp. 969–983, 2020.

[17] J. C. Chen and J. C. Chen, "An artificial-neural-networks-based in-process tool wear prediction system in milling operations," *International Journal of Advanced Manufacturing Technology*, vol. 25, no. 5-6, pp. 427–434, 2005.

[18] D. Wu, C. Jennings, J. Terpenny, R. X. Gao, and S. Kumara, "A comparative study on machine learning algorithms for smart manufacturing: tool wear prediction using random forests," *Journal of Manufacturing Science and Engineering*, vol. 139, no. 7, 2017.

[19] M. García-Ordás, *Wear Characterization of the Cutting Tool in Milling Processes Using Shape and Texture Descriptors*, PhD Thesis, Universidad de León, León, Spain, 2017.

[20] P. Krishnakumar, K. Rameshkumar, and K. I. Ramachandran, "Tool wear condition prediction using vibration signals in high speed machining (HSM) of titanium (Ti-6Al-4 V) alloy," *Procedia Computer Science*, vol. 50, pp. 270–275, 2015.

[21] B. Ozcelik, H. Oktem, and H. Kurtaran, "Optimum surface roughness in end milling Inconel 718 by coupling neural network model and genetic algorithm," *International Journal of Advanced Manufacturing Technology*, vol. 27, no. 3-4, pp. 234–241, 2005.

[22] V. Pare, G. Agnihotri, and C. Krishna, "Selection of optimum process parameters in high speed CNC end-milling of composite materials using meta heuristic techniques – a comparative study," *Strojniški vestnik – Journal of Mechanical Engineering*, vol. 61, no. 3, pp. 176–186, 2015.

[23] R. Quiza Sardiñas, M. Rivas Santana, and E. Alfonso Brindis, "Genetic algorithm-based multi-objective optimization of cutting parameters in turning processes," *Engineering Applications of Artificial Intelligence*, vol. 19, no. 2, pp. 127–133, 2006.

[24] J. Yan and L. Li, "Multi-objective optimization of milling parameters–the trade-offs between energy, production rate and cutting quality," *Journal of Cleaner Production*, vol. 52, pp. 462–471, 2013.

[25] D. R. Unune, C. K. Nirala, and H. S. Mali, "ANN-NSGA-II dual approach for modeling and optimization in abrasive mixed electro discharge diamond grinding of Monel K-500," *Engineering Science and Technology, an International Journal*, vol. 21, no. 3, pp. 322–329, 2018.

[26] P. Kayaroganam, V. Krishnan, E. Natarajan, S. Natarajan, and K. Muthusamy, "Drilling parameters analysis on in-situ Al/B4C/mica hybrid composite and an integrated optimization approach using fuzzy model and non-dominated sorting genetic algorithm," *Metals*, vol. 11, no. 12, p. 2060, 2021.

[27] C.-H. Kuo and Z.-Y. Lin, "Optimizing the high-performance milling of thin aluminum alloy plates using the taguchi method," *Metals*, vol. 11, no. 10, p. 1526, 2021.

[28] R. Viswanathan, S. Ramesh, S. Maniraj, and V. Subburam, "Measurement and multi-response optimization of turning parameters for magnesium alloy using hybrid combination of Taguchi-GRA-PCA technique," *Measurement*, vol. 159, Article ID 107800, 2020.

[29] T.-T. Le, "Practical hybrid machine learning approach for estimation of ultimate load of elliptical concrete-filled steel tubular columns under axial loading," *Advances in Civil Engineering*, vol. 2020, Article ID 8832522, 19 pages, 2020.

[30] V. Vapnik, *The Nature of Statistical Learning Theory*, Springer, New York, 2nd edition, 1999.

[31] N. X. Ho and T.-T. Le, "Effects of variability in experimental database on machine-learning-based prediction of ultimate load of circular concrete-filled steel tubes," *Measurement*, vol. 176, 2021.

[32] T.-T. Le and H. C. Phan, "Prediction of ultimate load of rectangular CFST columns using interpretable machine learning method," *Advances in Civil Engineering*, vol. 2020, Article ID 8855069, 16 pages, 2020.

[33] M. S. Alajmi and A. M. Almeshal, "Predicting the tool wear of a drilling process using novel machine learning XGBoost-SDA," *Materials*, vol. 13, no. 21, p. 4952, 2020.

[34] X. Chen, L. Huang, D. Xie, and Q. Zhao, "EGBMMDA: extreme gradient boosting machine for MiRNA-disease association prediction," *Cell Death & Disease*, vol. 9, pp. 3–16, 2018.

[35] P. G. Asteris, M. E. Lemonis, T.-T. Le, and K. D. Tsavdaridis, "Evaluation of the ultimate eccentric load of rectangular CFSTs using advanced neural network modeling," *Engineering Structures*, vol. 248, p. 113297, 2021.

[36] T.-T. Le and M. V. Le, "Prediction model for tensile modulus of carbon nanotube–polymer composites," in *Adv. Eng. Res. Appl*, D. C. Nguyen, N. P. Vu, B. T. Long, H. Puta, and K.-U. Sattler, Eds., Springer International Publishing, Cham, pp. 786–792, 2022.

[37] H. T. Duong, H. C. Phan, and T.-T. Le, "Critical buckling load evaluation of functionally graded material plate using Gaussian process regression," in *Adv. Eng. Res. Appl*, D. C. Nguyen, N. P. Vu, B. T. Long, H. Puta, and K.-U. Sattler, Eds., Springer International Publishing, Cham, pp. 286–292, 2022.

[38] O. Ghorbanzadeh, T. Blaschke, K. Gholamnia, S. R. Meena, D. Tiede, and J. Aryal, "Evaluation of different machine learning methods and deep-learning convolutional neural networks for landslide detection," *Remote Sensing*, vol. 11, no. 2, p. 196, 2019.

[39] A. C. Tsoi and A. Back, "Discrete time recurrent neural network architectures: a unifying review," *Neurocomputing*, vol. 15, no. 3-4, pp. 183–223, 1997.

[40] J. Cheng, L. Dong, and M. Lapata, *Long Short-Term Memory-Networks for Machine reading*, 2016, https://arxiv.org/abs/1601.06733.

[41] F. Kara, K. Aslantas, and A. Çiçek, "ANN and multiple regression method-based modelling of cutting forces in orthogonal machining of AISI 316L stainless steel," *Neural Computing & Applications*, vol. 26, no. 1, pp. 237–250, 2015.

[42] T.-T. Le, V.-H. Nguyen, and M. V. Le, "Development of deep learning model for the recognition of cracks on concrete surfaces," *Applied Computational Intelligence and Soft Computing*, vol. 2021, Article ID 8858545, 10 pages, 2021.

[43] T.-T. Le and M. V. Le, "Development of user-friendly kernel-based Gaussian process regression model for prediction of load-bearing capacity of square concrete-filled steel tubular members," *Materials and Structures*, vol. 54, no. 2, p. 59, 2021.

[44] K. Deb, A. Pratap, S. Agarwal, and T. Meyarivan, "A fast and elitist multiobjective genetic algorithm: nsga-II," *IEEE Transactions on Evolutionary Computation*, vol. 6, no. 2, pp. 182–197, 2002.

[45] C. A. C. Coello, G. B. Lamont, and D. A. Van Veldhuizen, "Evolutionary Algorithms for Solving Multi-Objective Problems," *Springer*, vol. 5, 2007.

[46] V. Modrak, R. S. Pandian, and S. S. Kumar, "Parametric study of wire-EDM process in Al-Mg-MoS2 composite using NSGA-II and MOPSO algorithms," *Processes*, vol. 9, no. 3, p. 469, 2021.

[47] S. Ramesh, N. Vijayakumar, R. Viswanathan, and S. Saravanan, "Optimization of EDM machining of high carbon high chromium steel using zirconium and nickel powder mixed dielectric by grey relational analysis," in *Recent Trends Mech. Eng*, C. S. Ramesh, P. Ghosh, and E. Natarajan, Eds., Springer, Singapore, pp. 167–185, 2021.

[48] R. Viswanathan, S. Ramesh, and V. Subburam, "Measurement and optimization of performance characteristics in turning of Mg alloy under dry and MQL conditions," *Measurement*, vol. 120, pp. 107–113, 2018.

[49] S. Ramesh, R. Viswanathan, and S. Ambika, "Measurement and optimization of surface roughness and tool wear via grey relational analysis, TOPSIS and RSA techniques," *Measurement*, vol. 78, pp. 63–72, 2016.

[50] S. Kalpakjian, S. R. Schmid, and H. Musa, *Manufacturing Engineering and Technology: Machining*, China Machine Press, Baiwanzhuang, 2011.

[51] C. Ming, S. Fanghong, W. Haili, Y. Renwei, Q. Zhenghong, and Z. Shuqiao, "Experimental research on the dynamic characteristics of the cutting temperature in the process of high-speed milling," *Journal of Materials Processing Technology*, vol. 138, no. 1-3, pp. 468–471, 2003.

[52] I. Zaghbani, V. Songmene, and R. Khettabi, "Fine and ultrafine particle characterization and modeling in high-speed milling of 6061-T6 aluminum alloy," *Journal of Materials Engineering and Performance*, vol. 18, no. 1, pp. 38–48, 2009.

[53] A. R. Meyers and T. J. Slattery, *Basic Machining Reference Handbook*, Industrial Press Inc, South Norwalk, 2001.

[54] H. Chang, S. Li, and R. Shi, "Design and manufacturing technology of high speed milling cutter for aluminum alloy," *Procedia Engineering*, vol. 174, pp. 630–637, 2017.

[55] J. Wu, X.-Y. Chen, H. Zhang, L.-D. Xiong, H. Lei, and S.-H. Deng, "Hyperparameter optimization for machine learning models based on Bayesian optimization," *J. Electron. Sci. Technol.*vol. 17, pp. 26–40, 2019.

[56] M. Injadat, A. Moubayed, A. B. Nassif, and A. Shami, "Systematic ensemble model selection approach for educational data mining," *Knowledge-Based Systems*, vol. 200, Article ID 105992, 2020.

[57] J.-M. Dufour and J. Neves, "Finite-sample inference and nonstandard asymptotics with Monte Carlo tests and R," *Handb. Stat*, vol. 41, pp. 3–31, 2019.

[58] M.-A. Zöller and M. F. Huber, "Benchmark and survey of automated machine learning frameworks," *Journal of Artificial Intelligence Research*, vol. 70, pp. 409–472, 2021.

[59] I. S. Al-Mejibli, J. K. Alwan, and D. H. Abd, "The effect of gamma value on support vector machine performance with different kernels," *International Journal of Electrical and Computer Engineering*, vol. 10, no. 5, p. 5497, 2020.

[60] A. Géron, *Hands-on Machine Learning with Scikit-Learn, Keras, and TensorFlow: Concepts, Tools, and Techniques to Build Intelligent Systems*, O'Reilly Media, Sebastopol, California, USA, 2019.

[61] Ö. Erkan, B. Işık, A. Çiçek, and F. Kara, "Prediction of damage factor in end milling of glass fibre reinforced plastic composites using artificial neural network," *Applied Composite Materials*, vol. 20, no. 4, pp. 517–536, 2013.

[62] K. Deb and H. Jain, "An evolutionary many-objective optimization algorithm using reference-point-based nondominated sorting approach, part I: solving problems with box constraints," *IEEE Transactions on Evolutionary Computation*, vol. 18, no. 4, pp. 577–601, 2014.

[63] J. Blank and K. Deb, "pymoo: multi-objective optimization in python," *IEEE Access*, vol. 8, pp. 89497–89509, 2020.

[64] K. A. Venugopal, S. Paul, and A. B. Chattopadhyay, "Tool wear in cryogenic turning of Ti-6Al-4V alloy," *Cryogenics*, vol. 47, no. 1, pp. 12–18, 2007.

[65] A. R. Zareena and S. C. Veldhuis, "Tool wear mechanisms and tool life enhancement in ultra-precision machining of titanium," *Journal of Materials Processing Technology*, vol. 212, no. 3, pp. 560–570, 2012.

Hindawi
Advances in Materials Science and Engineering
Volume 2022, Article ID 9481566, 9 pages
https://doi.org/10.1155/2022/9481566

Research Article

Analysis of Drilling of Coir Fiber-Reinforced Polyester Composites Using Multifaceted Drill Bit

T. V. Rajamurugan,[1] C. Rajaganapathy,[1] S. P. Jani,[2] Claris Snigdha Gurram,[3] Haiter Lenin Allasi,[4] and Samson Zerihun Damtew[4]

[1]*Mechanical Engineering, Government College of Engineering Srirangam, Trichy 620012, Tamilnadu, India*
[2]*Department of Mechanical Engineering, Marri Laxman Reddy Institute of Technology and Management, Hyderabad 500043, India*
[3]*Monash University, Melbourne, Australia*
[4]*Department of Mechanical Engineering, WOLLO University, Kombolcha Institute of Technology, Post box no: 208, Kombolcha, Ethiopia*

Correspondence should be addressed to Haiter Lenin Allasi; drahlenin@kiot.edu.et

Received 17 March 2022; Revised 2 May 2022; Accepted 5 May 2022; Published 24 May 2022

Academic Editor: Sengottuvelu Ramesh

Composite materials are continuously replacing the conventional materials and alloys owing to their weight reduction. Biodegradable fiber-reinforced composite materials are one of the prime attractions to the researcher due to their easy availability and low cost. During drilling of these Natural Fiber Reinforced Plastic composites (NFRP), delamination and surface roughness are the problems encountered, which are to be minimized to get better output by adopting different cutting conditions and tools. This work aims at the drilling of naturally available coir fiber-reinforced composite materials by using a multifaceted drill bit. Material thickness, spindle speed, feed rate, and multifaceted bit diameter are input against the output delamination. After modeling of the output result, a sensitivity analysis tool is introduced to rate the input factor to minimize delamination. SEM images are used to analyze the fracture morphology.

1. Introduction

Composites reinforced with natural fibers were reported in the early twentieth century. Green composites are made up of polymeric matrix-reinforced by natural fibers. Green composites are ecofriendly, economic, and easy to dispose of. Green composites are a mixture of natural fibers and plastics which can easily be replacing conventional glass-fiber composites since they have the advantages such as biodegradability and low density. Nowadays, work has been going on to use natural fibers instead of carbon, glass fibers because of their strength to weight ratio. Rajamurugan et al. [1] compared mechanical testing of composites reinforced with coir and luffa. The qualities of the fibers determine the performance of composites. Drilling of these composites is needed in automotive industries such as flax, sisal, and jute for bolting two different parts in assembling. The drilling process is difficult because of the soft matrix and hard fiber reinforcement. During drilling operation, the thrust force is induced, which in turn leads to damage like fiber pull-out and delamination concerning input parameters. Srinivasan et. al. [2]and Mudhukrishnan et al. [3] conducted experiments on glass fiber-reinforced polypropylene composites. They observed the impact of tool materials over surface roughness in drilling, and they inferred that solid carbide drills with low tool feed and high speed give a good surface finish to drilled holes. Raj and Karunamoorthy [4] discovered that tool wear caused by abrasive fibers is a major cause of damage. To overcome this, they recommended that the drill bit is to be properly selected. Tool wear increases with the increase in thrust force. Voss et al. [5] calculated the tool lifetime based on hole quality. Latha et al. [6] conducted

experiments on glass fiber-reinforced plastic drilling for delamination analysis. The most influential parameters that affect hole quality are feed rate and drill diameter. Increased feed causes an increase in strain rate, which increases the surface roughness of the hybrid composite [7]. Response Surface Methodology is a numerical tool used for modeling and analyzing the problem. The aim of the RSM is a correlation among the factors and the responses. The important step of RSM is to select the suitable design matrix for conducting the experiment. Myers [8], Dhakal, and Gowda [9] conducted tensile, flexural, and impact tests to characterize the mechanical properties of a short raw banana fiber polyester composite. Similarly, Chaudhary [10] et al. compared the glass fiber-reinforced epoxy laminates using hand lay-up with vacuum bagging, as well as the flexural strength of a glass fiber polymer laminate. Harikumar and Devaraju [11] evaluated the mechanical characteristics of GFRP composites with copper wire embedded glass-fiber reinforced polymer and concluded that copper wire incorporated composites pose high tensile strength and impact strength.

The influence of various treatments on composites was studied by Sature and Mache [12], and they found that moisture treatment possesses good strength to composites. Senthilkumaran and Kannan [13] used sensitivity analysis to identify and prioritize process variables based on their impact on welded mild steel components. To attain less delamination and maximum tensile strength, Babu et al. [14] used Taguchi and ANOVA techniques. According to them, feed and speed possess more impact on delamination and tensile strength. Ficici et al. [15] used carbide drill bits to achieve the best surface quality and minimum thrust. Mohanraj et al [16] focused on neural network optimization, teaching learning-based optimization to minimize thrust force, torque, and delamination in the drilling of GFRP composites. The backpropagation network algorithm was used by Zhu et. al. [17] to forecast the drilling force, and the findings show that the estimated drilling force based on the upgraded network algorithm is consistent and accurate. In fiber laser processing of GFRP composites, Rao et al. [18] correlated anticipated and experimental values, to evaluate damages such as loose fibers, interlayer fractures, matrix material evaporation, and fiber breakages. Liping Liu et al. [19] investigated the role of drill tool geometry to minimize delamination and thrust force in the drilling of composites. Rajamurugan et al. [20] have formulated an empirical relationship by using the response surface technique to predict the delamination in machining. Ramesh et al. [21], Viswanathan. R et al. [22], and Srinivasan M et al. [23] conducted machining experiments and did optimization by using various techniques such as ANOVA Techniques and gray relation analysis to minimize delamination and surface roughness. Palanikumar. K et al. [24] evaluated the mechanical properties of coconut flower-reinforced composites and concluded that the materials can be used in the automotive sector. Kaviarasan et al. [25] experimented on a new Delrin material to minimize the surface roughness by using neural network optimization techniques under dry conditions. The literature revealed that the damage analysis caused by the machining parameters, such as spindle speed, feed rate, drill diameter, and the properties of the material-like fiber orientation angle on natural fiber-reinforced composites is limited. Hence, an attempt has been made of optimizing the abovementioned input drilling parameters with delamination as the output response with sensitivity analysis in coir fiber-reinforced composites drilling.

Table 1: The coir fiber's physical properties.

Physical property	Coir fiber	Units
Density	0.93	gm/cc
Young's modulus	166	Mpa
Tensile strength	15.75	Mpa
Shear strength	13.7	Mpa
Flexural strength	34.63	Mpa
Impact strength	283	Kj/m^2

2. Materials and Methods

Coir fiber was purchased from Agasteeswaram (Kanyakumari district, Tamilnadu). P-502 type polyester resin and methyl ethyl ketone peroxide hardener were purchased to produce the samples. The fibers of coconut were chopped into a mat, and these coir fibers were used to make a composite laminate with polyester resin. The length of the coir fiber is 15–20 cm, and the fiber orientation angle is 0, 22.5, 45, 67.5, 90. The fiber has been oriented at 0° one over the other as sample 1, similarly, 22.5° are laid one over the other, and sample 2 is prepared. Similarly, sample 3 with 45°, sample 4 with 67.5°, and sample 5 with 90° were prepared. A mixture of polyester resin and 1% radar hardener is used to fabricate laminate using coir fiber reinforcement using constant fiber weight fraction. Mold release spray and releasing agent were used to remove composite laminate. The specimen is cured at room temperature for 48 hours (Rajamurugan et al). The compression molding technique was used to prepare the samples with a size of 140 × 90 mm with three different thicknesses such as 8, 12, and 16 mm. Physical properties of the fiber are indicated in Table 1.

Response surface methodology—central composite design is used to plan the designed trials.

Table 2 lists the input parameters utilized in the experiments.

The drilling experiments are performed on coir fiber-reinforced composites in Computer Numeric Control Vertical Machining Center with a capable speed range of 5000 rpm. The experiments were conducted using "Multi-faceted" carbide K10 drill of five various diameters with an overall shank length of 5 inches and shank size 1/2′ solid carbide of 140° point angle and 28° helix angle, purchased from "Wood Tech Enterprises, USA." Delamination is a type of damage caused by the anisotropy and brittleness of composite materials. The delamination factor was calculated using a toolmaker microscope. The machine used for drilling is shown in Figure 1.

RSM-based central composite rotatable design was used to model and optimize process parameters. The output

Table 2: Parameters in drilling experiments.

S. No	Parameter	Symbol	Unit	Levels				
				(−2)	(−1)	(0)	(1)	(2)
1	Spindle speed	V	Rpm	500	875	1250	1625	2000
2	Tool feed rate	F	mm/min	50	112.5	175	237.5	300
3	Drill diameter (mm)	D	Mm	4	6	8	10	12
4	Fiber orientation angle	Θ	Degrees	0	22.5	45	67.5	90

Figure 1: Machine used for drilling.

function for response surface analysis, which includes interaction and square effects, can be represented as follows:

$$Y = \beta_o + \beta_1 x_1 + \beta_2 x_2 + \ldots + \beta_i x_i + \varepsilon, \quad (1)$$

where y indicates response, β_0, β_1,..., β_i indicates regression coefficient, x_1, x_2,..., x_i indicates the estimated variables, and $\varepsilon\varepsilon$ indicates an error. Equation (1) represents first-order linear form.

Equation (2) represents the linear response surface model:

$$y = \beta_o + \sum_{i=1}^{n} \beta_i X_i + \varepsilon, \quad (2)$$

where β_0 and β_i are called coefficients, x_1, x_2,...x_i represents the variables, and $\varepsilon\varepsilon$ is the residual. Considering the interaction terms, the above equation is modified as in equation (3):

$$\mathrm{y} = \beta_o + \sum_{i=1}^{n} \beta_i X_i + \sum_{i} \sum_{j>1} \beta_{ij} X_i X_j + \varepsilon. \quad (3)$$

Equation (4) expresses the quadratic response model, which includes all linear, square, and interaction factors:

$$\mathrm{y} = \beta_o + \sum_{i=1}^{n} \beta_i X_i + \sum_{i=1}^{n} \beta_i X^2 + \sum_{i=1}^{n} \sum_{j=1}^{n} \beta_{ij} X_i X_j + \varepsilon, \quad (4)$$

where β_0, βi, and βij are drilling parameters and n is the number of model parameters. The coefficients in the aforementioned model can be compared using the least square approach or the second-order model.

Table 3: Central composite rotatable design.

S. no.	Design													
	A (X_1)	B (X_2)	C (X_3)	D (X_4)	A^2 ($X_1{}^2$)	B^2 (X_2)	C^2 (X_3)	D^2 (X_4)	AB (X_1X_2)	AC (X_1X_3)	AD (X_1X_4)	BC (X_2X_3)	BD (X_2X_4)	CD (X_3X_4)
1.	−1	−1	−1	−1	1	1	1	1	1	1	1	1	1	1
2.	1	−1	−1	−1	1	1	1	1	−1	−1	−1	1	1	1
3.	−1	1	−1	−1	1	1	1	1	−1	1	1	−1	−1	1
4.	1	1	−1	−1	1	1	1	1	1	−1	−1	−1	−1	1
5.	−1	−1	1	−1	1	1	1	1	1	−1	1	−1	1	−1
6.	1	−1	1	−1	1	1	1	1	−1	1	−1	−1	1	−1
7.	−1	1	1	−1	1	1	1	1	−1	−1	1	1	−1	−1
8.	1	1	1	−1	1	1	1	1	1	1	−1	1	−1	−1
9.	−1	−1	−1	1	1	1	1	1	1	1	−1	1	−1	−1
10.	1	−1	−1	1	1	1	1	1	−1	−1	1	1	−1	−1
11.	−1	1	−1	1	1	1	1	1	−1	1	−1	−1	1	−1
12.	1	1	−1	1	1	1	1	1	1	−1	1	−1	1	−1
13.	−1	−1	1	1	1	1	1	1	1	−1	−1	−1	−1	1
14.	1	−1	1	1	1	1	1	1	−1	1	1	−1	−1	1
15.	−1	1	1	1	1	1	1	1	−1	−1	−1	1	1	1
16.	1	1	1	1	1	1	1	1	1	1	1	1	1	1
17.	-2	0	0	0	4	0	0	0	0	0	0	0	0	0
18.	2	0	0	0	4	0	0	0	0	0	0	0	0	0
19.	0	−2	0	0	0	4	0	0	0	0	0	0	0	0
20.	0	2	0	0	0	4	0	0	0	0	0	0	0	0
21.	0	0	−2	0	0	0	4	0	0	0	0	0	0	0
22.	0	0	2	0	0	0	4	0	0	0	0	0	0	0
23.	0	0	0	−2	0	0	0	4	0	0	0	0	0	0
24.	0	0	0	2	0	0	0	4	0	0	0	0	0	0
25.	0	0	0	0	0	0	0	0	0	0	0	0	0	0
26.	0	0	0	0	0	0	0	0	0	0	0	0	0	0
27.	0	0	0	0	0	0	0	0	0	0	0	0	0	0
28.	0	0	0	0	0	0	0	0	0	0	0	0	0	0
29.	0	0	0	0	0	0	0	0	0	0	0	0	0	0
30.	0	0	0	0	0	0	0	0	0	0	0	0	0	0

The variables are coded as follows: (0) represents the center; (−2) represents the lowest value; and (+2) represents the highest value. The linear, quadratic, and two-way interactive effects of the factors on the response were estimated using the 31 experimental runs (Rajamurugan et al. 2013). The primary machining factors that have more effects on the responses in drilling coir fiber-reinforced polyester composites have been discovered as being independently controllable. The parameters' limits were determined after a thorough investigation. The machining operations are conducted as per the design matrix (Table 3) randomly to avoid errors and also Table 3 shows the coded values. The parameters and responses are presented in Table 4. Table 5 represents the adjusted and predicted R^2 values and the graph is shown in Figure 2. The positive variables show an increasing trend, whereas the negative ones represent a falling trend. The contour plot is generally used to study the relation between two independent factors and one input response. Here we have the output response as the delamination factor, and the contour plot is plotted against the combined effect of drill diameter and tool feed rate. As observed in the figure, increasing drill diameter shows a minimum effect on delamination; however, increasing tool feed rate causes a rise in delamination. The equation in Table 6 shows a model summary for carbide multifaceted drill bit.

The quadratic model for output response delamination was created using the Design-Expert software. The model is designed concerning delamination for multifaceted drill material for coir fiber-reinforced composite materials. In this experimentation, all the R^2 values are greater than 0.96, which relies on the formulated empirical models that are fine enough to predict the drilling output response concerning process parameters.

3. Results and Discussion

Natural FRP composites, especially coir fiber-reinforced composites demonstrated suitable alternatives for glass fiber-reinforced composites due to their superior strength and easy availability. Delamination is a key cause of concern during composite drilling, and it must be avoided. During drilling, thrust force increases, and delamination also increases. While drilling composites, the thrust force exerted on the plate by the drill bit causes delamination on the periphery of the holes. This is due to inhomogeneity between the soft polyester matrix and the rigid coir fiber. The geometry of the drill bit like the chisel edge and cutting lip makes contact with the workpiece and the graph of the thrust force reaches its peak. Whereas during the drilling process, the graph will be normal as there is no friction between the tool and workpiece. Figure 3, 3(a) depicts the

Table 4: Coded values, real values, and delamination.

Exp. no.	Coded value				Real value				Delamination
	Spindle speed (rpm)	Tool feed rate (mm/min)	Drill diameter (mm)	Fiber orientation angle, degrees	Spindle speed (rpm)	Tool feed rate (mm/min)	Drill diameter (mm)	Fiber orientation angle, degrees	
1	−1	−1	−1	−1	875	112.5	6	22.5	1.36
2	1	−1	−1	−1	1625	112.5	6	22.5	1.26
3	−1	1	−1	−1	875	237.5	6	22.5	1.25
4	1	1	−1	−1	1625	237.5	6	22.5	1.83
5	−1	−1	1	−1	875	112.5	10	22.5	1.43
6	1	−1	1	−1	1625	112.5	10	22.5	1.12
7	−1	1	1	−1	875	237.5	10	22.5	1.36
8	1	1	1	−1	1625	237.5	10	22.5	1.56
9	−1	−1	−1	1	875	112.5	6	67.5	1.46
10	1	−1	−1	1	1625	112.5	6	67.5	1.15
11	−1	1	−1	1	875	237.5	6	67.5	1.32
12	1	1	−1	1	1625	237.5	6	67.5	1.5
13	−1	−1	1	1	875	112.5	10	67.5	1.79
14	1	−1	1	1	1625	112.5	10	67.5	1.15
15	−1	1	1	1	875	237.5	10	67.5	1.7
16	1	1	1	1	1625	237.5	10	67.5	1.5
17	−2	0	0	0	500	175	8	45	1.48
18	2	0	0	0	2000	175	8	45	1.31
19	0	−2	0	0	1250	50	8	45	1.27
20	0	2	0	0	1250	300	8	45	1.54
21	0	0	−2	0	1250	175	4	45	1.38
22	0	0	2	0	1250	175	12	45	1.49
23	0	0	0	−2	1250	175	8	0	1.42
24	0	0	0	2	1250	175	8	90	1.5
25	0	0	0	0	1250	175	8	45	1.26
26	0	0	0	0	1250	175	8	45	1.31
27	0	0	0	0	1250	175	8	45	1.27
28	0	0	0	0	1250	175	8	45	1.36
29	0	0	0	0	1250	175	8	45	1.35
30	0	0	0	0	1250	175	8	45	1.42

Table 5: ANOVA—delamination for multifaceted drill.

Source	DF	Seq SS	Adj SS	Adj MS	F	P
Regression	14	0.820967	0.820967	0.058640	29.42	0.000
Linear	4	0.211367	0.211367	0.052842	26.51	0.000
Square	4	0.047425	0.047425	0.011856	5.95	0.005
Interaction	6	0.562175	0.562175	0.093696	47.00	0.000
Residual error	15	0.029900	0.029900	0.001993		
Total	29	0.850867				

R-Sq = 96.49%

influence of rotational speed on delamination, which illustrates that increasing spindle speed reduces the delamination factor in drilling. The reason is, that at high spindle speed, the adhesives in the composite materials got melted, which makes the material soften, and it causes the low delamination in drilling. As the spindle speed is raised, delamination in drilling of coir FR-polyester composites increases. This is due to the length of short fiber for all the thicknesses say 8 mm, 12 mm, and 16 mm. Each graph shows the same pattern, so it can be asserted that the thickness of the laminate does not have any influence on spindle speed while drilling coir fiber-reinforced polyester composites using a multifaceted drill bit. The feed rate is a highly predominant criterion that influences the delamination in the drilling of coir FR-polyester composites, so the thrust force increases as the feed rate increases in the drilling of coir FR-polyester composites because the shear area increases. Furthermore, increasing the feed rate increases the area of the uncut chip, which enhances delamination. Figure 3(b) shows as delamination develops as the feed rates increases. This is common for all the three thicknesses of laminate. This is because the coir fiber has the highest toughness among all-natural fiber *S*. For 50 mm feed, the delamination will be around 1.4, whereas it reaches the maximum of 1.6 at 300 mm/rev. The effect of drill diameter on delamination in composite material drilling suggests that when drill diameter

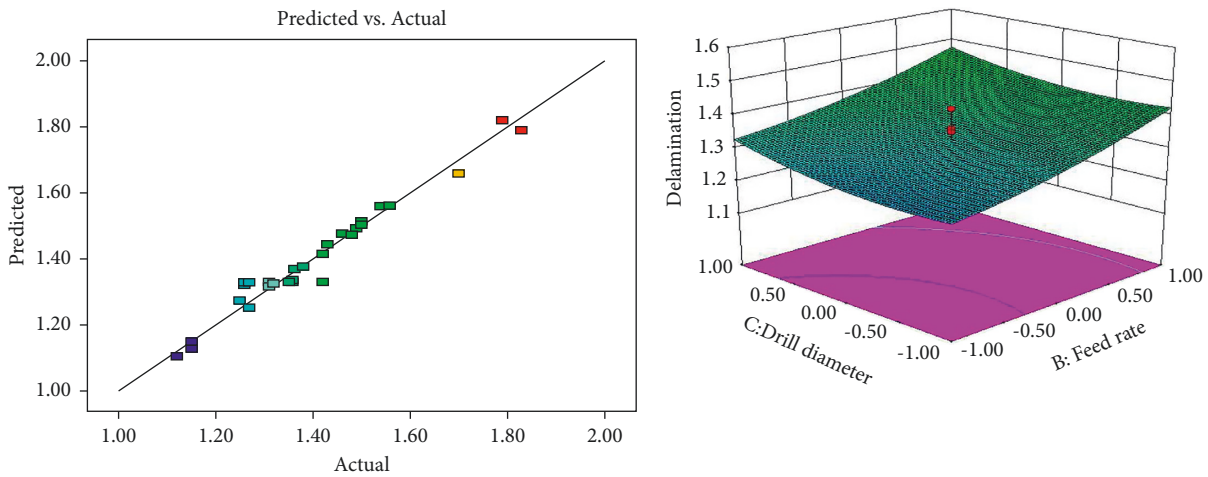

Figure 2: (a) Correlation graph; (b) 3-D response graphs for delamination.

Table 6: . Model summary for carbide multifaceted drill.

Output responses	Model expression	R^2 (%)
Delamination	$-1.32833 - 0.039167 * v + 0.076667 * f + 0.029167 * d + 0.023333 * \theta + 0.13250 * v^2 - 0.081250 * f^2$ $-0.083750 * d^2 - 2.50000E - 003 * \theta^2 - 0.022500 * v * f + 0.058750 * V * d + 0.016250 * V * \theta$ $+0.018750 f * d + 0.026250 * f * \theta + 0.032500 * d * \theta$	96.49

increases, the thrust force and torque increase because the peripheral area of the undeformed chip and shear area grows.

Figure 3(c) shows the effect of drill diameter on the thickness of the coir fiber-reinforced polyester laminate at various drill diameters. The graph displays varied patterns, which could be attributed to the induced frictional characteristics at the interface between the tool's cutting edge and the composite's surface. The effect of fiber orientation angle concerning delamination factor using a multifaceted drill bit of various thicknesses in coir fiber-reinforced polyester composites is presented in Figure 3(d). From the plotted graph it is inferred that no drastic increases in delamination occurs. This may be due to the alignment of fiber and length to diameter ratio of the fiber because coir fiber has low cellulose content. The input parameters of speed 1625 rpm, feed 237.5 mm/min, drill diameter 10 mm, fiber orientation angle 67.5° have minimum delamination. From the graphs, it is clear that a high feed rate and moderate speed reduce delamination. Similar results have been reported by Jayapal et al. [26].

Sensitivity analysis was defined as the systematic investigation of the reaction of the simulation response to either extreme values of the model's quantitative factors or too drastic changes in the model's qualitative factors Kleijnen (2015). The sensitivity equations are obtained by differentiating the developed empirical relation concerning the factors of interest such as spindle speed, tool feed rate, drill diameter, and fiber orientation angle that are explored here. To obtain the sensitivity equation for delamination, the sensitivity equation (5), (6), (7), and (8) represent the sensitivity of delamination for spindle speed, tool feed rate, drill diameter, and fiber orientation angle, respectively:

$$\frac{\partial D}{\partial V} = -0.04 + 2 * 0.13 * v + 0.02 * f + 0.06 * d + 0.02 * q, \tag{5}$$

$$\frac{\partial D}{\partial f} = 0.08 - 2 * 0.08 * f - 0.02 * v + 0.02 * d + 0.03 * q, \tag{6}$$

$$\frac{\partial D}{\partial d} = 0.03 - 2 * 0.08 * d + 0.06 * v + 0.02 * f + 0.03 * q, \tag{7}$$

$$\frac{\partial D}{\partial \theta} = 0.02 - 2 * 0.01 * q + 0.02 * v + 0.03 * f + 0.03 * d. \tag{8}$$

Sensitivities of input parameters on delamination are shown in Figure 4. The sensitivity of process parameters can be ranked based on their slope. On that basis, the ranking in this experiment reveals that the tool feed rate is highly sensitive to fiber orientation angle, spindle speed, and drill diameter, respectively, for drilling coir fiber-reinforced polyester composites using a multifaceted drill bit.

After the hole was drilled, the hole with and without protruded fibers was captured using a digital image with a high-resolution camera at the entry side of the hole. Figure 5

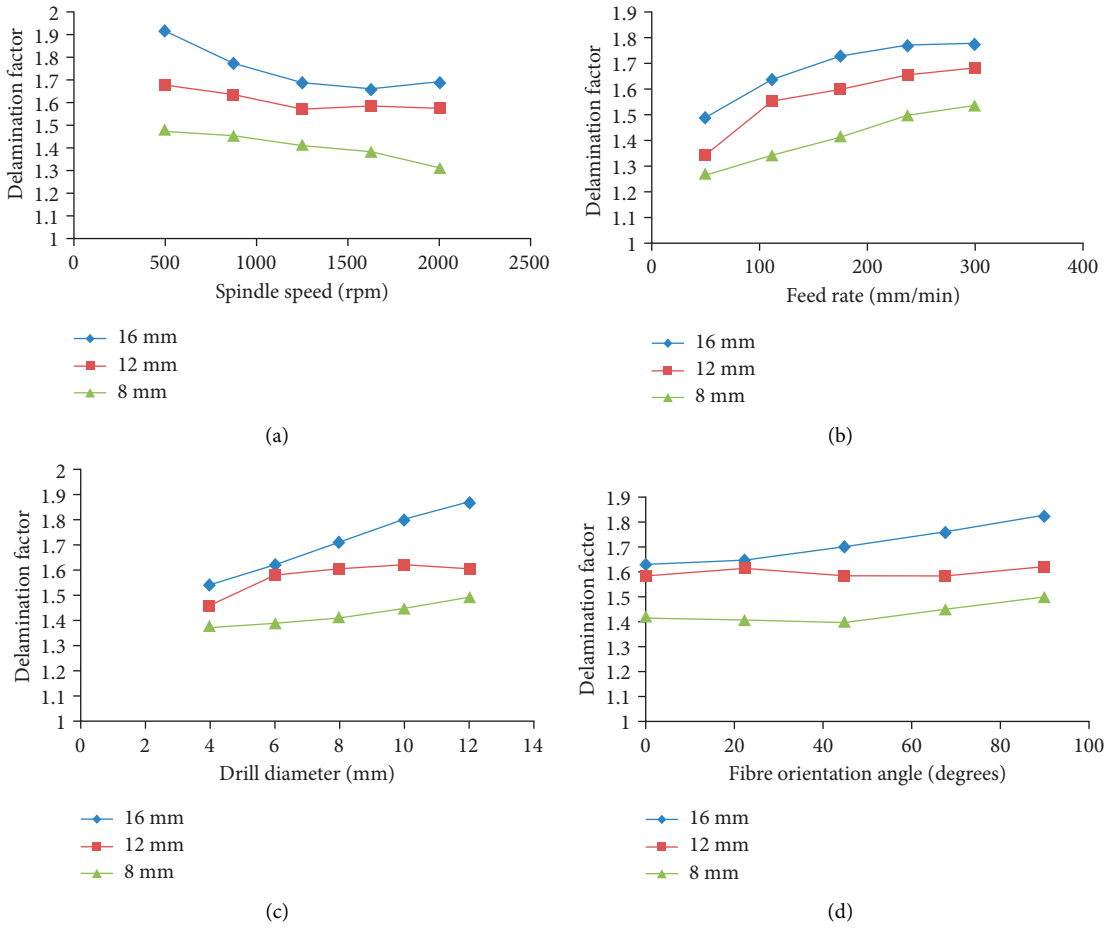

FIGURE 3: Effect of various input parameters on delamination factor (a) spindle speed, (b) tool feed rate, (c) drill diameter, (d) and fiber orientation angle.

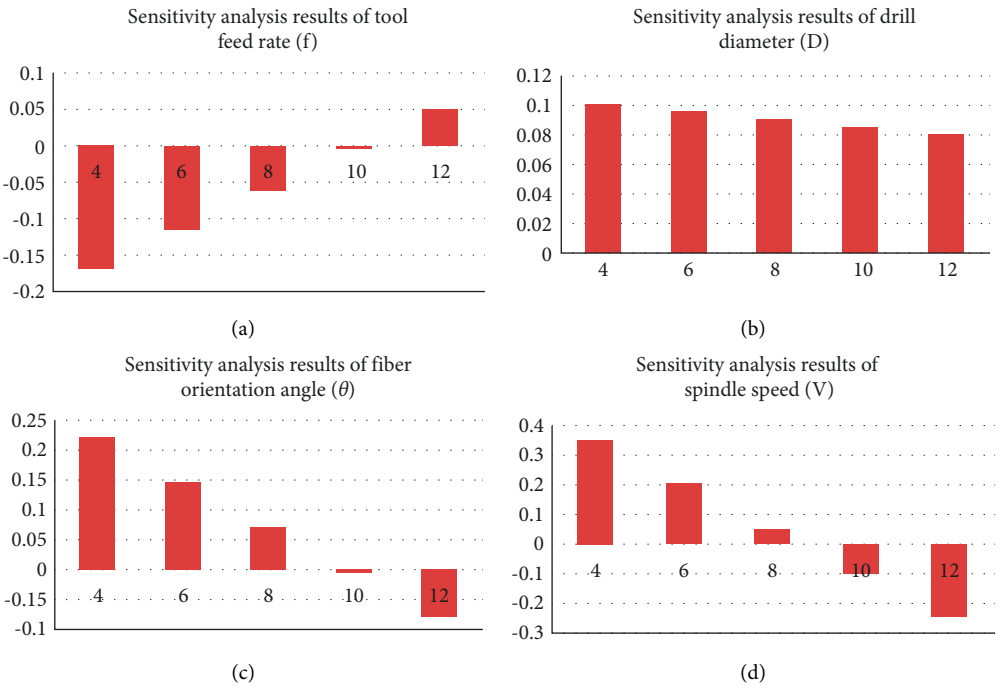

FIGURE 4: Sensitivity analysis of (a) tool feed rate, (b) (f) drill diameter, (c) orientation angle, and (d) spindle speed.

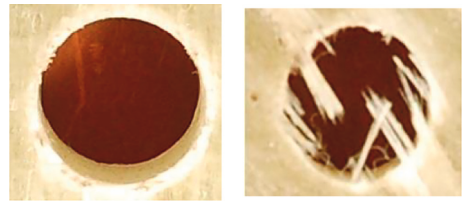

V=1625 rpm, f=112.5 mm/min, d=6 mm, θ=22.5

V=1625 rpm, f=237.5 mm/min, d=6 mm, θ=22.5

Figure 5: Quality of the holes with varying feed rates.

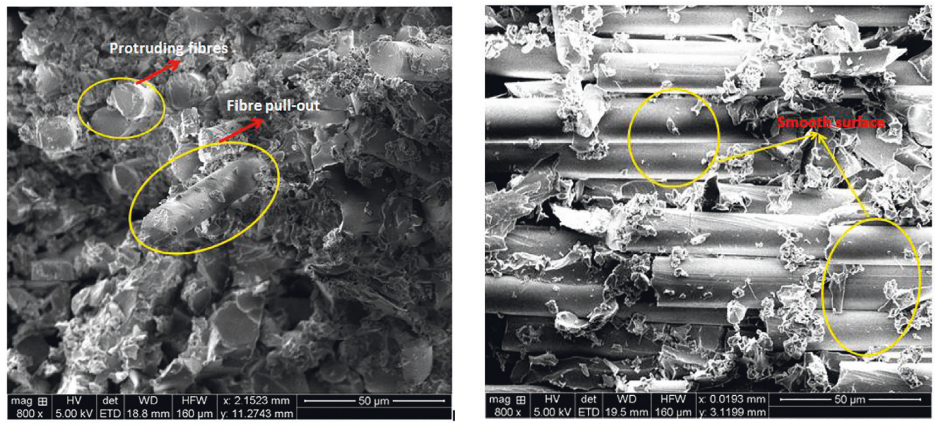

(a) (b)

Figure 6: ((a, b) shows the SEM photographs of the inner surface of the drilled hole.

indicates the photograph of the hole observed with a speed of 1625 rpm, feed 112.5 mm/min, tool diameter 6 mm, and fiber orientation angle of 22.5°. The distance of the hole center from the center of the drilled face is not equal, that is, ovality is observed with a low feed rate. Whereas for the same cutting condition except for changing the tool feed rate to 237.5 mm/min, a fine circular hole is observed, which may be due to matrix cracking and burn lead by the greater wear of the drill corner, which is shown in Figure 5(b). Generally, a multifaceted drill point has a flat primary cutting edge and a flat secondary edge. The primary and secondary ground cutting edges are parallel to the face of the point which decreases the thrust force and minimizes the delamination in the drilling of coir fiber-reinforced composites. Figure 6(a) shows the SEM photographs of the inner surface of the drilled hole with maximum delamination rotational speed of 875 rpm, a feed rate of 112.5, a tool diameter of 10 mm, and a fiber orientation angle of 67.5°. The figure shows a non-uniform wall surface and fiber pull-out due to the cutting action of a 10 mm diameter drill bit with a high feed rate. This condition favors the irregular inner wall surface, which is clearly shown in the figure. Figure 6(b) shows the SEM photographs of the inner diameter of the drilled hole with optimum cutting conditions which result in a smooth surface without any protruding fibers, which may be due to the influence of feed rate and the bonding between the matrix and coir fiber reinforcement.

4. Conclusion

(1) Even though coir fiber-reinforced composites have high mechanical strength, and the introduction of coir fibers did not improve or reduce delamination in coir fiber-reinforced composites drilling.

(2) From the ANOVA results, it is asserted that among other input parameters, tool feed rate plays an important impact in increasing delamination in drilling.

(3) The sensitivity analysis confirms the same phenomenon, such that feed rate is the most influential aspect.

(4) However, coir fiber-reinforced composites possess a good alternative to glass fiber-reinforced composites in all aspects such as low expensive, environmentally friendly, and long-term solutions to increase the composites' qualities.

(5) Proper care should be taken while drilling coir fiber-reinforced composites to avoid health hazards.

(6) SEM images were analyzed concerning the optimum and nonoptimum cutting conditions.

Data Availability

There is no data available.

Conflicts of Interest

The authors declare that they have no conflicts of interest.

References

[1] T. V. Rajamurugan, A. Baskaran, S. Matheswaran, and S. E. Lavanya, "Comparative analysis on mechanical properties of Luffa and coconut coir fiber reinforced polyester composites, Springer Proceedings in Materials," in *Advances in Materials and Manufacturing Engineering*, pp. 245–251, Springer, Singapore, 2021.

[2] T. Srinivasan, K. Palanikumar, K. Rajagopal, and B. Latha, "Optimization of delamination factor in drilling GFR-polypropylene composites," *Materials and Manufacturing Processes*, vol. 32, no. 2, pp. 226–233, 2017.

[3] M. Mudhukrishnan, P. Hariharan, K. Palanikumar, and B. Latha, "Tool materials influence on surface roughness and oversize in machining glass fiber reinforced polypropylene (GFR-PP) composites," *Materials and Manufacturing Processes*, vol. 32, no. 9, pp. 988–997, 2017.

[4] D. S. Raj and L. Karunamoorthy, "Study of the effect of tool wear on hole quality in drilling CFRP to select a suitable drill for multi-criteria hole quality," *Materials and Manufacturing Processes*, vol. 31, no. 5, pp. 587–592, 2016.

[5] R. Voss, M. Henerichs, S. Rupp, F. Kuster, and K. Wegener, "Evaluation of bore exit quality for fibre reinforced plastics including delamination and uncut fibres," *CIRP J Manuf Sci Technol*, vol. 12, pp. 56–66, 2016.

[6] B. Latha, V. S. Senthilkumar, and K. Palanikumar, "Modeling and optimization of process parameters for delamination in drilling glass fiber reinforced plastic (GFRP) composites," *Machining Science and Technology*, vol. 15, no. 2, pp. 172–191, 2011.

[7] C. L. Tan, A. I. Azmi, and N. Muhammad, "Surface roughness analysis of carbon/glass hybrid polymer composites in drilling process based on Taguchi and response surface methodology," in *Advanced Materials Research*vol. 1119, , pp. 622–627, Trans Tech Publications Ltd, 2015.

[8] R. H. Myers, D. C. Montgomery, and C. M. Anderson-Cook, *Response Surface Methodology: Process and Product Optimization Using Designed Experiments*, John Wiley & Sons, Hoboken, NJ, USA, 2016.

[9] S. Dhakal and B. S. Keerthi Gowda, "An experimental study on mechanical properties of banana polyester composite," *Materials Today Proceedings*, vol. 4, no. 8, pp. 7592–7598, 2017.

[10] S. K. Chaudhary, K. K. Singh, and R. Venugopal, "Experimental and numerical analysis of flexural test of unfilled glass fiber reinforced polymer composite laminate," *Materials Today Proceedings*, vol. 5, no. 1, pp. 184–192, 2018.

[11] R. Harikumar and A. Devaraju, "Fabrication and experimental analysis of copper wire embedded with GFRP composites," *Materials Today Proceedings*, vol. 5, no. 6, pp. 14327–14332, 2018.

[12] P. Sature and A. Mache, "Experimental and numerical study on moisture diffusion phenomenon of natural fiber based composites," *Materials Today Proceedings*, vol. 4, no. 9, pp. 10293–10297, 2017.

[13] B. Senthilkumar and T. Kannan, "Sensitivity analysis of flux cored arc welding process variables in super duplex stainless steel claddings," *Procedia Engineering*, vol. 64, pp. 1030–1039, 2013.

[14] G. D. Babu, K. S. Babu, and B. Gowd, "Optimization of Machining Parameters in Drilling Hemp Fiber Reinforced Composites to Maximize the Tensile Strength Using Design Experiments," *Indian Journal of Engineering and Materials Sciences*, vol. 20, no. 5, pp. 385–390, 2013.

[15] F. Ficici, "IInvestigation of Thrust Force in Drilling Polyphthalamide (PPA) Composites," *Measurement*, vol. 182, Article ID 109505, 2021.

[16] M. Mohanraj, R. S. Kumar, T. Venugopal, P. Natarajan, and S. Ganesan, "Study and analysis of drilling parameters using TLBO algorithm on GFRP composites," *Materials Today Proceedings*, vol. 7, no. 2.31, 2021.

[17] C. Zhu, Y. Wu, P. Gu, Z. Tao, and Y. Yu, "Prediction of drilling force for high volume fraction SiCp/Al composite based on neural network," *Procedia CIRP*, vol. 99, pp. 414–419, 2021.

[18] S. D. Rao B, A. Sethi, and A. K. Das, "Fiber laser processing of GFRP composites and multi-objective optimization of the process using response surface methodology," *Journal of Composite Materials*, vol. 53, no. 11, pp. 1459–1473, 2019.

[19] L. Liu, C. Qi, F. Wu, X. Zhang, and X. Zhu, "Analysis of thrust force and delamination in drilling GFRP composites with candle stick drills," *International Journal of Advanced Manufacturing Technology*, vol. 95, no. 5, pp. 2585–2600, 2018.

[20] T. V. Rajamurugan, K. Shanmugam, and K. Palanikumar, "Analysis of delamination in drilling glass fiber reinforced polyester composites," *Materials & Design*, vol. 45, pp. 80–87, 2013.

[21] S. Ramesh, R. Viswanathan, and S. Ambika, "Measurement and optimization of surface roughness and tool wear via grey relational analysis, TOPSIS and RSA techniques," *Measurement*, vol. 78, pp. 63–72, 2016.

[22] R. Viswanathan, S. Ramesh, N. Elango, and D. Kamesh Kumar, "Temperature measurement and optimisation in machining magnesium alloy using RSM and ANOVA," *Pertanika Journal of Science & Technology*, vol. 25, no. 1, 2017.

[23] M. Srinivasan, S. Ramesh, S. Sundaram, and R. Viswanathan, "Minimization of delamination, surface roughness and thrust force in drilling of Al2O3 ceramic particle filled CFRP composites," *Journal of Ceramic Processing Research*, vol. 22, no. 3, pp. 345–355, 2021.

[24] K. Palani Kumar, D. Keshavan, E. Natarajan et al., "Evaluation of mechanical properties of coconut flower cover fibre-reinforced polymer composites for industrial applications," *Progress in Rubber, Plastics and Recycling Technology*, vol. 37, no. 1, pp. 3–18, 2021.

[25] V. Kaviarasan, R. Venkatesan, and E. Natarajan, "Prediction of surface quality and optimization of process parameters in drilling of Delrin using neural network," *Progress in Rubber, Plastics and Recycling Technology*, vol. 35, no. 3, pp. 149–169, 2019.

[26] S. Jayabal and U. Natarajan, "Drilling analysis of coir-fibre-reinforced polyester composites," *Bulletin of Materials Science*, vol. 34, no. 7, pp. 1563–1567, 2011.

Hindawi
Advances in Materials Science and Engineering
Volume 2022, Article ID 3147586, 29 pages
https://doi.org/10.1155/2022/3147586

Research Article

Investigation of Machinability Characteristics of EDMed Inconel 825 Alloy under Multidimensional Parametric Modeling by Using Holistic Grey-PCA Statistical Models

Nitin Kumar Sahu,[1] **Mukesh Kumar Singh**,[1] **Bupe Getrude Mutono-Mwanza**,[2] **and Atul Kumar Sahu**[1]

[1]*Department of Industrial and Production Engineering, Guru Ghasidas (Central) Vishwavidyalaya, Bilaspur 495009, Chhattisgarh, India*
[2]*Graduate School of Business, University of Zambia, Great East Road Campus, Lusaka, Zambia*

Correspondence should be addressed to Bupe Getrude Mutono-Mwanza; bupe.mwanza@gmail.com

Received 15 February 2022; Accepted 19 April 2022; Published 14 May 2022

Academic Editor: Thanigaivelan R

The current social and industrial communities exceedingly demanded the materials that dealt with rich mechanical properties, i.e., the rich strength, hardness, reliability, high resistance against corrosion and oxidation, and high toughness and refractoriness. Recently, the researchers ascertained the comprehensive applications of these difficult to machine materials in the domain of automotive, aeronautical, nuclear industries etc. It is claimed that it is quite hard and expensive for machining these super-advanced materials by traditional machining operations. In the present study, worldwide promising nickel-based superalloy Inconel 825 material is used due to its outstanding mechanical and thermal properties at eminent temperatures and also having broad application in imperative engineering fields. The authors probed that machining cost and smart machinability index have become the gigantic concern in EDM operation; however, these can be minimized by adapting a conduit of evaluation of the optimum setting among multiple input parameters. It was a challenging task, which is respected by authors as the research gaps to be sorted out. To fulfill research gaps, the authors encountered imperative significant EDM input parameters, i.e., spark gap (Sg), gap voltage (Vg), pulse on time (Ton), pulse off time (Toff), Peak Current (Ip), Servo feed (Sf), Depth of Cut (Dc) and difficulty index (Di) corresponding to output responses, i.e., power consumption (Pc), machining time (Mt), and material removal rate (MRR) for framing the machinability index/model for conducting experiments and collecting objectives/responses/outputs. Next, the authors conducted experiments using the Taguchi L27 orthogonal array model in the nonvibratory domain for recording output responses. Later, to potentially access the results, the authors integrated the computational Taguchi methodology with dual models which is called as Taguchi-grey relational analysis (T-GRA) and Taguchi-principal component analysis (T-PCA). The optimum setting condition among considered inputs is discussed in the conclusion section. Later, confirmatory test gratified the evaluated optimum settings which is yielding an improvement of 0.16262 and 0.34398 score in executing T-GRA and T-PCA, respectively. In continuation, the current research evidenced that pulse off time is the chief significant process parameter having p values 0.005 and 0.001 for T-GRA and T-PCA, respectively. It is also seen that the depth of cut is also another important significant process parameter having p values 0.061 and 0.073 for T-GRA and T-PCA, respectively. Moreover, the current research work also investigated the effect of variation of momentous input process parameters over the surface topography and their utility in improving surface integrity and eliminating the micropores and cracks.

1. Introduction

Electrical discharge machining (EDM) has recently gained the high momentum among the various nontraditional manufacturing machining operations due to its less maintenance cost and rapid machining operations. EDM is capable for shaping, chamfering, drilling etc., of hard, tough, and refractory materials. EDM is turned out to be the most renowned nontraditional manufacturing machines at global standard due to its thermoelectric machining process. In EDM, the material removal phenomenon establishes by a series of discrete electrical discharges between the work piece and electrode immersed in a dielectric fluid. In EDM, the tiny material removes from the work piece and flushes away along with a continuously flowing dielectric fluid at a controlled rate. EDM is especially worldwide prioritized for cutting complex/intricate shapes and delicate cavities in various moulds or dyes that might be difficult with other conventional machining processes. A general structure of EDM is shown in Figure 1, which is used to remove the metal by means of electric spark erosion. Here, an electric pulse generates electric spark that is used as the cutting tool to erode the work piece and produce the finished work piece in the form of a customized shape as shown in Figure 2.

Currently, Inconel 825 (nickel-chromium-based superalloys) is invented and designed to provide outstanding resistance at numerous critical working environments. This material reveals the excellent resistance to oxidation and corrosion and also possesses well resiliency against tremendous high heat and pressure. Inconel 825 preserves its potency over an extensive range of temperature and is suitable for high temperature applications as shown by Prabhu and Vinayagam [1]. This superalloy has been become more demanding in the current scenario due to their inherent application in various engineering sectors such as nuclear, power, chemical, and production of moulds and dyes. However, shaping and machining operations of Inconel superalloys has become incredibly hard and costly via conventional machining processes. The conventional machining processes are found in the line of uneconomic production in machining the hard Inconel superalloys due to the grounds of excessive heat generation; rapid tool wear; and short tool life at the work-tool interfaces. It is probed that the conventional machining process also affected the properties of Inconel 825 superalloy such as high wear resistance, high hardness, high temperature strength, and high tendency to weld to the conventional cutting tool reported by Rajyalakshmi and Ramaiah [2]. In numerous observations, the conventional machining process also resulted in changes of work material characteristics and mechanical properties. Owing to aforesaid problems, it seemed to be an enormous challenge in front of current researchers for machining Inconel superalloys by conventional machining processes. Therefore, the necessity of nontraditional machining operations for finishing the Inconel superalloys is really experienced by the current manufacturing communities. Nowadays, EDM is found in the area of nontraditional machining process and widely employed in industries for obtaining high accuracy in machining Inconel 825 superalloys and all variety of conductive materials (regardless of their hardness) such as graphite, metals, metallic alloys, and even some ceramic materials.

2. Motivation and Research Objective

As we know that, in EDM operations, both work piece and the tool electrode are submerged inside a dielectric fluid. A spark channel is established in between the electrode and work piece at high temperature about 10,000°C, which enables EDM for machining the hard materials. It is found by systematic literature survey that extensive research documents are floated in the different domains of EDM; a few are briefly discussed to find superior models and EDM parameters and building the machinability index.

Prasad et al. [3] carried out their work on EN-42 spring steel using zinc-coated brass wire and distilled water as a dielectric in wire electrical discharge machining. The authors added WS_2 powder in distilled water to evaluate the impact of dielectric on metal removal rate and surface roughness. It is found that the concentration of powder suspended in dielectric that flows in the gap between a work piece and electrode plays a leading role for improving the surface integrity. It is a well-known fact that efficient flushing rate between the tool and work piece drastically affects the machining conditions of the EDM process. Furthermore, it is also probed that exploration of different dielectric fluids might have marvelous effect over material removal depth, the surface roughness, the electrode wear rate, and other output parameters. Singh and Singh [4] focused on statistical data modeling of various machining parameters to obtain the best combination of parameters for desired machining performances in the EDM process. It is determined via experimental auditing that the size of particle, particle concentration, the electrical resistivity, the particle density, and the thermal conductivity of powders drastically affect the various machining performance and operations of EDM reported by Chow et al. [5]. Appropriate mixing of powders into the dielectric fluid greatly influences the TWR as well as MRR. Guo et al. [6] utilized Ti-6Al-4V work material, acoustic emission (AE) sensor and compressed air, and kerosene and water-based emulsion as a dielectric medium to investigate the material removal process based on expansion and contraction of gas bubble around the discharge plasma. Goyal et al. [7] utilized normal diffused and cryogenic treated diffused wires as electrode on Inconel 625 to investigate the effects of tool electrode, peak current, pulse on time, pulse off time, wire feed and wire tension on the response MRR.

Recently, numerous number of researches divert their senses to use the statistical mathematical models and multiobjective evolutionary algorithms (MOEAs) for evaluating and optimizing the multiple objectives/responses vs. input parameters under EDM operations discussed by Golshan et al. [8]. Yang et al. [9] proposed the counterpropagation neural network for examining the experimental data against input variables for maximizing the material removal rate in parallel to minimize the surface roughness. Singh et al. [10] proposed the multiple statistical

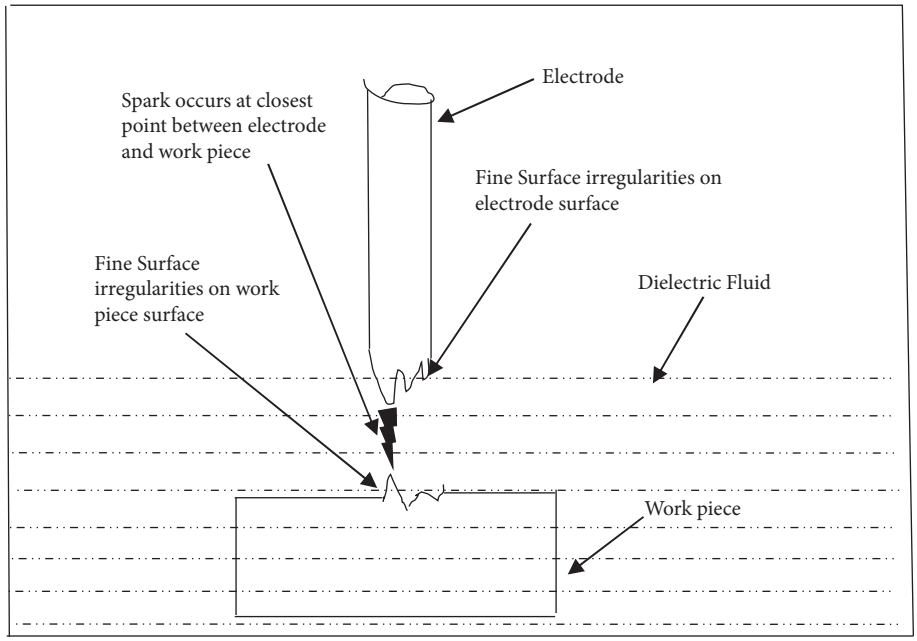

Figure 1: Schematic of sparking occurs at the nearest point in the EDM experimental setup.

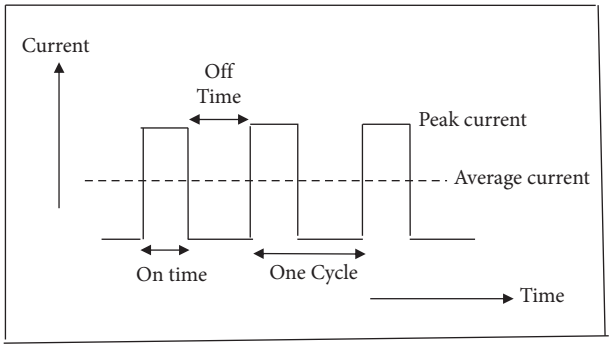

Figure 2: Typical EDM pulse current train for controlled pulse generator.

mathematical models such as adaptive neuro-fuzzy inference system (ANFIS), artificial neural network (ANN) with back-propagation algorithm, and response surface methodology (RSM) for computing and anticipating the MRR and SR for D3 die steel material. Jampana et al. [11] performed thermal investigation to identify the effects of powder having different thermo physical properties in powder-mixed EDM (PMEDM) process. There, the authors have modeled the machining characteristic by utilizing artificial neural networks and FEM for determining optimal selection of process variables. Nas et al. [12] selected AISI D2 cold work tool steel and utilized grey relational degree to identify the impact of crucial machining parameters on output responses, where it is found that amperage and pulse on time significantly affects the surface roughness and hole diameter in EDM. Devarasiddappa et al. [13] utilized the modified teaching learning-based optimization algorithm to experimentally investigate Ti6Al4V alloy in WEDM process by varying the process parameters, i.e., wire speed, current, pulse on time, and pulse off time to identify their impact on surface roughness. Kulkarni and Kulkarni [14] applied the heuristic grey wolf Optimizer algorithm in wire electrical discharge machining (WEDM) for optimizing pulse on time, pulse off time, wire feed, wire tension, upper flush, and lower flush on high carbon high chromium steel material. Kumar and Narasimhamu [15] studied the effect of WEDM parameters, i.e., wire feed rate, pulse on time, pulse off time, and water pressure on Inconel 750 alloy by embedding TOPSIS with grey wolf optimizer in estimating cutting speed and surface roughness. Abed et al. [16] proposed a sequential discharge model based on FEM simulation for EDM. Their results are experimentally validated, and it is found that simulated results and experimental results have relative error, and thus there is need to develop appropriate mathematical modeling to minimize the extent of errors. Saffaran et al. [17] employed metaheuristics algorithms, i.e., artificial neural network (ANN) along with particle swarm optimization (PSO) and simulated annealing (SA) on AISI2312 hot worked steel parts in order to carry out optimization of surface roughness, tool wear rate, and material removal rate in electrical discharge machining (EDM) process. Yunus and Alsoufi [18] investigated the effect of pulse on duration, pulse off duration, current, and voltage on MRR and SR in WEDM on nitinol alloys by utilizing particle swarm optimization, where the authors found significant effects of process parameters on responses. Sen et al. [19] tried to establish a correlation between pulse on time, pulse off time, peak current, and servo voltage and wire tension by means of neural network model in order to optimize performance characteristics, i.e., surface roughness, cutting speed, and kerf width.

Optimization of the responses such as MRR, surface roughness, and tool wear rate etc., depends on the crucial evaluation and selection of inputs process parameters as Aich et al. [20] and Tanveer et al. [21] mentioned. Moreover,

the examination and evaluation of optimum condition setting among multiple control parameters is so complex process in the context of nontraditional machining process as Luan et al. [22] and Jain and Parashar [23] mentioned. The satisfactory evaluation as well as selection of manufacturing conditions is one of the significant aspects to be focused for optimizing the multiple responses in EDM environment reported by Wang et al. [24]. The balance between the machining inputs and outputs in the context of EDM is very important to achieve desired objective as discussed by Gostimirovic et al. [25]. It is significant to determine the crucial machining characteristics and optimum setting for extracting elevated outputs from the group of inputs [26, 27]. Additionally, it is fruitful to evaluate multiple outputs for assuming effectiveness and efficacy from implicated resources [28, 29]. Kumar et al. [30] proposed the RSM accompanied with GRA on Inconel 825 in order to optimize multiple output objectives during wire-cut EDM. Prakash et al. [31] investigated the hybrid composites (Al-Si12/B4C/fly ash) in WEDM to identify the effect of WEDM process parameters on the material removal rate (MRR) and surface roughness (SR) responses and found that the MRR can be increased by increasing pulse on time and reinforcement. It is also found that increase in gap voltage, pulse on time, pulse off time, wire feed, and reinforcement increases the SR. Manikandan et al. [32] proposed the grey relational analysis for electrochemical drilling on Inconel 625 to analyze the effect of machining variables such as feed rate, flow rate, and concentration of electrolyte on MRR, SR, and other geometric measures. Muni et al. [33] performed experimental analysis on rice husk ash/Cu/Mg-reinforced hybrid Al-0.7Fe-0.6Si-0.375Cr-0.25Zn metal matrix nanocomposites in EDM and identified the effects of various process parameters on output objectives. It is found that MRR and SR, both are decreasing with increased content of rice husk ash. Mouralova et al. [34] carried out their investigation on pure aluminum 99.5 to optimize machined surface integrity and kerf width for precision machining. Perumal et al. [35] examined the effect of pulse on duration, wire tension, and wire feed on MRR and SR while performing machining of Ti-6Al-2Sn-4Zr-2Mo (α-β) alloy using the grey relational approach in WEDM, where significant thrust has been received by the authors to review the process parameters for sustainable outcomes. Sharma et al. [36] applied the hybrid approach on Inconel 706 for optimizing the material removal rate and surface roughness. The authors have also carried out energy dispersive X-ray spectroscopy (EDAX) for topography analysis of EDMed material. Mouralova et al. [37] used a transmission electron microscope to study the impact of the orientation direction of the cut on cutting speed and machined surface quality in wire electrical discharge machining (WEDM). Singh et al. [38] carried out their investigation on copper, SS-EN 24, and Ti-6Al-4V material for understanding the effect of thermophysical properties of workpiece materials on MRR.

The aim of the present study is to provide robust decision modeling and valuable insights to the current manufacturing organization for processing smart alloys. Moreover, the present study can be used by the manufacturing organization to decide significant levels of process parameters that provides efficient working condition, enhances profitability and productivity, and takes environmental responsibility, while performing machining operation in EDM. It is found that EDM is an advanced machining operation and requires driving fuels and mechanical energy. Thus, the present study has considered the green and productivity aspects in the form of appropriate selection of machining parameters as their proper selection against desired output which is very prominent and plays a keen role in reducing power consumption, enhancing productivity, and reducing machining time. Appropriate selection of process parametric setting enables the EDM in the direction of correct utilization of resources, reduction in negative environmental loads, and reduces wastes. The modeling proposed in the present study assists in the reduction of power consumption in EDM, which will lead towards less consumption of natural resources/fossil fuels and participates in environmental responsiveness. Additionally, the reduction in machining time leads in the faster manufacturing of the components and results in profitability and less cost and supports in gaining competitive advantage, which is the major achievement of the present study.

It is summarized that evaluation and selection of the outstanding optimum condition setting among multiple machining inputs parameters in addressing to minimize the power consumption, machining time, and maximize the material removal rate has become so critical occupation. From systematic literature review, it is accessed that a few authors are fruitfully attempted towards parametric modeling and optimization of outputs for evaluating the best optimum condition setting among input parameters under EDM considering Inconel 825 materials. Furthermore, it is also observed that few research documents are published and dealt with multiobjective optimization of limited or single or two outputs with respect to inadequate inputs variables/parameters for Inconel 825 with EDM operation. No authors are available which have considered the spark gap (Sg), gap voltage (Vg), pulse on time (Ton), pulse off time (Toff), peak current (Ip), servo feed (Sf), depth of cut (Dc), and difficulty index (Di) as inputs parameters for optimizing power consumption (Pc), machining time (Mt), and material removal rate (MRR) in multiobjective optimization realm in addition to surface topography analysis. The presented work has considered the optimization of EDM input parameters on Inconel 825 in order to optimize the responses using Taguchi-based grey relational analysis (T-GRA) accompanied with principal component analysis (T-PCA). Twenty-seven experiments are conducted systematically using Taguchi-based L_{27} orthogonal array model to fullfill aforesaid agendas.

3. Materials And Methods

3.1. Work Piece Material. In today's era of industry 4.0, technologies and competitiveness enforced industries to more focus on optimization of the EDM process by executing optimization methodologies and models reported by Zhou et al. [39]. The authors found that EDM operation is

subjected to multiple limitations along with controllable inputs parameters discussed by Baldin et al. [40]. A vigilant evaluation and selection of inputs machining parameters with right value leads to achieve the optimum output or smatter machining results discussed by Muthuramalingam et al. [41]. In the current market, various super-advanced material, composite, and other materials encompass the high resistance against heating as well as corrosion; rich mechanical properties with least machining cost are demanded with curiosity by different industrial sectors for fabricating various customized goods reported by Payal et al. [42]. It is ascertained that EDM operation is faster and feasible among all nontraditional machining operations discussed by Kumar and Rao [43]. Therefore, in the presented research forum, Inconel 825, composed by mixing the nickel-iron-chromium alloy with molybdenum and copper as well, is chosen due to its unique and exceptional characteristics such as rich hardness and strength, resiliency against reducing and oxidizing acids, voiding stress-corrosion cracking, and neutralizing the localize attack (pitting and crevice cavitations and rusting). Currently, the said Inconel 825 material is highly respected at global standard by many sectors such as chemical processing, aerospace, missile, nuclear fuel reprocessing, chemical and petrochemical, and marine. The material and EDM process evaluation and selection is respected preliminary so that sustainable manufacturing practices can be pushed out in manufacturing firms by evaluating and finding the best inputs or machining parameters at different values.

3.2. EDMed Controllable Parameters and Output Responses

(i) *Spark Gap (Sg):* it is an appropriate "gap" between electrode and work part to produce the spark under EDM process. Spark gap is needed to be maintained for generating the spark and is controllable by servo system setup.

(ii) *Gap Voltage (Vg):* it is gained by maintaining the potential gap or difference between the electrode and work piece. Gap voltage is known as the total energy of the spark. Increase in the gap voltage outcomes the improvement in flushing conditions and material removal rate and straightly supports to stabilize the machining.

(iii) *Pulse on Time (Ton):* it reflects the spark generation over short-timing or pulse timing. It is also known as the period (per cycle) in performing the machining operation, i.e., the current is allowed to flow through the discharge gap. The machining process is straightly proportional to Ton and becomes rapid in nature and thus results in augmentation in material removal rate.

(iv) *Pulse off Time (Ton):* it is the time consumed between the two consecutive sparks on nonsupply of current to the electrodes. During the period of pulse off time, deionization of dielectric occurs as well as dielectric also flushes the machining debris.

(v) *Peak Current (Ip):* peak current is the maximum current and occurs against each pulse on power supply. It is found that an expansion in peak discharge current fosters the intensification of input heat rate, which results in increased material removal rate and tool wear rate. It is also called as the peak discharge current in EDM operation.

(vi) *Servo Feed (Sf):* it maintains and controls the working gap corresponding to the set value. It also represents the distance, maintained the between the tool electrode and the work-piece in the appropriate manner on EDM machine process to avoid the inefficient sparking. Currently, EDMs are assisted by a servo feed mechanism, which automatically manages the servo feed.

(vii) *Depth of Cut (Dc):* it reflects the total quantity of the metal, which left from work part upto defined depth over each pass of the tool. Generally, it is expressed in mm.

(viii) *Difficulty Index (Di):* the difficulty index is the proportion or probability that the machine provides to an experimental test for reading input correctly. It ranges between 0 and 100%, and its higher value indicates effectiveness of the machine.

(ix) *Power consumption (Pc):* it is the consumption of AC/DC electrical energy per unit time by EDM machine. It is basically mapped in the unit of watt (W) or kilowatts (kW). Mathematically, $Power\ (W) = V * I$

(x) *Machining Time (Mt):* it is the amount of time, consumed by EDM machine to shape the work piece in meeting the given dimensions. It is typically mapped in minutes.

(xi) *Material Removal Rate (MRR):* it states the amount of material removed from the work part over per unit time. It can be computed by weighing the volume of material removal from work part or by measuring the weight of work part prior to and after EDM machining operation. Here, MRR (mg/min) = (initial weight of work piece − final weight of work piece/machining time)

3.3. Taguchi Model. It is known that the invention of innovative and novel materials is a ceaseless process. Various kind of new conductive, hard, and tough materials are introduced recently due to industrial and market demand. It is observed that empirical optimization and hypothetical auditing of input parameters of EDM process reflects the unreliable and inconsistent results as shown by Shao and Rajurkar [44]. The necessity of statistical mathematical models has been comprehensively realized, which can interpret the structured experimental data discussed by Reddy et al. [45] and Li et al. [46]. Shabgard and Khosrozadeh [47] reported that the Taguchi's models are most reliable and consistent in nature for executing experiments designs. Taguchi's model is used to frame the favorable setting of input process parameters against unavoidable variations or

external noise on the experiments reported by Singh et al. [48] and Werner [49]. The signal to noise (S/N) ratio is an idyllic metric nomenclature under Taguchi's model that eliminates the variability and carries forward the improvement of measurement as discussed by Choudhury et al. [50]. The S/N ratios are bifurcated into three standards: lower the better (LB), higher the better (HB), and nominal is the best (NB), as shown in equations (1)–(3), respectively, by Zhang et al. [51]. Furthermore, under the curriculum of Taguchi's model, the ANOVA analysis is also executed on experimental data towards accessing the most significant and influencing input parameters with respect to output responses.

3.3.1. Lower the Better (LB). This machining characteristic is associated with minimum is better (objective). Lower values are desirable corresponding to objectives or outputs, i.e., power consumption, machining time, etc.

$$\left(\frac{S}{N}\right)_{LB} = -10\text{Log}\frac{1}{n}\left[\sum_{j=1}^{n} y_j^2\right]. \quad (1)$$

3.3.2. Higher the Better (HB). This machining characteristic is associated with maximum is better (objective). High values are desirable corresponding to objectives or outputs, i.e., material removal rate etc.

$$\left(\frac{S}{N}\right)_{HB} = -10\text{Log}\frac{1}{n}\left[\sum_{j=1}^{n} \frac{1}{y_j^2}\right]. \quad (2)$$

3.3.3. Nominal the Best (NB). This machining characteristic is associated with nominal is better (objective). Nominal values are desirable corresponding to objectives or outputs, i.e., dimensions etc.

$$\left(\frac{S}{N}\right)_{NB} = -10\text{Log}\frac{1}{n}\left[\sum_{j=1}^{n} \left(y_j - y_0\right)^2\right], \quad (3)$$

where y_j = characteristic value in an observation j, y_0 = characteristic nominal value, and n = total experiment conducted.

3.4. Theory of Grey Relational Analysis. Prof. Deng's has designed the grey incidence analysis model or grey relational analysis model. He proposed the model to analysis the black and white information simultaneously, i.e., in any contingency, the situation has no information is represented as black and has complete information is represented as white discussed by Rajyalakshmi and Ramaiah [2] and Kumar et al. [30]. However, the realistic engineering problems usually dealing with partial information and can be fruitfully undertaken by the grey theory by Singh and Singh. The Grey relational analysis (GRA) model is executed to undertake the unsure, vague, imprecise, and inexact information by Manikandan et al. [32]. Hoverer, GRA model also has advanced features analysis and synchronizes the statistical or experimental data and has aptitude to provide the efficient solution to real social problems and manufacturing operations. The subsequent steps are engaged in the GRA model:

Step 1. Data preprocessing

In information preprocessing, the mapped machining characteristics are normalized from 0 to 1, which is called as grey relational generation. In grey relational generation, the normalized objective values corresponding to experimental data; lower the better (LB) and larger-the-better can be calculated by executing (4) and (5), respectively,

$$x_i(k) = \frac{\max y_i(k) - y_i(k)}{\max y_i(k) - \min y_i(k)}, \quad (4)$$

$$x_i(k) = \frac{y_i(k) - \min y_i(k)}{\max y_i(k) - \min y_i(k)}, \quad (5)$$

where $x_i(k)$ = the normalized value, $\min y_i(k)$ is the minimum value of $y_i(k)$ for the k$^{\text{th}}$ response, and $\max y_i(k))$ is the maximum value of $y_i(k)$ for the k$^{\text{th}}$ response.

Step 2. Evaluation of Δ_{oi}

It illustrates the divergence from the ideal sequence for the experimental responses/objectives

$$\Delta_{oi}\,(\text{difference of the absolute value}) = \left\|x_0(k) - x_i(k)\right\|, \quad (6)$$

where $x_0(k)$ $(k = 1, 2, 3, ..., 9)$ for the experimental responses.

Step 3. Grey relational coefficient

The grey relational coefficient $\xi_i(k)$ can be estimated as

$$\xi_i(k) = \frac{\Delta_{\min} + \psi\Delta_{\max}}{\Delta_{0i}(k) + \psi\Delta_{\max}}, \quad (7)$$

where ψ is the distinguishing coefficient $0 \le \psi \le 1$; $\Delta_{\min} = \forall j^{\min} \in i \forall k^{\min} \|x_0(k) - x_j(k)\|$ is the smallest value of Δ_{oi}; $\Delta_{\max} = \forall j^{\max} \in i \forall k^{\max} \|x_0(k) - x_j(k)\|$ is the largest value of Δ_{oi}.

Step 4. Grey relational grade γ_i

Grey relational grade γ_i can be computed by using (8) as

$$\gamma_i = \frac{1}{n}\sum \xi_i(k), \quad (8)$$

where n = number of output responses.

3.5. Principal Component Analysis (PCA). The purpose of principal component analysis (PCA) is to interpret and recognize the variance as well as covariance of entire performance characteristics or output objectives by integrating them linearly by Payal et al. [42]. The key benefit of PCA is that data can be compressed once the pattern is recorded, i.e., dimensional reduction without sacrificing accuracy as discussed by Saha and Mondal [52]. The steps are associated with the PCA model which is explained by Kasdekaret al. [53] as follows:

(1) Getting some data
(2) Normalization of data
(3) Computation of covariance matrix
(4) Analysis and interpretation of covariance matrix

Step 5. Construct a variance-covariance matrix M via executing the normalized data, illustrated as follows:

$$M = \begin{bmatrix} N_{1,1} & N_{1,2} & \dots & N_{1,u} \\ N_{2,1} & N_{2,2} & \dots & N_{2,p} \\ \vdots & \vdots & \dots & \vdots \\ N_{q,1} & N_{q,2} & \dots & N_{q,p} \end{bmatrix}, \quad (9)$$

where u reflects the number of machining characteristics and p reflects the number of experimental runs.

Step 6. The correlation coefficient array can be written as follows:

$$N_{k,l} = \frac{\mathrm{Cov}\left(Y^*_{i,k}, Y^*_{i,l}\right)}{\sqrt{\mathrm{Var}\left(Y^*_{i,k}\right)\mathrm{Var}\left(Y^*_{i,l}\right)}}, \quad (10)$$

where $\mathrm{Cov}(Y^*_{i,k}, Y^*_{i,l})$ expressed the covariance of sequence $Y^*_{i,k}$ and $Y^*_{i,l}$. $\sqrt{\mathrm{Var}(Y^*_{i,k})}$ is the standard deviation of $Y^*_{i,k}$, $\sqrt{\mathrm{Var}(Y^*_{i,l})}$ is the standard deviation of $Y^*_{i,l}$ and $N_{k,l}$ is the correlation coefficient.

Step 7. Evaluation of Eigen vectors and Eigen values of matrix M are denoted by $\overrightarrow{V_J}$ and λ_j, respectively.

In the PCA model, the eigenvector $\overrightarrow{V_J}$ expresses the weighting factor of j number of machining characteristics of the j^{th} principal component. For example, if Q_j expresses the j^{th} machining characteristic, then the j^{th} principal component ψ_j can be respected as a quality indicator along with the operating machining characteristic and might be calculated by equation (11). It is to be understood that each principal component ψ_j depicts a certain degree of clarification of the variation of machining characteristics such as the accountability proportion (AP). AP of machining characteristics increase in the case of numerous gathering of principal components which is called as cumulative accountability proportion (CAP). Evaluation and selection of individual principal components (ψ_j), those need to be associated with composite machining indicator ψ depends on their individual accountability proportion.

$$\begin{aligned} \psi_j &= V_{J1} * Q_1 + V_{J2} * Q_2, \\ V_{JJ} * Q_J &= \overrightarrow{V_J}.\overrightarrow{Q}. \end{aligned} \quad (11)$$

In the conducted research work, the composite principal component ψ is defined as the combination of principal components with their individual eigen values, and it serves as the representative of multiresponses, called as multi/composite response indicators.

If a machining characteristic Q_j is robustly governed by the j^{th} principal component, this principal component becomes the chief indicator of such a machining characteristic. It ought to be sensed that one machining indicator might frequently represent entire multimachining characteristics.

Step 8. After computing the individual principal components, the composite machining indicator must be defined, which is the representative of multicharacteristics of the output responses. In the presented research work, the composite principal component ψ can be calculated as follows:

$$\psi = \left(\psi^2_{2i} + \psi^2_{2i} + \psi^2_{3i} + \psi^2_{4i}\right)^{1/2}, \quad (12)$$

where i is the experiment conducted.

4. Experimentation Setup Details

4.1. Detail of Experimental Setup and Problem Formulation. In current investigation, experiments are robustly conducted upon EDM using Inconel 825 material specimen Both the mechanical properties and chemical composition of composed Inconel 825 are tabulated in Tables 1 and 2, respectively.

To conduct experiments, the authors availed the EDM setup (manufacturer: Electronica India Limited, model no: Electronica Electrapuls PS 50ZNC), provided by Central Institute of Petrochemicals Engineering and Technology (CIPET), Raipur, C.G, India. The specification of EDM setup is tabulated in Table 3. Figure 3 depicts the flow chart of conducted experiments for EDMed Inconel 825 specimen. To attain the high degree of precision in experiments, it was highly concern to assess irregularities or roughness of electrode's bottom surface.

The copper was prioritized as a tool material which was having surface irregularities and is requisite for machining. Copper electrode (dimensions: diameter 10 mm and length 35 mm) along with its mechanical properties and images at various orientations and stages are depicted in Table 4 and Figure 4, respectively. The work piece size of $150 * 100 * 10$ mm (length $*$ width $*$ thickness) was employed for experiments.

Prior to conduct the experiments on EDM, initial weight of copper electrode and Inconel 825 specimen was measured by executing the Chemico Complete Lab Ware White Weighing Scale (digital capacity: 200gm, accuracy: 1 mg). The weight of electrode and work piece was found as 60.91 gm and 785.24 gm, respectively. Commercial grade EDM oil at freezing point = 94°C and specific gravity = 0.763 was employed as dielectric fluid with a constant flushing pressure of Fp = 2.1 bar in the EDM operation. Work piece and electrode has been kept at a positive and negative polarity, respectively, throughout the experimentation.

After finishing the aforesaid prerequisite, the process parameters optimization problem is formulated or machinability assessing index was framed. The experiments were conducted on EDMed Inconel 825 specimen with

Table 1: Chemical composition of Inconel 825 properties.

Chemical composition											
Element	S	Ni	Cu	Al	Cr	Si	Fe	Mn	Ti	Mo	C
Weight (%)	0.03	38–46	1.5–3.0	0.2	19.5–23.5	0.5	22	1	0.6–1.2	2.5–3.5	0.05

Table 2: Mechanical properties of Inconel 825.

Mechanical properties									
Properties	Modulus of elasticity	Melting point	Density	Coefficient of expansion	Thermal conductivity	Modulus of rigidity	Poisson's ratio	Specific heat	Tensile strength
Values	196 kN/mm^2	1400°C	8.14 g/cm^3	14.0 m/m/°C (20–100°C)	12.3 W/moC at 100°C	75.9 N/mm^2	0.29	440 Joules/kg-C	550 N/mm^2

Table 3: Specification of EDM setup.

Item (s)	Value/range	Item (s)	Value/range
Mounting surface (length × width)	600 × 400 mm	Maximum work piece height	250 mm
Width of the work tank	900 mm	Maximum job weight	50 kg
Depth of the work tank	600 mm	Height of the work tank	400 mm
X-axis travel	400 mm	Current range (Ip)	0–50 A
Y-axis travel	300 mm	Pulse on time range (ton)	0.5–3000 μs
Transverse (X,Y, Z)	400, 300, 250 mm	Duty factor range (τ)	8–100%
Open circuit voltage range (Vg)		0–100 V	

considering eight controllable EDM input process parameters, i.e., spark gap (Sg), gap voltage (Vg), pulse on time (Ton), pulse off time (Toff), peak current (Ip), servo feed (Sf), depth of cut (Dc), and difficulty index (Di). Each input parameter is varied at three discrete levels as shown in Table 5. The authors are supposed to conduct many experiments under compliance of the full factorial rule for optimizing inputs. But because of many challenges and constraints, i.e., framing more specimens, time, operating cost, and machining cost, the authors evaluated the twenty-seven (27) experiments by executing the statistical Taguchi's based L_{27} orthogonal array model. The total number of 27 experiments to be conducted corresponding to eight controllable EDM input process parameters at three discrete levels are shown in Table 6. Figure 5 shows the images for experiment 1 and 2, after data entry of process parameters into control panel or computer, embedded with EDM machine.

The responses/objectives, i.e., power consumption, machining time, and material removal rate corresponding to entered inputs parameters are tabulated in Table 7. After performing the twenty-seven experiments, the captured image of EDMed Inconel 825 specimen is depicted in Figure 6. The presented research has intention to determine the effective conditions of favorable input process parameters for Inconel 825, which might aid the manufacturers for producing their products at least cost with high production.

4.2. Parametric Optimization of EDMed Inconel 825

4.2.1. Evaluation of Optimal Process Condition. It is undoubtedly required to convert the multiobjective responses into single response, i.e., multiresponse performance indicator (MRPI) in order to calculate the optimal process condition. To transform the variety of dimensions of investigational data into comparable platform, (4) and (5) are employed in the case of grey relational analysis, whereas (9) is applied in the case of principal component analysis.

After computing single response/MRPI, the authors executed equations (6)–(8) towards estimating the overall grey relational grade (OGRG), and the sequential tables are depicted in Tables 8–11.

Moreover, equations (10)–(12) are employed towards estimating composite principal components (CPC), and sequential tables are depicted in Tables 12–14. Evaluated OGRG and CRC were subjected to maximization function, and therefore, their higher value is respected close to the optimal objective index. The mean response against OGRG and CRC with main effect plot, S/N plot, interaction plot, matrix plot, and residual plots are depicted in Figures 7–10 and Figures 11–14, respectively.

The total mean of OGRG and CRC for each level of parameter is computed and depicted in Tables 15 and 16, respectively. Figures 11–14 resulted the optimal parametric setting such as $Sg_2Vg_3Ton_1Toff_1Ip_3Sf_1Dc_1Di_1$.

4.2.2. Analysis of Variance (ANOVA). After assurance or confirmatory against evaluated/predicted optimal condition among multiple input parameters, the authors focused on evaluating the effectual and significant (important) input among multiple input parameters and is called as factor (input parameters) analysis. The authors' fruitfully adapted analysis of variance (ANOVA) statistical model. ANOVA assisted the authors to interpret the output responses (data) for evaluating the most significance input parameters. The evaluation of most important input guides the EDM operator to focus and control more the identified most important input, as low controlling or nonstrong traceability

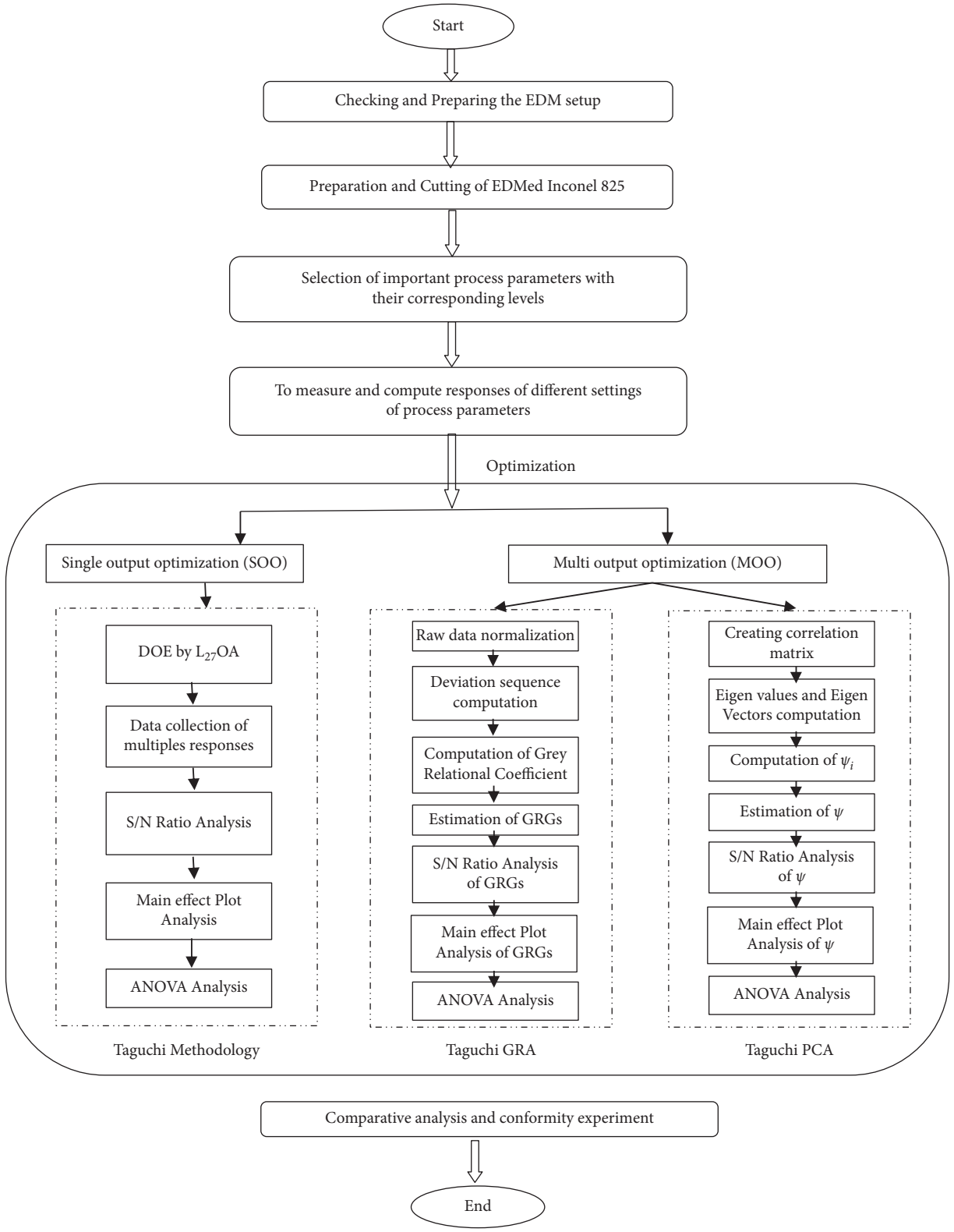

Figure 3: Flow chart of conducted experimental research for EDMed Inconel 825 material.

Table 4: Mechanical properties of pure copper electrode.

Physical properties	Electrical resistivity ($\mu\Omega$/cm)	Thermal conductivity (W/m·K)	Melting point (°C)	Specific gravity at 20°C (g/cc)	Density (g/cc)
Value	1.96	268.389	1083	8.9	8.92

(a) (b)

Figure 4: Electrode images at various stages. (a) Image of requisite machining performed on lathe on copper tool electrode. (b) Image of copper tool electrode after requisite machining performed and before starting experiment 1.

Table 5: Domain of experiments: bounded machining process parameters.

Parameters		Spark gap	Gap voltage	Pulse on time	Pulse off time	Peak current	Servo feed	Depth of cut	Difficulty index
Notations		(Sg)	(Vg)	(Ton)	(Toff)	(Ip)	(Sf)	(Dc)	(Di)
Units		mm	v	μs	μs	amp	mm/min	mm	—
Level of variations	1	0.05	25	500	10	15	40	0.5	30
	2	0.075	50	750	20	30	60	1	60
	3	0.1	75	1000	30	45	80	1.5	90

on identified input might cause the bad quality of goods. The total variability of the global desirably value is measured by sum of squared deviations about the grand mean of global desirability value is shown as follows. Thus,

$$SS_T = SS_F + SS_E,$$
$$SS_T = \sum_{j=1}^{p} \left(\gamma_j - \gamma_m\right)^2. \quad (13)$$

where SS_T = total sum of squared deviations about the mean, $\gamma_j = j^{\text{th}}$ experiment mean response, γ_m = grand mean of the response, P = number of experiments in the orthogonal array, SS_F = sum of squared deviations due to each factor, and SS_E = sum of squared deviations due to error.

In ANOVA table mean square deviation is defined as

$$SS = \frac{\text{SS (sum of squared deviation)}}{\text{DF (degree of freedom)}}. \quad (14)$$

F-value of Fisher's F ratio (variance ratio) is defined as

$$F = \frac{\text{MS of a term}}{\text{MS for the error term}}. \quad (15)$$

Equations (13)–(16) are employed for estimating ANOVA for OGRG and CPC are shown in Tables 17 and 18, respectively. After assessing the F value, probability of significance, i.e., p value is determined and estimated by MINITAB-16 software release 13.1. It is probed that p value for pulse off time is found such as 0.005 and 0.001 corresponding to OGRG and CPC, respectively.

Therefore, it is ascertained and marked that pulse off time is the key significant among multiple input parameters. In addition to that depth of cut is found the second significant input parameter, while the influences of other six factors were found insignificant. Furthermore, proportion of contribution encountered by each process parameters is also estimated for both T-GRA AND T-PCA and tabulated in Table 19.

4.2.3. Confirmatory Experiment and Validation. After determining the optimal process conditions/parametric setting of EDMed Inconel 825 material, the authors were not potentially sure to implement and install evaluated optimal parametric setting for machining on EDM. Therefore, the authors reconducted one more experiment on same material to confirm the obtained optimal parametric setting, i.e.,

Table 6: Taguchi's *L27* orthogonal array structure.

Exp no.	Spark gap (Sg)	Gap voltage (Vg)	Pulse on time (Ton)	Pulse off Time (Toff)	Peak current (Ip)	Servo feed (Sf)	Depth of cut (Dc)	Difficulty index (Di)
δ_1	0.05	25	500	10	15	40	0.5	30
δ_2	0.05	25	500	10	30	60	1	60
δ_3	0.05	25	500	10	45	80	1.5	90
δ_4	0.05	50	750	20	15	40	0.5	60
δ_5	0.05	50	750	20	30	60	1	90
δ_6	0.05	50	750	20	45	80	1.5	30
δ_7	0.05	75	1000	30	15	40	0.5	90
δ_8	0.05	75	1000	30	30	60	1	30
δ_9	0.05	75	1000	30	45	80	1.5	60
δ_{10}	0.075	25	750	30	15	60	1.5	30
δ_{11}	0.075	25	750	30	30	80	0.5	60
δ_{12}	0.075	25	750	30	45	40	1	90
δ_{13}	0.075	50	1000	10	15	60	1.5	60
δ_{14}	0.075	50	1000	10	30	80	0.5	90
δ_{15}	0.075	50	1000	10	45	40	1	30
δ_{16}	0.075	75	500	20	15	60	1.5	90
δ_{17}	0.075	75	500	20	30	80	0.5	30
δ_{18}	0.075	75	500	20	45	40	1	60
δ_{19}	0.1	25	1000	20	15	80	1	30
δ_{20}	0.1	25	1000	20	30	40	1.5	60
δ_{21}	0.1	25	1000	20	45	60	0.5	90
δ_{22}	0.1	50	500	30	15	80	1	60
δ_{23}	0.1	50	500	30	30	40	1.5	90
δ_{24}	0.1	50	500	30	45	60	0.5	30
δ_{25}	0.1	75	750	10	15	80	1	90
δ_{26}	0.1	75	750	10	30	40	1.5	30
δ_{27}	0.1	75	750	10	45	60	0.5	60

(a) (b)

Figure 5: Images showing details of experimentation 1 and experimentation 2. (a) Experiment 1 (run 1). (b) Experiment 2 (run 2).

$Sg_2Vg_3Ton_1Toff_1Ip_3Sf_1Dc_1Di_1$. Thereafter, the contrast between the obtained results and the predicted theoretical results is critically audited by employing (16), as shown in Tables 20 and 21. The estimated index $\hat{\gamma}$ of the optimal parametric setting of the design parameters is calculated as

$$\hat{\gamma} = \gamma_m + \sum_{i=1}^{0} \left(\bar{\gamma}_i - \gamma_m\right), \tag{16}$$

where γ_m and $\bar{\gamma}_i$ expressed the total means and mean at the optimal level, corresponding to GRG and CPC as well. 0 expressed the number of core design parameters might be responsive for good and poor quality characteristics of work part. After statistical interpretation and analysis, it is determined that there is the best synergy and compliance among OGRG and CPC. It is concluded that the proposed models are valid to evaluate the optimal parametric setting amongst multiple input parameters in addressing the multiple objectives/responses.

5. Analysis of Surface Topography

After, evaluation of optimal process condition, confirmatory test and ANOVA analysis, the authors acted to investigate

Table 7: Design of experiment (*L*27) orthogonal array and collected response experimental data.

δ_i	δ_1	δ_2	δ_3	δ_4	δ_5	δ_6	δ_7	δ_8	δ_9	δ_{10}	δ_{11}	δ_{12}	δ_{13}	δ_{14}	δ_{15}	δ_{16}	δ_{17}	δ_{18}	δ_{19}	δ_{20}	δ_{21}	δ_{22}	δ_{23}	δ_{24}	δ_{25}	δ_{26}	δ_{27}
Power consumption (KW)	1.125	4.625	7.100	1.250	7.625	9.750	4.250	7.500	10.000	1.875	8.750	12.500	2.625	5.150	7.500	4.500	6.225	8.500	2.000	5.000	9.875	5.125	9.000	9.500	2.500	4.438	6.000
Machining time (min)	6.900	2.450	2.480	2.130	2.700	4.670	2.920	3.950	3.930	10.300	2.230	3.880	8.830	0.980	0.765	3.620	1.500	2.100	11.270	5.120	1.770	10.980	5.190	1.370	3.280	3.420	1.150
MRR (mg/min)	32.394	232.653	370.968	67.265	159.259	209.850	48.077	149.367	83.969	66.990	116.592	153.846	95.130	193.878	168.831	204.420	373.333	328.000	65.661	172.862	101.695	59.199	161.654	153.285	201.22	295.322	356.522

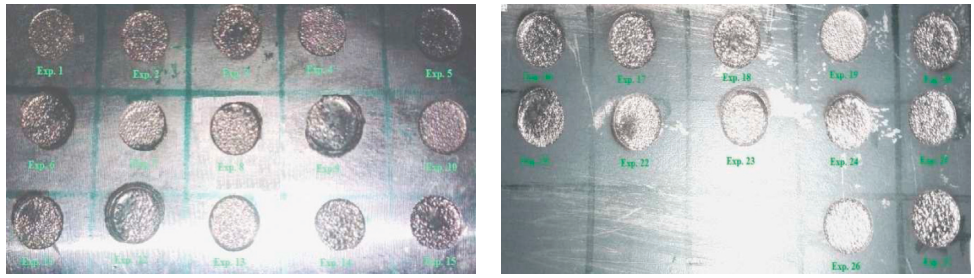

(a) (b)

Figure 6: Images of EDMed Work piece after completion of 27 experimentation.

the topography of the machined surface of EDMed Inconel 825 specimen using an Optical Microscope (Model-Carl Zeiss Microscope AXIO). The investigation of work part topography aids the authors to redesign the inputs and adapt the other robust optimal process condition evaluation models. To investigate topography, at first, preliminary invigilation is conducted on evaluated initial parametric setting $Sg_1Vg_1Ton_1Toff_1Ip_1Sf_1Dc_1Di_1$ which had low value of constrained process parameters for the evaluation of metallurgical structure and cracks. It has been found that initial parametric setting will have an acceptable metallurgical structure and crack. Tiny or very small amount of microvoids, resolidified debris, droplets, and molten pool are examined and depicted in Figure 15. Moreover, increasing value of spark gap allows vast amount of electrical current transferred to the work piece and results in higher thermal energy generation at projected surface which ultimately results in high material removal and lower machining time. However, on the other hand, it increases the deep craters and deposition of molten metal along with tendency of more crack formation on the machined surface as depicted in Figure 16 for parametric setting $Sg_3Vg_1Ton_3Toff_2Ip_1Sf_3Dc_2Di_1$.

Moreover, it is also observed from surface topography snapshots analysis that increased value in peak current also allowed enormous amount of thermal energy on the work piece that results in the generation of spherical globules and acceleration in molten metal deposition. Hence, in order to trim down these irregularities, the authors advised to increase the dielectric flashing circulation pressure in conjunction with increased value of process parameters as in present investigation, it was set at constant Fp = 2.1 bar. Also, increase in gap voltage results in spacious gap between the electrode and work piece, which delivers the extra efficient flushing rate of melted metal and debris. Hence, in the present investigation, the surface topography reconfirmed the results of ANOVA analysis, it is recertified that pulse off time as well as depth of cut broadly enhanced the surface integrity of the EDMed surface. Parallel enhancement in both pulse off time and depth of cut results in the efficient improvement in removal of the debris and melted metal which ultimately enhance material removal rate and decrease machining time. Moreover, efficient flushing can take place during pulse off time which reduces the thermal stress on the EDMed surface that generated due to extreme heat and cooling rates.

Table 8: Assessment of Δ0i for each of the responses.

δ_i	δ_1	δ_2	δ_3	δ_4	δ_5	δ_6	δ_7	δ_8	δ_9	δ_{10}	δ_{11}	δ_{12}	δ_{13}	δ_{14}	δ_{15}	δ_{16}	δ_{17}	δ_{18}	δ_{19}	δ_{20}	δ_{21}	δ_{22}	δ_{23}	δ_{24}	δ_{25}	δ_{26}	δ_{27}
Pc	0.0000	0.3077	0.5253	0.0110	0.5714	0.7582	0.2747	0.5604	0.7802	0.0659	0.6703	1.0000	0.1319	0.3538	0.5604	0.2967	0.4484	0.6484	0.0769	0.3407	0.7692	0.3516	0.6923	0.7363	0.1209	0.2912	0.4286
Mt	0.5840	0.1604	0.1633	0.1299	0.1842	0.3717	0.2051	0.3032	0.3013	0.9077	0.1395	0.2965	0.7677	0.0205	0.0000	0.2718	0.0700	0.1271	1.0000	0.4146	0.0957	0.9724	0.4212	0.0576	0.2394	0.2527	0.0366
MRR	1.0000	0.4126	0.0069	0.8977	0.6279	0.4795	0.9540	0.6569	0.8487	0.8985	0.7530	0.6438	0.8160	0.5264	0.5998	0.4954	0.0000	0.1330	0.9024	0.5880	0.7967	0.9214	0.6209	0.6454	0.5048	0.2288	0.0493

Table 9: Grey relational coefficient ξ_i (k) of each machining characteristics (with $\psi = 0.5$).

δ_i	δ_1	δ_2	δ_3	δ_4	δ_5	δ_6	δ_7	δ_8	δ_9	δ_{10}	δ_{11}	δ_{12}	δ_{13}	δ_{14}	δ_{15}	δ_{16}	δ_{17}	δ_{18}	δ_{19}	δ_{20}	δ_{21}	δ_{22}	δ_{23}	δ_{24}	δ_{25}	δ_{26}	δ_{27}
Pc	1.0000	0.6190	0.4877	0.9785	0.4667	0.3974	0.6454	0.4715	0.3906	0.8835	0.4272	0.3333	0.7913	0.5856	0.4715	0.6276	0.5272	0.4354	0.8667	0.5948	0.3939	0.5871	0.4194	0.4044	0.8053	0.6319	0.5385
Mt	0.4613	0.7571	0.7539	0.7937	0.7308	0.5736	0.7091	0.6225	0.6240	0.3552	0.7819	0.6277	0.3944	0.9607	1.0000	0.6479	0.8772	0.7973	0.3333	0.5467	0.8394	0.3396	0.5428	0.8967	0.6762	0.6642	0.9317
MRR	0.3333	0.5479	0.9863	0.3577	0.4433	0.5105	0.3439	0.4322	0.3707	0.3575	0.3990	0.4371	0.3799	0.4872	0.4546	0.5023	1.0000	0.7899	0.3565	0.4596	0.3856	0.3518	0.4461	0.4365	0.4976	0.686	0.9102

Table 10: Data preprocessing of each machining characteristic (grey relational generation).

δ_i	δ_1	δ_2	δ_3	δ_4	δ_5	δ_6	δ_7	δ_8	δ_9	δ_{10}	δ_{11}	δ_{12}	δ_{13}	δ_{14}	δ_{15}	δ_{16}	δ_{17}	δ_{18}	δ_{19}	δ_{20}	δ_{21}	δ_{22}	δ_{23}	δ_{24}	δ_{25}	δ_{26}	δ_{27}
Pc	1.000	0.692	0.475	0.989	0.429	0.242	0.725	0.440	0.220	0.934	0.330	0.000	0.868	0.646	0.440	0.703	0.552	0.352	0.923	0.659	0.231	0.648	0.308	0.264	0.879	0.709	0.571
Mt	0.416	0.840	0.837	0.870	0.816	0.628	0.795	0.697	0.699	0.092	0.861	0.703	0.232	0.980	1.000	0.728	0.930	0.873	0.000	0.585	0.904	0.028	0.579	0.942	0.761	0.747	0.963
MRR	0.000	0.587	0.993	0.102	0.372	0.520	0.046	0.343	0.151	0.101	0.247	0.356	0.184	0.474	0.400	0.505	1.000	0.867	0.098	0.412	0.203	0.079	0.379	0.355	0.495	0.771	0.951

Table 11: Grey relational grade γ_i.

δ_i	δ_1	δ_2	δ_3	δ_4	δ_5	δ_6	δ_7	δ_8	δ_9	δ_{10}	δ_{11}	δ_{12}	δ_{13}	δ_{14}	δ_{15}	δ_{16}	δ_{17}	δ_{18}	δ_{19}	δ_{20}	δ_{21}	δ_{22}	δ_{23}	δ_{24}	δ_{25}	δ_{26}	δ_{27}
Grey relational grade γ_i	0.59819	0.64134	0.74281	0.70998	0.54692	0.49380	0.56612	0.50874	0.46176	0.53207	0.53606	0.46607	0.52188	0.67781	0.64204	0.59258	0.80149	0.67423	0.51884	0.53368	0.53964	0.42615	0.46940	0.57923	0.65971	0.66074	0.79347
S/N ratio (higher-the-better)	−4.46315	−3.85817	−2.58473	−2.97504	−5.24156	−6.12890	−4.94190	−5.87016	−6.71170	−5.48061	−5.41578	−6.63098	−5.64852	−3.37787	−3.84875	−4.45508	−1.92202	−3.42387	−5.69930	−5.45438	−5.35794	−7.40875	−6.56920	−4.74303	−3.61586	−3.59933	−2.00942

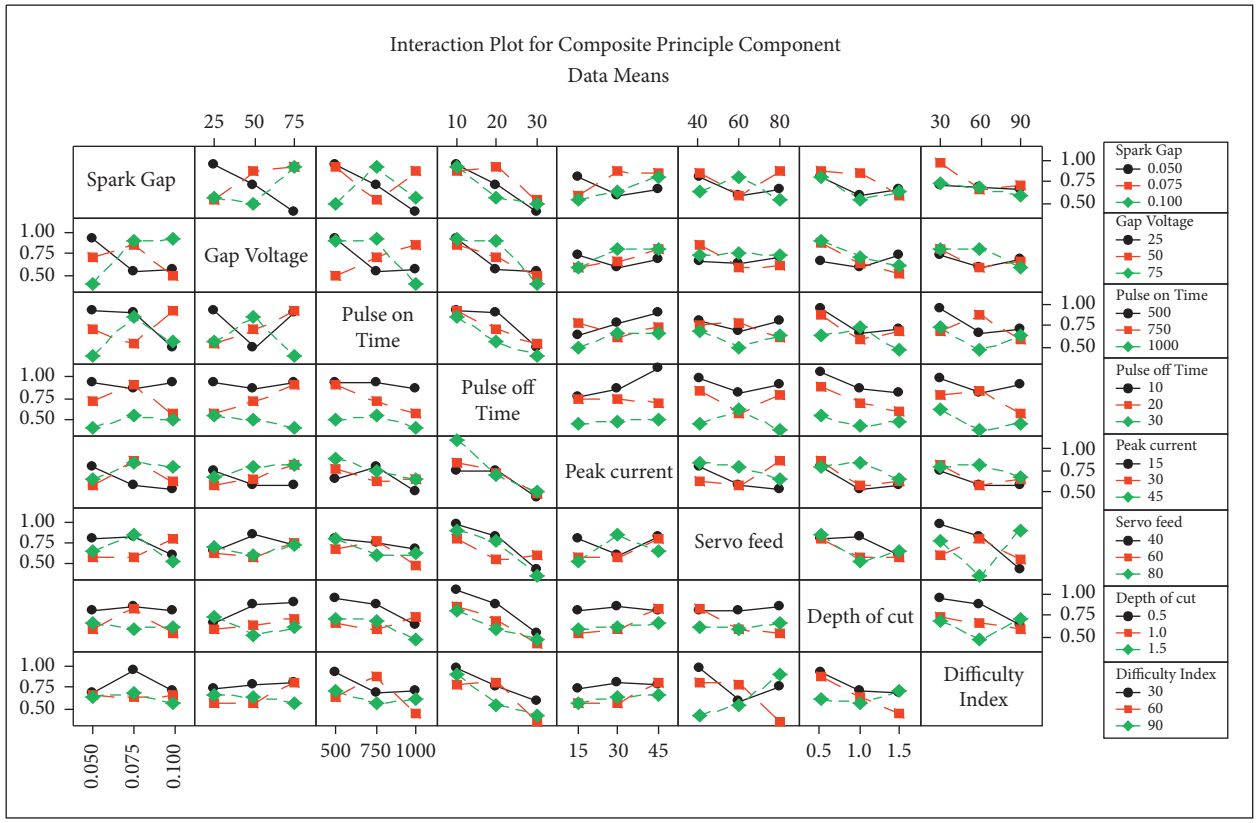

Figure 7: Interaction plot for the composite principal component.

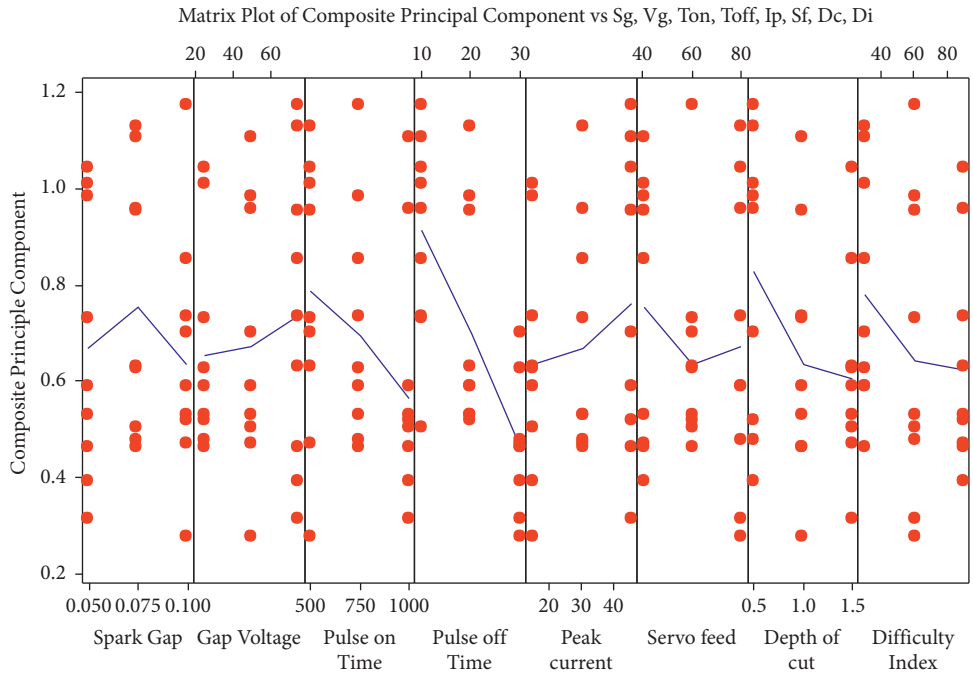

Figure 8: Matrix plot for the composite principal component.

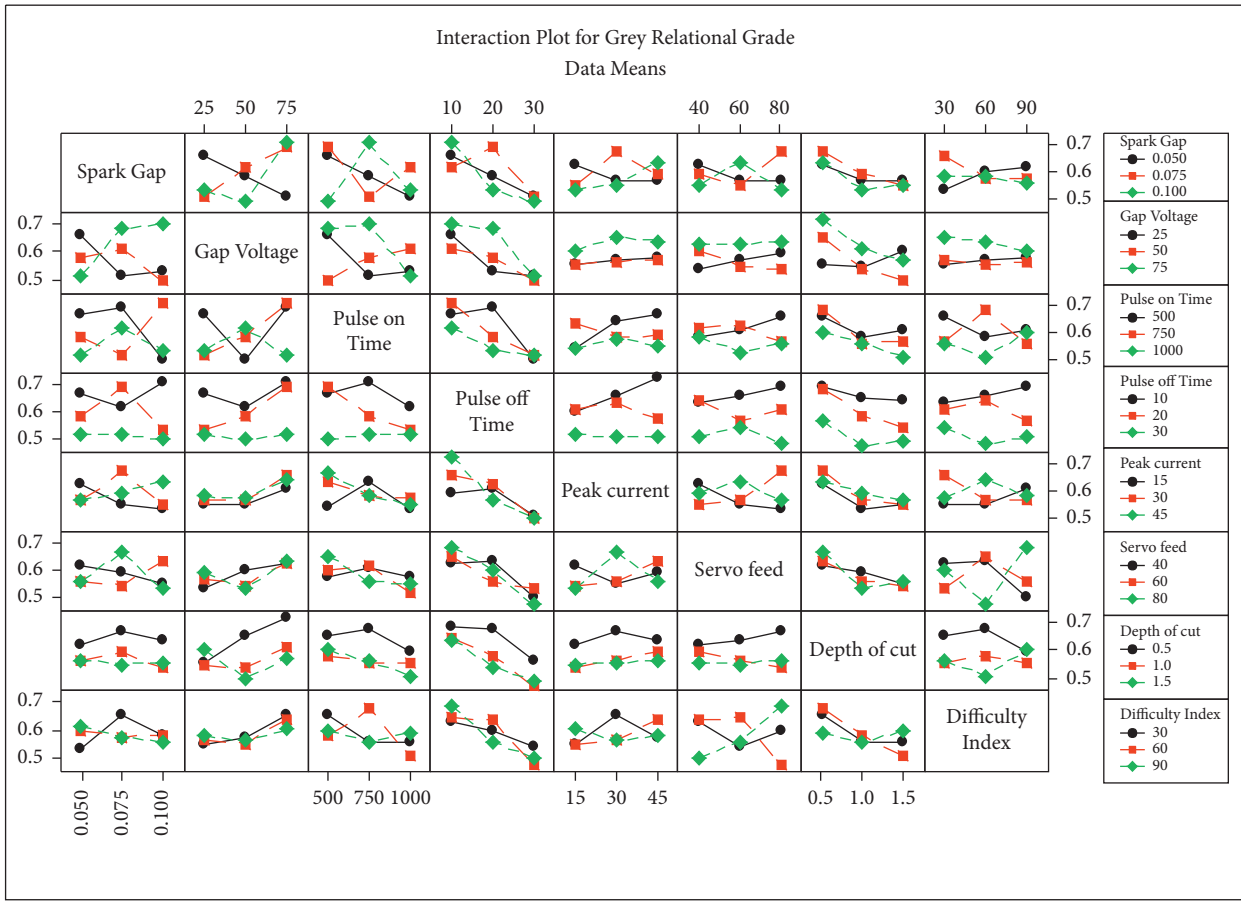

Figure 9: Interaction plot for overall grey relational grade (OGRG).

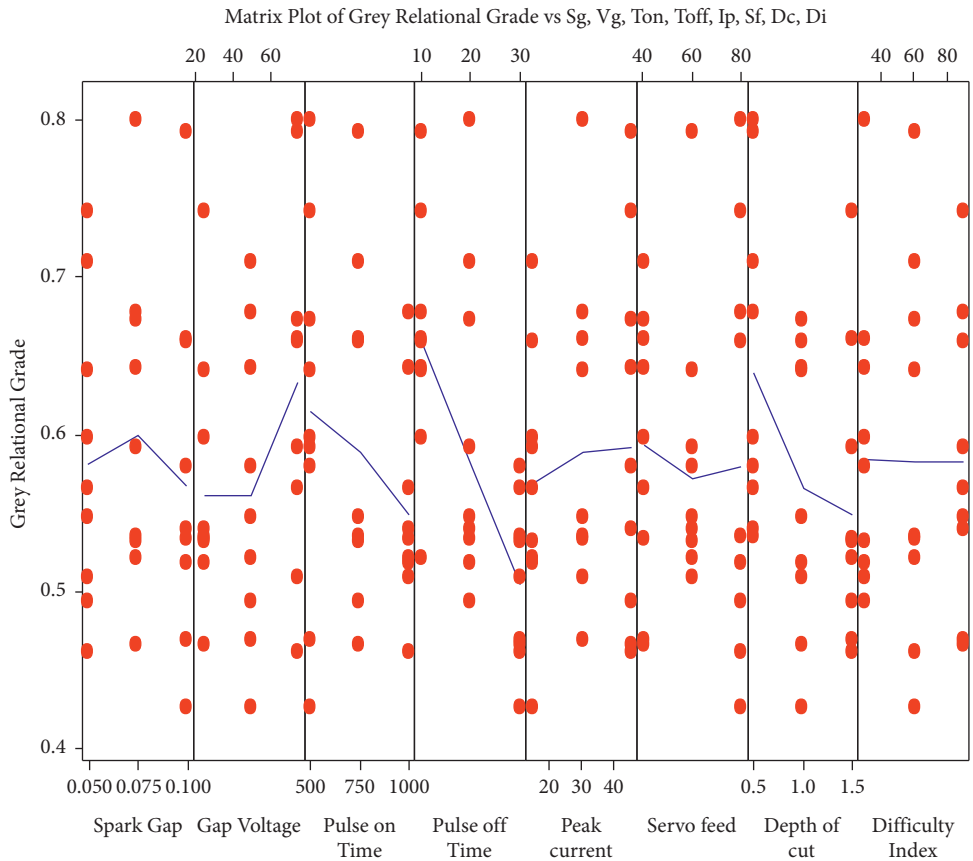

Figure 10: Matrix plot for overall grey relational grade (OGRG).

Table 12: Principal component (ψ_j) for L27 OA experimental observations.

δ_i	δ_1	δ_2	δ_3	δ_4	δ_5	δ_6	δ_7	δ_8	δ_9	δ_{10}	δ_{11}	δ_{12}	δ_{13}	δ_{14}	δ_{15}	δ_{16}	δ_{17}	δ_{18}	δ_{19}	δ_{20}	δ_{21}	δ_{22}	δ_{23}	δ_{24}	δ_{25}	δ_{26}	δ_{27}
ψ_1 (1st PC)	−0.41484	0.46194	0.77318	−0.18403	0.35718	0.41905	0.07032	0.29680	0.19018	−0.15324	0.31100	0.33866	−0.00282	0.60824	0.69336	0.35872	0.85571	0.72844	−0.13890	0.28314	0.32951	0.03012	0.31321	0.48334	0.25686	0.53865	0.88861
ψ_2 (2nd PC)	−0.55547	−0.27027	−0.15886	−0.70430	−0.23583	−0.09294	−0.32774	−0.16474	−0.17979	−0.31664	−0.29907	−0.13699	−0.23188	−0.68027	−0.84864	−0.20054	−0.34162	−0.21551	−0.29394	−0.15086	−0.37607	−0.13539	−0.10702	−0.46145	−0.31615	−0.16828	−0.48658
ψ_3 (3rd PC)	0.73434	0.50223	0.68606	0.66344	0.31316	0.40890	0.20599	0.31978	0.17836	0.52211	0.21012	0.28447	0.44756	0.30056	0.15396	0.48249	0.65593	0.57843	0.49493	0.42485	0.15155	0.24134	0.33519	0.21394	0.61244	0.64139	0.59272

Table 13: (Analysis of covariance matrix) eigen values, eigenvectors, accountability proportion (AP) and cumulative accountability proportion (CAP) computed for EDM major quality measures.

Principle component	ψ_1	ψ_2	ψ_3
Eigen vectors	(−0.527, 0.445, 0.724)	(−0.476, −0.860, 0.183)	(0.705, −0.248, 0.655)
Eigen value	0.10826	0.03817	0.03426
AP	0.599	0.211	0.190
CAP	0.599	0.81	1.00

Table 14: Composite principal component (ψ) for EDMed machining characteristics and corresponding S/N ratios.

	δ_1	δ_1	δ_2	δ_3	δ_4	δ_5	δ_6	δ_7	δ_8	δ_9	δ_{10}	δ_{11}	δ_{12}	δ_{13}	δ_{14}	δ_{15}	δ_{16}	δ_{17}	δ_{18}	δ_{19}	δ_{20}	δ_{21}	δ_{22}	δ_{23}	δ_{24}	δ_{25}	δ_{26}	δ_{27}
ψ	1.00990	0.73394	1.04581	0.98492	0.53034	0.59282	0.39344	0.46636	0.31671	0.62956	0.47992	0.46301	0.50407	0.96076	1.10664	0.63379	1.13101	0.95481	0.59215	0.53238	0.52247	0.27836	0.47107	0.70166	0.73553	0.85431	1.17375
S/N ratio	0.08554	−2.68675	0.38904	−0.13199	−5.50885	−4.54157	−8.10248	−6.62566	−9.98679	−4.01930	−6.37669	−6.68815	−5.95022	−0.34770	0.88011	−3.96109	1.06935	−0.40170	−4.55130	−5.47556	−5.63878	−11.10799	−6.53833	−3.07749	−2.66795	−1.36772	1.39153

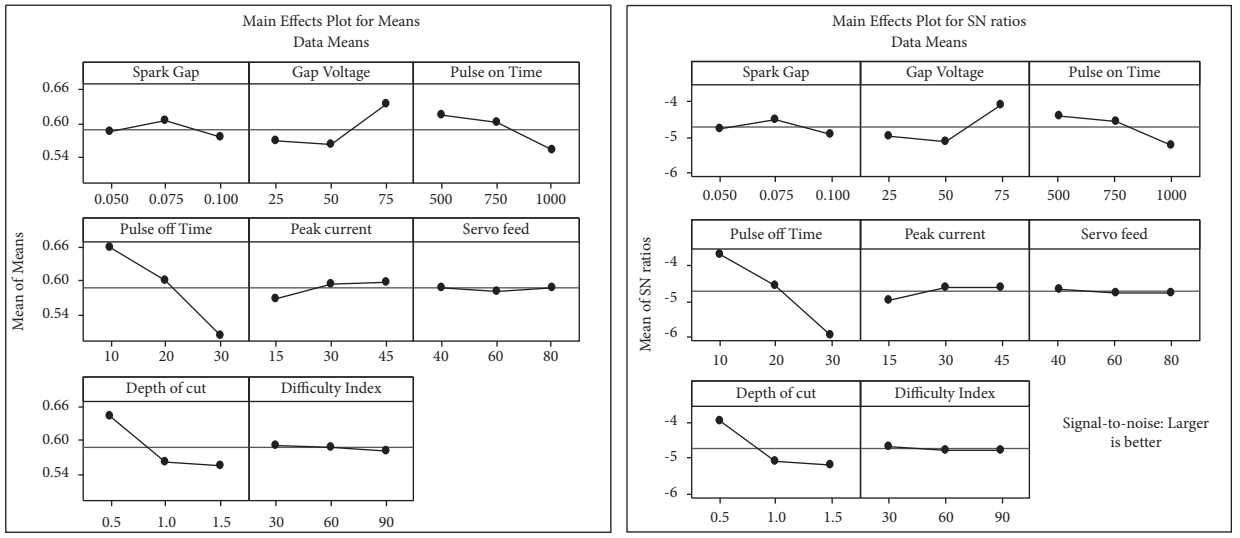

Figure 11: Main effect plot and S/N plot for overall grey relational grade (OGRG).

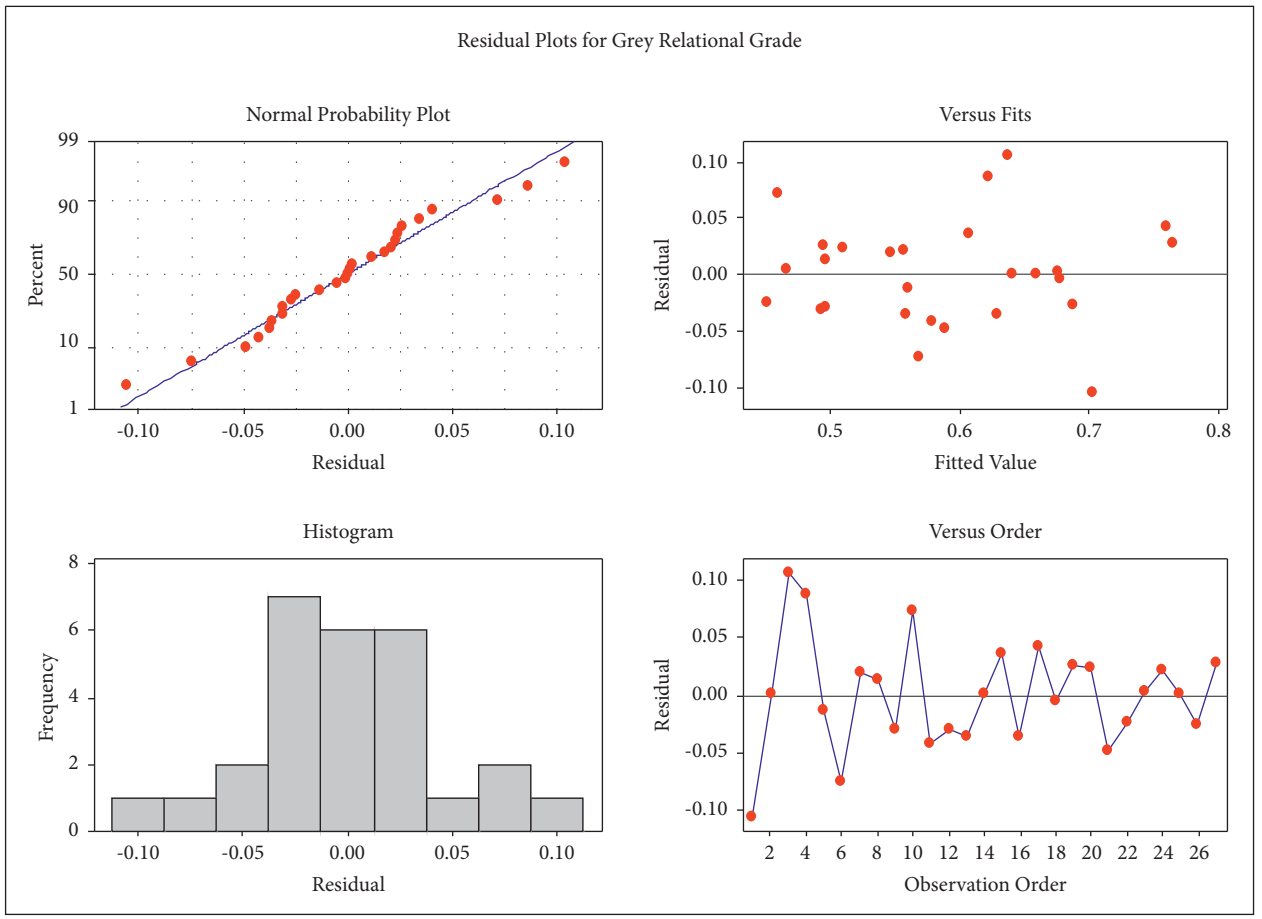

Figure 12: Residual plots for overall grey relational grade (OGRG).

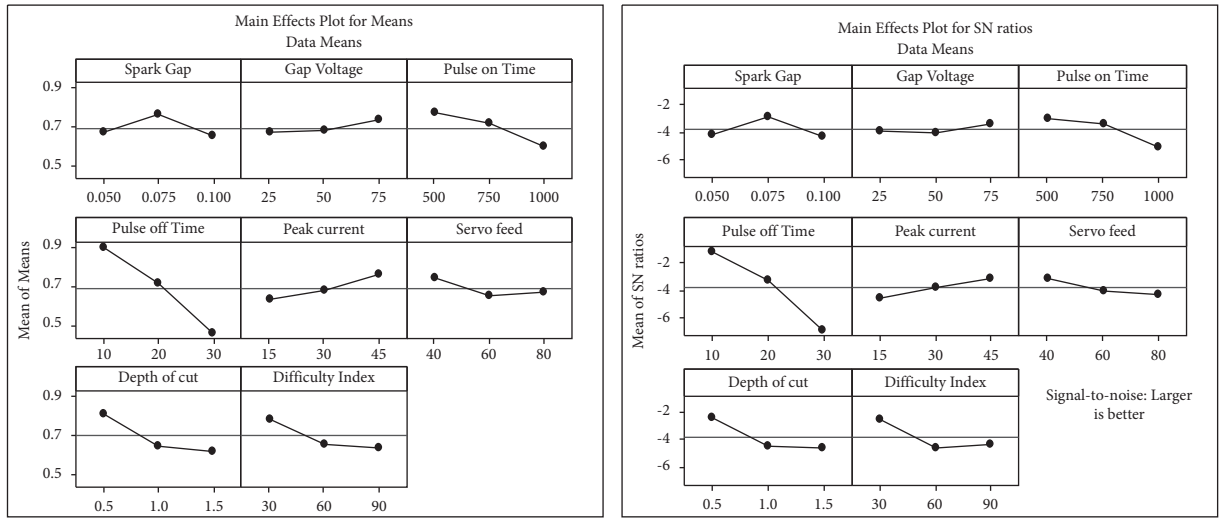

Figure 13: Main effect plot and S/N plot for composite principal component.

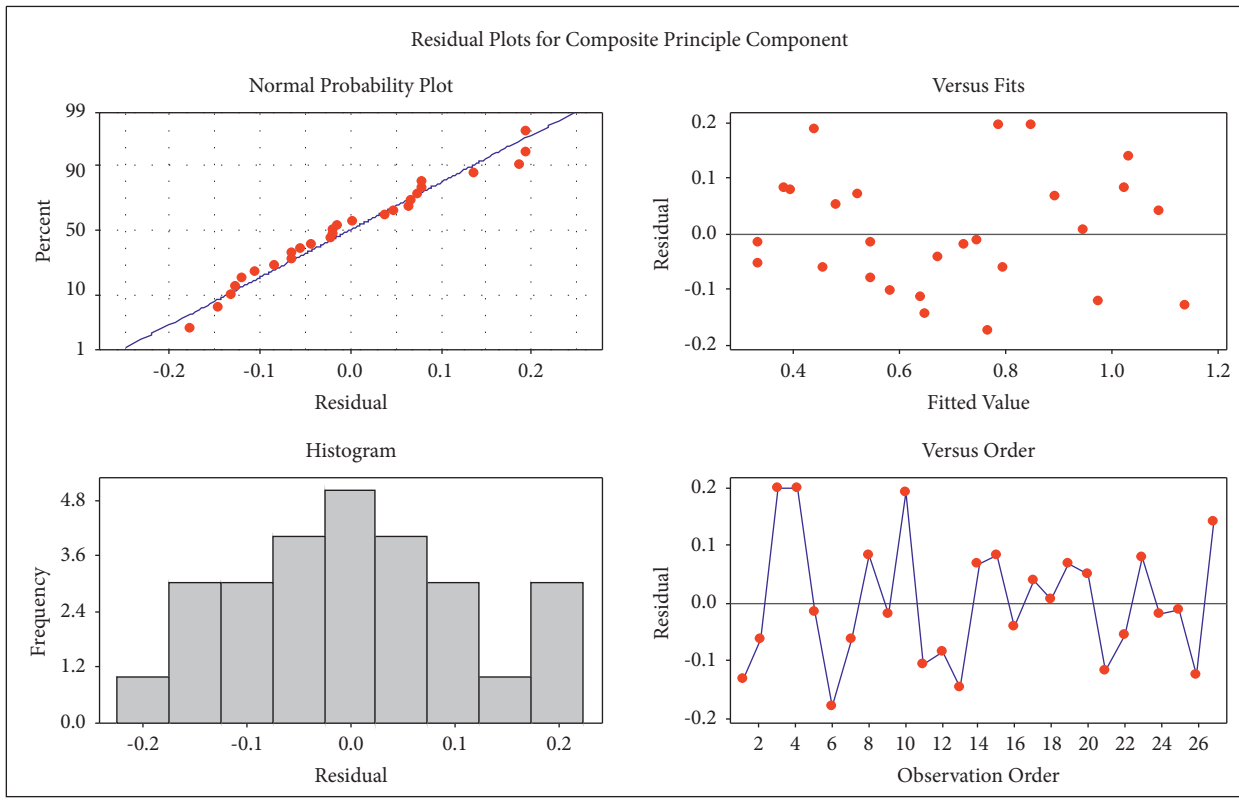

Figure 14: Residual plots for the composite principal component.

Table 15: Response table (mean) for grey relational grade.

Grey Relational Grade	Parameters							
	Sg	*Vg*	*Ton*	*Toff*	*Ip*	*Sf*	*Dc*	*Di*
Level 1	0.58550	0.56761	0.61391	0.65976	0.56950	0.59116	0.64466	0.59279
Level 2	0.60491	0.56302	0.59987	0.60124	0.59735	0.58398	0.56489	0.58873
Level 3	0.57565	0.63543	0.55228	0.50506	0.59921	0.59091	0.55650	0.58454
Delta	0.02926	0.07240	0.06164	0.15469	0.02970	0.00718	0.08816	0.00826
Mean of γ_i = 0.58869								

Delta = range, i.e., maximum – minimum.

Table 16: Response table (mean) for composite principal component (ψ).

Composite Principal Component	Parameters							
	Sg	Vg	Ton	Toff	Ip	Sf	Dc	Di
Level 1	0.67491	0.66768	0.77337	0.90275	0.64019	0.75227	0.81754	0.78716
Level 2	0.76262	0.68118	0.71602	0.71941	0.68445	0.6551	0.65124	0.66209
Level 3	0.6513	0.73997	0.59944	0.46667	0.76419	0.68145	0.62006	0.63958
Delta	0.11132	0.07228	0.17393	0.43607	0.124	0.09717	0.19748	0.14758
Mean of ψ = 0.69628								

Delta = range, i.e., maximum – minimum.

Table 17: ANOVA for γ_i using adjusted SS for tests.

Source	DF	Sequential SS	Adj SS	Adj MS	*F*	*p*
Sg	2	0.003991	0.003991	0.001996	0.35	0.712
Vg	2	0.029585	0.029585	0.014793	2.61	0.123
Ton	2	0.018783	0.018783	0.009392	1.65	0.239
Toff	2	0.109810	0.109810	0.054905	9.67	0.005
Ip	2	0.004984	0.004984	0.002492	0.44	0.656
Sf	2	0.000299	0.000299	0.000149	0.03	0.974
Dc	2	0.042619	0.042619	0.021309	3.75	0.061
Di	2	0.000307	0.000307	0.000153	0.03	0.973
Error	10	0.056751	0.056751	0.005675		
Total	26	0.267129				

Table 18: ANOVA for composite principal component (ψ) using adjusted SS for tests.

Source	DF	Sequential SS	Adj SS	Adj MS	*F*	*p*
Sg	2	0.06193	0.06193	0.03096	1.05	0.385
Vg	2	0.02659	0.02659	0.01329	0.45	0.649
Ton	2	0.14139	0.14139	0.07070	2.40	0.141
Toff	2	0.86294	0.86294	0.43147	14.64	0.001
Ip	2	0.07107	0.07107	0.03554	1.21	0.339
Sf	2	0.04546	0.04546	0.02273	0.77	0.488
Dc	2	0.20288	0.20288	0.10144	3.44	0.073
Di	2	0.11378	0.11378	0.05689	1.93	0.195
Error	10	0.29464	0.29464	0.02946		
Total	26	1.82067				

Table 19: Proportion of contribution encountered by the process parameters.

Parameters	Unit	γ_{MRPI}^{GRG}		ψ_{MRPI}^{PCA}	
		Adj SS	Percentage contribution (%)	Adj SS	Percentage contribution (%)
Spark gap	mm	0.00399	1.49	0.06193	3.40
Gap voltage	v	0.02959	11.08	0.02659	1.46
Pulse on time	μs	0.01878	7.03	0.14139	7.77
Pulse off time	μs	0.10981	41.11	0.86294	47.40
Peak current	amp	0.00498	1.87	0.07107	3.90
Servo feed	mm/min	0.0003	0.11	0.04546	2.50
Depth of cut	Mm	0.04262	15.95	0.20288	11.14
Difficulty index	—	0.00031	0.11	0.11378	6.25

Table 20: Results of confirmatory experiment for overall grey relational grade (OGRG).

	Initial factor setting	Optimal process condition	
		Prediction	Experiment
Level of factors	$Sg_1Vg_1Ton_1Toff_1$ $Ip_1Sf_1Dc_1Di_1$	$Sg_2Vg_3Ton_1Toff_1$ $Ip_3Sf_1Dc_1Di_1$	$Sg_2Vg_3Ton_1Toff_1$ $Ip_3Sf_1Dc_1Di$
Power consumption (Pc)	1.125		6.125
Machining time (Mt)	6.900		1.950
Material removal rate (MRR)	32.394		355.610
S/N ratio of γ_{MRPI}^{GRG}	−4.46315	−1.71286	−2.48370
γ_{MRPI}^{GRG}	0.59819	0.82103	0.75130

Improvement in $\gamma_{MRPI}^{GRG} = 0.16262$.

Table 21: Results of confirmatory experiment for composite principal component (ψ).

	Initial factor setting	Optimal process condition	
		Prediction	Experiment
Level of factors	$Sg_1Vg_1Ton_1Toff_1$ $Ip_1Sf_1Dc_1Di_1$	$Sg_2Vg_3Ton_1Toff_1$ $Ip_3Sf_1Dc_1Di_1$	$Sg_2Vg_3Ton_1Toff_1$ $Ip_3Sf_1Dc_1Di$
Power consumption (Pc)	1.125		6.125
Machining time (Mt)	6.900		1.950
Material removal rate (MRR)	32.394		355.610
S/N ratio of ψ_{MRPI}^{PCA}	0.08554	3.08187	0.34283
ψ_{MRPI}^{PCA}	1.00990	1.42592	1.04026

Improvement in $\psi_{MRPI}^{PCA} = 0.34398$.

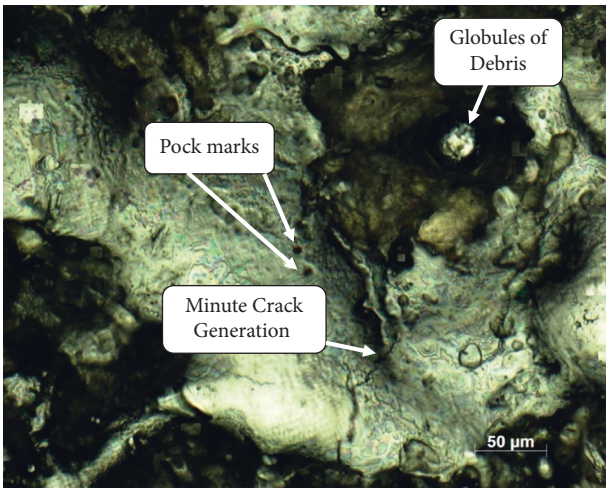

Figure 15: Analysis of surface topography for experimental run 1 using the initial parametric.

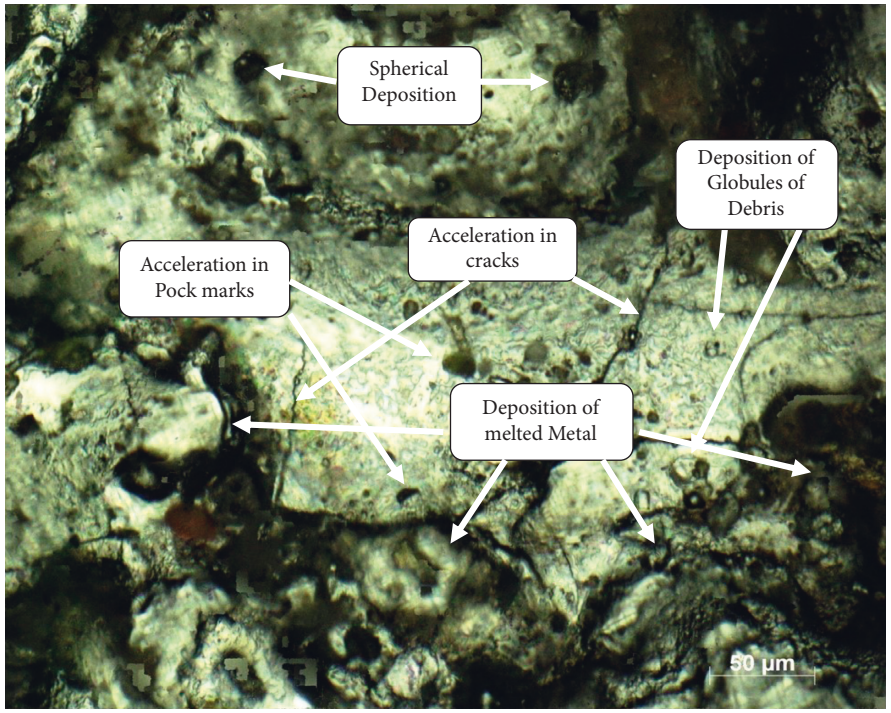

Figure 16: Analysis of surface topography for experimental run 19 using the parametric setting.

6. Conclusions

EDM is searched as a challenging, dynamic, and majestic machine and has short payback period for investors. EDM became the honeywell for entire production communities industry 4.0 in the current era. In the presented research forum, Taguchi-based L_{27} orthogonal array model is fruitfully adapted for conducting the experiments on Inconel 825 specimen using EDM operation. Preliminary, to conclude the reliable optimum setting among defined eight input parameters, a novel integrated Taguchi-grey relational analysis (T-GRA) and principal component analysis (T-PCA) is implemented. Two MRPIs are calculated by executing the T-GRA and T-PCA models over triple responses, i.e., Pc, Mt, and MRR. The computed MRPIs are examined for determining the optimum condition setting among eight input parameters which is found as $Sg_2Vg_3Ton_1Toff_1Ip_3Sf_1Dc_1Di_1$. Next, evaluated optimum setting is reconfirmed and validated with 100% assurance after conducting one more experiment on the same specimen with the same identical setup against evaluated optimum setting. The upshots of the confirmation test yielded an improvement of 0.16262 and 0.34398 corresponding to evaluated MRPIs by T-GRA and T-PCA, respectively, as a part first contribution or finding.

Furthermore, the analysis of variance (ANOVA) statistical model is adapted to find the priority ratings against eight inputs. The pulse off time and depth of cut is prioritized as the first and second significant input factor, respectively, on resulted p value as 0.005, 0.001, and 0.061, 0.073 in application of T-GRA and T-PCA, respectively, respected as a part second contribution/finding. Pulse off time is found as a most significant parameter by both T-GRA and T-PCA methodologies, where T-GRA reflected 41.11%% of contribution while T-PCA reflected 47.40% of contribution of pulse off time, respectively. In addition to this, the authors audited the effects of varying values of input parameters over the surface topography such as metallurgical structure, deep craters, and cracks, as discussed in Section 5; however, to overcome awful surface topography, a few remediates are proposed by authors as a part of third contribution/finding.

The research works is constrained or limited up to discussed problems, namely, the optimum parameters setting, significance inputs, and surface topography evaluation problems. The problems such as linear, programmable, and alternative evaluation problems is not in the curriculum of research work. From industrial value and applications perspectives, the nontraditional material scholars and investigators can prolifically adapt the proposed insights, models, methodology to audit the same materials with different nontraditional machines such as ECM and LBM. From the future scope standing point, the proposed integrated models, T-GRA and T-PCA in conjunction with ANOVA models can be employed to investigate the smart or forthcoming materials with different nontraditional machining process/operations. From the point of interdisciplinary view, the same protocol of the proposed research forum can be executed by the researchers of chemistry, physics, civil, electronic engineering etc., realms.

Data Availability

The data used to support the findings of this study are available in Tables 1–21.

Conflicts of Interest

The authors declare that there are no conflicts of interest regarding the publication of this manuscript.

References

[1] S. Prabhu and B. K. Vinayagam, "AFM surface investigation of Inconel 825 with multi wall carbon nano tube in electrical discharge machining process using Taguchi analysis," *Archives of Civil and Mechanical Engineering*, vol. 11, no. 1, pp. 149–170, 2011.

[2] G. Rajyalakshmi and P. Venkata Ramaiah, "Multiple process parameter optimization of wire electrical discharge machining on Inconel 825 using Taguchi grey relational analysis," *International Journal of Advanced Manufacturing Technology*, vol. 69, no. 5-8, pp. 1249–1262, 2013.

[3] L. Prasad, M. Upreti, A. Yadav, R. V. Patel, V. Kumar, and A. Kumar, "Optimization of process parameters during WEDM of EN42 spring steel," *SN Applied Sciences*, vol. 2, pp. 1–11, 2020.

[4] V. K. Singh and S. Singh, "Multi-objective optimization using Taguchi based grey relational analysis for wire EDM of Inconel 625," *J Mater Sci Mech Eng*, vol. 2, pp. 38–42, 2015.

[5] H.-M. Chow, B.-H. Yan, F.-Y. Huang, and J.-C. Hung, "Study of added powder in kerosene for the micro-slit machining of titanium alloy using electro-discharge machining," *Journal of Materials Processing Technology*, vol. 101, no. 1-3, pp. 95–103, 2000.

[6] C. Guo, S. Sun, S. Di, and D. Wei, "Study of working medium performance by acoustic emission in EDM machining of Ti6Al4V," *Advances in Materials Science and Engineering*, vol. 2020, Article ID 5452490, 10 pages, 2020.

[7] A. Goyal, A. Pandey, and P. Sharma, "Machinability of Inconel 625 aerospace material using cryogenically treated WEDM," *Solid State Phenomena*, vol. 266, pp. 38–42, 2017.

[8] A. Golshan, S. Gohari, and A. Ayob, "Modeling and optimization of cylindrical wire electro discharge machining of AISI D3 tool steel using non-dominated sorting genetic algorithm," *International Conference on Graphic and Image Processing (ICGIP 2011)*, vol. 8285, pp. 1–7, 2011.

[9] S.-H. Yang, J. Srinivas, S. Mohan, D.-M. Lee, and S. Balaji, "Optimization of electric discharge machining using simulated annealing," *Journal of Materials Processing Technology*, vol. 209, no. 9, pp. 4471–4475, 2009.

[10] N. K. Singh, Y. Singh, S. Kumar, and A. Sharma, "Comparative study of statistical and soft computing-based predictive models for material removal rate and surface roughness during helium-assisted EDM of D3 die steel," *SN Applied Sciences*, vol. 1, pp. 1–12, 2019.

[11] V. N. R. Jampana, P. S. V. Ramana Rao, and A. Sampathkumar, "Experimental and thermal investigation on powder mixed EDM using FEM and artificial neural networks," *Advances in Materials Science and Engineering*, vol. 2021, Article ID 8138294, 12 pages, 2021.

[12] E. Nas, O. Özbek, F. Bayraktar, and F. Kara, "Experimental and statistical investigation of machinability of AISI D2 steel using electroerosion machining method in different machining parameters," *Advances in Materials Science and Engineering*, vol. 2021, Article ID 1241797, 17 pages, 2021.

[13] D. Devarasiddappa, M. Chandrasekaran, and R. Arunachalam, "Experimental investigation and parametric optimization for minimizing surface roughness during WEDM of Ti6Al4V alloy using modified TLBO algorithm," *Journal of the Brazilian Society of Mechanical Sciences and Engineering*, vol. 42, pp. 1–18, 2020.

[14] O. Kulkarni and S. Kulkarni, "Process parameter optimization in WEDM by grey wolf optimizer," *Materials Today Proceedings*, vol. 5, no. 2, pp. 4402–4412, 2018.

[15] G. V. A. Kumar and K. L. Narasimhamu, "Multi-objective optimization in WEDM of Inconel 750 Alloy: application of TOPSIS embedded grey wolf optimizer," *Advanced engineering optimization through intelligent techniques*, vol. 949, pp. 231–240, 2020.

[16] F. N. Abed, V. Ramesh, M. Fadhil Jwaid, N. Agarwal, D. Koundal, and A. Mohamed Ibrahim, "Enhancement modelling based on electrical discharge machining successive discharges," *Advances in Materials Science and Engineering*, vol. 2022, Article ID 8017375, 7 pages, 2022.

[17] A. Saffaran, M. A. Moghaddam, and F. Kolahan, "Optimization of backpropagation neural network-based models in EDM process using particle swarm optimization and simulated annealing algorithms," *Journal of the Brazilian Society of Mechanical Sciences and Engineering*, vol. 1, pp. 1–14, 2020.

[18] M. Yunus and M. S. Alsoufi, "Multiresponse particle swarm optimization of wire-electro-discharge machining parameters of Nitinol alloys," *Mathematical Problems in Engineering*, vol. 2021, Article ID 9059722, 12 pages, 2021.

[19] R. Sen, B. Choudhuri, J. D. Barma, and P. Chakraborti, "Experimental investigation and optimisation of WEDM process for machining maraging steel using neural network based Jaya algorithm," *International Journal of Machining and Machinability of Materials*, vol. 20, no. 4, pp. 387–399, 2018.

[20] U. Aich, A. K. Pal, D. Laha, and S. Banerjee, "Searching for a pareto optimal solution set of edm responses applying multi-objective simulated annealing on rsm model," *Advanced Materials Research*, vol. 622, pp. 51–55, 2013.

[21] A. Tanveer, S. G. Kapoor, and S. S. Mujumdar, "Modeling of material removal in atomized dielectric-based electrical discharge machining (EDM)," in *Proceedings of the ASME 2019 14th International Manufacturing Science and Engineering Conference, MSEC 2019*, vol. 1–9, Pennsylvania, PA, USA, June 2019.

[22] N. D. Luan, N. D. Minh, and L. T. P. Thanh, "Multi-objective optimization of PMEDM process parameter by topsis method," *International Journal of Trend in Scientific Research and Development*, vol. 3, no. 4, pp. 112–115, 2019.

[23] S. Jain and V. Parashar, "Application of multi-objective BAT algorithm for EDM process parameters optimization," *International Journal of Advanced Science and Technology*, vol. 29, pp. 5214–5225, 2020.

[24] H. J. Wang, D. W. Zuo, H. Miao, H. F. Wang, and M. Wang, "Effect of discharge parameters on micro-surface topography of NAK80 by mirror-like surface EDM," *Key Engineering Materials*, vol. 431-432, pp. 438–441, 2010.

[25] M. Gostimirovic, V. Pucovsky, M. Sekulic, M. Radovanovic, and M. Madic, "Evolutionary multi-objective optimization of energy efficiency in electrical discharge machining," *Journal of Mechanical Science and Technology*, vol. 32, no. 10, pp. 4775–4785, 2018.

[26] N. K. Sahu, A. K. Sahu, and A. K. Sahu, "Optimization of weld bead geometry of MS plate (Grade: IS 2062) in the context of welding: a comparative analysis of GRA and PCA–Taguchi approaches," *Indian Academy of Sciences*, vol. 8, no. 3, pp. 234–259, 2017.

[27] Z. He, X. Ma, J. Luo, A. K. Sahu, A. k. Sahu, and N. K. Sahu, "Exploitation of the advanced manufacturing machine tool evaluation model under objective-grey information: a

knowledge-based cluster with the grey relational analysis approach," *Grey Systems: Theory and Application*, vol. 11, no. 3, pp. 394–417, 2021.

[28] A. K. Sahu, N. K. Sahu, A. K. Sahu, M. S. Rajput, and H. K. Narang, "T-SAW methodology for parametric evaluation of surface integrity aspects in AlMg3 (AA5754) alloy: c," *Measurement*, vol. 132, pp. 309–323, 2019.

[29] X. Guo, A. K. Sahu, N. K. Sahu, and A. K. Sahu, "A novel integrated computational TRIFMRG approach with grey relational analysis toward parametric evaluation of weld bead geometry of ms-grade: IS 2062," *Grey Systems: Theory and Application*, vol. 12, no. 1, pp. 117–141, 2022.

[30] P. Kumar, M. Meenu, and V. Kumar, "Optimization of process parameters for WEDM of Inconel 825 using grey relational analysis," *Decision Science Letters*, vol. 7, pp. 405–416, 2018.

[31] J. U. Prakash, P. Sivaprakasam, I. Garip et al., "Wire electrical discharge machining (WEDM) of hybrid composites (Al-Si12/B4C/fly Ash)," *Journal of Nanomaterials*, vol. 2021, Article ID 2503673, 10 pages, 2021.

[32] N. Manikandan, S. Kumanan, and C. Sathiyanarayanan, "Multiple performance optimization of electrochemical drilling of Inconel 625 using Taguchi based grey relational analysis," *Engineering Science and Technology, an International Journal*, vol. 20, no. 2, pp. 662–671, 2017.

[33] R. N. Muni, J. Singh, V. Kumar et al., "Multiobjective optimization of EDM parameters for rice husk Ash/Cu/Mg-reinforced hybrid Al-0.7Fe-0.6Si-0.375Cr-0.25Zn metal matrix Nanocomposites for engineering applications: fabrication and morphological analysis," *Journal of Nanomaterials*, vol. 2022, Article ID 2188705, 15 pages, 2022.

[34] K. Mouralova, J. Kovar, L. Klakurkova, J. Bednar, L. Benes, and R. Zahradnicek, "Analysis of surface morphology and topography of pure aluminium machined using WEDM," *Measurement*, vol. 114, pp. 169–176, 2018.

[35] A. Perumal, C. Kailasanathan, B. Stalin et al., "Multiresponse optimization of wire electrical discharge machining parameters for Ti-6Al-2Sn-4Zr-2Mo (α-β) alloy using taguchi-grey relational approach," *Advances in Materials Science and Engineering*, vol. 2022, Article ID 6905239, 13 pages, 2022.

[36] P. Sharma, D. Chakradhar, and N. S, "Analysis and optimization of WEDM performance characteristics of Inconel 706 for aerospace application," *Silicon*, vol. 10, no. 3, pp. 921–930, 2018.

[37] K. Mouralova, L. Benes, R. Zahradnicek et al., "Analysis of cut orientation through half-finished product using WEDM," *Materials and Manufacturing Processes*, vol. 34, no. 1, pp. 70–82, 2019.

[38] M. Singh, P. Saxena, J. Ramkumar, and R. V. Rao, "Multi-spark numerical simulation of the micro-EDM process: an extension of a single-spark numerical study," *International Journal of Advanced Manufacturing Technology*, vol. 108, no. 9-10, pp. 2701–2715, 2020.

[39] S. Zhou, Y. Yang, M. Zhou, and H. Sun, "Electrical discharge machining Inconel 718 with adaptively regulating gap servo-voltage," *International Journal of Advanced Manufacturing Technology*, vol. 109, no. 9-12, pp. 2575–2585, 2020.

[40] V. Baldin, C. R. B. Baldin, A. R. Machado, and F. L. Amorim, "Machining of Inconel 718 with a defined geometry tool or by electrical discharge machining," *International Journal of the Brazilian Society of Mechanical Sciences and Engineering*, vol. 42, pp. 1–14, 2020.

[41] T. Muthuramalingam, L. Ganesh Babu, K. Sridharan, T. Geethapriyan, and K. P. Srinivasan, "Multi-response optimization of WEDM process parameters of inconel 718 alloy using TGRA method," *Advances in Engineering Research and Application*, vol. 104, pp. 487–492, 2020.

[42] H. Payal, S. Maheshwari, and P. S. Bharti, "Parametric optimization of EDM process for Inconel 825 using GRA and PCA approach," *Journal of Information and Optimization Sciences*, vol. 40, no. 2, pp. 291–307, 2019.

[43] D. N. M. Kumar and M. P. C. Rao, "Optimization of EDM process parameters using response surface methodology for AISI D3 steel," *International Journal of Trend in Scientific Research and Development*, vol. 3, no. 3, pp. 1651–1656, 2019.

[44] B. Shao and K. P. Rajurkar, "Modelling of the crater formation in micro-EDM," *Procedia CIRP*, vol. 33, pp. 376–381, 2015.

[45] P. R. Reddy, G. J. Reddy, and G. Prasanthi, "Mathematical Modeling of Material Removal Rate Using Buckingham Pi Theorem in Electrical Discharge Machining of Hastelloy C276," *Lecture Notes in Mechanical Engineering*, pp. 843–852, Springer, Berlin, Germany, 2020.

[46] L. Li, Z. W. Niu, F. S. Yin, and Y. Y. Liu, "Surface integrity of sintered NdFeB permanent magnet after EDM," *Advanced Materials Research*, vol. 503-504, no. 504, pp. 27–30, 2012.

[47] M. Shabgard and B. Khosrozadeh, "Investigation of carbon nanotube added dielectric on the surface characteristics and machining performance of Ti-6Al-4V alloy in EDM process," *Journal of Manufacturing Processes*, vol. 25, pp. 212–219, 2017.

[48] A. K. Singh, R. Mahajan, A. Tiwari, D. Kumar, and R. K. Ghadai, "Effect of dielectric on electrical discharge machining: a review," *IOP Conference Series: Materials Science and Engineering*, vol. 377, pp. 1–9, 2018.

[49] A. Werner, "Method for enhanced accuracy in machining curvilinear profiles on wire-cut electrical discharge machines," *Precision Engineering*, vol. 44, pp. 75–80, 2016.

[50] S. D. Choudhury, N. J. Saharia, B. Surekha, and G. Mondal, "Study on the influence of hybridized powder mixed dielectric in electric discharge machining of alloy steels," *Materials Today Proceedings*, vol. 5, no. 9, pp. 18410–18415, 2018.

[51] Y. Zhang, Y. Liu, Y. Shen, R. Ji, Z. Li, and C. Zheng, "Investigation on the influence of the dielectrics on the material removal characteristics of EDM," *Journal of Materials Processing Technology*, vol. 214, no. 5, pp. 1052–1061, 2014.

[52] A. Saha and S. C. Mondal, "Multi-objective optimization in WEDM process of nanostructured hardfacing materials through hybrid techniques," *Measurement*, vol. 94, pp. 46–59, 2016.

[53] D. K. Kasdekar, V. Parashar, and P. Soni, "Optimization of machining parameters in electro discharge machining of Al6061-Cu-Sic-graphite metal matrix composite," *Materials Science Forum*, vol. 860, pp. 61–64, 2016.

Hindawi
Advances in Materials Science and Engineering
Volume 2022, Article ID 5791263, 9 pages
https://doi.org/10.1155/2022/5791263

Research Article

Effect of Ti-Based Thin Solid Films on Tribological and Mechanical Properties of AL7075-T7351

Dohyeon Kim,[1] **Hyunji Kim**,[2] **Sunghoon Im**,[3] **Hyomin Jeong**,[4] **Jungpil Noh**,[4] **and Sunchul Huh**[4]

[1]*Dept. of Energy and Mech. Eng. Graduate School of GNU, 2,Tongyeonghaean-ro, Tongyeong-si 53064, Republic of Korea*
[2]*Dept. of Steel Industry, Suncheon Jeil College, 17,Jeildaehak-gil, Suncheon-si 57997, Republic of Korea*
[3]*Dept. of Computer Applied Machinery, Changwon Campus of Korea Polytechnic, 51-88,Oedongballim-ro, Changwon-si, Republic of Korea*
[4]*Dept. of Energy and Mech. Eng. of GNU, 2,Tongyeonghaean-ro, Tongyeong-si 53064, Republic of Korea*

Correspondence should be addressed to Sunchul Huh; schuh@gnu.ac.kr

Received 15 February 2022; Revised 6 April 2022; Accepted 8 April 2022; Published 25 April 2022

Academic Editor: R. Thanigaivelan

Aluminum alloy itself does not provide sufficient wear resistance for structural parts. Therefore, there is need to protect against the wear issue in practical applications. The objective of this study is to investigate different parameters wear characteristics of direct current (dc) magnetron sputtered titanium films on Al7075-T7351 using a wear test. Each parameter has three levels which include the direct current (DC) power, deposition time, and substrate surface roughness. The thickness of the coatings was measured using a focused ion beam scanning electron microscopy (FIB-SEM) from approximately 0.5 μm to 4.4 μm. The titanium thin film coatings were then evaluated using a PD102 wear tester under conditions of 60 rpm, 2N, 30 minutes. As a result, the coefficient of friction of the coating was reduced, and the wear resistance of the coating was improved as the applied power and deposition time increased. The hardness of titanium-coated specimens is increased significantly up to 272 HV, while the hardness of uncoated specimens was 160 HV.

1. Introduction

Generally, aerospace, automobile parts, and energy-saving strategies have promoted research studies in the field of lightweight materials, especially on alloys based on aluminum. Aluminum has low hardness and does not provide sufficient mechanical strength for structural parts. Therefore, it is necessary to improve surface properties required in practical applications, especially when aluminum is in contact with other parts to protect against wear issues [1–4]. The resistance of the materials can be increased by improving surface conditions such as hardness and roughness [5, 6]. The creation of a titanium coating is one of the most effective methods to improve the wear resistance of a material surface undergoing contact motion. Surface coating technology using titanium thin films with high strength, corrosion resistance, and excellent mechanical properties is widely used to protect materials from external environments [7–13]. Many studies on developing wear resistance thin films for machining applications exist; for example, according to Nguyen et al. [14], the advantage of the titanium nitride coatings on aluminum alloy, which are well known for cutting tools, could be greatly enhanced with improved surface finishing in appearance, corrosion resistance, and wear resistance. Singh et al. showed that Ti-MoS2 films tribological performance is influenced by humidity, temperature, and deposition process and attributed titanium content with the increase in load-bearing capacity, higher wear resistance, and lower humidity [15]. Many of the coatings that can be applied by wet plating, sputtering, and thermal evaporation are used for some physical properties, but the coatings that have importance in tribological systems are comparatively few. Disadvantages of thermal evaporation and wet plating are deposits that may have poor

Table 1: Mechanical properties of Al7075-T7351.

Mechanical properties	Tensile strength (MPa)	Yield strength (MPa)	Elongation (%)	Modulus of elasticity (GPa)	Hardness, Vickers (Hv)
AL7075- T7351	462~505	386~435	8	72	155

adhesion. Magnetron sputter coating is a basic vacuum coating process, and a target (or cathode) plate is bombarded by energetic ions generated in a glow discharge plasma, situated in front of the target, which is used in this study because of its flexible coating technique that can be used to coat almost any material [16–18]. Magnetron sputtering is deposited by a titanium thin film and typically has crystallographic orientations of crystals (100), (001), and (101) parallel to the surface [19, 20]. The properties of nanoscale thin films are different from those of bulk materials, and the properties of these thin films start from the growth of nuclei of adsorption atoms that reach the substrate. The properties of thin films show different growth patterns depending on the substrate, deposition equipment, and process parameters. Thin films have properties distinguished from those of bulk materials, and they show delicate changes in their properties within a few nanoscales. Changes in the microstructure and surface condition determine this change in properties according to the thin film deposition equipment's process parameters, which affects the mechanical properties of the thin film material [21–23]. The number of various and independent deposition parameters reliable for optimizing deposited layers is limited. Achieving thin films of desired properties for specific applications is limited due to the lack of suitable methods for sputtering process control parameters. It is difficult for the sputtering to control the film properties such as film thickness, grain size, and step coverage. Many studies on magnetron sputtered Ti thin films have been reported. For example, Martin et al. researched the influence of bias power on some properties of Ti coatings [24], Chawla et al. reported that the average surface roughness of the Ti films has increased with an increase in substrate temperature [25]. However, these studies do not deal with a systematic investigation of the wear characteristic of Ti films in the sputtering process with respect to deposition parameters. The objective of this study is to investigate different parameters wear characteristics of direct current (dc) magnetron sputtered titanium films on Al7075-T7351 using a wear test. Each parameter has three levels which include the direct current (DC) power, deposition time, and substrate surface roughness. The surface roughness was calculated through applying a surface roughness to the base metal, and a Ti thin film was deposited to perform the wear test [26]. The objectives in such cases are to extend the wear resistance performance of the sputtering process beyond which either process can achieve on its own and allow the use of suitable base coating materials in high-performance aerospace applications.

2. Experimental Work

2.1. Experimental Material. In this study, experimental work was carried out on Al7075-T7351 alloyed specimens with dimensions of 10 mm in length and 32 mm in diameter in accordance with standard ISO 7148 [27]. To investigate wear resistance according to the surface roughness of the aluminum alloys and thin film DC power, working pressure, and deposition time, a total of 8 specimens were prepared. Table 1 shows the physical properties of the substrate. Polishing was performed using #400 abrasive paper and alumina hardener (0.3 um) powder. Table 2 shows the chemical composition of the Al7075-T7351. The roughness values according to the polishing type and data on average values were calculated using a surface roughness tester (model: AR-132C, manufacturer: AMITTARI, China). Table 3 shows that the average roughness value was 0.45 μm and 0.25 μm, respectively.

2.2. DC Magnetron Sputtering Process. Ti thin films were fabricated on Al alloy by DC magnetron sputtering system with pure Ti (99.9%) target for the development of titanium coating. Each specimen was washed for 15 minutes with an ultrasonic cleaner (model: SD-300H, manufacturer: SUNGDONG, Korea) using ethyl alcohol. Ultrasonically cleaned specimens were positioned in the coating chamber and loaded with pure titanium target. The distance between the Ti target and Al7075 substrates was 80 mm. Figure 1 shows a schematic diagram of the DC magnetron sputtering process. The sputtering device (model: SDC1022A, manufacturer: PSPLASMA, Korea) was composed of a vacuum system, sputtering target, D.C power supply device, substrate material support, and gas injection device. First, Ti was deposited under the following conditions: substrate temperature room temperature, Ar gas flow rate of 20 sccm, initial pressure of 5.0×10^{-6} Torr, working pressure of 2.0×10^{-3} Torr, and 3.0×10^{-3} Torr. The deposition time was 30 min and 90 min, and DC power of the Ti target was 100 W and 300 W. Before starting the actual experiment, the presputtering was performed for 15 minutes to remove the surface oxide of the Ti target. Experimental work was carried out on DC power and deposition time as variables to find optimum conditions for wear resistance of the titanium thin film. Table 4 shows the sputtering conditions for titanium thin film deposition process.

2.3. Coating Surface Characterization. The coating method was implemented for approximately 30 to 90 min to achieve coating thickness in the range of 0.5–4.5 μm. The cross section view and surface changes in the morphology of the Ti films were characterized using a focused ion beam scanning electron microscope (model: AMBER G, manufacturer: TESCAN). In addition, the component analysis was carried out using EDS (energy dispersive spectroscopy). A platinum (Pt) coating was fabricated locally to the specimen surface to

Table 2: Chemical compositions of Al7075-T7351.

	Al	Zn	Cu	Mg	Zr	Fe	Si	Mn	Cr	Ti	Etc.
Al7075	Bal.	5.7~6.7	2.0~2.6	1.9~2.6	0.08~0.15	0.15	0.12	0.1	0.04	0.06	0.15

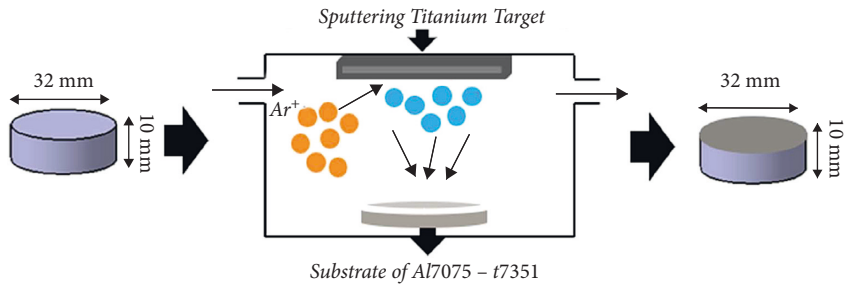

Figure 1: Schematic of the DC magnetron sputtering.

Table 3: Experimental parameters of surface roughness tests.

Parameters	Conditions
Surface roughness (μm)	0.45, 0.25

Table 4: Experimental parameters of DC magnetron sputtering.

Deposition condition	DC magnetron sputtering
Target material	Titanium
Base pressure (Torr)	5.0×10^{-6}
Working pressure (Torr)	2.0×10^{-3}
Pressure gas	Argon
Power (W)	100, 300
Deposition time (min)	30, 90
Temperature	RT

prevent damage to the titanium thin film layer's surface during FIB processing. After FIB processing, the titanium thin film's cross section was observed by tilting it at an angle of 55 degrees.

2.4. Wear Test. The friction and wear tests were conducted using a wear tester (model: PD102, manufacturer: R&B, Korea). The wear tests were conducted at a laboratory condition temperature of 20°C and under dry friction. During the wear test, a zirconia (ZrO_2) ball with a diameter of 12.7 mm and a hardness of 1400Hv was used as a counter body. Table 5 shows that the tribological conditions were performed by ball-on disc type and rotation speed of 60 RPM and a normal load of 2 N for 30 minutes. The wear test sliding track diameter was 11.5 mm. The wear test parameter was set to a low-speed rotation to prevent the generation of frictional heat and to set the linear speed to 100 mm/sec or less to prevent the lifting phenomenon. The amount of wear was based on the specimen's average weight before and after the experiment measured ten times. The wear track was observed using a scanning electron microscope (model: JSM6010LA, manufacturer: JEOL, Japan).

Table 5: Experimental parameters of wear tests.

Test parameters	Test
Materials	ZrO^2
Diameter (mm)	12.7
Sliding speed (RPM)	60
Time (sec)	1800
Load (N)	2
Temperature	RT

2.5. Hardness Test. The hardness tests were conducted using a nanoindentation tester (model: AIS 3000, manufacturer: Frontics, Korea). The nanoindentation tests were conducted at depth load resolutions of 10 μm, which were performed across the point at 2 mm intervals. The maximum applied load and testing speed were 50 kgf and 0.3 mm/min. 10 indentation measurements were made under a controlled load of 0.5 kgf for each measurement. The hardness values we conducted by using a quadrilateral conical indentation tip.

3. Results and Discussion

3.1. Characterization of Titanium Thin Films. To evaluate the surface features of Ti thin films, FIB-SEM images were collected at various DC magnetron sputtering processes and different fields of view. Figure 2 shows an image of the shape of the thickness measured by FIB-SEM. Figure 2 shows four sets of surface morphologies of Ti films deposited on Al7075 alloy with different sputtering DC power ranging from 100 W to 300 W and deposition time ranging from 30 min to 90 min. The lower part of the interface is an aluminum alloy layer, and titanium thin film was located between the Pt coating layer and the aluminum alloy layer [28]. The thickness of the titanium thin film in Figures 2(a), 2(b), 2(c), and 2(d) was approximately 0.5 μm, 1.6 μm, 1.5 μm, and 4.4 μm, respectively. Figure 3 shows a cross section of the titanium thin film after FIB processing through EDS (energy dispersive spectrometer mapping). Figure 3(a) shows a cross section image before composition analysis. The components

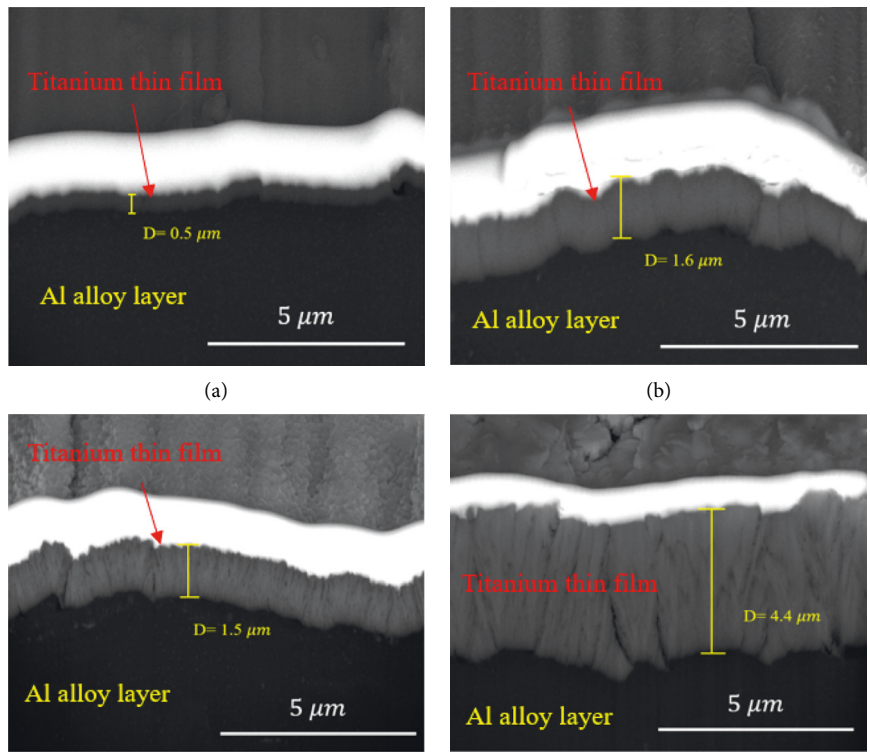

Figure 2: SEM image of cross-sectional view: (a) 30 min 100 W; (b) 90 min 100 W; (c) 30 min 300 W; (d) 90 min 300 W.

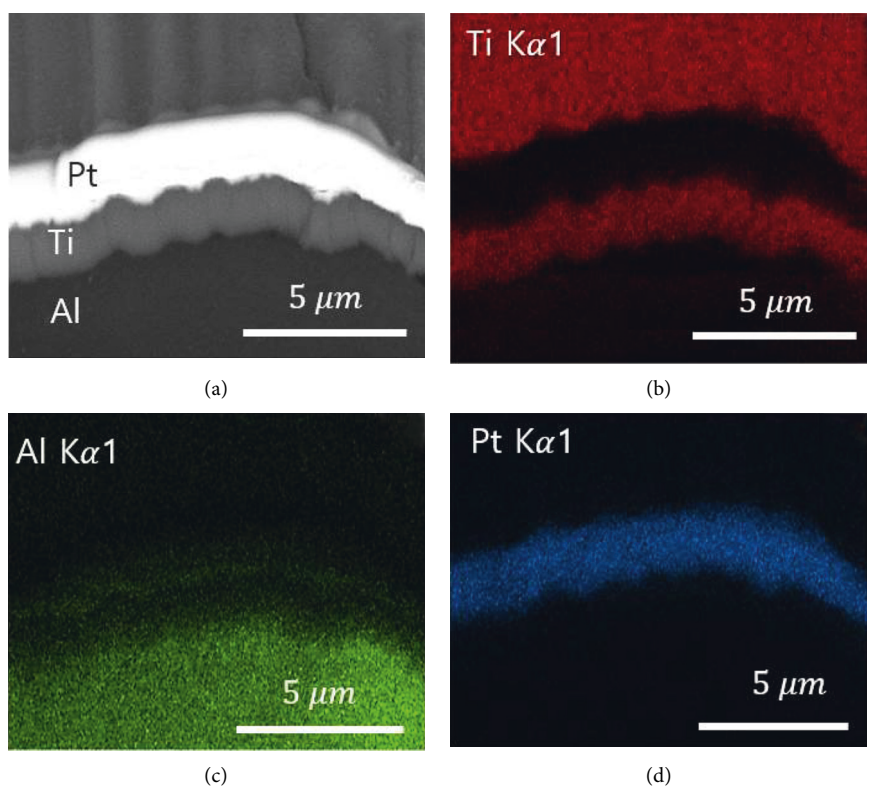

Figure 3: EDS mapping image of the interface: (a) cross-sectional view of sample; (b) Ti layer; (c) Al layer; (d) Pt layer.

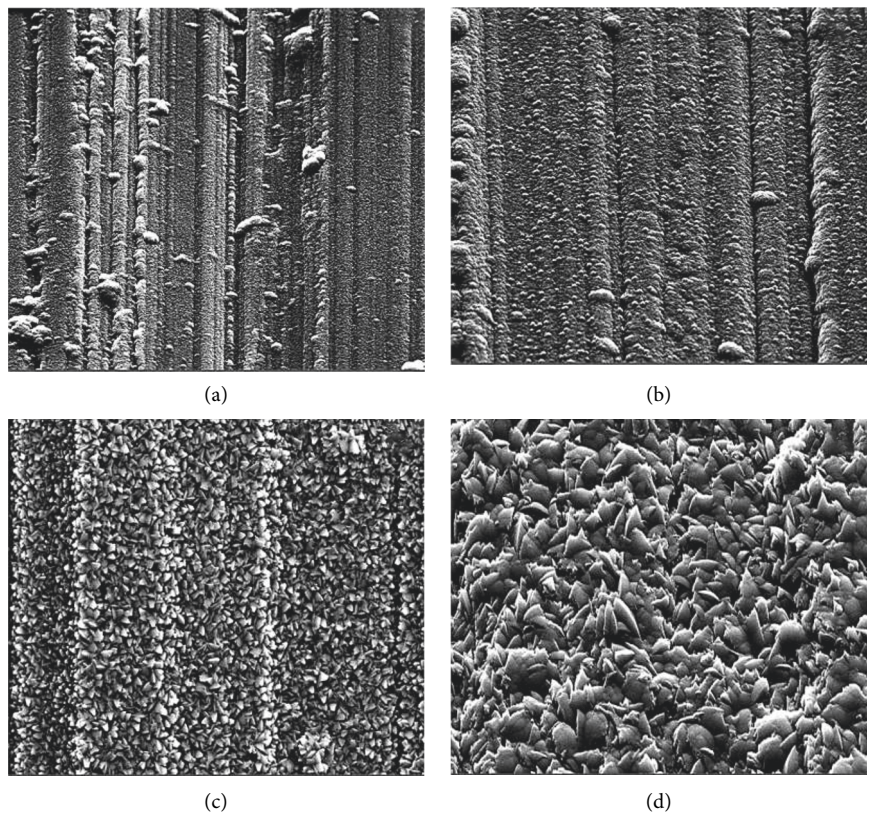

Figure 4: SEM image of surface morphology (×20000): (a) 30 min 100 W; (b) 90 min 100 W; (c) 30 min 300 W; (d) 90 min 300 W.

were separately graphed into a titanium layer through EDS mapping analysis as shown in Figure 3(b), an aluminum layer as shown in Figure 3(c), and a platinum layer as shown in Figure 3(d). The platinum layer component was got from a platinum coating component that was used to prevent surface damage for internal processing with an ion beam. The component analysis results confirmed that the titanium thin film was uniformly formed on the aluminum alloy's surface.

3.2. Surface Morphology. Figures 4(a)~4(d) show the surface morphology of the coated titanium thin film on aluminum alloys [(a) deposition time of 30 minutes and applied power of 100 W; (b) deposition time of 90 minutes and applied power of 100 W; (c) deposition time of 30 minutes and applied power of 300 W; (d) deposition time of 90 minutes and applied power of 300 W]. In Figure 4, the fine-grained structure of thin film samples are more explicitly revealed in images (c) and (d). The larger grains in the structure of (c) and (d) films compared with (a) and (b) films could be easily perceived. This phenomenon affects showing rough surface morphology with an increase in the plasma applied power. According to In-Kwon Oh [29], the acceleration of charged electrons or argon ions occurs, and the energy released after collision with a target increased too when plasma applied electric power increases, resulting in the rise of high temperature due to atomic momentum when high-energy titanium collides with the substrate. As a result, it increases the mobility of titanium atoms on the surface, which in turn roughens the surface. As seen in Figures 4(b) and 4(c), the thin film has a similar thickness. However, small and dense shapes were observed in Titanium thin film surface morphology. The developed coatings are characterized by fine particles exhibiting crystallinity, and their size increases when the applied DC power is increased from 100 W to 300 W. The titanium thin film particles' size was the largest with a deposition time of 90 minutes and applied power of 300 W as shown in Figure 4(d). According to Jin et al. [30], crystallization was not observed at a low sputtering power of 100 W for depositing a titanium thin film, and the microstructure property with 100 W applied power was amorphous. On the other hand, the specimen with 300 W applied power showed spherical hexagonal particles with a uniform distribution. This change in the surface's shape was attributed to the fact that the particles' size grew as the applied DC power increased.

3.3. Wear Behavior. Figure 5 shows a graph of the friction coefficients according to the deposition time and DC power during the sputtering process. Figure 5(a) is a graph comparing friction coefficients of specimens A0, A1, A2, A3, and A4 polished with #400 abrasive paper. Graphs were compared based on the substrate material. The friction coefficients of A1 and A2 deposited with 100 W were higher than those of the substrate material, while the friction coefficients of A3 and A4 deposited with 300 W were lower than those of

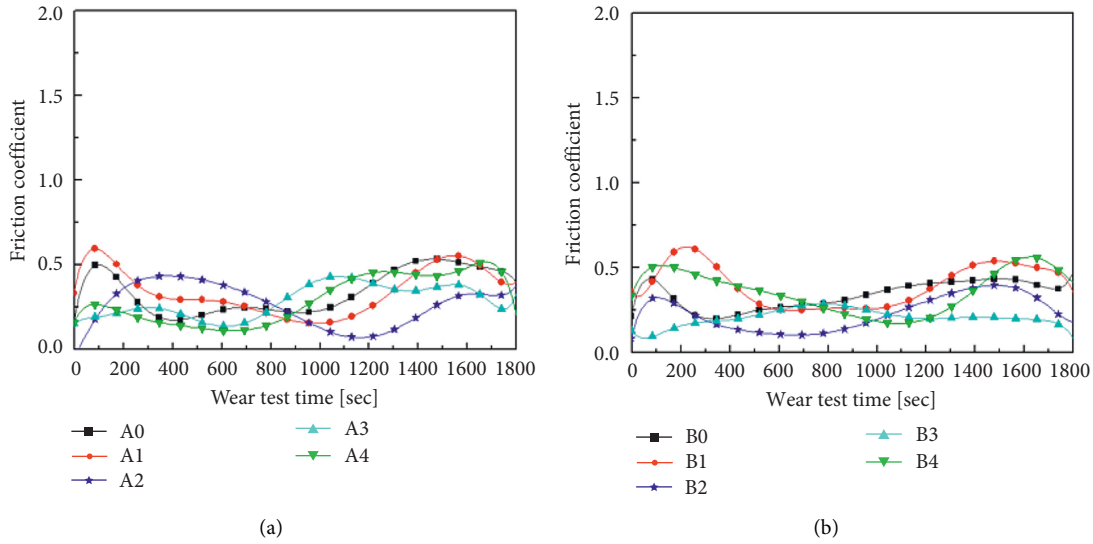

Figure 5: Friction coefficient curves by deposition conditions: (a) A0~A4; (b) B0~B4.

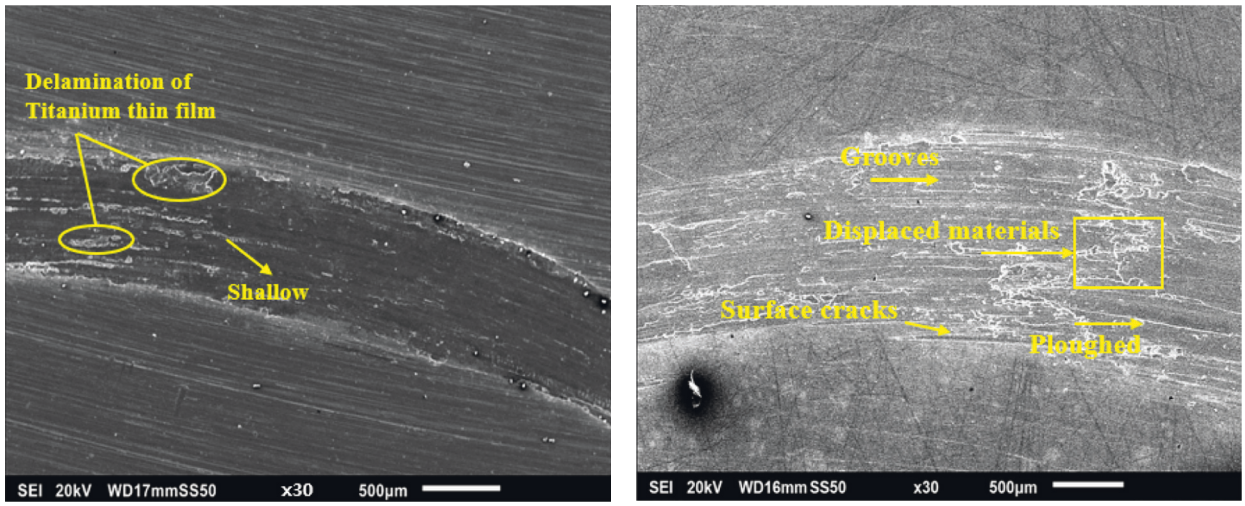

Figure 6: SEM image of the wear track surface morphology (×30): (a) A4; (b) B1.

the substrate material. The shape of the particles covering the thin film's surface changed from amorphous particles to crystalline particles as the applied DC power increased during the deposition of the titanium thin film. Wear resistance for crystallized particles was improved because the crystallized particles increased in size and strength. Therefore, the A4 specimen, which had the thickest crystalline particles, showed the best friction coefficient. Figure 5(b) shows the comparison between friction coefficients of specimens B0, B1, B2, B3, and B4 polished with alumina. Figure 5(a) shows that the friction coefficients of B1 and B2 deposited with 100 W showed a similar pattern to those of the substrate material, and friction coefficients of B3 and B4 deposited with 300 W showed a relatively linear curve. However, unlike the A4 specimen, the friction coefficient of the B4 specimen was high from the beginning of the experiment because a thick titanium thin film was deposited on the surface with low surface roughness, resulting in the weakening of the bonding strength with the substrate material.

Figure 6 shows the result of SEM analysis of the wear track formed on the titanium thin film's surface after the wear test. Wear analysis was performed on only two samples (A4 and B1) using a ball-on-disc wear machine. Figure 6(a) shows the wear track of the A4 specimen with the best wear resistance and a width of 0.79 mm. In the A4 specimen, the titanium thin film shows diminished and shallow wear tracks and small-scale delamination of titanium thin film particles from the aluminum substrate matrix [31]. Such properties display the pattern of grinding wear. Figure 6(b) shows that the track width of the B1 specimen was the worst result at 1.43 mm. The worn-out surface was relatively coarse and had many irregular pits due to the removal and sliding of the titanium thin films particles. Majority of debris was

Table 6: Results of hardness and wear behavior.

Specimens	Parameters A	B	C	Hardness (Hv)	Wear track (mm)	Friction coefficient	Wear loss (mg)
A0	0	0	0.45	160	1.37	0.343	2.67
A1	30 min	100 W	0.45	272	1.18	0.345	2.00
A2	90 min	100 W	0.45	251	1.23	0.263	2.50
A3	30 min	300 W	0.45	248	1.12	0.284	1.70
A4	90 min	300 W	0.45	173	0.79	0.294	0.93
B0	0	0	0.25	166	1.34	0.338	2.17
B1	30 min	100 W	0.25	196	1.43	0.397	2.13
B2	90 min	100 W	0.25	270	0.93	0.233	1.10
B3	30 min	300 W	0.25	237	0.85	0.204	1.37
B4	90 min	300 W	0.25	148	1.06	0.361	1.20

formed in irregular pits due to the thin film whose bonding strength was weakened and peeled off by the wear test, thus indicating an abrasive type of wear mechanism [32]. This is an adhesive wear pattern in which loose debris adheres to the wear track's edge along the turning radius. The repeated sliding action of the abrasive wear on the B1 sample caused grooves, surface cracks, and ploughed. The displaced materials can be observed in the SEM image shown in Figure 6(b) [33]. Table 6 shows the amount of hardness, the width of the wear track, and the average friction coefficient for each deposition condition of the titanium thin film. The wear amounts of A0 and B0 were 2.67 mg and 2.17 mg, respectively, for two types of substrate materials with different surface roughness, showing a difference of approximately 0.50 mg. It was confirmed that the width of the wear track for B0 was relatively narrow. This indicates that the lower the surface roughness value of the substrate material on which the thin film was not deposited, the better the wear resistance was improved after the wear test. Specimens A1, A3, and A4 processed with #400 abrasive paper showed that the amount of wear was 0.67 ~ 1.7 mg lower than that of the substrate material. On the other hand, the amount of wear of specimens A2 was similar to that of the substrate material. The amount of wear for the B specimens was lower than that of the substrate material in most cases. However, the amount of wear for the B1 specimen was similar to that of the substrate material. This can be because the comparatively thin film reduces the adhesive force with the substrate and easily peels off [26]. As shown in Figure 6(a), the amount of wear for the A4 specimen can be observed as a minimum according to shallow grooves and narrow wear track width. The amount of wear of the titanium thin film can be adjusted for better stability by increasing applied power and deposition time. It was confirmed that the amount of wear on all the specimens coated with titanium thin film formed was lower than that of the substrate material. These results confirmed that the A4 specimen deposited with a thin film with 300 W applied DC power for 90 minutes after polishing with #400 abrasive paper had the best wear resistance.

3.4. Hardness of the Titanium Thin Films. Nanoindentation measurements indicate that the hardness values of the films are 173 Hv to 272 Hv. The results of the nanoindentation test on titanium thin film confirm the shape change of the non-stress-free film according to the press-in load curve as shown in. Figure 7 shows the concave depth of the same load-displacement curve 10 um. This indicates that the loading and unloading curves are all nonlinear. As a result of the measurement, the hardness tends to decrease as DC power increases from 100 W to

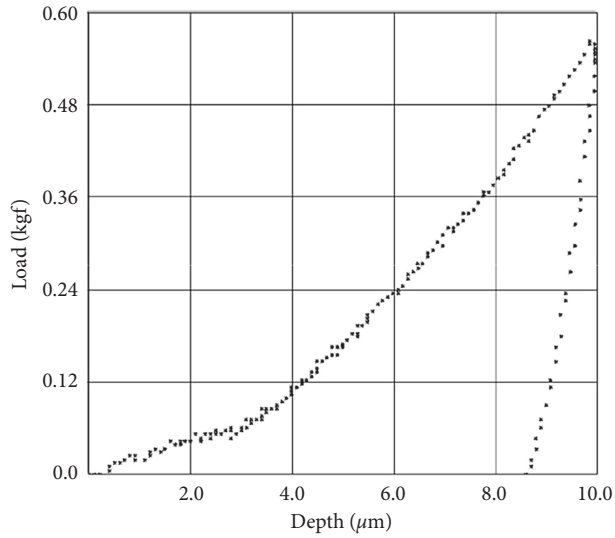

Figure 7: Nanoindentation force curves by penetration depth.

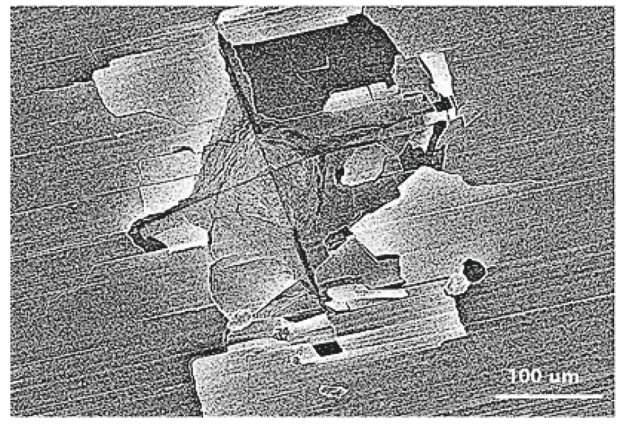

Figure 8: SEM image of the nanoindentation region.

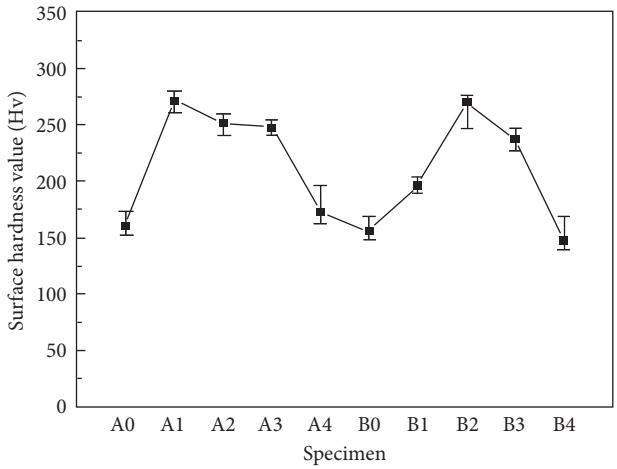

Figure 9: Surface hardness curves by deposition conditions.

300 W as shown in Figure 8. It can be observed that the hardness of the coating is affected by the change in DC power. If the thickness of the film is too small, the size effect will increase and plastic deformation under the nano-indentation will occur because the area is expanded and the hardness of the substrate material affects the measured hardness value [34]. Figure 8 shows traces of nano-indentation press-in by SEM for hardness measurement. Traces of pressing into the shape of diamond press-in can be seen, compressive stress was applied to the film, and peeling of the film layer can be seen. Figure 9 shows that the hardness of Ti deposited parameters tends to be higher than that of the parent material. The hardness of A4 and B4 is low, but it is assumed that the adhesion between the parent material and the thin film is low and the hardness is not improved. Hardness changes due to surface roughness conditions of the parent material have no effect.

4. Conclusions

In this study, an Al7075-T7351 aluminum material was polished under two roughness conditions: #400 abrasive and alumina, and then sputtering was performed using different applied electric power and deposition time. A wear test was performed on the prepared specimen under such conditions. The surface shape and thickness of the titanium thin film were then compared and analyzed through SEM.

(1) As a result of the titanium thin film thickness measurement, the titanium thin film was measured from approximately 0.5 μm to 4.4 μm. The sample polished with #400 abrasive paper and the sample polished with alumina has a roughness of approximately 0.45 μm and 0.25 μm, respectively.

(2) As a result of titanium thin film surface morphology, the rough surface fine-grained structure is observed when direct current power of 300 W is applied. This phenomenon has an effect on the rough surface fine-grained structure showing a rough surface morphology as plasma applied power increases.

(3) As a result of the friction coefficient analysis, the increasing deposition time of the test causes a decrease in friction coefficient value. Observing the wear track indicated that the wear track's width of specimens deposited with 100 W power was relatively broader than that of specimens deposited with 300 W power, indicating that applied direct current power has a significant effect on the improvement of wear resistance. This indicates that the A4 specimen in which a thin film was deposited with 300 W power for 90 minutes after polishing with #400 abrasive paper had the best wear resistance.

(4) In the titanium coating on Al7075-T7351 alloy by sputtering, to obtain the highest surface hardness for the specific test range 272 HV, the use of 100 W power is recommended. The applied direct current power of 100 W showed a higher hardness of the film than that of 300 W, and a higher hardness was observed when the titanium was deposited compared to the substrate material.

Data Availability

All data used to support the findings of this study are included in the article.

Conflicts of Interest

The authors declare that they have no conflicts of interest.

Acknowledgments

This study was carried out with the support of basic research projects in the field of science and engineering by the Ministry of Science and ICT (no. 2021R1H1A2094016).

References

[1] E. Zalnezhad, A. A. D. Sarhan, and M. Hamdi, "Optimizing the PVD TiN thin film coating's parameters on aerospace AL7075-T6 alloy for higher coating hardness and adhesion with better tribological properties of the coating surface," *International Journal of Advanced Manufacturing Technology*, vol. 64, no. 1-4, pp. 281–290, 2013.

[2] R. R. Boyer, "An overview on the use of titanium in the aerospace industry," *Materials Science and Engineering A*, vol. 213, no. 1-2, pp. 103–114, 1996.

[3] R. Figueroa, C. M. Abreu, M. J. Cristóbal, and G. Pena, "Effect of nitrogen and molybdenum ion implantation in the tribological behavior of AA7075 aluminum alloy," *Wear*, vol. 276-277, pp. 53–60, 2012.

[4] YH. Jin and JK. Yang, "Study of PEO process for Al 7075 and effect of additives," *Journal of the Korean institute of surface engineering*, vol. 53, pp. 53–58, 2020.

[5] S. Forero Sotomonte, C. Blanco Pinzon, and S. García Vergara, "Growth of PEO ceramic coatings on AA 2024-T3 aluminium alloy," *Journal of Physics: Conference Series*, vol. 687, Article ID 012037, 2016.

[6] C. M. Abreu, M. J. Cristóbal, R. Figueroa, and G. Pena, "Wear and corrosion performance of two different tempers (T6 and

T73) of AA7075 aluminium alloy after nitrogen implantation," *Applied Surface Science*, vol. 327, pp. 51–61, 2015.

[7] Y. M. Wang, P. F. Zhang, L. X. Guo, J. H. Ouyang, Y. Zhou, and D. C. Jia, "Effect of microarc oxidation coating on fatigue performance of Ti-Al-Zr alloy," *Applied Surface Science*, vol. 255, no. 20, pp. 8616–8623, 2009.

[8] N. Arshi, J. Lu, C. G. Lee, J. H. Yoon, B. H. Koo, and F. Ahmed, "Thickness effect on properties of titanium film deposited by d.c. magnetron sputtering and electron beam evaporation techniques," *Bulletin of Materials Science*, vol. 36, no. 5, pp. 807–812, 2013.

[9] H. Cho and JK. Kim, "Parametric study of diamond/Ti thin film deposition in microwave plasma CVD," *Journal of the Korean Crystal Growth and Crystal Technology*, vol. 15, pp. 10–15, 2005.

[10] S. M. Deambrosis, V. Zin, F. Montagner, C. Mortalò, and E. Miorin, "Effect of temperature and deposition technology on the microstructure, chemistry and tribo-mechanical characteristics of Ti-B based thin films by magnetron sputtering," *Surface and Coatings Technology*, vol. 405, Article ID 126556, 2021.

[11] S. Ghasemi, A. Shanaghi, and P. K. Chu, "Nano mechanical and wear properties of multi-layer Ti/TiN coatings deposited on Al 7075 by high-vacuum magnetron sputtering," *Thin Solid Films*, vol. 638, pp. 96–104, 2017.

[12] J.-H. Huang, F.-Y. Ouyang, and G.-P. Yu, "Effect of film thickness and Ti interlayer on the structure and properties of nanocrystalline TiN thin films on AISI D2 steel," *Surface and Coatings Technology*, vol. 201, no. 16-17, pp. 7043–7053, 2007.

[13] L.-J. Meng and M. P. dos Santos, "Investigations of titanium oxide films deposited by d.c. reactive magnetron sputtering in different sputtering pressures," *Thin Solid Films*, vol. 226, no. 1, pp. 22–29, 1993.

[14] C. L. Nguyen, A. Preston, M. Dickinson, A. T. T. Tran, M. Dickinson, and J. B. Metson, "Adhesion enhancement of titanium nitride coating on aluminum casting alloy by intrinsic microstructures," *Applied Surface Science*, vol. 377, pp. 174–179, 2016.

[15] H. Singh, K. C. Mutyala, H. Mohseni, T. W. Scharf, R. D. Evans, and G. L. Doll, "Tribological performance and coating characteristics of sputter-deposited Ti-doped MoS2in rolling and sliding contact," *Tribology Transactions*, vol. 58, no. 5, pp. 767–777, 2015.

[16] Y.-J. Kang, J.-H. Baeg, H. Park, and Y.-R. Cho, "Measurement of intrinsic hardness of deposited chromium thin films by nanoindentation method and influencing factors," *Korean Journal of Metals and Materials*, vol. 58, no. 3, pp. 207–215, 2020.

[17] D. Merche, N. Vandencasteele, and F. Reniers, "Atmospheric plasmas for thin film deposition: a critical review," *Thin Solid Films*, vol. 520, no. 13, pp. 4219–4236, 2012.

[18] E. Zalnezhad, A. A. D. Sarhan, and M. Hamdi, "A fuzzy logic based model to predict surface hardness of thin film TiN coating on aerospace AL7075-T6 alloy," *International Journal of Advanced Manufacturing Technology*, vol. 68, no. 1-4, pp. 415–423, 2013.

[19] JH. Jang, SH. Tak, Q. Zhang, Z. Xu, and S. Lyu, "Effect of the Ti-series coating on the friction and wear characteristics of SCM415 steel," *Tribology and Lubricants*, vol. 26, pp. 162–166, 2010.

[20] I. Gablech, V. Svatoš, O. Caha et al., "Preparation of (001) preferentially oriented titanium thin films by ion-beam sputtering deposition on thermal silicon dioxide," *Journal of Materials Science*, vol. 51, no. 7, pp. 3329–3336, 2016.

[21] E. Alfonso, J. Olaya, and G. Cubillos, "Thin film growth through sputtering technique and its applications," *Crystallization-Science and technology*, vol. 23, pp. 11-12, 2012.

[22] D. W. Hoffman, "Stress and property control in sputtered metal films without substrate bias," *Thin Solid Films*, vol. 107, no. 4, pp. 353–358, 1983.

[23] C. V. Thompson, "Grain growth in thin films," *Annual Review of Materials Science*, vol. 20, no. 1, pp. 245–268, 1990.

[24] N. Martin, D. Baretti, C. Rousselot, and J.-Y. Rauch, "The effect of bias power on some properties of titanium and titanium oxide films prepared by r.f. magnetron sputtering," *Surface and Coatings Technology*, vol. 107, no. 2-3, pp. 172–182, 1998.

[25] V. Chawla, R. Jayaganthan, A. K. Chawla, and R. Chandra, "Morphological study of magnetron sputtered Ti thin films on silicon substrate," *Materials Chemistry and Physics*, vol. 111, pp. 414–418, 2008.

[26] J. An, S. Im, H. kang, Y. Yoo, J. Noh, and S. Huh, "A study on the wear characteristics of Al7075 with changes in surface roughness and Ti thin film deposition time," *Advances in Materials Science and Engineering*, vol. 2020, Article ID 7934842, 9 pages, 2020.

[27] M. Fellah, M. Labaız, O. Assala, L. Dekhil, and A. Iost, "Tribological behavior of Ti-6Al-4V and Ti-6Al-7Nb alloys for total hip prosthesis," *Advances in Tribology*, vol. 2014, Article ID 451387, 13 pages, 2014.

[28] A. R. Govande, J. K. Katiyar, B. R. Sunil, and R. Dumpala, "Effect of heat treatment environment on the structural characteristics and microhardness of high velocity oxy-fuel sprayed tungsten carbide-cobalt coatings," *Materialwissenschaft und Werkstofftechnik*, vol. 52, pp. 1346–1354, 2021.

[29] IK. Oh, CM. Yoon, JW. Jang, and H. Kim, "Film properties of Al thin films depending on process parameters and film thickness grown by sputter," *Korean Journal of Materials Research*, vol. 26, pp. 438–443, 2016.

[30] Y. Jin, W. Wu, L. Li et al., "Effect of sputtering power on surface topography of dc magnetron sputtered Ti thin films observed by AFM," *Applied Surface Science*, vol. 255, pp. 4673–4679, 2009.

[31] J. V. Christy, R. Arunachalam, A. H. I. Mourad, P. K. Krishnan, S. Piya, and M. Al-Maharbi, "Processing, properties, and microstructure of recycled aluminum alloy composites produced through an optimized stir and squeeze casting processes," *Journal of Manufacturing Processes*, vol. 59, pp. 287–301, 2020.

[32] R. Thiraviam, V. Ravisankar, P. Kumar, R. Thanigaivelan, and R. Arunachalam, "A novel approach for the production and characterisation of aluminium–alumina hybrid metal matrix composites," *Materials Research Express*, vol. 7, no. No. 4, 2020.

[33] P. K. Krishnan, J. V. Christy, R. Arunachalam et al., "Production of aluminum alloy-based metal matrix composites using scrap aluminum alloy and waste materials: influence on microstructure and mechanical properties," *Journal of Alloys and Compounds*, vol. 784, pp. 1047–1061, 2019.

[34] M. Wittling, A. Bendavid, P. J. Martin, and M. V. Swain, "Influence of thickness and substrate on the hardness and deformation of TiN films," *Thin Solid Films*, vol. 270, pp. 270–283, 1995.